



**US Army Corps  
of Engineers®**  
Engineer Research and  
Development Center

## **Initial Research into the Effects of Woody Vegetation on Levees**

Volume III of IV: Numerical Model Simulation

Maureen K. Corcoran, John F. Peters, Joseph B. Dunbar, Jose L. Llopis, Fred T. Tracy, Johannes L. Wibowo, Janet E. Simms, Christopher E. Kees, S. Kyle McKay, J. Craig Fischenich, Matthew W. Farthing, M. Eileen Glynn, Bryant A. Robbins, Ryan C. Strange, Martin T. Schultz, Joan U. Clarke, Thomas E. Berry, Charles D. Little, and Landris T. Lee

July 2011



# Initial Research into the Effects of Woody Vegetation on Levees

Volume III of V: Numerical Model Simulation

Maureen K. Corcoran, John F. Peters, Joseph B. Dunbar,  
Jose L. Llopis, Johannes L. Wibowo, Janet E. Simms,  
M. Eileen Glynn, Bryant A. Robbins, Ryan C. Strange,  
and Landris T. Lee

*Geotechnical and Structures Laboratory  
U.S. Army Engineer Research and Development Center  
3909 Halls Ferry Road  
Vicksburg, MS 39180-6199*

Fred T. Tracy

*Information Technology Laboratory  
U.S. Army Engineer Research and Development Center  
3909 Halls Ferry Road  
Vicksburg, MS 39180-6199*

S. Kyle McKay, Martin T. Schultz, Thomas E. Berry,  
Joan U. Clarke, and J. Craig Fischenich

*Environmental Laboratory  
U.S. Army Engineer Research and Development Center  
3909 Halls Ferry Road  
Vicksburg, MS 39180-6199*

Christopher E. Kees, Matthew W. Farthing, and Charles D. Little

*Coastal and Hydraulics Laboratory  
U.S. Army Engineer Research and Development Center  
3909 Halls Ferry Road  
Vicksburg, MS 39180-6199*

Final report

## Executive Summary

At the request of Headquarters, USACE (HQUSACE), in July 2007, the U.S. Army Engineer Research and Development Center (ERDC) conducted an extensive literature review focusing on the effects of woody vegetation on levees. The review indicated that minimal data exist on the scientific relationship between levees and woody vegetation. Because of the lack of scientific data, HQUSACE concluded that without further research, scientific questions regarding the effects of woody vegetation on levees would remain unanswered. In April 2008, HQUSACE requested that ERDC begin research on this issue. ERDC formed a team consisting of scientists and engineers with geotechnical, environmental, geological, biological and geophysical expertise to assess the impact of woody vegetation on the structural performance of earthen levees using scientific and engineering methods.

The ERDC team prepared a scope of work (SOW) to study the effect of living woody vegetation on slope stability, seepage analyses were used to assess changes in hydraulic conductivity and the effects of the initiation of internal erosion. These particular topics were selected based on input from federal and state agencies, which showed that directing the research toward the effects of woody vegetation on slope stability and internal erosion would advance the understanding of the interaction of roots within an engineered levee. However, the selection of slope stability and seepage for this research does not diminish the need for future research on other topics related to the effects of woody vegetation on levees. Rather, this study should be viewed as an initial research effort into a very complex issue.

This study consists of the following three interrelated components:

1. Site visits, field data collection, and laboratory testing to obtain pertinent information necessary to support subsequent modeling and simulation efforts.
2. Modeling and simulation of the engineering, geological and environmental conditions, and structural performance of the levee system, relative to the initiation of internal erosion and slope stability, under various loading conditions.

3. Developing results and conclusions regarding engineering impacts living of woody vegetation on slope stability and internal erosion.

Site investigations identified root system characteristics using geophysical survey methods, root excavation methods, and root strength (pull-out) tests. Root studies focused on living, healthy woody vegetation. Data collected by these methods were used in the seepage and slope stability analyses. One of the major findings from field investigations was the relative efficacy of electrical resistivity imaging (ERI) measurements in determining the size and extent of tree root balls, relative to other geophysical methods, such as ground penetrating radar (GPR) or electromagnetic (EM) techniques. Root excavation proved successful for validating GPR in sandy soils.

In addition to identifying root characteristics, field studies included soil permeameter testing for the purpose of calculating hydraulic conductivity to test the hypothesis that tree roots influence soil hydraulic properties. Permeameter tests were performed within the root system and in a nearby control area without a tree but within the same soil horizon. Soil samples were retrieved during permeameter testing for soil classification. Statistical methods were used to calculate and compare the mean values of the two data sets: root system versus the control area. The resulting mean values were not used directly in the model simulations because the modeling was performed prior to the field data collection. However, for consistency the resulting means and ranges of calculated hydraulic conductivities were compared to those found in the site engineering documents as well as the values used for seepage models. The statistical comparison of means did not produce conclusive evidence that tree roots influence the average hydraulic conductivity of a soil layer. Only one test showed evidence of an existing macropore associated with a tree site. These analyses were conducted for Sacramento, CA; Burlington, WA; Portland, OR; Lewisville, TX; Vicksburg, MS; Albuquerque, NM; Boca Raton, FL, and Danville, PA.

Slope stability models and seepage models used both two-dimensional (2-D) and three-dimensional (3-D) finite element computer codes. The stability analysis uses limit equilibrium methods for 2-D analyses and deformational analyses in three dimensions. Seepage models included analysis for internal erosion.

The ERDC research used SEEP2D for three analysis in the seepage analyses. These analyses included conducting a sensitivity analysis for hydraulic

conductivity as it affects the groundwater flow field, producing a random macropore heterogeneity in a block of soil representing a root system, and representing a root as a defect extending from the surface to the base of the blanket. The extended root system was depicted as a uniform area of low hydraulic conductivity, which is an extreme representation that may not reflect actual field conditions. The results from these analyses are specific only to the levees studied for this research.

In the first approach, extensive 2-D sensitivity analyses were performed where the hydraulic conductivity of the woody vegetation zone was systematically varied from the surrounding soil by a factor of  $\beta$ , ranging from 1,000 to 0.001. When  $\beta$  is equal to 1.0, the analysis simulates a levee without woody vegetation. In these analyses, the woody vegetation (tree) zone was modeled as a continuum of porous media with dimensions 6 ft wide by 5 ft deep. Various hydraulic loadings were also applied in the sensitivity analyses using steady state and transient conditions.

Sensitivity analyses also investigated the influence of woody vegetation location on model output. Simulations included woody vegetation zones located at the levee toe, beyond the levee toe, levee slope, and levee crest on both the riverside and landside of the studied levees. Pore pressure and the phreatic surface from the seepage analysis were used in the slope stability model to determine effective stresses for strength computations. Two-dimensional analyses were conducted for Sacramento, CA; Burlington, WA; Portland, OR; and Albuquerque, NM.

The second seepage analysis recognized the heterogeneity of macropores within both a root system and surrounding soil matrix by randomly distributing hydraulic conductivity throughout the rectangular configuration representing a root system. Velocity vectors show that a random heterogeneous zone can have flow paths that support large flow velocities. However, research does not exist on whether high velocities result in the initiation of internal erosion.

The third approach in the seepage analysis considers the probability of a tree root creating a seepage exit thereby initiating internal erosion in the soil foundation. This analysis follows the procedure described by Schaefer et al. (2010). Results from this analysis are specific only to the levees studied for this research. Because of the complexity of processes related to seepage and piping and the lack of research supporting such processes, only

the initiation of processes leading to internal erosion is addressed in this research. Analyses were conducted for Burlington, WA, Portland, OR, and Albuquerque, NM. Based on these analyses, the probability of initiation of internal erosion is negligible from woody vegetation at the toe of the levee for the Burlington and Portland sites. The results for Albuquerque yielded a factor of safety slightly higher than 1.0 but the probability of internal erosion occurring is negligible to 0.25.

Two-dimensional stability analyses were conducted using the Spencer Limit Equilibrium Method available within the UTEXAS4 slope stability software. Fixed input parameters for the analysis were soil properties, levee geometry, and root properties. Root reinforcement properties were derived from field test data collected by ERDC for this research. Variable input parameters included: tree position on the levee slope, tree weight, pore pressure, phreatic surface, river elevation, wind load, and failure criteria. In a simplified slope stability analysis, effective stresses for strength is to use the phreatic surface from the seepage analysis, and rather than using the pore pressures computed in the finite element analysis, an assumption is made as to what the pore pressures are below the phreatic surface. However, in the ERDC study, an accurate method of using pore pressures, as computed from the seepage flow analysis, in the slope stability analysis is used. Tree weights and wind loads are divided by 6 based on the 6-ft width because only one foot-wide slice is considered. Because tree root growth is variable, even for a given species in the same region, the root extent used in the models was varied to accommodate the inconsistent patterns of root growth. In general, this study observed that trees on the upper part of the slope decreased the factor of safety because they add weight. Trees near the toe increased the factor of safety because of the reinforcing effects of the roots and the increased counterweight effect of the tree to slope movement. Trees at midslope had lesser effect on the factor of safety because they acted as a load, but not a counterweight, and the roots are too shallow to reach the failure zone within the midslope region.

The objectives of the 3-D seepage and stability analyses were to validate the results of the more simplified 2-D model simulation. The 2-D model geometry and material properties of the woody vegetation zone were imported into the 3-D model. These analyses were made for the Sacramento, CA, and Burlington, WA, sites. The 3-D model modified the geometry to include three woody vegetation zones located at the toe (landslide toe, Sacramento; riverside toe, Burlington) and positioned 20 ft

apart, thereby creating a 3-D version of the 2-D model simulating a row of trees. Only steady state simulations were considered. Local 3-D effects were observed in the flow field around the zones, but resulted change was not apparent to the global flow field, location of the seepage face, or pore pressure gradients. The lack of change is attributed to the particularly shallow depth of the zones relative to the deeper confining layers.

Trees and their root systems were found to have an effect on overall levee stability. Results indicated that a tree can increase or decrease the factor of safety with respect to slope stability depending on the location of the tree on the levee. Additionally, when wind speeds greater than 40 MPH are considered, the factor of safety decreases for all tree locations evaluated for this study (top of slope, midslope, and toe of slope). In this study, reductions in factor of safety reflect specific conditions and may not represent the worst case scenario at these sites. Because of the extreme variability in geology, tree species, climate, and soils, the impact of trees on levees must be analyzed on a case-by-case basis. However, this study does reveal that the tree weight, tree location, root system, and wind loads are all significant parameters that must be taken into account when evaluating the effect of a tree on slope stability for a particular site.

There are many other possible effects of woody vegetation on a levee that were not studied in this research. These are equally important in attempting to fully understand the impact of woody vegetation on levee integrity as those selected for the ERDC research. The possibility of dead or decaying root systems providing preferential flow paths for piping to occur is a topic that requires further study. In addition, the seepage analysis is limited to studying the onset of internal erosion through addressing the contributing factors. Additional research is needed outside the ERDC scope of work to fully evaluate the progression of piping. Until advances are made in this area, it is difficult to fully assess the impact of woody vegetation on the progression of piping.

Efforts reported in this research were focused on living, healthy woody vegetation. Results from numerical analyses were based on models from sandy or silty sand levees. Levees consisting of clay were not included in the ERDC numerical analyses. This research did not address performance of levee systems with the presence of dead, woody vegetation and decaying roots. Other areas of concern that lie outside the scope of work are the contribution, if any, of windthrow and animal burrows to seepage; the

impact of woody vegetation within a levee channel on the hydraulic conveyance of a river; biological impacts, such as the prevention of growth of protective grass cover beneath a tree; and the contribution of woody vegetation to scour and erosion. The effect of woody vegetation on levee inspection, maintenance, and accessibility to the levee for flood fighting were not considered in this study. To have a more complex understanding of potential impacts of woody vegetation on levees, further research in these areas is needed.

**DISCLAIMER:** The contents of this report are not to be used for advertising, publication, or promotional purposes. Citation of trade names does not constitute an official endorsement or approval of the use of such commercial products. All product names and trademarks cited are the property of their respective owners. The findings of this report are not to be construed as an official Department of the Army position unless so designated by other authorized documents.

**DESTROY THIS REPORT WHEN NO LONGER NEEDED. DO NOT RETURN IT TO THE ORIGINATOR.**

# Contents

<b>Executive Summary .....</b>	<b>ii</b>
<b>Figures and Tables.....</b>	<b>xii</b>
<b>Preface .....</b>	<b>xxv</b>
<b>Unit Conversion Factors.....</b>	<b>xxvi</b>
<b>Acknowledgements.....</b>	<b>xxvii</b>
<b>1 Numerical Modeling.....</b>	<b>1</b>
2-D seepage analyses.....	2
General procedure for SEEP2-D.....	4
Governing equations.....	4
Flow equation .....	4
Relative hydraulic conductivity and moisture content .....	6
Study locations.....	7
Changes in hydraulic conductivity.....	7
Sacramento, CA.....	8
Soil properties .....	13
Steady-state results for elevation 29 ft.....	13
No woody vegetation zone .....	13
Woody vegetation (single tree) zone beyond the toe of the levee.....	15
Woody vegetation zone on the toe of the levee.....	18
Woody vegetation zone midway on the steeper landside slope of the levee .....	21
Woody vegetation zone near the top of the landside of the levee .....	21
Woody vegetation zone at the river height on the riverside.....	21
Woody vegetation zone at the change in slope on the riverside .....	21
Woody vegetation zone near the end of the levee sand on the riverside.....	27
Steady-state results for elevation 26 ft.....	27
No woody vegetation zone .....	27
Woody vegetation zone on the toe of the levee.....	27
Woody vegetation zone midslope on the steeper landside slope of the levee .....	27
Woody vegetation zone at the river height on the riverside.....	29
Steady-state results for elevation 23 ft.....	29
No woody vegetation zone .....	29
Woody vegetation zone on the toe of the levee.....	29
Woody vegetation zone midway on the steeper landside slope of the levee .....	34
Woody vegetation zone at the river height on the riverside.....	34
Transient analysis .....	34
No woody vegetation zone .....	39
Woody vegetation (single tree) zone on the toe of the levee.....	41
Woody vegetation zone near the end of the levee on the riverside .....	44
Woody vegetation (single tree) zone with extended lateral root systems .....	44
Effect of a deep root system on the Pocket Levee, Sacramento, CA .....	51
Parameter study of the blanket thickness of the Pocket Levee .....	54

<i>Mesh refinement study for the Pocket Levee</i> .....	55
<i>Degradation of the slurry wall</i> .....	57
<i>Burlington, WA</i> .....	60
<i>First cross section</i> .....	60
<i>Description of the 2-D model</i> .....	60
<i>Soil properties</i> .....	61
<i>Steady-state results for woody vegetation zones</i> .....	62
<i>No woody vegetation</i> .....	62
<i>Woody vegetation zone beyond the toe of the levee</i> .....	63
<i>Woody vegetation zone on the toe of the levee</i> .....	66
<i>Woody vegetation zone nearly midslope to the top of the levee on the landside</i> .....	69
<i>Woody vegetation zone nearly midslope to the levee crown on the riverside</i> .....	69
<i>Woody vegetation zone near the heel on the riverside</i> .....	69
<i>Transient analysis</i> .....	73
<i>No woody vegetation zone</i> .....	73
<i>Woody vegetation zone on the toe of the levee</i> .....	74
<i>Woody vegetation zone nearly midslope to the levee crown on the riverside</i> .....	78
<i>Extended woody vegetation zone</i> .....	78
<i>Second cross section</i> .....	83
<i>Description of the 2-D model</i> .....	83
<i>Soil properties</i> .....	83
<i>No woody vegetation zone</i> .....	84
<i>Steady-state results for a single woody vegetation zone</i> .....	85
<i>Woody vegetation zone at the toe of the levee</i> .....	85
<i>Woody vegetation zone on the lower slope of the levee on the riverside</i> .....	85
<i>Transient simulation</i> .....	89
<i>No woody vegetation zone</i> .....	89
<i>Woody vegetation zone on the toe of the levee</i> .....	89
<i>Woody vegetation zone on the lower slope of the levee on the riverside</i> .....	89
<i>Third cross section</i> .....	94
<i>Description of the 2-D model</i> .....	94
<i>Soil properties</i> .....	94
<i>No woody vegetation zone</i> .....	96
<i>Woody vegetation zone just beyond the toe</i> .....	96
<i>Transient simulation</i> .....	97
<i>No woody vegetation</i> .....	97
<i>Woody vegetation zone beyond the toe of the levee</i> .....	97
<i>Albuquerque, NM</i> .....	103
<i>Description of the 2-D model</i> .....	103
<i>Soil properties</i> .....	104
<i>Steady-state results for woody vegetation zones at El. 4992 ft.</i> .....	104
<i>No woody vegetation zone</i> .....	104
<i>Woody vegetation zone near the toe of the levee</i> .....	104
<i>Woody vegetation zone at the bottom of the ditch</i> .....	108
<i>Steady-state results for El. 4989 ft for woody vegetation zones</i> .....	108
<i>No woody vegetation zone</i> .....	108
<i>Woody vegetation zone near the toe of the levee</i> .....	111
<i>Woody vegetation zone at the bottom of the ditch</i> .....	111
<i>Transient solution</i> .....	111
<i>No woody vegetation zone</i> .....	111
<i>Woody vegetation zone at the bottom of the ditch</i> .....	115
<i>Portland, OR</i> .....	116
<i>Description of the 2-D model</i> .....	116

<i>Soil properties</i> .....	117
<i>Steady-state results for woody vegetation zones</i> .....	118
<i>No woody vegetation zone</i> .....	118
<i>Woody vegetation zone beyond the lower toe of the levee</i> .....	119
<i>Woody vegetation zone just beyond the upper toe of the levee</i> .....	119
<i>Woody vegetation zone nearly midslope to the levee crown on the riverside</i> .....	123
<i>Woody vegetation zone at the river elevation on the riverside</i> .....	123
<i>Transient analysis</i> .....	123
<i>No woody vegetation zone</i> .....	127
<i>Woody vegetation zone beyond the lower toe of the levee</i> .....	127
<i>Woody vegetation zone at the river elevation on the riverside</i> .....	127
<i>Summary</i> .....	132
<i>Macropore heterogeneity</i> .....	134
<i>3-D seepage model</i> .....	139
<i>Simplified extended root</i> .....	139
<i>Random root zone</i> .....	142
<b>2 Defects Produced from Woody Vegetation .....</b>	<b>152</b>
<i>Background</i> .....	152
<i>Observation sites, Lake Providence, LA</i> .....	152
<i>Geologic history</i> .....	153
<i>Sand boils</i> .....	157
<i>2-D model of defects from woody vegetation at the toe of the levee</i> .....	157
<i>Background</i> .....	157
<i>Defect A – Root defect as a vertical column</i> .....	164
<i>Sacramento, CA</i> .....	164
<i>Burlington, WA</i> .....	166
<i>Portland, OR, and Albuquerque, NM</i> .....	167
<i>Defect B – Root defect as a non-vertical column</i> .....	167
<b>3 2-D Slope Stability Analysis.....</b>	<b>171</b>
<i>Root strength</i> .....	171
<i>Tree weight</i> .....	177
<i>Wind load</i> .....	180
<i>Procedure</i> .....	181
<i>Study locations for analyses</i> .....	185
<i>Sacramento, CA</i> .....	185
<i>Sensitivity analysis</i> .....	188
<i>Landside analysis</i> .....	189
<i>Riverside analysis</i> .....	193
<i>Sensitivity analysis of wind load</i> .....	201
<i>Burlington, WA</i> .....	203
<i>Albuquerque, NM</i> .....	215
<i>Vicksburg, MS</i> .....	219
<i>Introduction</i> .....	219
<i>Geologic setting</i> .....	224
<i>Laboratory soils data and hydraulic conductivity</i> .....	226
<i>Groundwater conditions</i> .....	226
<i>Danville, PA</i> .....	226

<i>Introduction</i> .....	226
<i>Geologic setting</i> .....	227
<i>Danville Borough levee assessment and results</i> .....	232
<i>Laboratory soils data and hydraulic conductivity</i> .....	233
<i>Groundwater conditions</i> .....	233
<i>Boca Raton, FL</i> .....	234
<i>Introduction</i> .....	234
<i>Geologic setting</i> .....	234
<i>Laboratory soils data and hydraulic conductivity</i> .....	234
<i>Groundwater conditions</i> .....	238
<b>4 3-D Numerical Modeling.....</b>	<b>239</b>
Model input.....	240
Conceptual models for seepage and slope stability .....	245
Sensitivity analysis .....	247
Complex root zone geometry .....	251
<i>Cutout domain seepage and stability</i> .....	266
Discussion .....	270
<i>Limitations</i> .....	272
<i>Conclusions</i> .....	272
<i>Future research</i> .....	272
<b>References.....</b>	<b>273</b>
<b>Appendix A: Glossary<sup>1</sup> .....</b>	<b>279</b>
<b>Appendix B: Mississippi River Stage Data.....</b>	<b>288</b>
<b>Appendix C: Review of VPlants Model.....</b>	<b>294</b>

# Figures and Tables

## Figures

Figure 1. Procedure used by ERDC for the seepage analysis.....	5
Figure 2. Plot of finite elements with pressure head given at the nodes, and the resulting phreatic surface.....	6
Figure 3. Boundary conditions used in SEEP2D, Pocket Levee, Sacramento, CA.....	9
Figure 4. Position of woody vegetation zones as approximated from ERDC geophysical surveys, Pocket Levee, Sacramento, CA.....	11
Figure 5. Pocket Levee cross section with material types.....	11
Figure 6. A section of the finite element mesh, Pocket Levee, Sacramento, CA. The total mesh contains 22,139 nodes and 42,868 triangular elements.....	12
Figure 7. Close-up of the SBC slurry wall of the Pocket Levee, Sacramento, CA.....	12
Figure 8. Phreatic surface computed for the Pocket Levee, Sacramento, CA, model.....	14
Figure 9. Total head (ft) contours with phreatic surface, Pocket Levee, Sacramento, CA.....	14
Figure 10. Velocity vectors with phreatic surface, Pocket Levee, Sacramento, CA.....	15
Figure 11. Total head (ft) contours, phreatic surface, and velocity vectors for El. 29 ft versus $\beta$ , Pocket Levee, Sacramento, CA.....	16
Figure 12. Selected nodes, Pocket Levee, Sacramento, CA.....	17
Figure 13. Total head (ft) contours, phreatic surface, and velocity vectors for El. 29 ft versus $\beta$ , Pocket Levee, Sacramento, CA.....	19
Figure 14. Selected nodes, Pocket Levee, Sacramento, CA.....	20
Figure 15. Total head (ft) contours and phreatic surface for El. 29 ft, Pocket Levee, Sacramento, CA.....	22
Figure 16. Selected nodes, Pocket Levee, Sacramento, CA.....	23
Figure 17. Total head (ft) contours and phreatic surface for El. 29 ft, Pocket Levee, Sacramento, CA.....	24
Figure 18. Total head (ft) contours and phreatic surface for El. 29 ft versus $\beta$ , Pocket Levee, Sacramento, CA.....	25
Figure 19. Total head (ft) contours and phreatic surface El. 29 ft versus $\beta$ , Pocket Levee, Sacramento, CA.....	26
Figure 20. Total head (ft) contours and phreatic surface for El. 29 ft versus $\beta$ , Pocket Levee, Sacramento, CA.....	28
Figure 21. Total head (ft) contours, velocity vectors, and phreatic surface for river El. 26 ft, Pocket Levee, Sacramento, CA.....	29
Figure 22. Total head (ft) contours, phreatic surface, and velocity vectors for El. 26 ft versus $\beta$ , Pocket Levee, Sacramento, CA.....	30
Figure 23. Selected nodes, Pocket Levee, Sacramento, CA.....	31
Figure 24. Total head (ft) contours and phreatic surface for El. 26 ft versus $\beta$ , Pocket Levee, Sacramento, CA.....	32

Figure 25. Total head (ft) contours and phreatic surface for El. 26 ft versus $\beta$ , Pocket Levee, Sacramento, CA.....	33
Figure 26. Total head (ft) contours, velocity vectors, and phreatic surface for the river El. 23 ft Pocket Levee, Sacramento, CA.....	34
Figure 27. Total head (ft) contours, phreatic surface, and velocity vectors for El. 23 ft versus $\beta$ , Pocket Levee, Sacramento, CA.....	35
Figure 28. Selected nodes, Pocket Levee, Sacramento, CA.....	36
Figure 29. Total head (ft) contours and phreatic surface for El. 23 ft versus $\beta$ , Pocket Levee, Sacramento, CA.....	37
Figure 30. Total head (ft) contours and phreatic surface for El. 23 ft versus $\beta$ , Pocket Levee, Sacramento, CA.....	38
Figure 31. Hydrograph of the 1986 Flood, Sacramento River, at River Mile (RM) 52. Pocket Levee, Sacramento, CA.....	39
Figure 32. Initial phreatic surface.....	40
Figure 33. Phreatic surface after 3 hr.....	40
Figure 34. Phreatic surface after 4 hr.....	40
Figure 35. Phreatic surface after 5 hr.....	40
Figure 36. Phreatic surface near the woody vegetation zone for the transient case versus $\beta$ , Pocket Levee, Sacramento, CA.....	42
Figure 37. Selected nodes, Pocket Levee, Sacramento, CA.....	43
Figure 38. Phreatic surface for $\beta = 1$ ( $k_{veg} = 1 k_{no-veg}$ ), Pocket Levee, Sacramento, CA.....	45
Figure 39. Phreatic surface for $\beta = 100$ ( $k_{veg} = 100 k_{no-veg}$ ), Pocket Levee, Sacramento, CA.....	46
Figure 40. Phreatic surface for $\beta = 0.01$ ( $k_{veg} = 0.01 k_{no-veg}$ ), Pocket Levee, Sacramento, CA.....	47
Figure 41. Woody vegetation zone with extended root system, Pocket Levee, Sacramento, CA.....	48
Figure 42. Total head contours, phreatic surface, and velocity vectors for $\beta = 1$ ( $k_{veg} = 1 k_{no-veg}$ ), Pocket Levee, Sacramento, CA.....	48
Figure 43. Total head contours, phreatic surface, and velocity vectors for $\beta = 100$ ( $k_{veg} = 100 k_{no-veg}$ ), Pocket Levee, Sacramento, CA.....	49
Figure 44. Total head contours, phreatic surface, and velocity vectors for $\beta = 0.01$ ( $k_{veg} = 0.01 k_{no-veg}$ ), Pocket Levee, Sacramento, CA.....	49
Figure 45. Selected nodes, Pocket Levee, Sacramento, CA.....	50
Figure 46. Woody vegetation zone with dimensions of 6 ft $\times$ 5 ft.....	52
Figure 47. Woody vegetation zone with dimensions of 6 ft $\times$ 10 ft.....	53
Figure 48. Selected nodes.....	54
Figure 49. Original mesh, Pocket Levee, Sacramento, CA.....	56
Figure 50. Slightly refined mesh, Pocket Levee, Sacramento, CA.....	57
Figure 51. Significantly refined mesh, Pocket Levee, Sacramento, CA.....	57
Figure 52. Zone representing degradation of the slurry wall.....	58
Figure 53. Original total head contours and phreatic surface.....	58
Figure 54. Total head contours and phreatic surface with the degradation zone as sand.....	59
Figure 55. Selected nodes.....	59

Figure 56. First cross section with material types and woody vegetation zones, Burlington, WA.....	61
Figure 57. Portion of the finite element mesh for the first cross section of the Burlington Levee. The total mesh contains 19,560 nodes and 37,688 triangular elements.....	61
Figure 58. Total head contours and phreatic surface, Burlington, WA.....	63
Figure 59. Velocity vectors showing the flow pattern, Burlington, WA.....	63
Figure 60. Total head (ft) contours, phreatic surface, and velocity vectors, Burlington, WA.....	64
Figure 61. Selected nodes, Burlington, WA.....	65
Figure 62. Total head (ft) contours, phreatic surface, and velocity vectors, Burlington, WA.....	67
Figure 63. Selected nodes, Burlington, WA.....	68
Figure 64. Total head (ft) contours and phreatic surface, Burlington, WA.....	70
Figure 65. Total head (ft) contours and phreatic surface, Burlington, WA.....	71
Figure 66. Total head (ft) contours and phreatic surface, Burlington, WA.....	72
Figure 67. Selected nodes, Burlington, WA.....	73
Figure 68. Hydrograph of the 1995 Flood, Burlington, WA.....	75
Figure 69. Initial position of the phreatic surface, Burlington, WA.....	75
Figure 70. Phreatic surface at the maximum flood stage, Burlington, WA.....	75
Figure 71. Phreatic surface for the transient case, Burlington, WA.....	76
Figure 72. Selected nodes, Burlington, WA.....	77
Figure 73. Phreatic surface for the transient case, Burlington, WA.....	79
Figure 74. Finite element mesh with woody vegetation zone and extended zone, Burlington, WA.....	80
Figure 75. Total head contours and phreatic surface for $\beta = 1$ ( $k_{veg} = k_{no-veg}$ ), Burlington, WA.....	80
Figure 76. Total head contours and phreatic surface for $\beta = 100$ ( $k_{veg} = 100 k_{no-veg}$ ), Burlington, WA.....	81
Figure 77. Total head contours and phreatic surface for $\beta = 0.01$ ( $k_{veg} = 0.01 k_{no-veg}$ ), Burlington, WA.....	81
Figure 78. Selected nodes, Burlington, WA.....	82
Figure 79. Second cross section with material types and woody vegetation zones, Burlington, WA.....	83
Figure 80. Portion of the finite element for the second cross section of the Burlington Levee. The total mesh consists of 20,280 nodes and 39,569 triangular elements.....	84
Figure 81. Total head contours and phreatic surface, Burlington, WA.....	85
Figure 82. Total head (ft) contours, phreatic surface, and velocity vectors, Burlington, WA.....	86
Figure 83. Selected nodes, Burlington, WA.....	87
Figure 84. Total head contours and phreatic surface, Burlington, WA.....	88
Figure 85. Initial conditions at El. 32 ft, Burlington, WA.....	90
Figure 86. Phreatic surface and total head contours for the transient case, Burlington, WA.....	90
Figure 87. Phreatic surface for transient flow, Burlington, WA.....	91
Figure 88. Selected nodes, Burlington, WA.....	92

Figure 89. Phreatic surface for different values of $\beta$ for the transient solution, Burlington, WA .....	93
Figure 90. Enlargement of the woody vegetation zone for $\beta = 0.01$ ( $K_{veg} = 0.01 K_{no-veg}$ ), Burlington, WA .....	94
Figure 91. Third cross section with material types and woody vegetation zone, Burlington, WA .....	95
Figure 92. Portion of finite element mesh for the third cross section of the Burlington Levee. The total mesh consists of 19,844 nodes and 38,690 triangular elements.....	95
Figure 93. Total head contours and phreatic surface, Burlington, WA .....	97
Figure 94. Total head (ft) contours, phreatic surface, and velocity vectors, Burlington, WA .....	98
Figure 95. Selected nodes, Burlington, WA .....	99
Figure 96. Initial condition of phreatic surface, Burlington, WA .....	100
Figure 97. Phreatic surface at the end of the simulation, Burlington, WA .....	100
Figure 98. Total head contours and phreatic surface for the transient case, Burlington, WA .....	101
Figure 99. Selected nodes, Burlington, WA .....	102
Figure 100. Cross section with material types and woody vegetation zones, Albuquerque, NM .....	103
Figure 101. A portion of the finite element mesh for the Albuquerque Levee. The total mesh contains 13,800 nodes 26,614 triangular elements.....	104
Figure 102. Total head (ft) contours and phreatic surface, Albuquerque, NM .....	105
Figure 103. Total head (ft) contours, phreatic surface, and velocity vectors, Albuquerque, NM .....	106
Figure 104. Selected nodes, Albuquerque, NM .....	107
Figure 105. Total head (ft) contours, phreatic surface, and velocity vectors, Albuquerque, NM .....	109
Figure 106. Selected nodes, Albuquerque, NM .....	110
Figure 107. Total head (ft) contours and phreatic surface, Albuquerque, NM .....	111
Figure 108. Total head (ft) contours and phreatic surface, Albuquerque, NM .....	112
Figure 109. Selected nodes, Albuquerque, NM .....	113
Figure 110. Hydrograph of the 1942 Flood, Albuquerque, NM .....	114
Figure 111. Initial position of the phreatic surface.....	114
Figure 112. Final position of the phreatic surface.....	114
Figure 113. Selected nodes, Albuquerque, NM .....	115
Figure 114. Cross section with material types and woody vegetation zones, Portland, OR .....	117
Figure 115. A section of the Portland Levee finite element mesh. The total mesh contains 12,802 nodes and 24,589 triangular elements.....	117
Figure 116. Total head contours and phreatic surface, Portland, OR.....	118
Figure 117. Total head (ft) contours, phreatic surface, and velocity vectors, Portland, OR .....	120
Figure 118. Selected nodes, Portland, OR .....	121
Figure 119. Total head (ft) contours, phreatic surface, and velocity vectors, Portland, OR.....	122
Figure 120. Selected nodes, Portland, OR .....	124
Figure 121. Total head (ft) contours and phreatic surface, Portland, OR.....	125

Figure 122. Total head (ft) contours and phreatic surface, Portland, OR .....	126
Figure 123. Hydrograph of the Columbia River, Portland, OR .....	128
Figure 124. Initial position of the phreatic surface, Portland, OR .....	128
Figure 125. Phreatic surface at the maximum flood stage, Portland, OR.....	128
Figure 126. Phreatic surface for the transient case, Portland, OR.....	129
Figure 127. Selected nodes, Portland, OR.....	130
Figure 128. Total head (ft) contours and phreatic surface, Portland, OR .....	131
Figure 129. Total head contours (red) and flow lines (blue) without the effect of a woody vegetation zone.....	135
Figure 130. Total head contours (red) and flow lines (blue) with the effect of a woody vegetation zone for the first set of random $\beta$ values.....	135
Figure 131. Total head contours (red) and flow lines (blue) with the effect of a woody vegetation zone for the second set of random $\beta$ values.....	136
Figure 132. Total head contours (red) and flow lines (blue) with the effect of a woody vegetation zone for the third set of random $\beta$ values.....	136
Figure 133. Velocity vectors for the first random example.....	137
Figure 134. Velocity vectors for the second random example.....	137
Figure 135. Velocity vectors for the third random example.....	138
Figure 136. An enlarged section of the 3-D mesh surface to show mesh details. There are 350,820 nodes and 627,616 prism elements in the entire 3-D mesh.....	140
Figure 137. An enlarged section of the 3-D mesh surface with a tree root defect .....	140
Figure 138. Total head contours on the surface of the mesh .....	141
Figure 139. Velocity vectors on the surface of the mesh.....	141
Figure 140. Total head isosurfaces.....	142
Figure 141. Surface of the mesh showing the 6-ft $\times$ 6-ft $\times$ 5-ft woody vegetation zone. There are 3,017,367 nodes and 5,836,072 prism elements in this mesh.....	143
Figure 142. Portion of the 3-D mesh for the 6-ft $\times$ 6-ft $\times$ 5-ft woody vegetation zone .....	143
Figure 143. Total head contours with no tree in the 6-ft $\times$ 6-ft $\times$ 5-ft woody vegetation zone.....	144
Figure 144. Isosurfaces for total head with no tree in the 6-ft $\times$ 6-ft $\times$ 5-ft woody vegetation zone.....	144
Figure 145. Vector plot of velocity with no tree in the 6-ft $\times$ 6-ft $\times$ 5-ft woody vegetation zone.....	145
Figure 146. First oblique view of total head contours for the 6-ft $\times$ 6-ft $\times$ 5-ft random hydraulic conductivity zone.....	145
Figure 147. Second oblique view of total head contours for the 6-ft $\times$ 6-ft $\times$ 5-ft random hydraulic conductivity zone .....	146
Figure 148. Front view of total head contours for the 6-ft $\times$ 6-ft $\times$ 5-ft random hydraulic conductivity zone at the beginning of the hydraulic conductivity zone ( $y = 32$ ft). ....	146
Figure 149. Oblique view of total head contours for the 6-ft $\times$ 6-ft $\times$ 5-ft random woody vegetation zone for a 0.5-ft slab starting in the middle of the zone ( $y = 35$ ft).....	147
Figure 150. Front view of total head contours for the 6-ft $\times$ 6-ft $\times$ 5-ft random hydraulic conductivity zone for a 0.5-ft slab starting in the middle of the hydraulic conductivity zone ( $y = 35$ ft).....	147

Figure 151. Isosurfaces for the 6-ft × 6-ft × 5-ft random hydraulic conductivity zone.....	148
Figure 152. Isosurfaces for the 0.5-ft slice in the middle ( $y = 35$ ft) of the 6-ft × 6-ft × 5-ft random hydraulic conductivity zone.....	148
Figure 153. Front view of isosurfaces for the 0.5-ft slice in the middle ( $y = 35$ ft) of the 6-ft × 6-ft × 5-ft random hydraulic conductivity zone.....	150
Figure 154. Oblique view of velocity vector plots for the 6-ft × 6-ft × 5-ft random hydraulic conductivity zone.....	150
Figure 155. Front view of velocity vector plots for the 6-ft × 6-ft × 5-ft random hydraulic conductivity zone.....	151
Figure 156. Location map of Lake Providence showing sand boils and cross sections (Fisk 1947).....	154
Figure 157. Sedimentary units and elevations for cross section A-A' (Fisk 1947).....	155
Figure 158. Sedimentary units and elevations for cross section B-B' (Fisk 1947).....	156
Figure 159. Lake Providence during high water levels in May 2009 (A, B, C, and E), and at low water levels in October 2010 (D and F).....	158
Figure 160. Active sand boils during high river stage of May 2009.....	159
Figure 161. Water flowing out of cypress roots during May 2009 flood stage.....	160
Figure 162. Crawfish burrow at Lake Providence; photo was taken during low water levels.....	161
Figure 163. Woody vegetation zone with root system.....	168
Figure 164. Finite elements selected to form a root system.....	169
Figure 165. Defect along the left edge shown by the red zone.....	170
Figure 166. Schematic diagram of initially vertical position of a root fiber during the shearing process (Wu 1976, after Gray and Leiser 1982).....	172
Figure 167. Initially inclined position of a root fiber during shear (after Gray and Leiser 1982).....	174
Figure 168. Shear stress [kilo-pound per square foot (KSF)] of sand reinforced with No. 2 reed fibers versus normal stress; one specimen reinforced using fiber in vertical direction and the other with random direction (Gray and Ohashi 1983).....	175
Figure 169. Relationship between weight and DBH for different heights of black oak tree.....	178
Figure 170. Relationship between weight and DBH for different heights of white oak tree.....	178
Figure 171. Relationship between weight and DBH for different heights of red oak tree.....	179
Figure 172. Relationship between weight and DBH for different heights of hickory tree.....	179
Figure 173. Procedure used by ERDC for the slope stability analysis.....	182
Figure 174. Conceptual diagram of tree and levee interaction in slope stability analysis.....	183
Figure 175. Three failure criteria used for calculating the factor of safety on the landside at the Pocket Levee, Sacramento, CA.....	186
Figure 176. Typical levee profile of the Pocket Levee area, Sacramento, CA.....	186
Figure 177. Tree 2 Failure Criterion 1 .....	188
Figure 178. The cottonwood tree in Portland, OR, used in the slope stability analyses for the Pocket Levee, Sacramento, CA.....	189
Figure 179. Tree positions and water levels used in the sensitivity analysis for the slope stability analyses, Pocket Levee, Sacramento, CA.....	190

Figure 180. Landside slope stability analysis with no tree, assuming Failure Criterion 2, El. 29 ft, Pocket Levee, Sacramento, CA. This analysis serves as a baseline comparison for failure criterion to different positions of a single tree. ....	191
Figure 181. Landside slope stability analysis with a single tree at the toe of the levee, assuming Failure Criteria 2, Pocket Levee, Sacramento, CA. ....	192
Figure 182. The factor of safety with a single tree at the toe of the levee, Failure Criterion 1, Pocket Levee, Sacramento, CA. ....	193
Figure 183. The factor of safety with a single tree at the toe of the levee, Failure Criteria 3, El. 29 ft, Pocket Levee, Sacramento, CA.....	194
Figure 184. Sensitivity analysis of the factor of safety for Failure Criterion 1 on the landside of the levee with no tree, and three different locations of a single tree. Three different flood elevations are used in the analysis for the Pocket Levee, Sacramento, CA.....	195
Figure 185. Sensitivity analysis of the factor of safety for Failure Criterion 2 on the landside of the levee with no tree, and three different locations of a single tree. Three different flood elevations are used in the analysis for the Pocket Levee, Sacramento, CA.....	196
Figure 186. Sensitivity analysis of the factor of safety for Failure Criterion 3 on the landside of the levee with no tree, and three different locations of a single tree. Three different flood elevations are used in the analysis for the Pocket Levee, Sacramento, CA.....	196
Figure 187. Riverside slope stability analysis with no tree, assuming Failure Criterion 2, Pocket Levee, Sacramento, CA. This analysis serves as a baseline comparison for additional analyses using different locations of a single tree.....	197
Figure 188. Riverside slope stability analysis with a single tree at the toe of the levee, assuming Failure Criterion 2, Pocket Levee, Sacramento, CA.....	197
Figure 189. Riverside slope stability analysis with a single tree at the toe of the levee, assuming Failure Criterion 1, Pocket Levee, Sacramento, CA.....	199
Figure 190. Riverside slope stability analysis with a single tree at the toe of the levee, assuming Failure Criterion 3, Pocket Levee, Sacramento, CA.....	199
Figure 191. Sensitivity analysis of the factor of safety for Failure Criterion 1 on the riverside of the levee with no tree, and three different locations of a single tree. Three different flood elevations are used in the analysis for the Pocket Levee, Sacramento, CA.....	200
Figure 192. Sensitivity analysis of the factor of safety for Failure Criterion 3 on the riverside of the levee with no tree, and three different locations of a single tree. Three different flood elevations are used in the analysis for the Pocket Levee, Sacramento, CA.....	200
Figure 193. Sensitivity analysis of the factor of safety for Failure Criterion 3 on the riverside of the levee with no tree, and three different locations of a single tree. Three different flood elevations are used in the analysis for the Pocket Levee, Sacramento, CA.....	201
Figure 194. Monthly maximum and average wind speed in Sacramento, CA.....	202
Figure 195. Sensitivity analysis of factor of safety of landside levee attributable to varying wind speed using no tree, and a single tree at three different locations on the levee. The analysis also uses three different flood elevations, and Failure Criterion 2.....	203
Figure 196. Typical section of the levee in Burlington, WA.....	204
Figure 197. Tree position and water elevation scenarios. ....	205
Figure 198. The Western cedar used in the Burlington Levee analysis.....	207
Figure 199. Tree representation in UTEXAS4, Burlington, WA.....	208
Figure 200. The locations of the failure criteria used in the slope stability analysis for Burlington, WA. ....	209

Figure 201. Typical failure circles used in the slope stability analyses for the Burlington Levee.....	210
Figure 202. Sensitivity analysis of the factor of safety for Failure Criterion 1 with no tree, and five different locations of a single tree.....	211
Figure 203. Sensitivity analysis of the factor of safety for Failure Criterion 2 with no tree, and five different locations of a single tree.....	211
Figure 204. Sensitivity analysis of the factor of safety for Failure Criterion 3 with no tree, and five different locations of a single tree.....	212
Figure 205. Tree 2 Failure Criterion 1.....	213
Figure 206. The variation in pore pressures between no tree, and a tree near the levee toe.....	214
Figure 207. Wind loading effects on the factor of safety.....	215
Figure 208. A typical section for a levee in Albuquerque, NM.....	216
Figure 209. The tree position at the toe drain used in the slope stability analysis for Albuquerque, NM.....	217
Figure 210. The results of the slope stability analysis for Albuquerque, NM.....	217
Figure 211. Typical failure circle for the Albuquerque Levee.....	218
Figure 212. Location of the Vicksburg study site. The study site is in a gravel pit south of Vicksburg in hills bordering the Mississippi River Alluvial Valley. These hills are composed of Tertiary Age sediments veneered by windblown silt (loess) derived from exposed fine-grained Mississippi River sediments from melting Pleistocene Age glaciers in the northern latitudes.....	219
Figure 213. Aerial view of the Vicksburg Site where an oak tree and pine tree were studied. The pine tree lies within an active sand and gravel operation. Geophysical surveys were performed at both sites. LiDAR surveys were performed only at the Oak site. Excavation of roots was performed at both tree sites. Hamer Creek is the local drainage and is a tributary to the Big Black River, which in turn drains into the Mississippi River.....	220
Figure 214. Closeup view of the oak tree where LiDAR and geophysical surveys were conducted.....	221
Figure 215. Top photo is view of pine tree at the Warren County gravel pit used to test ground-penetrating radar for mapping roots. Bottom photo shows the underlying sand and gravel foundation being mined for aggregate. The tree being studied is the farthest tree in the right side of photograph.....	222
Figure 216. Study area along the Susquehanna River at Danville, Pennsylvania. Closeup view in bottom of photo shows the levee centerline and the site studied at station 122 + 90. Note the trees growing at the edge of the vegetation-free zone (VFZ). .....	223
Figure 217. View of Danville levee looking southwest at station 122 + 90. Silver maple stumps along edge of the vegetation free zone were removed in 2009.....	228
Figure 218. Center line boring from Station 122 + 90, continued (Schnabel 2010).....	229
Figure 219. Study site at Boca Raton, FL, where a fig tree was evaluated. ....	235
Figure 220. View of fig trees studied at the Boca Raton, FL. Top photo is view looking south on the east side of the canal. This tree was tested for soil hydraulic conductivity using a permeameter. Bottom photo is view looking north and shows another fig tree adjacent to the wildlife refuge. Levee is to the right of photo. Both trees were measured with the Troxler for soil moisture and density. ....	236
Figure 221. View looking south of the levee system adjacent to the Arthur R. Marshall Loxahatchee National Wildlife Refuge. Top photo shows the canal on the protected side	

---

and marsh on the flood side. Pervious nature of the levee soils are reflected by seepage at the levee toe on the landside. Water level in the marsh was about 1 to 2 ft higher than the protected side. ....	237
Figure 222. Periodic domain and material layout for 3-D modeling with the woody vegetation zone (red) and separation zone (yellow), Pocket Levee, Sacramento, CA. ....	242
Figure 223. Mesh for the 10-ft half-period cell used as the computational domain, Pocket Levee, Sacramento, CA. ....	242
Figure 224. Levee domain (grey) and cutout domain (red)....	243
Figure 225. Poisson surface reconstruction of ERDC LiDAR scan, Vicksburg, MS. ....	244
Figure 226. Reconstructed surface mesh for root system from the ERDC LiDAR scan, Vicksburg, MS. ....	245
Figure 227. Soil-root zone for intermediate (Level 2) computational mesh.....	246
Figure 228. Soil-root zone for highest resolution (Level 3) computational mesh. ....	246
Figure 229. Periodic domain and material layout for 3-D root geometry (red) embedded in 5 ft clay blanket (light blue) at the toe of the Pocket Levee, Sacramento, CA.....	247
Figure 230. (Top) total head gradients for 2-D (red) and 3-D (blue) cases, $\beta = 0.001$ , (Bottom) location of slice in the 3-D domain, Pocket Levee, Sacramento, CA.....	249
Figure 231. Total head contours of 2-D (red) and 3-D (blue) cases, $\beta = 0.001$ , Pocket Levee, Sacramento, CA.....	250
Figure 232. Phreatic surface and flow lines for 2-D (red) and 3-D (blue) cases, $\beta = 0.001$ , Pocket Levee, Sacramento, CA. ....	250
Figure 233. Total head gradients in 2-D (red, top) and 3-D (blue, bottom) cases along the plane $y = 0$ , $\beta = 0.001$ , Pocket Levee, Sacramento, CA. ....	252
Figure 234. Total head gradients for 2-D (red) and 3-D (blue) cases, $\beta=1000.0$ , Pocket Levee, Sacramento, CA.....	253
Figure 235. Total head contours of 2-D (red) and 3-D (blue) cases, $\beta=1000.0$ , Pocket Levee, Sacramento, CA.....	253
Figure 236. Phreatic surface and flow lines for 2-D (red) and 3-D (blue) cases, $\beta=1000.0$ , Pocket Levee, Sacramento, CA. ....	254
Figure 237. Total head gradients for 2-D (red, top) and 3-D (blue, bottom) cases along the plane $y=0$ , $\beta=1000.0$ , Pocket Levee, Sacramento, CA. ....	255
Figure 238. Total head contours of 2-D (red) and 3-D (blue) cases, $\beta=0.1$ , Pocket Levee, Sacramento, CA. ....	256
Figure 239. Flow lines for 2-D (red) and 3-D (blue) test cases near the woody vegetation zone, $\beta=0.01$ , Levee Profile 1, Burlington, WA. ....	256
Figure 240. Total head contours near the woody vegetation zone, $\beta=0.01$ , Levee Profile 1, Burlington, WA. ....	257
Figure 241. Total head contours and flow lines for 2-D (red) and 3-D (blue) test cases, $\beta=10.0$ , Levee Profile 1, Burlington, WA. ....	257
Figure 242. Total head contours for 2-D (red) and 3-D (blue) cases near the woody vegetation zone, $\beta=10.0$ , Levee Profile 1, Burlington, WA. ....	258
Figure 243. Flow lines for 2-D (red) and 3-D (blue) cases near the woody vegetation zone, $\beta=10.0$ , Levee Profile 1, Burlington, WA. ....	258
Figure 244. Phreatic surface and flow lines for 2-D (red) and 3-D (blue) cases, $\beta=0.01$ , Levee Profile 1, Burlington, WA. ....	259

Figure 245. Intersection of the root system at the levee toe with the clay blanket, Pocket Levee, Sacramento, CA.....	259
Figure 246. Phreatic surface with total head contours and flow lines colored by pressure head gradient, $\beta=1$ , Pocket Levee, Sacramento, CA .....	260
Figure 247. Phreatic surface with total head contours and flow lines colored by pressure head gradient, $\beta=100$ , Pocket Levee, Sacramento, CA .....	260
Figure 248. Phreatic surface with total head contours and flow lines colored by pressure head gradient, $\beta = 0.01$ , Pocket Levee, Sacramento, CA.....	261
Figure 249. Close-up of soil-root region, $\beta = 1$ (unmodified case), Pocket Levee, Sacramento, CA.....	261
Figure 250. Close-up of soil-root zone, $\beta = 100$ , Pocket Levee, Sacramento, CA.....	262
Figure 251. Close-up of soil-root zone, $\beta = 0.01$ , Pocket Levee, Sacramento, CA.....	262
Figure 252. Root geometry with projected pressure head gradient, $\beta=0.01, 1$ , and $100$ , Level 2, Pocket Levee, Sacramento CA.....	263
Figure 253. Groundwater velocity field in (ft/day) around root zone, $\beta = 1$ (unmodified case), Pocket Levee, Sacramento, CA.....	263
Figure 254. Comparison of groundwater velocity field around soil-root zone for unmodified case (red) and $\beta = 0.01$ (green), Pocket Levee, Sacramento, CA.....	264
Figure 255. Groundwater velocity field in (ft/day) around root zone for $\beta = 100$ , Pocket Levee, Sacramento, CA.....	264
Figure 256. Average and maximum total head gradients at levee toe excluding vegetated region.....	265
Figure 257. Average and maximum total head gradients at levee toe.....	265
Figure 258. Average pressure at base of clay blanket beneath root zone. ....	265
Figure 259. Root system location at levee toe.....	267
Figure 260. Cutout domain contours (1-ft intervals) and flow lines.....	267
Figure 261. Total head contours and pressure head gradients in root zone. ....	268
Figure 262. Root zone flow lines and pressure head gradients.....	268
Figure 263. Close-up of root zone flow lines and pressure head gradients with large three-dimensional effects on the flow lines.....	269
Figure 264. Scaled deformation at failure (SRF=factor of safety=0.80) for the case $\Gamma=1$ . ....	269
Figure 265. Scaled displacements at failure (SRF=factor of safety=1.10) for $\Gamma=1000$ . ....	270
Figure 266. Scaled displacements at failure (SRF=factor of safety=0.90) for $\Gamma=1$ and $\beta=1$ . ....	271

## Tables

Table 1. Hydraulic conductivity values assigned to layer soils, Pocket Levee, Sacramento, CA. ....	13
Table 2. Moisture content and van Genuchten soil properties, Pocket Levee, Sacramento, CA (Baker et al. 2006). ....	13
Table 3. Magnitude of gradient at selected nodes for different values of $\beta$ for El. 29 ft.....	17
Table 4. Pore pressure (lb/ft <sup>2</sup> ) at selected nodes for different values of hydraulic conductivity for El. 29 ft, Pocket Levee, Sacramento, CA.....	17

Table 5. Magnitude of gradient at selected nodes for different values of hydraulic conductivity for El. 29 ft, Pocket Levee, Sacramento, CA.....	20
Table 6. Pore pressure (lb/ft <sup>2</sup> ) at selected nodes for different values of hydraulic conductivity for El. 29 ft, Pocket Levee, Sacramento, CA.....	20
Table 7. Magnitude of gradient at selected nodes for different values of hydraulic conductivity for El. 29 ft, Pocket Levee, Sacramento, CA.....	23
Table 8. Pore pressure (lb/ft <sup>2</sup> ) at selected nodes for different values of hydraulic conductivity for El. 29 ft, Pocket Levee, Sacramento, CA.....	23
Table 9. Magnitude of gradient at selected nodes for different values of hydraulic conductivity for El. 26 ft, Pocket Levee, Sacramento, CA.....	31
Table 10. Pore pressure (lb/ft <sup>2</sup> ) at selected nodes for different values of hydraulic conductivity for El. 26 ft, Pocket Levee, Sacramento, CA.....	31
Table 11. Magnitude of gradient at selected nodes for different values of hydraulic conductivity for El. 23 ft, Pocket Levee, Sacramento, CA.....	36
Table 12. Pore pressure (lb/ft <sup>2</sup> ) at selected nodes for different values of hydraulic conductivity for El. 23 ft, Pocket Levee, Sacramento, CA.....	36
Table 13. Magnitude of gradient at selected nodes for different values of hydraulic conductivity for transient case, Pocket Levee, Sacramento, CA.....	43
Table 14. Pore pressure (lb/ft <sup>2</sup> ) at selected nodes for different values of hydraulic conductivity for transient case, Pocket Levee, Sacramento, CA.....	43
Table 15. Magnitude of gradient at selected nodes for different values of hydraulic conductivity for the extended root case, Pocket Levee, Sacramento, CA.....	50
Table 16. Pore pressure (lb/ft <sup>2</sup> ) at selected nodes for different values of hydraulic conductivity for the extended root case, Pocket Levee, Sacramento, CA.....	50
Table 17. Magnitude of gradient at selected nodes for different values of $\beta$ for the 6 ft $\times$ 5 ft zone.....	52
Table 18. Pore pressure (lb/ft <sup>2</sup> ) at selected nodes for different values of $\beta$ for the 6 ft $\times$ 5 ft zone.....	52
Table 19. Magnitude of gradient at selected nodes for different values of $\beta$ for the 6 ft $\times$ 10 ft zone.....	53
Table 20. Pore pressure (lb/ft <sup>2</sup> ) at selected nodes for different values of $\beta$ for the 6 ft $\times$ 10 ft zone.....	53
Table 21. Magnitude of gradient at selected nodes for different values of $\beta$ and for different blanket thicknesses.....	55
Table 22. Magnitude of gradient at selected nodes for the different meshes.....	56
Table 23. Pore pressure at selected nodes for the different meshes.....	56
Table 24. Magnitude of gradient and pore pressure (lb/ft <sup>2</sup> ) at selected points for the degradation of the slurry wall case.....	60
Table 25. First Burlington Levee model hydraulic conductivities.....	62
Table 26. First Burlington Levee model moisture content and van Genuchten soil properties.....	62
Table 27. Magnitude of gradient at selected nodes for different values of $\beta$ .....	65
Table 28. Pore pressure (lb/ft <sup>2</sup> ) at selected nodes for different values of $\beta$ .....	65
Table 29. Magnitude of gradient at selected nodes for different values of $\beta$ .....	68
Table 30. Pore pressure (lb/ft <sup>2</sup> ) at selected nodes for different values of $\beta$ .....	68

Table 31. Magnitude of gradient at selected nodes for different values of $\beta$ .....	74
Table 32. Pore pressure (lb/ft <sup>2</sup> ) at selected nodes for different values of $\beta$ .....	74
Table 33. Magnitude of gradient at selected nodes for different values of $\beta$ .....	77
Table 34. Pore pressure (lb/ft <sup>2</sup> ) at selected nodes for different values of $\beta$ .....	77
Table 35. Magnitude of gradient at selected nodes for different values of $\beta$ .....	82
Table 36. Pore pressure (lb/ft <sup>2</sup> ) at selected nodes for different values of $\beta$ .....	82
Table 37. Second Burlington levee model hydraulic conductivities.....	84
Table 38. Second and third Burlington Levee model moisture content and van Genuchten soil properties.....	84
Table 39. Magnitude of gradient at selected nodes for different values of $\beta$ .....	87
Table 40. Pore pressure (lb/ft <sup>2</sup> ) at selected nodes for different values of $\beta$ .....	87
Table 41. Magnitude of gradient at selected nodes for different values of $\beta$ .....	92
Table 42. Pore pressure (lb/ft <sup>2</sup> ) at selected nodes for different values of $\beta$ .....	92
Table 43. Third Burlington Levee model hydraulic conductivities.....	96
Table 44. Magnitude of gradient at selected nodes for different values of $\beta$ .....	99
Table 45. Pore pressure (lb/ft <sup>2</sup> ) at selected nodes for different values of $\beta$ .....	99
Table 46. Magnitude of gradient at selected nodes for different values of $\beta$ .....	102
Table 47. Pore pressure (lb/ft <sup>2</sup> ) at selected nodes for different values of $\beta$ .....	102
Table 48. Albuquerque Levee model hydraulic conductivities.....	105
Table 49. Albuquerque Levee model moisture content and van Genuchten soil properties. ....	105
Table 50. Magnitude of gradient at selected nodes for different values of $\beta$ .....	107
Table 51. Pore pressure (lb/ft <sup>2</sup> ) at selected nodes for different values of $\beta$ .....	107
Table 52. Magnitude of gradient at selected nodes for different values of $\beta$ .....	110
Table 53. Pore pressure (lb/ft <sup>2</sup> ) at selected nodes for different values of $\beta$ .....	110
Table 54. Magnitude of gradient at selected nodes for different values of $\beta$ .....	113
Table 55. Pore pressure (lb/ft <sup>2</sup> ) at selected nodes for different values of $\beta$ .....	113
Table 56. Magnitude of gradient at selected nodes for different values of $\beta$ .....	116
Table 57. Pore pressure (lb/ft <sup>2</sup> ) at selected nodes for different values of $\beta$ .....	116
Table 58. Portland Levee model hydraulic conductivities.....	118
Table 59. Portland Levee model moisture content and van Genuchten soil properties.....	118
Table 60. Magnitude of gradient at selected nodes for different values of $\beta$ .....	121
Table 61. Pore pressure (lb/ft <sup>2</sup> ) at selected nodes for different values of $\beta$ .....	121
Table 62. Magnitude of gradient at selected nodes for different values of $\beta$ .....	124
Table 63. Pore pressure (lb/ft <sup>2</sup> ) at selected nodes for different values of $\beta$ .....	124
Table 64. Magnitude of gradient at selected nodes for different values of $\beta$ .....	130
Table 65. Pore pressure (lb/ft <sup>2</sup> ) at selected nodes for different values of $\beta$ .....	130
Table 66. Exit gradient at nodes for woody vegetation zones for each levee site using different values of $\beta$ .....	132
Table 67. Exit gradient from the levee toe to 8 in. from the toe.....	138
Table 68. Comparison of pore pressure at the bottom of the 5-ft blanket below the toe for both the 2-D and 3-D models.....	141

---

Table 69. Probability of a seepage exit through the confining layer versus calculated factor of safety against heave.....	163
Table 70. Probability of initiation of backward erosion in the foundation given a seepage exit is predicted.....	164
Table 71. Average vertical seepage gradient through the confining layer, factor of safety for this exit gradient, average horizontal seepage gradient in the foundation, and probability of initiation of erosion in the foundation for different blanket thicknesses and slurry wall options for the Pocket Levee.....	165
Table 72. Exit gradient and velocity at the toe and pore pressure at the bottom of the blanket below the toe for different thicknesses of the blanket .....	166
Table 73. Average vertical seepage gradient through the confining layer, factor of safety for this exit gradient, average horizontal seepage gradient in the foundation, and probability of initiation of erosion in the foundation for different cross sections of the Burlington levee.....	167
Table 74. Average vertical seepage gradient through the confining layer, factor of safety for this exit gradient, average horizontal seepage gradient in the foundation, and probability of initiation of erosion in the foundation for the Portland and Albuquerque levees.....	168
Table 75. Exit gradient and velocity at the toe and pore pressure at the bottom of the blanket below the toe for the root system model.....	169
Table 76. Additional shear strength caused by tree roots of different species (Norris and Greenwood 2006).....	176
Table 77. Summary of TGW of four species (Myers et al. 1976). ....	177
Table 78. Foundation material properties of the Pocket Levee, Sacramento, CA. ....	187
Table 79. Factor of Safety for the Pocket Levee (landside) with no tree, three different tree locations, and three different flood water levels. ....	194
Table 80. Factor of Safety for the Pocket Levee (riverside) with no tree, three different tree locations, and three different flood water levels. ....	201
Table 81. Factor of Safety for the Pocket Levee, Sacramento, CA, (landside) with three different tree locations, and flood water elevation at 29 ft with varying wind speeds. The crown area of the cottonwood is 2625 ft <sup>2</sup> . ....	203
Table 82. Burlington Levee material properties. ....	204
Table 83. Factor of Safety for the Burlington, WA, Levee (landside) with no tree, five different tree locations, and three different flood water levels.....	212
Table 84. Factor of Safety for Burlington, WA, Levee (riverside) with five different tree locations and three different flood water levels. ....	212
Table 85. Wind load results for downstream tree positions. The crown area of the cedar tree is 1828 ft <sup>2</sup> . ....	215
Table 86. Soil properties for the levee section in Figure 208, Albuquerque, NM. ....	216
Table 87. Stratum designation for the SEEPW analysis of the Danville Levee system Schnabel 2010). See Figure 218 for stratum designation of this boring. ....	231
Table 88. Stability sensitivity study to root system strength. ....	271

## Preface

This research of the effects of woody vegetation on the structural integrity of levees was sponsored by Headquarters, U.S. Army Corps of Engineers (HQUSACE).

This investigation was conducted during the period of October 2009 to September 2010. The project manager for the study was Dr. Maureen K. Corcoran, Engineer Research and Development Center (ERDC), Geotechnical and Structures Laboratory (GSL). Dr. John F. Peters, GSL, provided the technical oversight. The principal investigators for the research are Dr. Joseph B. Dunbar, M. Eileen Glynn, Jose L. Llopis, Dr. Janet E. Simms, and Dr. Johannes Wibowo, GSL; Dr. Christopher Kees, ERDC, Coastal and Hydraulics Laboratory; S. Kyle McKay and Dr. J. Craig Fischenich, ERDC, Environmental Laboratory; and Dr. Fred T. Tracy, ERDC, Information Technology Laboratory.

The research direction was provided by Dr. Michael K. Sharp, ERDC Technical Director for Water Resources Infrastructure (WRI), and Dr. Maureen K. Corcoran, Associate Technical Director for WRI. This publication was prepared under the general supervision of Dr. William P. Grogan, Deputy Director, GSL; and Dr. David W. Pittman, Director, GSL.

At the time of publication of this report, COL Kevin J. Wilson was Commander and Executive Director of ERDC, and Dr. Jeffery P. Holland was Director.

This volume is one of four volumes documenting research conducted by ERDC on the effects of woody vegetation on levees. The fifth volume includes a description of the agency technical review (ATR) process and the comments from the review. The research includes data collected and analyzed during this study, as well as those data previously collected by state and federal agencies and their contractors. Major components of this project included site selection, characterization, and analysis (including levee location, geometry, geology, and soils within and underlying the levee); field studies (including tree properties and identification), and estimation of root and root ball dimensions using electrical resistivity, electromagnetic induction, and ground-penetrating radar, as well as root excavation); and numerical simulation modeling (including sensitivity and deformation analysis).

## Unit Conversion Factors

Multiply	By	To Obtain
Feet	0.3048	meters
Inches	2.54	centimeters
Inches	0.0254	meters
miles (U.S. statute)	1,609.347	meters
Miles	1.61	kilometers

## Acknowledgements

The U.S. Army Engineer Research and Development Center (ERDC) would like to acknowledge and greatly thank the support of many individuals who contributed their time and resources to ensure the success of this research. The following engineers and scientists from the U.S. Army Corps of Engineers (USACE) Districts and Divisions were instrumental in providing input on field locations, local knowledge of woody vegetation, field support, and geotechnical reports: U.S. Army Engineer District, Albuquerque (SPA) – Ondrea C. Hummel, William J. Trujillo, Deborah A. Foley, Bruce A. Jordan, Kristopher T. Schafer, and Dwayne E. Lillard (retired); U.S. Army Engineer District, Sacramento (SPK) – Mary P. Perlea, Kevin Knuuti, Meegan G. Nagy, Michael D. Ramsbotham, Edward A. Ketchum, Pamlyn K. Hill, and Ben Gompers; U.S. Army Division, South Pacific Division (SPD) – Kenneth G. Harrington, and Lester Tong (retired); U.S. Army Engineer District, New Orleans (MVN) – Stephen F. Finnegan, and Michael L. Stout (Contractor); Mississippi Valley Division (MVD) – Ken Klaus; U.S. Army Engineer District, Portland (NWP) – Les D. Miller; U.S. Army Engineer District, Ft. Worth (SWF) – Anita Hill, Ramanuja C. Kannan, and Les Perrin (retired); U.S. Army Engineer District, Seattle (NWS) – Charles H. Ifft, Douglas T. Weber, and Catherine A. Desjardin; Northwestern Division (NWD) – Steven J. Fink ; and U.S. Army Engineer District, Jacksonville (SAJ) – Randy L. Rabb.

In addition to the principal investigators listed as authors of this report, the following people at ERDC and its contractors supported field efforts, literature searches, and data analyses and are gratefully acknowledged: Dr. Monte L. Pearson Raju V. Kala, Isaac J. Stephens, Clinton J. Forsha, and Jerry Ballard, ERDC, Geotechnical and Structures Laboratory; Jim A. Dolan, ERDC, Information Technology Laboratory (ITL); Daniel A. Leavell, Bowhead Science & Technology; Dr. David Biedenharn and Dr. Chester Watson, Biedenharn Group; Rae Gore and Chelsea Thomas, Bevilacqua Research Corporation; Lyndsey Freeney and Daniel Chausse, ERDC- Contractors; Pam Bailey, Bobby W. McComas, Tyler D. Tharp, Megan English, and Leah McMahon, ERDC, Environmental Laboratory.

Cheri T. Loden, InfoPro; Marilyn Holt and Karen Taylor, U.S. Army Corps of Engineers-Information Technology Laboratory, compiled and formatted

the report. Mark Hardenberg, (STEM International), Bill Mullen (Bowhead Science and Technology), and Pamela Harrion (ITL) edited the report.

Agencies and individuals outside of USACE were outstanding in their support of our research. The ERDC field activities could not have been completed without the assistance of the following people and organizations: Danville, PA - Tom Graham, Danville Bureau Secretary, Joe V. Bellini, AMEC and Scott Raschke, Schnabel Engineering; Albuquerque, NM – Jerry Lovato, Albuquerque Metropolitan Arroyo Flood Control Authority, Ray Gomez, Middle Rio Grande Conservation District, and Mark Stone and students, (University of New Mexico); Sacramento, CA – Richard E. Marshall (retired), California Central Valley Flood Control Association), Dr. Alison Berry, Shih-Ming Chung, and Jaylee Tuil, University of California (UC)-Davis, Roy Kroll, California Department of Water Resources, and River Partners; Jacksonville, FL – Steve Partney, South Florida Water Management District; Burlington, WA – Chuck Bennett, Skagit River Drainage District No. 12; Portland, OR – Dave Hendricks, Multnomah County Drainage District No. 1; and Vicksburg, MS – James Marble, Vicksburg Sand and Gravel.

The participation of Ben Gouldby, HR Wallingford, UK, and Dr. Kenneth Cumming, National Marine Fisheries Service, in the ERDC/California Science Team workshop is greatly appreciated. The expertise of John Greenwood, University at Nottingham-Trent, UK, on root pullout tests greatly increased our knowledge of the procedure and data analysis. Dr. Philip Soar, University of Portsmouth, UK, is acknowledged for his detailed review of a root system model. We appreciate the time Dr. Natasha Pollen-Bankhead and Dr. Andrew Simon, U.S. Department of Agriculture, Agricultural Research Service, National Sedimentation Laboratory, spent relating their experiences on permeameter tests. Loren Murray, URS Corporation, provided the Light Detection and Ranging (LiDAR) scans for the Pocket Levee in Sacramento, CA.

A special thanks to the California Science Team for the many discussions and their input concerning this research: George Sills, Sills Engineering; Dr. Leslie F. Harder, Jr., HDR Engineering, Inc.; Dr. F. Douglas Shields, Jr., Consulting Hydraulic Engineer; Keith Swanson, California Department of Water Resources; Laura Kaplan, Center for Collaborative Policy; Dr. Donald Gray, University of Michigan; Peter Buck and Mick Klasson, Sacramento Area Flood Control Agency; Dr. Alison Berry, UC-Davis; Dr. Chris Peterson,

University of Georgia; Roy Kroll and Mike Inamine, California Department of Water Resources; Dr. Jonathan Bray, University of California, Berkeley; Sujan Punyamurthula, Richard Millet, and Franz Campero, URS Corporation; and Steven Chainey, AECOM.

## 1 Numerical Modeling

In this study, numerical models were used to address conditions using a single, living tree that contribute to the initiation of internal erosion and affect the stability of a levee. The concept for the U.S. Army Engineer Research and Development Center (ERDC) research is to use two-dimensional (2-D) models to identify parameters, which may affect underseepage where a woody vegetation zone is present, and then further investigate these parameters in three-dimensional (3-D). Although more complicated, 3-D modeling of a root system will produce more detail. However, data gathered in the 2-D models are essential to quantify potential effects of the zone on a levee. The 2-D seepage model will also provide sensitivity analysis of input parameters that influence the model output.

There are issues concerning the interaction of a root system with the surrounding soil matrix that are not thoroughly addressed in the ERDC field studies because of time limitations and the complexity of these topics. These include field evidence to evaluate the contribution of roots to the development, connectivity, longevity, and distribution of macropores, which may serve as preferential flow paths; influence of roots on soil properties and soil heterogeneity; and additional field evaluation on accurate definition of roots through non-destructive techniques. Therefore, because of the range of variability and the lack of research in soils and root systems, the model output the ERDC research should be considered as site specific.

Noguchi et al. (1997) found that living roots impede flow, but that flow can be diverted around the perimeter of roots. Their work consisted of field investigations to observe water movement through soil profiles by using liquid white paint sprinkled on the surface after watering. After 24 hr, the study sites were excavated to record the stained flow patterns. In support of this field observation, Johnson and Lehmann (2006) conclude that infiltrating water is channeled along roots through preferential flow pathways that are formed by means of root action on bulk soil. They describe these root-derived preferential flow pathways as a result of localized compaction of soil by roots and the addition of the cementing action of substances exuded by roots to the adjacent soil. Angers and Caron (1998) note though that the exudation of this cementing agent may

contribute to stabilizing soil structure. Johnson and Lehmann further state that increased soil heterogeneity found around trees is a result of water and nutrient fluxes delivered to localized zones around the trunk of the tree, which is then channeled into and through the soil by preferential pathways. Because of this previous research, hydraulic conductivity of a root is not considered in the ERDC models, but rather the flow path coincidental to the roots is modeled.

The ERDC assessment was made using both 2-D seepage and slope stability codes to analyze levee cross sections described in Volume II, and to establish a relationship between factor of safety and flood level. To make a realistic assessment, the 3-D nature of the problem is also taken into account.

Another model of interest is VPlants (Virtual Plants), a model designed for vegetation root architecture. An evaluation directed by ERDC was conducted by Dr. Philip J. Soar at the University of Portsmouth, UK. Dr. Soar met with Dr. Fredric Danjon, the developer of VPlants, to discuss the possibility of using this model in the ERDC research. However, ERDC decided to incorporate root systems into traditional slope stability and seepage models. For research focused on specific root properties, VPlants is a valuable tool. The evaluation of VPlants is included in Appendix C.

Numerical model simulations for seepage were used to better understand the effects of woody vegetation on seepage, and are described by (1) changes in hydraulic conductivity, (2) macropore heterogeneity, and (3) defect in a levee blanket produced by a single root.

For critical conditions (i.e., those nearing failure), levee stability was reassessed with differing locations of trees. From these analyses, the cases in which stability was most affected by the woody vegetation were selected for 3-D simulations using a seepage-deformation model. Levee performance was gauged by its stability under flood conditions.

## **2-D seepage analyses**

The objectives of the 2-D seepage analyses are to provide a better understanding of the effect of woody vegetation on the flow field, identify if woody vegetation contributes to the initiation of piping, and compute pore pressures for the slope stability models. The 2-D model implemented in this research uses the finite element (FE) method in SEEP2D (Tracy

1983; Jones 1999) within the Department of Defense (DoD) Groundwater Modeling System (GMS). The DoD, in partnership with the Department of Energy (DOE), the U.S. Environmental Protection Agency (EPA), the U.S. Nuclear Regulatory Commission (NRC), and 20 academic partners, developed GMS. GMS is widely applied in addressing groundwater issues (Yang et al. 2009; Toto et al. 2009; Gurwin and Lubczynski 2005), and it is commercially available.

SEEP2D is designed by the ERDC to compute seepage on profile models, such as a levee cross section. The model is internationally known in the engineering community as a model for complicated seepage analysis of dams and levees (Baker 2003; Guardo and Rohrer 2000; Zee and Zee 2006). The SEEP2D model developer conducted the seepage analyses described in this report.

Pore pressures in the steady-state analysis are indicative of a “snapshot” during a specific river elevation and do not account for the process involved in producing these pressures. Because of this, a transient analysis is used to capture changes in the pore pressures from a fluctuating water level. Seepage and/or piping incidents were not provided with the hydrographs, so these occurrences are not used for model validation. Flood elevations and head differential were low for the Portland site because of a dam located upstream of the selected levee section. For all sites, the highest water levels recorded were used from hydrograph information provided by USACE district offices. Transient computations were performed by a transient version of SEEP2D, developed specifically for this study.

The following are assumptions based on methods inherent in SEEP2D:

- Seepage analyses are based on Darcy's Law and do not include turbulent flow.
- A soil layer is considered an incompressible medium in that the soil-water matrix does not volumetrically change size when pressure changes.
- Richards' equation is used to model flow.
- The van Genuchten equation is used to model relative hydraulic conductivity and moisture content in saturated soils.
- Hydraulic conductivity of a soil type remains constant inside each finite element that is assigned that particular soil.
- Only linear, triangular finite elements are allowed.

- Only one boundary condition was used on the landside. A specified total head equal to a water level at ground surface 2,000 ft downstream of the levee was placed on the vertical boundary of the finite element mesh at the landside.
- The phreatic surface is computed by nodes on the landside of the levee and is changed iteratively between pressure head = 0 and flow = 0.

### **General procedure for SEEP2-D**

Seepage analysis for the ERDC research uses three approaches:

(1) changes in hydraulic conductivity, (2) macropore heterogeneity, and (3) defect in a blanket of a levee. The general procedure for the 2-D model is applicable to all of the approaches and is shown in Figure 1. To generate a FE mesh, cross sections described in Volume II were placed into GMS using the Conceptual Model component. Soil properties used in the cross sections are described later in this volume.

The phreatic surface used in the seepage analysis is computed by SEEP2D as a boundary condition equivalent to the pressure head = zero contour (Figure 2). Using linear interpolation, the respective positions where pressure head is zero are computed along the boundaries of the finite elements. Lines are then used to connect the two intersection points of a given element to form the phreatic surface plot. This boundary is also used in the stability analysis discussed in Chapter 3 of this volume.

### **Governing equations**

#### *Flow equation*

SEEP2D is based on Darcian flow and incorporates Richards' equation to account for flow in an unsaturated soil. However, in soils with macropores, such as those produced by tree roots, turbulent flow may occur (Beven and Germann 1982). In the analyses for this study, infiltration and evapotranspiration are not considered. The version of this equation where the angle between the first principal hydraulic conductivity axis and the  $x$ -axis is zero is given by

$$\frac{\partial}{\partial x} \left( k_r k_H \frac{\partial \phi}{\partial x} \right) + \frac{\partial}{\partial y} \left( k_r k_V \frac{\partial \phi}{\partial y} \right) = \frac{\partial \theta}{\partial t} \quad (1)$$

where:

- $k_H$  = the saturated hydraulic conductivity in the horizontal direction
- $k_V$  = the saturated hydraulic conductivity in the vertical direction
- $k_r$  = the relative hydraulic conductivity
- $\phi$  = total head
- $\theta$  = moisture content
- $x$  = the horizontal coordinate
- $y$  = the vertical coordinate.

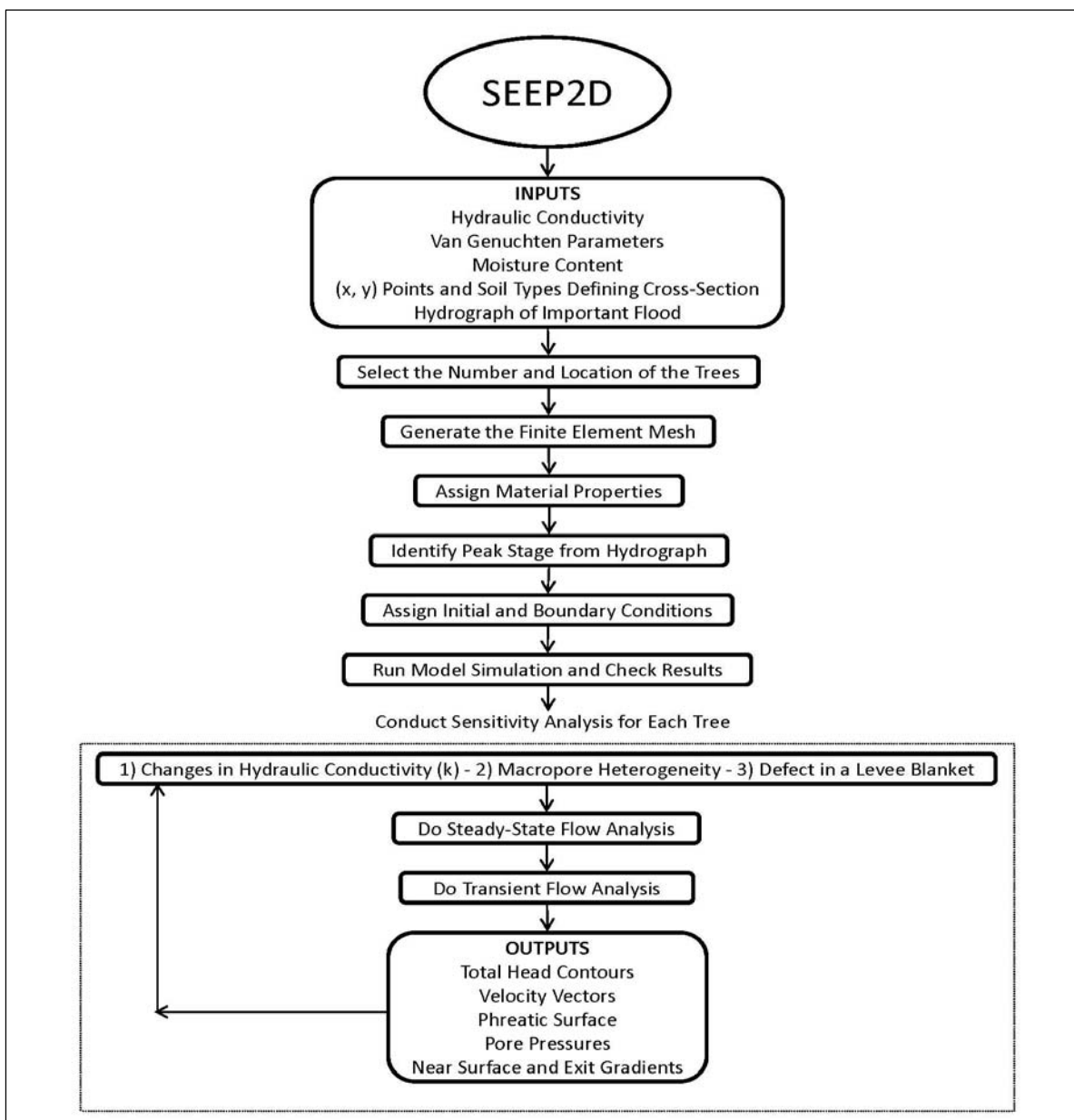


Figure 1. Procedure used by ERDC for the seepage analysis.

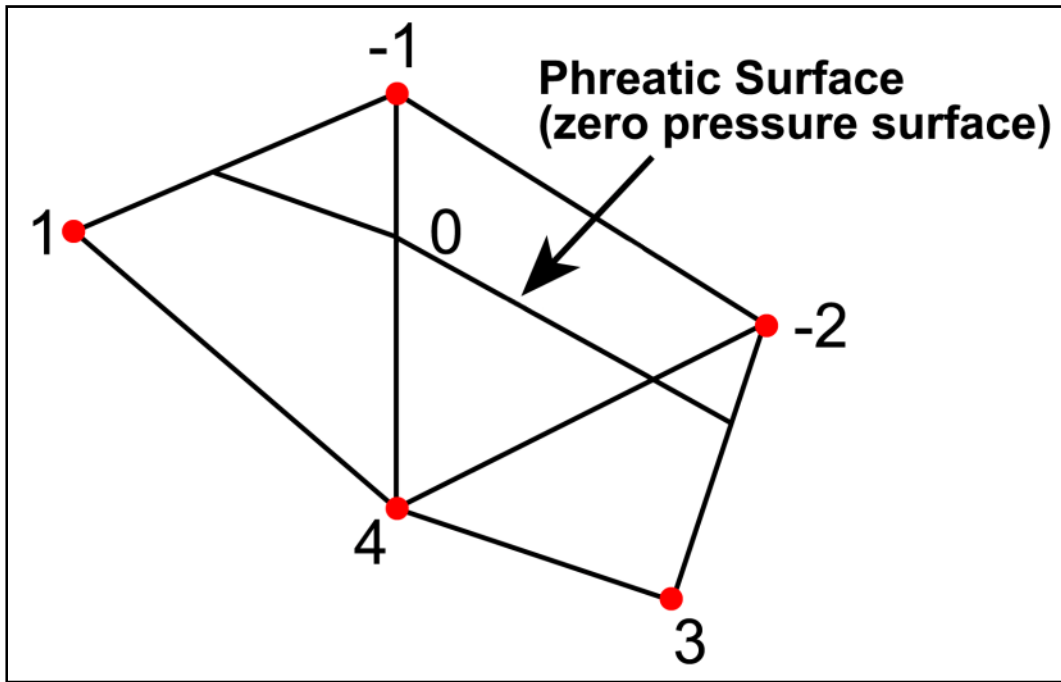


Figure 2. Plot of finite elements with pressure head given at the nodes, and the resulting phreatic surface.

As the soil becomes saturated and  $k_r$  approaches 1.0, Equation 1 reduces to the time-transient equation for saturation flow and is represented as,

$$\frac{\partial}{\partial x} \left( k_H \frac{\partial \phi}{\partial x} \right) + \frac{\partial}{\partial y} \left( k_V \frac{\partial \phi}{\partial y} \right) = S_s \frac{\partial \phi}{\partial t} \quad (2)$$

where:

$S_s$  = the specific storage (volume of water stored or released per unit volume of saturated soil per unit change in total head).

#### *Relative hydraulic conductivity and moisture content*

The van Genuchten equation (van Genuchten 1980) is used for modeling both relative hydraulic conductivity and moisture content. The equation is based on the Mualem (1976) model for predicting the relative hydraulic conductivity ( $k_r$ ) developed from knowledge of the soil-water retention curve. The SEEP2D model contains the van Genuchten equation. First,

$$S_e = [1 + \alpha(-h)^n]^{-m}, m = 1 - \frac{1}{n}, h \leq 0 \\ = 1, h \geq 0 \quad (3)$$

$$h = \varphi - y \quad (4)$$

where:

$h$  = pressure head

$a, n, m$  = material parameters based on experiments by van Genuchten (1980) unique to a specific soil type

$S_e$  = effective saturation

then,

$$\theta = \theta_r + (\theta_s - \theta_r) S_e \quad (5)$$

and

$$k_r = \sqrt{S_e} \left[ 1 - (1 - S_e^{1/m})^m \right]^2, \quad h \leq 0 \quad (6)$$

$$= 1, \quad h \geq 0$$

where:

$\theta_r$  = residual moisture content when the soil is very dry

$\theta_s$  = moisture content when the soil is saturated.

### Study locations

Seepage analyses for three approaches, (1) changes in hydraulic conductivity, (2) macropore heterogeneity, and (3) defect in a blanket of a levee, were conducted for Sacramento, CA; Burlington, WA; Albuquerque, NM; and Portland, OR. The following discussion is separated by site and approach, and described in the order listed above. The third approach is described in Chapter 2 because of the relationship between conditions observed at one of the sites selected to study for the ERDC research, and modeling a defect in a levee blanket. Labels for contour intervals and water levels are not included in all the figures in this section. The purpose of these figures is to convey the overall flow pattern.

### Changes in hydraulic conductivity

The first analysis concerns changes in hydraulic conductivity ( $k$ ). This analysis does not consider the average gradient under a levee, but rather

focuses on exit gradients. Additional analyses described in Chapter 2 computed the average gradient for addressing the probability for the initiation of erosion. A lower case  $k$  is used because it represents a scalar quantity as compared to a matrix quantity. In the numerical model, both horizontal and vertical components of hydraulic conductivity are used. A rectangular configuration, interpreted from geophysical surveys conducted for this study, as the possible extent of a root system from a single tree, is used in the model to depict an area of specific hydraulic conductivity. Geophysical surveys conducted for the ERDC research show high variability in soil around a tree at most study sites. In this report, the rectangular block is described as the woody vegetation zone. A single hydraulic conductivity value is assigned to this block and varied by orders of magnitude. This process is based on the possibility that root systems influence soil permeability, either by increasing or decreasing it, and is the same process followed by Schnabel (2010) to study the potential impact of a root mass system on steady state underseepage in Danville, PA.

However, with such soil variability, hydraulic conductivity may not be a consistent value, as shown in this analysis. An unknown is how the root system of a tree is affecting hydraulic conductivity and contributing to preferential flow. It is conceivable and very likely that other factors (i.e., decayed roots, roots from multiple trees, animal burrows, and/or worm holes) also contribute to modifying the soil permeability by producing a network of macropores. This analysis on hydraulic conductivity reveals the influence of these changes on pore pressure and, therefore, on slope stability. Because of time limitations to conduct this research, only pore pressures for the seepage model results for  $\beta = 100$  were used in the slope stability analysis. This value is considered as what might be a critical condition in the slope stability analysis.

The initial model for each site was based on a hydrograph representative of the site. River elevation was increased according to the hydrograph from low stage to flood stage, and an evaluation was performed at selected stages. An important load case was to extend the landside portion of the computational domain 2,000 ft, and then apply the river elevation at ground surface.

Sacramento, CA

Boundary conditions used in the Pocket Levee model are applied at the nodes of the mesh, and consist of three types: head boundary, impervious

(bottom) boundary, and exit face. The beginning of the exit face, referred to as the exit point, is calculated iteratively in the solution process. The head boundary condition, the total specified head in Figure 3, is a boundary where the head is known, such as an elevation of a river. This boundary condition represents locations where flow enters or exits a system. The total head boundary condition on the riverside used in the Pocket Levee is the elevation of the Sacramento River arbitrarily selected at 3-ft intervals (i.e., 23 ft, 26 ft, and 29 ft). The flood stage is 26 ft. The landside elevation for the Pocket Levee is always set at 12 ft.

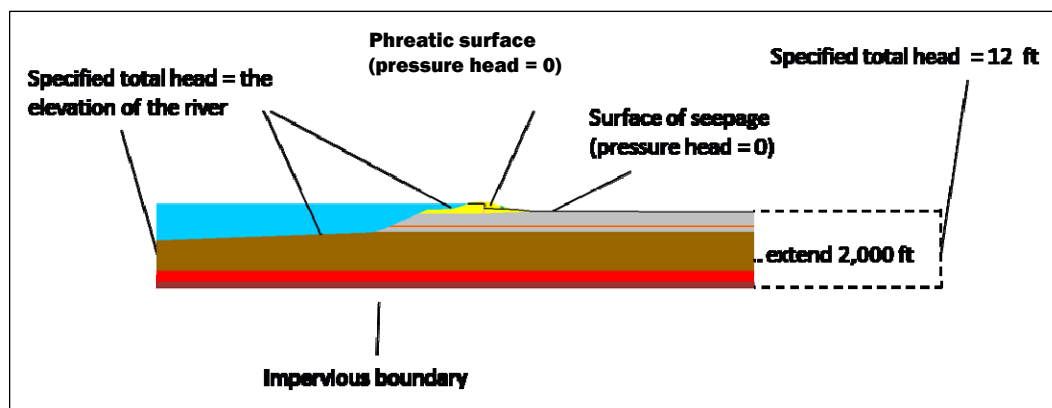


Figure 3. Boundary conditions used in SEEP2D, Pocket Levee, Sacramento, CA.

The exit face boundary condition, identified as surface of seepage in Figure 3, is where the pressure head is equal to the elevation, assuming that the datum is zero. The exit face is not known at the beginning of a solution (i.e., where the phreatic surface hits the downstream face), so the program must iterate to a solution. The boundary condition above the exit point is impervious because the soil is unsaturated, and thus “thirsty,” so no water can exit this part of the downstream boundary.

Boundary conditions are as follows:

Impervious boundary – defines the bottom boundary

- Riverside – (1) nodes below or at the river elevation have a total head = river elevation.  
 (2) nodes above the river elevation are treated as impervious.

- Landside – (1) the phreatic surface hits the landside at the exit point (pressure head = 0).  
 (2) nodes above the exit point are considered impervious.

- (3) nodes below the exit point and above the landside water elevation are on the surface of seepage. These nodes are set to pressure head = 0.
- (4) nodes on or below the landside water elevation (12 ft) (vertical line segment) have a total head applied of 12 ft.

The purpose of the analysis is to determine changes in the hydraulic conductivity of the assumed woody vegetation zone. Data collected from the geophysical surveys, described in Chapter 4 of Volume II of this series, show the root ball of a tree under observation to be approximately 6 ft × 5 ft. Because of time limitations on this research, field data collection and model analyses were conducted simultaneously; therefore, these are the dimensions of each woody vegetation zone used in all of the model analyses. In the model, a woody vegetation zone is defined as the portion of the mesh where the hydraulic conductivity ( $k$ ) for this zone is modified by the multiplier  $\beta$  in Equation 1:

$$k_{veg} = \beta k_{no-veg} \quad (7)$$

where:

$k_{no-veg}$  = hydraulic conductivity of the zone without woody vegetation

$k_{veg}$  = hydraulic conductivity of the zone with woody vegetation

$\beta$  = a parameter set to various values (e.g., 0.001, 0.01, 0.1, 0.5, 1, 2, 10, 100).

Increasing the hydraulic conductivity implies that the soil in the woody vegetation zone is more pervious due to the soil being unconsolidated, or preferred paths being developed in the root system. Conversely, decreasing the hydraulic conductivity means that the roots are an impediment to flow, and thus the soil is less pervious than without the roots. A parametric study was performed for each position of the woody vegetation zone shown in Figure 4, by varying the value of  $\beta$ , so that it is greater than the woody vegetation-free zone, and also less than the woody vegetation-free zone.

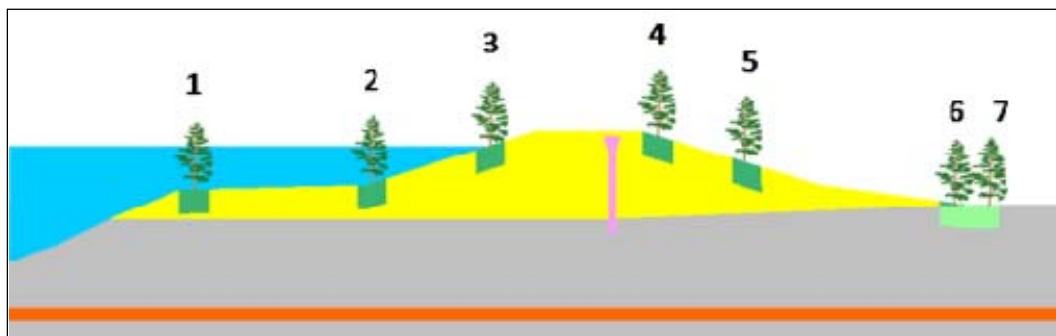


Figure 4. Position of woody vegetation zones as approximated from ERDC geophysical surveys, Pocket Levee, Sacramento, CA.

Figure 4 shows examples of woody vegetation zones (always shown in green) at different locations along the levee for the Pocket Levee cross section. The locations of the woody vegetation trees do not necessarily correspond to specific locations studied at this site. Rather, these are where roots could have engineering significance to the performance of the levee.

As discussed in Volume II of this series, the cross section (Figure 5) used in this analysis was generated from field data collected by ERDC, in addition to boring logs and soil properties from previous geotechnical analyses.

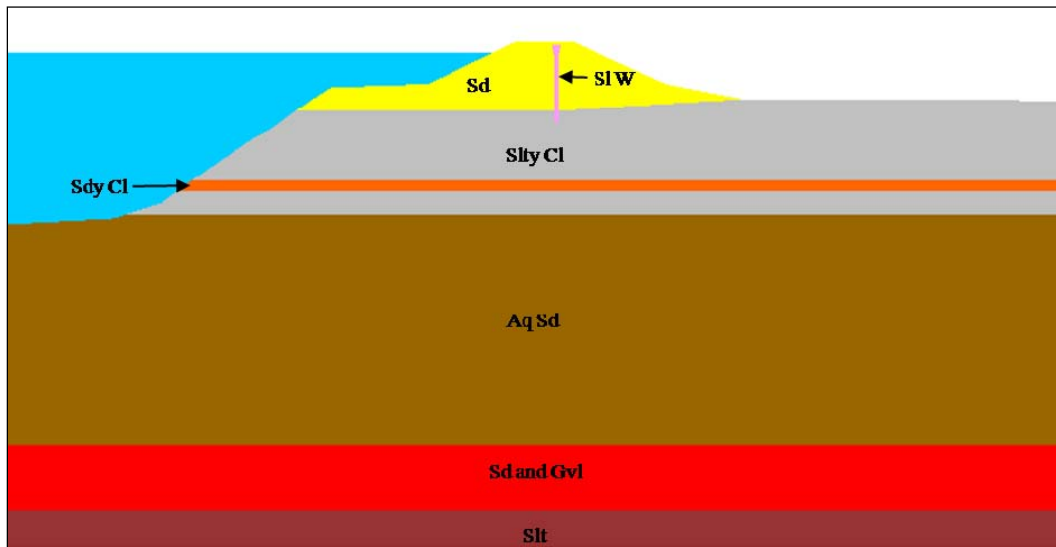


Figure 5. Pocket Levee cross section with material types.

Figure 6 shows a portion of the FE mesh generated for the analysis. A soilbentonite-cement (SBC) slurry wall was constructed on the Pocket Levee to reduce through-seepage. Figure 7 is a close-up of the SBC slurry wall.

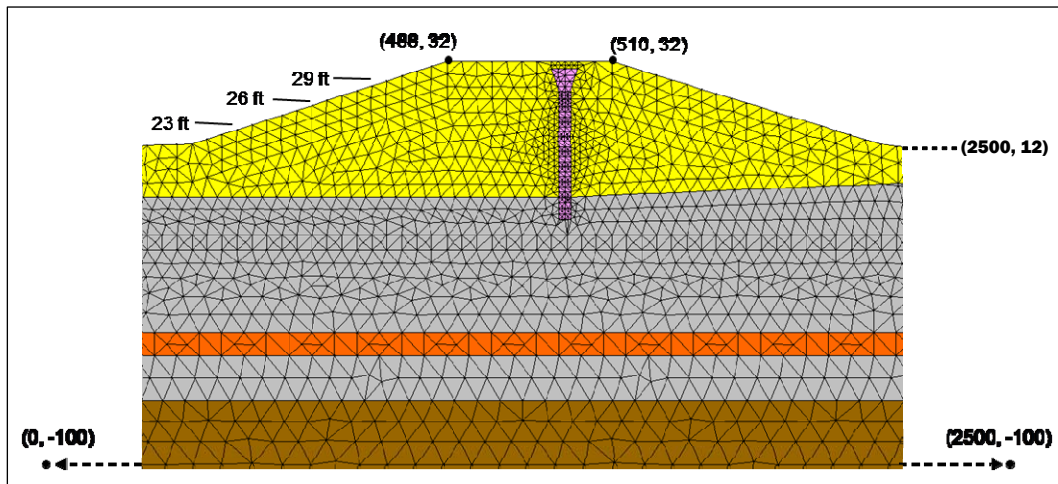


Figure 6. A section of the finite element mesh, Pocket Levee, Sacramento, CA.  
The total mesh contains 22,139 nodes and 42,868 triangular elements.

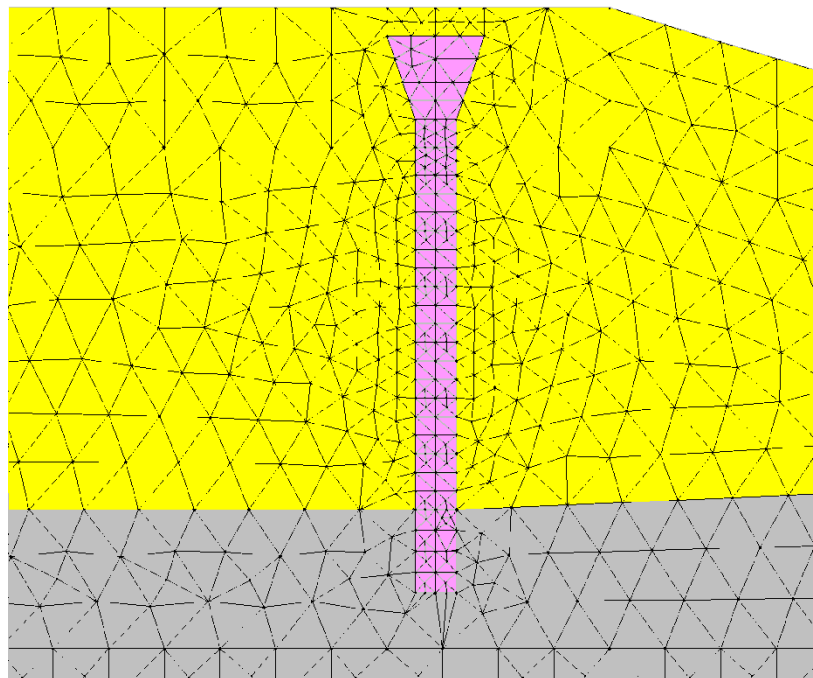


Figure 7. Close-up of the SBC slurry wall  
of the Pocket Levee, Sacramento, CA.

This site has sandy levee embankment with a SBC wall through the levee embankment. The levee is founded on a 30-ft-thick deposit of silty clay underlain by a 25-ft-thick layer of aquifer sand. A steady-state seepage analysis (USACE 2005a) indicates that underseepage exit gradients are acceptable for flood loadings up to 28.55 ft. The threat of failure from underseepage (piping) appears to be low. Through-seepage (due to the slurry wall) and underseepage (due to the thick confining layer) are not a likely concern for this levee. Because of the engineering of this levee, the

blanket thickness was reduced in subsequent analyses after the initial model to reflect a levee that is not as stable as the Pocket Levee at this particular location.

#### *Soil properties*

Soil properties used for the Pocket Levee model are given in Table 1. Table 2 provides the saturated hydraulic conductivities for the soil layers, moisture content, and van Genuchten parameters.

**Table 1. Hydraulic conductivity values assigned to layer soils, Pocket Levee, Sacramento, CA.**

Material	$k_H$ (cm/sec)	$k_H$ (ft/day)	$k_v$ (cm/sec)	$k_v$ (ft/day)
Levee sand (Sd)	$8.00 \times 10^{-3}$	22.7	$2.00 \times 10^{-3}$	5.67
Clay silty clay (Sly Cl)	$8.00 \times 10^{-4}$	2.27	$2.00 \times 10^{-4}$	0.567
Clay mixed with sand (Sdy Cl)	$3.00 \times 10^{-5}$	0.085	$1.00 \times 10^{-5}$	0.0283
Aquifer sand (Aq Sd)	$8.00 \times 10^{-2}$	227.0	$2.00 \times 10^{-2}$	56.7
Gravel (Gvl)	$2.00 \times 10^{-2}$	56.7	$2.00 \times 10^{-2}$	56.7
Silt (Slt)	$1.00 \times 10^{-4}$	0.283	$1.00 \times 10^{-4}$	0.283
SBC slurry wall (SIW)	$1.00 \times 10^{-6}$	0.00283	$1.00 \times 10^{-6}$	0.00283

**Table 2. Moisture content and van Genuchten soil properties, Pocket Levee, Sacramento, CA (Baker et al. 2006).**

Material	$\theta_r$	$\theta_s$	$\alpha$ (1/m)	$\alpha$ (1/ft)	$n$
Levee sand (Sd)	0.057	0.410	12.4	3.78	2.28
Clay silty clay (Sly Cl)	0.089	0.43	1.00	0.305	1.23
Clay mixed with sand (Sdy Cl)	0.100	0.390	5.90	1.80	1.48
Aquifer sand (Aq Sd)	0.045	0.430	14.5	4.42	2.68
Gravel (Gvl)	0.045	0.430	14.5	4.42	2.68
Silt (Slt)	0.034	0.460	1.60	0.488	1.37
SBC slurry wall (SIW)	0.068	0.380	0.80	0.244	1.09

Steady-state results for elevation 29 ft

#### **No woody vegetation zone**

The model was first run without a woody vegetation zone to provide a baseline comparison with the model runs where a zone is present. As previously discussed, this zone is defined as a rectangular block in the

model, which is assigned a hydraulic conductivity value. In this case, the hydraulic conductivity of the zone is equal to the surrounding soil matrix, as indicated by  $\beta = 1$ . This baseline model is represented by bold numbers in the tables of this chapter for ease of comparison. The phreatic surface computed in SEEP2D without zone is shown in Figure 8. Figure 9 is a subset of the total head contours used in the model. The numbers are the total heads represented by the associated contour lines, and are used in calculating the total head loss. For this case, the total head contours range from a maximum of 29 ft (river elevation) to a minimum of 12 ft (landslide elevation). Using these elevations as an example, the total head drop between 29 ft and 12 ft would be 17 ft. Figure 10 shows velocity direction vectors. The length of the vectors does not indicate velocity magnitude but rather direction, and should not be used to imply that there is significant flow in the unsaturated zone.

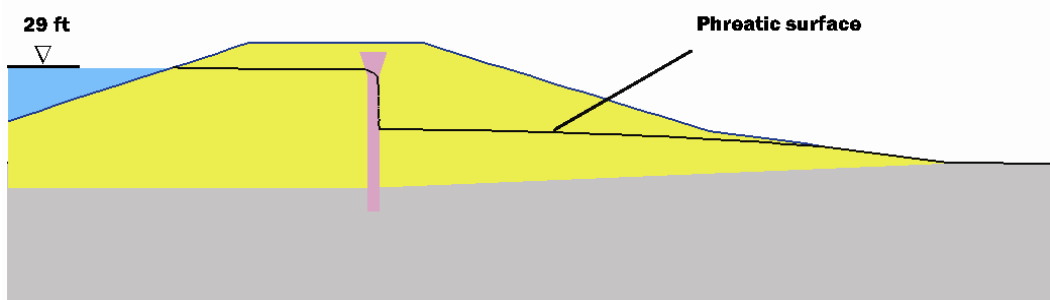


Figure 8. Phreatic surface computed for the Pocket Levee, Sacramento, CA, model.

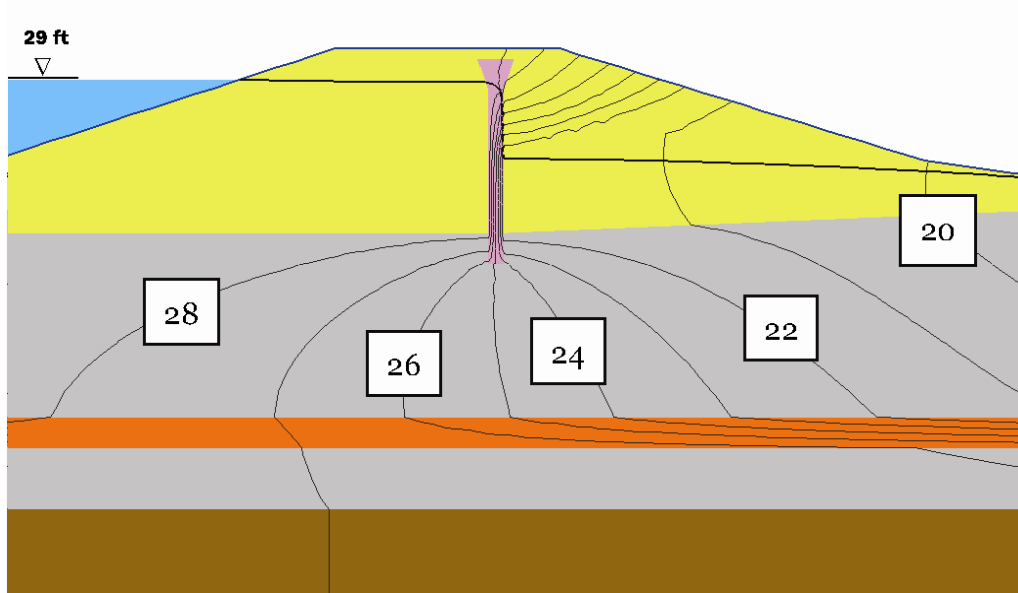


Figure 9. Total head (ft) contours with phreatic surface, Pocket Levee, Sacramento, CA.

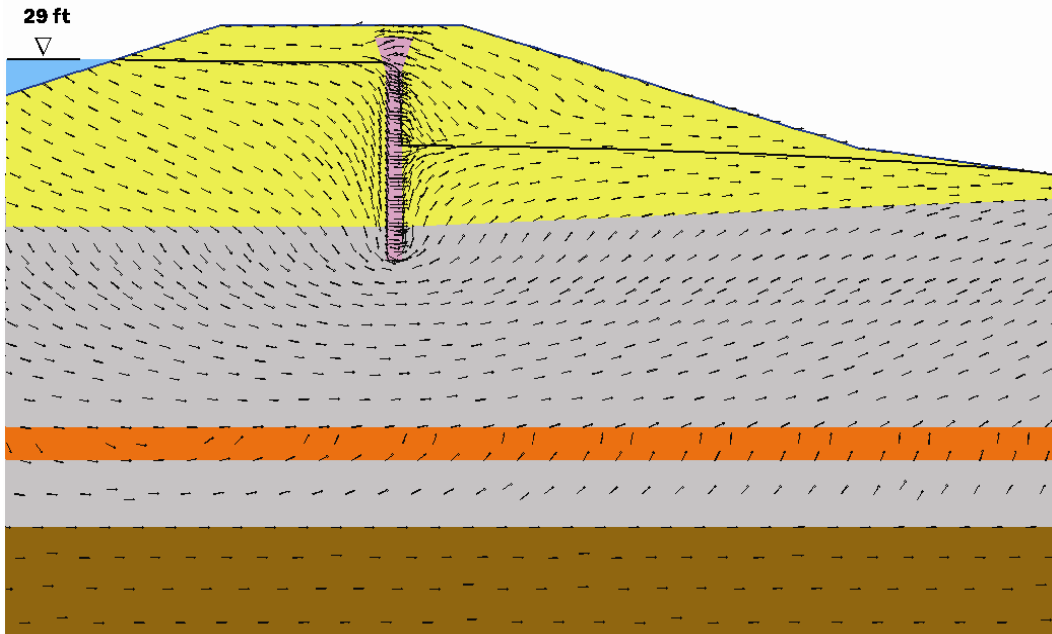


Figure 10. Velocity vectors with phreatic surface, Pocket Levee, Sacramento, CA.

### ***Woody vegetation (single tree) zone beyond the toe of the levee***

This case is represented by the seventh zone in Figure 4, and is within 15 ft of the toe of the levee. Figure 11 shows the mesh near the woody vegetation zone along with total head contours and velocity vectors for various values of hydraulic conductivity, as given in Equation 7. Nodes within the zone and also outside the zone were selected, as shown in Figure 12, for tabulating the magnitude of gradient (Table 3) and pore pressure (Table 4). Gradient is a vector quantity, and has an  $x$ -component and a  $y$ -component in two dimensions. The magnitude of any vector in two dimensions, and thus the gradient, is the square root of the sum of the squares of the  $x$ -component and  $y$ -component.

The research included only an individual tree in the analyses and did not consider the impact of multiple trees at one location. A variety of conditions were modeled that reflect both the waterside and landside conditions. Critical locations are different, depending on the circumstances (i.e., geology, levee geometry, blanket thickness, and mode of failure) at each site. The critical condition of a zone at the landside toe with a thin blanket and high water conditions were not stated, but the impact of the zone along the levee profile was evaluated for any impact to the critical location.

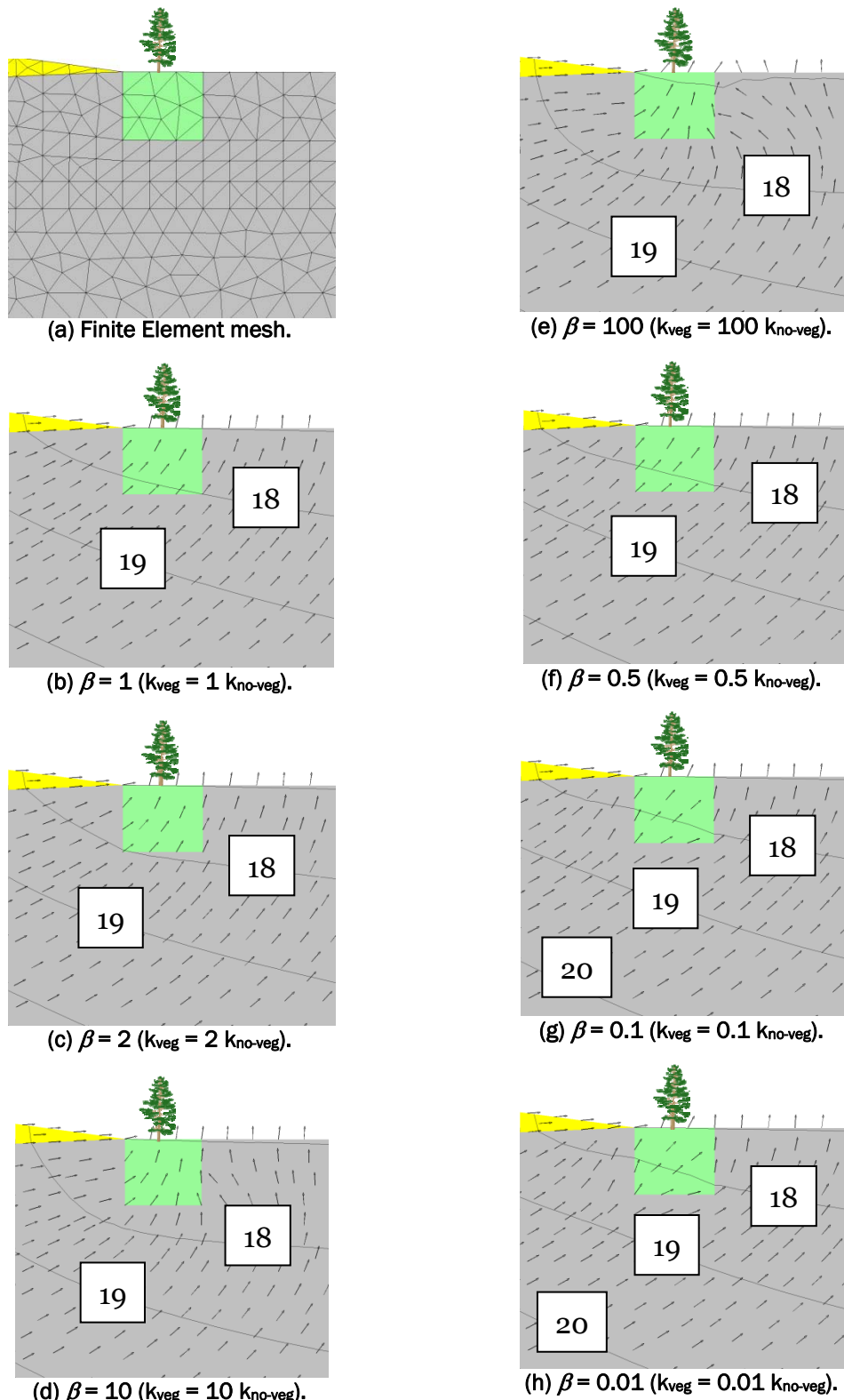


Figure 11. Total head (ft) contours, phreatic surface, and velocity vectors  
for El. 29 ft. versus  $\beta$ , Pocket Levee, Sacramento, CA.

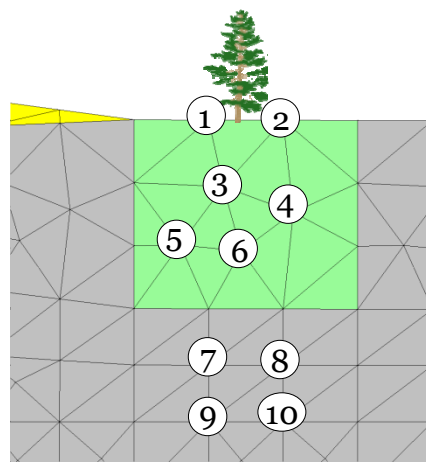


Figure 12. Selected nodes, Pocket Levee, Sacramento, CA.

Table 3. Magnitude of gradient at selected nodes for different values of  $\beta$  for El. 29 ft.

Nodes	$\beta = 0.5$	$\beta = 0.1$	$\beta = 0.01$	$\beta = 1$	$\beta = 2$	$\beta = 10$	$\beta = 100$
1	0.323	0.369	0.382	<b>0.284</b>	0.230	0.093	0.011
2	0.257	0.265	0.263	<b>0.239</b>	0.202	0.087	0.013
3	0.271	0.305	0.314	<b>0.241</b>	0.197	0.081	0.011
4	0.246	0.285	0.297	<b>0.217</b>	0.171	0.072	0.010
5	0.245	0.275	0.282	<b>0.218</b>	0.178	0.073	0.010
6	0.245	0.296	0.312	<b>0.209</b>	0.165	0.065	0.009
7	0.145	0.115	0.106	<b>0.168</b>	0.198	0.284	0.302
8	0.153	0.137	0.134	<b>0.167</b>	0.188	0.248	0.288
9	0.142	0.128	0.124	<b>0.154</b>	0.170	0.212	0.237
10	0.145	0.135	0.132	<b>0.154</b>	0.167	0.203	0.226

Table 4. Pore pressure (lb/ft<sup>2</sup>) at selected nodes for different values of hydraulic conductivity for El. 29 ft, Pocket Levee, Sacramento, CA.

Node	$\beta = 0.5$	$\beta = 0.1$	$\beta = 0.01$	$\beta = 1$	$\beta = 2$	$\beta = 10$	$\beta = 100$
1	0.0	0.0	0.0	<b>0.0</b>	0.0	0.0	0.0
2	0.0	0.0	0.0	<b>0.0</b>	0.0	0.0	0.0
3	142.8	147.0	148.1	<b>139.1</b>	133.6	119.4	110.8
4	191.8	193.7	193.9	<b>188.8</b>	183.1	165.7	154.5
5	269.1	278.4	281.1	<b>261.4</b>	250.9	224.5	208.8
6	275.1	282.7	284.7	<b>268.6</b>	259.0	233.9	218.6
7	501.6	510.0	512.3	<b>494.5</b>	484.3	457.8	441.6
8	495.7	503.4	505.5	<b>489.2</b>	479.7	454.2	438.4
9	607.8	614.1	615.8	<b>602.4</b>	594.5	573.4	560.4
10	602.2	608.1	609.6	<b>597.0</b>	589.4	568.8	556.0

The observations from the model output are as follows:

- As hydraulic conductivity is increased, the magnitude of gradient in the woody vegetation zone is decreased, and the magnitude of gradient below the zone is increased.
- Conversely, as the hydraulic conductivity is decreased, the magnitude of gradient in the woody vegetation zone is increased, and the magnitude of gradient below the zone is decreased.
- As the hydraulic conductivity is increased, the total head contours move away from the woody vegetation zone.
- Conversely, as the hydraulic conductivity is decreased, the total head contours move toward the woody vegetation zone, thereby increasing the gradient.

When  $\beta = 10$  or greater, pore pressures are reduced enough to become less than zero at the top of the woody vegetation zone. This causes the phreatic surface (pressure = 0) to fall within the zone leaving it in a partially saturated and partially unsaturated condition. This, in turn, makes the slope even safer from piping than was seen in the analysis for the seventh zone. For  $\beta > 1$ , a woody vegetation zone acts as a typical drain, drawing seepage into it. This is true if the zone stays saturated. However, in the case of  $\beta \geq 10$  for this particular levee and zone location, a careful look at Figure 13 shows that the phreatic surface drops below the ground surface in the zone. In this case, no water flows to the top of the woody vegetation zone, and flow lines become almost parallel to the surface. With no water leaving the surface and very little vertical gradient being realized, the above conclusion that piping is even less likely than was seen in the analysis for the seventh zone is established.

### ***Woody vegetation zone on the toe of the levee***

The sixth woody vegetation zone in Figure 4 is at the toe of the levee. Figure 13 shows the mesh near the woody vegetation zone along with total head contours, phreatic surface, and velocity vectors for various values of hydraulic conductivity. As before, certain nodes in the region were selected, as shown in Figure 14, for tabulating the magnitude of gradient (Table 5) and pore pressure (Table 6). The observations from the previous zone are valid for this location. Additional observations are as follows:

- Gradients are smaller and pore pressures are greater than in the previous location of the woody vegetation zone.

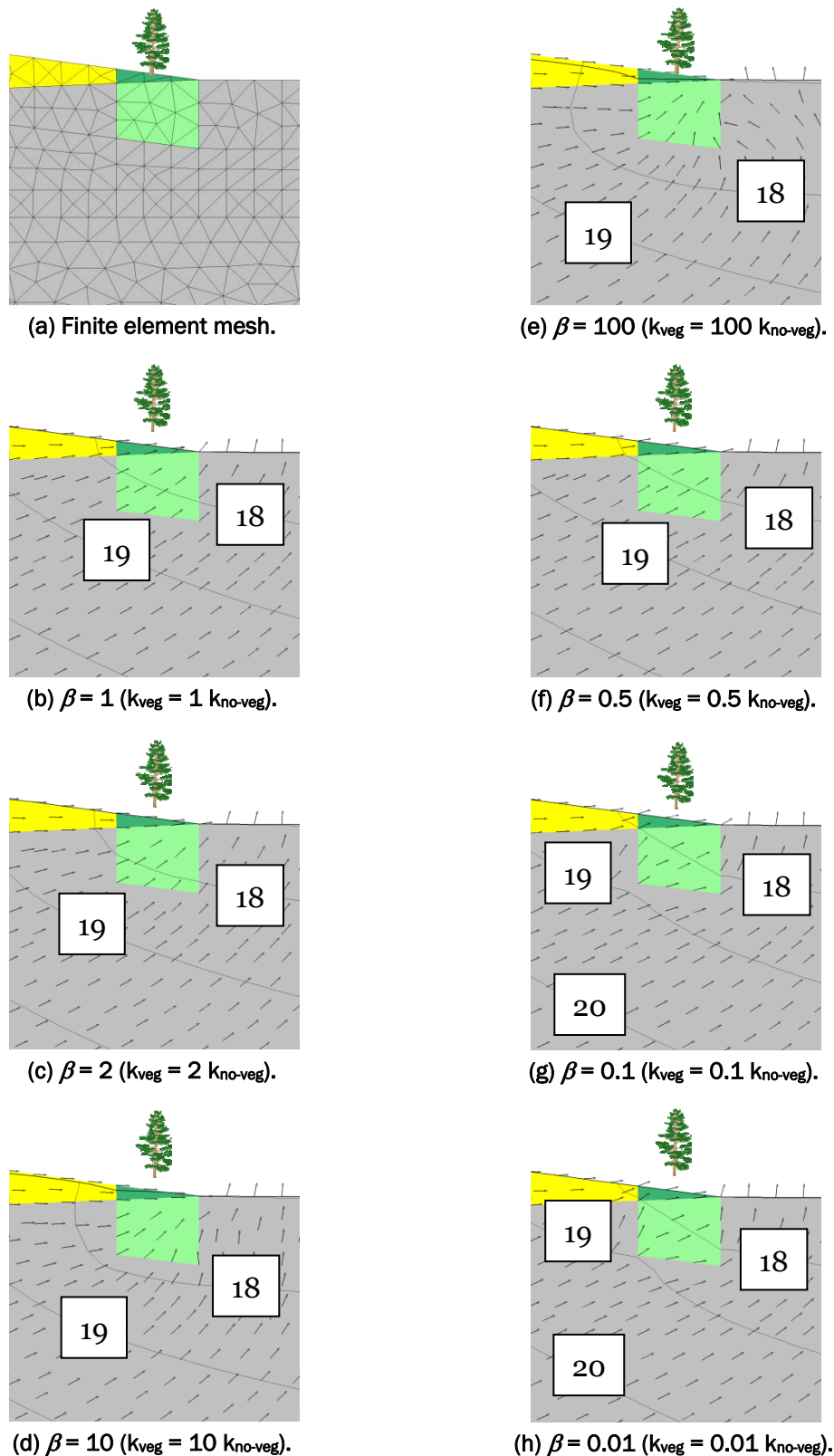


Figure 13. Total head (ft) contours, phreatic surface, and velocity vectors for El. 29 ft versus  $\beta$ , Pocket Levee, Sacramento, CA.

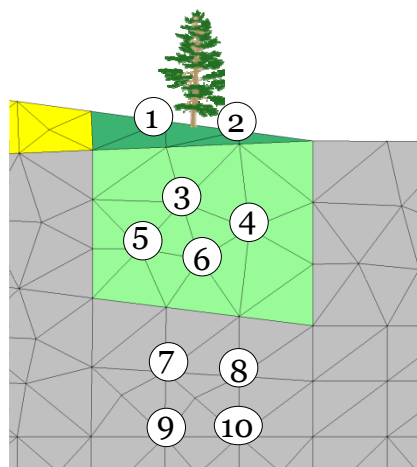


Figure 14. Selected nodes, Pocket Levee, Sacramento, CA.

Table 5. Magnitude of gradient at selected nodes for different values of hydraulic conductivity for El. 29 ft, Pocket Levee, Sacramento, CA.

Node	$\beta = 0.5$	$\beta = 0.1$	$\beta = 0.01$	$\beta = 1$	$\beta = 2$	$\beta = 10$	$\beta = 100$
1	0.172	0.226	0.246	<b>0.143</b>	0.119	0.038	0.006
2	0.154	0.167	0.171	<b>0.146</b>	0.138	0.078	0.011
3	0.279	0.331	0.348	<b>0.239</b>	0.188	0.069	0.010
4	0.276	0.332	0.353	<b>0.237</b>	0.191	0.074	0.011
5	0.235	0.276	0.290	<b>0.199</b>	0.158	0.062	0.009
6	0.253	0.322	0.347	<b>0.208</b>	0.158	0.060	0.009
7	0.141	0.115	0.107	<b>0.163</b>	0.190	0.251	0.302
8	0.154	0.145	0.144	<b>0.167</b>	0.186	0.245	0.305
9	0.138	0.126	0.120	<b>0.149</b>	0.164	0.202	0.236
10	0.145	0.137	0.135	<b>0.153</b>	0.164	0.199	0.234

Table 6. Pore pressure (lb/ft<sup>2</sup>) at selected nodes for different values of hydraulic conductivity for El. 29 ft, Pocket Levee, Sacramento, CA.

Node	$\beta = 0.5$	$\beta = 0.1$	$\beta = 0.01$	$\beta = 1$	$\beta = 2$	$\beta = 10$	$\beta = 100$
1	0.0	0.0	0.0	<b>0.0</b>	0.0	-10.7	-30.2
2	0.0	0.0	0.0	<b>0.0</b>	0.0	-0.2	-14.5
3	161.0	166.1	167.5	<b>156.6</b>	150.6	130.7	107.5
4	204.1	204.3	203.7	<b>201.7</b>	196.7	176.2	152.3
5	265.3	276.3	279.8	<b>256.5</b>	245.5	214.9	186.5
6	276.1	283.8	286.0	<b>269.3</b>	260.0	231.8	204.0
7	503.4	511.8	514.4	<b>496.4</b>	487.0	459.5	434.1
8	504.2	511.2	513.3	<b>498.0</b>	489.5	463.1	437.8
9	626.6	634.4	634.2	<b>621.4</b>	614.4	592.6	571.8
10	619.5	624.9	626.5	<b>614.6</b>	607.9	586.5	565.8

- When  $\beta = 10$  or greater, pore pressures are reduced enough to cause the phreatic surface (pressure = 0) to fall within the woody vegetation zone leaving the zone in an unsaturated condition.

### ***Woody vegetation zone midway on the steeper landside slope of the levee***

The fifth woody vegetation zone in Figure 4 is about midway on the steeper landside slope of the levee. Plots of total head contours and the phreatic surface for this zone for  $\beta = 1, 100$ , and 0.01 are given in Figure 15. From these plots, it is seen that the woody vegetation zone is mostly above the phreatic surface, and the overall flow patterns are affected very little by this zone, regardless of the change in hydraulic conductivity. To verify this, a detailed study as before was conducted in the vicinity of the woody vegetation zone by using all of the seven different values of hydraulic conductivity. Figure 16 shows selected nodes where the magnitude of the gradient is given in Table 7, and pore pressure is given in Table 8. There are very few differences among these data in the saturated zone for any value of hydraulic conductivity.

### ***Woody vegetation zone near the top of the landside of the levee***

The fourth woody vegetation zone in Figure 4 is near the top of the landside slope of the levee. Total head contours and the phreatic surface for this zone using  $\beta = 1, 100$ , and 0.01 are given in Figure 17. From these plots, it is seen that although the total head contours are modified significantly in the unsaturated zone, the phreatic surface, and total head on the downstream part of the levee are essentially the same for all three plots.

### ***Woody vegetation zone at the river height on the riverside***

The third woody vegetation zone in Figure 4 is placed at the river elevation on the riverside. From the plots in Figure 18, this zone does not have an effect on the flow field on the landside.

### ***Woody vegetation zone at the change in slope on the riverside***

The second woody vegetation zone in Figure 4 is on the change in slope of the levee on the riverside. As with Figure 18, Figure 19 shows that the zone at this location does not influence the flow field.

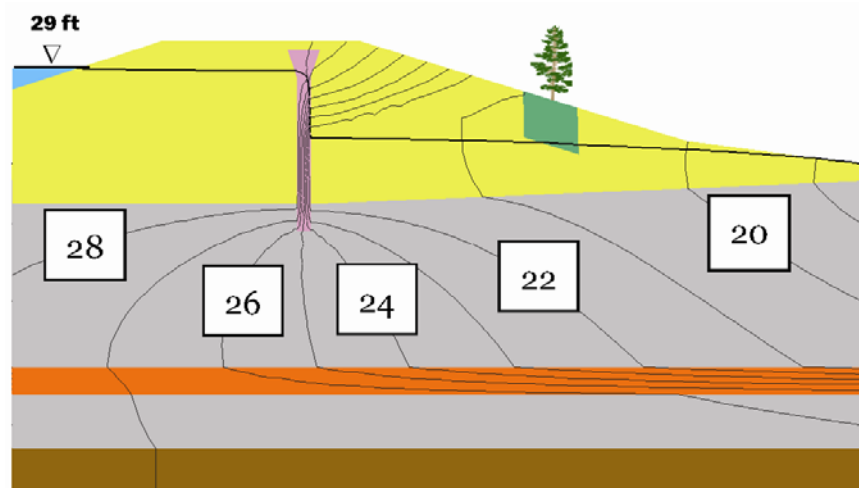
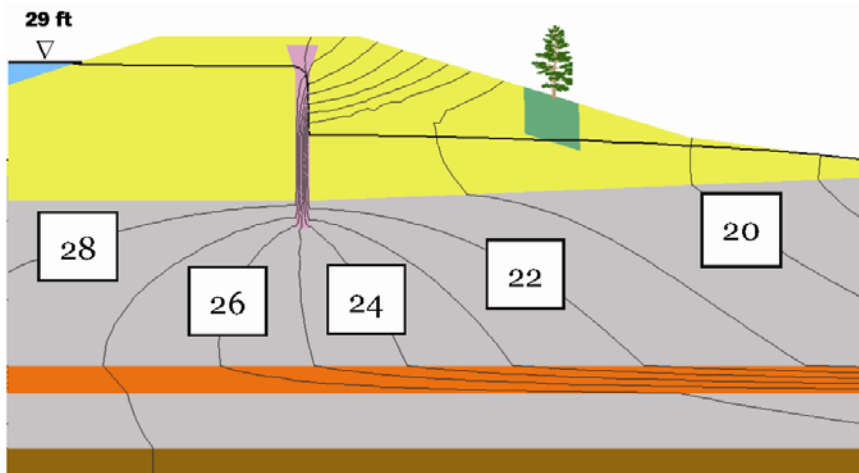
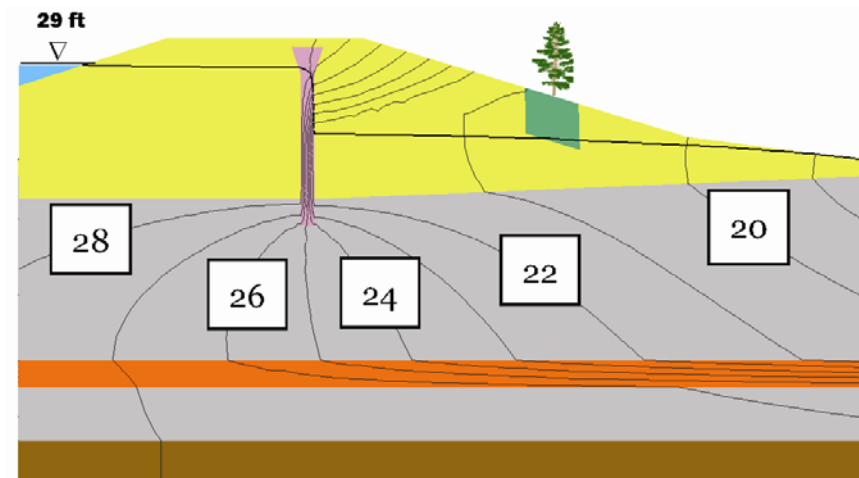
(a)  $\beta = 1$  ( $k_{veg} = 1 k_{no-veg}$ ).(b)  $\beta = 100$  ( $k_{veg} = 100 k_{no-veg}$ ).(c)  $\beta = 0.01$  ( $k_{veg} = 0.01 k_{no-veg}$ ).

Figure 15. Total head (ft) contours and phreatic surface for El. 29 ft,  
Pocket Levee, Sacramento, CA.

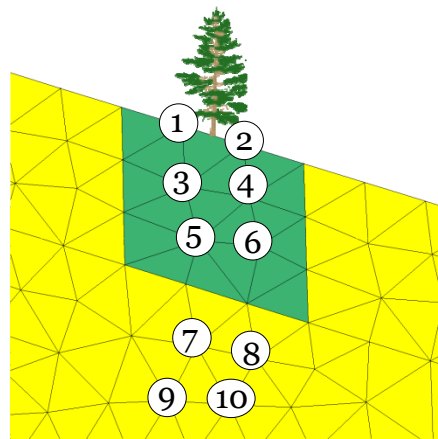


Figure 16. Selected nodes, Pocket Levee, Sacramento, CA.

Table 7. Magnitude of gradient at selected nodes for different values of hydraulic conductivity for El. 29 ft, Pocket Levee, Sacramento, CA.

Node	$\beta = 0.5$	$\beta = 0.1$	$\beta = 0.01$	$\beta = 1$	$\beta = 2$	$\beta = 10$	$\beta = 100$
1	0.060	0.080	0.087	<b>0.047</b>	0.033	0.011	0.002
2	0.054	0.080	0.092	<b>0.040</b>	0.027	0.010	0.003
3	0.047	0.065	0.071	<b>0.036</b>	0.027	0.011	0.004
4	0.054	0.079	0.090	<b>0.040</b>	0.028	0.011	0.003
5	0.042	0.054	0.058	<b>0.036</b>	0.030	0.021	0.012
6	0.054	0.078	0.089	<b>0.041</b>	0.029	0.013	0.002
7	0.038	0.039	0.040	<b>0.037</b>	0.036	0.035	0.035
8	0.041	0.045	0.047	<b>0.039</b>	0.036	0.032	0.029
9	0.038	0.039	0.039	<b>0.038</b>	0.037	0.036	0.012
10	0.040	0.042	0.042	<b>0.040</b>	0.039	0.036	0.035

Table 8. Pore pressure (lb/ft<sup>2</sup>) at selected nodes for different values of hydraulic conductivity for El. 29 ft, Pocket Levee, Sacramento, CA.

Node	$\beta = 0.5$	$\beta = 0.1$	$\beta = 0.01$	$\beta = 1$	$\beta = 2$	$\beta = 10$	$\beta = 100$
1	-318.4	-316.3	-315.7	<b>-320.0</b>	-322.0	-326.6	-329.5
2	-287.3	-288.3	-288.9	<b>-287.1</b>	-297.4	-289.6	-291.6
3	-198.5	-197.4	-197.0	<b>-199.4</b>	-200.7	-204.1	-206.5
4	-182.5	-183.6	-184.1	<b>-182.1</b>	-182.1	-183.4	-184.8
5	-90.0	-89.3	-89.1	<b>-90.8</b>	-91.8	-95.1	-97.4
6	-86.3	-87.4	-87.9	<b>-85.9</b>	-85.8	-86.6	-87.5
7	121.6	122.4	122.6	<b>121.2</b>	120.7	119.7	119.17
8	143.4	143.8	143.9	<b>143.2</b>	143.0	142.8	142.7
9	236.8	237.3	237.5	<b>236.5</b>	236.1	235.4	234.9
10	239.4	239.7	239.9	<b>239.1</b>	238.9	238.4	238.1

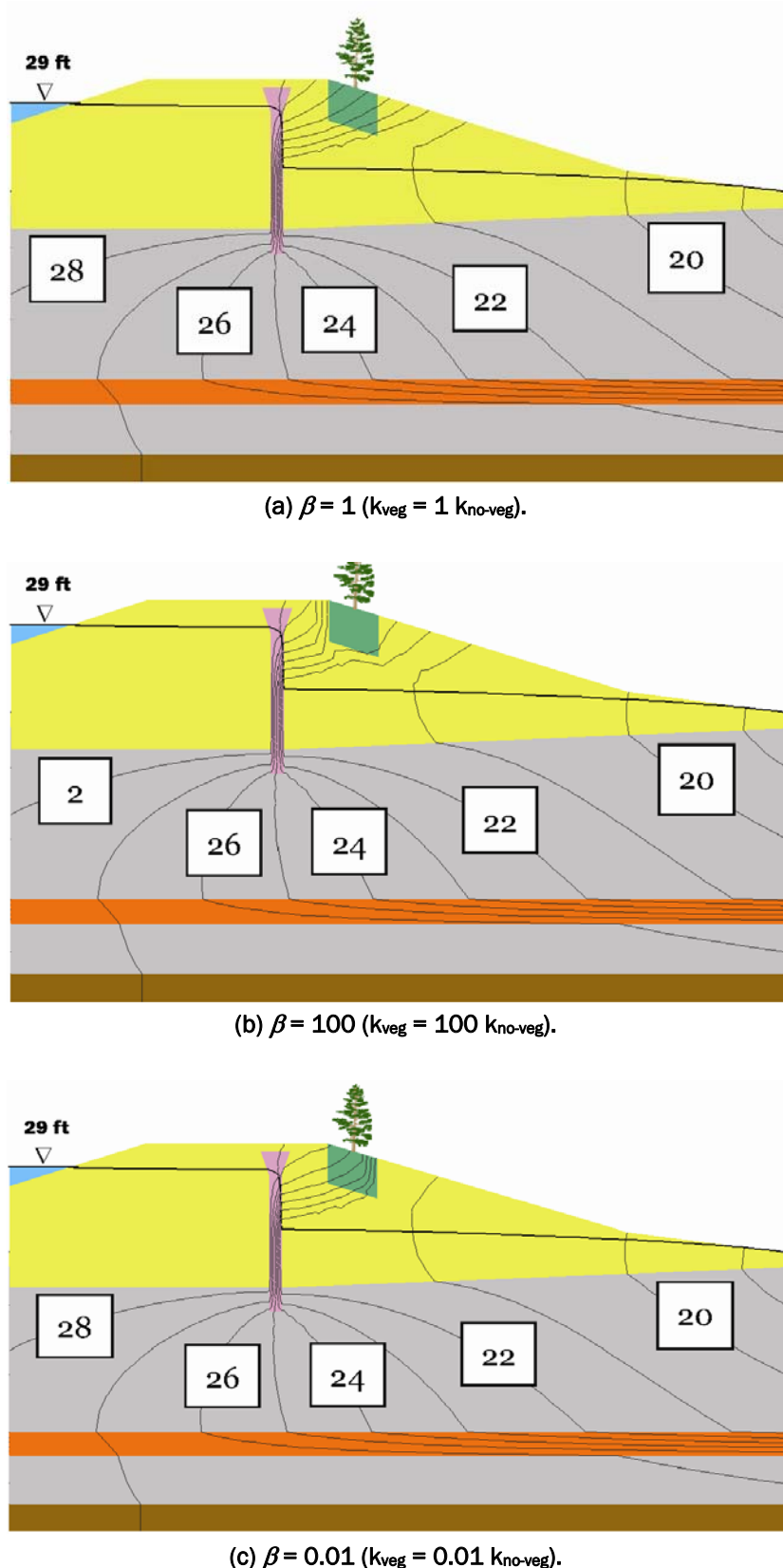


Figure 17. Total head (ft) contours and phreatic surface for El. 29 ft, Pocket Levee, Sacramento, CA.

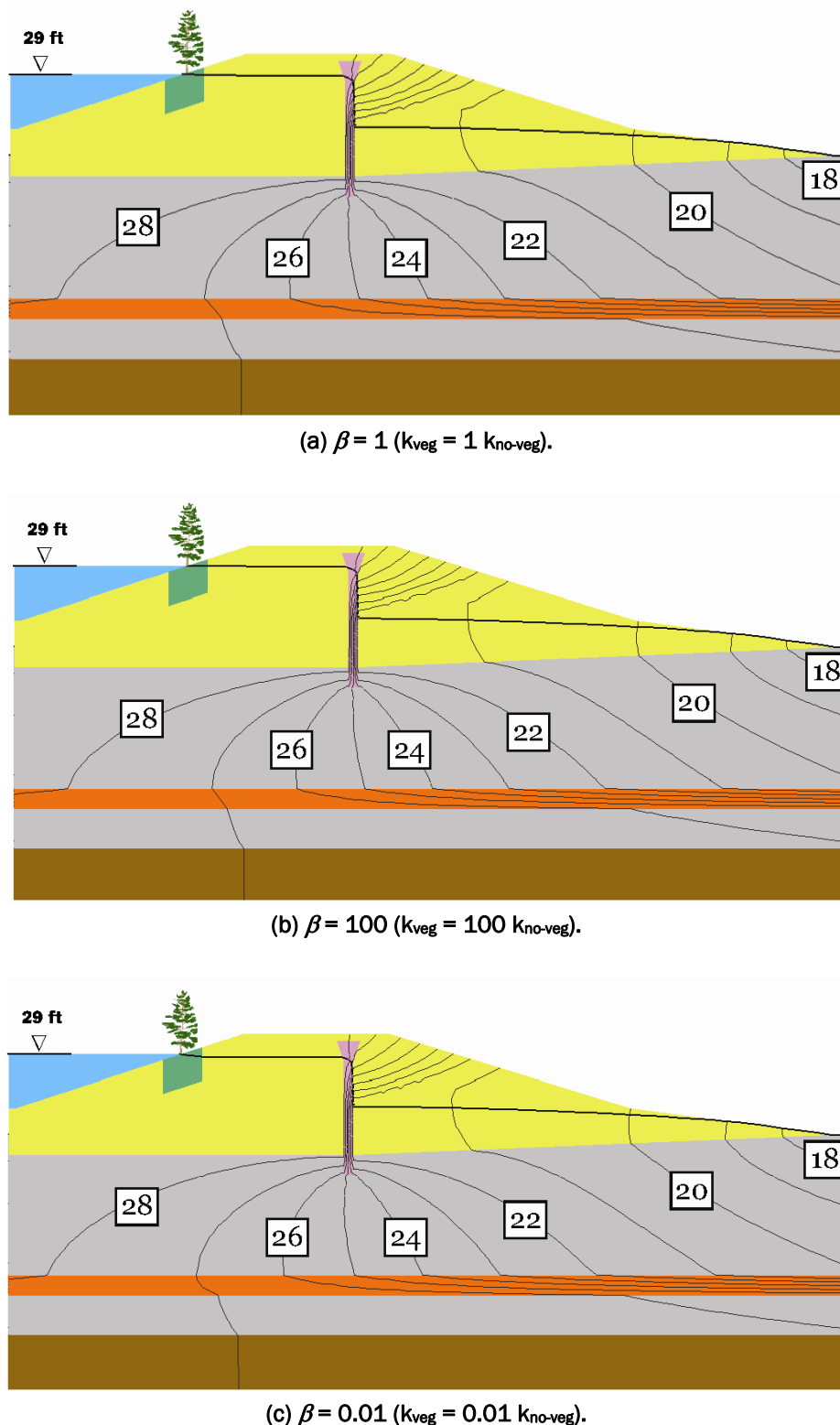


Figure 18. Total head (ft) contours and phreatic surface for El. 29 ft versus  $\beta$ , Pocket Levee, Sacramento, CA.

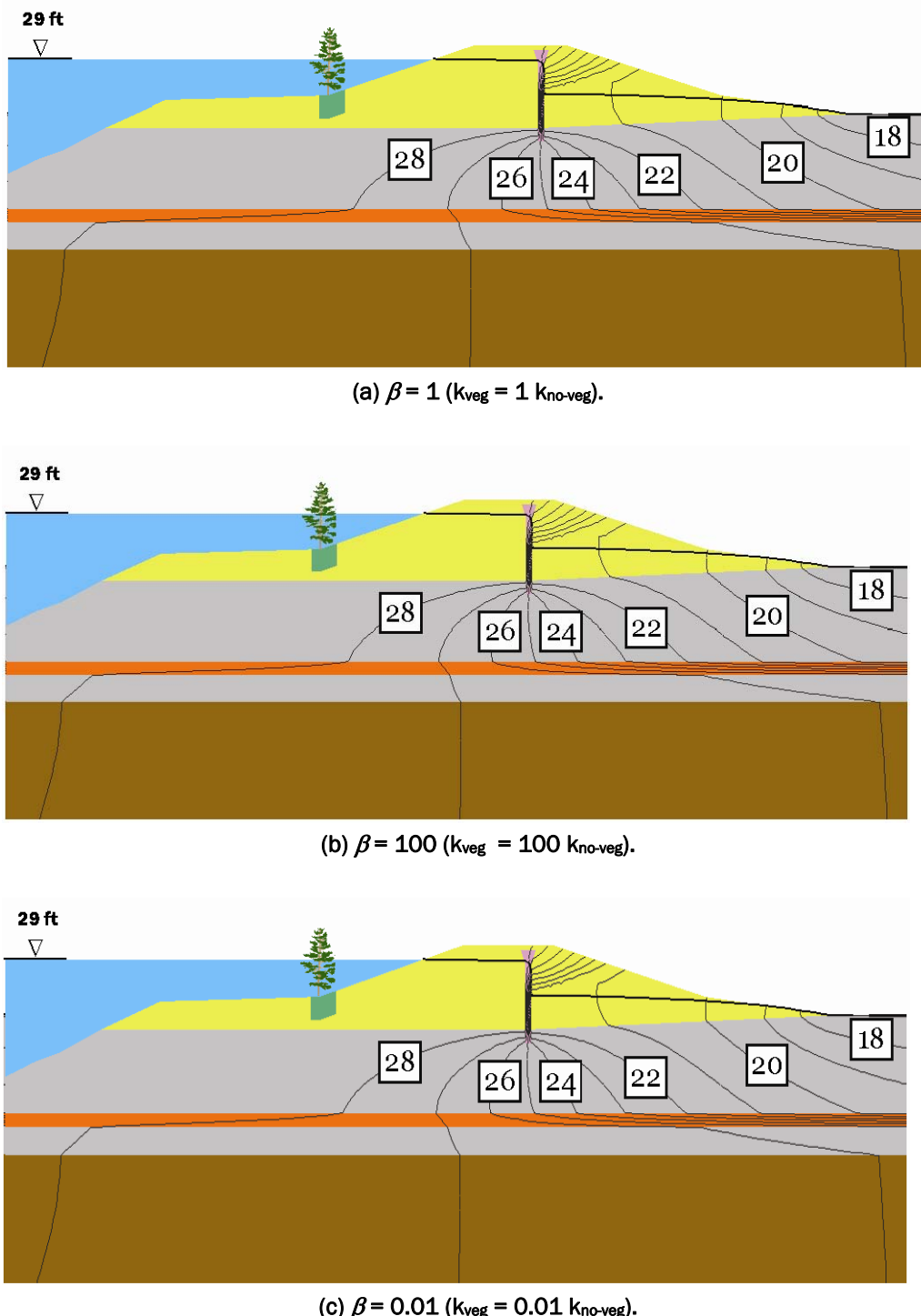


Figure 19. Total head (ft) contours and phreatic surface El. 29 ft versus  $\beta$ ,  
Pocket Levee, Sacramento, CA.

### ***Woody vegetation zone near the end of the levee sand on the riverside***

The first woody vegetation zone in Figure 4 is near the end of the levee sand on the riverside. Figure 20 again shows negligible influence on the flow field at this location.

*Steady-state results for elevation 26 ft*

Because similar results occur at a lower elevation (from 29 ft to 26 ft), a reduced number of woody vegetation zones are considered for El. 26 ft as follows: (1) woody vegetation zone on the toe of the levee, (2) zone midway on the steeper landside slope of the levee, and (3) zone at river height on the riverside.

#### ***No woody vegetation zone***

Figure 21 shows the flow pattern for the river at El. 26 ft. Results for this lower elevation are very similar to the previous results.

#### ***Woody vegetation zone on the toe of the levee***

Figure 22 shows the mesh near the woody vegetation zone along with total head contours, phreatic surface, and velocity vectors for various values of the hydraulic conductivity for the sixth zone in Figure 4. The same nodes used for El. 29 ft for tabulating magnitude of gradient (Table 9) and pore pressure (Table 10) were selected and are shown in Figure 23. The observations about the sixth zone for El. 29 ft in Figure 4 are valid, as well as the following:

- Total head contours for El. 26 ft are farther apart than those of El. 29 ft signifying a lower gradient.
- Magnitudes of gradient and pore pressures for El. 26 ft are less than those for El. 29 ft because of lower head across the levee but the affect remains the same on the flow field.

#### ***Woody vegetation zone midslope on the steeper landside slope of the levee***

The fifth woody vegetation zone in Figure 4 is midway on the steeper landside slope of the levee. Plots of total head contours and the phreatic

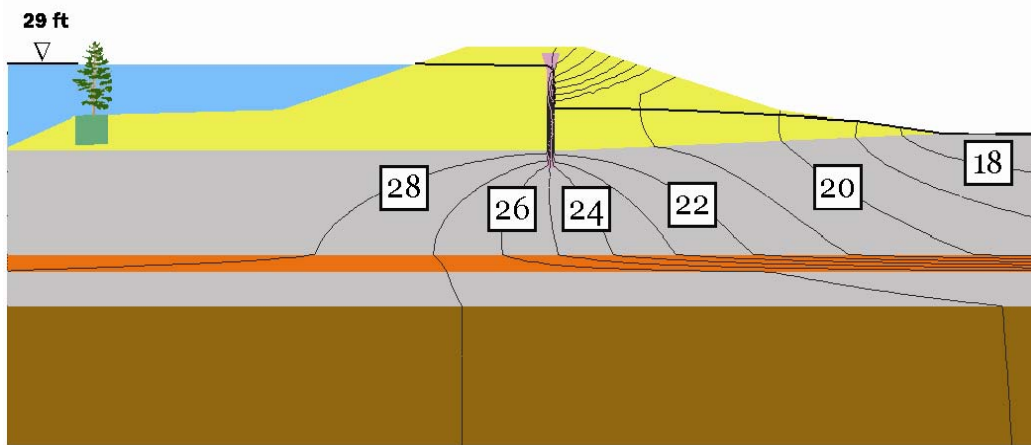
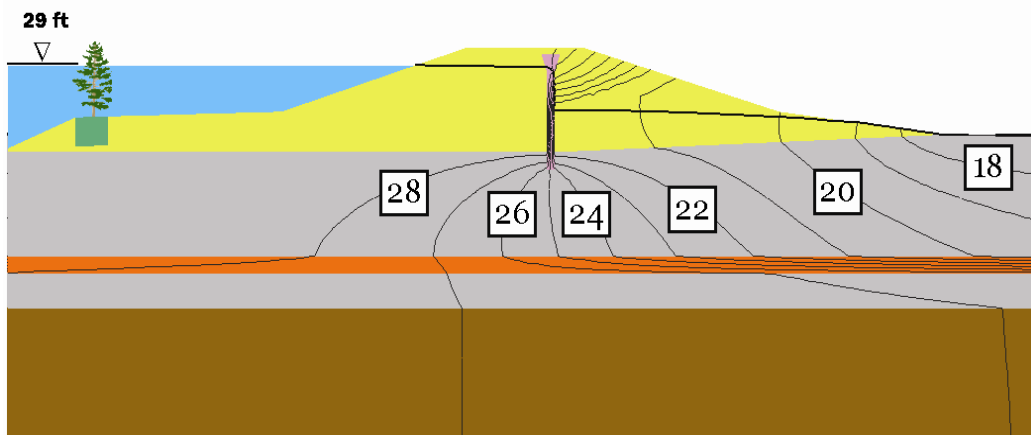
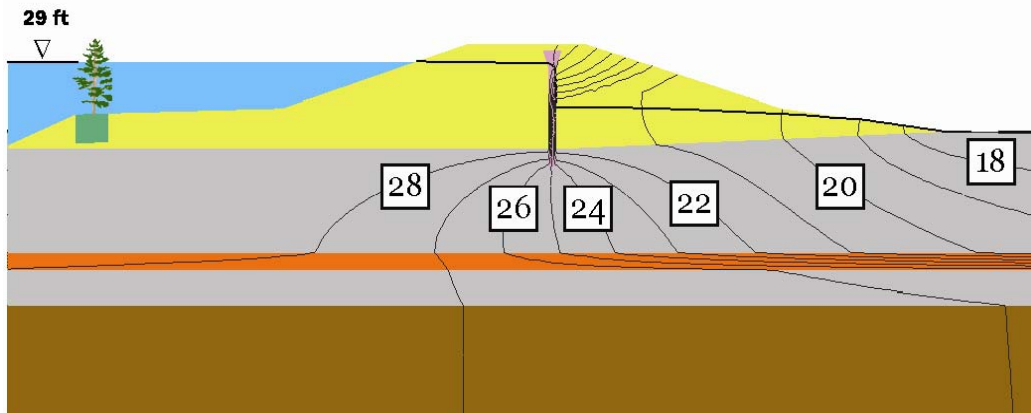
(a)  $\beta = 1$  ( $k_{veg} = 1 k_{no-veg}$ ).(b)  $\beta = 100$  ( $k_{veg} = 100 k_{no-veg}$ ).(c)  $\beta = 0.01$  ( $k_{veg} = 0.01 k_{no-veg}$ ).

Figure 20. Total head (ft) contours and phreatic surface for El. 29 ft versus  $\beta$ ,  
Pocket Levee, Sacramento, CA.

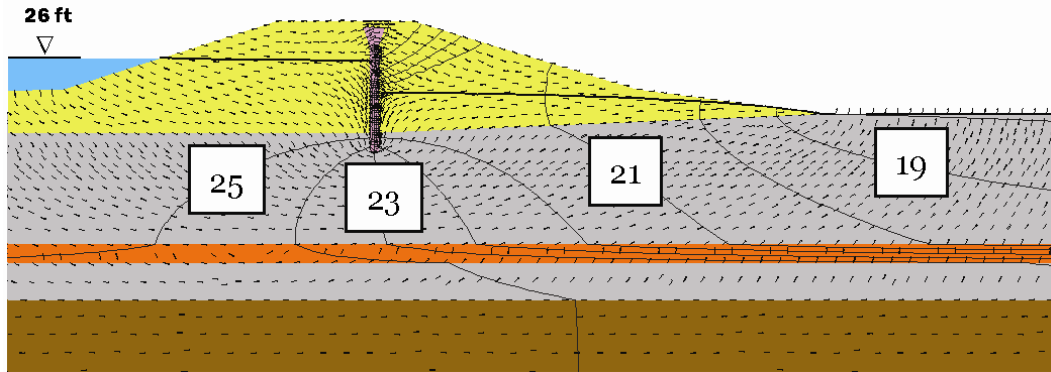


Figure 21. Total head (ft) contours, velocity vectors, and phreatic surface for river El. 26 ft, Pocket Levee, Sacramento, CA.

surface for this zone using  $\beta = 1, 100$ , and  $0.01$  are given in Figure 24. From these plots, it is seen, even more than before, that the zone is mostly above the phreatic surface, and the overall effect on flow patterns is negligible.

### ***Woody vegetation zone at the river height on the riverside***

A woody vegetation zone similar to the third zone in Figure 4 is placed at El. 26 ft. Plots of the flow pattern for  $\beta = 1, 100$ , and  $0.01$  are generated, and presented in Figure 25. As seen in the analysis of this zone for El 29 ft, changes in hydraulic conductivity do not significantly alter the flow pattern downstream.

*Steady-state results for elevation 23 ft*

### ***No woody vegetation zone***

Figure 26 shows total head contours, phreatic surface, and velocity vectors for the river at El. 23 ft. It is important to note that as the river elevation is lowered, the phreatic surface is lowered, and the exit point starting at the landside surface of seepage is also lower.

### ***Woody vegetation zone on the toe of the levee***

The sixth woody vegetation zone in Figure 4 was examined in this analysis. Plots of total head contours and the phreatic surface for  $\beta = 1, 100$ , and  $0.01$  are given in Figure 27. Figure 28 uses the same nodes as the analyses for El. 29 ft and El. 26 ft with Tables 11 and 12 giving the magnitude of gradient and pore pressure for these selections, respectively. The

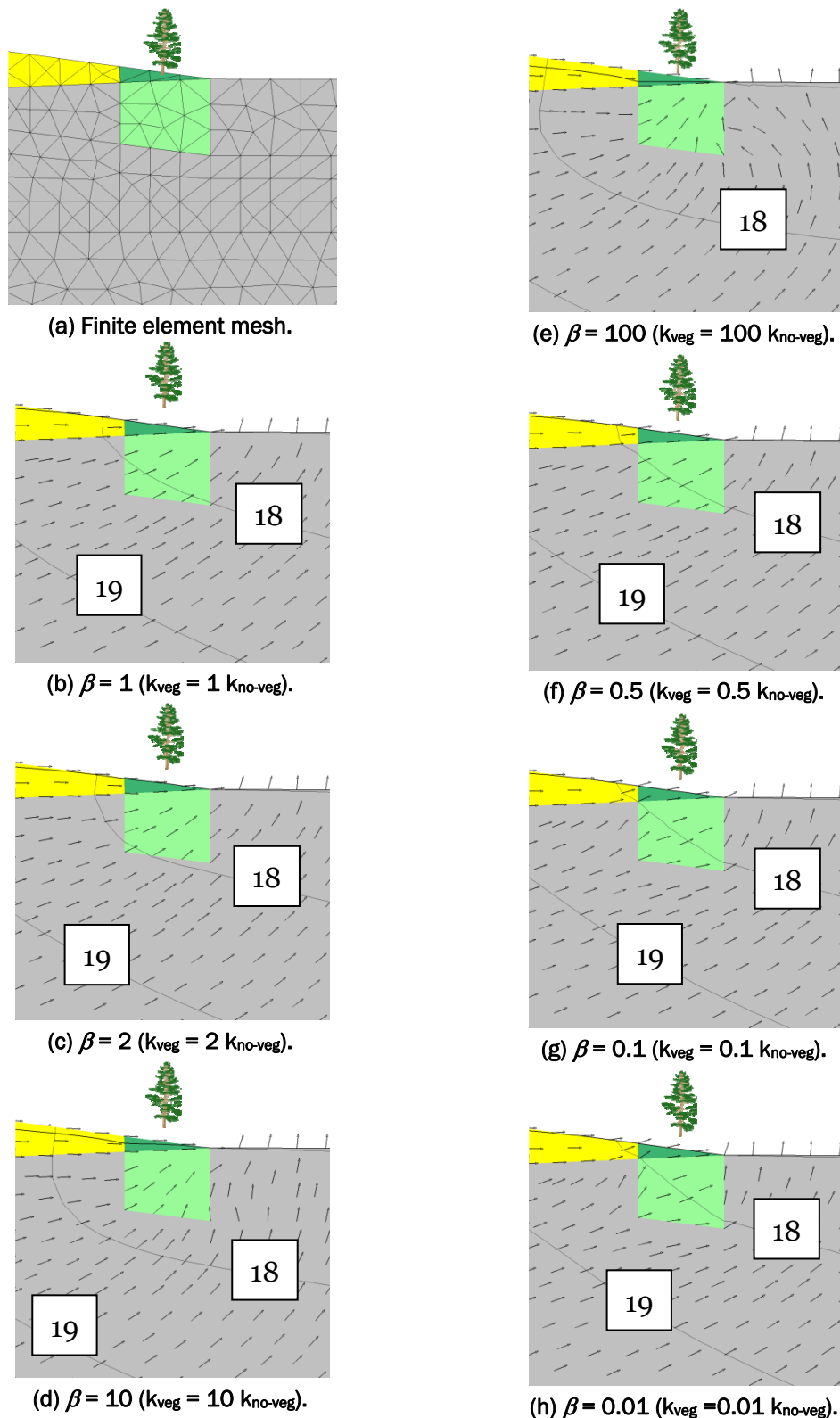


Figure 22. Total head (ft) contours, phreatic surface, and velocity vectors for El. 26 ft versus  $\beta$ , Pocket Levee, Sacramento, CA.

**Table 9.** Magnitude of gradient at selected nodes for different values of hydraulic conductivity for El. 26 ft, Pocket Levee, Sacramento, CA.

Node	$\beta = 0.5$	$\beta = 0.1$	$\beta = 0.01$	$\beta = 1$	$\beta = 2$	$\beta = 10$	$\beta = 100$
1	0.164	0.214	0.234	<b>0.139</b>	0.109	0.030	0.005
2	0.150	0.162	0.166	<b>0.143</b>	0.135	0.057	0.008
3	0.221	0.268	0.284	<b>0.186</b>	0.142	0.054	0.008
4	0.220	0.270	0.289	<b>0.188</b>	0.149	0.057	0.008
5	0.176	0.214	0.227	<b>0.149</b>	0.116	0.047	0.007
6	0.195	0.252	0.274	<b>0.158</b>	0.118	0.046	0.006
7	0.106	0.088	0.084	<b>0.121</b>	0.141	0.190	0.227
8	0.118	0.114	0.115	<b>0.125</b>	0.138	0.185	0.229
9	0.102	0.093	0.090	<b>0.110</b>	0.121	0.152	0.177
10	0.109	0.104	0.103	<b>0.114</b>	0.122	0.150	0.175

**Table 10.** Pore pressure (lb/ft<sup>2</sup>) at selected nodes for different values of hydraulic conductivity for El. 26 ft, Pocket Levee, Sacramento, CA.

Node	$\beta = 0.5$	$\beta = 0.1$	$\beta = 0.01$	$\beta = 1$	$\beta = 2$	$\beta = 10$	$\beta = 100$
1	0.0	0.0	0.0	<b>0.0</b>	0.0	-16.9	-31.1
2	0.0	0.0	0.0	<b>0.0</b>	0.0	-4.9	-15.1
3	154.4	159.0	160.3	<b>150.6</b>	145.0	123.7	106.5
4	195.5	195.4	194.8	<b>193.8</b>	189.6	169.1	151.2
5	253.1	262.9	266.0	<b>245.7</b>	235.8	206.5	185.3
6	263.8	270.2	272.0	<b>258.4</b>	260.3	223.6	202.8
7	481.8	488.7	490.8	<b>476.1</b>	468.0	442.2	423.2
8	483.3	489.0	490.7	<b>478.5</b>	471.2	446.8	427.8
9	600.9	605.9	607.4	<b>596.8</b>	590.4	569.5	553.9
10	594.9	599.4	600.7	<b>591.0</b>	585.0	564.7	549.2

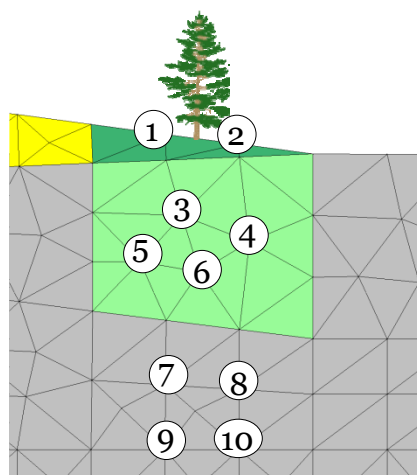


**Figure 23.** Selected nodes, Pocket Levee, Sacramento, CA.

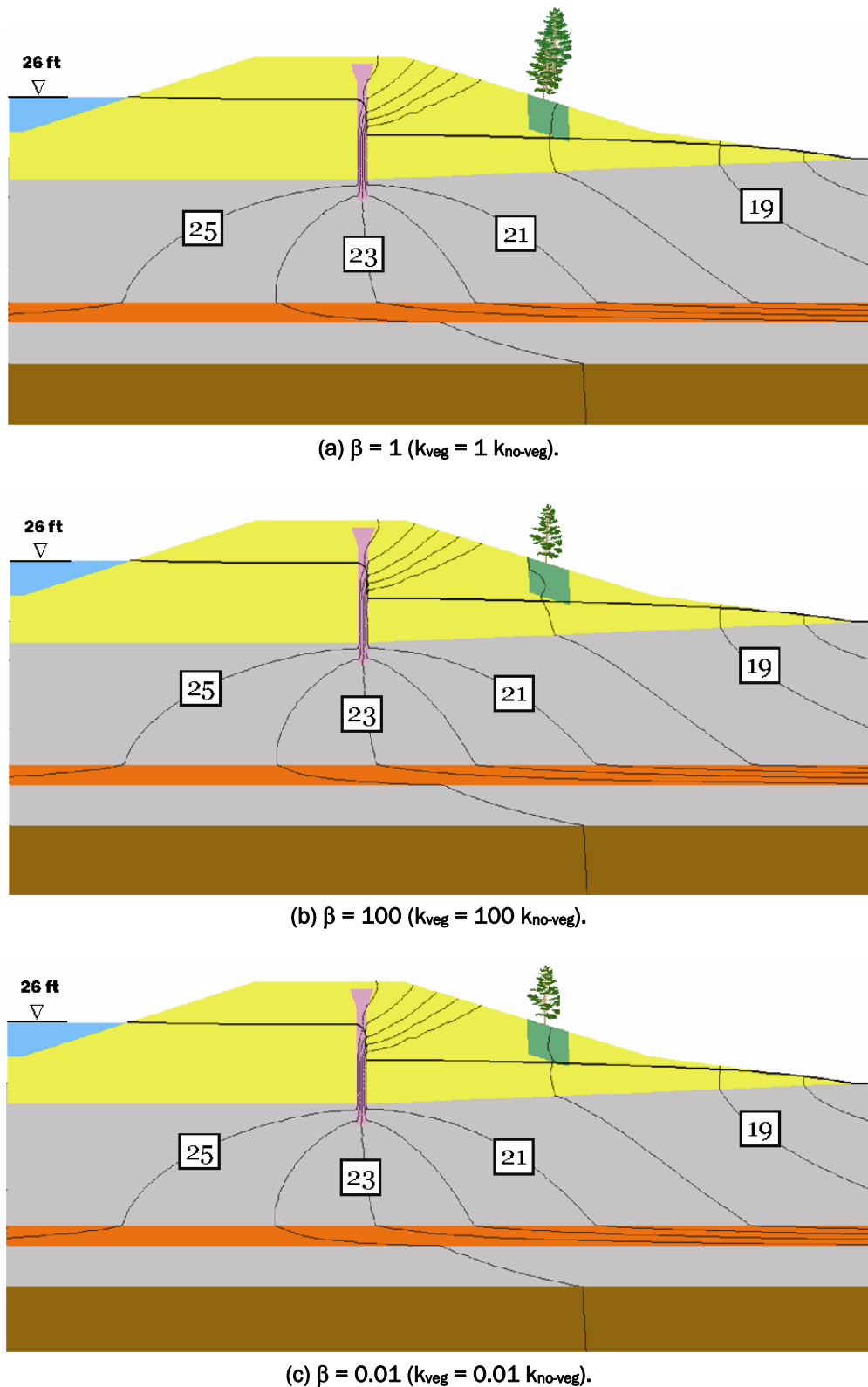


Figure 24. Total head (ft) contours and phreatic surface for El. 26 ft versus  $\beta$ , Pocket Levee, Sacramento, CA.

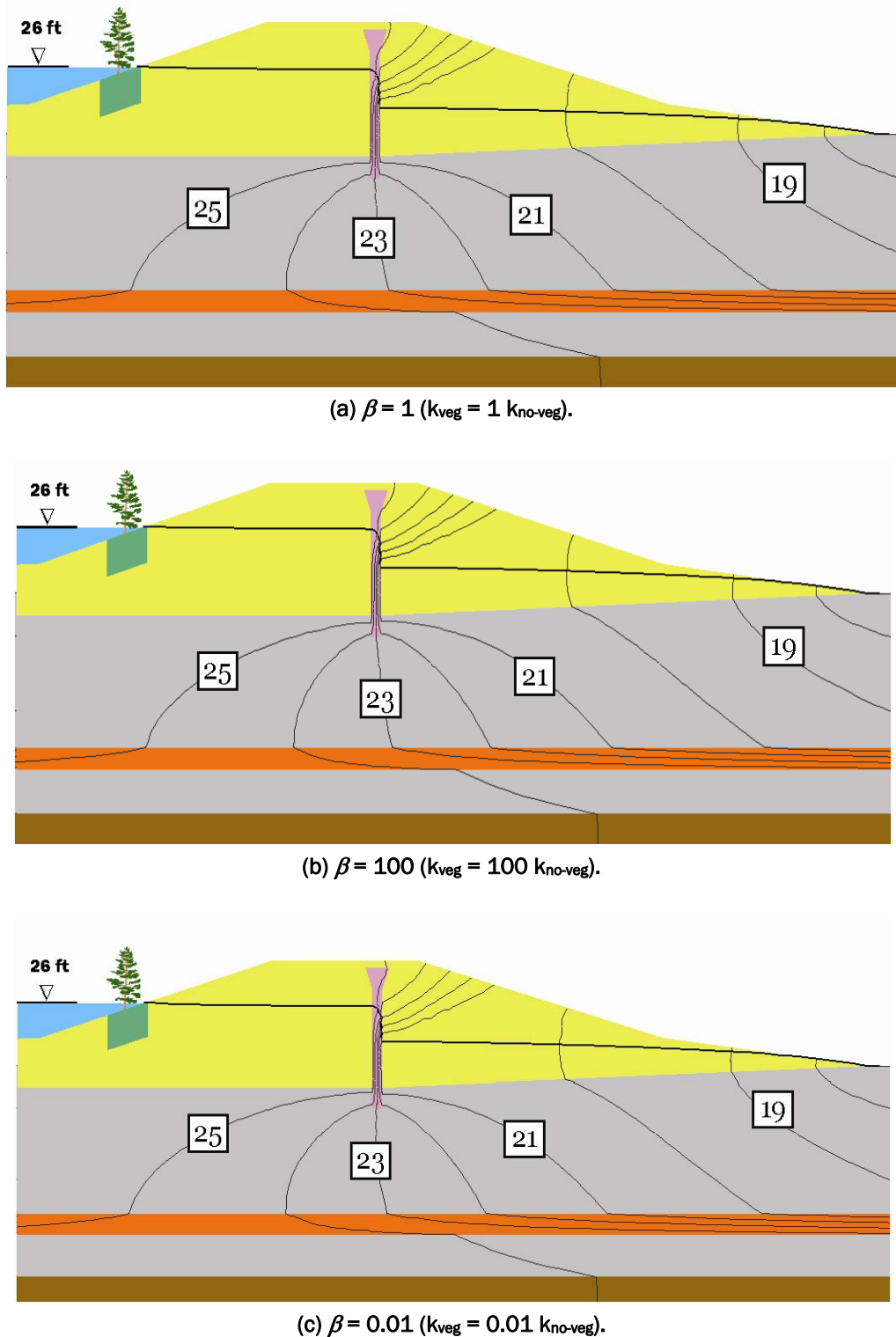


Figure 25. Total head (ft) contours and phreatic surface for El. 26 ft versus  $\beta$ , Pocket Levee, Sacramento, CA.

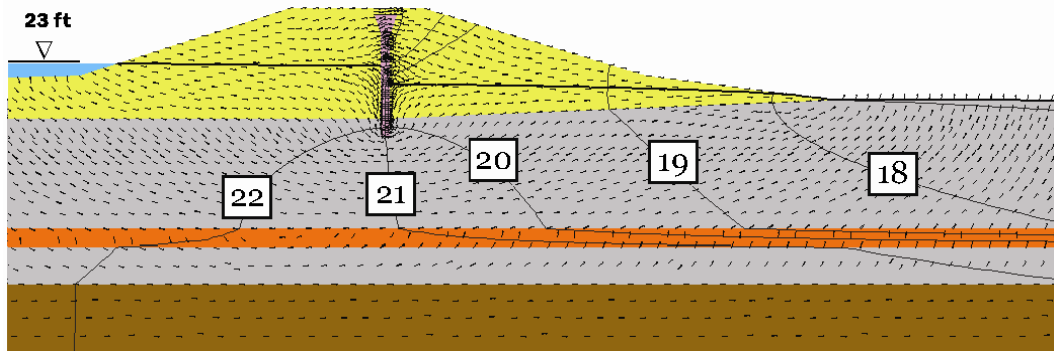


Figure 26. Total head (ft) contours, velocity vectors, and phreatic surface for the river El. 23 ft Pocket Levee, Sacramento, CA.

observations in the analyses for the previous elevations for this zone are valid, as well as the following:

- The phreatic surface was drawn into the woody vegetation zone earlier for  $\beta = 2$  than for this same value at higher elevations. Thus, changes in hydraulic conductivity at this location have less influence on the flow field.

### ***Woody vegetation zone midway on the steeper landside slope of the levee***

The fifth woody vegetation zone in Figure 4 is midway on the steeper landside slope of the levee. Total head contours and the phreatic surface for this woody vegetation zone for  $\beta = 1, 100$ , and  $0.01$  are given in Figure 29. From these plots, it is seen, even more than before, that the zone is mostly above the phreatic surface, and the effect on the overall flow patterns at this zone are negligible.

### ***Woody vegetation zone at the river height on the riverside***

The third woody vegetation zone in Figure 4 is placed at El. 23 ft. Plots of the flow pattern for  $\beta = 1, 100$ , and  $0.01$  are constructed, and presented in Figure 30. As in the analysis of the previous zone, the changes in hydraulic conductivity for this zone do not influence the flow pattern downstream.

#### *Transient analysis*

The transient version of SEEP2D is a fully implicit solution to Equation 1. After development, the program was tested against analytical solutions derived by Tracy (2006) and applied to the Pocket Levee model. Figure 31 shows the hydrograph of the 1986 flood used to establish the riverside

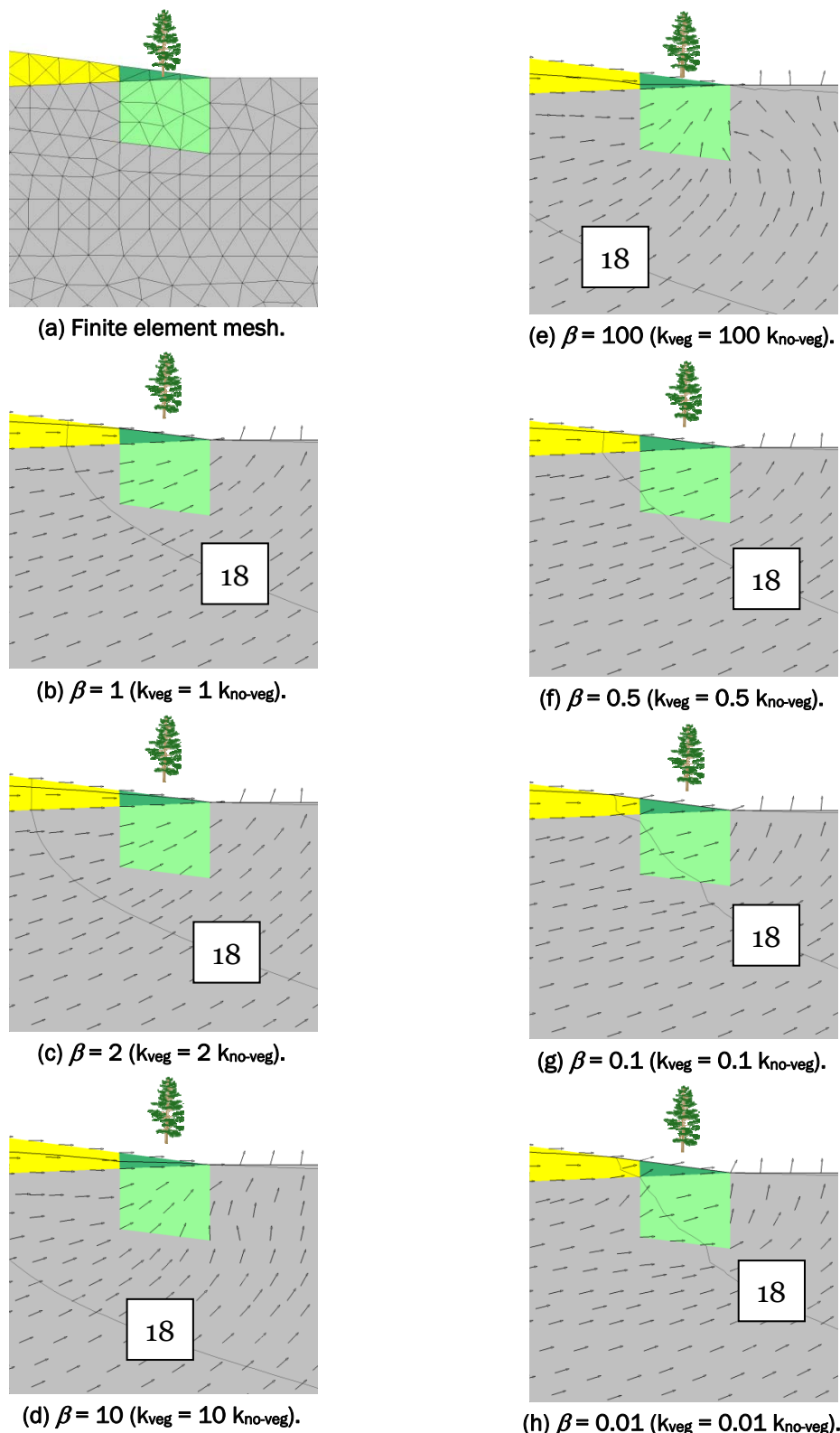


Figure 27. Total head (ft) contours, phreatic surface, and velocity vectors for El. 23 ft versus  $\beta$ , Pocket Levee, Sacramento, CA.

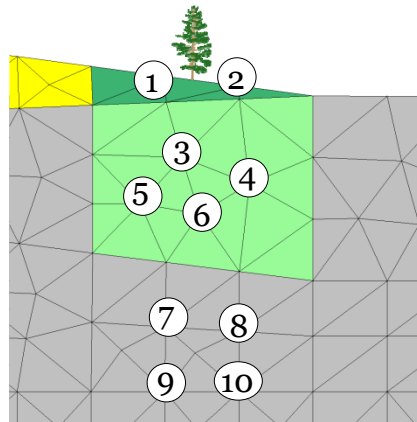


Figure 28. Selected nodes, Pocket Levee, Sacramento, CA.

Table 11. Magnitude of gradient at selected nodes for different values of hydraulic conductivity for El. 23 ft, Pocket Levee, Sacramento, CA.

Node	$\beta = 0.5$	$\beta = 0.1$	$\beta = 0.01$	$\beta = 1$	$\beta = 2$	$\beta = 10$	$\beta = 100$
1	0.142	0.189	0.211	<b>0.116</b>	0.070	0.020	0.003
2	0.142	0.153	0.158	<b>0.135</b>	0.105	0.037	0.005
3	0.152	0.194	0.211	<b>0.122</b>	0.086	0.036	0.005
4	0.156	0.199	0.217	<b>0.128</b>	0.094	0.038	0.005
5	0.115	0.149	0.162	<b>0.094</b>	0.072	0.032	0.005
6	0.131	0.176	0.194	<b>0.103</b>	0.075	0.031	0.004
7	0.070	0.062	0.061	<b>0.078</b>	0.090	0.126	0.150
8	0.079	0.081	0.084	<b>0.082</b>	0.089	0.122	0.150
9	0.066	0.061	0.059	<b>0.070</b>	0.078	0.100	0.116
10	0.072	0.070	0.070	<b>0.074</b>	0.078	0.098	0.115

Table 12. Pore pressure (lb/ft<sup>2</sup>) at selected nodes for different values of hydraulic conductivity for El. 23 ft, Pocket Levee, Sacramento, CA.

Node	$\beta = 0.5$	$\beta = 0.1$	$\beta = 0.01$	$\beta = 1$	$\beta = 2$	$\beta = 10$	$\beta = 100$
1	0.0	0.0	0.0	<b>0.0</b>	-5.1	-22.8	-31.9
2	0.0	0.0	0.0	<b>0.0</b>	0.0	-9.2	-15.7
3	145.6	149.8	151.2	<b>142.0</b>	135.3	116.8	105.5
4	184.9	184.8	184.4	<b>183.5</b>	178.7	161.9	150.2
5	237.6	246.0	249.0	<b>231.0</b>	221.3	198.1	184.0
6	248.7	253.8	255.5	<b>244.2</b>	236.4	215.3	201.6
7	456.7	462.3	465.4	<b>451.9</b>	444.3	424.6	411.9
8	459.4	463.9	465.4	<b>455.4</b>	448.7	430.0	417.5
9	571.9	576.1	577.5	<b>568.2</b>	561.8	545.6	535.2
10	567.2	571.0	572.2	<b>563.8</b>	557.9	542.3	532.0

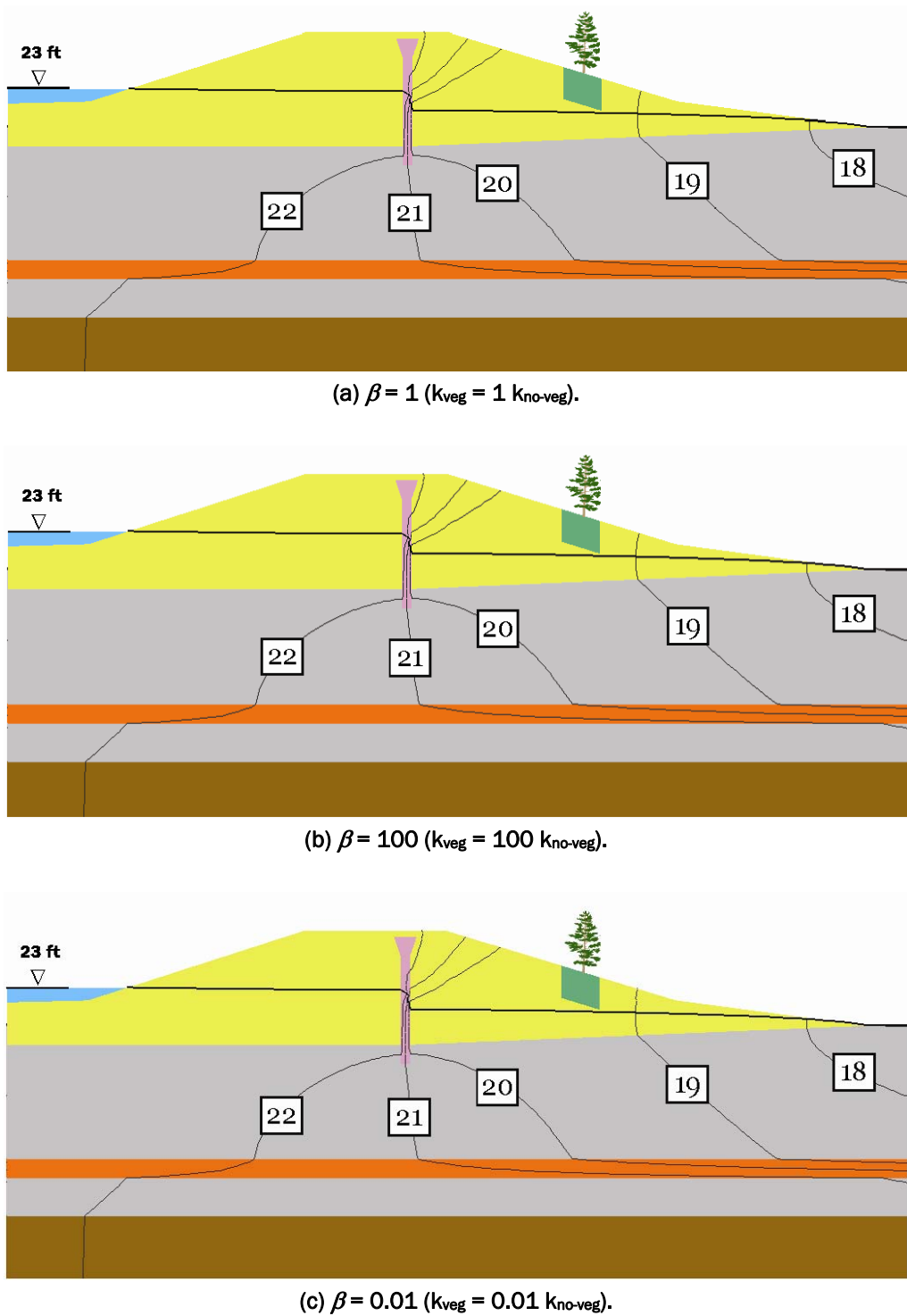


Figure 29. Total head (ft) contours and phreatic surface for El. 23 ft versus  $\beta$ , Pocket Levee, Sacramento, CA.

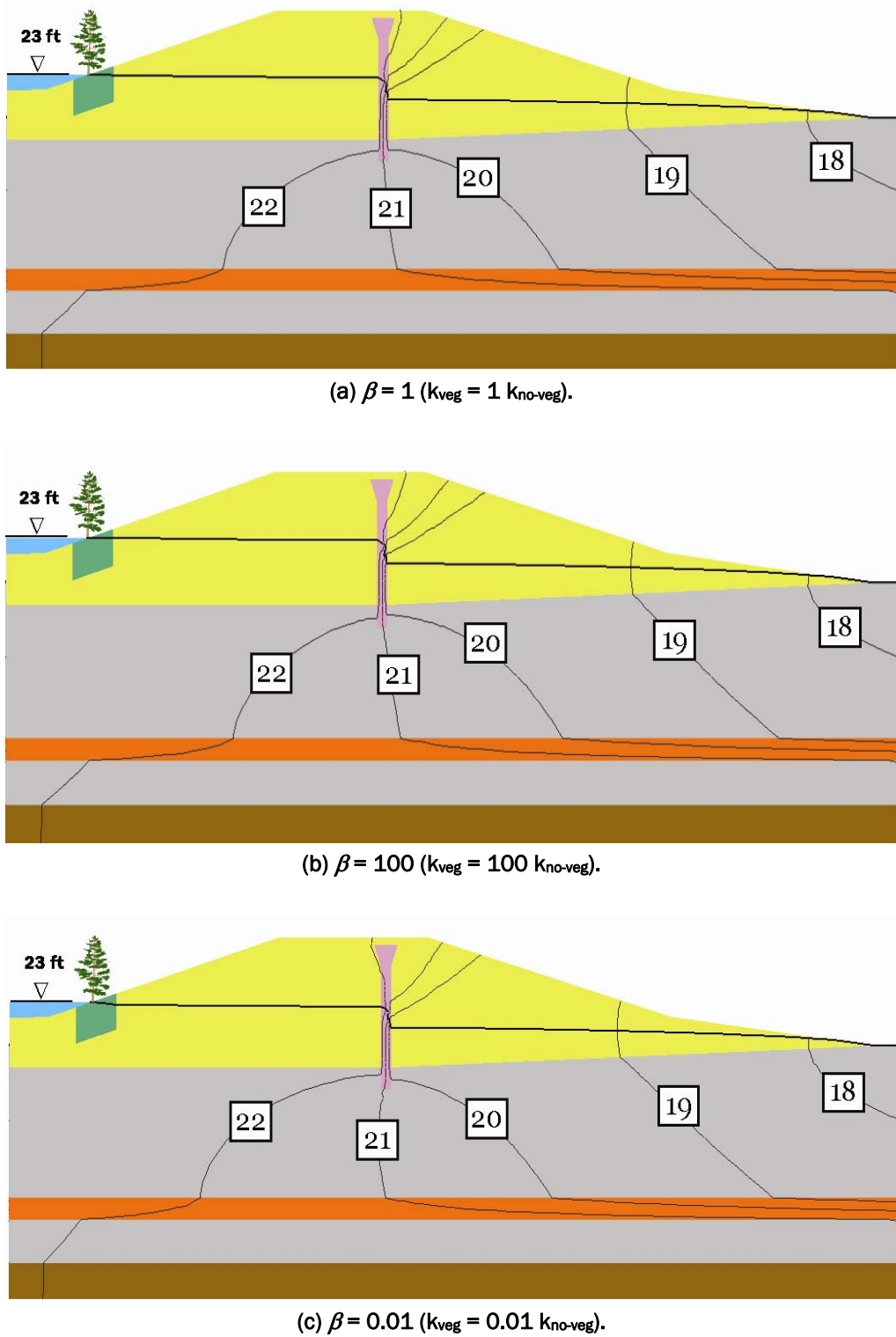
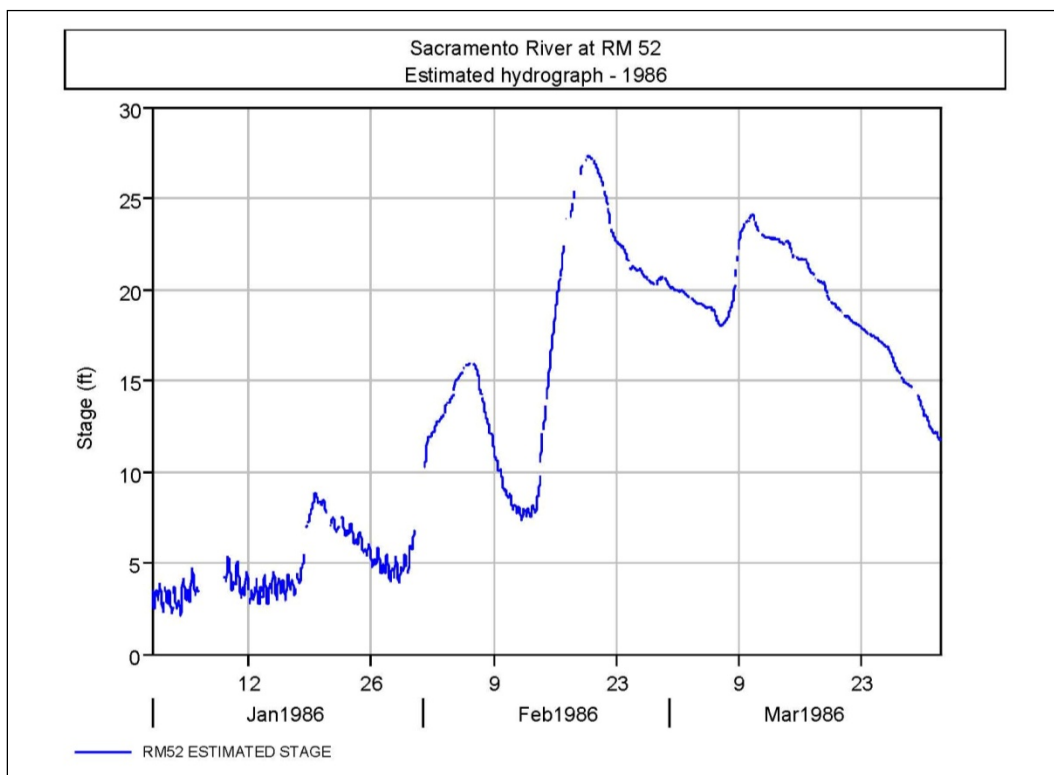


Figure 30. Total head (ft) contours and phreatic surface for El. 23 ft versus  $\beta$ , Pocket Levee, Sacramento, CA.



**Figure 31. Hydrograph of the 1986 Flood, Sacramento River, at River Mile (RM) 52. Pocket Levee, Sacramento, CA.**

boundary condition. The cross section for this study is approximately 1.6 miles downstream from the U.S. Geological Survey (USGS) gauge used to plot the hydrographs. Because of this, 0.8 ft was subtracted from the hydrograph values. The beginning point on the adjusted hydrograph was the elevation of the river at 12 ft. Thus, the initial solution applied a total head of 12 ft on both the riverside and landside boundaries and used the steady-state version of SEEP2D. With the initial solution from this output, the riverside boundary condition for the transient simulation was set according to the adjusted hydrograph.

### **No woody vegetation zone**

Figure 32 shows the initial phreatic surface and Figures 33 through 35 show the phreatic surface after 3, 4, and 5 hr, respectively. These runs were done without considering any change in hydraulic conductivity. The river level was 23.2 ft after 3 hr, 25.3 ft after 4 hr, and 26.5 ft after 5 hr. An observation from these results is as follows:

- For a given level of the river, the phreatic surface does not have time to reach the steady-state solution computed at this same river level.

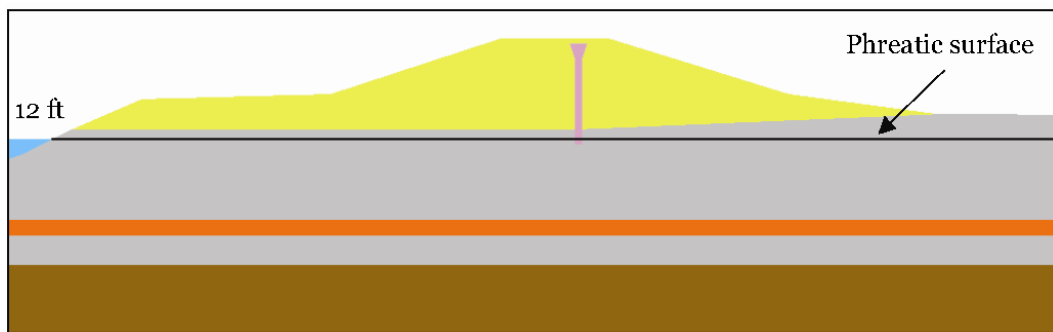


Figure 32. Initial phreatic surface.

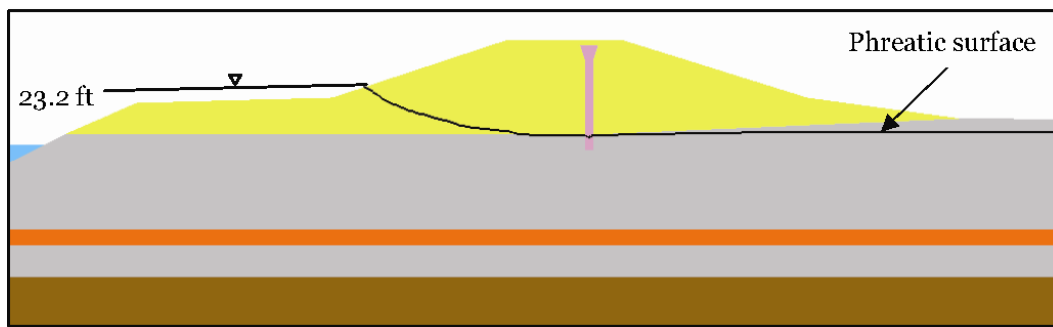


Figure 33. Phreatic surface after 3 hr.

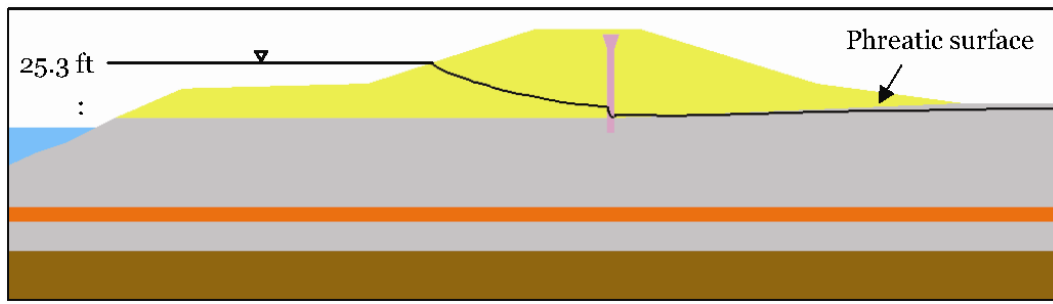


Figure 34. Phreatic surface after 4 hr.

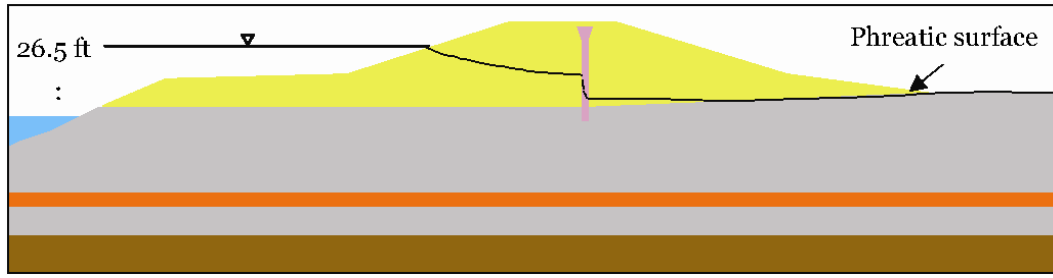


Figure 35. Phreatic surface after 5 hr.

***Woody vegetation (single tree) zone on the toe of the levee***

Although the phreatic surface does not reach the steady-state levels for a given river elevation, it does pass through woody vegetation zones near the toe of the levee. Therefore, the sixth zone in Figure 4 (i.e., the zone on the toe of the levee) is again considered. Figure 36 shows the effect of this zone on the phreatic surface for values of  $\beta = 1, 100$ , and  $0.01$ . Tables 13 and 14 give magnitude of gradient and pore pressure, respectively, for the selected nodes in Figure 37 in the transient case after the river reaches an elevation of 26 ft. Therefore, these results can be directly compared with the steady-state results given in Tables 9 and 10 containing steady-state results for El. 26 ft. Nodes that have negative pressures are not tabulated. Gradients are not of concern in the unsaturated zone because there is no upward pressing force to cause seepage or piping. The observations from these results are as follows:

- Magnitudes of gradient are lower in the transient case as compared to the steady-state case.
- Pore pressures are lower in the transient case as compared to the steady-state case.
- The lower the phreatic surface, the lower the exit point and the less the surface of seepage. The surface of seepage is defined as the portion of the levee face on the downstream side that starts at the exit point (where the phreatic surface intersects the levee face) and ends at the tailwater level. Water seeps out along this surface. When the woody vegetation zone is less pervious ( $\beta = 0.01$ ), the phreatic surface lags its position in the surrounding soil, thus making the zone a momentary barrier to the advancing surface. This effect does not last beyond the zone, as the phreatic surface comes back even closer to the landside slope than for the case where there is no zone. Exit gradients for nodes 5 and 6 are larger.
- When the woody vegetation zone is more pervious ( $\beta = 100$ ), the phreatic surface advances faster than the case without vegetation. However, this effect only lasts directly under the zone, and the phreatic surface returns very close to its original position beyond the zone. In this particular scenario, the phreatic surface, although closer, did not become part of the surface of seepage, and magnitudes of gradient were lower because of the zone. Therefore, for all values of  $\beta$ , the effect of changes in the hydraulic conductivity on the advancing phreatic line is local to the woody vegetation zone and is momentary.

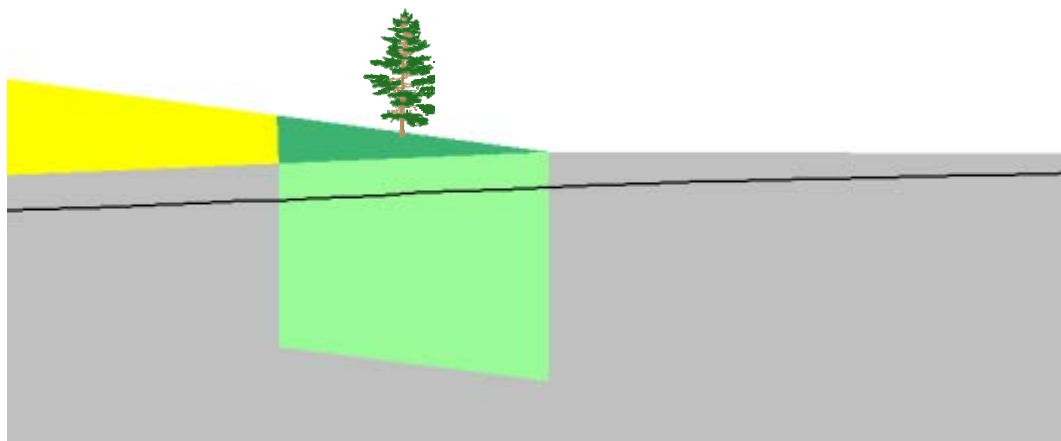
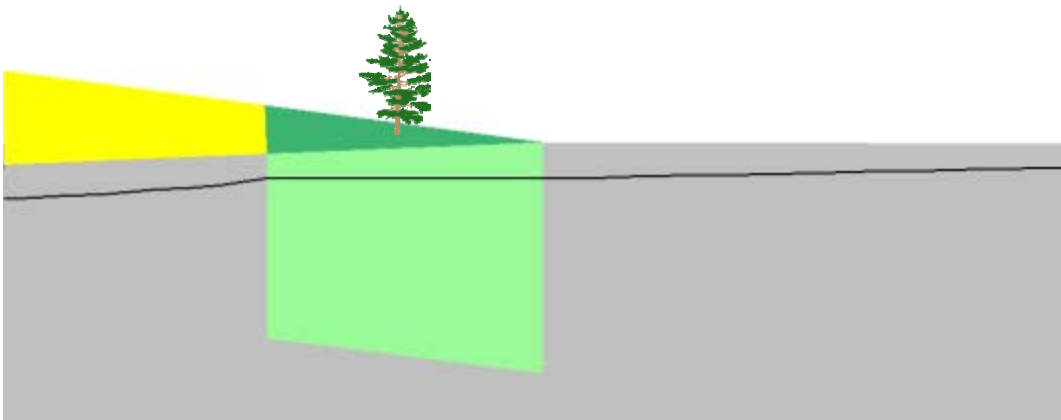
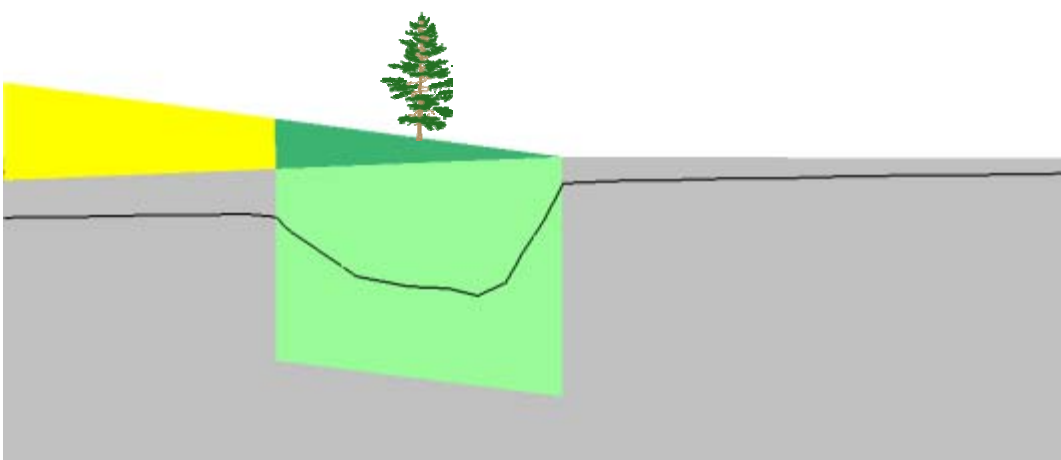
(a)  $\beta = 1$  ( $k_{veg} = k_{no-veg}$ ).(b)  $\beta = 100$  ( $k_{veg} = 100 k_{no-veg}$ ).(c)  $\beta = 0.01$  ( $k_{veg} = 0.01 k_{no-veg}$ ).

Figure 36. Phreatic surface near the woody vegetation zone for the transient case versus  $\beta$ , Pocket Levee, Sacramento, CA.

**Table 13. Magnitude of gradient at selected nodes for different values of hydraulic conductivity for transient case, Pocket Levee, Sacramento, CA.**

Node	$\beta = 0.01$	$\beta = 1$	$\beta = 100$
1	-	-	-
2	-	-	-
3	-	0.128	0.003
4	-	0.096	0.003
5	1.026	0.102	0.003
6	1.498	0.094	0.003
7	0.086	0.094	0.109
8	0.069	0.090	0.127
9	0.089	0.095	0.106
10	0.080	0.091	0.110

**Table 14. Pore pressure (lb/ft<sup>2</sup>) at selected nodes for different values of hydraulic conductivity for transient case, Pocket Levee, Sacramento, CA.**

Node	$\beta = 0.01$	$\beta = 1$	$\beta = 100$
1	-	-	-
2	-	-	-
3	-	51.0	54.9
4	-	104.1	99.5
5	94.7	133.8	133.1
6	88.0	136.5	150.8
7	370.1	362.3	352.8
8	383.1	373.8	362.4
9	488.1	481.5	473.7
10	491.6	484.1	485.5

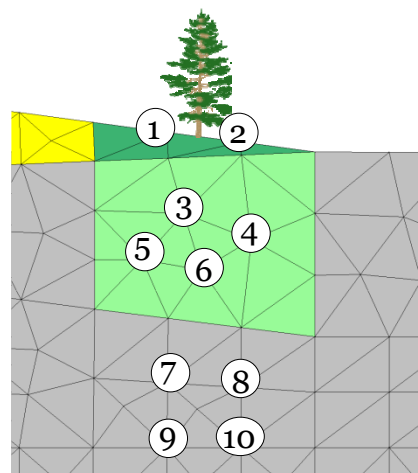


**Figure 37. Selected nodes, Pocket Levee, Sacramento, CA.**

### ***Woody vegetation zone near the end of the levee on the riverside***

The first woody vegetation zone in Figure 4 is near the end of the levee sand layer on the riverside, and is representative of zones on the riverside of the levee. Figure 38 shows the phreatic surface when the river is at El. 20 ft for  $\beta = 1$ , Figure 39 shows the phreatic surface when the river is at El. 20 ft for  $\beta = 100$ , and Figure 40 shows the phreatic surface when the river is at El. 20 ft for  $\beta = 0.01$ . The following observations can be gleaned from these figures:

- As seen earlier, the phreatic surface lags when  $\beta = 0.01$  and increases when  $\beta = 100$  [see (a) of Figures 38 through 40].
- However, by the time the phreatic surface reaches the SBC slurry wall, there is no noticeable difference in the position of the phreatic surface [see (b) of Figures 38 through 40] downstream of the SBC slurry wall on the landside.
- Changes in hydraulic conductivity on the riverside do not affect the landside flow conditions.

### ***Woody vegetation (single tree) zone with extended lateral root systems***

Some trees may exhibit extended lateral root systems. To simulate this phenomenon in 2-D, elements 18 ft on either side of the woody vegetation zone on the toe of the levee and near the surface were treated as part of the zone, as shown in 41. This number is arbitrary to test the effect of an extended lateral root and is not based on actual field measurements.

Figures 41 through 44 show the phreatic surface, total head contours, and velocity vectors for  $\beta = 1, 100$ , and  $0.01$ , respectively, for steady-state at El. 29 ft. Figure 45 shows nodes where the magnitude of the gradient (Table 15) and pore pressure (Table 16) are tabulated. To understand these results, the critical gradient is defined as

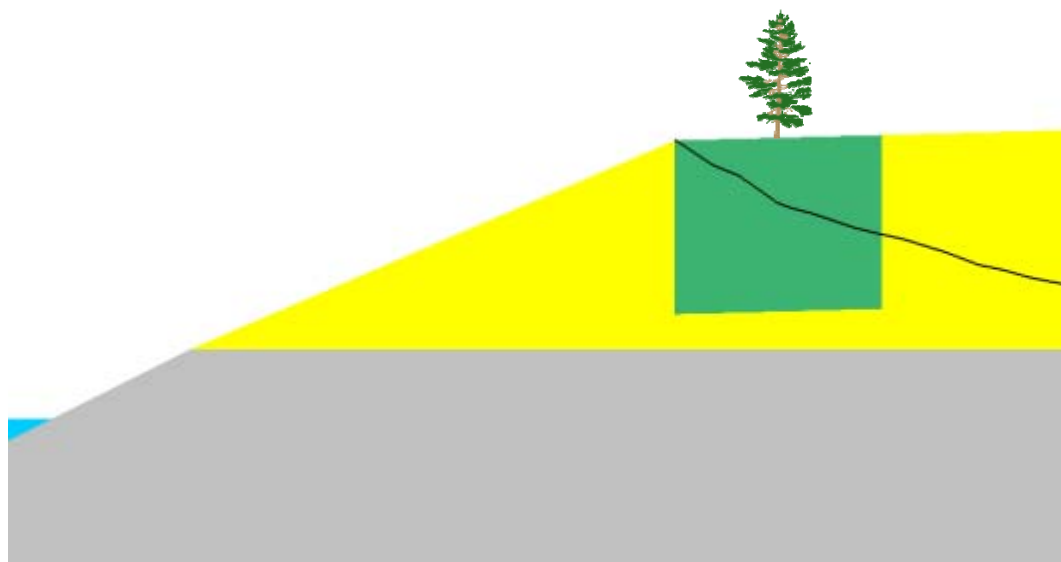
$$i_c = \frac{\gamma_{ss}}{\gamma_w} - 1 \quad (8)$$

where:

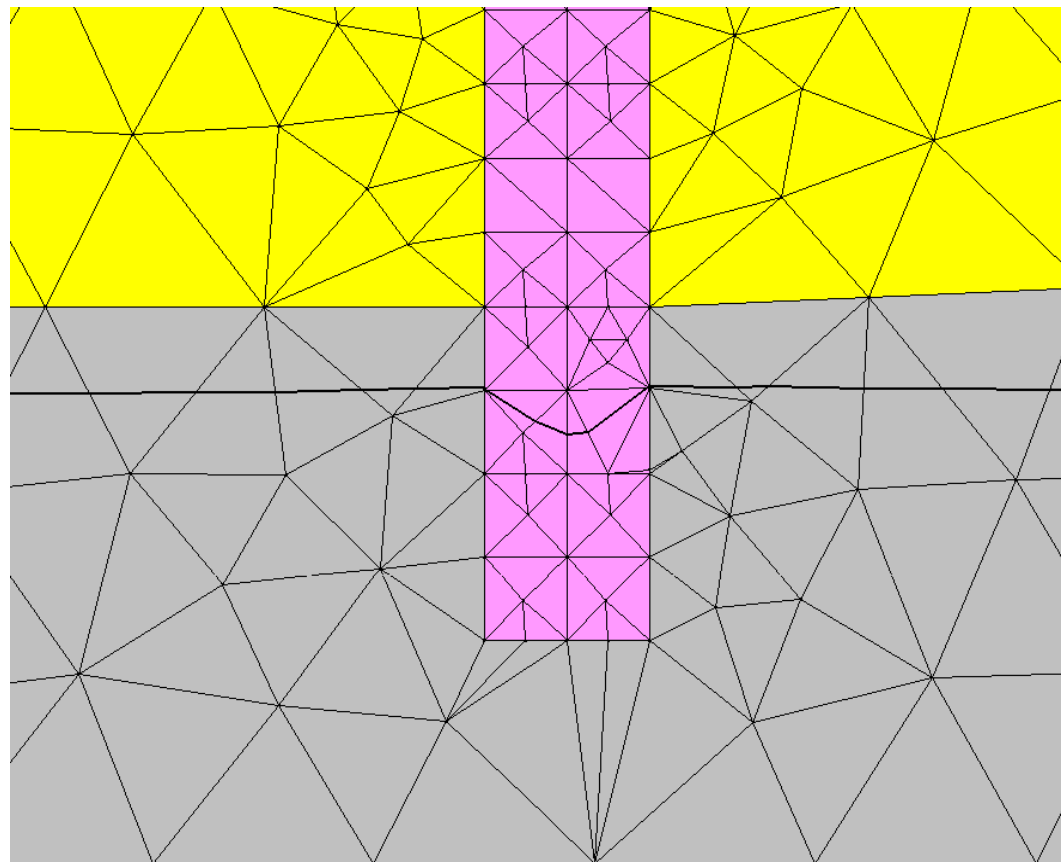
$i_c$  = critical gradient

$\gamma_{ss}$  = density of saturated soil

$\gamma_w$  = density of water.

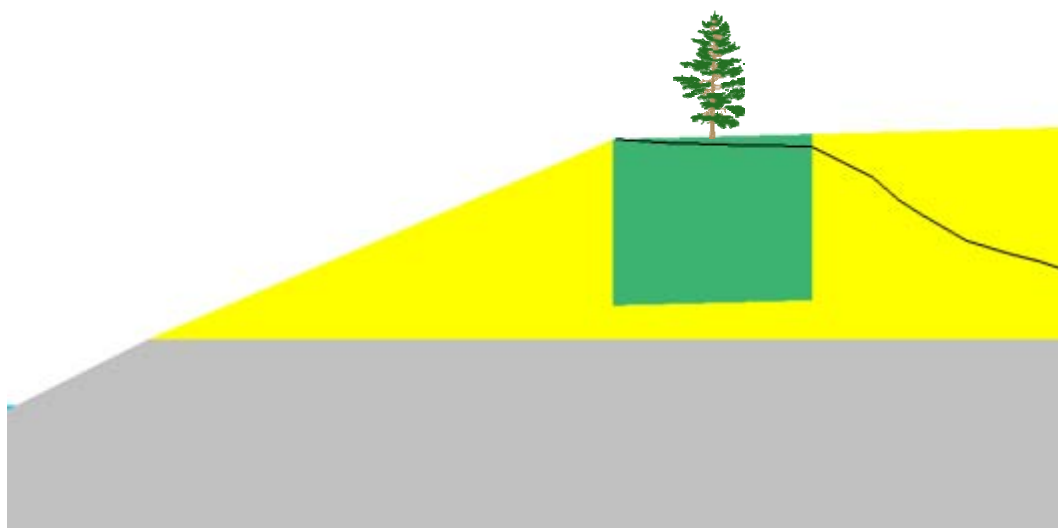


(a) Phreatic surface at the woody vegetation zone.

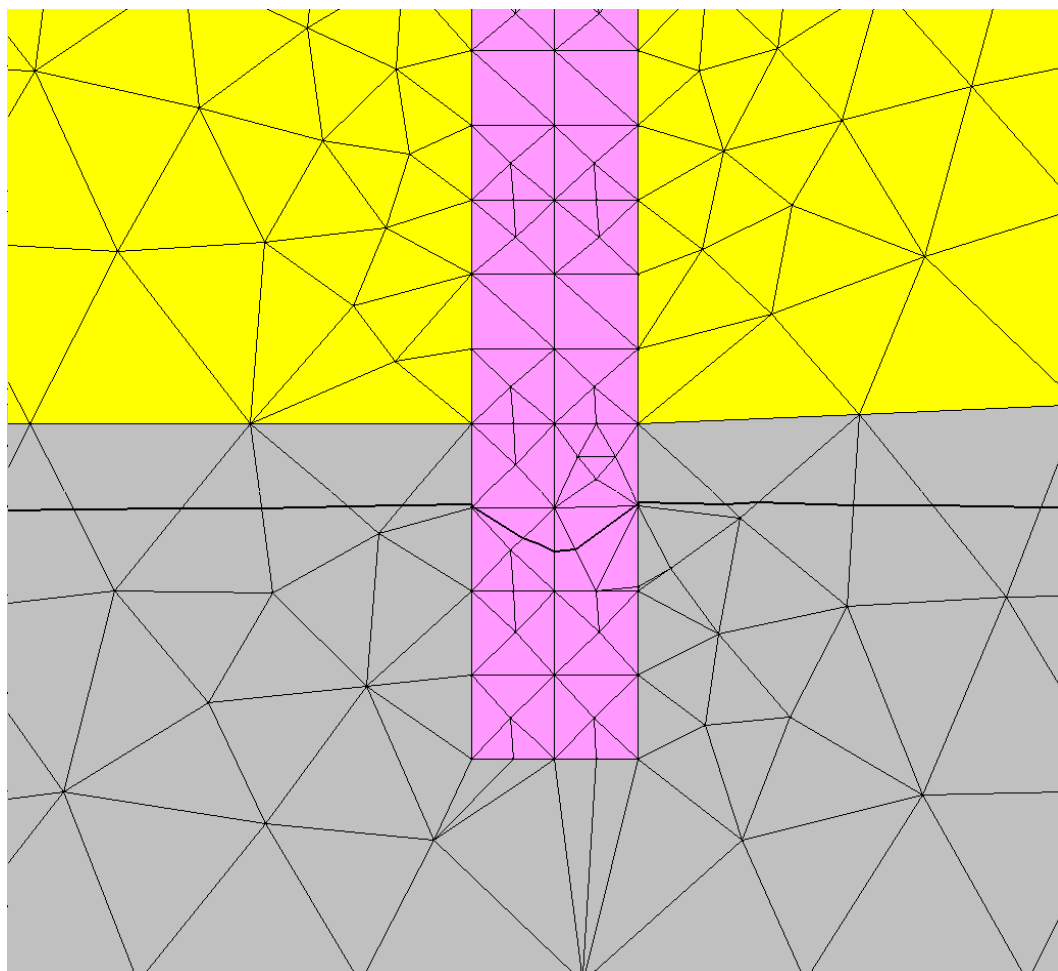


(b) Phreatic surface at the SBC slurry wall.

Figure 38. Phreatic surface for  $\beta = 1$  ( $k_{veg} = 1 k_{no-veg}$ ), Pocket Levee, Sacramento, CA.

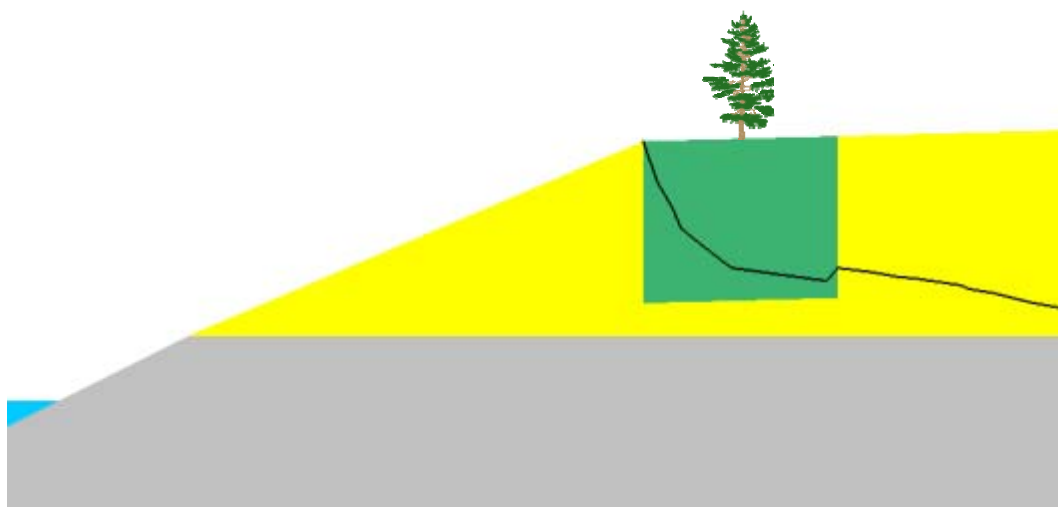


(a) Phreatic surface at the woody vegetation zone.

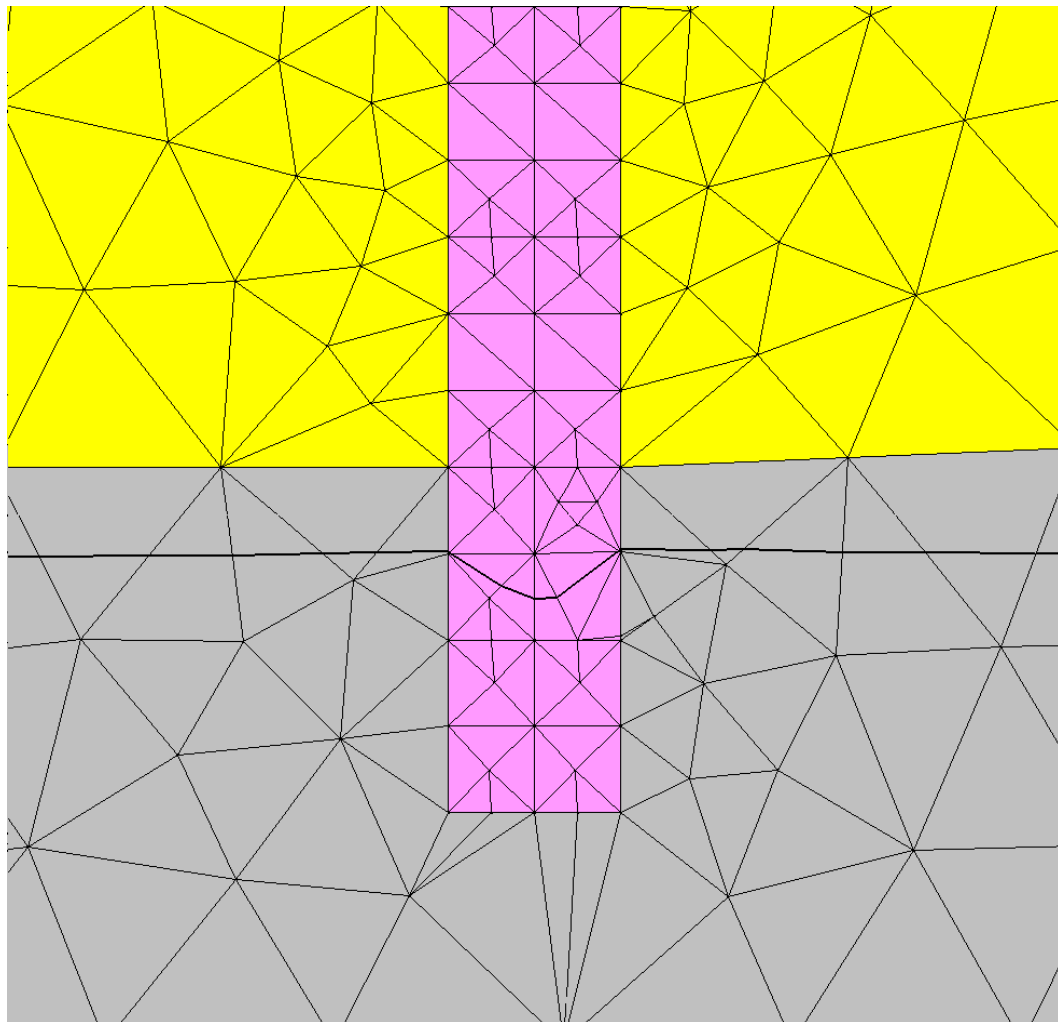


(b) Phreatic surface at the SBC slurry wall.

Figure 39. Phreatic surface for  $\beta = 100$  ( $k_{veg} = 100 k_{no-veg}$ ), Pocket Levee, Sacramento, CA.



(a) Phreatic surface at the woody vegetation zone.



(b) Phreatic surface at the SBC slurry wall.

Figure 40. Phreatic surface for  $\beta = 0.01$  ( $K_{veg} = 0.01 K_{no-veg}$ ),  
Pocket Levee, Sacramento, CA.

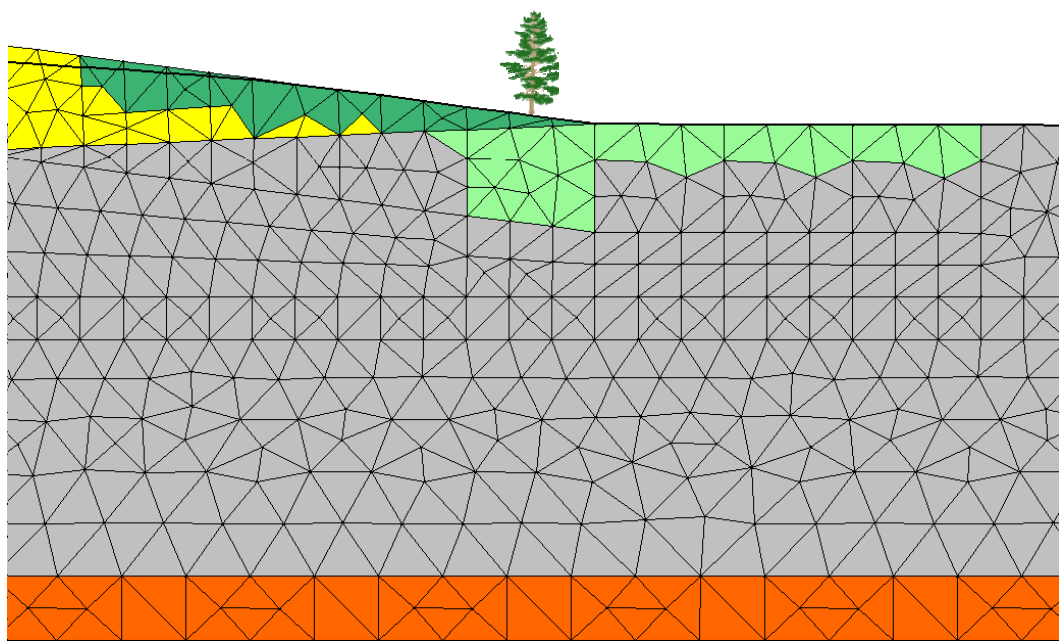


Figure 41. Woody vegetation zone with extended root system,  
Pocket Levee, Sacramento, CA.

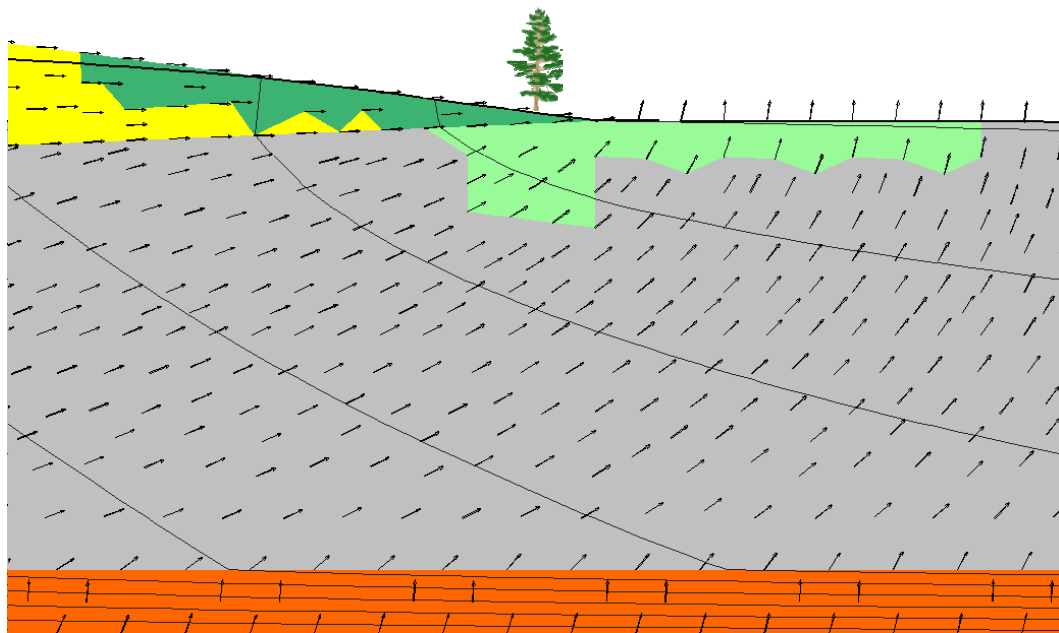


Figure 42. Total head contours, phreatic surface, and velocity vectors  
for  $\beta = 1$  ( $k_{veg} = 1 k_{no-veg}$ ), Pocket Levee, Sacramento, CA.

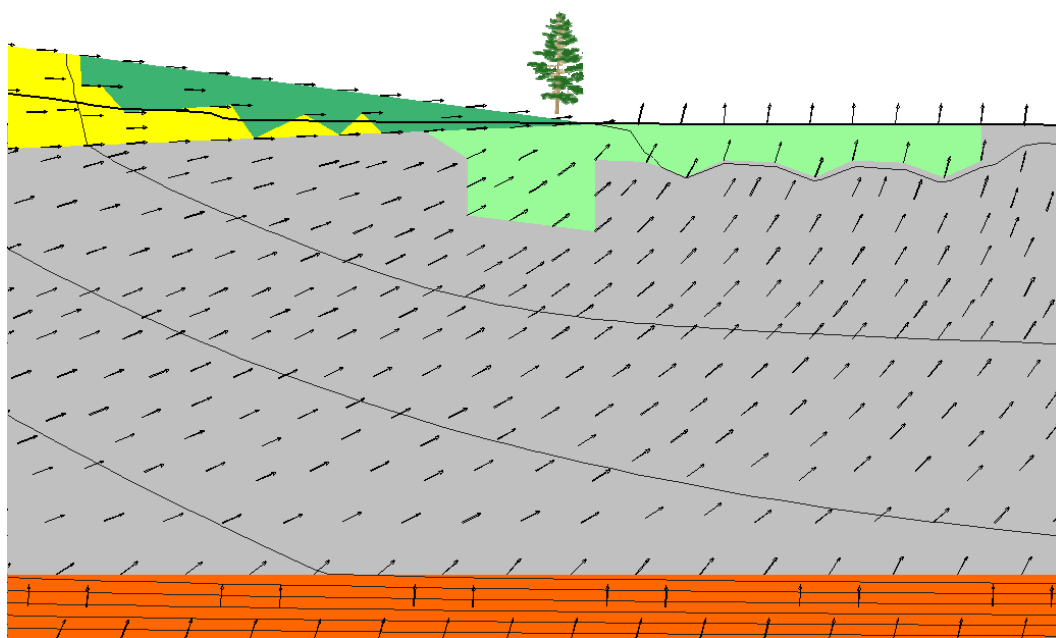


Figure 43. Total head contours, phreatic surface, and velocity vectors  
for  $\beta = 100$  ( $K_{veg} = 100 K_{no-veg}$ ), Pocket Levee, Sacramento, CA.

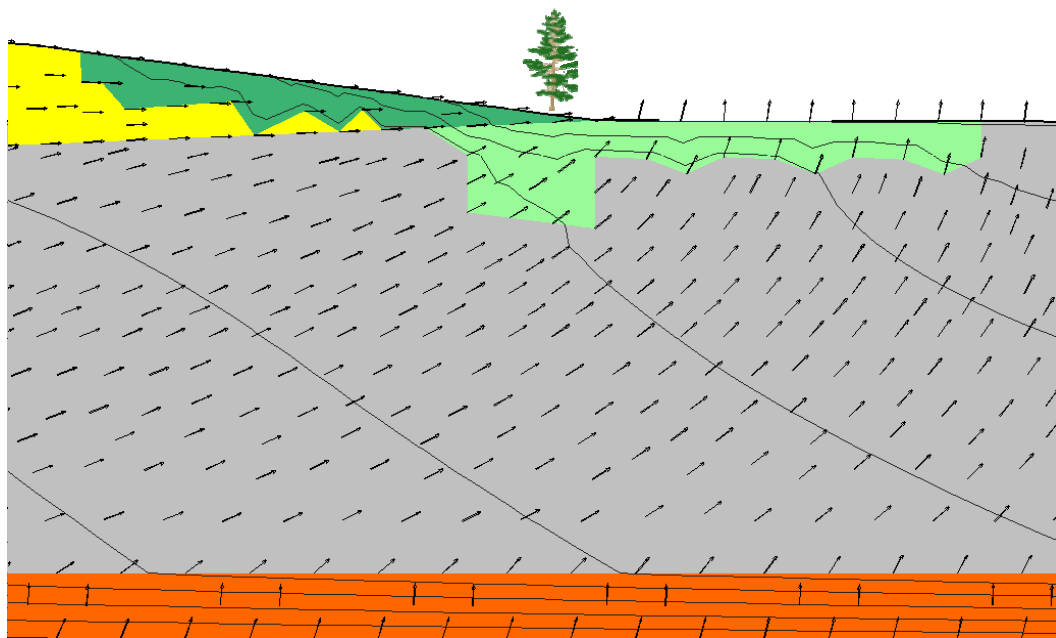


Figure 44. Total head contours, phreatic surface, and velocity vectors  
for  $\beta = 0.01$  ( $K_{veg} = 0.01 K_{no-veg}$ ), Pocket Levee, Sacramento, CA.

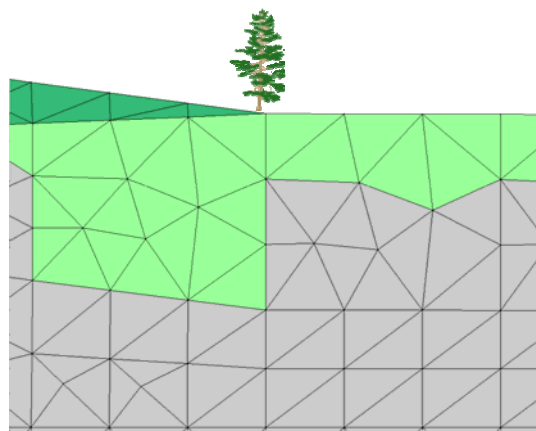


Figure 45. Selected nodes, Pocket Levee, Sacramento, CA.

**Table 15. Magnitude of gradient at selected nodes for different values of hydraulic conductivity for the extended root case, Pocket Levee, Sacramento, CA.**

Node	$\beta = 1$	$\beta = 100$	$\beta = 0.01$
1	0.235	0.015	1.013
2	0.284	0.009	1.434
3	0.239	0.005	0.982
4	9.221	0.004	1.370
5	0.241	0.020	0.620
6	0.217	0.050	0.217
7	0.218	0.038	0.092
8	0.209	0.066	0.080
9	0.188	0.150	0.113
10	0.188	0.135	0.096

**Table 16. Pore pressure (lb/ft<sup>2</sup>) at selected nodes for different values of hydraulic conductivity for the extended root case, Pocket Levee, Sacramento, CA.**

Node	$\beta = 1$	$\beta = 100$	$\beta = 0.01$
1	0.0	0.0	0.0
2	0.0	0.0	0.0
3	0.0	0.0	0.0
4	0.0	0.0	0.0
5	139.1	110.1	262.7
6	188.8	153.1	302.9
7	261.4	211.0	365.5
8	268.6	222.7	373.5
9	385.1	325.2	480.8
10	380.1	330.0	473.2

Effects from the woody vegetation zone are increased with the addition of the extended root. The observations from these results are as follows:

- The exit gradient increased dramatically when the extended root is much less pervious ( $\beta = 0.01$ ) than its surroundings.
- Conversely, if the extended root system is significantly more pervious ( $\beta = 100$ ), all the magnitudes of gradient are reduced, and those on the surface are reduced significantly, meaning that the probability of a seepage exit through the confining layer, and, therefore, the probability of initiation of erosion in the foundation is unlikely.
- Magnitudes of gradient are increased dramatically when the extended root is much less pervious ( $\beta = 0.01$ ) than its surroundings.
- Conversely, if the extended root system is significantly more pervious ( $\beta = 100$ ), the magnitudes of gradient are reduced, and those on the surface are significantly reduced.

*Effect of a deep root system on the Pocket Levee, Sacramento, CA*

Roots from woody vegetation may extend horizontally along and near the surface of the levee. Other times, they may grow more in a vertical direction. To continue the theme of conducting a study of the effects of woody vegetation on levees, a comparison was made for the effect of a zone of 6 ft  $\times$  5 ft versus one with dimensions of 6 ft  $\times$  10 ft. The zone considered for this exercise is just beyond the levee toe. Figure 46 shows this idealized zone without the extended depth, and Figure 47 shows the zone with the added depth. In both cases, the same nodes were analyzed for magnitude of gradient (Tables 17 and 19) and pore pressure (Tables 18 and 20).

The observations are as follows:

- Magnitude of gradient inside the woody vegetation zone decreased with increasing  $\beta$  and increased with decreasing  $\beta$  for most nodes.
- Pore pressure inside the woody vegetation zone decreased with increasing  $\beta$  and increased with decreasing  $\beta$  for most nodes.
- The longer woody vegetation zone resulted in less variation of both magnitude of gradient and pore pressure when varying  $\beta$  as compared to the original woody vegetation zone.

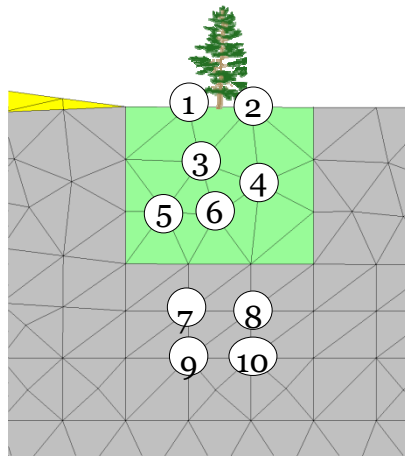


Figure 46. Woody vegetation zone with dimensions of 6 ft  $\times$  5 ft.

Table 17. Magnitude of gradient at selected nodes for different values of  $\beta$  for the 6 ft  $\times$  5 ft zone.

Point	$\beta = 0.5$	$\beta = 0.1$	$\beta = 0.01$	$\beta = 1$	$\beta = 2$	$\beta = 10$	$\beta = 100$
1	0.323	0.369	0.382	<b>0.284</b>	0.230	0.093	0.011
2	0.257	0.265	0.263	<b>0.239</b>	0.202	0.087	0.013
3	0.271	0.305	0.314	<b>0.241</b>	0.197	0.081	0.011
4	0.246	0.285	0.297	<b>0.217</b>	0.171	0.072	0.010
5	0.245	0.275	0.282	<b>0.218</b>	0.178	0.073	0.010
6	0.245	0.296	0.312	<b>0.209</b>	0.165	0.065	0.009
7	0.145	0.115	0.106	<b>0.168</b>	0.198	0.284	0.302
8	0.153	0.137	0.134	<b>0.167</b>	0.188	0.248	0.288
9	0.142	0.128	0.124	<b>0.154</b>	0.170	0.212	0.237
10	0.145	0.135	0.132	<b>0.154</b>	0.167	0.203	0.226

Table 18. Pore pressure (lb/ft<sup>2</sup>) at selected nodes for different values of  $\beta$  for the 6 ft  $\times$  5 ft zone.

Point	$\beta = 0.5$	$\beta = 0.1$	$\beta = 0.01$	$\beta = 1$	$\beta = 2$	$\beta = 10$	$\beta = 100$
1	0.0	0.0	0.0	<b>0.0</b>	0.0	0.0	0.0
2	0.0	0.0	0.0	<b>0.0</b>	0.0	0.0	0.0
3	142.8	147.0	148.1	<b>139.1</b>	133.6	119.4	110.8
4	191.8	193.7	193.9	<b>188.8</b>	183.1	165.7	154.5
5	269.1	278.4	281.1	<b>261.4</b>	250.9	224.5	208.8
6	275.1	282.7	284.7	<b>268.6</b>	259.0	233.9	218.6
7	501.6	510.0	512.3	<b>494.5</b>	484.3	457.8	441.6
8	495.7	503.4	505.5	<b>489.2</b>	479.7	454.2	438.4
9	607.8	614.1	615.8	<b>602.4</b>	594.5	573.4	560.4
10	602.2	608.1	609.6	<b>597.0</b>	589.4	568.8	556.0

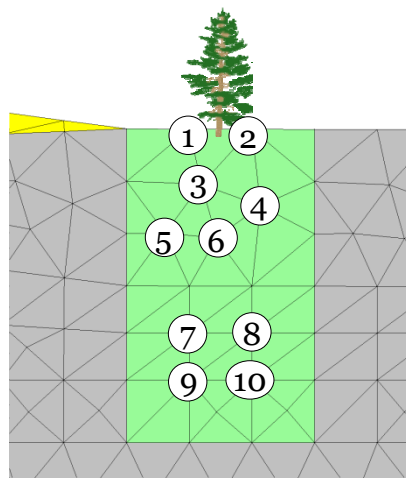


Figure 47. Woody vegetation zone with dimensions of 6 ft  $\times$  10 ft.

Table 19. Magnitude of gradient at selected nodes for different values of  $\beta$  for the 6 ft  $\times$  10 ft zone.

Point	$\beta = 0.5$	$\beta = 0.1$	$\beta = 0.01$	$\beta = 1$	$\beta = 2$	$\beta = 10$	$\beta = 100$
1	0.318	0.363	0.380	<b>0.284</b>	0.228	0.116	0.016
2	0.248	0.240	0.232	<b>0.239</b>	0.216	0.111	0.018
3	0.261	0.287	0.298	<b>0.241</b>	0.210	0.107	0.016
4	0.229	0.243	0.249	<b>0.217</b>	0.194	0.102	0.016
5	0.241	0.285	0.308	<b>0.218</b>	0.189	0.098	0.015
6	0.227	0.259	0.275	<b>0.209</b>	0.184	0.096	0.015
7	0.185	0.221	0.241	<b>0.168</b>	0.147	0.076	0.012
8	0.186	0.226	0.249	<b>0.167</b>	0.145	0.076	0.012
9	0.172	0.201	0.216	<b>0.154</b>	0.129	0.063	0.009
10	0.182	0.239	0.268	<b>0.154</b>	0.124	0.059	0.009

Table 20. Pore pressure (lb/ft<sup>2</sup>) at selected nodes for different values of  $\beta$  for the 6 ft  $\times$  10 ft zone.

Point	$\beta = 0.5$	$\beta = 0.1$	$\beta = 0.01$	$\beta = 1$	$\beta = 2$	$\beta = 10$	$\beta = 100$
1	0.0	0.0	0.0	<b>0.0</b>	0.0	0.0	0.0
2	0.0	0.0	0.0	<b>0.0</b>	0.0	0.0	0.0
3	142.1	145.9	147.1	<b>139.1</b>	134.8	122.0	111.4
4	190.5	190.2	189.2	<b>188.8</b>	185.2	169.3	155.3
5	268.0	277.7	281.7	<b>261.4</b>	252.8	229.4	209.9
6	272.9	277.3	278.5	<b>268.6</b>	260.2	239.4	219.8
7	502.0	400.2	514.4	<b>494.5</b>	483.2	445.2	411.4
8	493.5	494.8	493.9	<b>489.2</b>	480.8	444.7	411.5
9	611.0	621.0	624.5	<b>602.4</b>	589.4	545.2	505.9
10	602.6	605.5	605.2	<b>597.0</b>	586.8	544.5	505.8

*Parameter study of the blanket thickness of the Pocket Levee*

A parameter study of the blanket thickness was conducted to show the impact on the gradient. The effect of a woody vegetation zone for each of the selected blanket thicknesses was also determined. Figure 48 shows four selected nodes for which magnitude of gradient was obtained.

Table 21 gives the magnitudes of gradient for blanket thickness of 30 ft (original configuration), 25 ft, 20 ft, 15 ft, 10 ft, 5 ft, and no thickness of the blanket.

This was accomplished by replacing additional layers of clay and silty clay of the blanket with the aquifer sand. The different layers are constant, except the top one that starts out at a 5-ft thickness at the toe of the levee to zero at the end of the landside approximately 2,000 ft away. The observations that can be drawn are:

- The gradient in the blanket is calculated as the head loss in the blanket divided by the blanket thickness; therefore, as the blanket thickness decreases, the magnitude of gradient increases.
- When there is no blanket remaining (zero thickness), gradients are significantly lower.
- The global phenomenon of smaller gradients for  $\beta = 100$  (more pervious) and larger gradients for  $\beta = 0.01$  (less pervious) is again observed.
- At small values of the blanket thickness, the gradients are becoming high and could exceed the critical gradient.

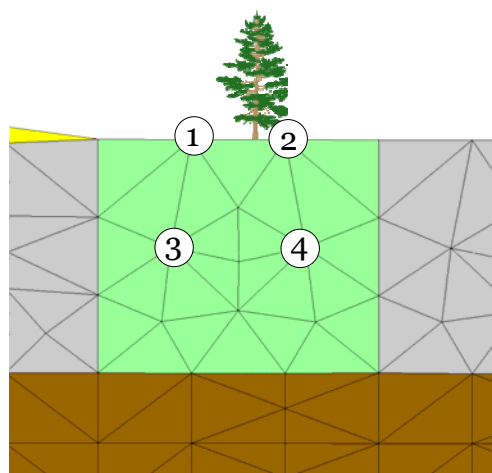


Figure 48. Selected nodes.

**Table 21. Magnitude of gradient at selected nodes for different values of  $\beta$  and for different blanket thicknesses.**

Blanket Thickness at the Toe (ft)	Node	$\beta = 0.01$	$\beta = 1$	$\beta = 100$
30	1	0.368	<b>0.275</b>	0.011
30	2	0.259	<b>0.237</b>	0.013
30	3	0.323	<b>0.241</b>	0.010
30	4	0.290	<b>0.222</b>	0.011
25	1	0.377	<b>0.283</b>	0.011
25	2	0.268	<b>0.244</b>	0.013
25	3	0.332	<b>0.248</b>	0.011
25	4	0.299	<b>0.230</b>	0.011
20	1	0.458	<b>0.354</b>	0.015
20	2	0.350	<b>0.316</b>	0.017
20	3	0.416	<b>0.318</b>	0.014
20	4	0.385	<b>0.300</b>	0.015
15	1	0.613	<b>0.491</b>	0.023
15	2	0.509	<b>0.453</b>	0.025
15	3	0.579	<b>0.453</b>	0.021
15	4	0.551	<b>0.438</b>	0.022
10	1	0.807	<b>0.672</b>	0.036
10	2	0.706	<b>0.636</b>	0.038
10	3	0.782	<b>0.634</b>	0.034
10	4	0.759	<b>0.621</b>	0.034
5	1	1.179	<b>1.125</b>	0.401
5	2	1.100	<b>1.093</b>	0.403
5	3	1.112	<b>1.093</b>	0.404
5	4	1.099	<b>1.083</b>	0.399
0	1	0.331	<b>0.200</b>	0.005
0	2	0.185	<b>0.156</b>	0.007
0	3	0.261	<b>0.162</b>	0.005
0	4	0.215	<b>0.141</b>	0.006

#### *Mesh refinement study for the Pocket Levee*

A rather large number of finite elements were used for the Pocket Levee. Although this could imply that the results are valid, a mesh refinement study was still conducted with results for magnitude of gradient (Table 22) and pore pressure (Table 23) for the woody vegetation zone just beyond the toe being especially scrutinized (Figures 49 through 51).

Table 22. Magnitude of gradient at selected nodes for the different meshes.

Node	Slightly Refined Mesh	Original Mesh	Significantly Refined Mesh
1	0.273	0.284	0.295
2	0.235	0.239	0.246
3	0.270	0.266	0.274
4	0.220	0.220	0.215
5	0.212	0.210	0.216
6	0.198	0.198	0.197
7	0.186	0.188	0.185
8	0.191	0.188	0.187

Table 23. Pore pressure at selected nodes for the different meshes.

Node	Slightly Refined Mesh	Original Mesh	Significantly Refined Mesh
1	0.0	0.0	0.0
2	0.0	0.0	0.0
3	138.2	138.3	139.0
4	287.0	266.9	267.1
5	126.8	127.0	127.0
6	252.2	252.2	252.4
7	385.2	385.1	385.1
8	380.2	380.1	380.0

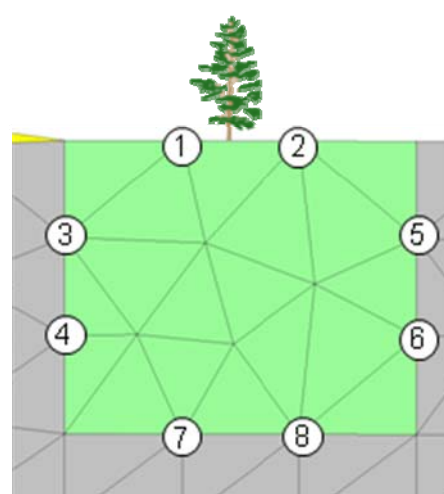


Figure 49. Original mesh, Pocket Levee, Sacramento, CA.

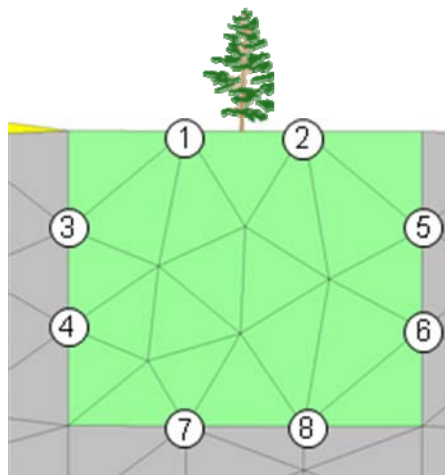


Figure 50. Slightly refined mesh,  
Pocket Levee, Sacramento, CA.

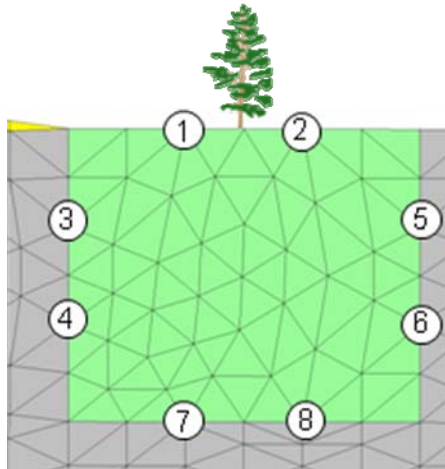


Figure 51. Significantly refined mesh,  
Pocket Levee, Sacramento, CA.

### Degradation of the slurry wall

It is feasible to accept that slurry walls may act as a root barrier, or that roots may actually penetrate and degrade a slurry wall. This section simulates what happens to the flow pattern when this occurs (see Figure 52 showing the degraded zone of the slurry wall in green). Figure 53 shows the original flow pattern, and Figure 54 shows the flow pattern (total head contours and free surface) when the degradation zone is considered as sand for the steady-state case of the river being at El. 29-ft. The primary difference in these two results is that the exit point for the original solution has coordinate, (564.0, 18.6), and the exit point for the modified case has coordinate, (550.0, 20.5). This represents some impact, as there is more surface of seepage. However, if the values of magnitude of gradient and pore pressure are considered for the nodes in Figure 55 (see Table 24), the

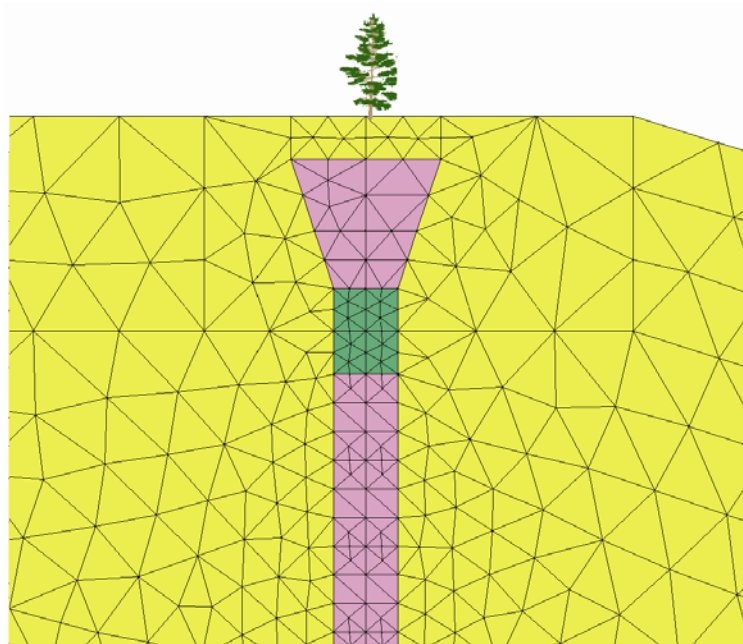


Figure 52. Zone representing degradation of the slurry wall.

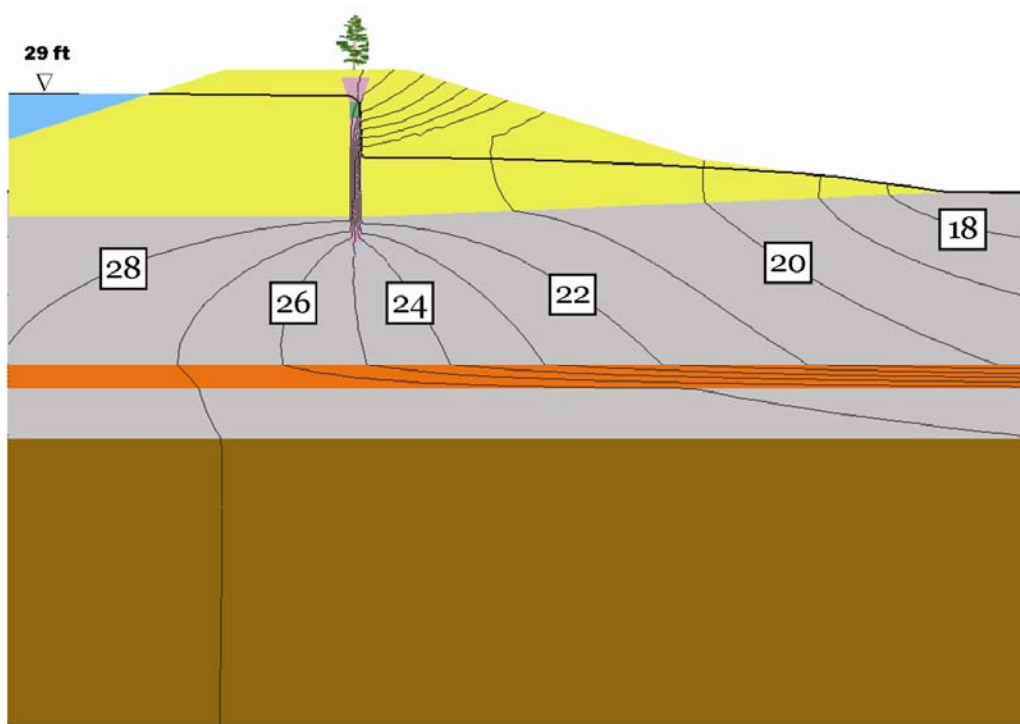


Figure 53. Original total head contours and phreatic surface.

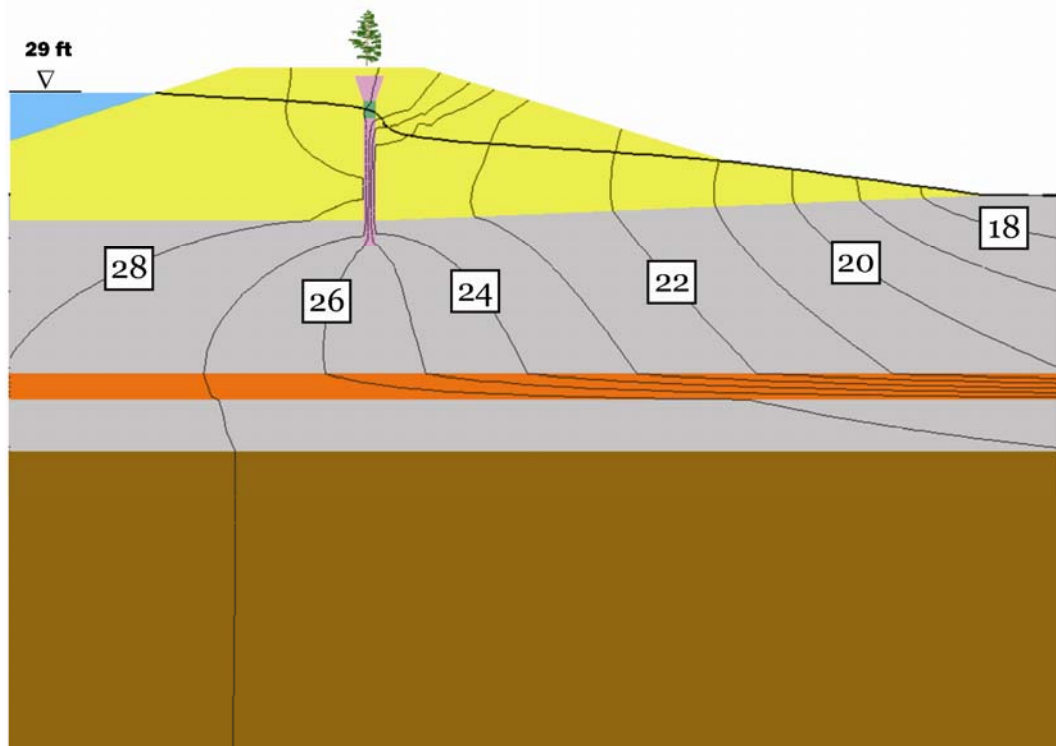


Figure 54. Total head contours and phreatic surface with the degradation zone as sand.

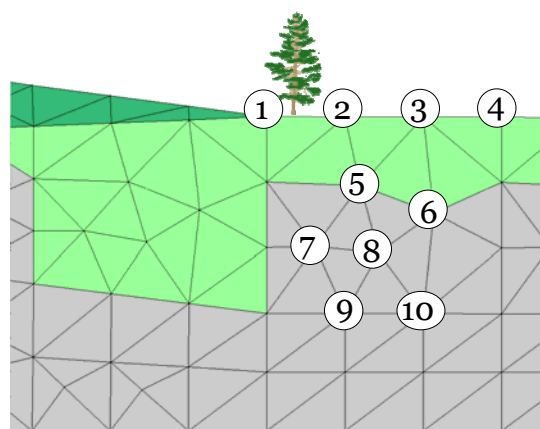


Figure 55. Selected nodes.

**Table 24.** Magnitude of gradient and pore pressure ( $\text{lb}/\text{ft}^2$ ) at selected points for the degradation of the slurry wall case.

Point	Magnitude of Gradient		Pore Pressure	
	Original	Modified	Original	Modified
1	0.235	0.251	0.0	0.0
2	0.284	0.307	0.0	0.0
3	0.239	0.258	0.0	0.0
4	9.221	0.239	0.0	0.0
5	0.241	0.262	139.1	141.5
6	0.217	0.236	188.8	191.8
7	0.218	0.240	261.4	266.2
8	0.209	0.229	268.6	273.1
9	0.188	0.207	385.1	391.7
10	0.188	0.205	380.1	386.1

numbers are only moderately larger. A detailed slope stability analysis is needed to realize the full impact for this case.

### Burlington, WA

Various phenomena were analyzed for the Pocket Levee model. As this is a nationwide study, other levees were also considered. The next three cross sections considered are from Burlington, WA, levees. These additional sites will either reveal characteristics of a woody vegetation zone on a levee, which are unique to the Pocket Levee, or observations from that modeling experience will apply to most levees in varying degrees of commonality.

#### *First cross section*

#### **Description of the 2-D model**

Figure 56 shows the levee with its material types and location of woody vegetation zones on the levee to be examined in detail. The first material is fill (levee) and is composed of silty sand (soil classification SM). The second material is overbank deposit (blanket) and contains silt (soil classification ML). Hydraulic conductivity for these materials is provided in Golder Associates (2009). These values are based on grain size analyses from representative samples from these major horizons. However, hydraulic conductivity for ML is lower than the expected value of  $10^{-4}$  for this soil type. The third material is channel deposit (aquifer), and is composed of the equivalent of poorly graded sand (soil classification SP).

Figure 57 shows a portion of the finite element mesh. The elevation used on the landside is always at 32.2 ft. The elevation of the river is set to 38.7 ft (which is the highest stage on the hydrograph used in the transient analysis) for steady-state flow analysis.

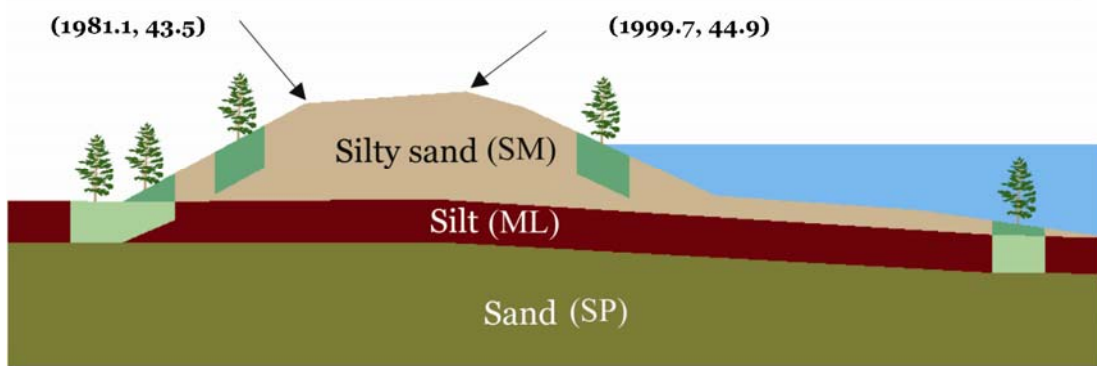


Figure 56. First cross section with material types and woody vegetation zones, Burlington, WA.

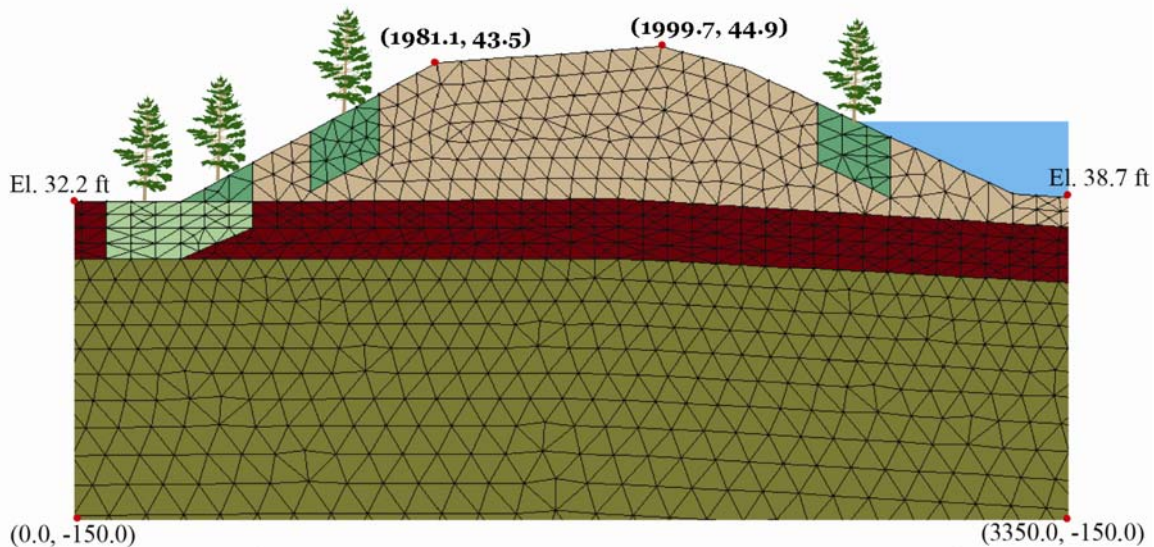


Figure 57. Portion of the finite element mesh for the first cross section of the Burlington Levee. The total mesh contains 19,560 nodes and 37,688 triangular elements.

### ***Soil properties***

Soil properties for the first Burlington Levee model are given in Tables 25 and 26. Table 25 shows saturated hydraulic conductivity for each soil layer and Table 26 provides the moisture content and van Genuchten parameters.

**Table 25.** First Burlington Levee model hydraulic conductivities.

Material	$k_H$ (cm/sec)	$k_H$ (ft/day)	$k_V$ (cm/sec)	$k_V$ (ft/day)
Silty sand (SM)	$1.17 \times 10^{-3}$	3.32	$1.17 \times 10^{-3}$	3.32
Silt (ML)	$2.00 \times 10^{-3}$	5.67	$1.00 \times 10^{-3}$	2.83
Sand (SP)	$4.00 \times 10^{-2}$	113.39	$4.00 \times 10^{-2}$	113.39

**Table 26.** First Burlington Levee model moisture content and van Genuchten soil properties.

Material	$\theta$	$\theta_s$	$\alpha$ (1/m)	$\alpha$ (1/ft)	$n$
Silty sand (SM)	0.041	0.440	10.2	3.11	2.24
Silt (ML)	0.034	0.460	1.60	0.488	1.37
Sand (SP)	0.045	0.430	14.5	4.42	2.68

The hydraulic conductivity values are from Golder Associates (2009). These values were based on grain size data from representative samples from these major horizons. However, the value for silt (ML) is higher than the usual hydraulic conductivity value of  $10^{-4}$  for a silt, according to the Unified Soil Classification System (USCS) and the CA Guidance of hydraulic conductivities.

*Steady-state results for woody vegetation zones*

### No woody vegetation

The model was first run without a woody vegetation zone. Figure 58 shows the location of the phreatic surface and total head contours, and Figure 59 shows the velocity vectors indicating the flow pattern. The following are observed:

- The phreatic surface is a flow line; therefore, the velocity vectors should appear essentially parallel to the phreatic surface.
- A surface of seepage exists where through-seepage could potentially be a problem. The effect of woody vegetation will be especially significant in this region.
- Underseepage begins just beyond the levee toe, as indicated by the vertical velocity vectors. This is a crucial area to investigate because of potential occurrence of a seepage exit through the confining layer.

Different positions of a woody vegetation zone on the levee are presented in the following figures.

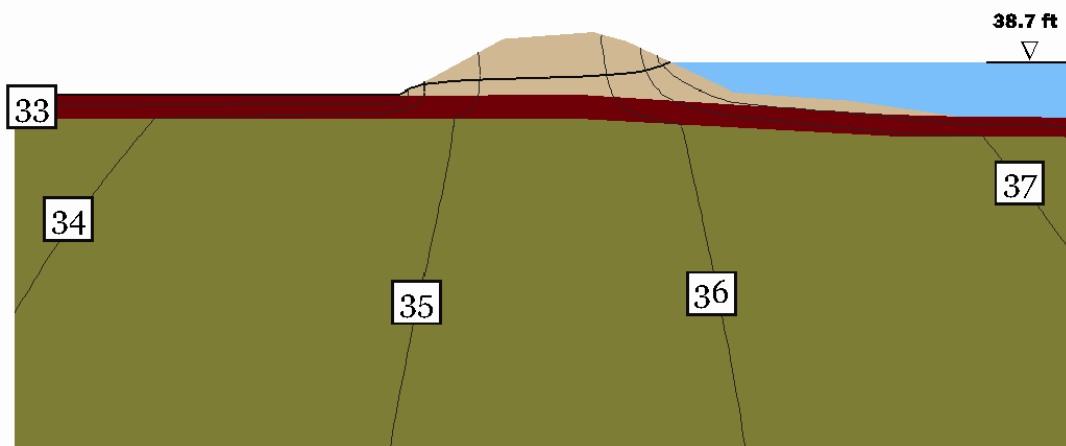


Figure 58. Total head contours and phreatic surface, Burlington, WA.

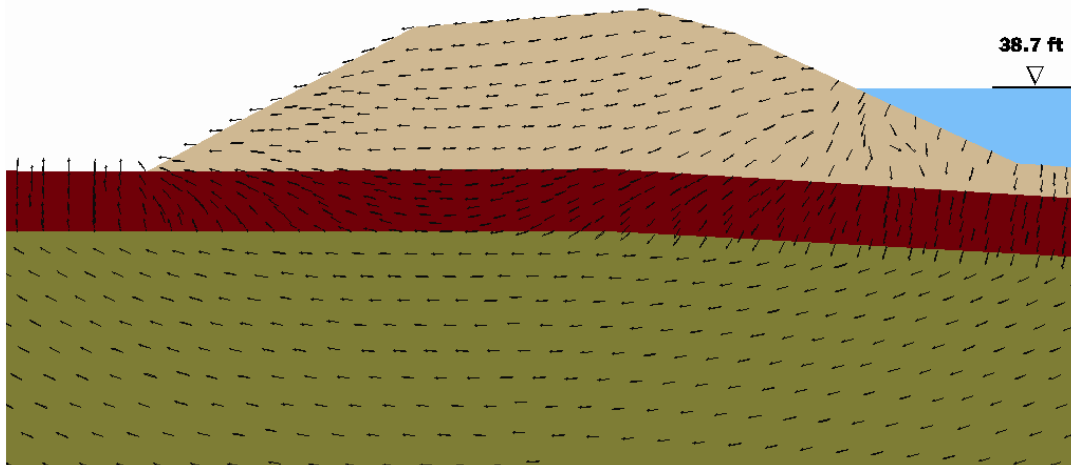


Figure 59. Velocity vectors showing the flow pattern, Burlington, WA.

### ***Woody vegetation zone beyond the toe of the levee***

The first woody vegetation zone in Figure 56 is just beyond the toe of the levee. Figure 60 shows the mesh near the zone along with total head contours, the phreatic surface, and velocity vectors for various values of  $\beta$ . Certain nodes in the region were then selected, as shown in Figure 61 for tabulating the magnitude of gradient (Table 27) and pore pressure (Table 28). This gives a consistent analysis with that done for the Pocket Levee. The following conclusions from the Pocket Levee study can also be made from the plots and data for the Burlington, WA, site:

- As  $\beta$  is increased, the magnitude of gradient in the woody vegetation zone is decreased, and the magnitude of gradient below the zone is increased.

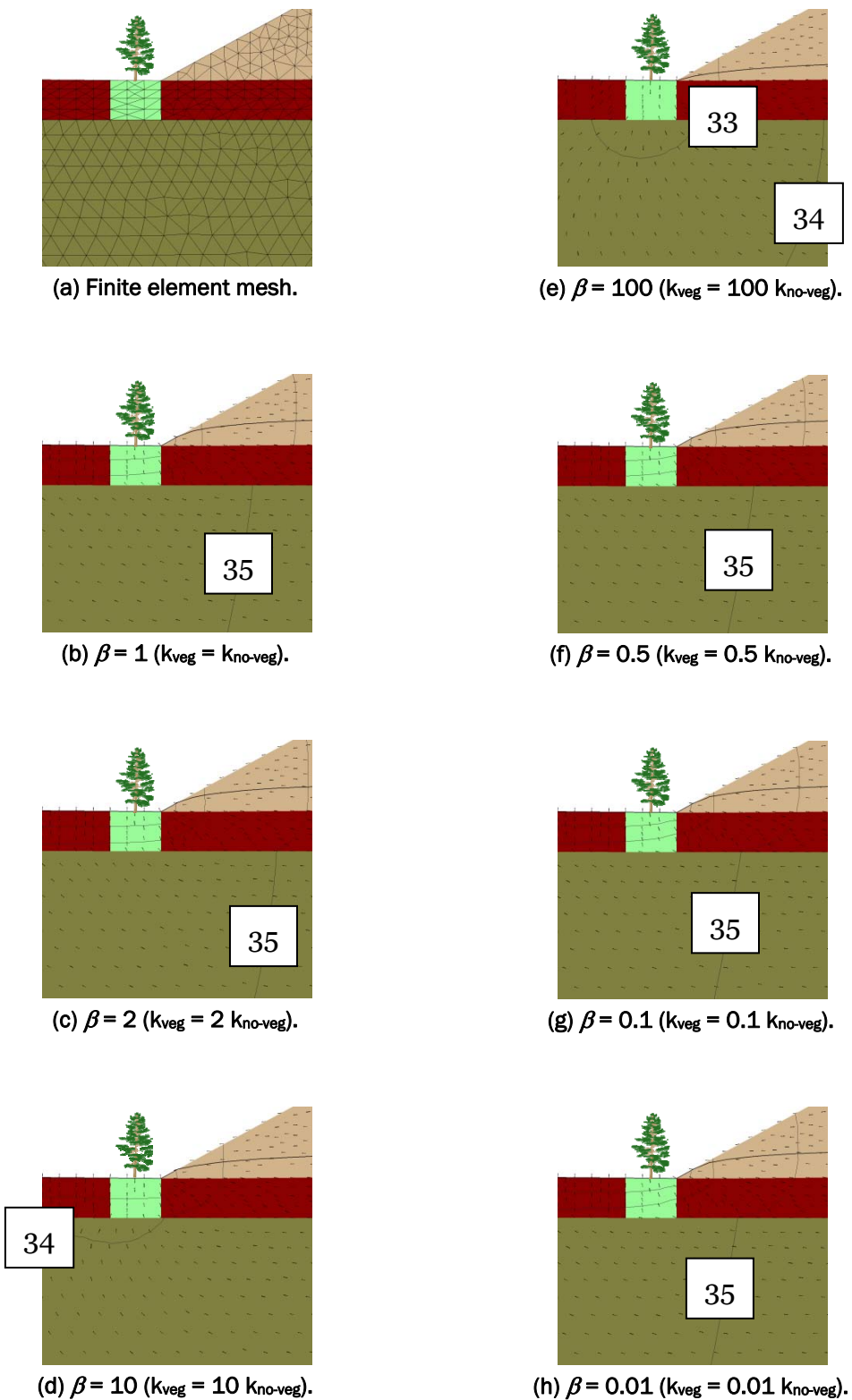


Figure 60. Total head (ft) contours, phreatic surface, and velocity vectors, Burlington, WA.

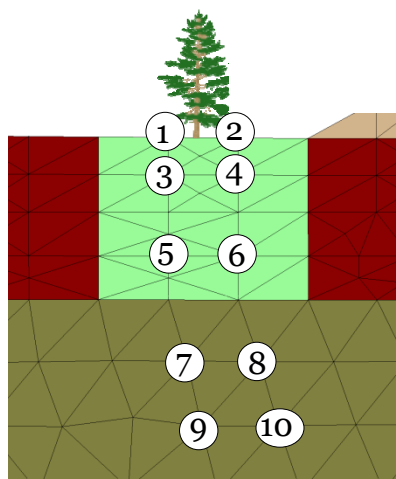


Figure 61. Selected nodes, Burlington, WA.

Table 27. Magnitude of gradient at selected nodes for different values of  $\beta$ .

Node	$\beta = 0.5$	$\beta = 0.1$	$\beta = 0.01$	$\beta = 1$	$\beta = 2$	$\beta = 10$	$\beta = 100$
1	0.587	0.605	0.610	<b>0.567</b>	0.534	0.381	0.092
2	0.662	0.710	0.725	<b>0.624</b>	0.574	0.398	0.010
3	0.579	0.597	0.602	<b>0.561</b>	0.530	0.382	0.094
4	0.665	0.714	0.729	<b>0.626</b>	0.576	0.400	0.101
5	0.532	0.540	0.541	<b>0.521</b>	0.499	0.363	0.086
6	0.512	0.505	0.502	<b>0.510</b>	0.497	0.371	0.091
7	0.023	0.022	0.022	<b>0.024</b>	0.028	0.061	0.123
8	0.022	0.021	0.020	<b>0.025</b>	0.030	0.065	0.134
9	0.022	0.021	0.021	<b>0.023</b>	0.026	0.049	0.098
10	0.022	0.021	0.021	<b>0.023</b>	0.028	0.050	0.098

Table 28. Pore pressure (lb/ft<sup>2</sup>) at selected nodes for different values of  $\beta$ .

Node	$\beta = 0.5$	$\beta = 0.1$	$\beta = 0.01$	$\beta = 1$	$\beta = 2$	$\beta = 10$	$\beta = 100$
1	0.0	0.0	0.0	<b>0.0</b>	0.0	0.0	0.0
2	0.0	0.0	0.0	<b>0.0</b>	0.0	0.0	0.0
3	108.5	109.8	110.1	<b>107.1</b>	104.9	94.5	74.7
4	114.1	117.9	119.0	<b>111.2</b>	107.6	95.3	74.8
5	339.2	352.2	342.9	<b>335.9</b>	329.9	298.7	236.9
6	345.0	350.0	351.4	<b>340.4</b>	333.2	300.2	237.3
7	575.9	579.0	579.7	<b>572.2</b>	565.5	527.9	451.3
8	578.5	581.5	582.2	<b>574.9</b>	568.2	531.2	454.4
9	693.0	695.8	696.4	<b>688.7</b>	683.6	649.9	579.7
10	695.0	697.7	698.3	<b>691.8</b>	686.0	653.5	585.2

- Conversely, as  $\beta$  is decreased, the magnitude of gradient in the woody vegetation zone is increased, and the magnitude of gradient below the zone is decreased.
- As  $\beta$  is increased, total head contours move away from the zone.
- Conversely, as  $\beta$  is decreased, total head contours move toward the zone.
- As  $\beta$  is increased, the flow of water moves toward the zone.
- Conversely, as  $\beta$  is increased, the flow of water moves away from the zone.
- As  $\beta$  is increased, pore pressures both in and just below the zone are decreased.
- Conversely, as  $\beta$  is decreased, pore pressures both in and just below the zone are increased.

For the elevation of 38.7 ft, the flow analysis indicates that a tree in this woody vegetation zone does not appreciably affect the flow field. However, for higher river elevations where the magnitude of gradient steadily increases, certain conditions of the woody vegetation zone could exacerbate the stability of the levee. An example is when the woody vegetation zone is less pervious than when there is no zone at the same location. The woody vegetation zone produces an increase in exit gradients from the original values. At elevations higher than 39.7 ft, this observation would be increased even more than what was apparent in the lower elevations.

### ***Woody vegetation zone on the toe of the levee***

The second woody vegetation zone in Figure 56 is on the toe of the levee. Figure 62 shows the mesh near the zone along with total head contours, phreatic surface, and velocity vectors for various values of  $\beta$ . As before, certain nodes in the region were then selected, as shown in Figure 63 for tabulating the magnitude of gradient (Table 29) and pore pressure (Table 30). As done with the Pocket Levee results, negative pore pressures were replaced with a dash. The following are observed for this location:

- As  $\beta$  is increased, magnitudes of gradient in the woody vegetation zone and downstream of the zone decrease.
- As  $\beta$  is increased, magnitude of gradient under the zone increases.
- As  $\beta$  is decreased, magnitudes of gradient in the zone increase.
- As  $\beta$  is decreased, magnitudes of gradient downstream of the zone both decrease and increase.

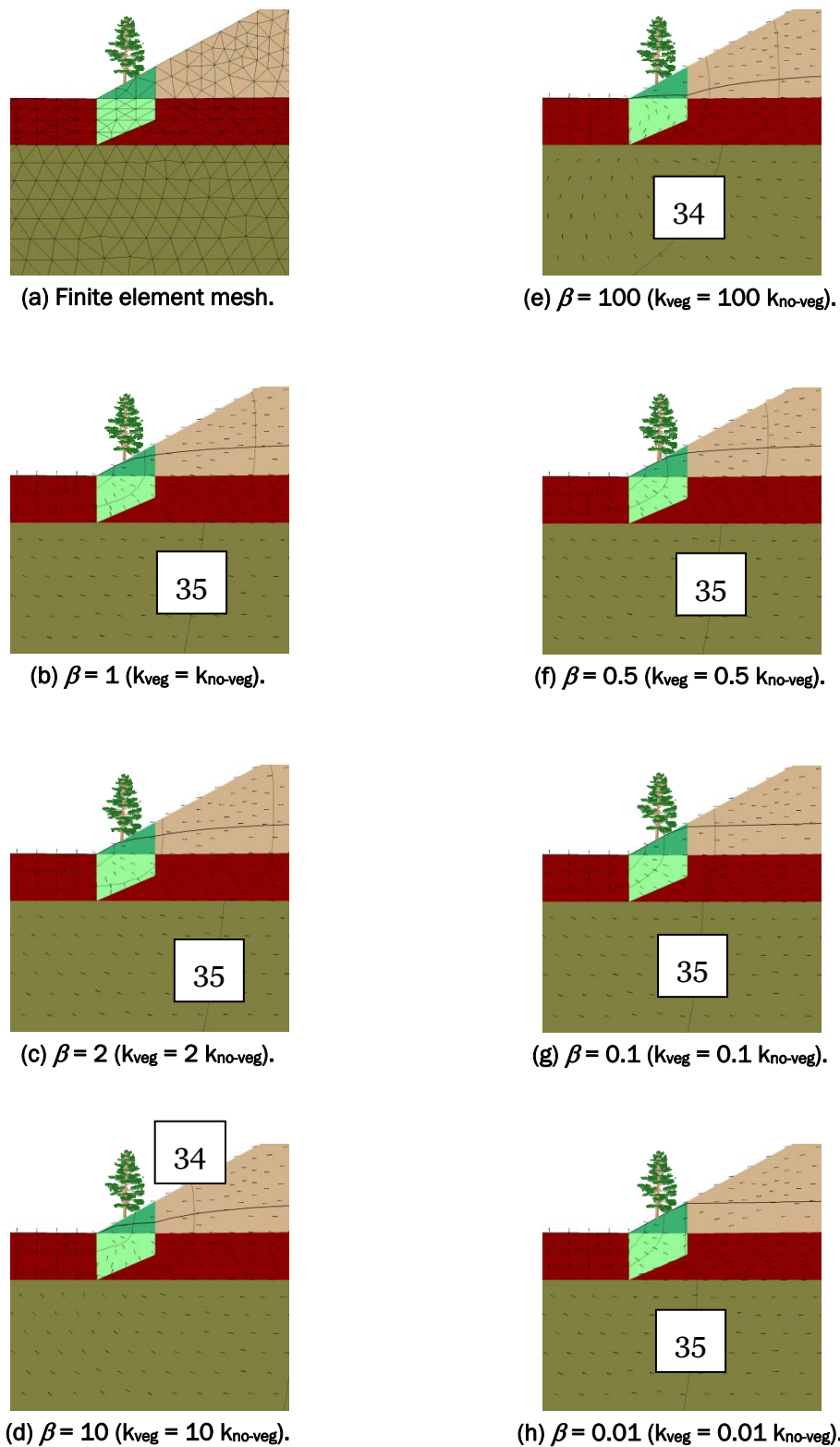


Figure 62. Total head (ft) contours, phreatic surface, and velocity vectors, Burlington, WA.

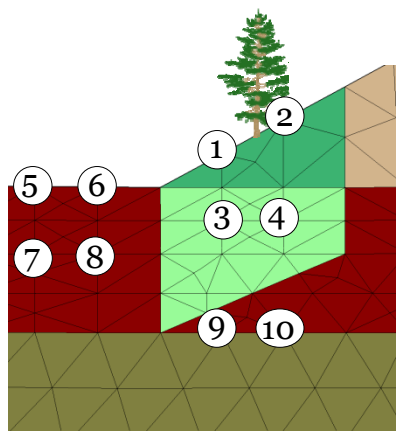


Figure 63. Selected nodes, Burlington, WA.

Table 29. Magnitude of gradient at selected nodes for different values of  $\beta$ .

Node	$\beta = 0.5$	$\beta = 0.1$	$\beta = 0.01$	$\beta = 1$	$\beta = 2$	$\beta = 10$	$\beta = 100$
1	0.508	0.582	0.598	<b>0.432</b>	0.347	0.199	0.067
2	0.333	0.446	0.496	<b>0.264</b>	0.188	0.089	0.029
3	0.466	0.534	0.558	<b>0.416</b>	0.357	0.226	0.075
4	0.320	0.393	0.422	<b>0.273</b>	0.221	0.117	0.032
5	0.567	0.557	0.552	<b>0.567</b>	0.557	0.482	0.282
6	0.615	0.582	0.567	<b>0.624</b>	0.616	0.508	0.252
7	0.553	0.555	0.555	<b>0.547</b>	0.536	0.474	0.292
8	0.562	0.566	0.566	<b>0.554</b>	0.536	0.451	0.250
9	0.116	0.039	0.030	<b>0.183</b>	0.272	0.507	0.574
10	0.101	0.033	0.028	<b>0.163</b>	0.239	0.424	0.458

Table 30. Pore pressure (lb/ft<sup>2</sup>) at selected nodes for different values of  $\beta$ .

Node	$\beta = 0.5$	$\beta = 0.1$	$\beta = 0.01$	$\beta = 1$	$\beta = 2$	$\beta = 10$	$\beta = 100$
1	0.0	0.0	0.0	<b>0.0</b>	0.0	-	-
2	-	0.0	0.0	-	-	-	-
3	162.8	166.4	167.1	<b>158.5</b>	152.0	125.2	86.8
4	198.5	212.1	216.6	<b>187.5</b>	174.1	135.2	89.2
5	0.0	0.0	0.0	<b>0.0</b>	0.0	0.0	0.0
6	0.0	0.0	0.0	<b>0.0</b>	0.0	0.0	0.0
7	213.6	212.9	212.5	<b>213.2</b>	211.8	202.3	175.7
8	217.7	214.7	213.2	<b>218.2</b>	216.6	202.2	168.6
9	469.2	472.1	473.0	<b>466.5</b>	462.5	443.6	362.8
10	472.4	475.3	476.2	<b>469.7</b>	465.8	448.5	396.9

- As  $\beta$  is decreased, magnitude of gradient under the zone is decreased.
- As  $\beta$  is increased, pore pressures are decreased for all the selected points.
- As  $\beta$  is decreased, the pore pressures are increased for all the selected points in and under the zone.
- When pore pressures become negative, the phreatic surface has fallen below these points.
- As  $\beta$  is decreased, pore pressures downstream of the zone are decreased.

### ***Woody vegetation zone nearly midslope to the top of the levee on the landside***

The third woody vegetation zone in Figure 56 is nearly halfway to the top of the levee on the landside. Plots of total head contours and the phreatic surface using  $\beta = 1, 100$ , and  $0.01$  for this zone are given in Figure 64. From these plots, it is seen that the phreatic surface flows through the lower part of the zone, but does not significantly affect the total head contours, except in the vicinity of the zone. Soil at the surface of the zone remains unsaturated, and, therefore, no flow exists. Given this situation, it is unlikely that significant exit gradients will form. Based on these model results, the integrity of the levee is not affected.

### ***Woody vegetation zone nearly midslope to the levee crown on the riverside***

The fourth woody vegetation zone in Figure 56 is nearly halfway to the top of the levee on the riverside. Plots of total head contours and the phreatic surface using  $\beta = 1, 100$ , and  $0.01$  for this zone are given in Figure 65. Although the total head contours were influenced significantly in the zone, there is no noticeable change in the flow pattern downstream.

### ***Woody vegetation zone near the heel on the riverside***

The fifth woody vegetation zone in Figure 56 is near the heel on the riverside. Plots of total head contours and the phreatic surface using  $\beta = 1, 100$ , and  $0.01$  for this zone are given in Figure 66. From these plots, it is seen that the total head contours are significantly affected. To examine closely, the nodes shown in Figure 67, repeated from Figure 61, will have

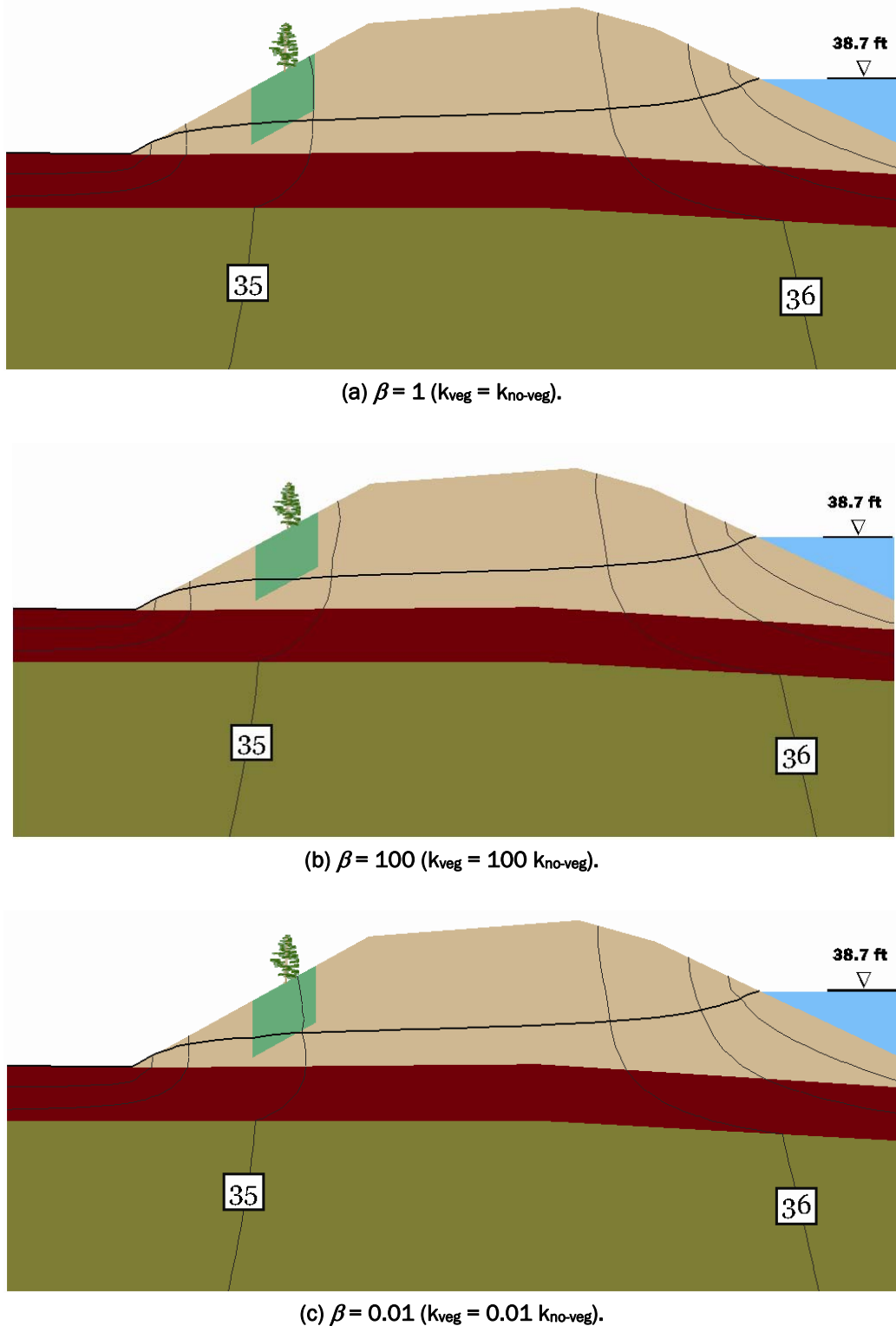


Figure 64. Total head (ft) contours and phreatic surface, Burlington, WA.

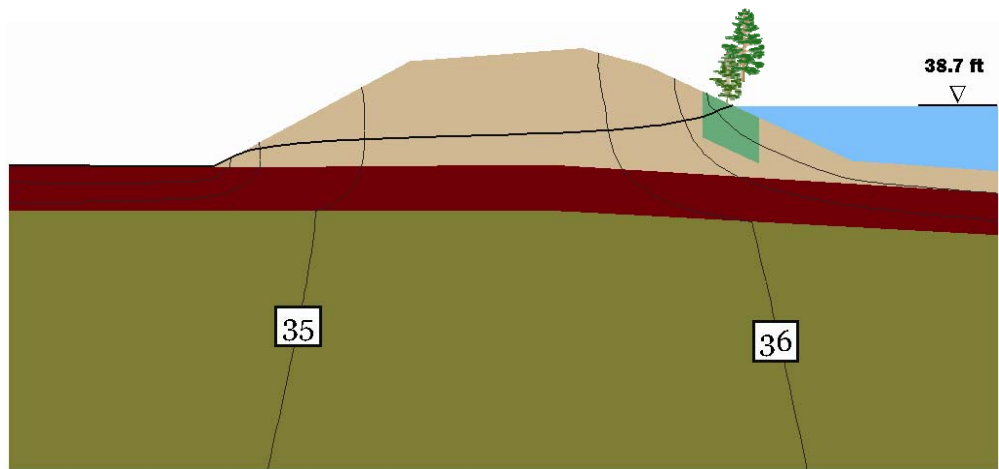
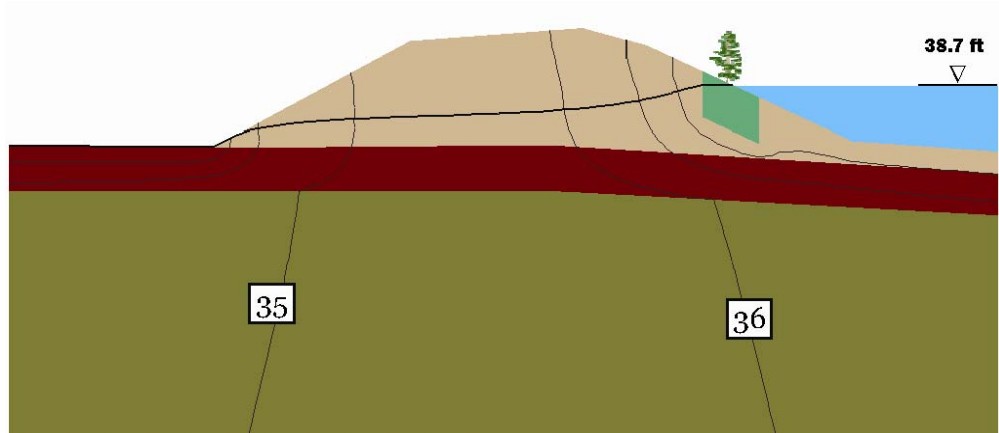
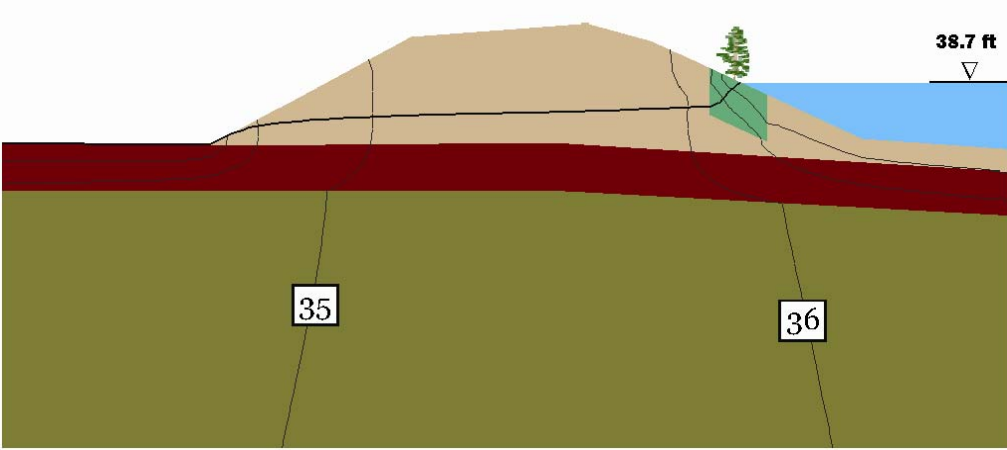
(a)  $\beta = 1$  ( $k_{veg} = k_{no-veg}$ ).(b)  $\beta = 100$  ( $k_{veg} = 100 k_{no-veg}$ ).(c)  $\beta = 0.01$  ( $k_{veg} = 0.01 k_{no-veg}$ ).

Figure 65. Total head (ft) contours and phreatic surface, Burlington, WA.

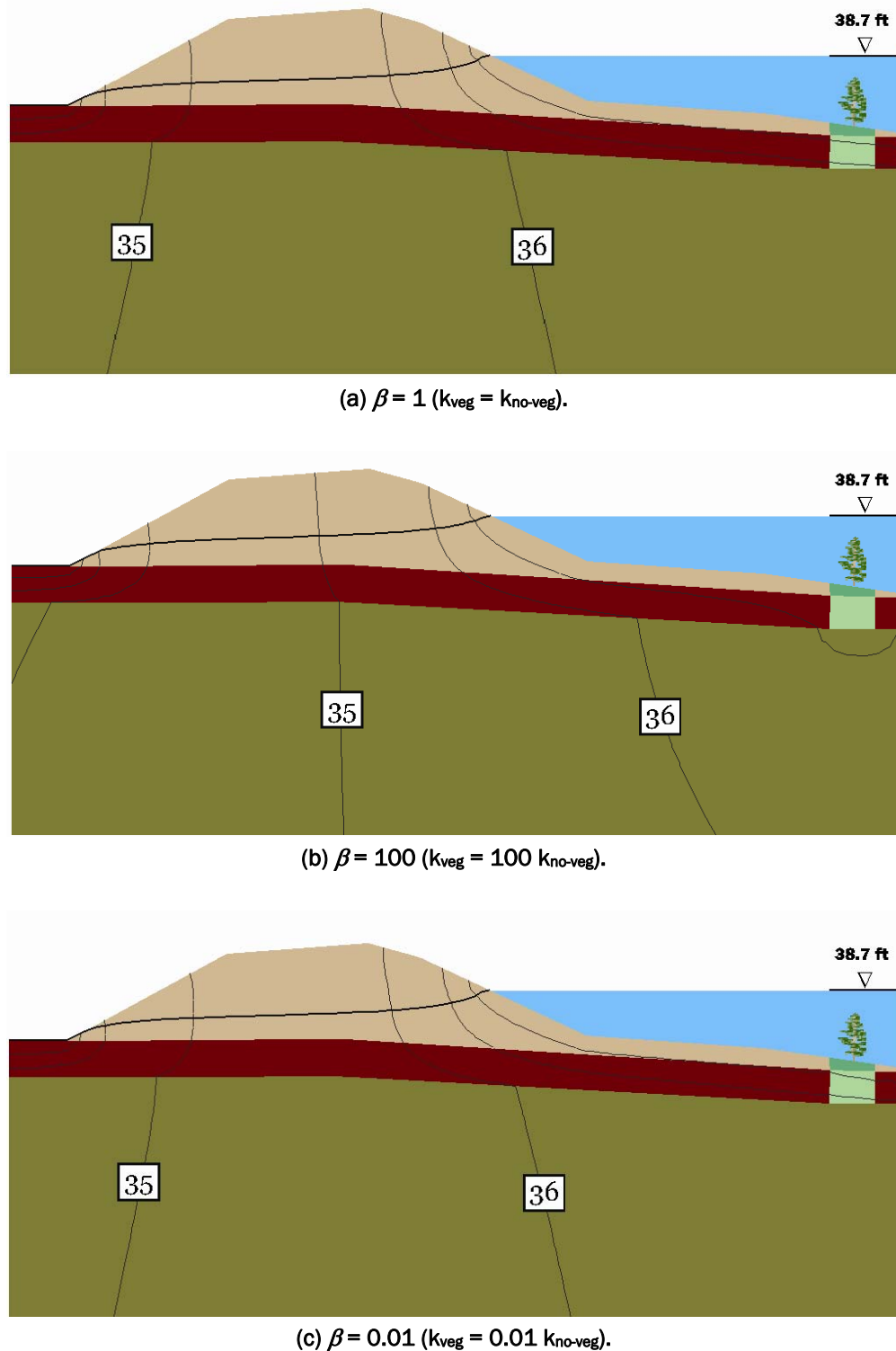


Figure 66. Total head (ft) contours and phreatic surface, Burlington, WA.

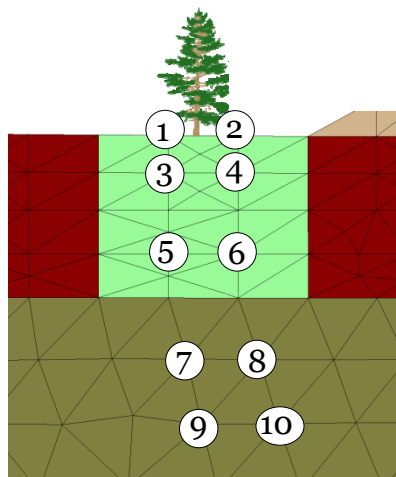


Figure 67. Selected nodes, Burlington, WA.

magnitude of gradient and pore pressure tabulated in Tables 31 and 32, respectively. Observations are as follows:

- Magnitudes of gradient were not affected very much as shown by the numbers in the tables.
- A close examination of the total head contours show that they are close to horizontal and appear much the same for the three plots. Thus, vertical flow just beyond the toe is essentially unchanged.
- Pore pressures are increased with increasing  $\beta$ .
- Conversely, pore pressures are decreased with decreasing  $\beta$ .

#### *Transient analysis*

A transient flow analysis followed the same procedure as used in the Pocket Levee model. The initial condition was selected as 32.2 ft on both the landside and riverside of the levee. The water level of the river was then increased according to the hydrograph, as given in Figure 68. The maximum stage is 38.7 ft.

#### **No woody vegetation zone**

Figure 69 shows the initial position of the phreatic surface, and Figure 70 shows the phreatic surface at its maximum height without a woody vegetation zone. From these results, the phreatic surface does not achieve the equivalent of steady state in the approximately 1.7 days it takes to rise from 32.2 ft to 38.7 ft. Two zones are considered in more detail for this analysis.

**Table 31.** Magnitude of gradient at selected nodes for different values of  $\beta$ .

Node	$\beta = 0.5$	$\beta = 0.1$	$\beta = 0.01$	$\beta = 1$	$\beta = 2$	$\beta = 10$	$\beta = 100$
1	0.565	0.563	0.562	<b>0.567</b>	0.570	0.590	0.638
2	0.622	0.620	0.620	<b>0.624</b>	0.628	0.649	0.701
3	0.559	0.557	0.557	<b>0.561</b>	0.564	0.584	0.632
4	0.624	0.622	0.622	<b>0.626</b>	0.630	0.651	0.703
5	0.519	0.518	0.518	<b>0.521</b>	0.524	0.543	0.589
6	0.509	0.507	0.507	<b>0.510</b>	0.513	0.532	0.577
7	0.024	0.024	0.024	<b>0.024</b>	0.024	0.025	0.027
8	0.025	0.025	0.025	<b>0.025</b>	0.025	0.026	0.029
9	0.023	0.023	0.023	<b>0.023</b>	0.024	0.025	0.027
10	0.024	0.024	0.024	<b>0.023</b>	0.024	0.025	0.028

**Table 32.** Pore pressure ( $\text{lb}/\text{ft}^2$ ) at selected nodes for different values of  $\beta$ .

Node	$\beta = 0.5$	$\beta = 0.1$	$\beta = 0.01$	$\beta = 1$	$\beta = 2$	$\beta = 10$	$\beta = 100$
1	0.0	0.0	0.0	<b>0.0</b>	0.0	0.0	0.0
2	0.0	0.0	0.0	<b>0.0</b>	0.0	0.0	0.0
3	107.0	106.9	106.9	<b>107.1</b>	107.3	108.7	112.0
4	111.1	111.0	111.0	<b>111.2</b>	111.5	113.0	116.6
5	335.5	335.2	335.1	<b>335.9</b>	336.6	340.9	351.1
6	340.0	339.7	339.7	<b>340.4</b>	341.2	345.5	356.2
7	571.7	571.3	571.2	<b>572.2</b>	573.2	579.1	593.2
8	574.3	573.9	573.8	<b>574.9</b>	575.9	581.9	596.3
9	689.3	688.7	688.6	<b>688.7</b>	690.7	696.7	711.1
10	691.2	690.8	690.7	<b>691.8</b>	692.8	698.9	713.7

### ***Woody vegetation zone on the toe of the levee***

The second woody vegetation zone in Figure 56 is again considered and is at the toe of the levee. Values of  $\beta$  of 1, 100, and 0.01 were chosen, and the same transient run as before was done. Figure 71 shows the phreatic surface at this zone for these values of  $\beta$ . Figure 72 shows the same selected nodes as before, and Tables 33 and 34 show magnitude of gradient and pore pressure, respectively. The observations are as follows:

- The phreatic surface dropped for both increasing and decreasing values of  $\beta$ .
- Gradients and pore pressures did not achieve the level of the steady-state solution.

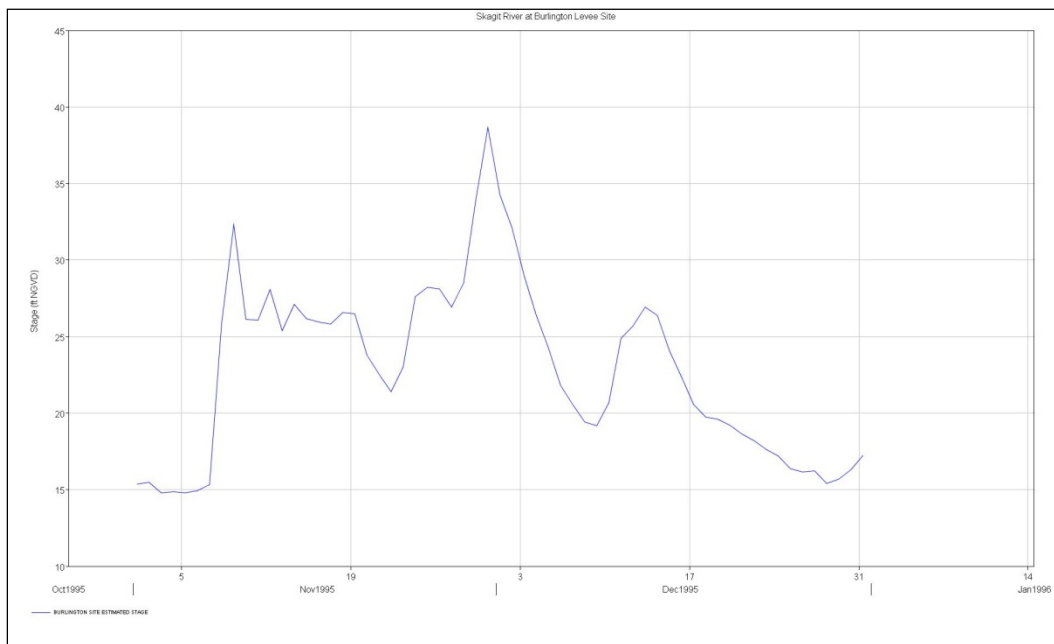


Figure 68. Hydrograph of the 1995 Flood, Burlington, WA.

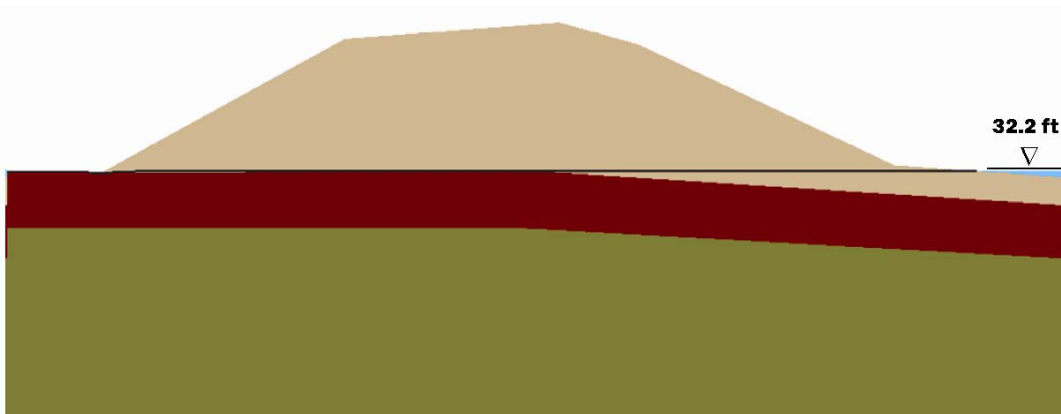


Figure 69. Initial position of the phreatic surface, Burlington, WA.

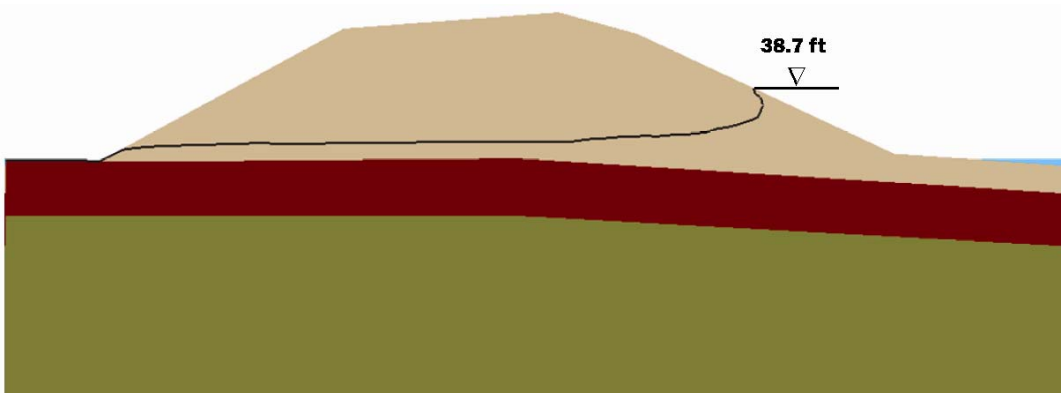


Figure 70. Phreatic surface at the maximum flood stage, Burlington, WA.

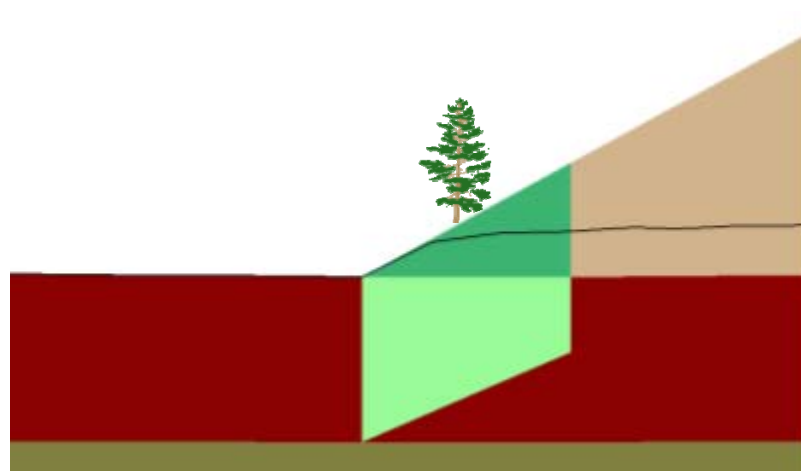
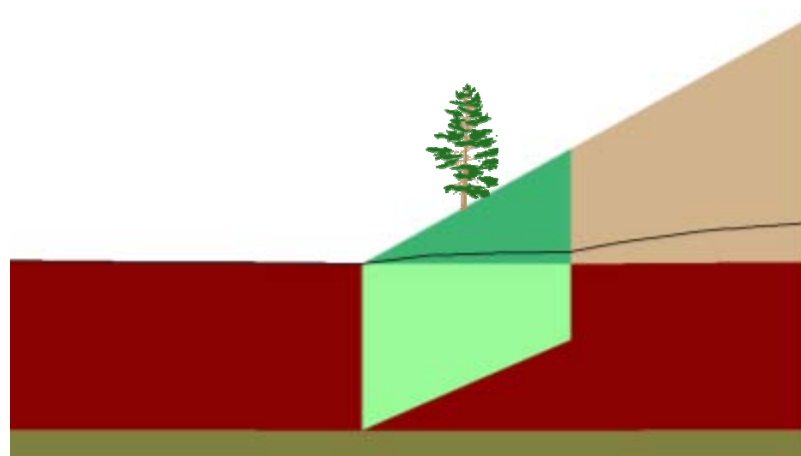
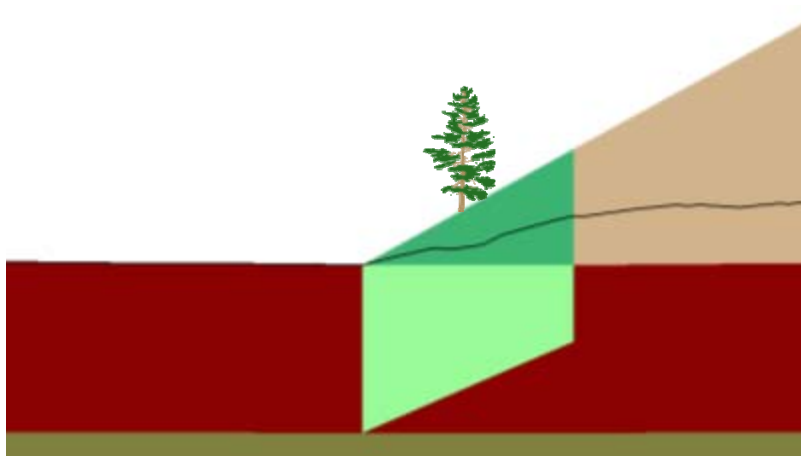
(a)  $\beta = 1$  ( $k_{veg} = k_{no-veg}$ ).(b)  $\beta = 100$  ( $k_{veg} = 100 k_{no-veg}$ ).(a)  $\beta = 0.01$  ( $k_{veg} = 0.01 k_{no-veg}$ ).

Figure 71. Phreatic surface for the transient case, Burlington, WA.

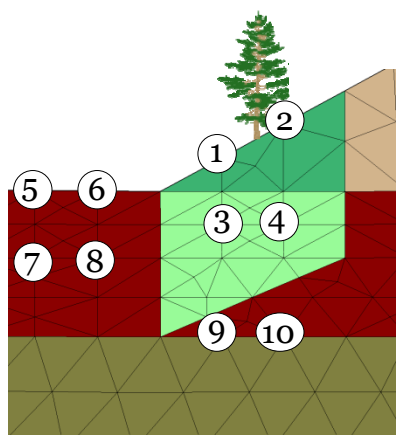


Figure 72. Selected nodes, Burlington, WA.

Table 33. Magnitude of gradient at selected nodes for different values of  $\beta$ .

Node	$\beta = 0.01$	$\beta = 1$	$\beta = 100$
1	0.393	<b>0.268</b>	0.062
2	0.579	<b>0.242</b>	0.040
3	0.524	<b>0.362</b>	0.072
4	0.453	<b>0.248</b>	0.030
5	0.508	<b>0.519</b>	0.266
6	0.521	<b>0.566</b>	0.237
7	0.510	<b>0.505</b>	0.276
8	0.520	<b>0.510</b>	0.238
9	0.022	<b>0.187</b>	0.534
10	0.031	<b>0.182</b>	0.429

Table 34. Pore pressure (lb/ft<sup>2</sup>) at selected nodes for different values of  $\beta$ .

Node	$\beta = 0.01$	$\beta = 1$	$\beta = 100$
1	-	-	-
2	-	-	-
3	140.8	<b>144.6</b>	85.6
4	171.7	<b>163.9</b>	87.8
5	0.0	<b>0.0</b>	0.0
6	0.0	<b>0.0</b>	0.0
7	206.4	<b>207.0</b>	173.6
8	206.9	<b>210.8</b>	166.8
9	457.8	<b>452.6</b>	377.7
10	460.2	<b>456.1</b>	389.8

- The emerging universal principle holds here; as  $\beta$  increases, the gradients become smaller at the ground surface of the woody vegetation zone but larger beneath it.
- Conversely, as  $\beta$  is decreased, the gradients become larger at the ground surface of the woody vegetation zone but smaller beneath it.

### ***Woody vegetation zone nearly midslope to the levee crown on the riverside***

The fourth woody vegetation zone in Figure 56 is nearly midslope to the levee crown on the riverside. Plots of total head contours and the phreatic surface using  $\beta = 1$ ,  $100$ , and  $0.01$  are given for this zone in Figure 73. Although the phreatic surface changes significantly at the woody vegetation zone, the phreatic surface remains very close to the same at the exit point.

### ***Extended woody vegetation zone***

As with the Pocket Levee model, the woody vegetation zone on the toe of the levee is extended. Figure 74 shows the mesh with the extended zone, and Figures 75 through 77 show the phreatic surface and total head contours for  $\beta = 1$ ,  $\beta = 100$ , and  $\beta = 0.01$ , respectively. From these plots, it is evident that changes in magnitude of gradient and pore pressure in the original configuration of this zone are magnified in the extended zone. To document the extent of these differences, Table 35 shows magnitude of gradient, and Table 36 gives pore pressure for the selected nodes in Figure 78. Observations are as follows:

- The amount to which magnitude of gradient and pore pressure are changed for different values of  $\beta$  are significant.
- When  $\beta = 100$ , the surface of seepage is completely eliminated and the magnitude of gradient is very small in the woody vegetation zone and downstream from it.
- When  $\beta = 0.01$ , the surface of seepage is increased and the magnitude of gradient is significantly larger in the woody vegetation zone.
- Pore pressures are greatly decreased with  $\beta = 100$  and greatly increased with  $\beta = 0.01$ .

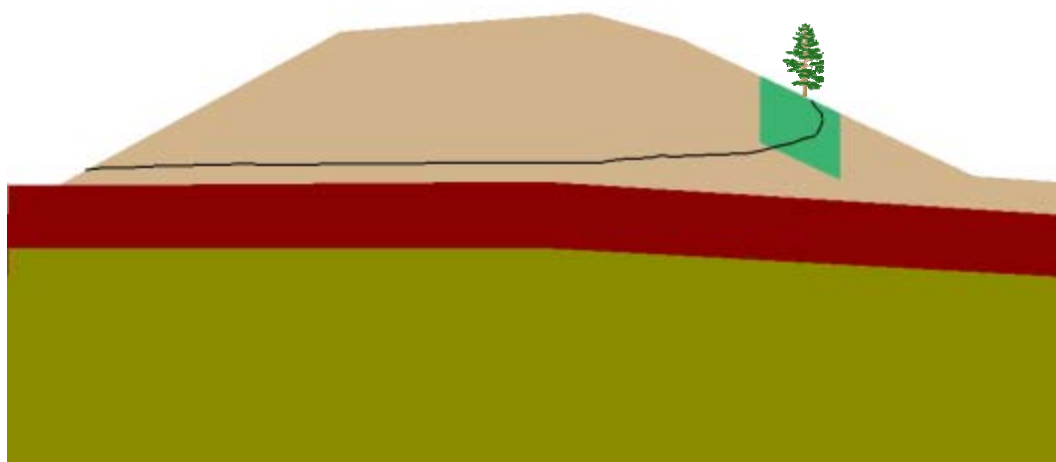
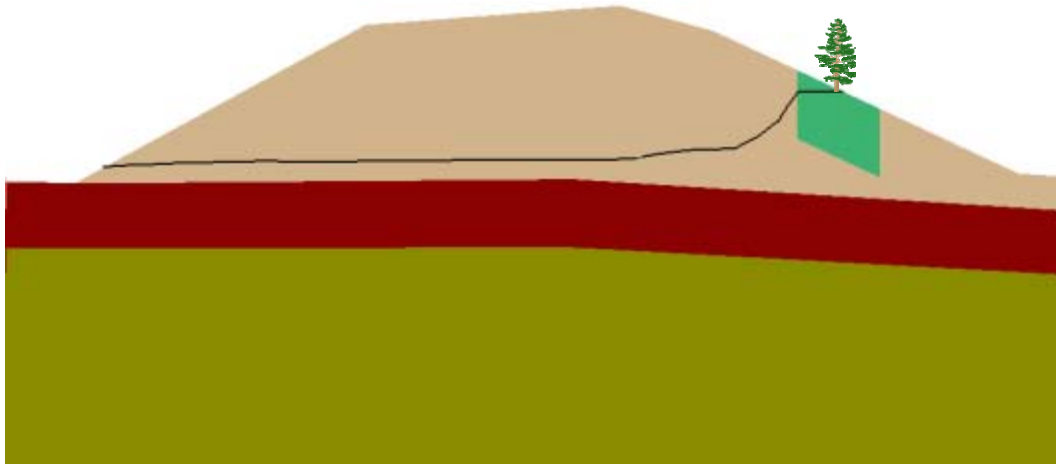
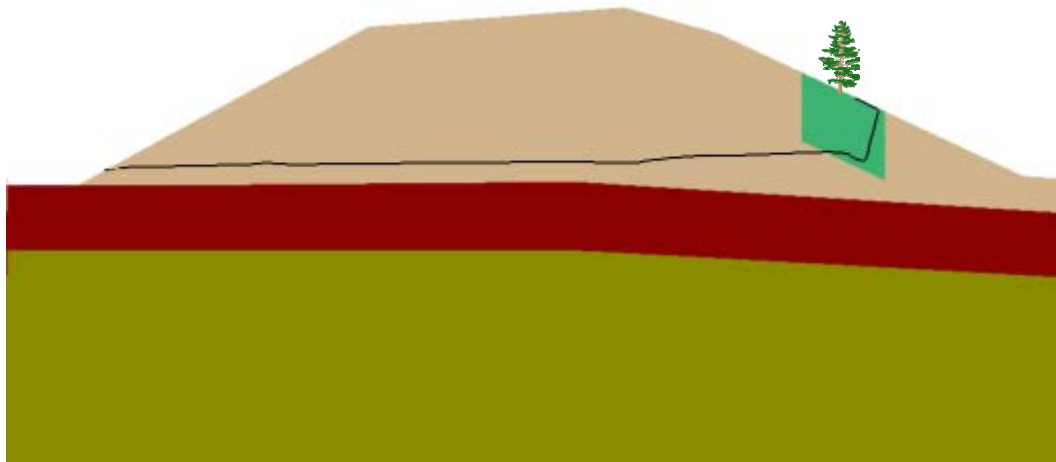
(a)  $\beta = 1$  ( $k_{\text{veg}} = k_{\text{no-veg}}$ ).(b)  $\beta = 100$  ( $k_{\text{veg}} = 100 k_{\text{no-veg}}$ ).(c)  $\beta = 0.01$  ( $k_{\text{veg}} = 0.01 k_{\text{no-veg}}$ ).

Figure 73. Phreatic surface for the transient case, Burlington, WA.

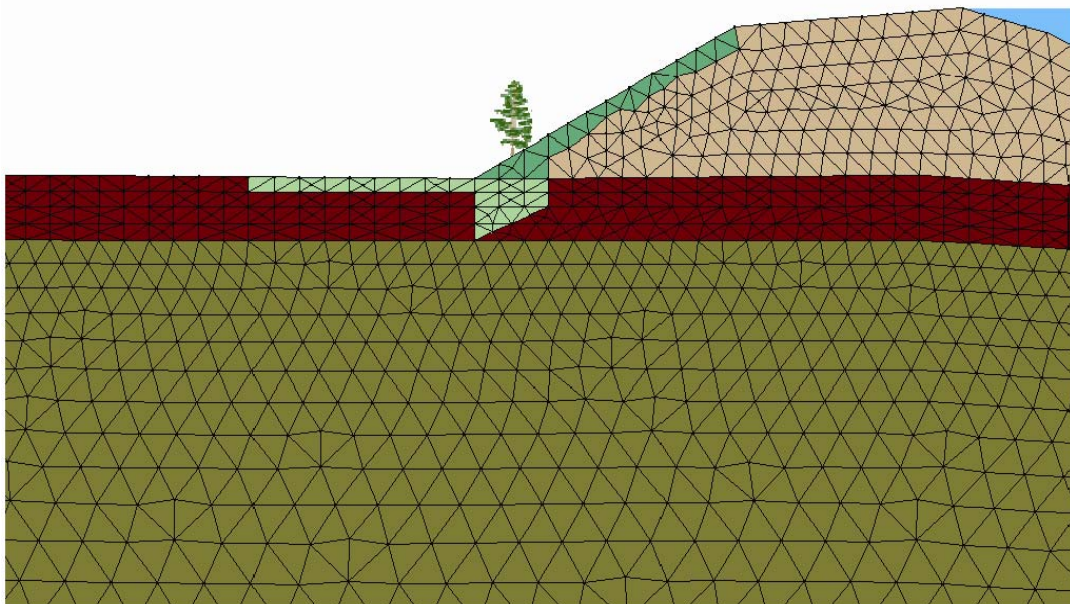


Figure 74. Finite element mesh with woody vegetation zone and extended zone, Burlington, WA.

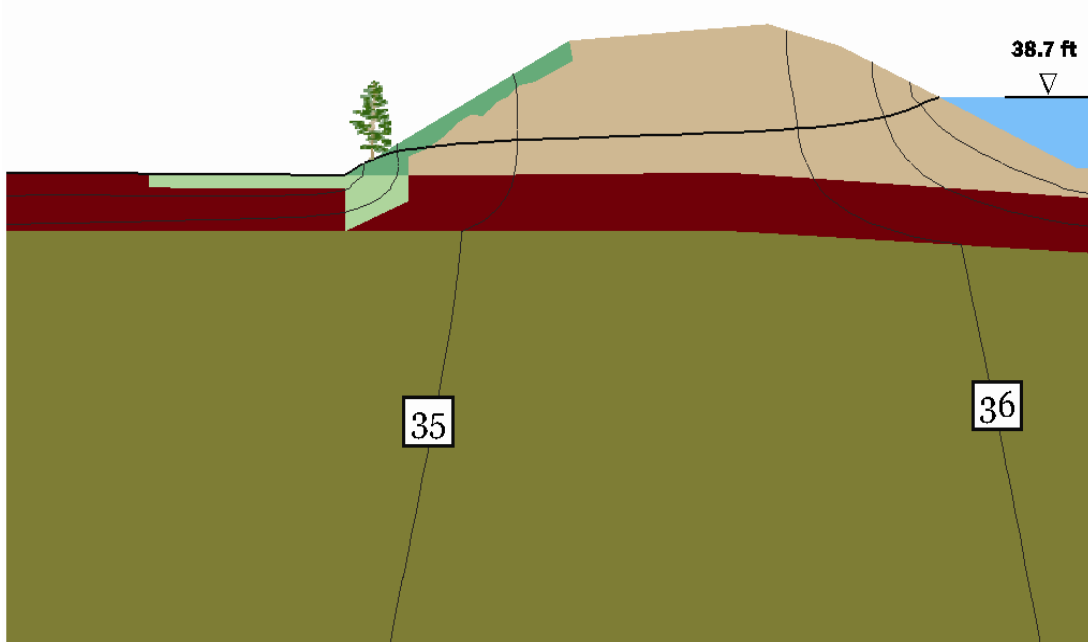


Figure 75. Total head contours and phreatic surface for  $\beta = 1$  ( $k_{veg} = k_{no-veg}$ ), Burlington, WA.

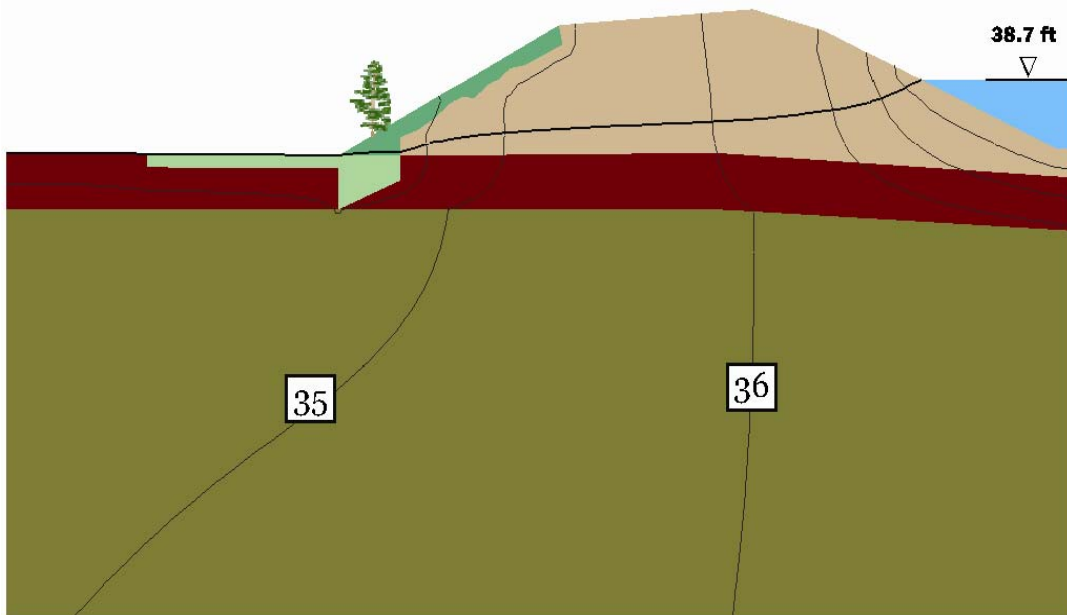


Figure 76. Total head contours and phreatic surface for  
 $\beta = 100$  ( $k_{veg} = 100 k_{no-veg}$ ), Burlington, WA.

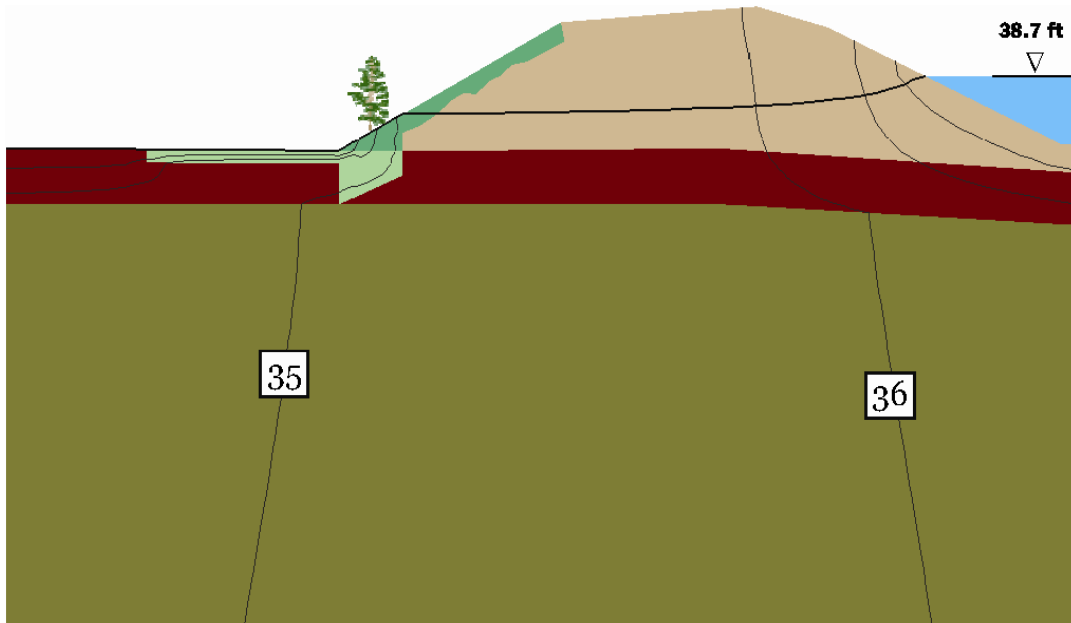


Figure 77. Total head contours and phreatic surface for  
 $\beta = 0.01$  ( $k_{veg} = 0.01 k_{no-veg}$ ), Burlington, WA.

**Table 35. Magnitude of gradient at selected nodes for different values of  $\beta$ .**

Node	$\beta = 0.01$	$\beta = 1$	$\beta = 100$
1	0.759	<b>0.432</b>	0.052
2	0.576	<b>0.264</b>	0.034
3	0.410	<b>0.416</b>	0.072
4	0.341	<b>0.273</b>	0.029
5	2.532	<b>0.567</b>	0.009
6	2.581	<b>0.624</b>	0.022
7	0.036	<b>0.547</b>	0.358
8	0.039	<b>0.554</b>	0.293
9	0.022	<b>0.183</b>	0.566
10	0.022	<b>0.163</b>	0.467

**Table 36. Pore pressure (lb/ft<sup>2</sup>) at selected nodes for different values of  $\beta$ .**

Node	$\beta = 0.01$	$\beta = 1$	$\beta = 100$
1	0.0	<b>0.0</b>	-
2	0.0	-	-
3	219.0	<b>158.5</b>	81.7
4	238.2	<b>187.5</b>	84.5
5	0.0	<b>0.0</b>	0.0
6	0.0	<b>0.0</b>	0.0
7	312.8	<b>213.2</b>	162.0
8	314.2	<b>218.2</b>	157.9
9	487.8	<b>466.5</b>	378.7
10	490.1	<b>469.7</b>	392.1

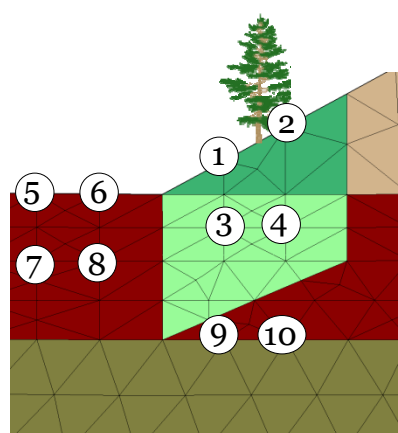


**Figure 78. Selected nodes, Burlington, WA.**

### Second cross section

#### **Description of the 2-D model**

Figure 79 shows the levee with its material types and location of woody vegetation zones on the levee to be examined in detail. Two woody vegetation zones, one at the levee toe and the other on the lower slope of the levee on the riverside, will be considered for this cross section. Other zones are not evaluated in this cross section because of the consistency of results for these zones in the previous cross section. The first material is fill (levee) and is composed of silty sand (soil classification SM). The second material is overbank deposit (blanket) and contains a mixture of the equivalent of poorly graded sand and silty sand (soil classification SP-SM). The third material is channel deposit (aquifer) and is composed of the equivalent of poorly graded sand and well graded sand (soil classification SP-SW). Figure 80 shows a portion of the FE mesh. The elevation of the river is set to 38.7 ft for steady-state flow analysis, which is the highest value on the hydrograph used for the transient analysis. The elevation of the landside is always set to 32.0 ft.

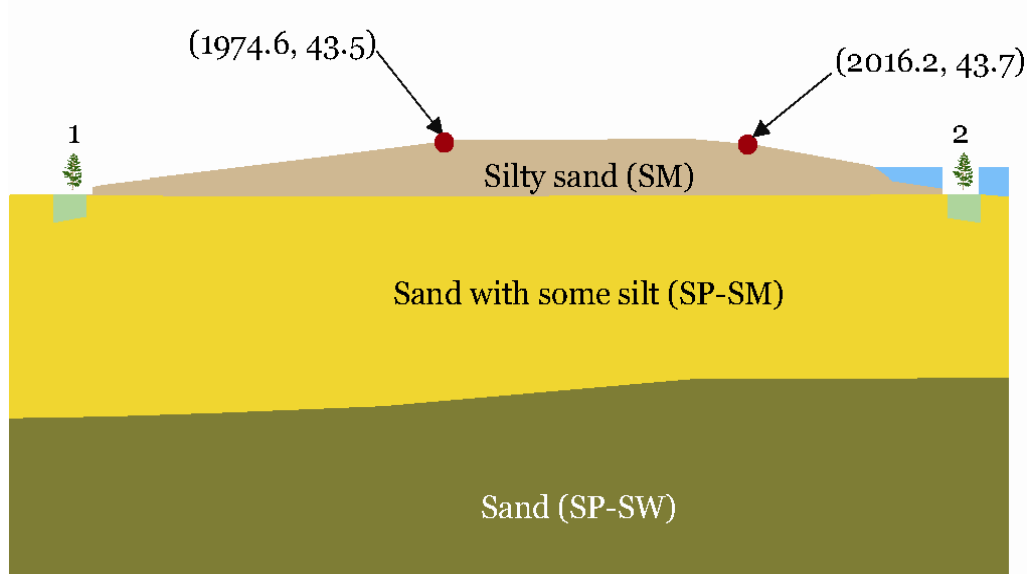


Figure 79. Second cross section with material types and woody vegetation zones, Burlington, WA.

#### **Soil properties**

Soil properties for the second Burlington Levee model are given in Tables 37 and 38. Table 37 gives the saturated hydraulic conductivity for the soil layers, and Table 38 provides the moisture content and van Genuchten parameters.

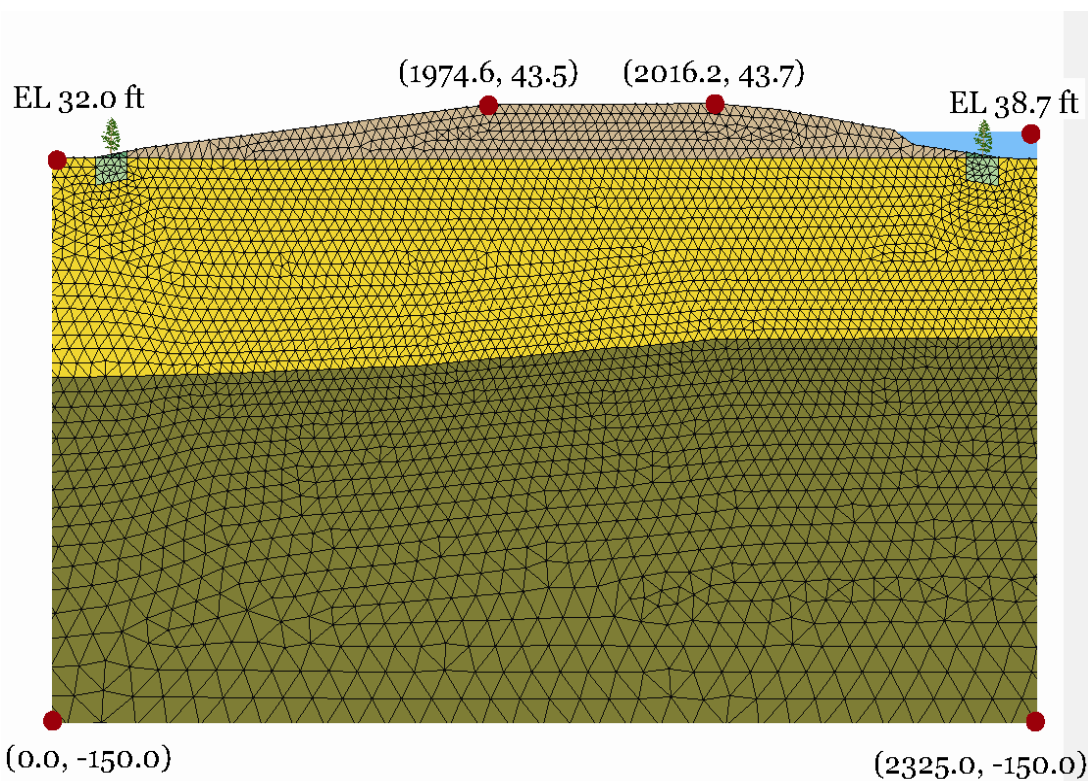


Figure 80. Portion of the finite element for the second cross section of the Burlington Levee. The total mesh consists of 20,280 nodes and 39,569 triangular elements.

Table 37. Second Burlington levee model hydraulic conductivities.

Material	$k_H$ (cm/sec)	$k_H$ (ft/day)	$k_V$ (cm/sec)	$k_V$ (ft/day)
Silty sand (SM)	$1.00 \times 10^{-4}$	0.28	$1.00 \times 10^{-4}$	0.28
Sand with some silt (SP-SM)	$2.00 \times 10^{-3}$	5.67	$1.00 \times 10^{-3}$	2.83
Sand (SP-SW)	$5.00 \times 10^{-2}$	141.73	$5.00 \times 10^{-2}$	141.73

Table 38. Second and third Burlington Levee model moisture content and van Genuchten soil properties.

Material	$\theta$	$\theta_s$	$\alpha(1/m)$	$\alpha(1/ft)$	$n$
Silty sand (SM)	0.041	0.440	10.2	3.11	2.24
Sand with some silt (SP-SM)	0.043	0.435	12.4	3.76	1.37
Sand (SP-SW)	0.045	0.430	14.5	4.42	2.46

#### No woody vegetation zone

The model was first run without a woody vegetation zone. Figure 81 shows the location of the phreatic surface and total head contours. The analyses for different zones are discussed in the following sections.

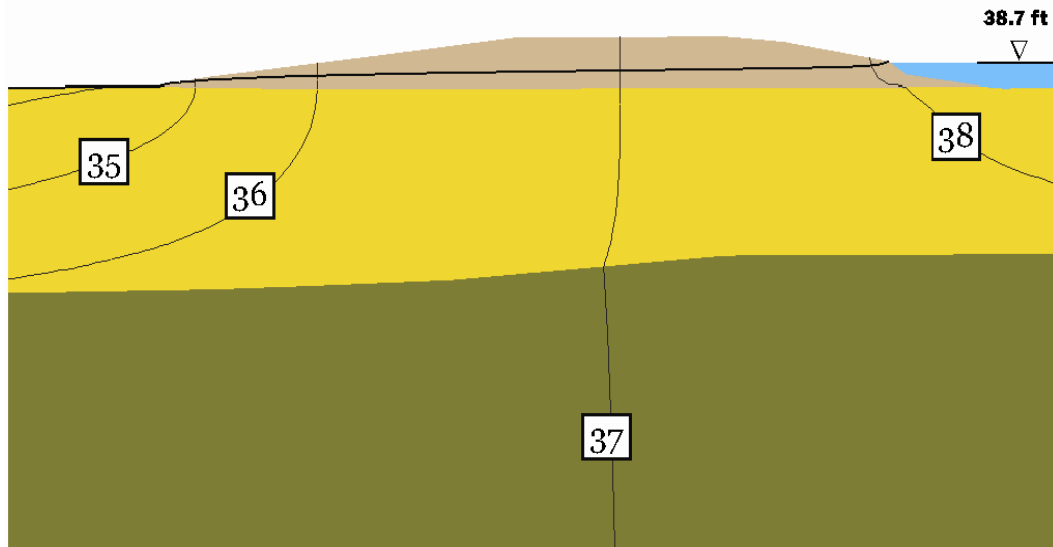


Figure 81. Total head contours and phreatic surface, Burlington, WA.

### ***Steady-state results for a single woody vegetation zone***

#### **Woody vegetation zone at the toe of the levee**

The first woody vegetation zone in Figure 79 is at the toe of the levee. Figure 82 shows the mesh near the zone along with total head contours, phreatic surface, and velocity vectors for various values of  $\beta$ . Nodes in the region were selected, as shown in Figure 83, for tabulating the magnitude of gradient in Table 39, and pore pressure in Table 40. The following concepts independent of the levee geometry are emerging:

- When the woody vegetation zone is more pervious, gradients are reduced in the woody vegetation zone and increased under it.
- Conversely, when the woody vegetation zone is less pervious, gradients are increased in the zone and mostly decreased under it.
- When the woody vegetation zone is more pervious, pore pressures are reduced in the zone and under it.
- Conversely, when the woody vegetation zone is less pervious, pore pressures are increased in the zone and under it.

#### **Woody vegetation zone on the lower slope of the levee on the riverside**

The second woody vegetation zone in Figure 79 is located on the lower slope of the levee on the riverside. Figure 84 shows the phreatic surface and total head contours for  $\beta = 1, 100$ , and  $0.01$  for this zone. Consistent with previous results, the effect on the downstream flow patterns is negligible.

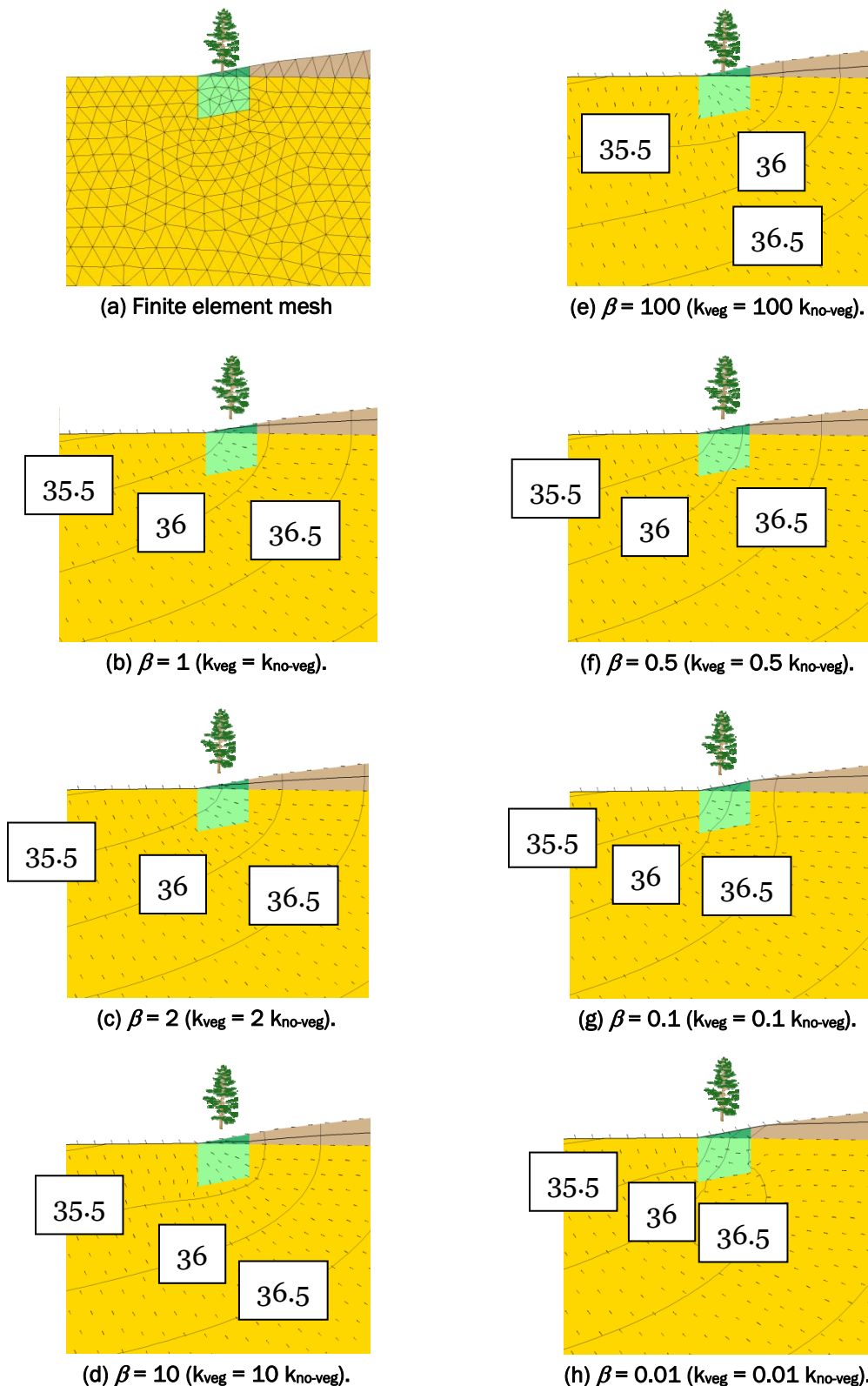


Figure 82. Total head (ft) contours, phreatic surface, and velocity vectors, Burlington, WA.

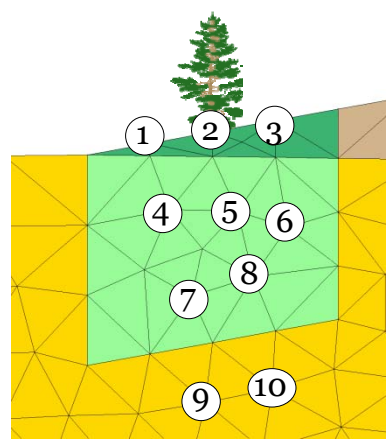


Figure 83. Selected nodes, Burlington, WA.

Table 39. Magnitude of gradient at selected nodes for different values of  $\beta$ .

Node	$\beta = 0.5$	$\beta = 0.1$	$\beta = 0.01$	$\beta = 1$	$\beta = 2$	$\beta = 10$	$\beta = 100$
1	0.272	0.420	0.476	<b>0.181</b>	0.123	0.050	0.007
2	0.205	0.363	0.433	<b>0.124</b>	0.081	0.029	0.004
3	0.152	0.314	0.398	<b>0.092</b>	0.060	0.018	0.002
4	0.157	0.213	0.235	<b>0.123</b>	0.091	0.035	0.005
5	0.133	0.191	0.215	<b>0.099</b>	0.069	0.024	0.003
6	0.114	0.173	0.198	<b>0.083</b>	0.057	0.019	0.002
7	0.127	0.187	0.212	<b>0.098</b>	0.063	0.021	0.003
8	0.113	0.160	0.179	<b>0.085</b>	0.061	0.021	0.003
9	0.072	0.076	0.080	<b>0.075</b>	0.083	0.110	0.128
10	0.064	0.065	0.068	<b>0.071</b>	0.084	0.118	0.136

Table 40. Pore pressure (lb/ft<sup>2</sup>) at selected nodes for different values of  $\beta$ .

Node	$\beta = 0.5$	$\beta = 0.1$	$\beta = 0.01$	$\beta = 1$	$\beta = 2$	$\beta = 10$	$\beta = 100$
1	0.0	0.0	0.0	<b>0.0</b>	-	-	-
2	0.0	0.0	0.0	-	-	-	-
3	0.0	0.0	0.0	-	-	-	-
4	113.5	117.5	118.8	<b>109.8</b>	104.7	91.0	82.3
5	129.5	139.4	143.2	<b>122.3</b>	114.0	95.7	85.2
6	163.2	177.8	183.4	<b>153.4</b>	142.7	121.3	109.4
7	255.7	263.8	266.6	<b>249.5</b>	241.9	223.0	211.2
8	233.7	245.6	249.9	<b>225.3</b>	215.8	194.6	182.3
9	424.1	433.0	436.2	<b>417.8</b>	410.2	392.0	380.6
10	408.8	419.3	423.1	<b>401.4</b>	392.6	372.8	361.0

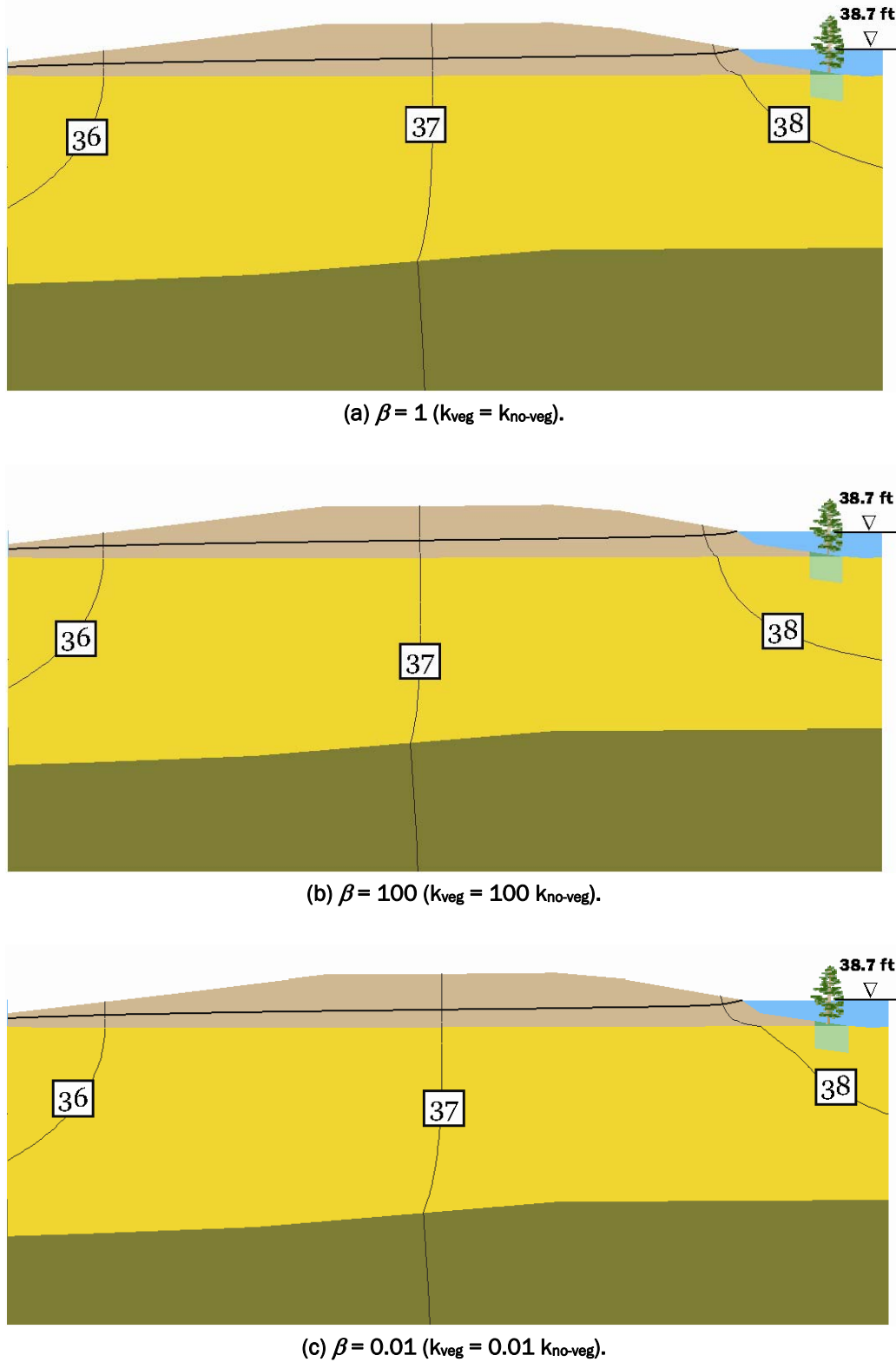


Figure 84. Total head contours and phreatic surface, Burlington, WA.

## ***Transient simulation***

### **No woody vegetation zone**

A transient solution was again performed. The initial condition was computed by setting both the landside and riverside water elevation boundary condition to 32.0 ft and solving the steady-state solution. The same hydrograph was used as before, and the simulation was run to the maximum point on the hydrograph of 38.7 ft. Figure 85 shows the phreatic surface at the initial condition, and Figure 86 shows total head and phreatic surface at the end of the transient simulation.

### **Woody vegetation zone on the toe of the levee**

The woody vegetation zone on the toe of the levee is used for the transient case. The phreatic surface for  $\beta = 1, 100$ , and  $0.01$  is shown in Figure 87. Magnitude of gradient (Table 41) and pore pressure (Table 42) are given in Table 41 and Table 42, respectively, at the nodes (Figure 88) selected for this analysis. Observations from these results are as follows:

- Gradients in the unsaturated zone can be high. Because pore pressure is also negative in this region, there is no upward force.
- Model results, which show a decreased gradient in the woody vegetation zone while increasing  $\beta$  and increased gradient as  $\beta$  is decreased, remain consistent observation throughout this study.
- Model results, which show an increased gradient under the woody vegetation zone as  $\beta$  is increased and a decreasing gradient while decreasing  $\beta$ , remain a consistent observation throughout this study.
- Pore pressures both increase and decrease when varying  $\beta$ .

### **Woody vegetation zone on the lower slope of the levee on the riverside**

The woody vegetation zone on the lower slope of the levee on the riverside is considered for the transient condition. Figure 89 shows the phreatic surface for various values of  $\beta$  for this zone. Clearly, there is no appreciable difference in the flow path on the landside from this zone. However, Figure 90 shows an enlargement of the zone for  $\beta = 0.01$ , where a pocket of negative pore pressure exists. This occurs at times when the rising water level hits a less pervious region.

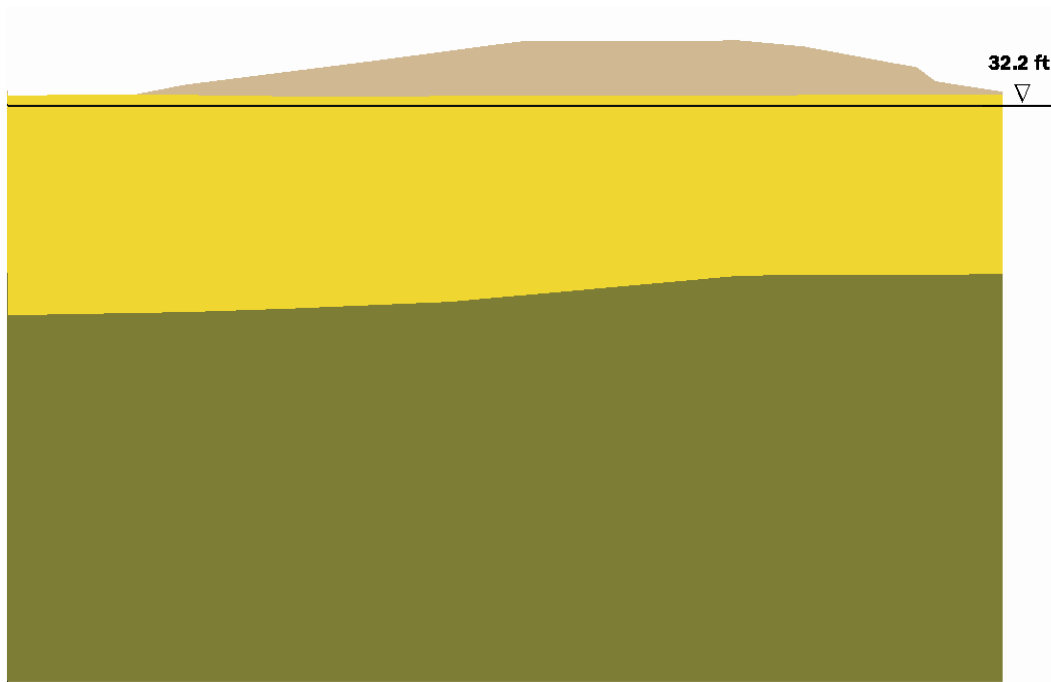


Figure 85. Initial conditions at El. 32 ft, Burlington, WA.

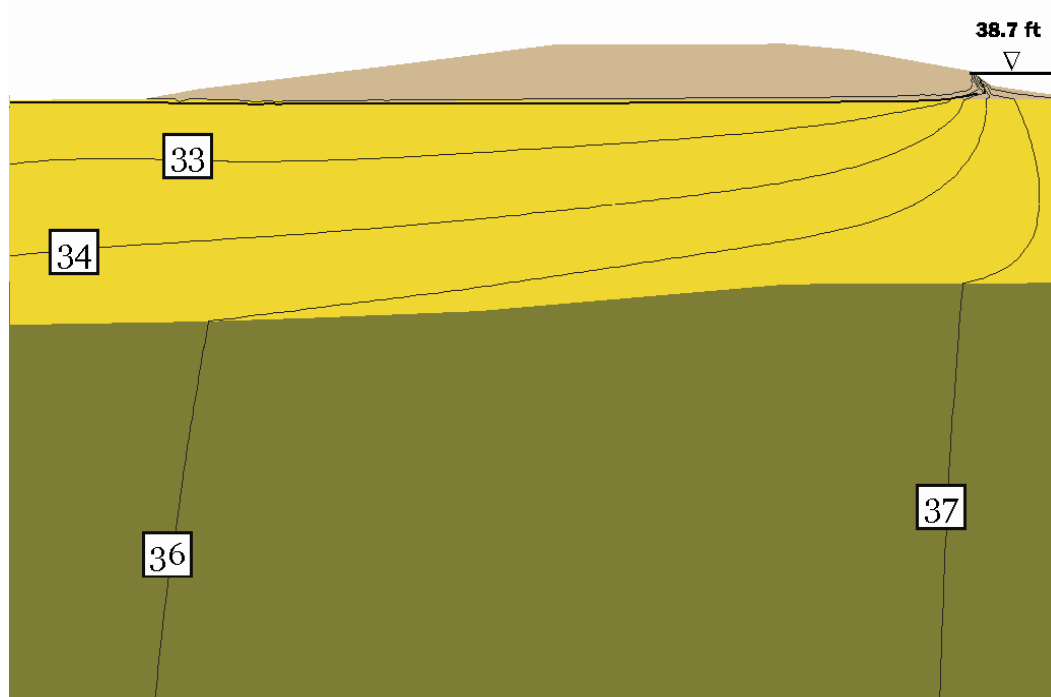


Figure 86. Phreatic surface and total head contours for the transient case, Burlington, WA.

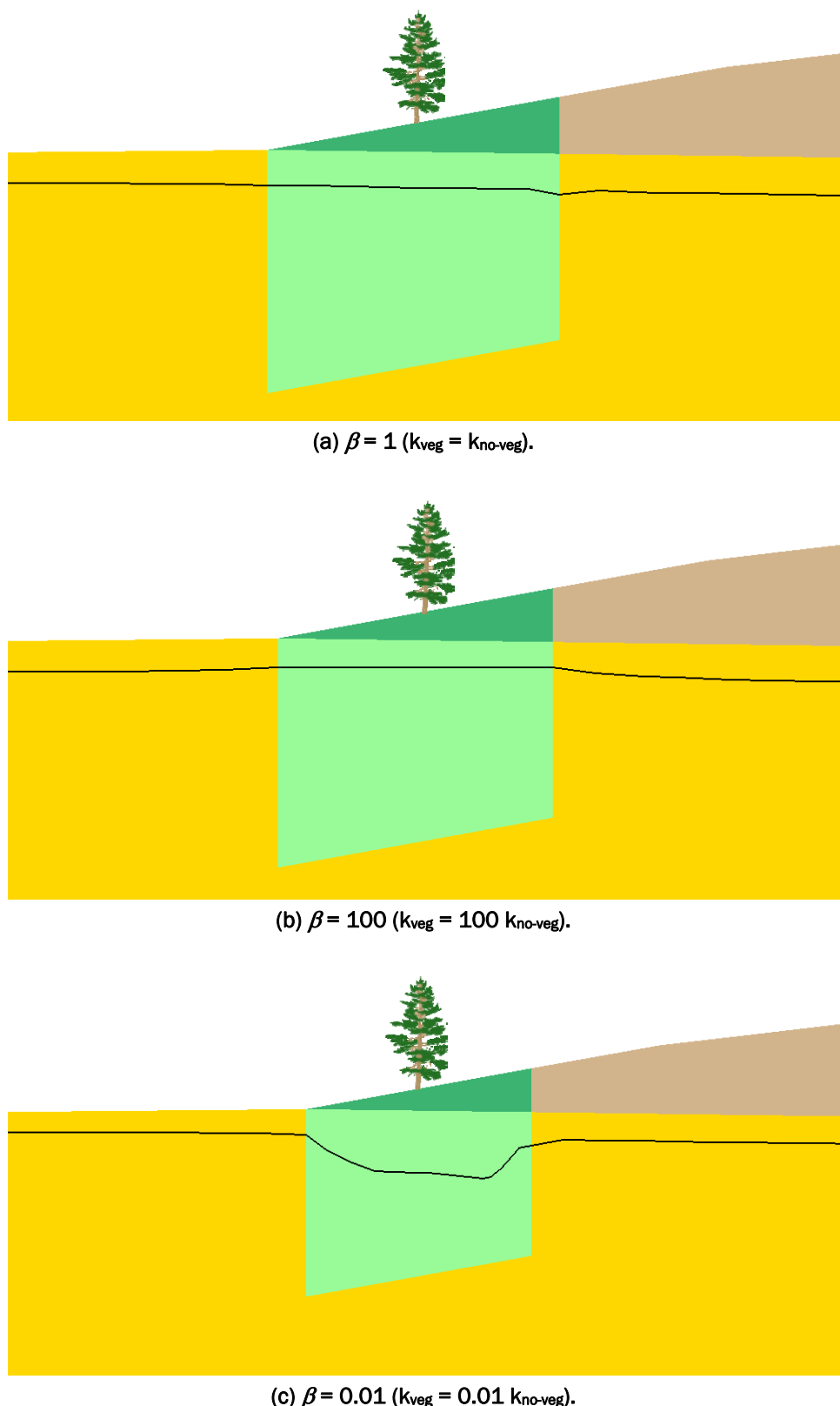


Figure 87. Phreatic surface for transient flow, Burlington, WA.

**Table 41.** Magnitude of gradient at selected nodes for different values of  $\beta$ .

Node	$\beta = 0.01$	$\beta = 1$	$\beta = 100$
1	0.296	<b>3.635</b>	0.876
2	0.000	<b>1.375</b>	1.414
3	0.168	<b>0.872</b>	1.211
4	0.517	<b>0.098</b>	0.002
5	0.435	<b>0.104</b>	0.002
6	0.563	<b>0.090</b>	0.002
7	0.371	<b>0.065</b>	0.001
8	0.607	<b>0.068</b>	0.001
9	0.037	<b>0.066</b>	0.083
10	0.049	<b>0.068</b>	0.080

**Table 42.** Pore pressure (lb/ft<sup>2</sup>) at selected nodes for different values of  $\beta$ .

Node	$\beta = 0.01$	$\beta = 1$	$\beta = 100$
1	-	-	-
2	-	-	-
3	-	-	-
4	-	<b>37.5</b>	40.8
5	-	<b>38.6</b>	43.4
6	-	<b>63.5</b>	67.5
7	166.5	<b>173.7</b>	169.4
8	123.6	<b>141.8</b>	140.4
9	350.0	<b>341.2</b>	334.2
10	327.2	<b>318.8</b>	313.0

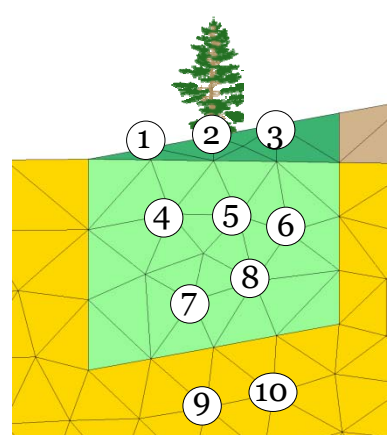


**Figure 88.** Selected nodes, Burlington, WA.

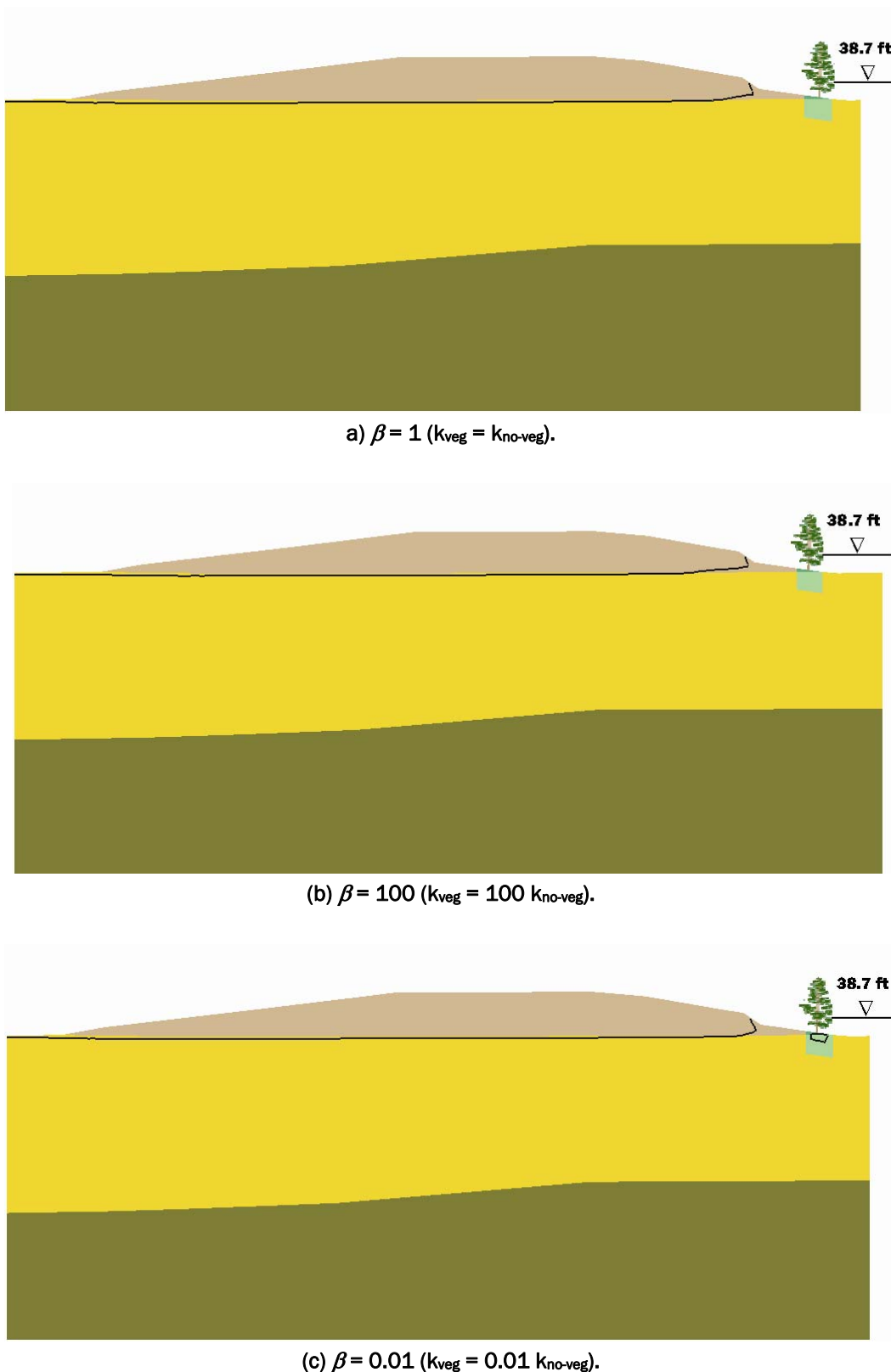


Figure 89. Phreatic surface for different values of  $\beta$  for the transient solution, Burlington, WA.

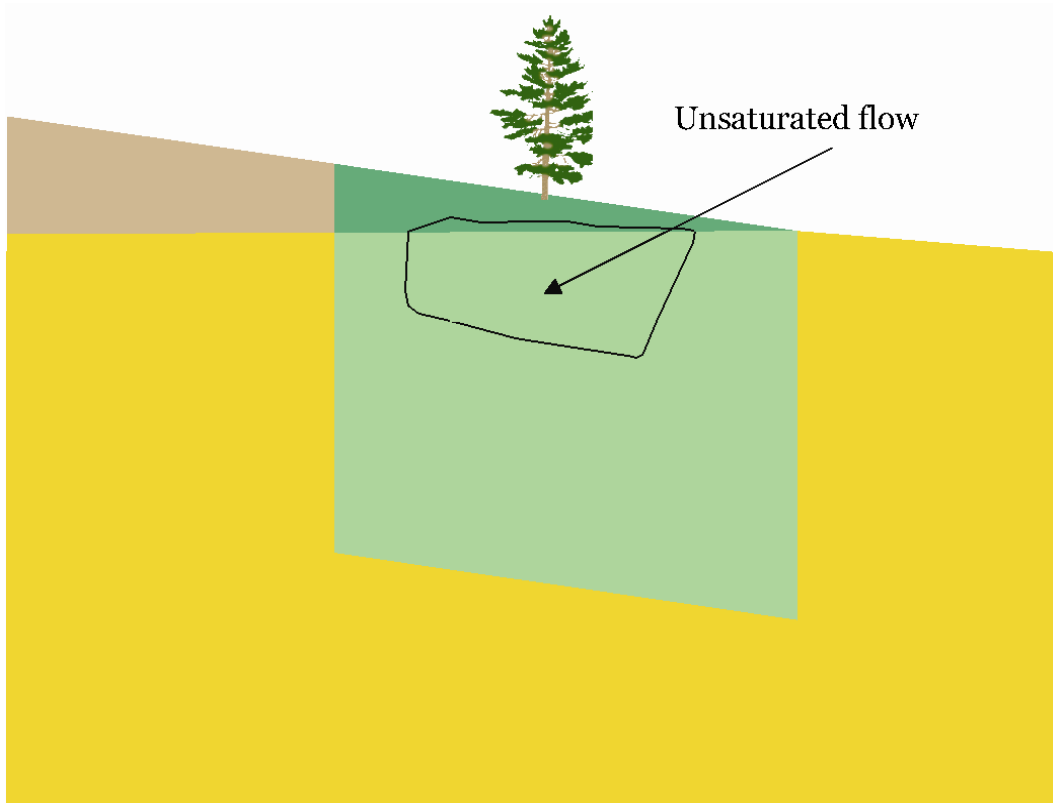


Figure 90. Enlargement of the woody vegetation zone for  $\beta = 0.01$   
( $k_{veg} = 0.01 k_{no-veg}$ ), Burlington, WA.

*Third cross section*

### **Description of the 2-D model**

Figure 91 shows the levee with its material types and location of the woody vegetation zone on the levee to be examined in detail. Only the zone beyond the toe of the levee is considered in this evaluation. Other zones were eliminated from this cross section because of consistency of model results, which show little effect on the flow field in the previous cross sections. Materials are very similar to the second cross section. Figure 92 shows a portion of the FE mesh. The elevation on the landside is always at El. 28.0 ft, and the river elevation is set to 38.7 ft, which is the highest value on the hydrograph, for steady-state flow analysis.

### **Soil properties**

Soil properties for the third Burlington Levee model are given in Tables 43 and 38. Table 43 gives the saturated hydraulic conductivities for the soil layers. Moisture content and van Genuchten parameters in Table 38 are the same values used in the previous two cross sections.

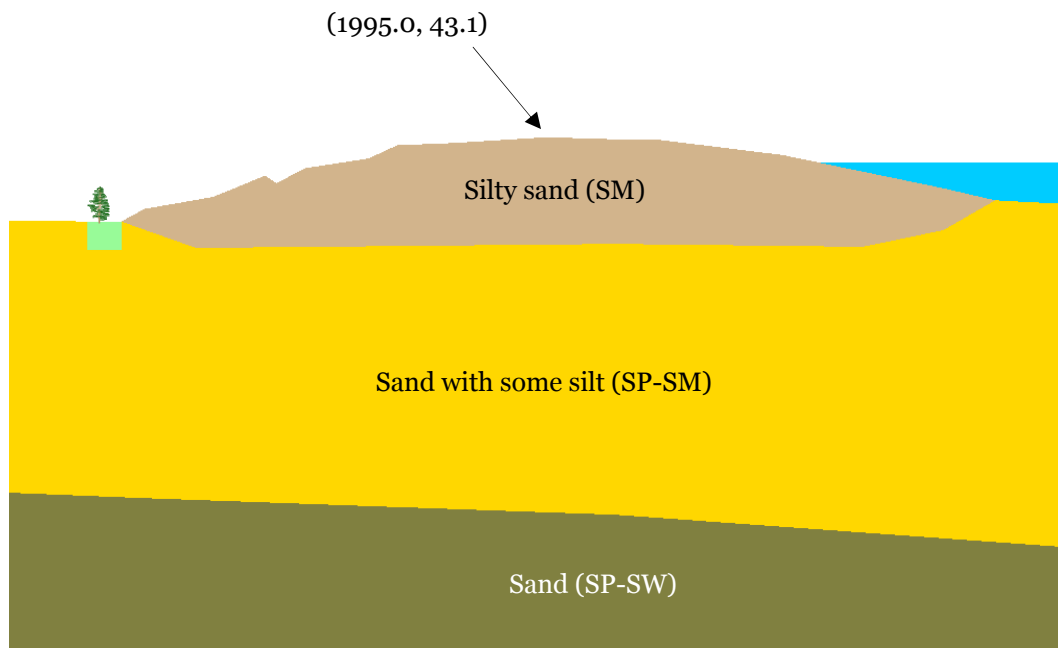


Figure 91. Third cross section with material types and woody vegetation zone, Burlington, WA.

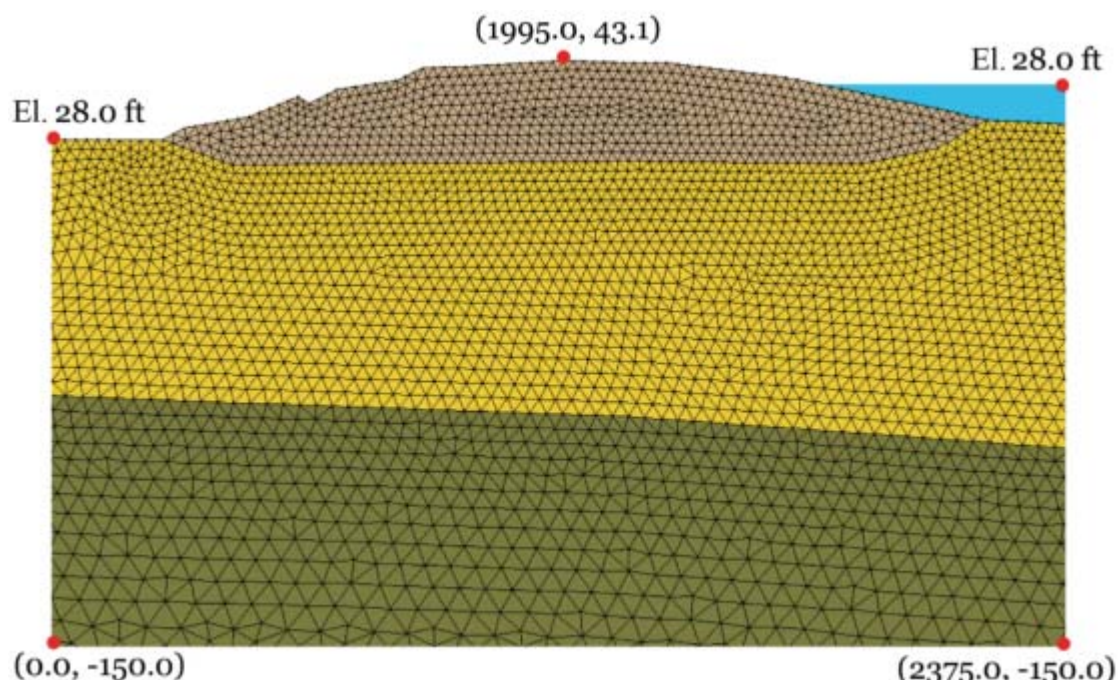


Figure 92. Portion of finite element mesh for the third cross section of the Burlington Levee. The total mesh consists of 19,844 nodes and 38,690 triangular elements.

**Table 43.** Third Burlington Levee model hydraulic conductivities.

Material	$k_H$ (cm/sec)	$k_H$ (ft/day)	$k_V$ (cm/sec)	$k_V$ (ft/day)
Silty sand (SM)	$1.00 \times 10^{-4}$	0.28	$1.00 \times 10^{-4}$	0.28
Sand with some silt (SP-SM)	$2.00 \times 10^{-3}$	5.67	$1.00 \times 10^{-3}$	2.83
Sand (SP-SW)	$9.10 \times 10^{-2}$	257.95	$9.10 \times 10^{-2}$	257.95

### No woody vegetation zone

The model was first run without a woody vegetation zone. Figure 93 shows the location of the phreatic surface and total head contours. The analyses for the different zones are discussed in the following sections.

### Woody vegetation zone just beyond the toe

Figure 94 shows the phreatic surface, velocity vectors, and total head contours for various values of  $\beta$  for the zone just beyond the toe. It is now clearly established that given a levee exhibiting unsaturated flow, the following are consistent observations:

- When the woody vegetation zone is more pervious, the total head contours are spread out, and the phreatic surface is lowered.
- Conversely, when the woody vegetation zone is less pervious, the total head contours are drawn closer, and the phreatic surface is raised.

Figure 95 shows specific nodes that are used to analyze results by tabulating the magnitude of gradient in Table 44 and pore pressure in Table 45. It is now also clearly established that given a levee exhibiting unsaturated flow, the following are true:

- When the woody vegetation zone is more pervious, gradients are reduced in the zone and increased under it.
- Conversely, when the woody vegetation zone is less pervious, gradients are increased in the zone and reduced under it.
- When the woody vegetation zone is more pervious, pore pressures are reduced inside and under the zone.
- Conversely, when the woody vegetation zone is less pervious, pore pressures are increased inside and under the zone.

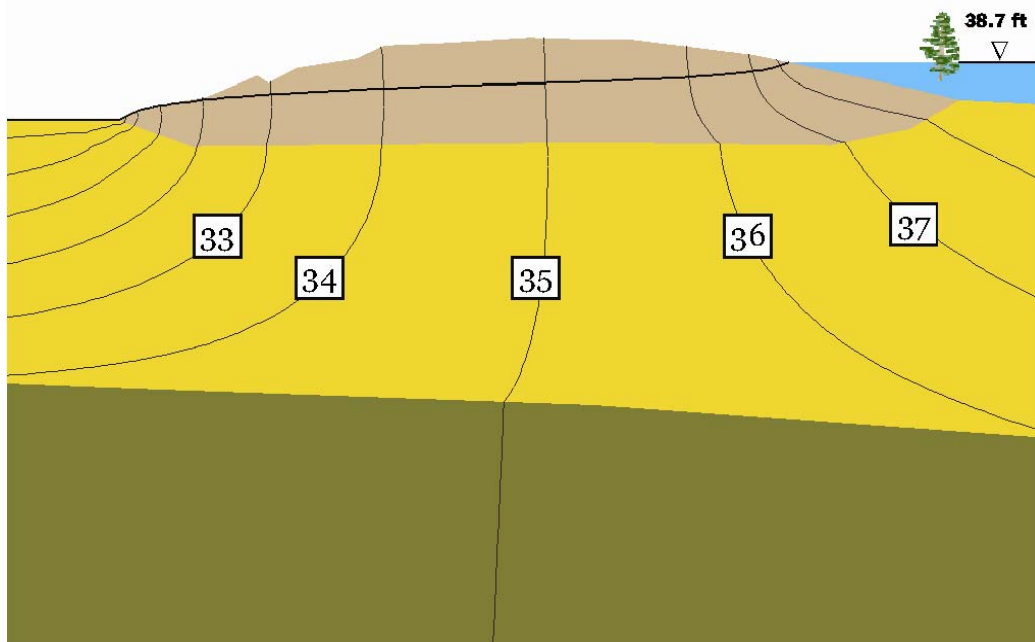


Figure 93. Total head contours and phreatic surface, Burlington, WA.

### ***Transient simulation***

#### **No woody vegetation**

The initial condition was computed for the transient simulation by setting both the landside and riverside water elevation boundary condition to 28 ft and solving the steady-state solution. The same hydrograph was used as before, and the simulation was run to the maximum point on the hydrograph of 38.7 ft. Figure 96 shows the phreatic surface at the initial condition and Figure 97 shows the phreatic surface at the end of the transient simulation.

#### **Woody vegetation zone beyond the toe of the levee**

The woody vegetation zone beyond the toe of the levee is considered for the transient case. Figure 98 shows the phreatic surface and total head contours for  $\beta = 1, 100$ , and  $0.01$ . Figure 99 shows the same selected nodes where magnitude of gradient (Table 46) and pore pressure (Table 47) are tabulated. Observations from these results are as follows:

- When the soil is less pervious, it serves as a deterrent to flow. Thus, the phreatic surface was lowered slightly in the woody vegetation zone.
- When values of magnitude of gradient and pore pressure were higher (lower) as a function of  $\beta$  in the steady-state case, they generally did not rise (go down) as much as in the transient case.

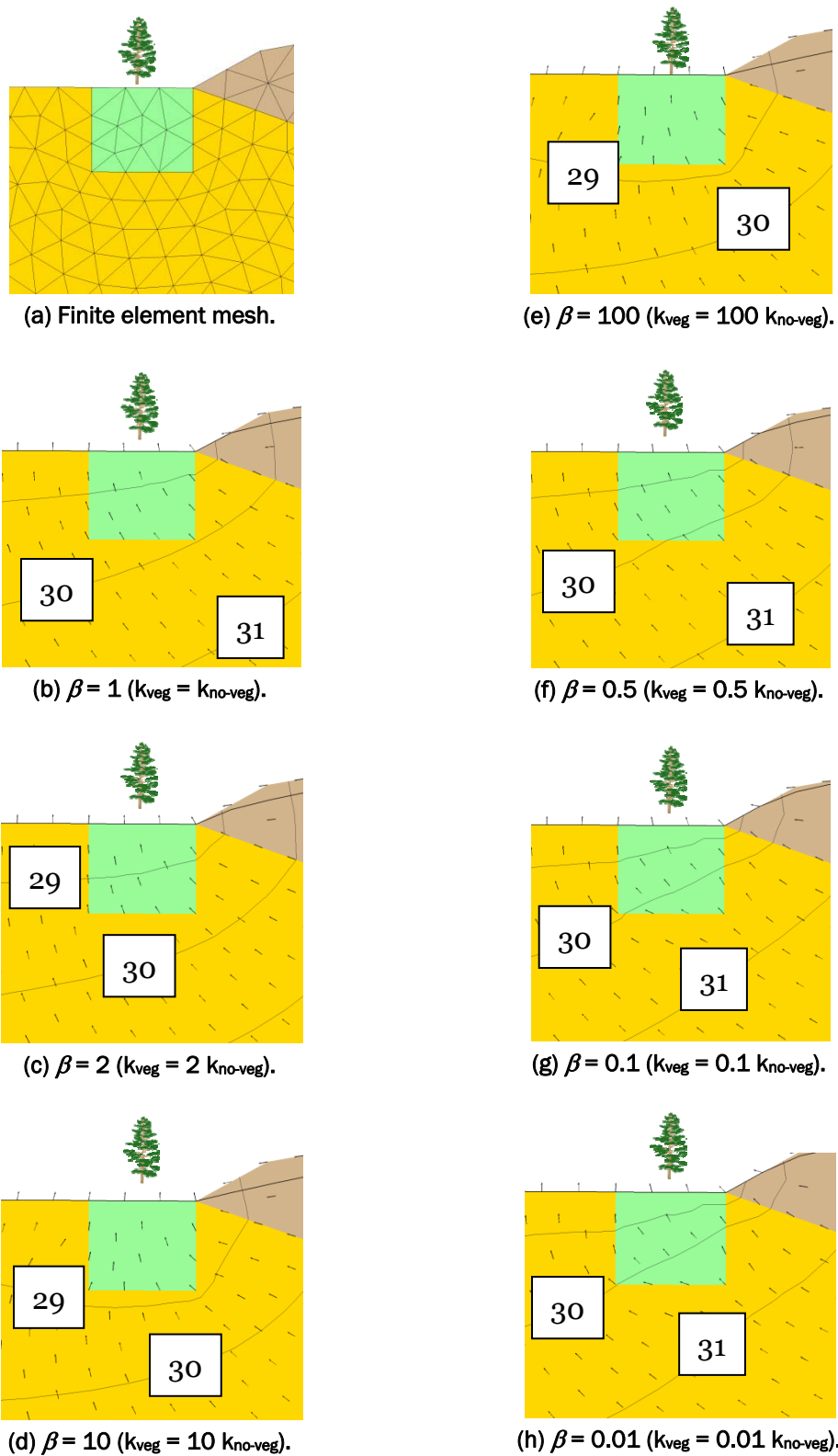


Figure 94. Total head (ft) contours, phreatic surface, and velocity vectors, Burlington, WA.

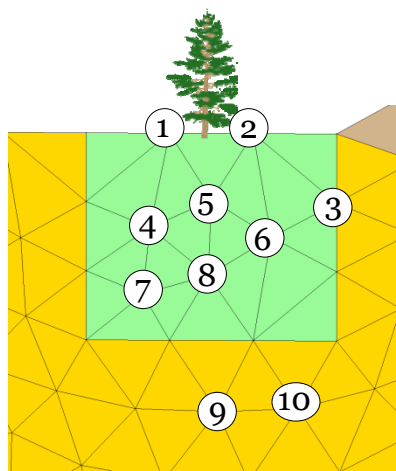


Figure 95. Selected nodes, Burlington, WA.

Table 44. Magnitude of gradient at selected nodes for different values of  $\beta$ .

Node	$\beta = 0.5$	$\beta = 0.1$	$\beta = 0.01$	$\beta = 1$	$\beta = 2$	$\beta = 10$	$\beta = 100$
1	0.316	0.365	0.377	<b>0.269</b>	0.206	0.071	0.007
2	0.436	0.534	0.609	<b>0.348</b>	0.252	0.083	0.012
3	0.426	0.535	0.572	<b>0.348</b>	0.264	0.122	0.078
4	0.303	0.374	0.398	<b>0.251</b>	0.189	0.065	0.007
5	0.349	0.433	0.460	<b>0.287</b>	0.212	0.071	0.008
6	0.350	0.440	0.470	<b>0.285</b>	0.211	0.071	0.009
7	0.286	0.393	0.433	<b>0.224</b>	0.161	0.054	0.006
8	0.305	0.393	0.423	<b>0.243</b>	0.176	0.057	0.007
9	0.162	0.135	0.130	<b>0.188</b>	0.218	0.274	0.297
10	0.156	0.117	0.107	<b>0.188</b>	0.227	0.303	0.337

Table 45. Pore pressure (lb/ft<sup>2</sup>) at selected nodes for different values of  $\beta$ .

Node	$\beta = 0.5$	$\beta = 0.1$	$\beta = 0.01$	$\beta = 1$	$\beta = 2$	$\beta = 10$	$\beta = 100$
1	0.0	0.0	0.0	<b>0.0</b>	0.0	0.0	0.0
2	0.0	0.0	0.0	<b>0.0</b>	0.0	0.0	0.0
3	166.7	190.7	199.8	<b>151.6</b>	136.9	114.3	105.7
4	186.7	193.6	195.3	<b>180.1</b>	171.3	152.4	143.4
5	137.9	146.5	149.3	<b>131.2</b>	123.4	108.4	101.6
6	223.2	242.3	248.9	<b>209.8</b>	195.2	169.2	158.1
7	314.6	327.4	330.9	<b>303.3</b>	289.0	258.8	244.5
8	286.8	303.5	308.8	<b>273.8</b>	258.5	228.9	215.6
9	535.8	553.7	559.4	<b>521.6</b>	504.8	471.6	456.4
10	540.2	559.4	565.4	<b>525.2</b>	507.4	472.3	456.1

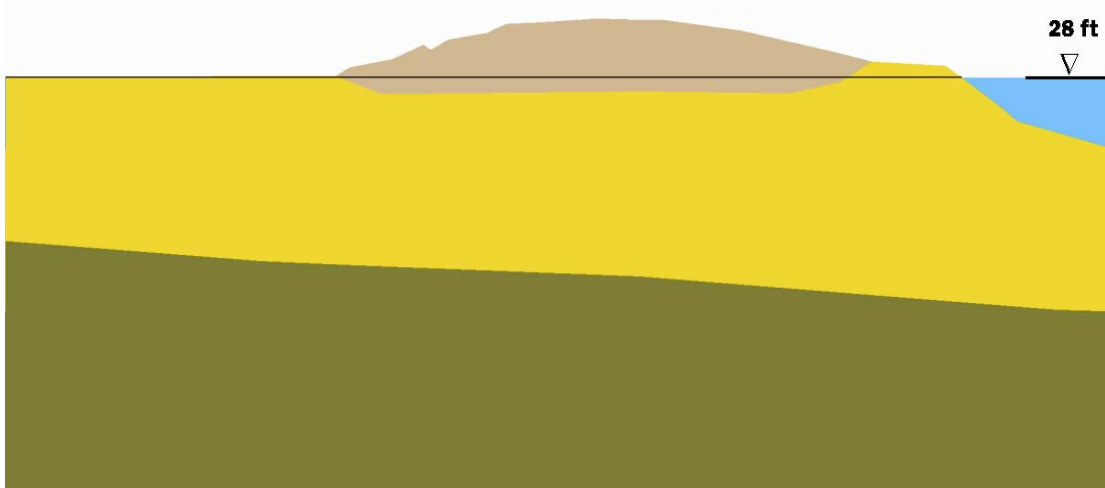


Figure 96. Initial condition of phreatic surface, Burlington, WA.

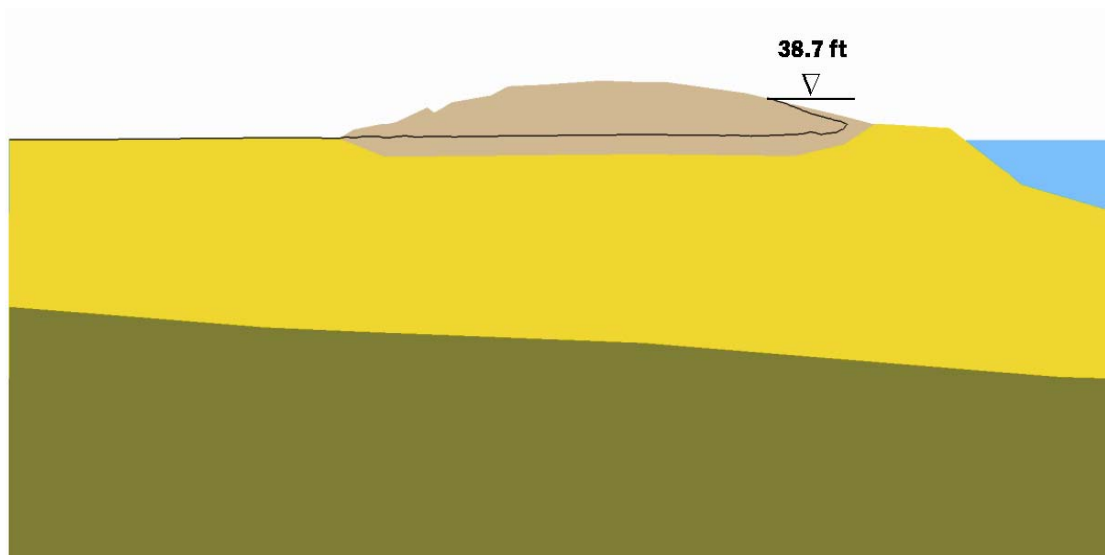


Figure 97. Phreatic surface at the end of the simulation, Burlington, WA.

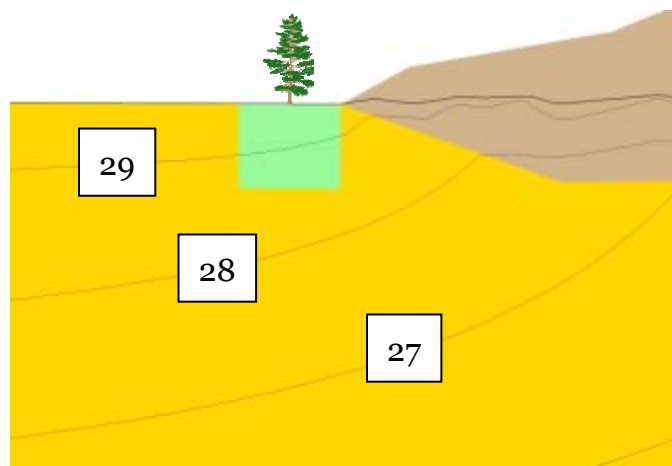
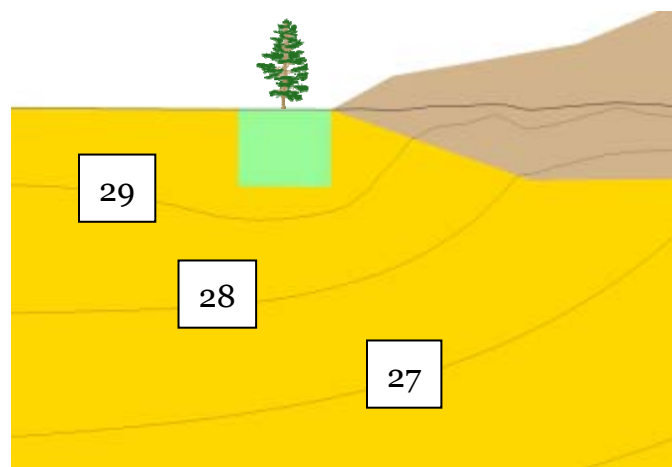
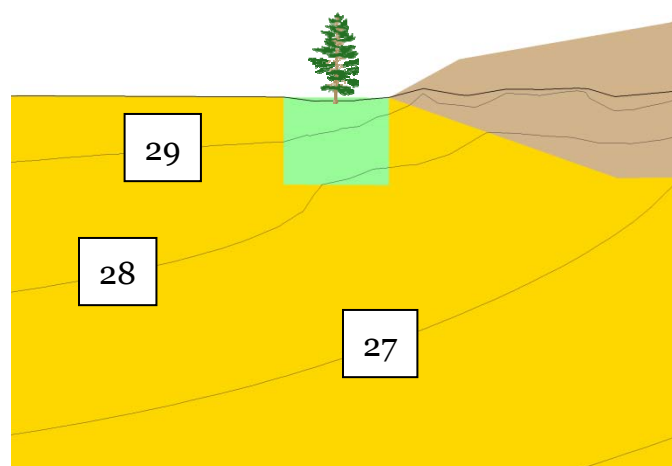
(a)  $\beta = 1$  ( $k_{veg} = k_{no-veg}$ ).(b)  $\beta = 100$  ( $k_{veg} = 100 k_{no-veg}$ ).(c)  $\beta = 0.01$  ( $k_{veg} = 0.01 k_{no-veg}$ ).

Figure 98. Total head contours and phreatic surface for the transient case, Burlington, WA.

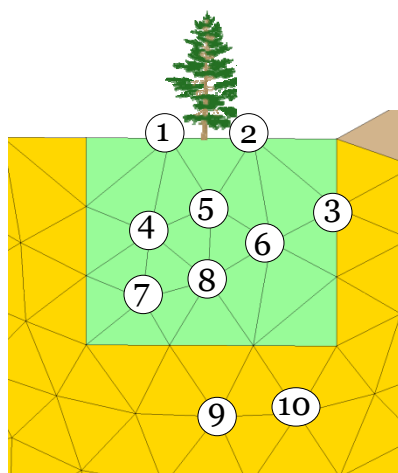


Figure 99. Selected nodes, Burlington, WA.

Table 46. Magnitude of gradient at selected nodes for different values of  $\beta$ .

Node	$\beta = 0.01$	$\beta = 1$	$\beta = 100$
1	0.386	<b>0.212</b>	0.006
2	0.544	<b>0.267</b>	0.010
3	0.447	<b>0.267</b>	0.052
4	0.351	<b>0.199</b>	0.005
5	0.441	<b>0.224</b>	0.007
6	0.399	<b>0.220</b>	0.008
7	0.345	<b>0.181</b>	0.005
8	0.352	<b>0.194</b>	0.006
9	0.096	<b>0.159</b>	0.253
10	0.086	<b>0.156</b>	0.281

Table 47. Pore pressure (lb/ft<sup>2</sup>) at selected nodes for different values of  $\beta$ .

Node	$\beta = 0.01$	$\beta = 1$	$\beta = 100$
1	-	<b>0.0</b>	0.0
2	-	<b>0.0</b>	0.0
3	169.6	<b>138.6</b>	105.5
4	181.1	<b>172.1</b>	143.2
5	130.5	<b>124.2</b>	101.5
6	221.3	<b>196.6</b>	157.8
7	311.7	<b>291.0</b>	244.1
8	284.8	<b>260.5</b>	215.3
9	528.9	<b>501.0</b>	450.4
10	530.2	<b>501.4</b>	448.6

## Albuquerque, NM

The levee in Albuquerque, NM, is the last in the series of levees to be analyzed.

### *Description of the 2-D model*

Figure 100 shows the levee with its material types and location of woody vegetation zones on the levee to be examined in detail. Figure 101 shows a portion of the finite element mesh. Materials are levee sand (soil classification SP), levee silty sand (soil classification SM), blanket sandy silt (soil classification ML), aquifer sand (soil classification SP), gravel and sand toe drain (soil classification GM), and pipe-type drain. River elevation is set to the maximum value (4989.0 ft) from the hydrograph for a steady-state flow analysis. Because this peak flood is not close to the levee crown of 4995.0 ft, a larger value of 4992.0 ft for the river elevation is selected for a second steady-state analysis. The elevation on the landside is always set to 4985.0 ft.

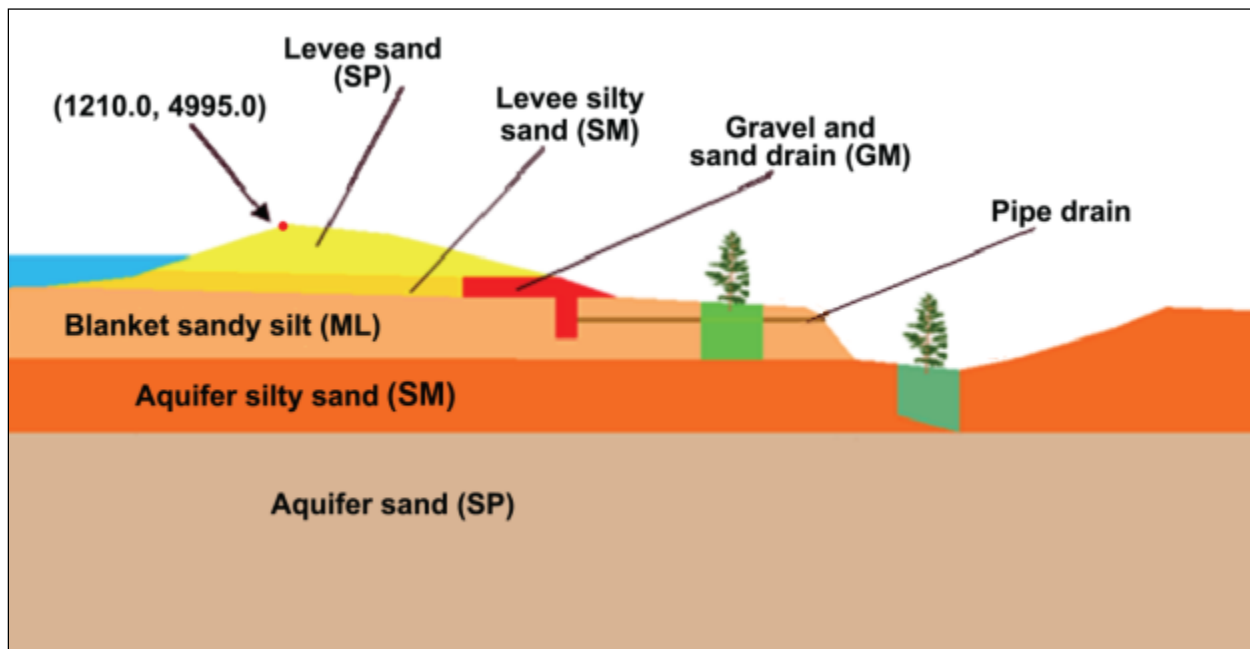


Figure 100. Cross section with material types and woody vegetation zones, Albuquerque, NM.

The ditch on the landside usually has some water in it, unless special permission is given to dewater a portion of the levee for construction. As extreme cases are often emphasized in this study, the ditch will be modeled as an exit face without water.

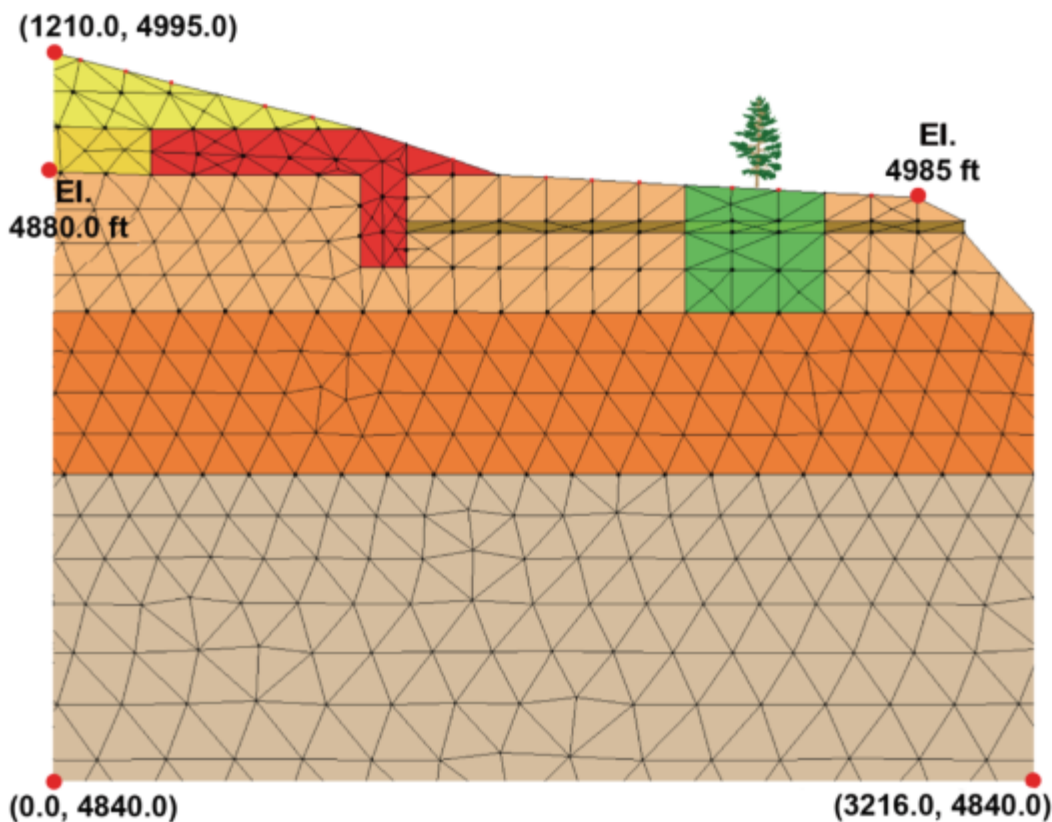


Figure 101. A portion of the finite element mesh for the Albuquerque Levee.  
The total mesh contains 13,800 nodes 26,614 triangular elements.

#### *Soil properties*

Soil properties for the Albuquerque Levee model are given in Tables 48 and 49. Table 48 gives the saturated hydraulic conductivity for the soil layers, and Table 49 provides the moisture content and van Genuchten parameters.

#### *Steady-state results for woody vegetation zones at El. 4992 ft*

#### **No woody vegetation zone**

The model was first run without a woody vegetation zone. Figure 102 shows the location of the phreatic surface and total head contours. Analyses for the different zones are discussed in the following sections.

#### **Woody vegetation zone near the toe of the levee**

The first woody vegetation zone in Figure 100 is near the levee toe. Figure 103 shows the mesh near the woody vegetation zone along with total head contours, the phreatic surface, and velocity vectors for various values

Table 48. Albuquerque Levee model hydraulic conductivities.

Material	$k_H$ (cm/sec)	$k_H$ (ft/day)	$k_V$ (cm/sec)	$k_V$ (ft/day)
Levee sand (SP)	$3.00 \times 10^{-3}$	8.50	$3.00 \times 10^{-3}$	8.50
Levee silty sand (SM)	$1.00 \times 10^{-4}$	0.283	$1.00 \times 10^{-4}$	0.283
Blanket sandy silt (ML)	$1.00 \times 10^{-5}$	0.0283	$1.00 \times 10^{-5}$	0.0283
Aquifer silty sand (SM)	$3.00 \times 10^{-4}$	0.850	$3.00 \times 10^{-4}$	0.850
Aquifer sand (SP)	$6.00 \times 10^{-3}$	17.0	$6.00 \times 10^{-3}$	17.0
Toe drain	$1.00 \times 10^{-3}$	2.83	$1.00 \times 10^{-3}$	2.83
Pipe drain	$1.00 \times 10^{-2}$	28.3	$1.00 \times 10^{-2}$	28.3

Table 49. Albuquerque Levee model moisture content and van Genuchten soil properties.

Material	$\theta_r$	$\theta_s$	$\alpha$ (1/m)	$\alpha$ (1/ft)	n
Levee sand (SP)	0.045	0.430	14.5	4.42	2.68
Levee silty sand (SM)	0.041	0.440	10.2	3.11	2.24
Blanket sandy silt (ML)	0.040	0.445	8.04	2.45	2.03
Aquifer silty sand (SM)	0.041	0.440	10.2	3.11	2.24
Aquifer sand (SP)	0.045	0.430	14.5	4.42	2.68
Toe drain	0.045	0.430	14.5	4.42	2.68
Pipe drain	0.045	0.430	14.5	4.42	2.68

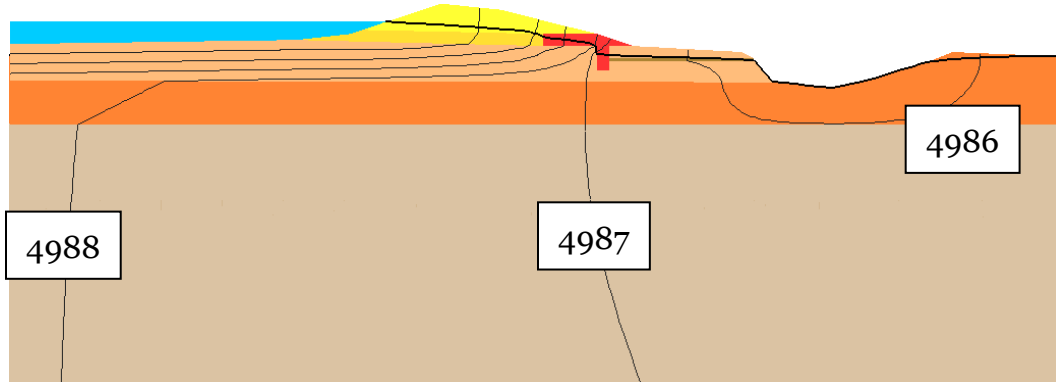


Figure 102. Total head (ft) contours and phreatic surface, Albuquerque, NM.

of  $\beta$ . For consistency with the procedure used in previous modes for this study, nodes were selected, as shown in Figure 104, for tabulating both magnitude of gradient (Table 50) and pore pressure (Table 51). Observations for this location are as follows:

- The phreatic surface never reached the ground surface, although gradients increased when the woody vegetation zone was considered less pervious.

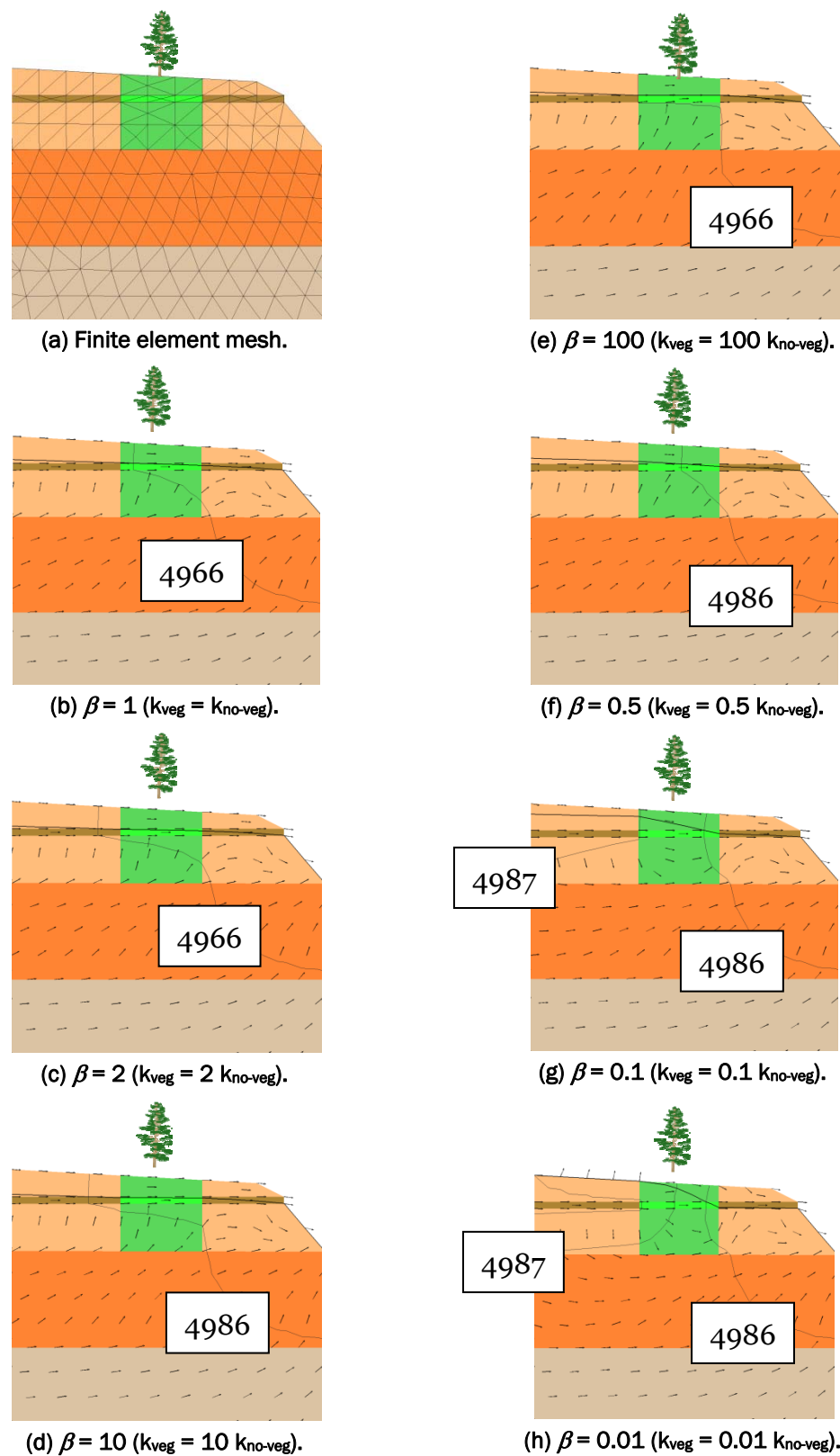


Figure 103. Total head (ft) contours, phreatic surface, and velocity vectors, Albuquerque, NM.

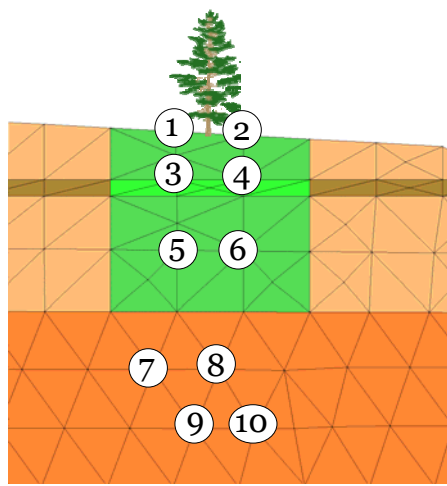


Figure 104. Selected nodes, Albuquerque, NM.

Table 50. Magnitude of gradient at selected nodes for different values of  $\beta$ .

$\beta = 0.5$	$\beta = 0.1$	$\beta = 0.01$	Node	$\beta = 1$	$\beta = 2$	$\beta = 10$	$\beta = 100$
0.060	0.195	0.236	1	<b>0.032</b>	0.017	0.004	0.004
0.062	0.216	0.392	2	<b>0.033</b>	0.018	0.004	0.005
0.060	0.208	0.400	3	<b>0.032</b>	0.017	0.004	0.004
0.062	0.214	0.418	4	<b>0.033</b>	0.018	0.004	0.005
0.130	0.147	0.332	5	<b>0.148</b>	0.154	0.120	0.033
0.129	0.168	0.280	6	<b>0.128</b>	0.124	0.089	0.020
0.056	0.058	0.062	7	<b>0.056</b>	0.058	0.058	0.092
0.075	0.078	0.081	8	<b>0.075</b>	0.075	0.076	0.080
0.066	0.066	0.067	9	<b>0.066</b>	0.067	0.074	0.087
0.088	0.088	0.089	10	<b>0.088</b>	0.088	0.091	0.094

Table 51. Pore pressure (lb/ft<sup>2</sup>) at selected nodes for different values of  $\beta$ .

Node	$\beta = 0.5$	$\beta = 0.1$	$\beta = 0.01$	$\beta = 1$	$\beta = 2$	$\beta = 10$	$\beta = 100$
1	-	-	-	-	-	-	-
2	-	-	-	-	-	-	-
3	-	37.6	78.9	-	-	-	-
4	-	11.6	29.0	-	-	-	-
5	158.5	166.5	188.6	<b>144.8</b>	142.5	139.6	136.1
6	140.8	149.5	159.7	<b>139.1</b>	138.1	137.0	135.9
7	389.1	390.9	392.7	<b>388.4</b>	387.4	382.9	373.4
8	380.4	381.8	393.2	<b>379.8</b>	378.9	374.7	367.2
9	498.1	499.4	500.6	<b>497.6</b>	497.0	494.2	488.7
10	491.1	492.2	493.2	<b>490.7</b>	490.1	487.7	483.4

- Neither the phreatic surface nor pore pressures were significantly changed.

### ***Woody vegetation zone at the bottom of the ditch***

The second woody vegetation zone in Figure 100 is at the bottom of the ditch. Figure 105 shows the mesh near the zone with total head contours, phreatic surface, and velocity vectors for various values of  $\beta$ . Figure 106 shows the nodes selected for tabulating both magnitude of gradient (Table 52) and pore pressure (Table 53). Observations are as follows:

- This woody vegetation zone has a significant impact on the magnitude of gradient and pore pressure.
- A flood at this level that is sustained to achieve close to this steady-state condition creates high gradients.
- When the woody vegetation zone is more pervious ( $\beta > 1$ ), high magnitudes of gradient are lowered within the zone and immediately upstream and downstream of the zone.
- Conversely, when the woody vegetation zone is less pervious, high magnitudes of gradient are increased immediately upstream of, in, and immediately downstream of the woody vegetation zone. Pore pressures are significantly lowered when the zone is more pervious.
- Pore pressures are slightly increased when the woody vegetation zone is less pervious.
- When the woody vegetation zone is more pervious, magnitudes of gradient are increased beneath it.
- Conversely, when the woody vegetation zone is less pervious, the magnitude of gradient is decreased beneath it.

#### *Steady-state results for El. 4989 ft for woody vegetation zones*

The model is run at elevation 4989 ft to compare with the results from elevation 4992 ft.

### ***No woody vegetation zone***

The model was first run without a woody vegetation zone. Figure 107 shows the location of the phreatic surface and total head contours. Analyses for the different zones are discussed in the following sections.

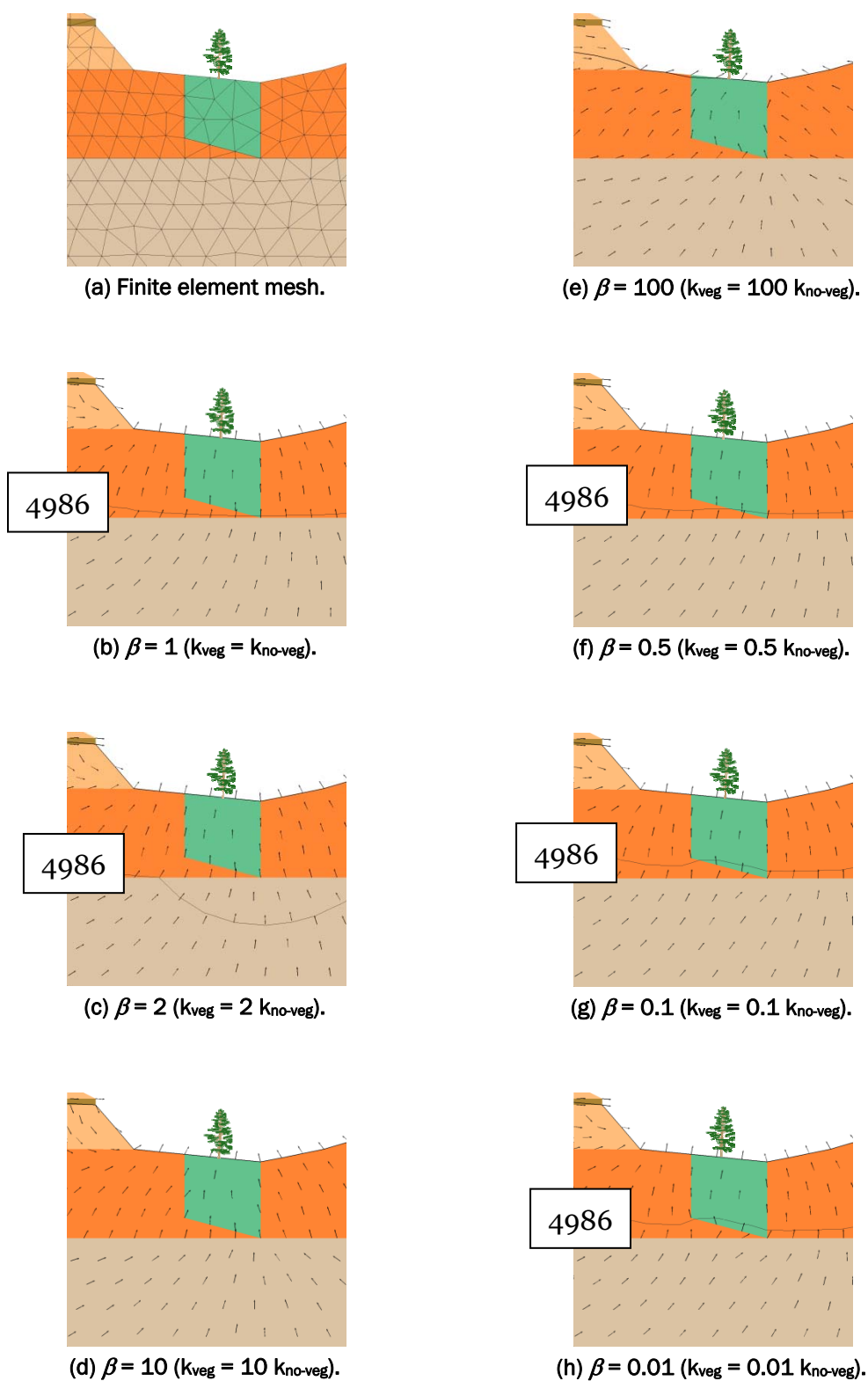


Figure 105. Total head (ft) contours, phreatic surface, and velocity vectors, Albuquerque, NM.

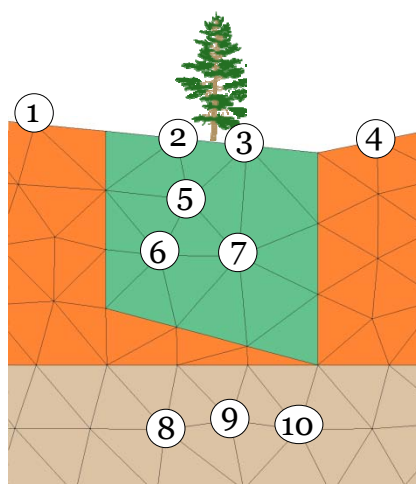


Figure 106. Selected nodes, Albuquerque, NM.

Table 52. Magnitude of gradient at selected nodes for different values of  $\beta$ .

Node	$\beta = 0.5$	$\beta = 0.1$	$\beta = 0.01$	$\beta = 1$	$\beta = 2$	$\beta = 10$	$\beta = 100$
1	0.826	0.896	0.914	<b>0.760</b>	0.664	0.386	0.208
2	0.860	0.948	0.971	<b>0.775</b>	0.653	0.303	0.039
3	0.937	0.999	1.014	<b>0.869</b>	0.763	0.426	0.102
4	0.849	0.875	0.880	<b>0.817</b>	0.764	0.567	0.275
5	0.864	0.939	0.958	<b>0.789</b>	0.676	0.336	0.047
6	0.809	0.887	0.905	<b>0.632</b>	0.618	0.281	0.032
7	0.856	0.926	0.944	<b>0.787</b>	0.686	0.377	0.067
8	0.026	0.017	0.015	<b>0.034</b>	0.047	0.088	0.127
9	0.025	0.017	0.016	<b>0.034</b>	0.049	0.102	0.166
10	0.026	0.023	0.023	<b>0.034</b>	0.046	0.117	0.236

Table 53. Pore pressure (lb/ft<sup>2</sup>) at selected nodes for different values of  $\beta$ .

Node	$\beta = 0.5$	$\beta = 0.1$	$\beta = 0.01$	$\beta = 1$	$\beta = 2$	$\beta = 10$	$\beta = 100$
1	0.0	0.0	0.0	<b>0.0</b>	0.0	0.0	0.0
2	0.0	0.0	0.0	<b>0.0</b>	0.0	0.0	0.0
3	0.0	0.0	0.0	<b>0.0</b>	0.0	0.0	0.0
4	0.0	0.0	0.0	<b>0.0</b>	0.0	0.0	0.0
5	195.4	203.3	205.4	<b>187.3</b>	175.4	139.6	105.4
6	382.2	398.7	402.9	<b>365.8</b>	341.5	269.9	208.0
7	370.9	383.2	386.1	<b>357.9</b>	337.7	273.4	208.9
8	824.1	833.8	836.3	<b>813.8</b>	797.4	730.9	614.9
9	806.2	816.2	818.7	<b>795.7</b>	778.7	708.4	585.3
10	821.6	830.9	833.2	<b>811.5</b>	795.1	723.5	591.8

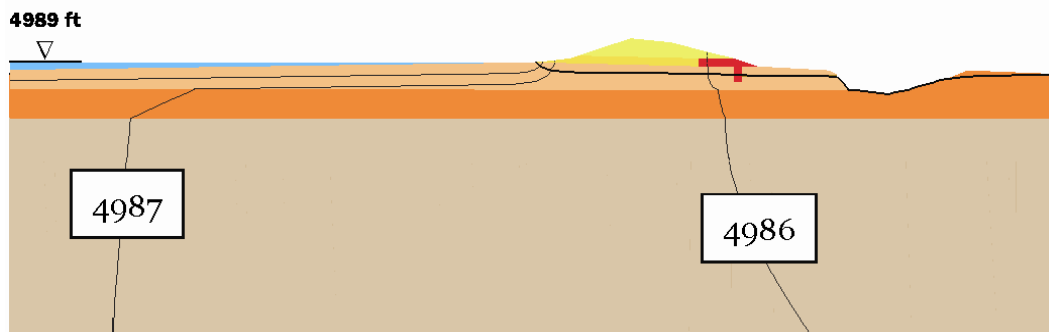


Figure 107. Total head (ft) contours and phreatic surface, Albuquerque, NM.

### ***Woody vegetation zone near the toe of the levee***

The first woody vegetation zone in Figure 100 near the toe of the levee is analyzed. Figure 108 shows the phreatic surface and total head contours for values of  $\beta = 1, 100$ , and  $0.01$ .

### ***Woody vegetation zone at the bottom of the ditch***

The second woody vegetation zone in Figure 100 at the bottom of the ditch is analyzed with a river elevation of 4989 ft. The same nodes in the region as before were selected, as shown in Figure 109, for tabulating the magnitude of gradient (Table 54) and pore pressure (Table 55). An observation is as follows:

- Magnitudes of gradient and pore pressures, which are expected for a lower river elevation, are smaller than those found for river elevation 4992 ft.

#### *Transient solution*

A transient solution was conducted using the hydrograph of the 1942 Flood, shown in Figure 110. Because of differences in the datum used, 2 ft are added to the values in this plot. The initial condition was set to 4985.0 ft on both the riverside and landside boundaries for a steady-state solution. The solution is then run for 21 days to achieve a stage of 4989.0 ft.

### ***No woody vegetation zone***

Figure 111 shows the initial position of the phreatic surface, and Figure 112 shows the phreatic surface at its maximum height without a woody vegetation zone. These results show that the phreatic surface does not achieve the equivalent of steady state. This is consistent with the results

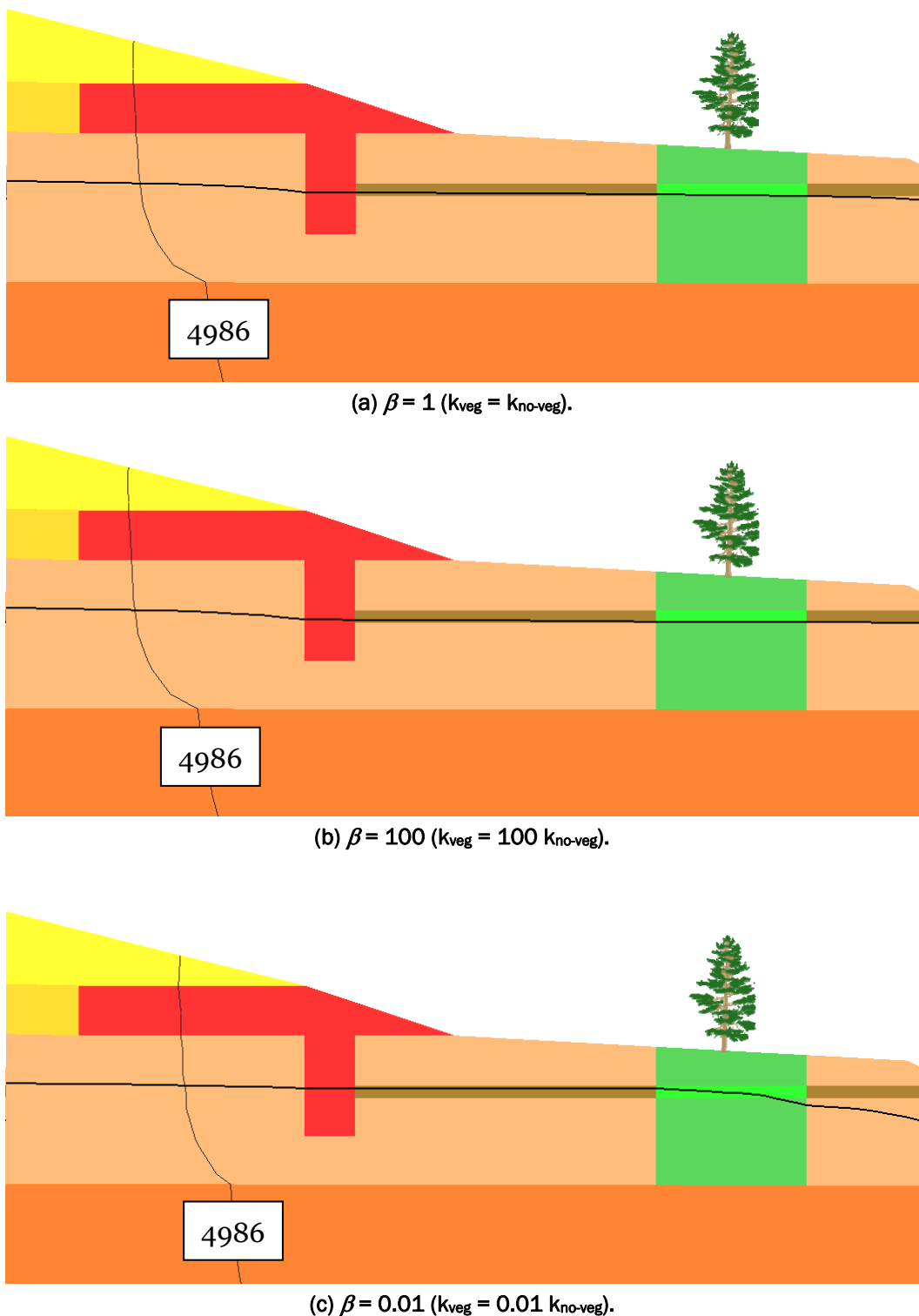


Figure 108. Total head (ft) contours and phreatic surface, Albuquerque, NM.

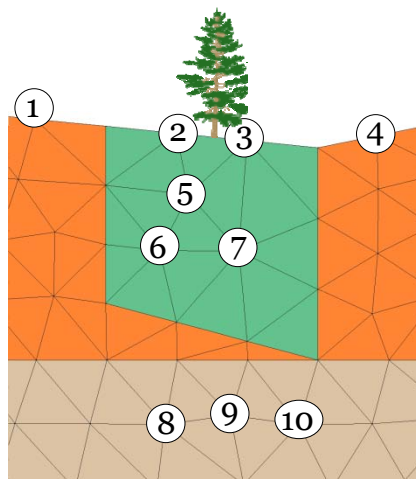


Figure 109. Selected nodes, Albuquerque, NM.

Table 54. Magnitude of gradient at selected nodes for different values of  $\beta$ .

Node	$\beta = 0.01$	$\beta = 1$	$\beta = 100$
1	0.778	0.630	0.271
2	0.838	0.654	0.222
3	0.886	0.745	0.329
4	0.773	0.704	0.435
5	0.828	0.668	0.250
6	0.776	0.615	0.205
7	0.815	0.668	0.283
8	0.011	0.028	0.065
9	0.011	0.028	0.075
10	0.017	0.027	0.087

Table 55. Pore pressure (lb/ft<sup>2</sup>) at selected nodes for different values of  $\beta$ .

Node	$\beta = 0.01$	$\beta = 1$	$\beta = 100$
1	0.0	0.0	0.0
2	0.0	0.0	0.0
3	0.0	0.0	0.0
4	0.0	0.0	0.0
5	191.6	174.6	130.3
6	375.6	340.7	252.5
7	361.2	333.9	254.5
8	790.7	766.3	673.2
9	773.7	748.8	652.5
10	788.9	765.1	668.0

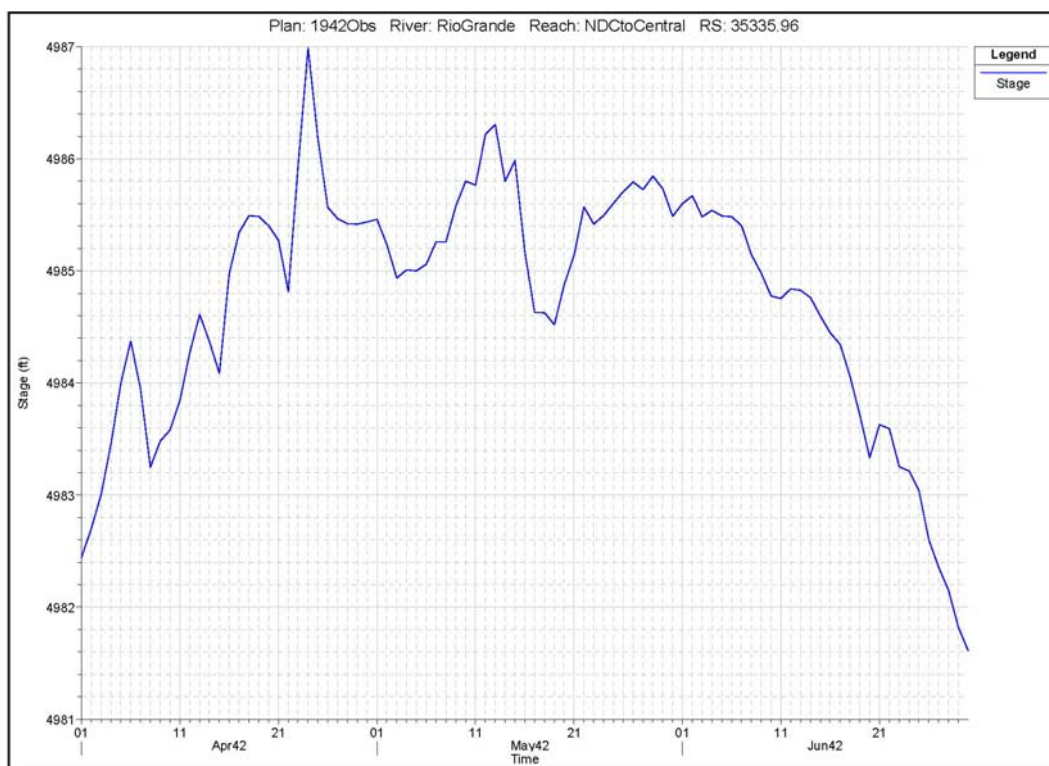


Figure 110. Hydrograph of the 1942 Flood, Albuquerque, NM.

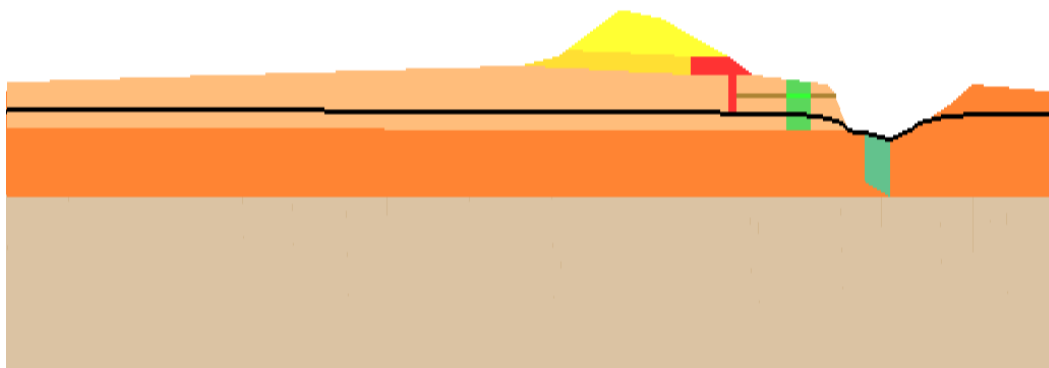


Figure 111. Initial position of the phreatic surface.

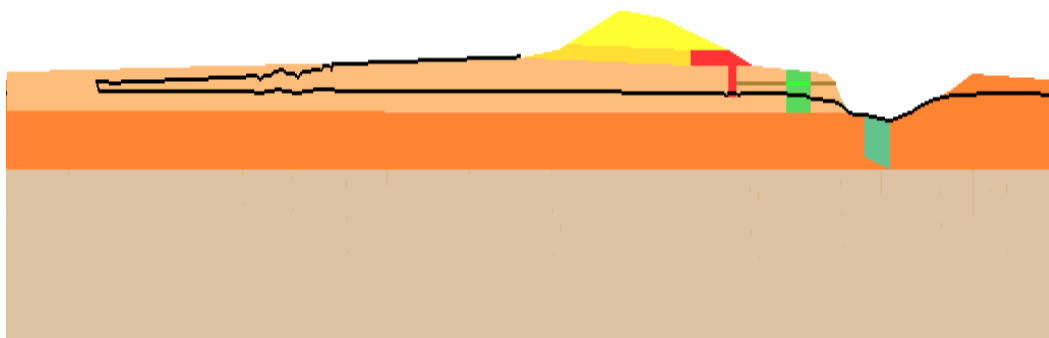


Figure 112. Final position of the phreatic surface.

from the models of all sites in this study. Because the zone on the toe of the levee did not have a significant impact on the flow pattern for the steady-state case, only the zone in the ditch is considered in more detail.

### ***Woody vegetation zone at the bottom of the ditch***

The second woody vegetation zone in Figure 100 at the bottom of the ditch is analyzed using the transient solution. Nodes in Figure 113 are used for tabulating both magnitudes of gradient (Table 56) and pore pressure (Table 57). These are the same nodes as selected for the previous model. Observations are as follows:

- This woody vegetation zone significantly affects both the magnitude of gradient and pore pressure for the transient case as it did for the steady-state cases.
- When the woody vegetation zone was more pervious, the phreatic surface was partially drawn away from the soil surface as demonstrated by the negative pore pressures.
- Magnitudes of gradient and pore pressure were not as high in the transient case as in the steady-state case at elevation 4989 ft.
- When the woody vegetation zone was less pervious, exit gradients became significant again.

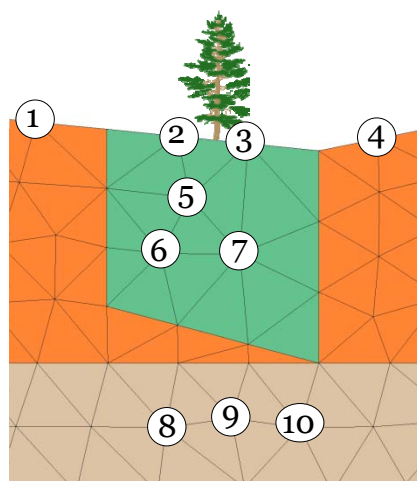


Figure 113. Selected nodes, Albuquerque, NM.

Table 56. Magnitude of gradient at selected nodes for different values of  $\beta$ .

Node	$\beta = 0.01$	$\beta = 1$	$\beta = 100$
1	0.624	<b>0.495</b>	0.189
2	0.687	<b>0.528</b>	0.024
3	0.734	<b>0.613</b>	0.075
4	0.640	<b>0.580</b>	0.215
5	0.678	<b>0.542</b>	0.029
6	0.627	<b>0.495</b>	0.020
7	0.666	<b>0.543</b>	0.043
8	0.009	<b>0.023</b>	0.084
9	0.010	<b>0.023</b>	0.111
10	0.015	<b>0.022</b>	0.157

Table 57. Pore pressure (lb/ft<sup>2</sup>) at selected nodes for different values of  $\beta$ .

Node	$\beta = 0.01$	$\beta = 1$	$\beta = 100$
1	0.0	<b>0.0</b>	-
2	0.0	<b>0.0</b>	0.0
3	0.0	<b>0.0</b>	-
4	0.0	<b>0.0</b>	0.0
5	175.8	<b>161.3</b>	101.4
6	344.3	<b>314.8</b>	202.4
7	331.8	<b>308.6</b>	203.0
8	738.2	<b>716.9</b>	575.5
9	721.2	<b>699.4</b>	550.4
10	736.4	<b>715.6</b>	560.1

## Portland, OR

### *Description of the 2-D model*

Figure 114 shows the levee with its material types and locations of the woody vegetation zones to be evaluated. Figure 115 shows a portion of the FE mesh. River elevation is set to the maximum value of 29.6 ft from the hydrograph used for steady-state flow analysis. The elevation on the landside is always 25 ft.

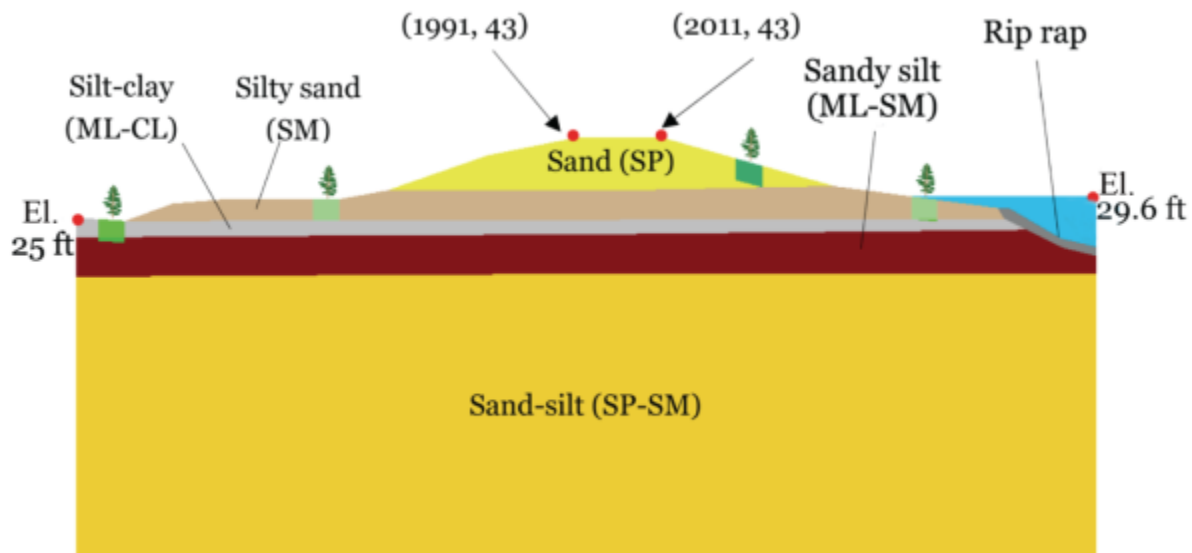


Figure 114. Cross section with material types and woody vegetation zones, Portland, OR.

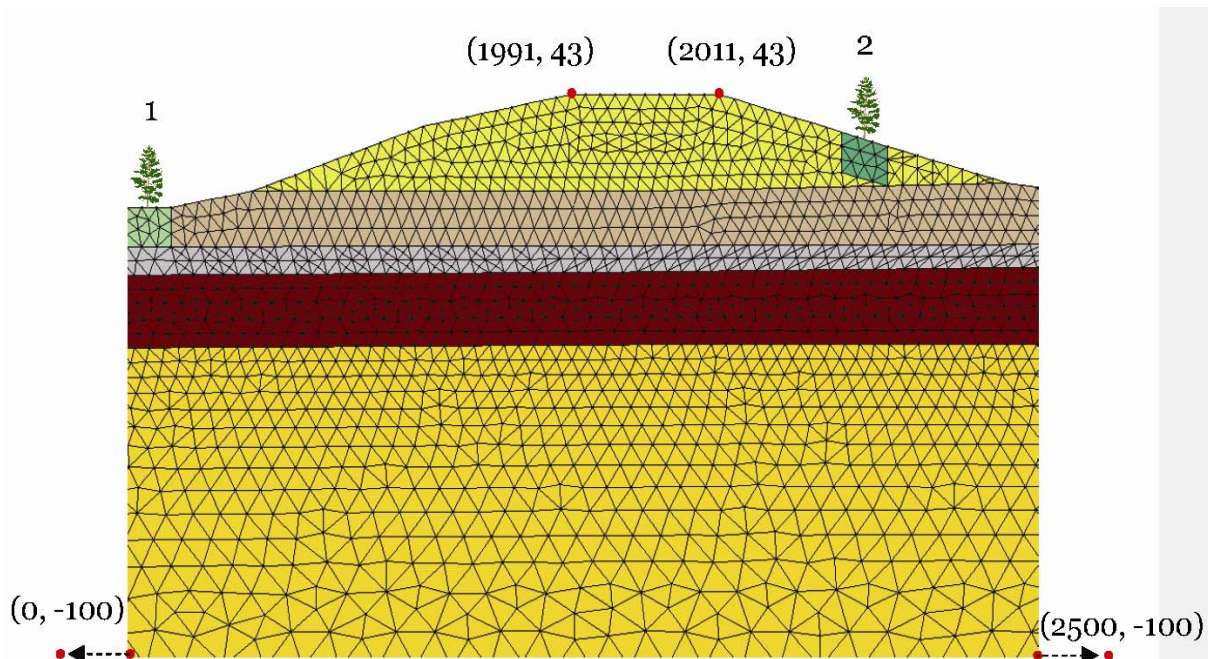


Figure 115. A section of the Portland Levee finite element mesh. The total mesh contains 12,802 nodes and 24,589 triangular elements.

#### *Soil properties*

Soil properties for the Portland Levee model are given in Tables 58 and 59. Table 58 gives the saturated hydraulic conductivities for the soil layers, and Table 59 provides the moisture content and van Genuchten parameters.

Table 58. Portland Levee model hydraulic conductivities.

Material	$k_H$ (cm/sec)	$k_H$ (ft/day)	$k_V$ (cm/sec)	$k_V$ (ft/day)
Sand (SP)	$1.94 \times 10^{-2}$	54.9	$9.66 \times 10^{-3}$	27.4
Silty sand (SM)	$1.94 \times 10^{-3}$	5.5	$9.52 \times 10^{-4}$	2.7
Silt-clay (MC-CL)	$7.05 \times 10^{-5}$	0.2	$3.52 \times 10^{-5}$	0.1
Sandy silt (ML)	$1.76 \times 10^{-4}$	0.5	$1.06 \times 10^{-4}$	0.3
Sand-silt (SP-SM)	$1.94 \times 10^{-3}$	5.5	$9.52 \times 10^{-4}$	2.7
Rip rap	0.645	1828.8	0.645	1828.8

Table 59. Portland Levee model moisture content and van Genuchten soil properties.

Material	$\theta$	$\theta_s$	$\alpha$ (1/m)	$\alpha$ (1/ft)	$n$
Sand (SP)	0.045	0.430	14.5	4.42	2.68
Silty sand (SM)	0.041	0.440	10.2	3.11	2.24
Silt-clay (MC-CL)	0.089	0.43	1.00	0.305	1.23
Sandy silt (ML)	0.040	0.445	8.04	2.45	2.03
Sand-silt (SP-SM)	0.041	0.440	10.2	3.11	2.24
Rip rap	0.045	0.430	14.5	4.42	2.68

Steady-state results for woody vegetation zones

### No woody vegetation zone

The model was first run without a woody vegetation zone. Figure 116 shows the location of the phreatic surface and total head contours.

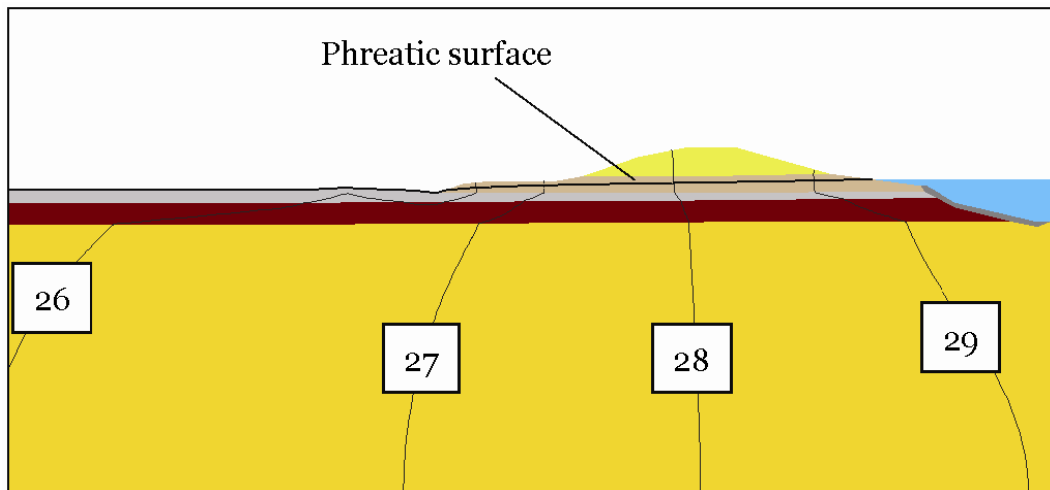


Figure 116. Total head contours and phreatic surface, Portland, OR.

***Woody vegetation zone beyond the lower toe of the levee***

The first woody vegetation zone in Figure 114 is just beyond the lower toe of the levee. Figure 117 shows the mesh near the woody vegetation zone along with total head contours, the phreatic surface, and velocity vectors for various values of  $\beta$ . Nodes in the region were selected, as shown in Figure 118, for tabulating both magnitude of gradient (Table 60) and pore pressure (Table 61). This is consistent with the analyses on the levees for the previous sites.

The following observations from the Pocket Levee and Burlington analyses for a woody vegetation zone just beyond the levee toe can also be made for the Portland Levee:

- As hydraulic conductivity is increased, the magnitude of gradient in the woody vegetation zone is decreased, and the magnitude of gradient below the zone is increased.
- Conversely, as hydraulic conductivity is decreased, the magnitude of gradient in the woody vegetation zone is increased, and the magnitude of gradient below the zone is decreased.
- As hydraulic conductivity is increased, total head contours move away from the woody vegetation zone.
- Conversely, as hydraulic conductivity is decreased, the total head contours move toward the zone.
- As hydraulic conductivity is increased, the flow of water moves toward the woody vegetation zone.
- Conversely, as hydraulic conductivity is increased, the flow of water moves away from the woody vegetation zone.
- As hydraulic conductivity is increased, pore pressures both in and just below the woody vegetation zone are decreased.
- Conversely, as hydraulic conductivity is decreased, pore pressures both in and just below the woody vegetation zone are increased.
- For this particular levee, this location does not produce a negative impact on this flow analysis.

***Woody vegetation zone just beyond the upper toe of the levee***

The second woody vegetation zone in Figure 114 is just beyond the toe of the sandy section of the levee. Figure 119 shows the mesh near the woody vegetation zone along with total head contours, phreatic surface, and velocity vectors for various values of  $\beta$ . As before, nodes in the region were

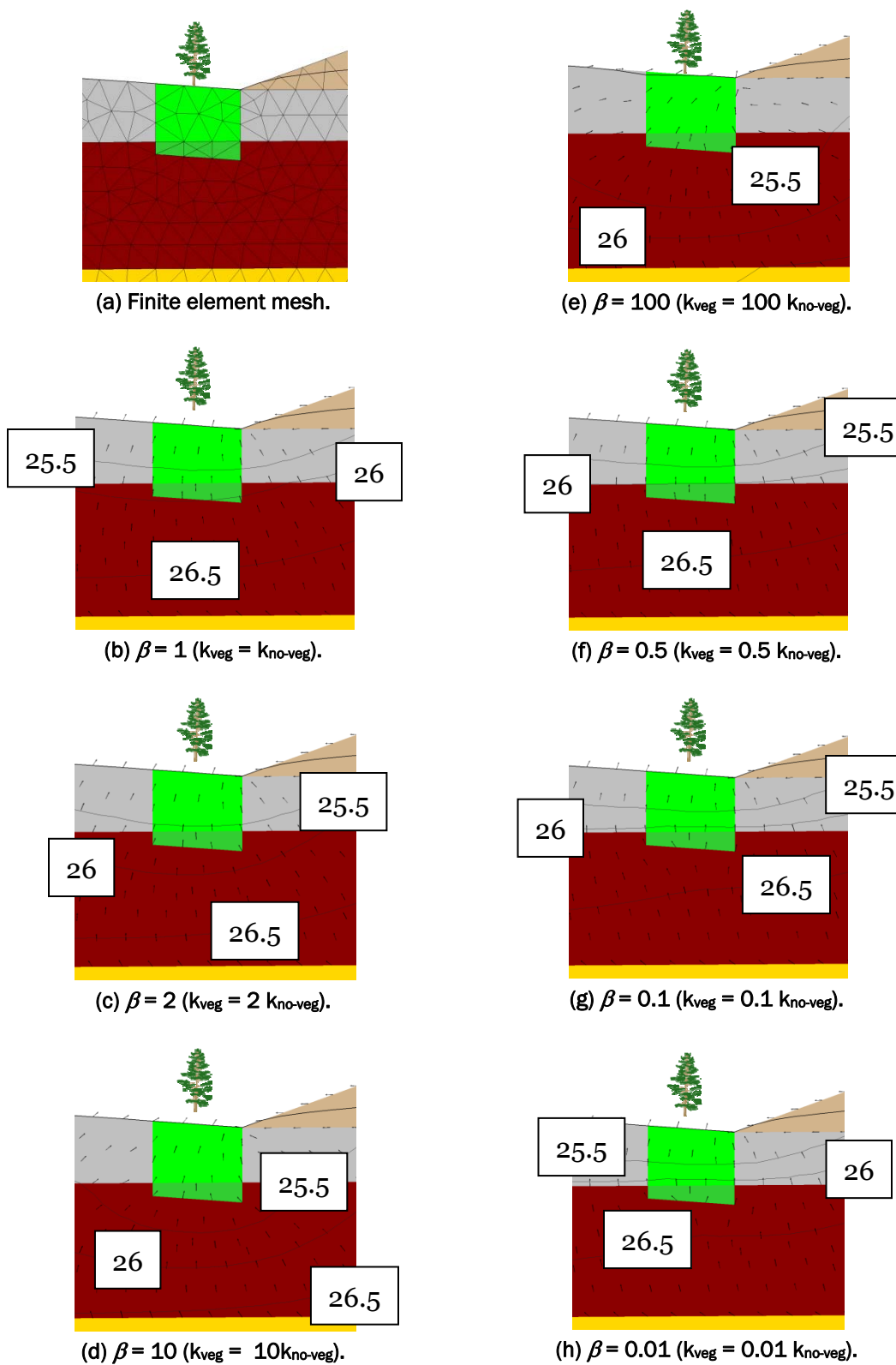


Figure 117. Total head (ft) contours, phreatic surface, and velocity vectors, Portland, OR.

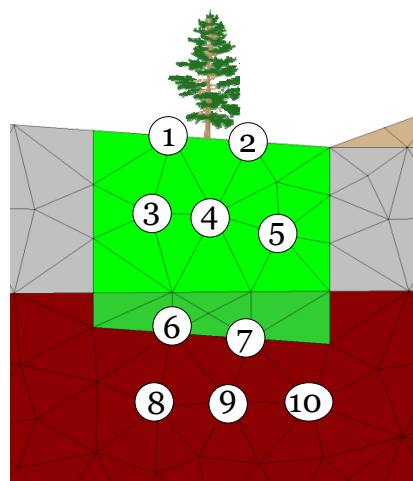


Figure 118. Selected nodes, Portland, OR.

Table 60. Magnitude of gradient at selected nodes for different values of  $\beta$ .

Node	$\beta = 0.5$	$\beta = 0.1$	$\beta = 0.01$	$\beta = 1$	$\beta = 2$	$\beta = 10$	$\beta = 100$
1	0.450	0.494	0.501	<b>0.407</b>	0.341	0.145	0.039
2	0.537	0.583	0.595	<b>0.491</b>	0.423	0.216	0.045
3	0.423	0.456	0.465	<b>0.387</b>	0.331	0.147	0.016
4	0.468	0.508	0.518	<b>0.428</b>	0.368	0.177	0.023
5	0.470	0.496	0.501	<b>0.439</b>	0.386	0.200	0.036
6	0.107	0.102	0.101	<b>0.114</b>	0.125	0.169	0.211
7	0.115	0.113	0.113	<b>0.119</b>	0.126	0.148	0.170
8	0.082	0.060	0.054	<b>0.104</b>	0.137	0.233	0.315
9	0.081	0.051	0.043	<b>0.108</b>	0.145	0.251	0.337
10	0.086	0.065	0.060	<b>0.108</b>	0.143	0.258	0.359

Table 61. Pore pressure (lb/ft<sup>2</sup>) at selected nodes for different values of  $\beta$ .

Node	$\beta = 0.5$	$\beta = 0.1$	$\beta = 0.01$	$\beta = 1$	$\beta = 2$	$\beta = 10$	$\beta = 100$
1	0.0	0.0	0.0	<b>0.0</b>	0.0	0.0	0.0
2	0.0	0.0	0.0	<b>0.0</b>	0.0	0.0	0.0
3	178.9	184.0	185.3	<b>173.7</b>	165.8	141.3	116.9
4	176.6	181.6	182.9	<b>171.5</b>	163.8	139.9	117.2
5	222.1	228.3	229.8	<b>215.8</b>	206.1	175.8	149.0
6	428.6	440.1	443.3	<b>4117.6</b>	401.3	351.7	309.2
7	439.2	450.8	453.9	<b>428.1</b>	411.8	371.3	318.1
8	555.5	562.7	564.5	<b>548.2</b>	537.0	501.0	469.2
9	544.8	552.7	554.8	<b>536.9</b>	524.8	486.2	452.5
10	551.9	558.6	560.3	<b>544.8</b>	533.7	496.5	463.3

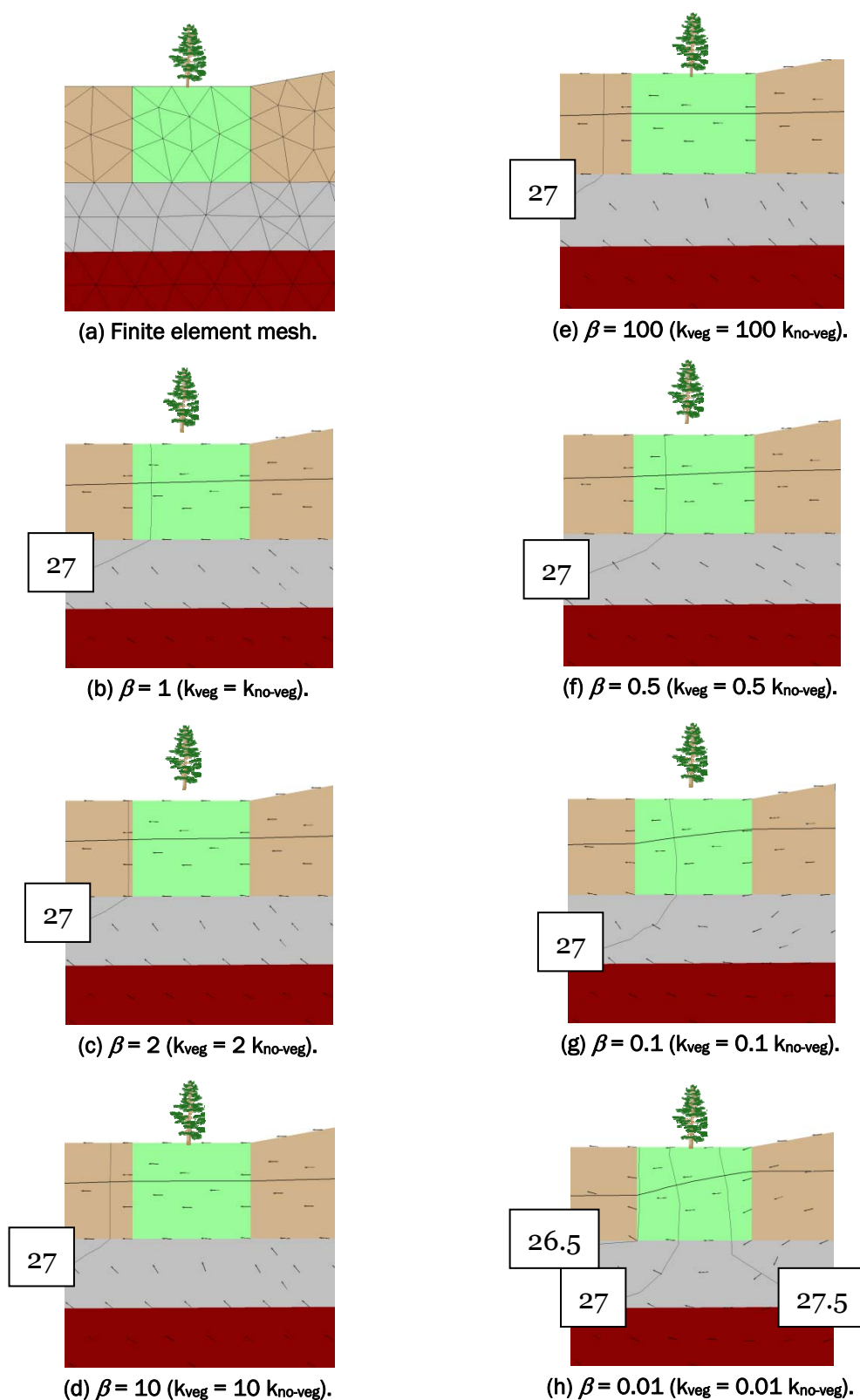


Figure 119. Total head (ft) contours, phreatic surface, and velocity vectors, Portland, OR.

selected, as shown in Figure 120, for tabulating the magnitude of gradient (Table 62) and pore pressure (Table 63). As with the previous levee results in this research, negative pore pressures were replaced with a dash. Observations that can be drawn are as follows:

- When the woody vegetation zone has higher hydraulic conductivity than the surrounding soil, the drop of potential of total head is delayed beyond the zone. However, the effect on gradient is negligible because the flow is parallel to the surface for this zone.
- When the woody vegetation zone has lower hydraulic conductivity than the surrounding soil, the zone becomes an obstacle to flow. Because of this, there is some change in flow, and the magnitude of gradient increases. However, gradients are still rather small and do not affect the stability of the levee.
- When the woody vegetation zone has lower hydraulic conductivity than the surrounding soil, the phreatic surface is lowered.

### ***Woody vegetation zone nearly midslope to the levee crown on the riverside***

The third woody vegetation zone in Figure 114 is nearly midslope to the levee crown on the riverside. Plots of total head contours and phreatic surface for this zone using  $\beta = 1, 100$ , and  $0.01$  are given in Figure 121. From these plots, it is seen that the flow is not affected by this zone, a result consistent with that of previous analyses.

### ***Woody vegetation zone at the river elevation on the riverside***

The fourth woody vegetation zone in Figure 114 is at the water level on the riverside. Plots of total head contours and the phreatic surface for this zone using  $\beta = 1, 100$ , and  $0.01$  are given in Figure 122. From these plots, it is seen that flow is not affected by this zone. This is consistent with previous results.

#### *Transient analysis*

A transient flow analysis was conducted, as in the previous seepage models, for changes in hydraulic conductivity described for this research. The initial condition was selected as 25.0 ft on the landside, and 26.0 ft on the riverside of the levee, given that this is the first point on the

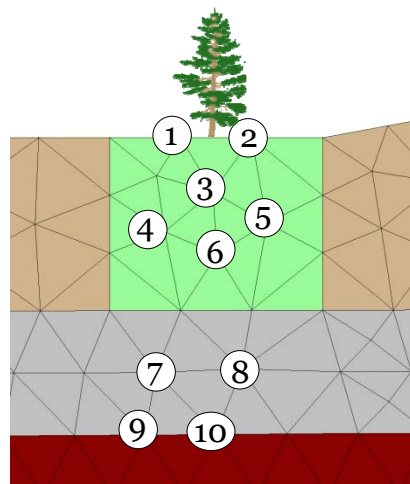


Figure 120. Selected nodes,  
Portland, OR.

Table 62. Magnitude of gradient at selected nodes for different values of  $\beta$ .

Node	$\beta = 0.5$	$\beta = 0.1$	$\beta = 0.01$	$\beta = 1$	$\beta = 2$	$\beta = 10$	$\beta = 100$
1	0.046	0.136	0.242	<b>0.025</b>	0.013	0.003	0.000
2	0.042	0.107	0.166	<b>0.024</b>	0.013	0.003	0.000
3	0.044	0.123	0.204	<b>0.025</b>	0.013	0.003	0.000
4	0.045	0.135	0.241	<b>0.025</b>	0.013	0.003	0.000
5	0.042	0.110	0.180	<b>0.023</b>	0.013	0.003	0.000
6	0.043	0.119	0.196	<b>0.024</b>	0.013	0.003	0.000
7	0.061	0.105	0.155	<b>0.051</b>	0.046	0.041	0.039
8	0.049	0.080	0.124	<b>0.047</b>	0.048	0.049	0.049
9	0.043	0.062	0.084	<b>0.039</b>	0.035	0.033	0.032
10	0.038	0.049	0.065	<b>0.035</b>	0.034	0.033	0.033

Table 63. Pore pressure (lb/ft<sup>2</sup>) at selected nodes for different values of  $\beta$ .

Node	$\beta = 0.5$	$\beta = 0.1$	$\beta = 0.01$	$\beta = 1$	$\beta = 2$	$\beta = 10$	$\beta = 100$
1	-	-	-	-	-	-	-
2	-	-	-	-	-	-	-
3	-	-	-	-	-	-	-
4	40.9	36.8	32.4	<b>42.1</b>	42.7	43.4	43.5
5	33.5	43.3	53.7	<b>31.2</b>	29.8	28.7	28.4
6	84.5	87.5	90.7	<b>83.9</b>	83.5	83.2	83.1
7	294.9	292.6	290.1	<b>295.4</b>	295.7	296.0	296.1
8	292.5	295.9	299.2	<b>291.7</b>	291.2	290.7	290.6
9	409.8	409.2	408.5	<b>409.9</b>	409.9	410.0	410.0
10	411.7	412.8	413.8	<b>411.4</b>	411.2	411.0	411.0

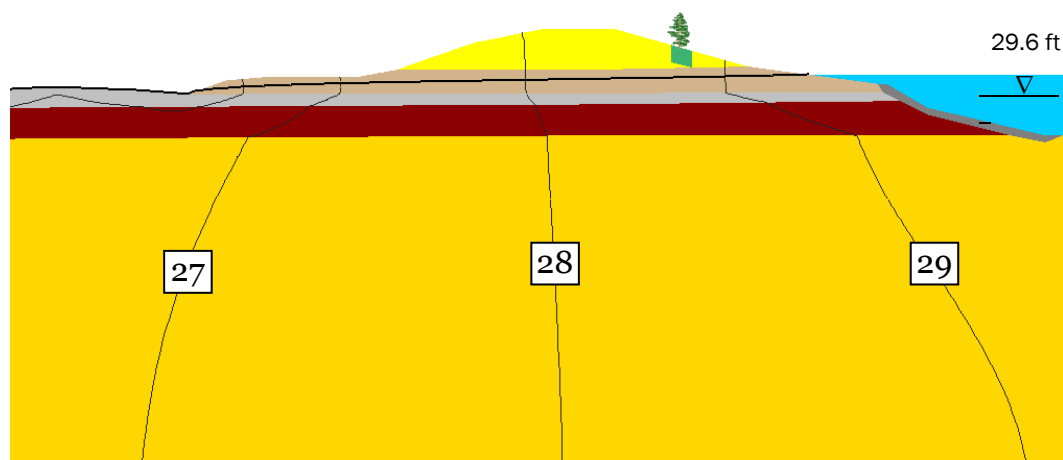
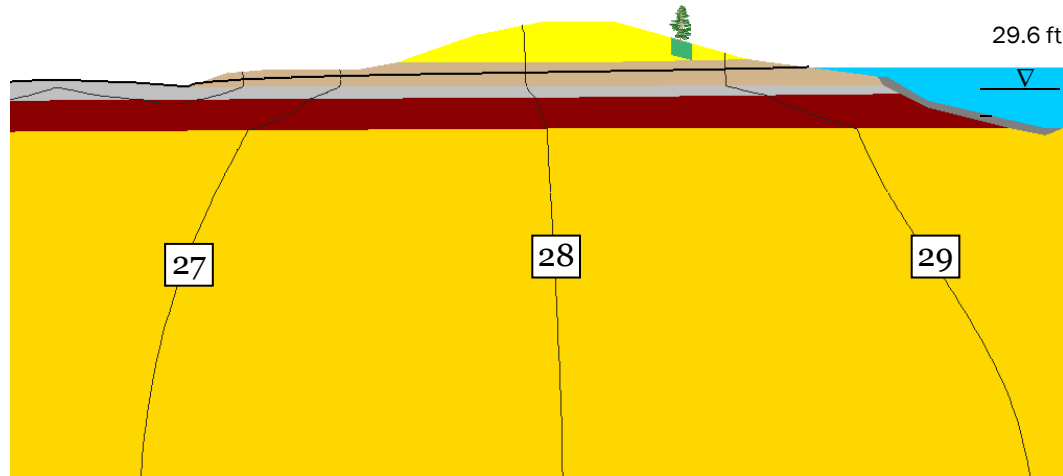
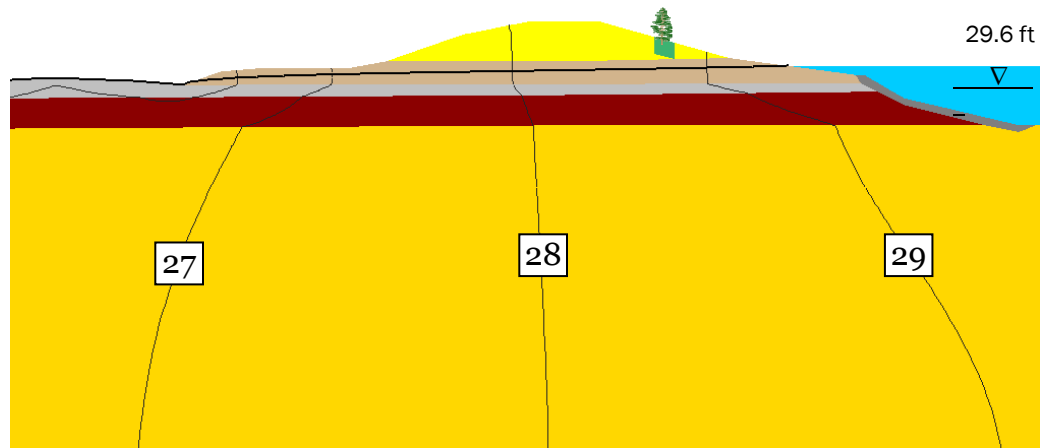
(a)  $\beta = 1$  ( $k_{\text{veg}} = k_{\text{no-veg}}$ ).(b)  $\beta = 100$  ( $k_{\text{veg}} = 100 k_{\text{no-veg}}$ ).(c)  $\beta = 0.01$  ( $k_{\text{veg}} = 0.01 k_{\text{no-veg}}$ ).

Figure 121. Total head (ft) contours and phreatic surface, Portland, OR.

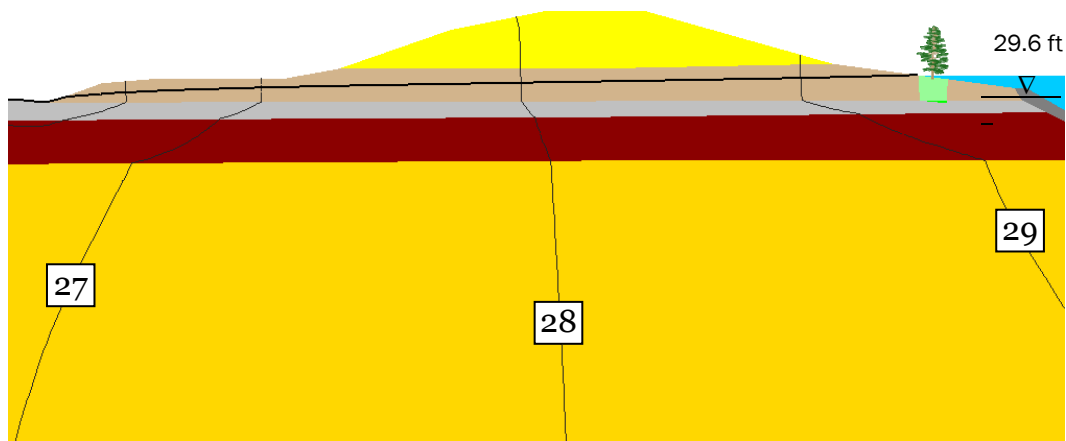
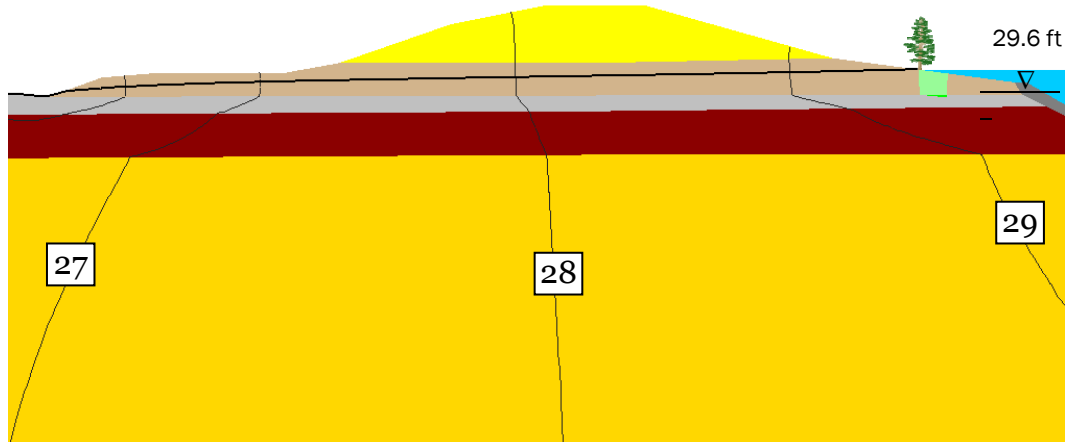
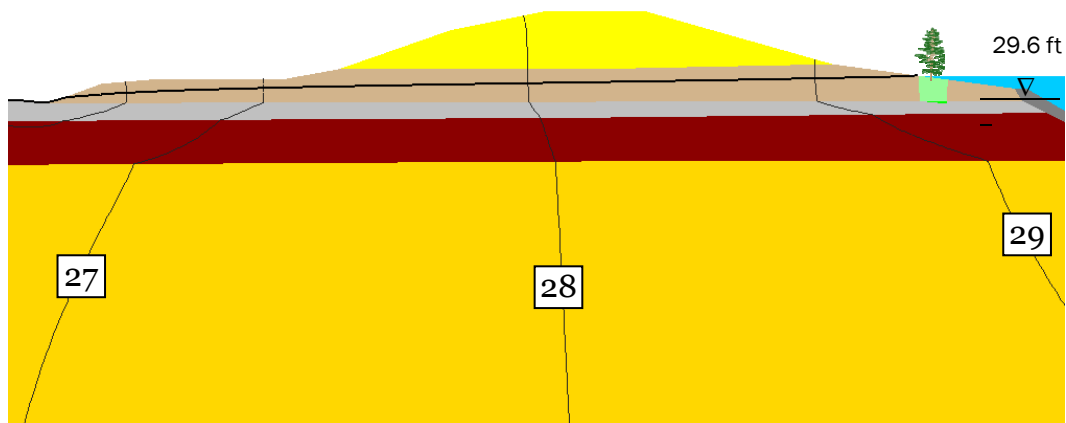
(a)  $\beta = 1$  ( $k_{\text{veg}} = k_{\text{no-veg}}$ ).(b)  $\beta = 100$  ( $k_{\text{veg}} = 100 k_{\text{no-veg}}$ ).(c)  $\beta = 0.01$  ( $k_{\text{veg}} = 0.01 k_{\text{no-veg}}$ ).

Figure 122. Total head (ft) contours and phreatic surface, Portland, OR.

hydrograph that is used in this study (Figure 123). The river elevation was then advanced to its maximum stage of 29.6 ft.

### **No woody vegetation zone**

Figure 124 shows the initial position of the phreatic surface, and Figure 125 shows the phreatic surface at its maximum height without a woody vegetation zone. It is clear from these results that the phreatic surface does not achieve the equivalent of steady state in the approximately 13 hr it took to computationally arrive at 29.6 ft from 26.0 ft.

Two woody vegetation zones at different locations are described in the following sections.

### **Woody vegetation zone beyond the lower toe of the levee**

The first zone in Figure 114 is just beyond the lower toe of the levee beginning with a ditch at El. 24 ft. Values of  $\beta$  equal to 0.01, 1, and 100 were used for this analysis, and the model was run from river elevation 26.0 ft to 29.6 ft. Figure 126 shows the phreatic surface at this zone for these values of  $\beta$ . Figure 127 shows the three nodes as previously selected, and Tables 64 and 65 show magnitude of gradient and pore pressure, respectively. Observations are as follows:

- Phreatic surface is not affected near the zone.
- All of the phenomena for the steady-state case exist in the transient case for this woody vegetation zone as listed above, except that their values are smaller. This is consistent with the seepage analyses conducted on other levees for this research.

### **Woody vegetation zone at the river elevation on the riverside**

The fourth woody vegetation zone in Figure 114 is at the river elevation on the riverside. Plots of total head contours and the phreatic surface for this zone for  $\beta = 1, 100$ , and 0.01 are given in Figure 128. From these plots, it is seen that although the phreatic surface and total head contours are affected at the riverside, they are not appreciably affected on the landside near the exit point and beyond. Again, this is consistent with previous results.

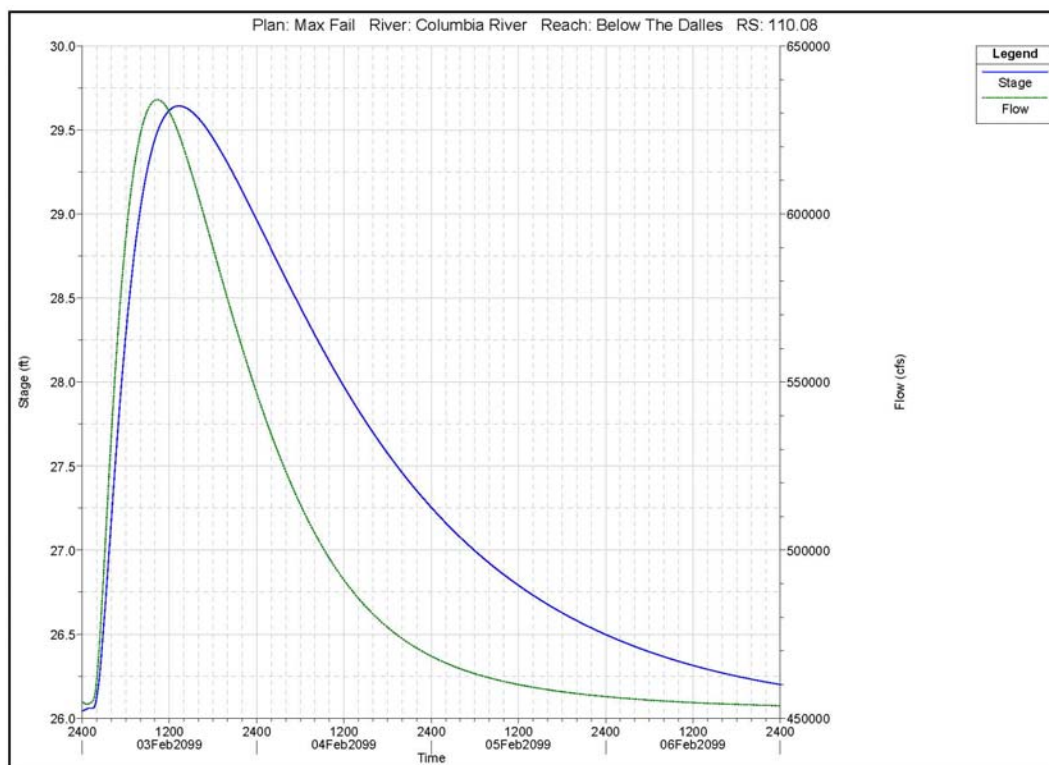


Figure 123. Hydrograph of the Columbia River, Portland, OR.

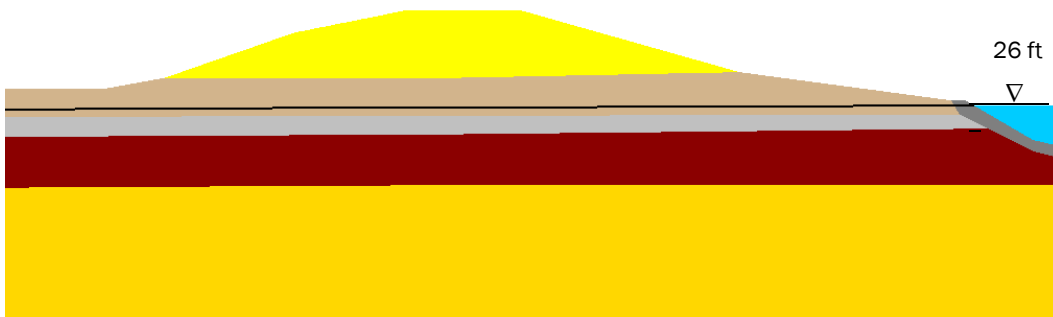


Figure 124. Initial position of the phreatic surface, Portland, OR.

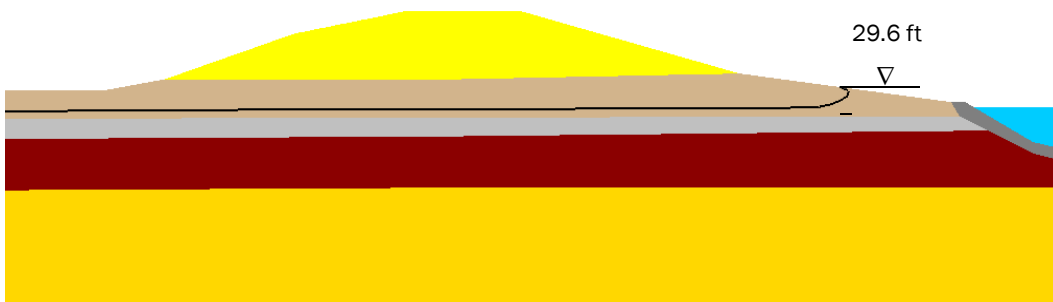


Figure 125. Phreatic surface at the maximum flood stage, Portland, OR.

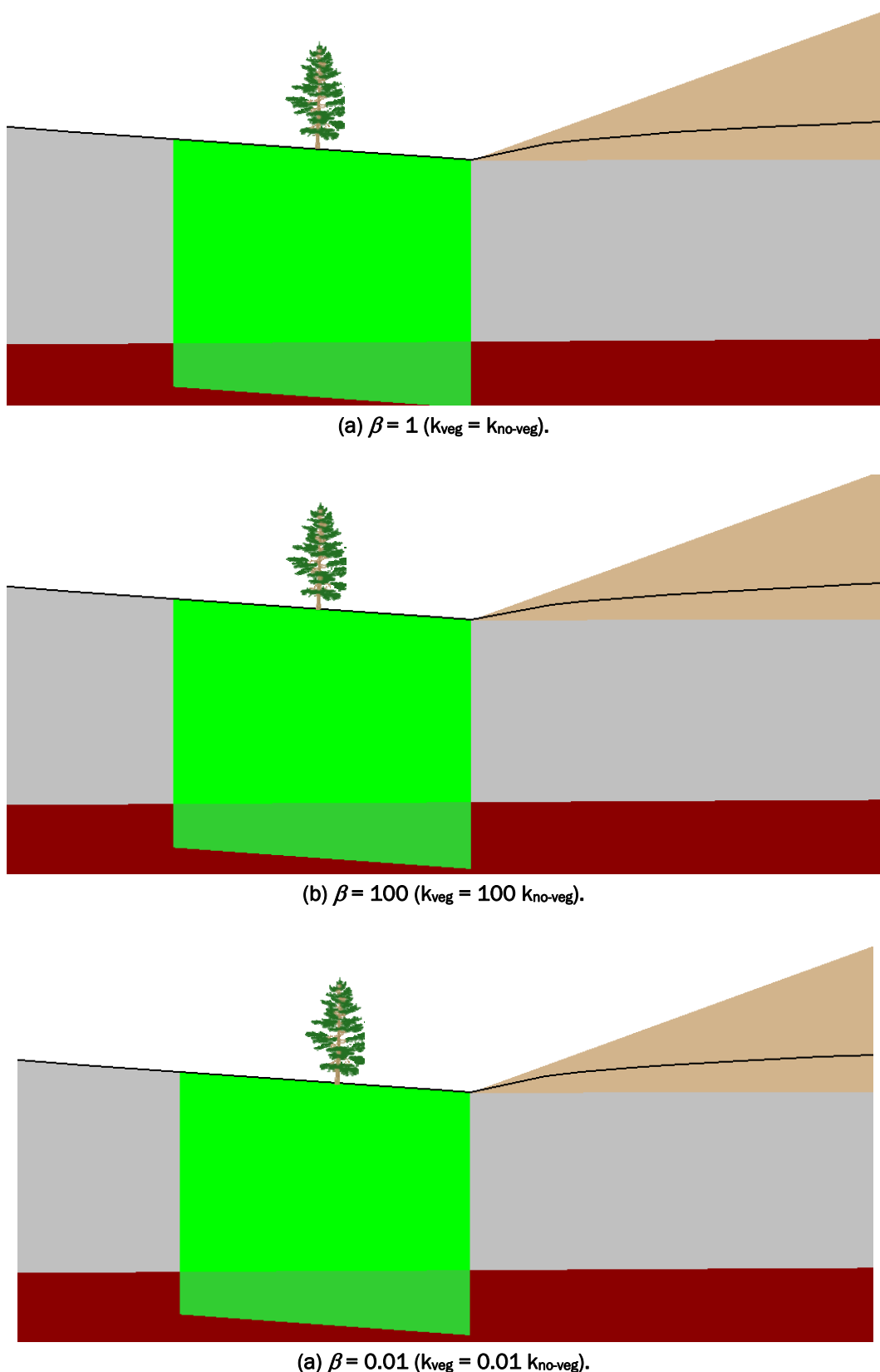


Figure 126. Phreatic surface for the transient case, Portland, OR.

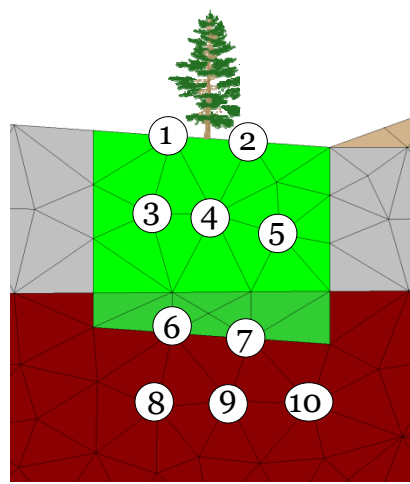


Figure 127. Selected nodes, Portland, OR.

Table 64. Magnitude of gradient at selected nodes for different values of  $\beta$ .

Node	$\beta = 0.01$	$\beta = 1$	$\beta = 100$
1	0.377	<b>0.297</b>	0.0516
2	0.431	<b>0.362</b>	0.071
3	0.342	<b>0.280</b>	0.020
4	0.381	<b>0.315</b>	0.034
5	0.375	<b>0.327</b>	0.042
6	0.073	<b>0.084</b>	0.154
7	0.094	<b>0.090</b>	0.124
8	0.036	<b>0.077</b>	0.230
9	0.033	<b>0.081</b>	0.246
10	0.053	<b>0.083</b>	0.264

Table 65. Pore pressure (lb/ft<sup>2</sup>) at selected nodes for different values of  $\beta$ .

Node	$\beta = 0.01$	$\beta = 1$	$\beta = 100$
1	0.0	<b>0.0</b>	0.0
2	0.0	<b>0.0</b>	0.0
3	169.2	<b>159.8</b>	121.5
4	165.1	<b>156.9</b>	120.4
5	204.8	<b>196.1</b>	151.2
6	407.2	<b>388.2</b>	311.7
7	415.9	<b>397.1</b>	320.3
8	527.6	<b>515.6</b>	460.2
9	516.4	<b>503.5</b>	444.8
10	520.7	<b>509.9</b>	453.7

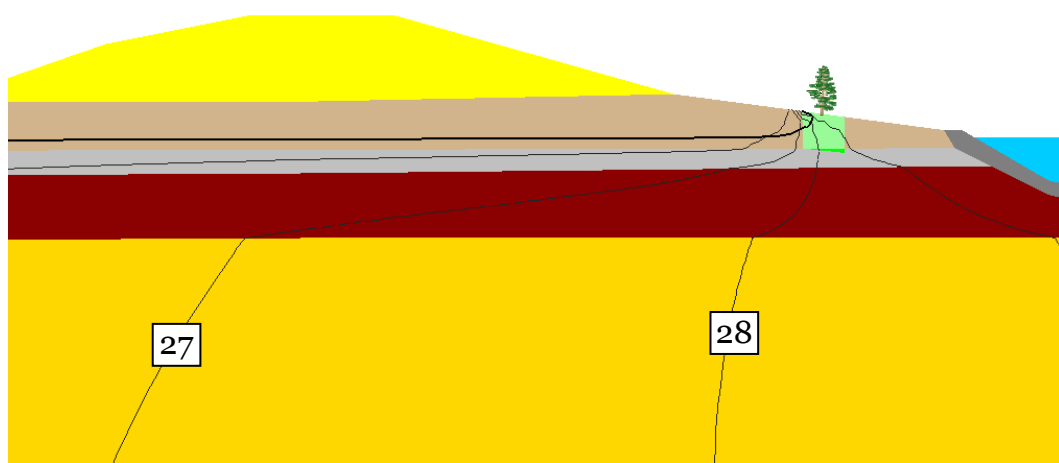
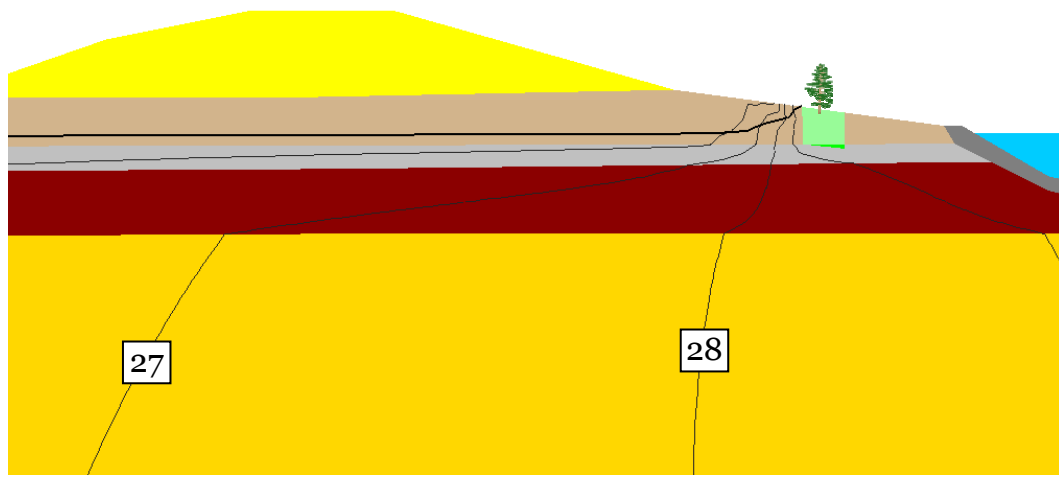
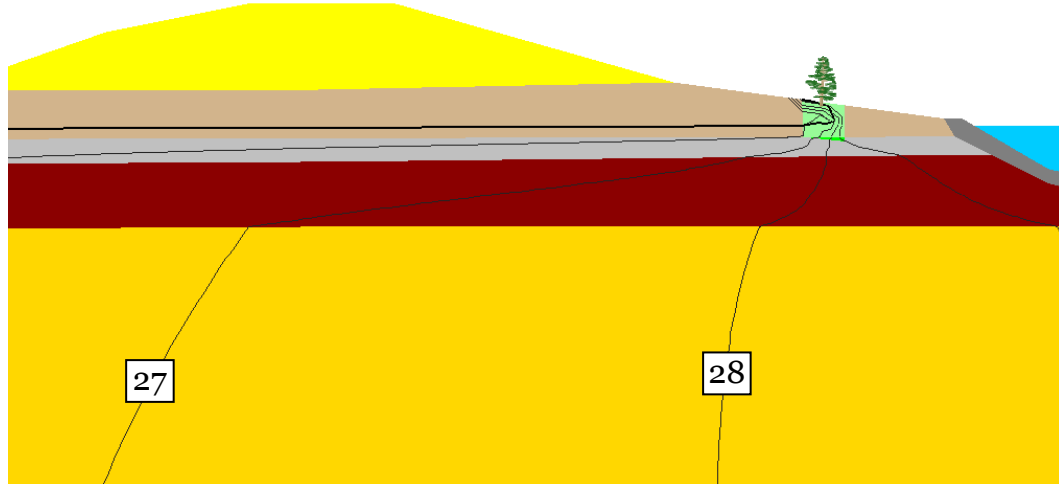
(a)  $\beta = 1$  ( $k_{veg} = k_{no-veg}$ ).(b)  $\beta = 100$  ( $k_{veg} = 100 k_{no-veg}$ ).(c)  $\beta = 0.01$  ( $k_{veg} = 0.01 k_{no-veg}$ ).

Figure 128. Total head (ft) contours and phreatic surface, Portland, OR.

## Summary

This study provides a detailed analysis of the impact of a zone with different hydraulic conductivity from the surrounding soil matrix which may affect the overall flow on a levee with specific properties described in these analyses. However, practicing engineers and others may only need a focused summary at key results. Table 66 satisfies this need by providing the exit gradient at significant points (toe of the levee or bottom of a drainage ditch) of the levee system for values of  $\beta = 1, 100$ , and  $0.01$ . Highlighted in red are positions of woody vegetation zones where underseepage may occur. A dash is given when the phreatic surface is below the given significant point. Results are from both steady-state and transient solutions. Transient solutions are highlighted in yellow. Only the zones just beyond the toe of the levee for the cross sections considered in this study and at the bottom of the dewatered drainage ditch in Albuquerque, NM, made any appreciable difference to the value of the exit gradient.

**Table 66. Exit gradient at nodes for woody vegetation zones for each levee site using different values of  $\beta$ .**

	$\beta = 0.01$	$\beta = 1$	$\beta = 100$
<b>Sacramento, CA, with river at EL 29 ft – Exit gradient calculated at levee toe</b>			
Zone beyond the toe	0.49	0.33	0.01
Zone on the toe	0.24	0.33	0.03
Zone midway on the steeper landside slope	0.33	0.33	0.33
Zone near the top of the landside	0.33	0.33	0.33
Zone at the river height on the riverside	0.33	0.33	0.33
Zone at the change in slope on the riverside	0.33	0.33	0.33
Zone near the end of the levee sand on the riverside	0.33	0.33	0.33
<b>Sacramento, CA, with river at El. 29 ft – Extended Woody Vegetation Zone Vertically – Exit gradient calculated at levee toe</b>			
Zone beyond the toe	0.52	0.33	0.01
<b>Sacramento, CA, with river at El. 29 ft – Extended Woody Vegetation Zone Horizontally – Exit gradient calculated at levee toe</b>			
Zone beyond the toe	1.48	0.33	0.01
<b>Sacramento, CA, with river at El. 29 ft – Degradation of Slurry Wall – Exit gradient calculated at levee toe</b>			
Zone beyond the toe	0.33	0.33	0.33
<b>Sacramento, CA, with river at El. 26 ft – Exit gradient calculated at levee toe</b>			
Zone beyond the toe	0.43	0.28	0.00
Zone beyond the toe – Transient	-	-	-

Zone on the toe	0.19	0.28	0.02
Zone midway on the steeper landside slope	0.28	0.28	0.28
Zone near the top of the landside	0.28	0.28	0.28
Zone at the river height on the riverside	0.28	0.28	0.28
Zone at the change in slope on the riverside	0.28	0.28	0.28
Zone near the end of the levee sand on the riverside	0.28	0.28	0.28
<b>Burlington, WA, first cross section – Exit gradient calculated at levee toe</b>			
Zone beyond the toe	<b>1.09</b>	0.81	0.11
Zone beyond the toe – Transient	0.99	0.74	0.11
Zone on the toe	0.59	0.81	0.22
Zone nearly halfway to the top of the levee on the landside	0.81	0.81	0.81
Zone nearly halfway to the top of the levee on the riverside	0.80	0.81	0.82
Zone near the heel on the river side	0.80	0.81	0.87
<b>Burlington, WA, second cross section – Exit gradient calculated at levee toe</b>			
Zone on the toe	0.11	0.18	0.01
Zone on the lower slope of the levee on the riverside	0.19	0.18	0.18
<b>Burlington, WA, third cross section – Exit gradient calculated at levee toe</b>			
Zone just beyond the toe	<b>0.92</b>	0.46	0.02
<b>Portland, OR - Exit gradient calculated at lower levee toe</b>			
Zone beyond the lower toe	<b>0.84</b>	0.69	0.11
Zone beyond the lower toe – Transient	0.64	0.53	0.13
Zone just beyond the upper toe of the levee	0.68	0.69	0.69
Zone nearly halfway to the top of the levee on the riverside	0.69	0.69	0.69
Zone at the river elevation on the river side	0.68	0.69	0.69
<b>Albuquerque, NM, with river at El. 4992 ft – Exit gradient calculated at bottom of dewatered drainage ditch</b>			
Zone near the toe	1.00	0.99	0.99
Zone at the bottom of the ditch	<b>1.11</b>	0.99	0.16
<b>Albuquerque, NM, with river at El. 4989 ft – Exit gradient calculated at bottom of dewatered drainage ditch</b>			
Zone near the toe	0.86	0.86	0.86
Zone at the bottom of the ditch	<b>0.98</b>	0.86	0.63
Zone at the bottom of the ditch – Transient	0.85	0.74	0.12

## Macropore heterogeneity

Several studies confirmed the existence of macropores produced by both living and decayed tree roots (Beven and Germann 1982). Beven and Germann observe that such macropores may last at least 50 to 100 years in a soil containing about 30% clay. They further mention that the effectiveness of macropores can be destroyed as a result of one rainstorm.

In a study by Noguchi et al. (1997) on preferential flow in macropores, they demonstrate that vertical porous zones had hydraulic conductivities 10 to 100 times higher than those in the surrounding mineral soil. They further note that the more porous zones are influenced by living and decayed roots, which might encourage preferential flow in the vertical direction.

This analysis recognizes the heterogeneity of macropores located within both a root system and surrounding soil matrix by randomly distributing hydraulic conductivity throughout the rectangular configuration. A random value for hydraulic conductivity was generated for each triangular finite element of approximately 1 in dimensions in the 6-ft × 5-ft woody vegetation zone (Figure 132) by multiplying the initial hydraulic conductivity by the factor ( $\beta$ ) between 0.01 and 100.0. Table 67 shows results for three different random number sets.

Figure 129 shows total head contours (red) and flow lines (blue) without the effect of a woody vegetation zone. These are not orthogonal because the horizontal to vertical hydraulic conductivity ratio is not 1 in the clay blanket because of the impermeable nature of the clay. Figure 130 through Figure 132 show similar results for the three random root ball idealizations. Figure 133 through Figure 135 show velocity vectors for the three random idealizations with the magnitude of each vector being proportional to its respective velocity.

Observations are as follows:

- Local modifications to the original exit gradients, as shown in Table 67, are much higher than a representative critical gradient for a sandy soil of 0.9.
- Total head contours and flow lines appear similar to the original ones but follow a more tortuous path.

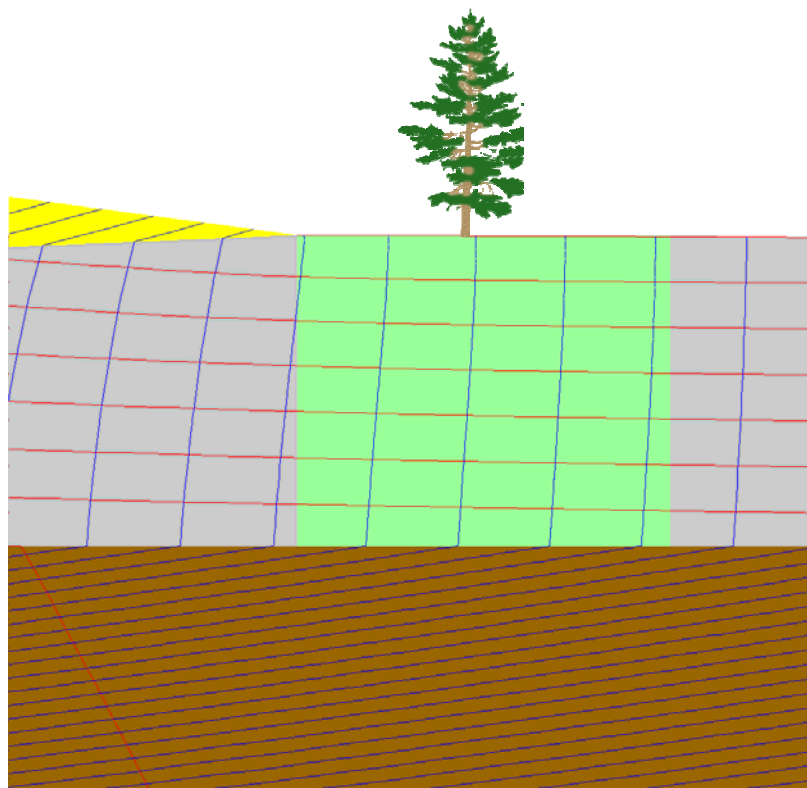


Figure 129. Total head contours (red) and flow lines (blue) without the effect of a woody vegetation zone.

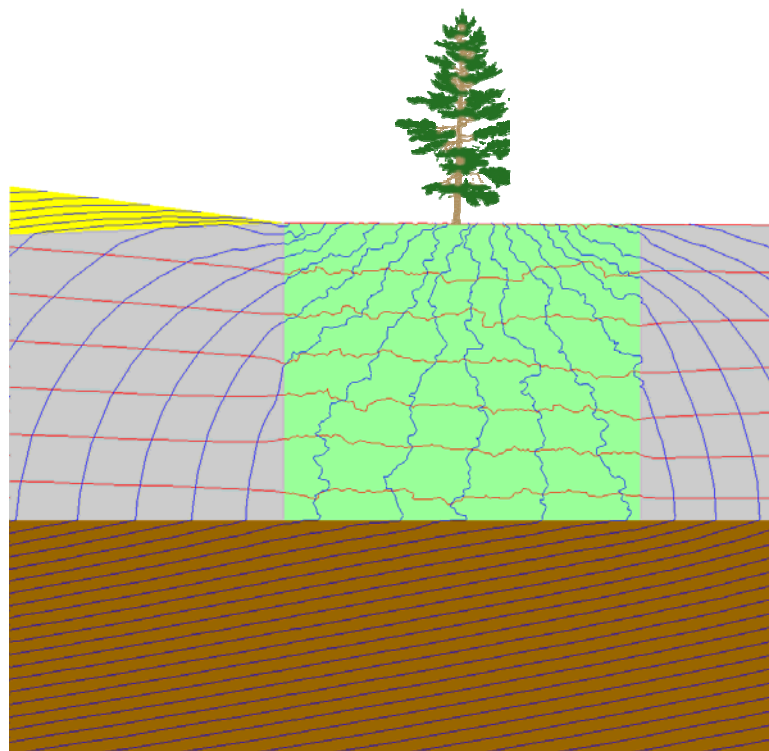


Figure 130. Total head contours (red) and flow lines (blue) with the effect of a woody vegetation zone for the first set of random  $\beta$  values.

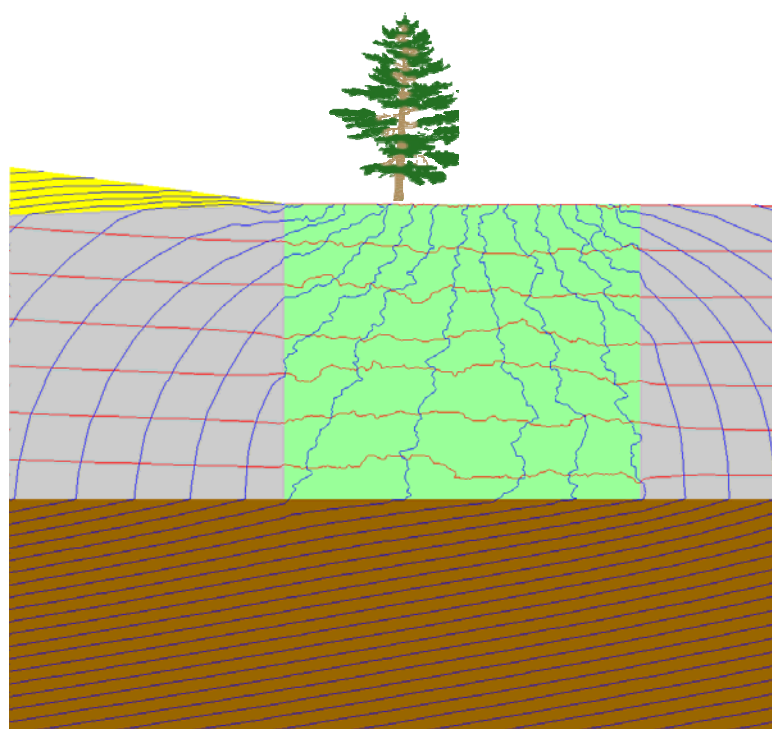


Figure 131. Total head contours (red) and flow lines (blue) with the effect of a woody vegetation zone for the second set of random  $\beta$  values.

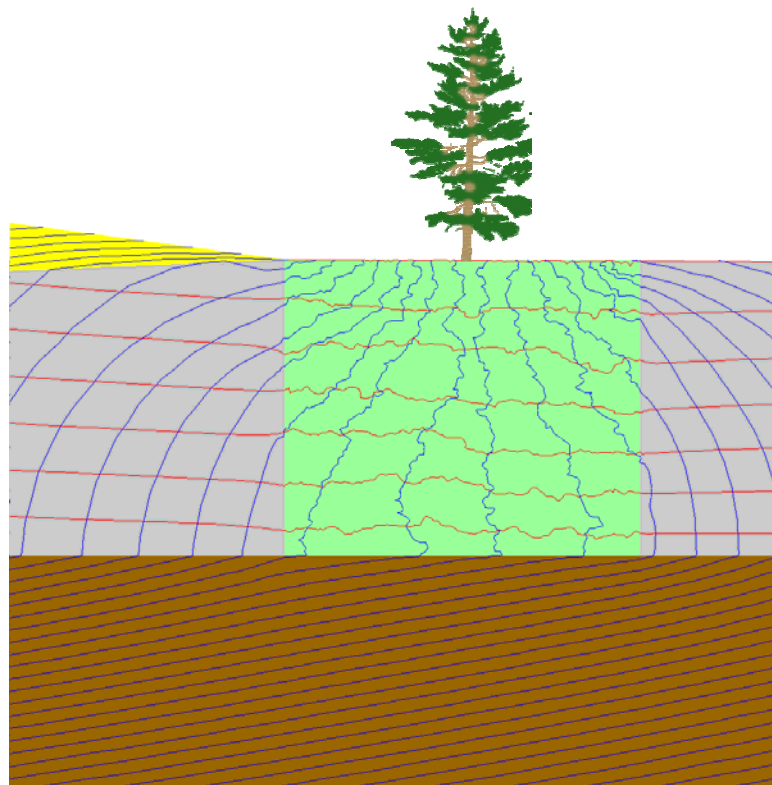


Figure 132. Total head contours (red) and flow lines (blue) with the effect of a woody vegetation zone for the third set of random  $\beta$  values.

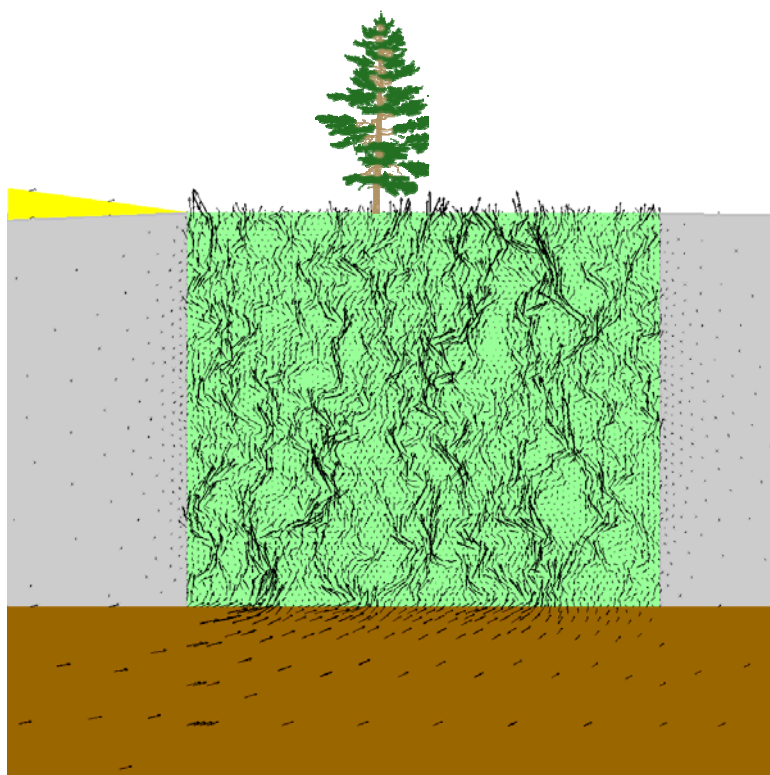


Figure 133. Velocity vectors for the first random example.

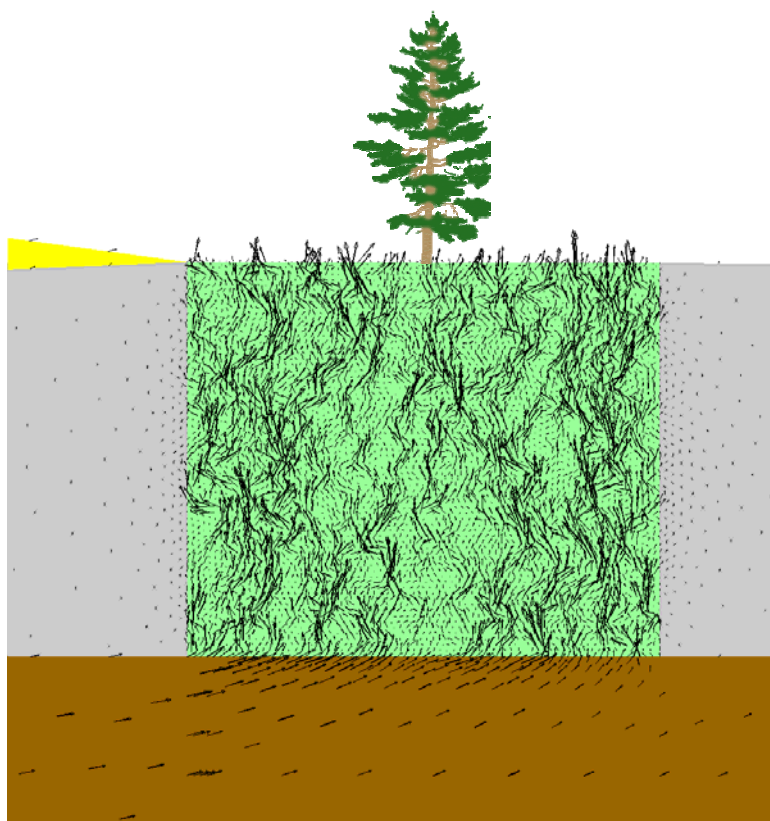


Figure 134. Velocity vectors for the second random example.

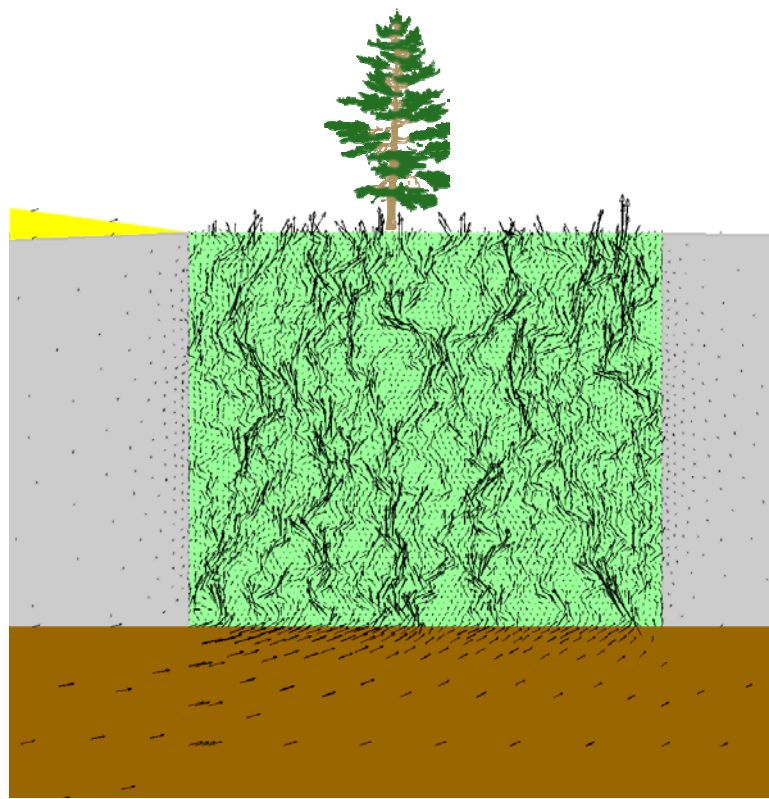


Figure 135. Velocity vectors for the third random example.

Table 67. Exit gradient from the levee toe to 8 in. from the toe.

Distance (in.) from Toe	No Woody Vegetation Zone	Random Set # 1	Random Set # 2	Random Set # 3
0 (levee toe)	1.57	1.57	1.47	1.69
1	1.55	2.29	0.58	1.75
2	1.53	1.02	1.33	1.77
4	1.61	1.01	1.71	0.16
5	1.49	1.47	1.73	0.27
6	1.47	1.96	2.88	0.54
7	1.46	1.29	2.88	0.75
8	1.46	0.38	1.92	0.88

- Velocity vectors in homogeneous soils are smaller than many of the velocity vectors in heterogeneous soils (e.g., where macropores exist)
- Velocity vectors show that a random heterogeneous woody vegetation zone can have flow paths that support large flow velocities. Such high velocity paths can also occur for the case where the zone with high

hydraulic conductivity values is represented by a continuous root, as discussed in Chapter 2. Research does not exist on whether high velocities result in initiation of piping; therefore, the actual impact of high velocities on piping is unknown.

### **3-D seepage model**

When comparing 2-D model results with those from a 3-D model, it is desirable to use the 2-D cross section mesh as the front view for the 3-D computations. In the following section, a parallel groundwater code for a 3-D model seepage model is used to provide comparison of pore pressure for both dimensions using this procedure. A second 3-D modeling effort discussed in Chapter 4 introduces the root system collected from Light Detection and Ranging (LiDAR) at the Vicksburg, MS, site for both slope stability and seepage analyses.

#### **Simplified extended root**

The 2-D mesh for the Sacramento cross section with the 5-ft blanket was converted to a 3-D mesh by extruding the 2-D mesh 11 times (Figures 136 and 137). Three 2-ft extrusions were completed, followed by two 0.5-ft extrusions, and a 1-in. extrusion. This process was repeated for two 0.5-ft and three 2-ft extrusions to complete the solid 3-D mesh. Each triangular 2-D element was converted to a 3-D prism element in the process.

Table 68 shows a comparison of both 2-D and 3-D results for the pore pressure at the bottom of the blanket. Figures 138, 139, and 140 show total head contours, velocity vectors on the surface of the 3-D mesh, and isosurfaces of the total head, respectively.

Observations are as follows:

- Results from 3-D computations are slightly different than those of the 2-D model because of more complex computational algorithms used in the 3-D analysis.
- Pore pressure was reduced 8.0 lb/ft<sup>3</sup> when using the 1-in. × 5-ft 2-D root defect, whereas the 3-D 1-in. × 1-in. × 5-ft root defect reduced the pore pressure only 0.2 lb/ft<sup>3</sup>. This further confirms the original assertion that a small defect would not appreciably reduce the pore pressure at the bottom of the blanket.

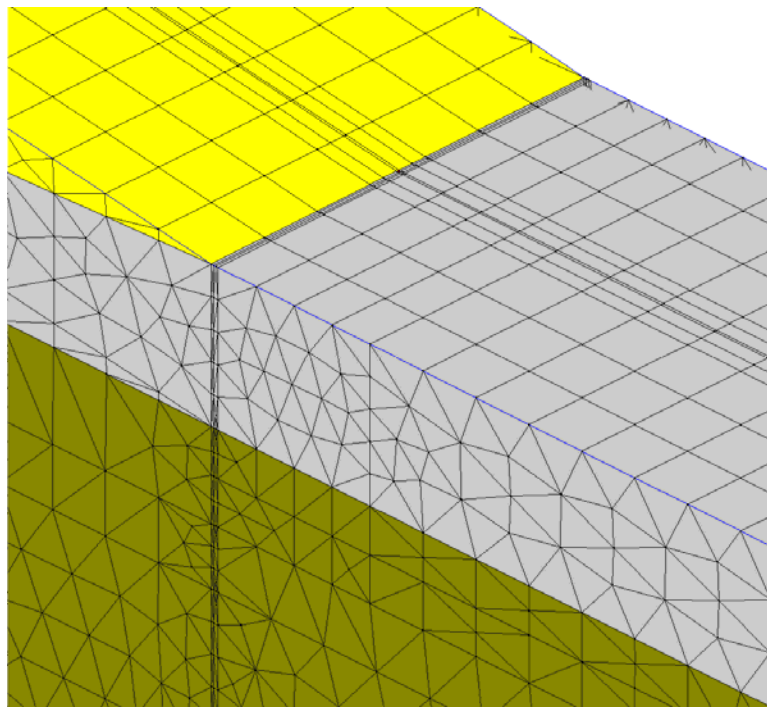


Figure 136. An enlarged section of the 3-D mesh surface to show mesh details. There are 350,820 nodes and 627,616 prism elements in the entire 3-D mesh.

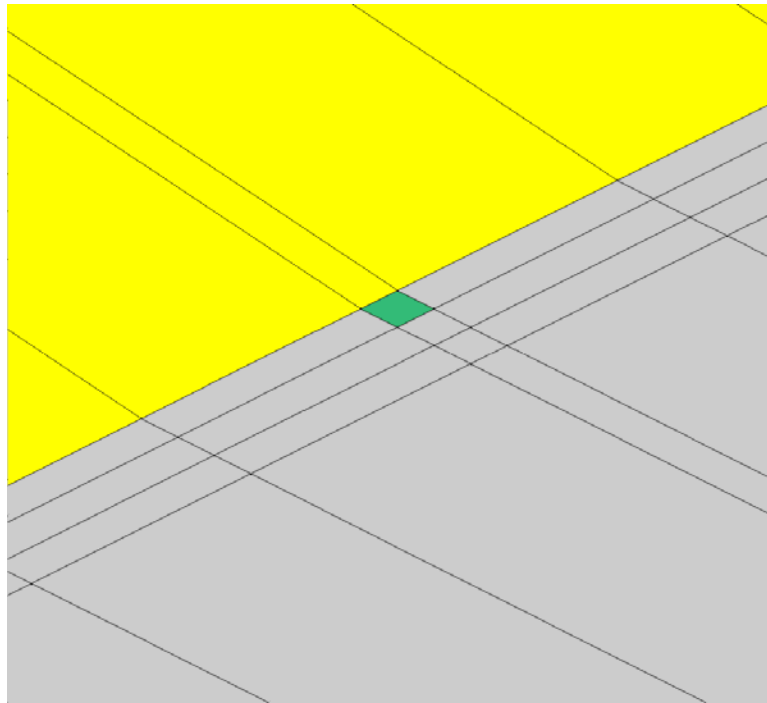


Figure 137. An enlarged section of the 3-D mesh surface with a tree root defect.

Table 68. Comparison of pore pressure at the bottom of the 5-ft blanket below the toe for both the 2-D and 3-D models.

Tree	Pore Pressure (2-D) (psf)	Pore Pressure (3-D) (psf)
No	742.4	743.6
Yes	734.4	743.4

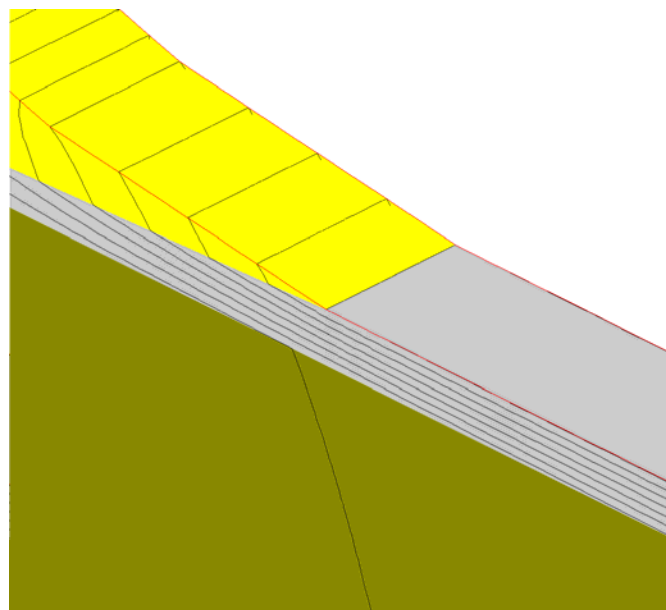


Figure 138. Total head contours on the surface of the mesh.

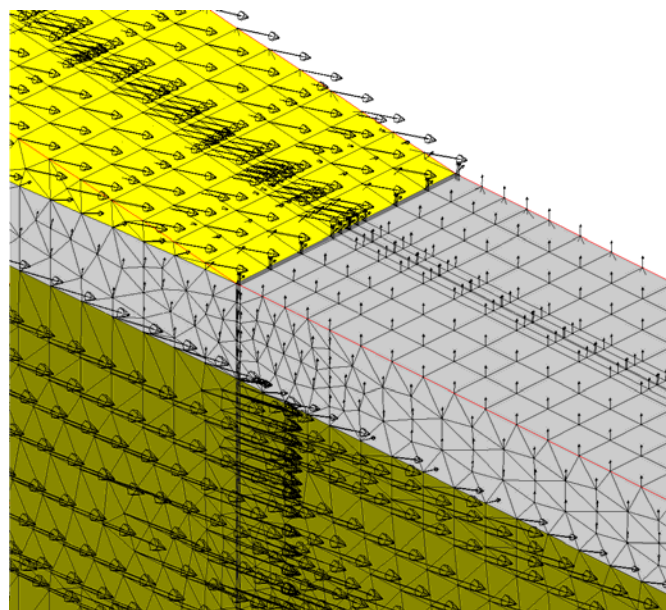


Figure 139. Velocity vectors on the surface of the mesh.

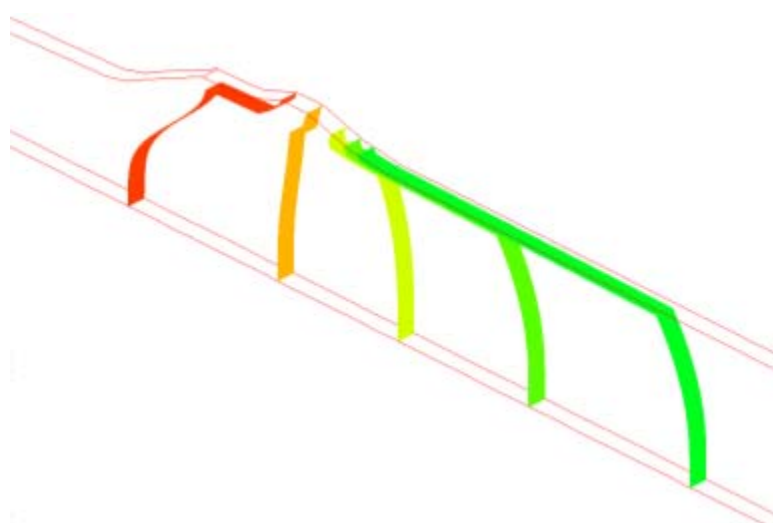


Figure 140. Total head isosurfaces.

- Contours on the 3-D mesh appear to be the same as the contours on the 2-D mesh. The defect is so small that the flow remains almost two-dimensional in the 3-D setting.

### Random root zone

This section discusses the 3-D version of the 6-ft × 5-ft woody vegetation zone. In 3-D, a 6-ft × 6-ft × 5-ft root zone is used. The 2-D cross section from the 2-D mesh was extruded in the following  $\Delta y$  amounts: 2 (10 ft), 1 (5 ft), 3 (2 ft), 2 (0.5 ft), 72 [1 in. (hydraulic conductivity zone)], 2 (0.5 ft), 3 (2 ft), and 2 (10 ft) to form the 3-D mesh containing 3-D prism elements generated from the respective 2-D triangular elements. Figure 141 shows the surface of the 3-D mesh with the zone shown in green, and Figure 142 shows a portion of the 3-D mesh of the zone. Contours of total head are shown in Figure 143 before a variation in hydraulic conductivity was introduced. Isosurfaces for total head in 3-D are equivalent to contour plots in 2-D. Figures 144 and 145 show isosurfaces inside the 6-ft × 6-ft × 5-ft zone and vector plots for every two-hundredth velocity vector, both with no tree.

Material properties of each 3-D element were randomly modified. The random hydraulic conductivity zone option took approximately 15 min on 128 cores to run using the ERDC Cray XE6 when starting from the non-randomized solution as an initial condition. Figures 146 and 147 show oblique views of the random hydraulic conductivity zone, and Figure 148 shows a front view of the same information at  $y = 32$  ft. Figure 149 shows

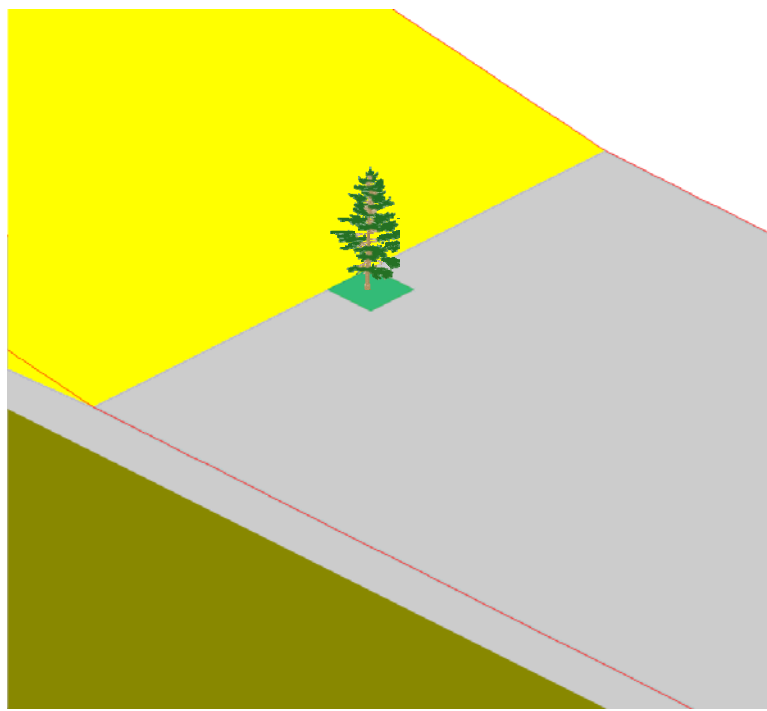


Figure 141. Surface of the mesh showing the 6-ft × 6-ft × 5-ft woody vegetation zone. There are 3,017,367 nodes and 5,836,072 prism elements in this mesh.

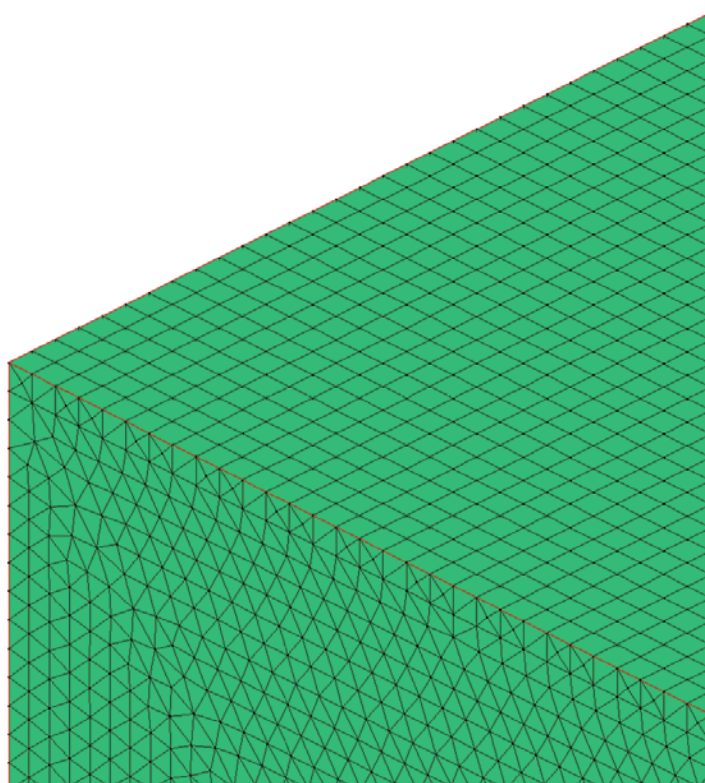


Figure 142. Portion of the 3-D mesh for the 6-ft × 6-ft × 5-ft woody vegetation zone.

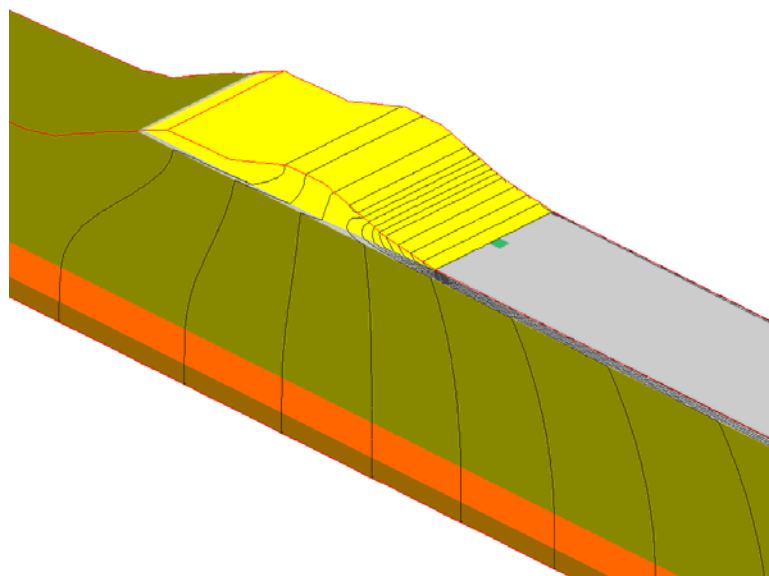


Figure 143. Total head contours with no tree in the 6-ft × 6-ft × 5-ft woody vegetation zone.

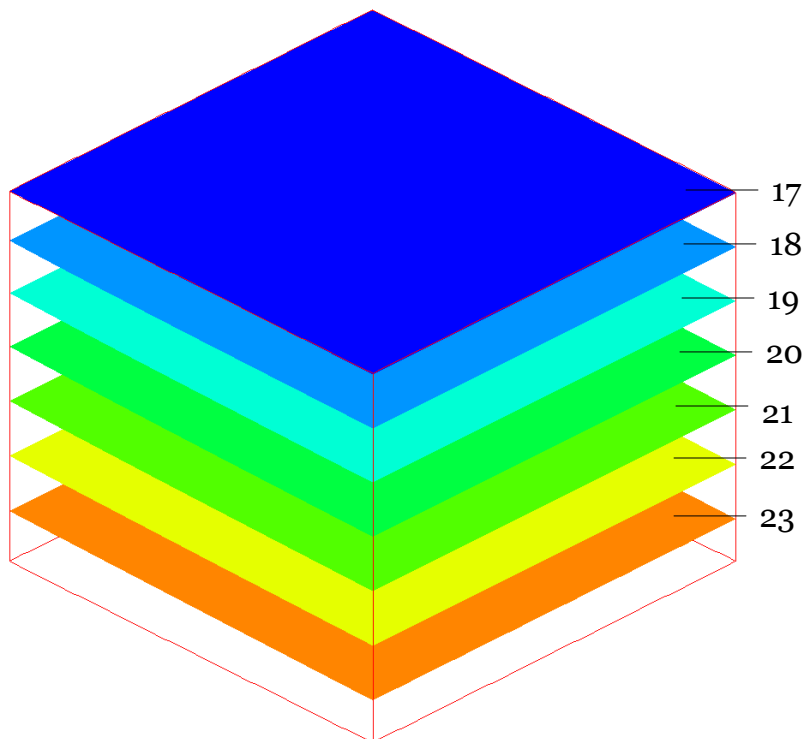


Figure 144. Isosurfaces for total head with no tree in the 6-ft × 6-ft × 5-ft woody vegetation zone.

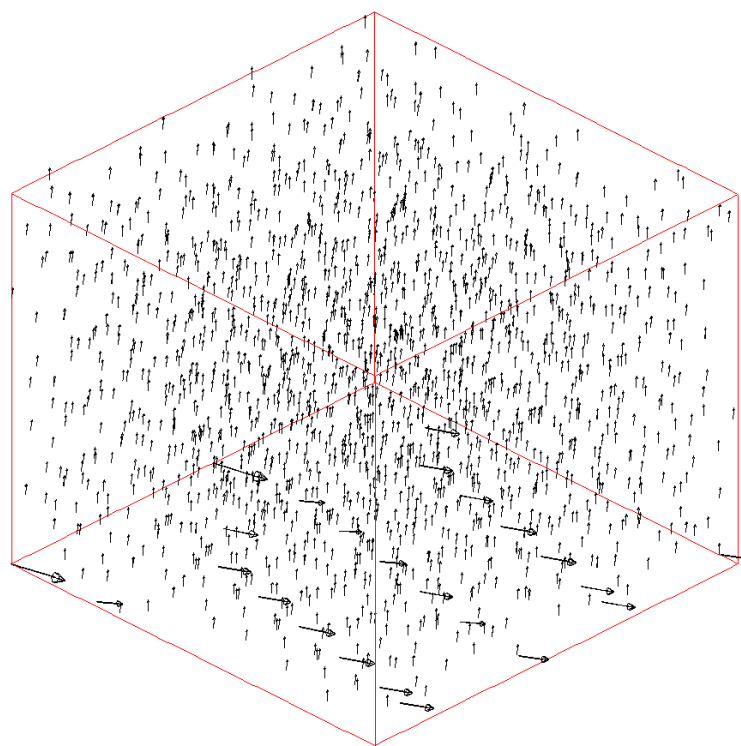


Figure 145. Vector plot of velocity with no tree in the 6-ft × 6-ft × 5-ft woody vegetation zone.

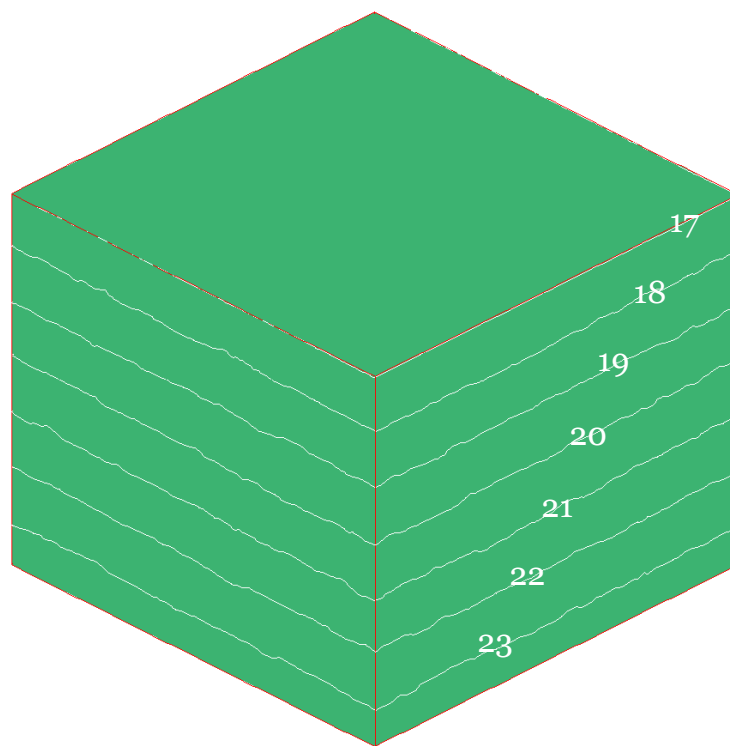


Figure 146. First oblique view of total head contours for the 6-ft × 6-ft × 5-ft random hydraulic conductivity zone.

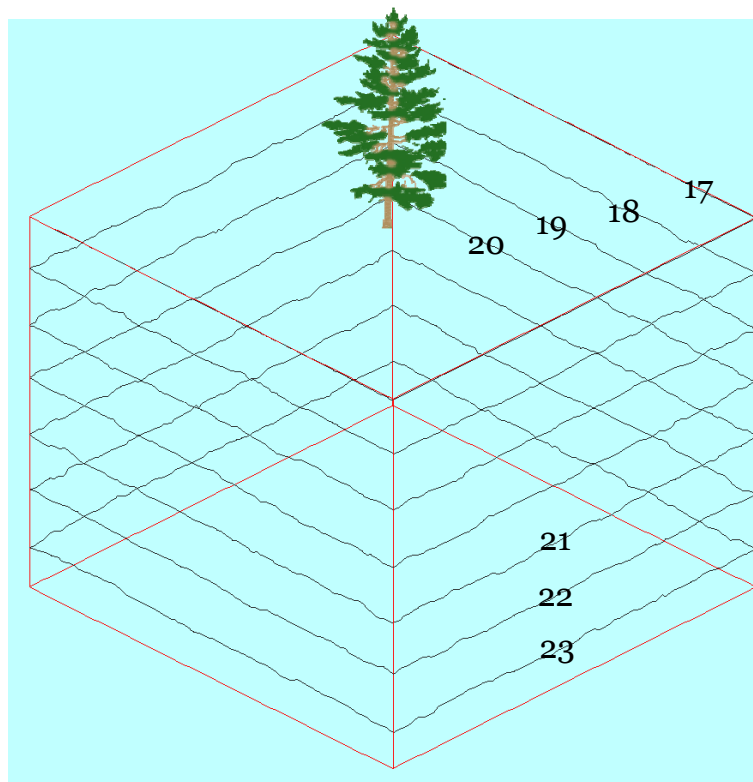


Figure 147. Second oblique view of total head contours for the 6-ft  $\times$  6-ft  $\times$  5-ft random hydraulic conductivity zone.

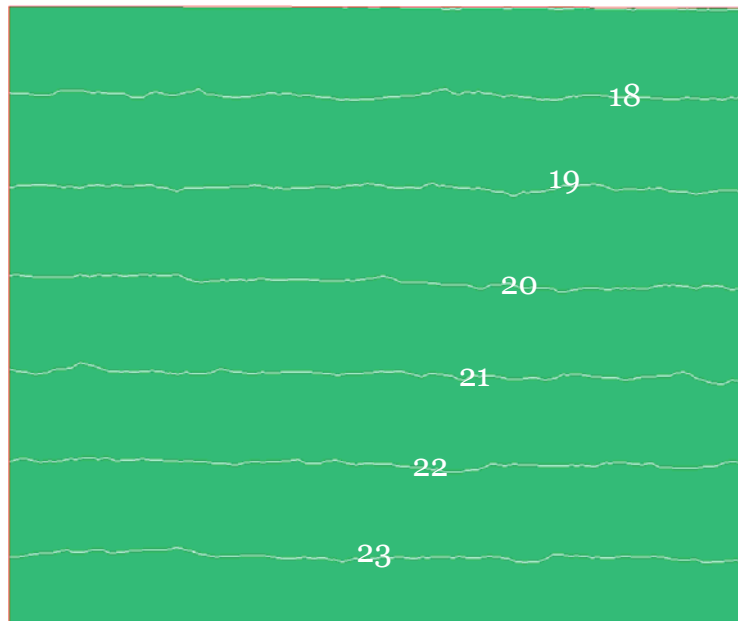


Figure 148. Front view of total head contours for the 6-ft  $\times$  6-ft  $\times$  5-ft random hydraulic conductivity zone at the beginning of the hydraulic conductivity zone ( $y = 32$  ft).

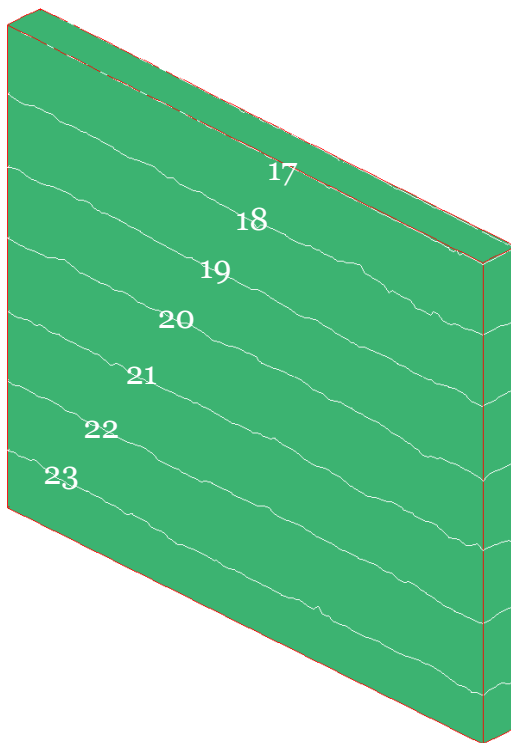


Figure 149. Oblique view of total head contours for the 6-ft x 6-ft x 5-ft random woody vegetation zone for a 0.5-ft slab starting in the middle of the zone ( $y = 35$  ft).

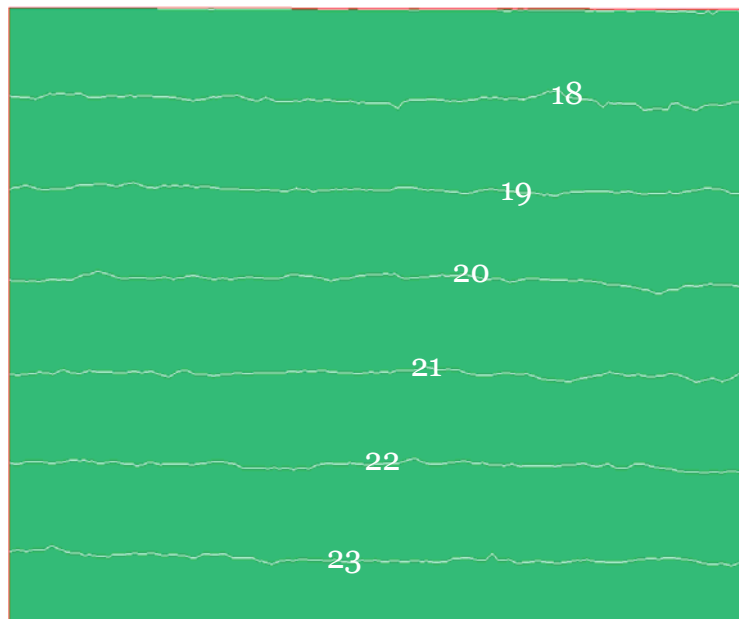


Figure 150. Front view of total head contours for the 6-ft x 6-ft x 5-ft random hydraulic conductivity zone for a 0.5-ft slab starting in the middle of the hydraulic conductivity zone ( $y = 35$  ft).

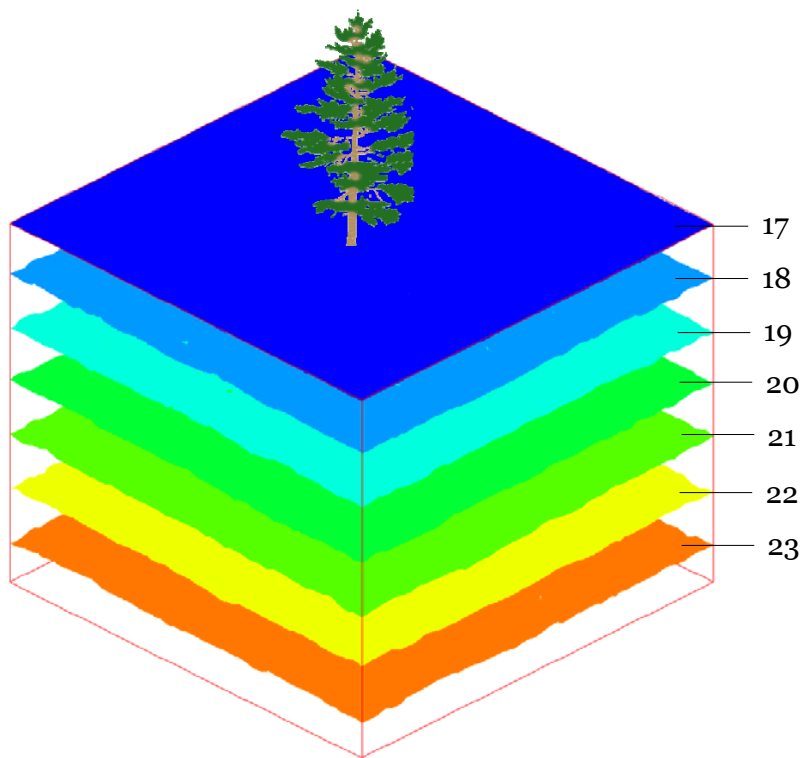


Figure 151. Isosurfaces for the 6-ft × 6-ft × 5-ft random hydraulic conductivity zone.

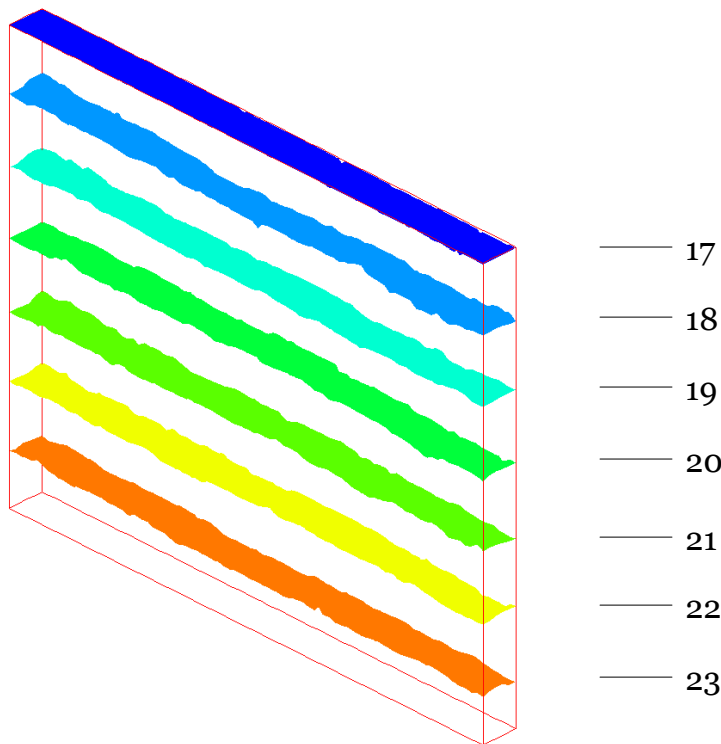


Figure 152. Isosurfaces for the 0.5-ft slice in the middle ( $y = 35$  ft) of the 6-ft × 6-ft × 5-ft random hydraulic conductivity zone.

an oblique view of a 0.5-ft portion of the hydraulic conductivity zone starting in the middle of the zone ( $y = 35$  ft). Figure 150 shows a front view of the same data as in Figure 149. Figures 151 and 152 show isosurfaces of total head for the entire hydraulic conductivity zone and isosurfaces of total head for the 0.5-ft piece of geometry for the random hydraulic conductivity zone, respectively. Figure 153 shows a front view of the isosurfaces of the 0.5-ft part of the hydraulic conductivity zone with both front and back showing. This illustrates both the variation in the  $x$ -direction and the variation vertically. Figures 154 and 155 show an oblique view and a front view of every two-hundredth vector of velocity for the random hydraulic conductivity zone, respectively.

Vectors are not scaled exactly the same in Figures 154 and 155. Figure 155 shows fewer vectors with the different directions created in the random woody vegetation zone.

The observations are as follows:

- Total heads and velocities are less affected by random hydraulic conductivity in the woody vegetation zone in the 3-D analysis as compared to the 2-D analysis, as shown by the isosurface (i.e., the isosurface exhibits a more uneven surface in 2-D). In addition, vectors in the 3-D analysis are slightly larger with random hydraulic conductivity (Figure 154) than that without the random value (Figure 145). Vectors for the 2-D analysis are much larger with random hydraulic conductivity than those without it.
- Numbers in the 2-D analysis of the root defect modified pore pressures more than in the 3-D analysis, so a well-known general trend is being demonstrated; a point source/sink has less effect than a line source/sink.

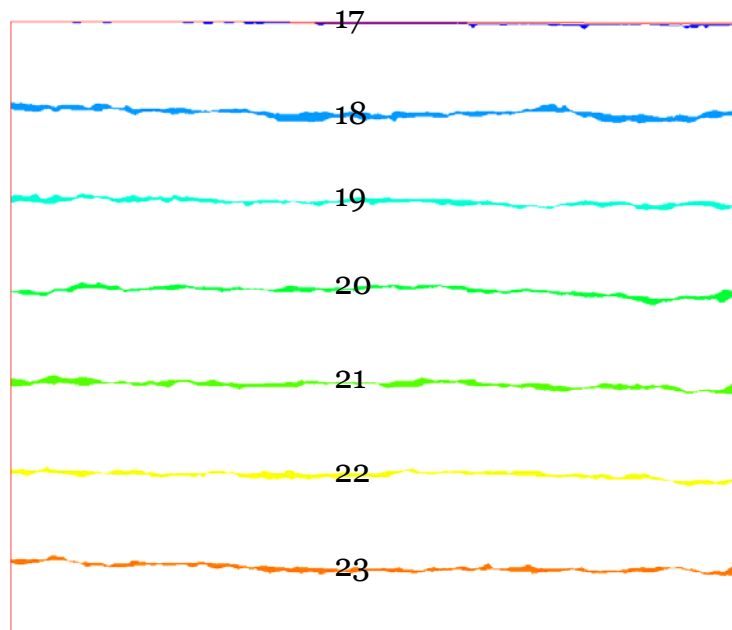


Figure 153. Front view of isosurfaces for the 0.5-ft slice in the middle ( $y = 35$  ft) of the 6-ft  $\times$  6-ft  $\times$  5-ft random hydraulic conductivity zone.

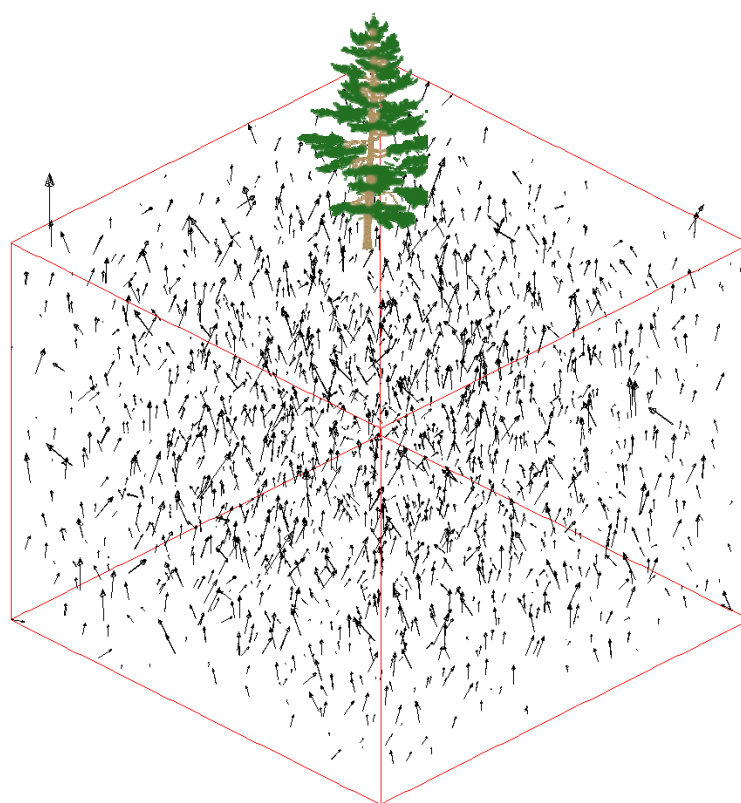


Figure 154. Oblique view of velocity vector plots for the 6-ft  $\times$  6-ft  $\times$  5-ft random hydraulic conductivity zone.

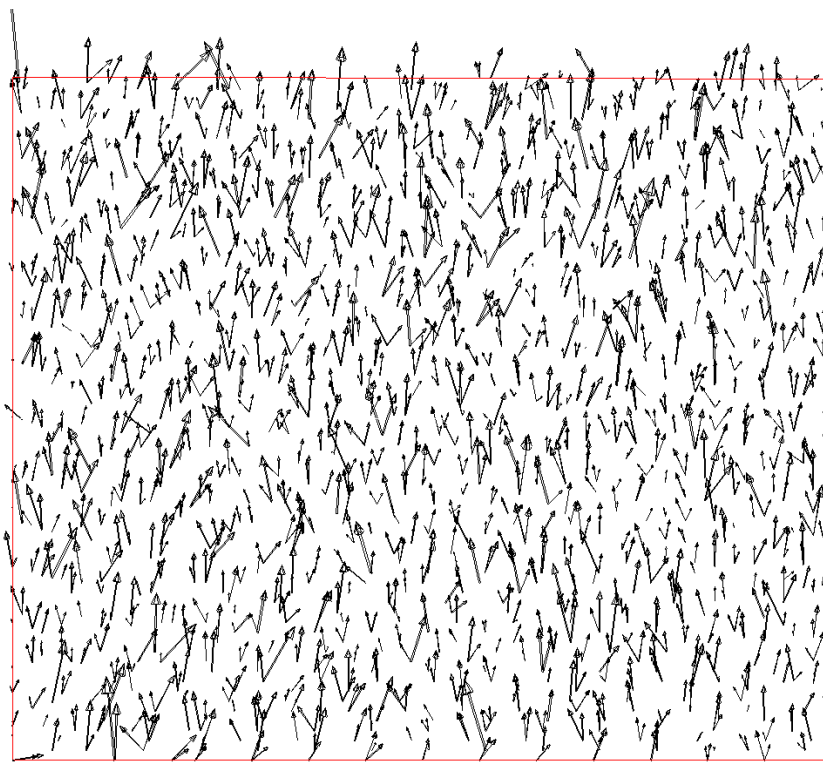


Figure 155. Front view of velocity vector plots for the 6-ft  
x 6-ft x 5-ft random hydraulic conductivity zone.

## 2 Defects Produced from Woody Vegetation

### Background

Previous research demonstrated that living trees contribute to preferential pathways on a forested slope (Noguchi et al. 1997). However, a difficulty in studying the influence of a root system on piping is the lack of research on both the mechanisms of piping and the contribution of macroporosity to flow, regardless of the presence of roots. In this section, roots are considered as a defect in a levee.

The ERDC research did not include field tests to explore the complex interaction of roots within a soil matrix, but surface observations made during field visits are reported in this section, as well as a 2-D model analysis of defects in the levee blanket produced by roots.

Field observations at two sites in Lake Providence, LA, during the ERDC research, revealed possible evidence that living trees and their root systems may produce defects in soil, or act as a conduit for flow, and thereby provide preferential flow paths for the occurrence of seepage and piping. Trees at one site are on an oxbow lake, not on a levee, but the observation of water flowing through tree roots is still significant regardless of the environment. However, it is important to note that the unstable geology (i.e., the thin impervious clay layer) at this site also greatly influences piping in these areas. Therefore, these observations do not conclude that trees are producing sand boils in these areas.

The 2-D model is based on a procedure outlined in Schaefer et al. (2010). This document is actually directed to studying dams, but procedures, such as this, for seepage analysis on levees do not exist. Obviously, this approach may have limitations when used for levees, but it does include details on piping and seepage that are inherent to soil regardless whether the structure is a dam or levee.

### Observation sites, Lake Providence, LA

On May 2009, a site visit to Lake Providence, LA, was made to observe and photograph seepage flow through living bald cypress (*Taxodium distichum*) tree roots. These trees surround the oxbow lake, a former

meander of the Mississippi River, and are well established. Cypress roots are exposed at the base of the tree and are easily visible during fluctuating water levels. Previous field evaluations by the U.S. Army Corps of Engineers, Vicksburg District, during high river stages of the Mississippi River in 2009, noted flow through several tree roots. The Mississippi River Valley Division (MVD) contacted ERDC about these observations, and coordinated the initial field visit.

### **Geologic history**

Lake Providence is a previous meander of the Mississippi River, and now exists as an oxbow lake within the Lower Mississippi Alluvial Valley (LMAV) (Figure 156). Sediments within the LMAV are the result of erosional and depositional processes from the last glacial period [15,000 Before Present (BP)]. Fisk (1947) identifies alluvial deposits within this area, and divided these deposits into substratum sands and gravels, and fine-grained, relatively impermeable topstratum, both which vary in thickness above an irregularly eroded surface identified as Tertiary (65 million years BP to 2.6 million years BP) bedrock. When erosional and depositional processes separated the meander, the former river channel filled with fine grained sediment that Fisk identifies as a clay plug. The clay plug is a mixture of blue mud, silty clays, and clayey silts, and is evident in the topstratum deposits.

Because of fluctuating erosive and depositional forces, both the substratum and topstratum deposits vary greatly in thickness. Kolb (1975) noted that the topstratum can vary in thickness from 2 ft to 100 ft within a lateral distance of 200 ft. Substratum sands and gravels are between -20 ft to 80 ft relative to mean sea level (MSL), and the topstratum unit is between 80 to 100 ft MSL (Figure 157 and Figure 158).

Fisk (1947) and Kolb (1975) conducted studies on the relationship of LMAV sediments and the effects of geology with the occurrence of sand boils. While Fisk (1947) identifies the fine-grained alluvium within the valley, Kolb (1975) explains the correlation of these sediments during high river stages, and the location of the sediments, with the occurrence of sand boils. For example, Kolb (1975) found that clay plugs have a marked effect on river meanders, channel stability, and where they lie beneath the levees, on underseepage. He concluded that a correlation exists between the geometry of clay plugs and the angle at which the clay plug crosses the levee.

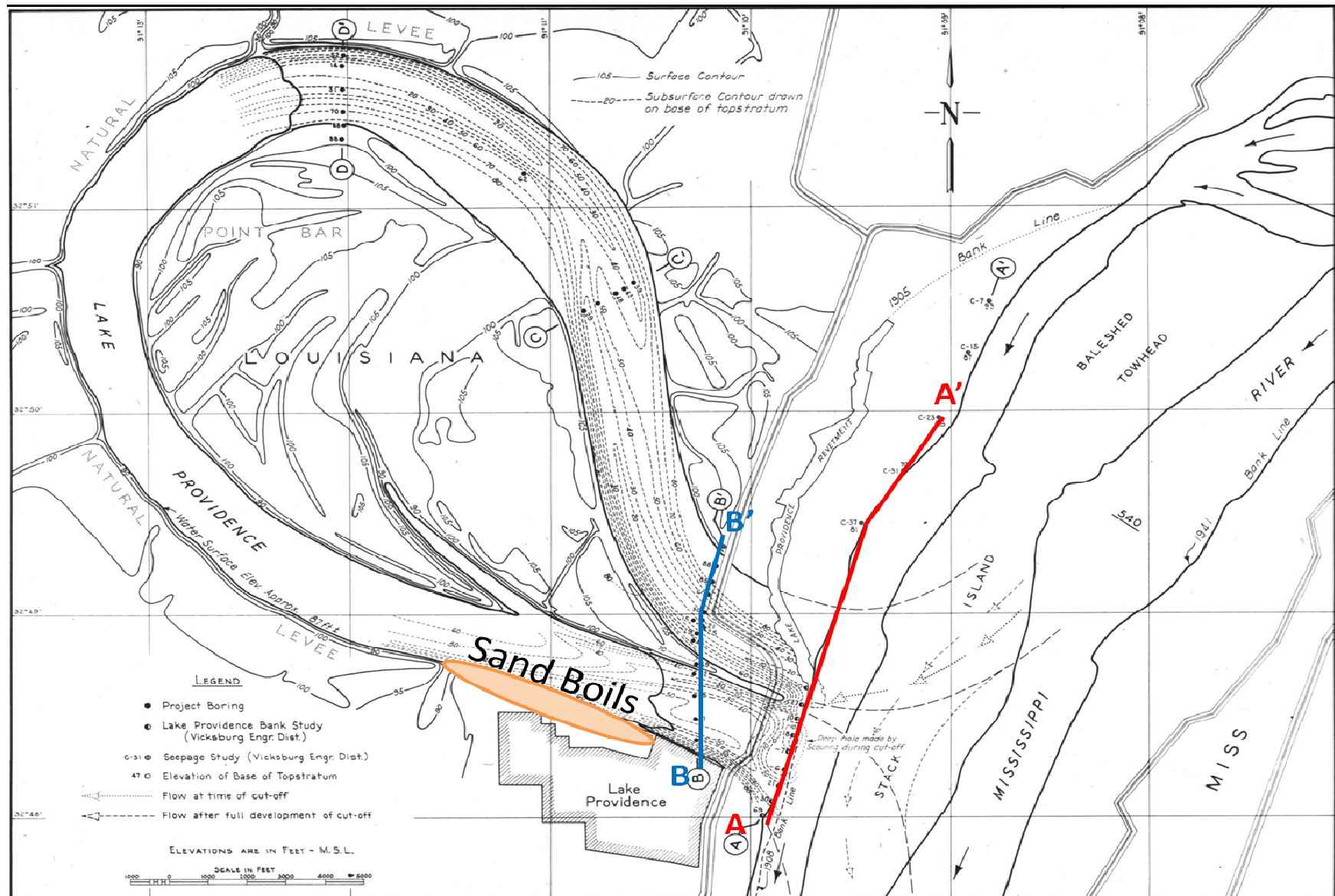


Figure 156. Location map of Lake Providence showing sand boils and cross sections (Fisk 1947).

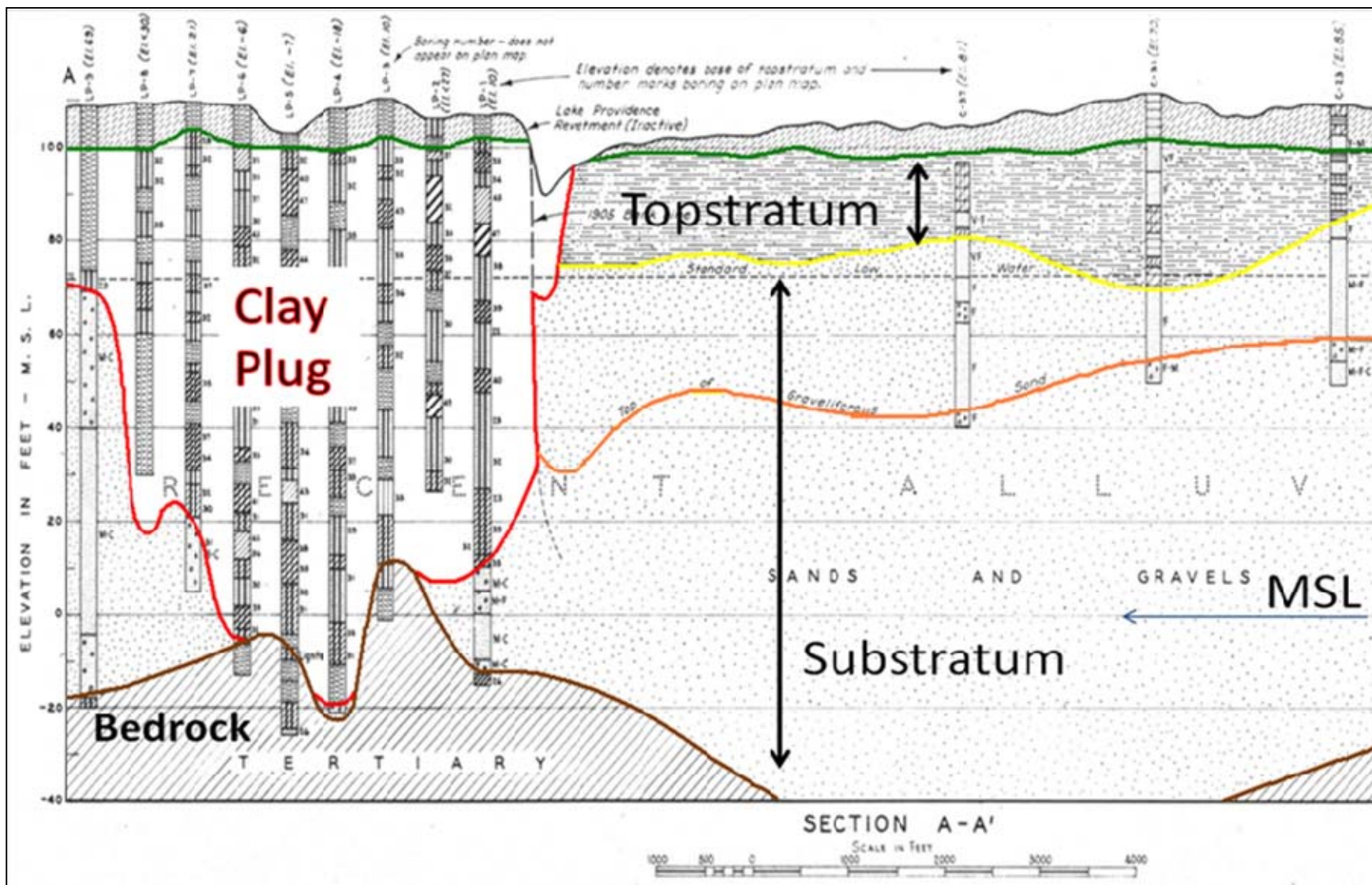


Figure 157. Sedimentary units and elevations for cross section A-A' (Fisk 1947).

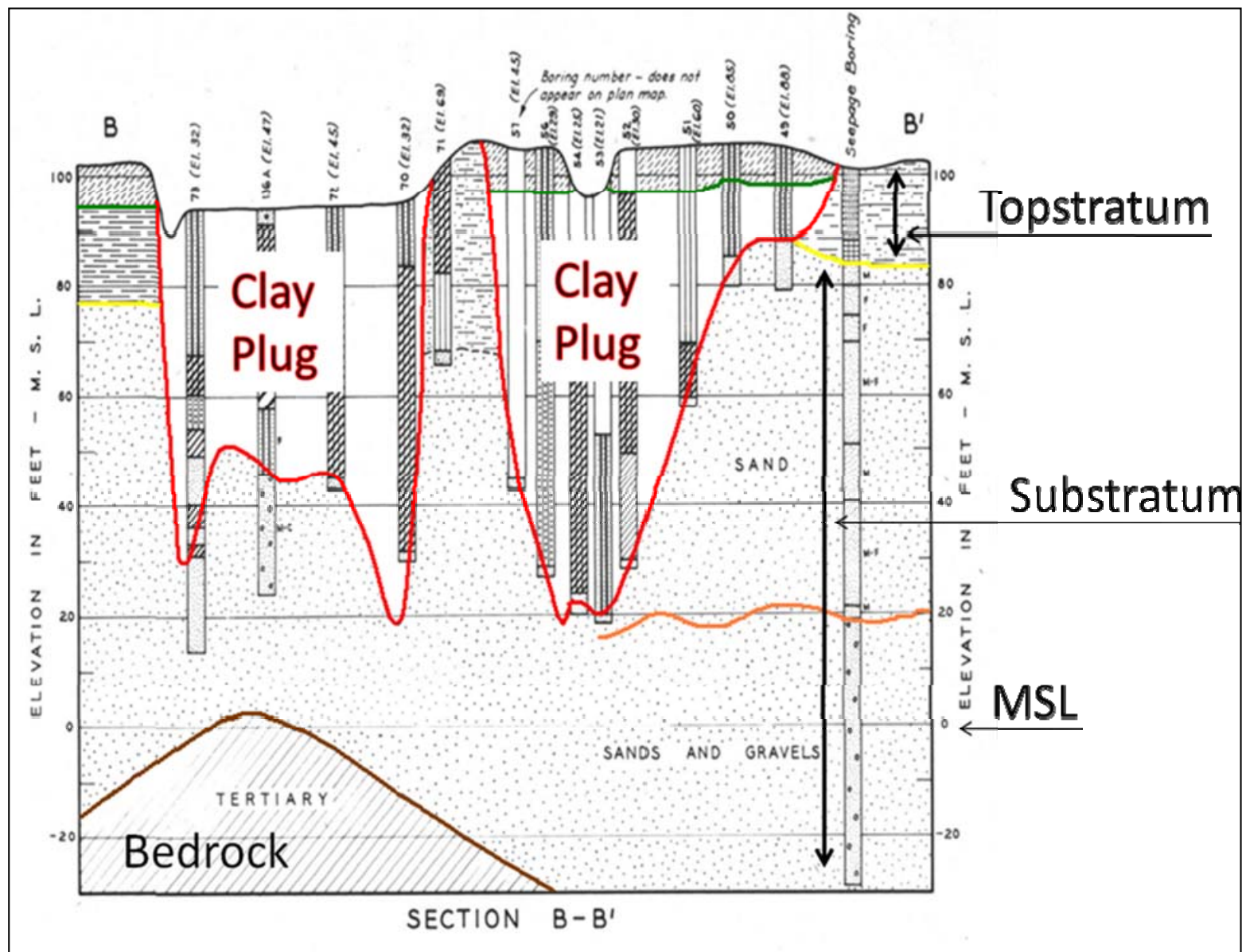


Figure 158. Sedimentary units and elevations for cross section B-B' (Fisk 1947).

### Sand boils

Sand boils on the landward side of levees are a common occurrence along the Lower Mississippi River, and are a result of an increase of hydrostatic pressure within substratum sands exceeding the weight of the topstratum. If this pressure is too great, heaving can occur and water will seep through a weakness of the topstratum. Kolb (1975) identified these potential weaknesses as root holes, shrinkage cracks, minute fissures, and animal burrows (i.e., crayfish holes).

In May 2009, the Mississippi River reached flood stage of 48.0 ft and 43.0 ft in Greenville, MS, and Vicksburg, MS, respectively. During a visit to Lake Providence at this time, sand boils were observed along the lakefront of Lake Providence (Figure 159). In addition to active sand boils (Figure 160 A-B), water flow was observed in two cypress roots (Figure 161 A-B). However, this observation does not conclude that these trees exacerbated the seepage or simply act as conduits for the water flow in an unstable geologic environment.

The site was observed again in October 2010 during low water levels. Sandbags used to stabilize the pressure difference provide evidence of previously active sand boils along the lakefront. Figure 159 presents a photographic comparison during these different stages.

Crayfish burrows were observed on 14 October 2010, when the lake was at lower water levels (Figure 162). Stage data are in Appendix A for stations in Greenville, MS, and Vicksburg, MS.

## 2-D model of defects from woody vegetation at the toe of the levee

### Background

The observations discussed in the previous section provide field evidence of a role woody vegetation may play in piping and seepage. The third approach in the seepage analysis considers the probability of tree root creating a seepage exit, thereby initiating internal erosion in the soil foundation. This analysis follows the procedure described by Schaefer et al. (2010). Results from this analysis are specific only to the levees studied for this research. Because of the complexity of processes related to seepage and piping and the lack of research supporting such processes, only the initiation of

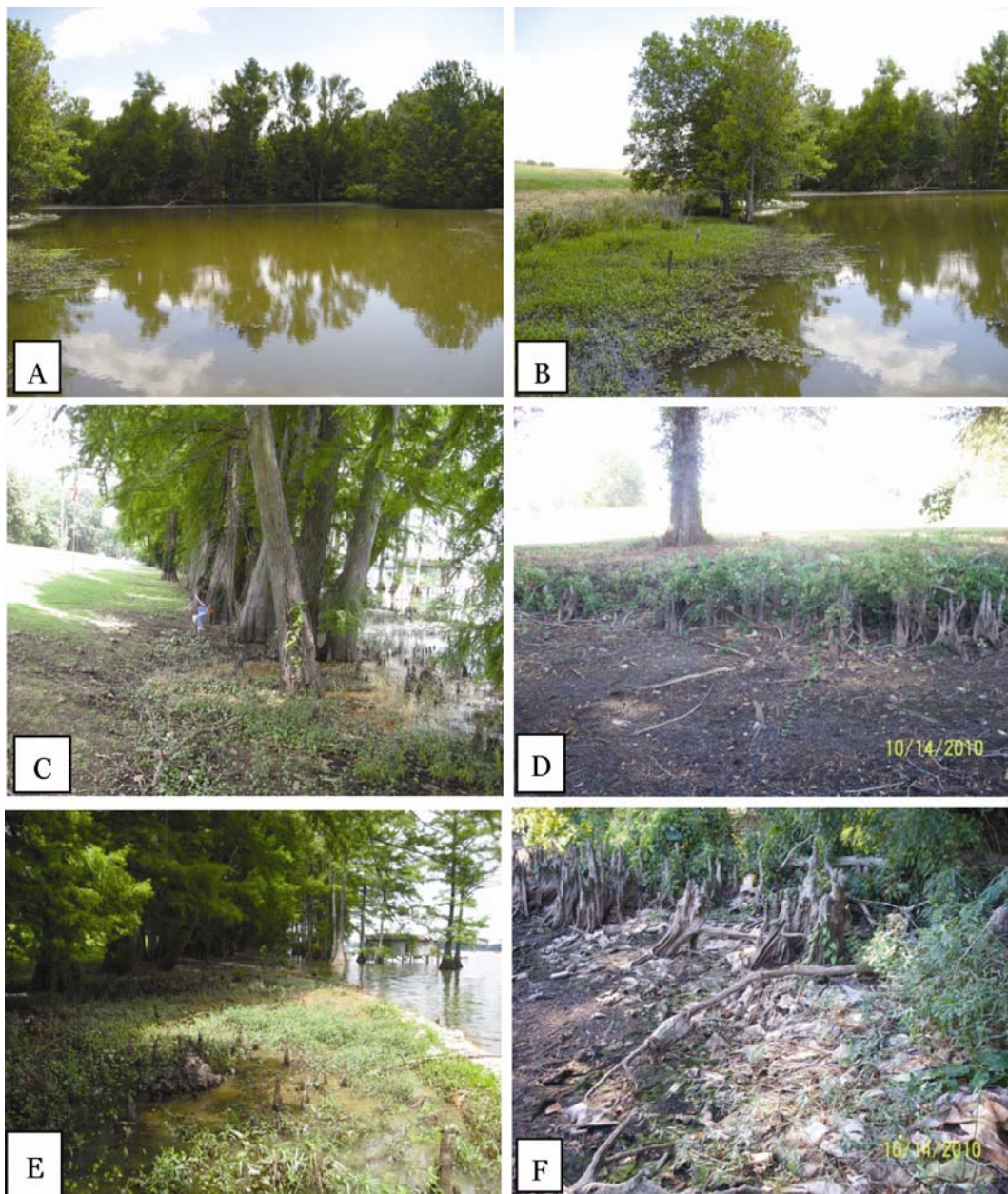


Figure 159. Lake Providence during high water levels in May 2009 (A, B, C, and E), and at low water levels in October 2010 (D and F).

processes leading to underseepage is addressed in these analyses. Schaefer et al. (2010) define initiation as the first phase of internal erosion, and consider the existence of a flaw, such as a continuous crack or poorly compacted layer in which a concentrated leak may form. They further note that if a flaw exists, erosion must begin to initiate for internal erosion to develop.

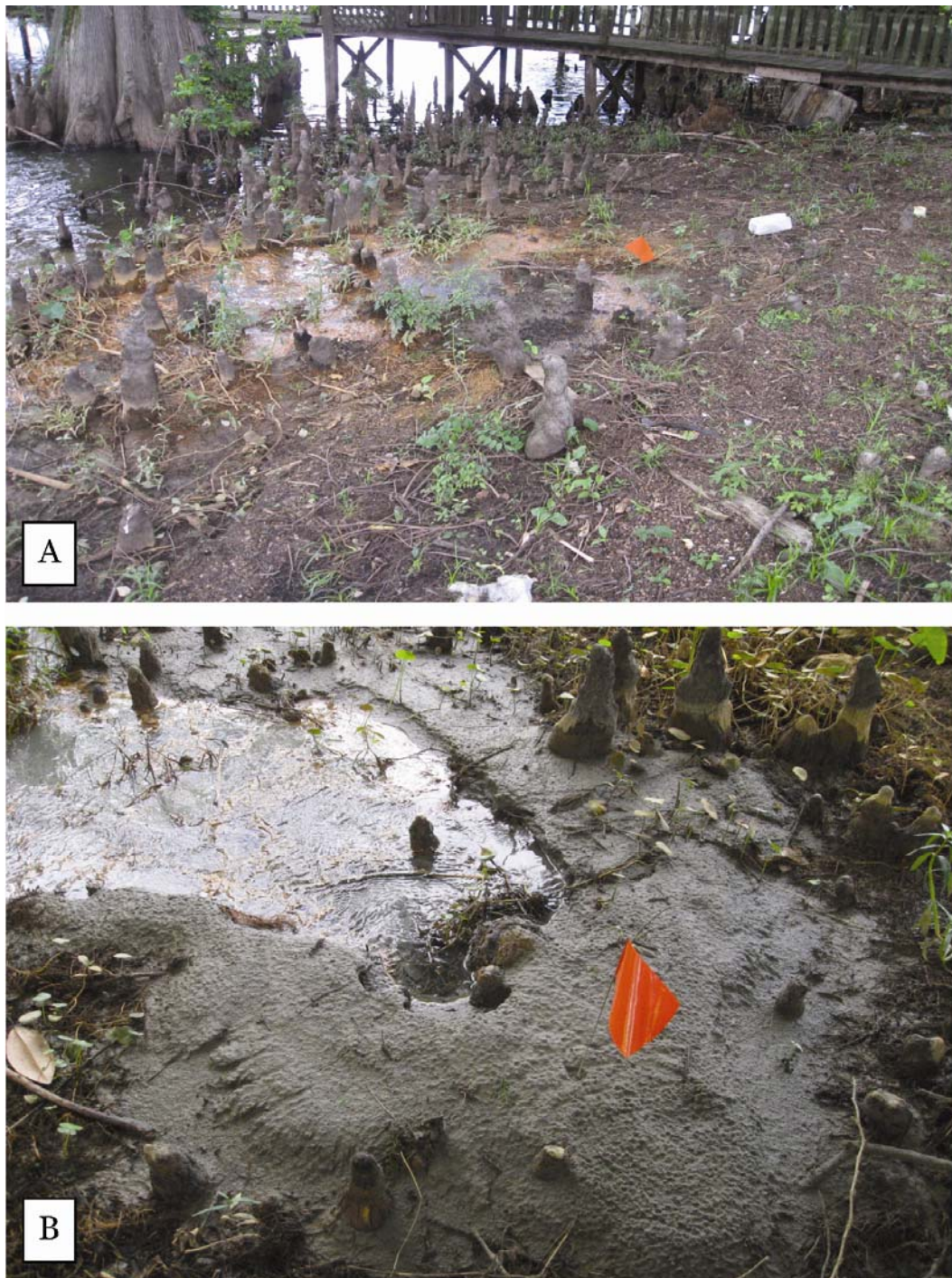


Figure 160. Active sand boils during high river stage of May 2009.

An assumption used by Schaefer et al. (2010) states that a defect where a small flow path is created does not appreciably reduce pore pressure at the bottom of the blanket.



Figure 161. Water flowing out of cypress roots  
during May 2009 flood stage.



Figure 162. Crawfish burrow at Lake Providence; photo was taken during low water levels.

The following generic sequence of events has been developed for internal erosion failure modes (Schaefer et al. 2010):

- Reservoir Rises.
  - ﴿ Initiation – Flaws exist <sup>(1)(2)</sup> – **this stage is the focus of ERDC study on seepage using the approach for modeling a defect in a levee blanket.**
  - ﴿ Initiation – Erosion starts.
  - ﴿ Continuation – Unfiltered or inadequately filtered exit exists.
  - ﴿ Progression – Roof forms to support a pipe.
  - ﴿ Progression – Upstream zone fails to fill crack.
  - ﴿ Progression – Upstream zone fails to limit flows.

- ↳ Intervention fails.
- ↳ Dam breaches (consider all likely breach mechanisms).
- ↳ Consequences occur.
  - (1) A flaw is a continuous crack or gap, poorly compacted or high permeability zone in which a concentrated leak may form.
  - (2) For Backward Erosion Piping (BEP), no flaw is required, but a continuous zone of cohesionless soil in the embankment or foundation is required.

This section addresses the likelihood of a seepage exit being created by a defect in the blanket, which in turn produces a subsequent initiation of internal erosion in the soil foundation. This modeling effort is divided into two analyses as follows:

- **Defect A** – Root defect as a vertical column: Model follows the procedure described by Schaefer et al. (2010), which calculates a range of probabilities for a defect caused by a single tree root represented as a 1-in.-thick vertical column.
- **Defect B** – Root defect as a non-vertical column. Model follows the procedure described by Schaefer et al. (2010), but instead of a vertical column, the modeled root follows a tortuous path.

A brief outline of the procedure in Schaefer et al. (2010) is as follows:

- Determine if a cohesionless soil such as sand is in the foundation. If not, a defect in the vertical layer does not result in erosion.
- Determine blanket thickness. If the blanket thickness is > 25 ft, the probability of a tree at the toe causing piping and erosion is considered negligible. It is important to note that the 25-ft criterion is based on a small sample of collected data. It is used here for the reported results in tables to give quantifiable results. For blanket thickness < 25 ft, continue with the steps below.
- For seepage exits through the overlying confining layer due to defects caused by woody vegetation, assume a continuous column

of sand from the base of the confining layer to the ground surface. Calculate the vertical exit gradient.

- Calculate the factor of safety for this exit gradient using sand as the material where flow occurs in the defect.
- Use Table 69 to compute the probability of a vertical seepage exit through the confining layer. Compute the average horizontal seepage gradient in the foundation.
- The standard procedure here is to compute the particle size distribution of the foundation material, and then estimate a representative uniformity coefficient ( $C_u$ ). If  $1 < C_u < 6$ , graphs given in (1) and (2) are used to determine a horizontal gradient that causes initiation of erosion back to the upstream. For  $C_u > 6$ , the vertical exit gradient is used instead for further calculation.

**Table 69. Probability of a seepage exit through the confining layer versus calculated factor of safety against heave.**

Factor of Safety Against Heave	Probability of a Seepage Exit through the Confining Layer
> 1.3	Negligible
1.3	0.005
1.23	0.02
1.12	0.05
1.05	0.1
1.0	0.9
0.92	0.99
0.80	0.999

Two deviations were made from the above procedure because of the focus considered in the ERDC research. In the first deviation, probabilities in Table 69 refer to factors of safety regarding heave instead of exit gradient. However, for the purpose of providing a reasonable computation, the table is used in this analysis with the additional criterion that if factor of safety < 0.8, the probability is 1.0. In the second adjustment, rather than using the particle size distribution calculation in Step 6 of the above procedure, Table 70 is used to obtain a range of the resulting probability. Therefore, the worst case is calculated from the highlighted row of Table 70. The smallest average horizontal gradient in the foundation list, Table 70, is 0.05. For those cases where the average horizontal gradient in the foundation is less than 0.05, linear interpolation is used to compute the

resulting probability. For example, if the probability is 0.64 when the horizontal gradient is 0.05 (shaded row of Table 70) and the actual horizontal gradient is instead 0.02, the computed probability is  $(0.02 / 0.05) * 0.64 = 0.26$ .

**Table 70. Probability of initiation of backward erosion in the foundation given a seepage exit is predicted.**

Average Seepage Gradient Required to Initiate and Progress Backward Erosion	Average Seepage Gradient in the Foundation						
	0.05	0.1	0.25	0.5	0.75	1.0	2.0
0.05	0.62	0.9285	0.9987	1.0000	1.0000	1.0000	1.0000
0.1	0.19	0.62	0.9671	0.9987	0.9999	1.0000	1.0000
0.25	0.008	0.11	0.62	0.93	0.98	0.9958	0.9999
0.5	0.0002	0.008	0.19	0.62	0.84	0.93	0.9958
0.75	0.00001	0.001	0.06	0.35	0.62	0.78	0.97
1.0	0.000001	0.0002	0.02	0.19	0.43	0.62	0.93

Because the levees used in this study have sand under the confining layer, they required further analysis based on the procedure described above. Each levee system is individually analyzed. Vertical gradients are calculated at the levee toe, and horizontal gradients are calculated at the mid-point of the levee foundation as recommended by Schaefer et al. (2010). Exit gradients were computed at the toe of the levee for each case, except the Albuquerque site where computations were taken at the bottom of the dewatered drainage ditch.

#### **Defect A – Root defect as a vertical column**

In this model, a defect is modeled as a continuous column of sand. A defect of 1-in. thickness, assuming a tree root, is extended from the toe through the blanket. The length of the column varied based on adjusting the blanket thickness. Steady-state runs were computed for different thicknesses of the blanket. Hydraulic conductivity used for the defect is 100 times more pervious than that of the soil. Models were analyzed for Sacramento, CA; Burlington, WA; Portland, OR; and Albuquerque, NM.

#### *Sacramento, CA*

Three cross sections are used for the Pocket Levee in Sacramento, CA, and are described as follows:

- Cross section 1: Levee geometry and soil profile are consistent with the model for the Pocket Levee described in Volume II. Blanket thickness is 30 ft, and the slurry wall is included.
- Cross section 2: Blanket thickness is reduced to 5 ft, and the slurry wall is included.
- Cross section 3: Blanket thickness is reduced to 5 ft, and the slurry wall is excluded.

In the first result for the 30-ft blanket with the slurry wall, the effect of the tree at the levee toe with regard to a defect is negligible. This is not just that the blanket thickness is greater than 25 ft, but also because the factor of safety is greater than 1.3. In cross sections 2 and 3, the blanket is reduced to 5 ft. In these scenarios, the factor of safety is 0.66, resulting in the probability of initiation of 1.0. Table 71 shows the results of the above computations for the Pocket Levee.

**Table 71. Average vertical seepage gradient through the confining layer, factor of safety for this exit gradient, average horizontal seepage gradient in the foundation, and probability of initiation of erosion in the foundation for different blanket thicknesses and slurry wall options for the Pocket Levee.**

Parameter	Cross section			
	1	2	3	
Variations in levee geometry	Blanket thickness (T)	30	5	5
	Slurry wall	Yes	Yes	No
Calculated from SEEP2D	Average vertical seepage gradient	0.29	1.37	1.37
	Factor of safety for exit gradient (FS)	3.10	0.66	0.66
	Horizontal gradient	0.01	0.03	0.03
Interpretation of calculated results based on Schaefer et al. (2010)	Probability of initiation	Negligible	1.0	1.0
	Criterion for probability estimate	T > 25 ft FS > 1.3	FS < 1	FS < 1

FS = factor of safety.

To further the analyses, different scenarios without the slurry wall and with a 5-ft-thick blanket are used to compute velocity, horizontal gradient, and pore pressure. These models considered both a tree on the levee toe and no tree for comparison. Results are shown in Table 72.

**Table 72. Exit gradient and velocity at the toe and pore pressure at the bottom of the blanket below the toe for different thicknesses of the blanket.**

Blanket thickness (ft)	5	10	20	30
Exit gradient at toe without tree	1.46	0.92	0.62	0.40
Exit gradient at toe with tree	1.39	0.84	0.53	0.31
Velocity at toe without tree	0.83	0.52	0.35	0.23
Velocity at toe with tree	78.8	47.6	30.1	17.6
Pore pressure at bottom of blanket without tree	742.4	1105.7	1763.0	2441.1
Pore pressure at bottom of blanket with tree	734.4	1100.9	1760.2	2440.3
Horizontal gradient in the foundation without tree	0.026	0.020	0.015	0.010
Horizontal gradient in the foundation with tree	0.026	0.020	0.015	0.010

Observations from the modeling are as follows:

- The model root penetrating the blanket does not appreciably lower the pore pressure at the bottom of the blanket. This observation supports the assumption in Schaefer et al. (2010) that a defect where a small flow path is created does not appreciably reduce the pore pressure at the bottom of the blanket.
- Water velocities within the defect are greater than those outside the defect.
- The smaller the blanket thickness, the larger the exit gradient and velocities.
- If the top blanket is penetrated, pore pressures at the bottom of the blanket are reduced. This effect is independent of top blanket thickness.

#### *Burlington, WA*

Three cross sections for the Burlington levees were analyzed with the same assumption that the defect from the tree extends from the toe of the levee through the blanket to the sand foundation below the blanket. The blanket thicknesses for these cross sections are directly from the model of the levee profile, and, therefore, are not round numbers. Three cross sections are used in the Burlington analysis. Parameters and results for each cross

section are summarized in Table 73. All three cases show negligible effect with respect to piping and internal erosion in the foundation.

**Table 73. Average vertical seepage gradient through the confining layer, factor of safety for this exit gradient, average horizontal seepage gradient in the foundation, and probability of initiation of erosion in the foundation for different cross sections of the Burlington levee.**

Parameter	Cross-section			
	1	2	3	
Variations in levee geometry	Blanket thickness (T) (ft)	4.10	39.0	48.1
Calculated from SEEP2D	Average vertical seepage gradient	0.43	0.06	0.12
	Factor of safety for exit gradient (FS)	2.10	15.0	7.5
	Horizontal gradient	0.20	0.01	0.01
Interpretation of calculated results based on IET procedure.	Probability of initiation	Negligible	Negligible	Negligible
	Criterion for probability estimate	FS > 1.3	T > 25 ft FS > 1.3	T > 25 ft FS > 1.3

FS = factor of safety.

#### *Portland, OR, and Albuquerque, NM*

The procedure for Portland, OR, and Albuquerque, NM, follows the assumption used in the previous analyses that a defect extends from the ground surface to the base of the blanket. These analyses use one cross section each for Portland and Albuquerque.

Based on these analyses, the probability of initiation of piping is negligible from woody vegetation at the toe of the levee for Portland. Because the model for the Albuquerque levee yielded a safety factor of 1.06, the analysis continued by computing the average horizontal seepage gradient in the foundation as described by Schaefer et al. (2010). A probability of 0.25 for initiation makes the conclusion uncertain. Results are given in Table 74.

#### **Defect B – Root defect as a non-vertical column**

The next model uses a finely discretized mesh of the 6-ft × 5-ft woody vegetation zone just beyond the levee toe such that the edges of the zone have nodes at 1-in. intervals. A root system was introduced into this fine mesh by selecting triangular elements (Figure 163 and Figure 164). The light green is the original woody vegetation zone, and the dark green is the material representing the root system. Table 75 gives exit gradient and

**Table 74.** Average vertical seepage gradient through the confining layer, factor of safety for this exit gradient, average horizontal seepage gradient in the foundation, and probability of initiation of erosion in the foundation for the Portland and Albuquerque levees.

Parameter		Levee	
		Portland	Albuquerque
Variations in levee geometry	Blanket thickness (T)	3.66	6.00
Calculated from SEEP2D	Average vertical seepage gradient	0.43	0.85
	Factor of safety for exit gradient (FS)	2.10	1.06
	Horizontal gradient	0.02	0.02
Interpretation of calculated results based on IET procedure.	Probability of initiation	Negligible	Negligible to 0.25
	Criterion for probability estimate	FS > 1.3	Best to worst case

FS = factor of safety.

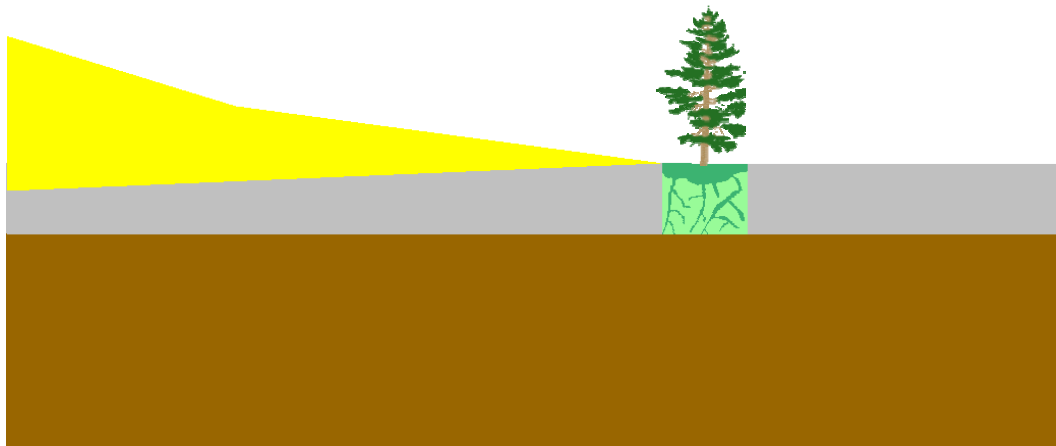


**Figure 163.** Woody vegetation zone with root system.

velocity at the toe of the levee and pore pressure at the bottom of the blanket directly below the toe for three cases: (1) no tree, (2) root system being 100 times less pervious than the original soil, and (3) a defect that formed along the edge of one of the roots that extends from the toe of the levee to the bottom of the blanket (see the red zone in Figure 165).

Observations are as follows:

- When the root system is tightly in place, the exit gradient at the toe is moderately increased, the velocity at the toe is significantly decreased, and the pore pressure at the bottom of the blanket directly below the toe remains the same.

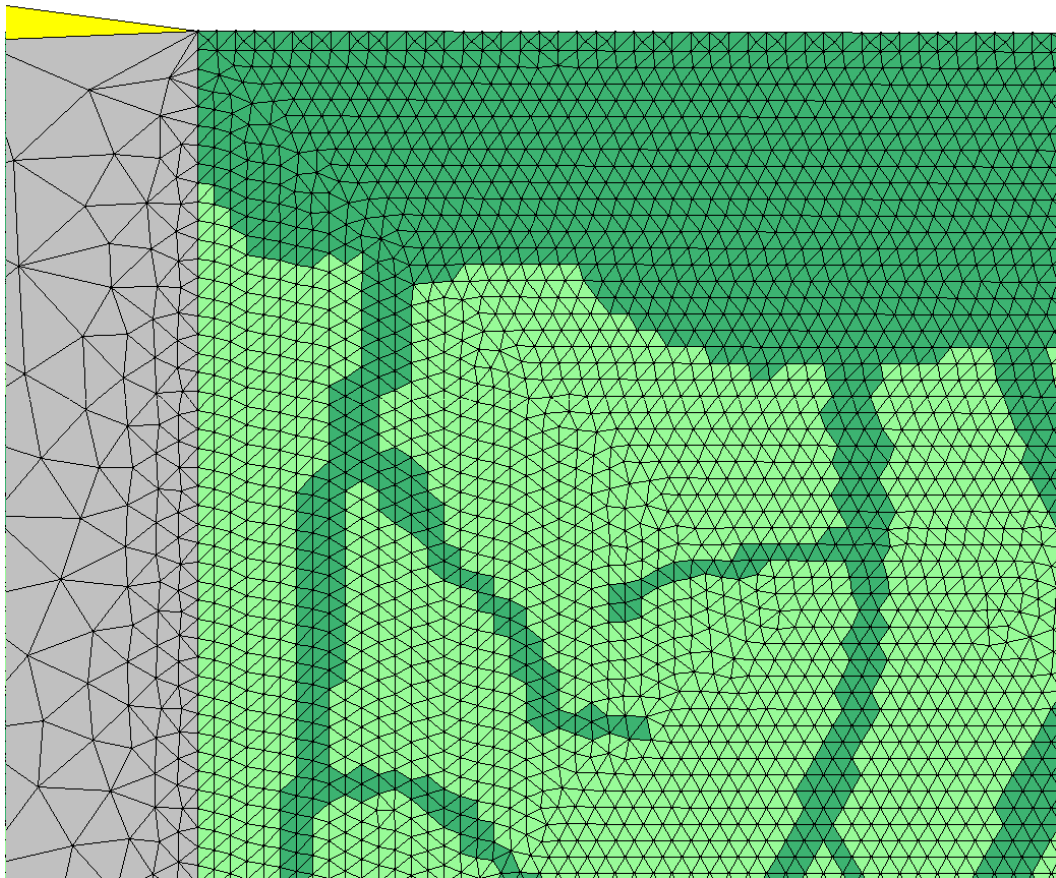


Figure 164. Finite elements selected to form a root system.

Table 75. Exit gradient and velocity at the toe and pore pressure at the bottom of the blanket below the toe for the root system model.

Tree case	No Tree	Root System	Defect
Exit gradient at toe	1.57	2.07	1.43
Velocity at toe	0.89	0.01	81.2
Pore pressure at bottom of blanket	740.6	740.6	737.6

- When the defect model is turned on, the exit gradient at the toe is slightly decreased, velocity at the toe is significantly increased, and pore pressure at the bottom of the blanket directly below the toe is only slightly reduced.
- Model results reveal that if a defect occurs in a complicated root structure, the result is the same as the simple continuous-column-of-soil model.

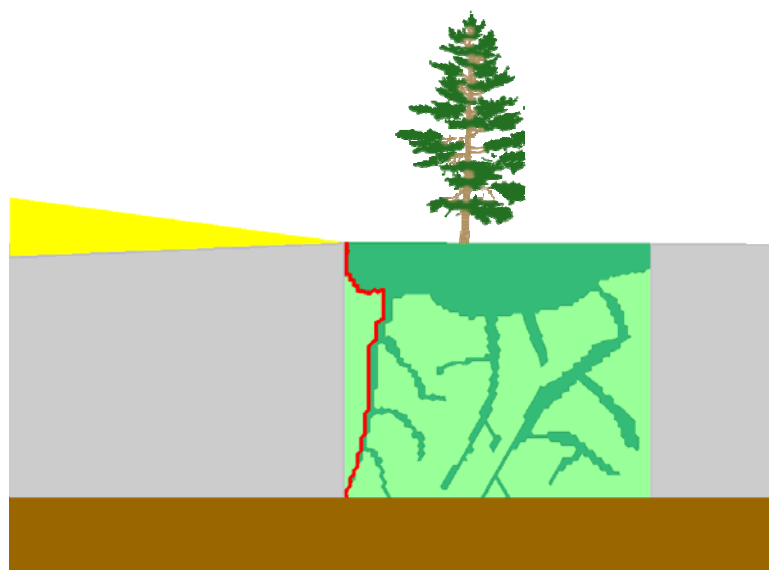


Figure 165. Defect along the left edge shown by the red zone.

- One of the assumptions used in Schaefer et al. (2010) is that a defect where a small flow path is created does not appreciably reduce the pore pressure at the bottom of the blanket. Modeling results using the Sacramento model verify that assumption.

### 3 2-D Slope Stability Analysis

The slope stability analysis was designed to investigate the influence of trees on levee integrity, specifically the levee stability factor of safety. An important aspect of this study was to incorporate the root system and root strength into a slope stability model. The procedure used in this study is discussed later in this section.

Previous researchers recognized the importance of root strength in soil reinforcement. Their work played an important role in developing the approach used in this study. In addition to the soil strength, tree weight and wind are important factors when studying the effect of trees on levee stability. This section also includes a discussion of the process of using root pullout data, described in Volume II of this report, in a slope stability model.

#### Root strength

Wu (1976), Wu et al. (1979), and Waldron (1977) independently initiated a straightforward approach to study the effects of root fibers on soil strength. The approach assumes that the roots are flexible and the initial positions of the root fibers are perpendicular to the shear plane (Figure 166). After a horizontal shear displacement of  $x$ , the upper part of the root fiber has a distortion angle of  $\theta$  relative to the original position. The additional shear strength attributable to this root fiber is

$$\Delta S_R = t_R (\sin \theta + \cos \theta \tan \varphi) \quad (9)$$

where:

$\Delta S_R$  = additional shear strength due to root, psi

$t_R$  = average tensile strength of root per unit area of soil, psi

$\theta$  = angle of shear distortion, degree

$\varphi$  = internal friction angle of soil, degree

$(\sin \theta + \cos \theta \tan \varphi)$  = root orientation factor.

According to Gray and Megahan (1981), the average tensile strength of a root,  $t_R$ , can be calculated from the following relationship:

$$t_R = T_R \left( \frac{A_R}{A} \right) \quad (10)$$

where:

$T_R$  = average of tensile strength of roots, psi  
 $(A_R/A)$  = root area ratio (RAR), fraction of soil occupied by roots.

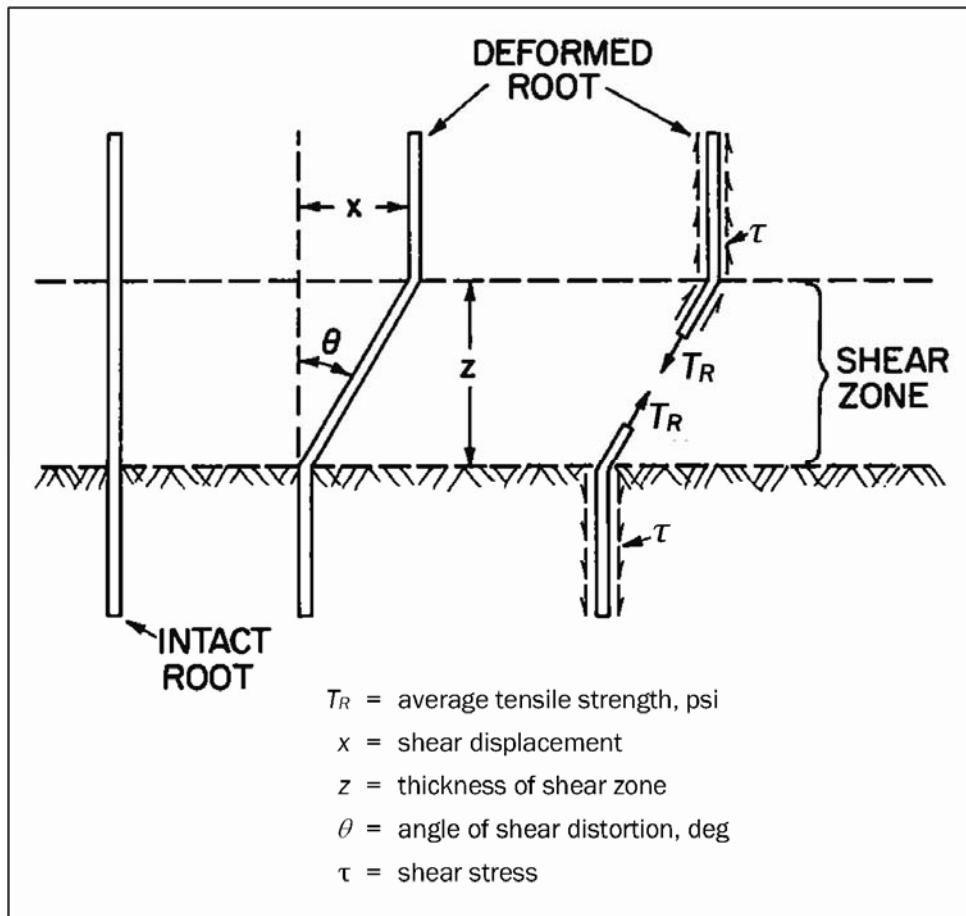


Figure 166. Schematic diagram of initially vertical position of a root fiber during the shearing process (Wu 1976, after Gray and Leiser 1982).

Wu (1976) observed that the angle  $\theta$  varies between 45 and 70 deg. He performed parametric studies on the sensitivity of friction angle  $\phi$ , and distortion angle  $\theta$  to the additional shear strength caused by the root in Equation 9. Considering the variation for  $25^\circ < \phi < 40^\circ$  and  $40^\circ < \theta < 70^\circ$ , Wu found that the root orientation factor varied from 1.0 to 1.3. Assuming the midpoint of the range to be the most probable value, Wu suggested the simplified form of Equation 8 as follows:

$$\Delta S_R = 1.2 t_R \quad (11)$$

Gray and Leiser (1982) investigated the additional soil shear strength when root fibers have an inclined position relative to the shear plane direction (Figure 167). Considering that a root has an initial inclined angle of  $i$  relative to the shear plane, they expressed the additional shear strength by the following relationship:

$$\Delta S_R = t_R [\sin(90 - \psi) + \cos[90 - \psi] \tan \phi] \quad (12)$$

where  $\psi$  is the angle between the root and shear plane during shear, defined by:

$$\psi = \tan^{-1} \left[ \frac{1}{k + (\tan i)^{-1}} \right] \quad (13)$$

and

- $i$  = initial angle of root inclination with respect to shear plane
- $x$  = shear displacement
- $z$  = thickness of shear zone
- $k = x/z$  = shear distortion ratio,

Using Equation 12, Gray and Leiser (1982) suggested using more variation in the value of the root orientation factor in Equation 10. Depending on the initial angle between the roots and the shear plane and the shear distortion ratio, the root orientation factor may vary from zero to 1.2. This theoretical calculation was confirmed by the experimental results of direct shear tests on sand material with fiber reinforcement at different initial orientations (Gray and Leiser 1982).

Gray and Ohashi (1983) investigated the effects of different types of fiber reinforcement in sand material. One of the experiments they conducted compared the results of shear tests of sand reinforced by fibers in a vertical orientation to sand reinforced with fibers in random orientations. The tests yielded nearly identical results (Figure 168). These results show that it is acceptable to assume that roots have an initial position perpendicular to the shear plane.

Pollen and Simon (2005) revisited Equation 11 by testing saturated direct shear on silt with switchgrass root. The direct shear test results were compared to Equation 9 and to a numerical analysis using a fiber bundle model. Equation 9 predicted shear strengths far above direct shear test

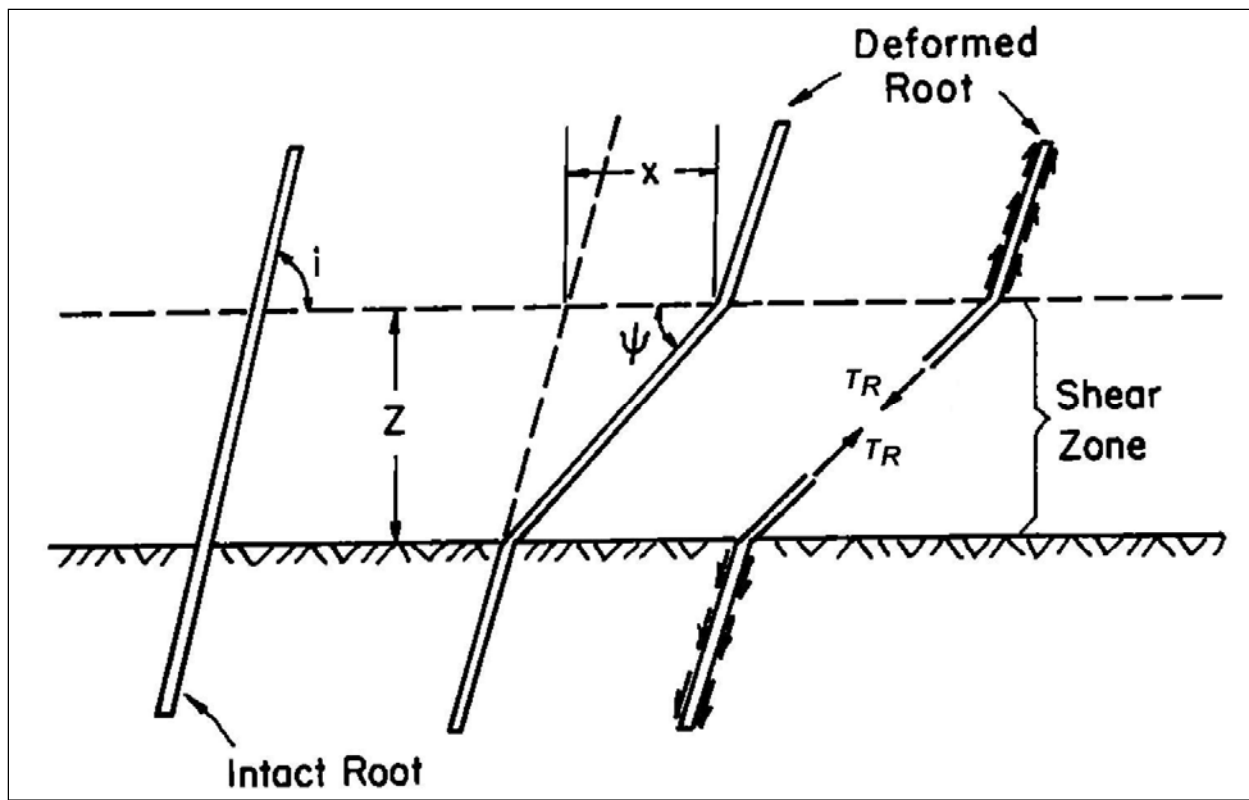


Figure 167. Initially inclined position of a root fiber during shear (after Gray and Leiser 1982).

results, while the numerical prediction method yields results close to the direct shear test results. The fiber bundle, first proposed by Daniels (1945), considered that the maximum load that can be held by the bundle of fibers is less than the sum of the individual strengths. Pollen and Simon (2005) concluded that this fiber bundle principle was the reason for the overestimations by Wu (1976) and Wu et al. (1979). This principle is very similar to pile group efficiency, determined using the Converse-Labarre equation in pile foundation engineering (Bowles 1995). For a cluster of piles, the soil pressure developed as resistance will overlap, and therefore as a group, the total bearing capacity of the piles is less than the sum of their individual bearing capacity. Pollen and Simon (2005) evaluated the difference of the two root reinforcements for six different species. The ratio of root reinforcement using Pollen and Simon's model to the equation used by Wu et al. ranges between 0.48 (switchgrass) to 0.82 (pine).

In calculating additional shear strength, Wu (1976) suggested using  $T_R$  as the full capacity of the tensile strength. Waldron (1977) independently studied the effects of four different types of roots in four different types of soils. His results show a non-brittle shear failure. The shear displacement

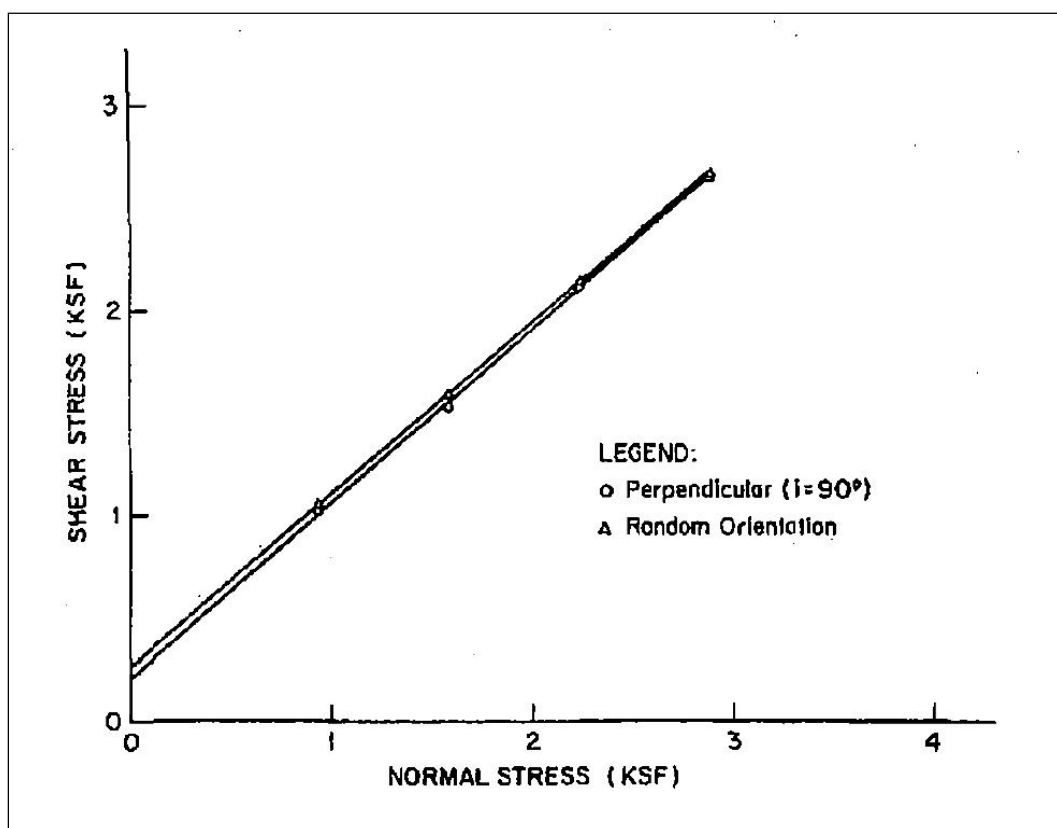


Figure 168. Shear stress [kilo-pound per square foot (KSF)] of sand reinforced with No. 2 reed fibers versus normal stress; one specimen reinforced using fiber in vertical direction and the other with random direction (Gray and Ohashi 1983).

versus shear resistance curve shows a relatively long period of residual shear resistance, indicating that the failures were not tension failure but more frictional failure. This finding is supported by Norris and Greenwood (2006), who compared root pullout strength to root tensile strength. Norris and Greenwood found that, in many cases, pullout strength is smaller than tensile strength. In general, the pullout strength is 50 to 70% of the root tensile strength. Norris and Greenwood (2006) calculated and summarized the additional shear strength caused by different species used in their research, along with test results from other researchers in Table 76.

The percentages calculated by Norris and Greenwood (2006) coincide with the finding of Pollen and Simon (2005). By doing pullout tests on a root of larger diameter, they included the partial effects of fiber bundles because a larger root is connected to or branched from smaller roots. The breaking of individual roots is not simultaneous, but similar to the predicted progressive failure of the fiber bundle model. A weaker root will break first, then

**Table 76. Additional shear strength caused by tree roots of different species  
(Norris and Greenwood 2006).**

Vegetation, Soil Type, and Location	Root Cohesion (c'v) kPa
Silt loam soils under alder ( <i>Alnus</i> ), nursery, Japan	2.0 - 12.0
Beech ( <i>Fagus</i> sp.), forest-soil, New Zealand	6.6
Bouldery, silty clay colluvium under sugar maple ( <i>Acer saccharum</i> ) forest, Ohio, USA	5.7
Industrial deciduous forest, colluvial soil (sandy loam), Oregon, USA	6.8 - 23.2
Mountain till soils under hemlock ( <i>Tsuga mertensiana</i> ) and spruce ( <i>Picea sitchensis</i> ), Alaska, USA	3.4 - 4.4
Mountain till soils under conifers ( <i>Pseudotsuga menziesii</i> ), British Columbia, Canada	1.0 - 3.0
Sitka spruce ( <i>Picea sitchensis</i> ) – western hemlock ( <i>Tsuga heterophylla</i> ), Alaska, USA	3.5 - 6.0
Mountain and hill soils under coastal Douglas fir and Rocky Mountain Douglas fir ( <i>Pseudotsuga menziesii</i> ), West Oregon and Idaho, USA	3.0 - 17.5
Mountain till soils under cedar ( <i>Thuja plicata</i> ), hemlock ( <i>Tsuga mertensiana</i> ) and spruce ( <i>Picea sitchensis</i> ), Alaska, USA	5.9
Lodgepole pine ( <i>Pinus contorta</i> ), coastal sands, California, USA	3.0 - 21.0
Yellow pine ( <i>Pinus ponderosa</i> ) seedlings grown in small containers of clay loam	5.0
Sandy loam soils under Ponderosa pine ( <i>Pinus ponderosa</i> ), Douglas fir ( <i>Pseudotsuga menziesii</i> ) and Engelmann spruce ( <i>Picea engelmannii</i> ), Idaho, USA	~10.3
Shallow stony loam till soils under mixed evergreen forests, New Zealand	3.3
Yellow pine ( <i>Pinus ponderosa</i> ) (54 months), laboratory	3.7 - 6.4
Hemlock ( <i>Tsuga</i> sp.), Sitka spruce ( <i>Picea sitchensis</i> ) and yellow cedar ( <i>Thuja occidentalis</i> ), Alaska, USA	5.6 - 12.6
Cryptomeria japonica (sugi) on loamy sand (Kanto loam), Ibaraki Prefecture, Japan	1.0 - 5.0
Hemlock ( <i>Tsuga</i> sp.), Douglas fir ( <i>Pseudotsuga</i> ), cedar ( <i>Thuja</i> ), glacial till soils, Washington, USA	2.5 - 3.0
<i>Pinus contorta</i> on coastal sand	2.3
Natural coniferous forest, colluvial soil (sandy loam), Oregon	25.6 - 94.3
<i>Pinus halepensis</i> , hill slopes, Almudaina, Spain	-0.4 - 18.2

transfer the load to the neighboring root. The process repeats until the last root breaks. Thus, the failure is not always a brittle failure. Pullout tests conducted by ERDC for this study in Portland, OR, Burlington, WA, and Albuquerque, NM, also confirm many cases of non-brittle failure. In analyzing slope stability in this study, the value used for  $T_R$  in Equation 9 was found to be the pullout strength value obtained from field tests.

## Tree weight

Trees will transfer their body weight through their root ball to the levee. To calculate the additional surcharge caused by the tree, the weight of a tree needs to be estimated. As discussed in this section, there are several research investigations on how to estimate the weight of a tree of different species.

Crow and Erdmann (1983) studied the weight of red maple from 150 trees at six different sites around Lake Michigan in Wisconsin and Michigan. The ages of the red maple varied between 40 and 70 years old, and the diameter at breast height (DBH) ranged from 4.0 to 21 in. They found a nonlinear relationship between the tree green weight (TGW), and its DBH and height.

Myers et al. (1976) developed equations for estimating full tree weight of four hardwood species: black oak (*Quercus velutina*), red oak (*Quercus rubra*), white oak (*Quercus alba*), and hickory (*Carya*). For each species, they use 40 trees over a range of diameters to build the equations. They used 20 trees to derive the equations and the other 20 to test the relationship. The DBH in the study ranged between 5.0 and 18+ in. Eight possible relationships were investigated. They found the TGW of the tree, in pounds, best related to DBH ( $D$ ), in inches, and tree height ( $H$ ) in feet, and in a nonlinear relationship to be the function of the highest correlation. Table 77 summarizes the final equations for each species.

**Table 77. Summary of TGW of four species (Myers et al. 1976).**

	Species	Equation
1	Black oak	$TGW = 0.2112 D^{2.154} H^{0.911}$
2	White oak	$TGW = 1.3426 D^{2.409} H^{0.4275}$
3	Red oak	$TGW = 0.06375 D^{2.285} H^{1.099}$
4	Hickory	$TGW = 0.784 D^{1.86} H^{0.813}$

Note:

$TGW$  = Tree Green Weight, lb.

$D$  = DBH (diameter at breast height), in.

$H$  = Tree Height, ft.

Figure 169 shows the relationship between the TGW, and DBH for different heights of black oak based on the equation for black oak in Table 77. The black oak tree DBH ranges between 6 and 30 in., and the heights range from 40 to 96 ft. The figure shows the tree weight ranging from 300 to 20,000 lb. Similarly, Figures 170, 171, and 172 depict the weight of white oak, red oak, and hickory trees, respectively.

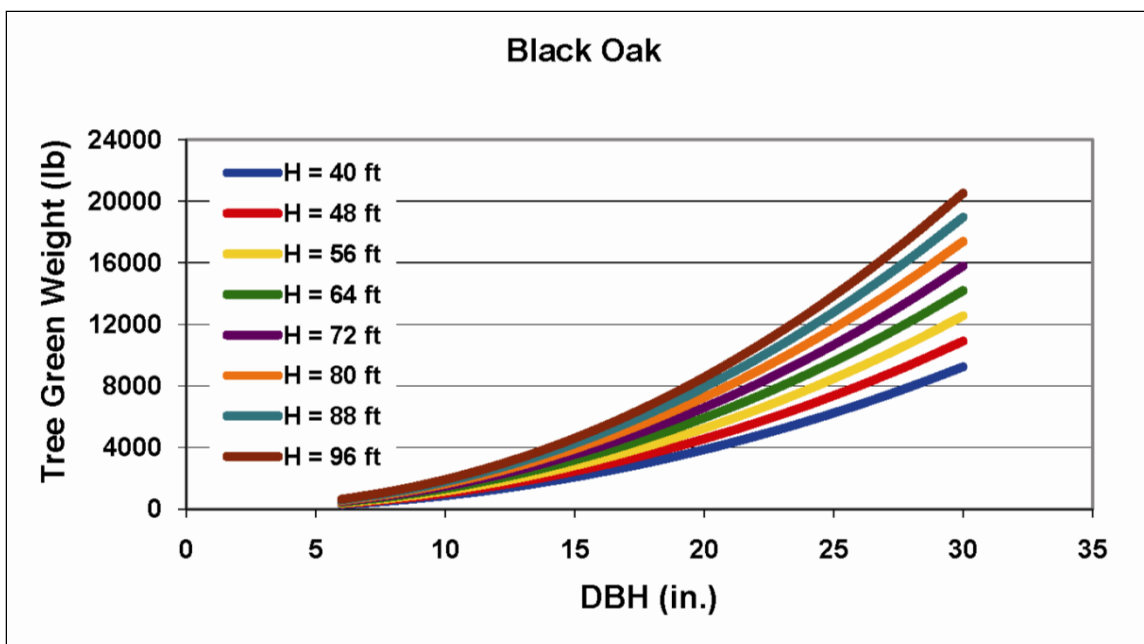


Figure 169. Relationship between weight and DBH for different heights of black oak tree.

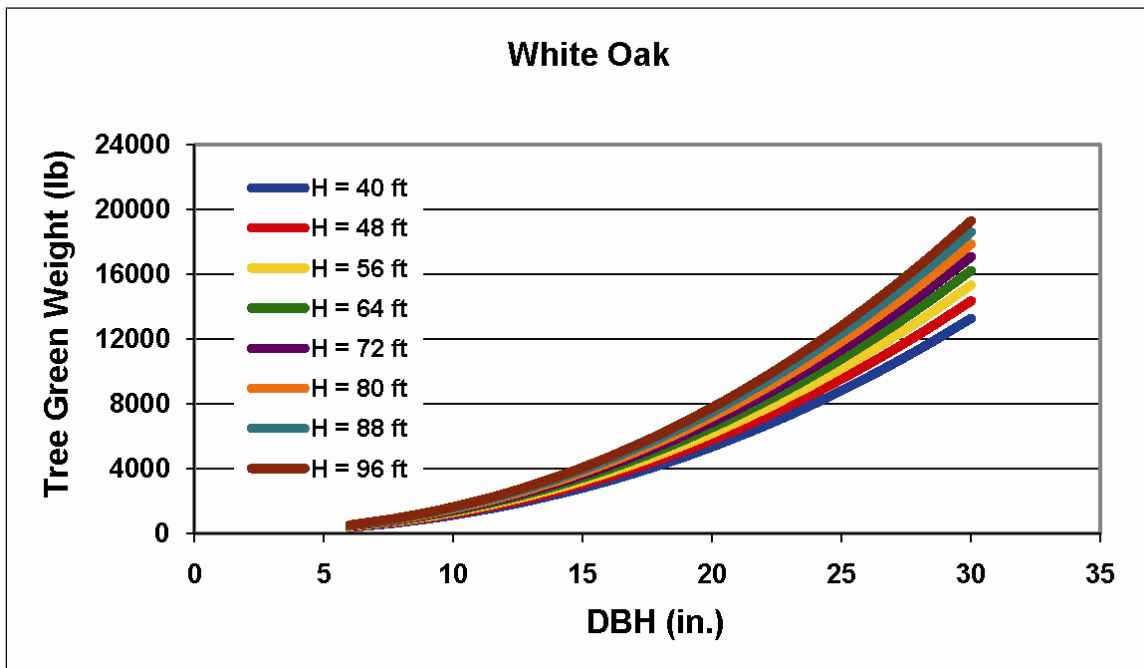


Figure 170. Relationship between weight and DBH for different heights of white oak tree.

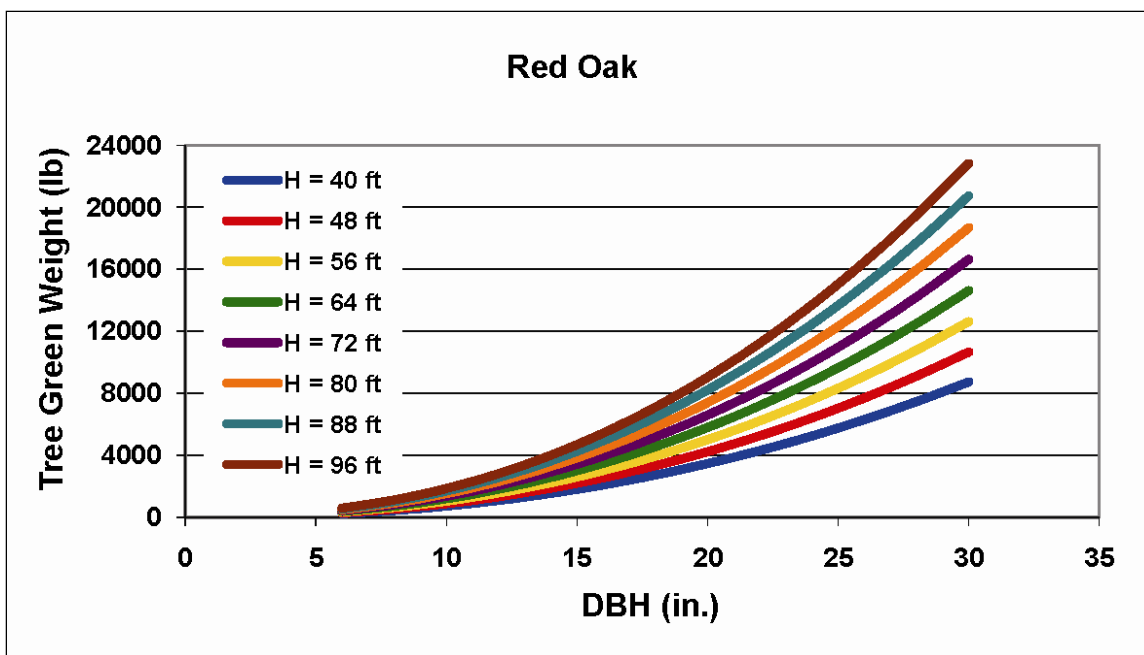


Figure 171. Relationship between weight and DBH for different heights of red oak tree.

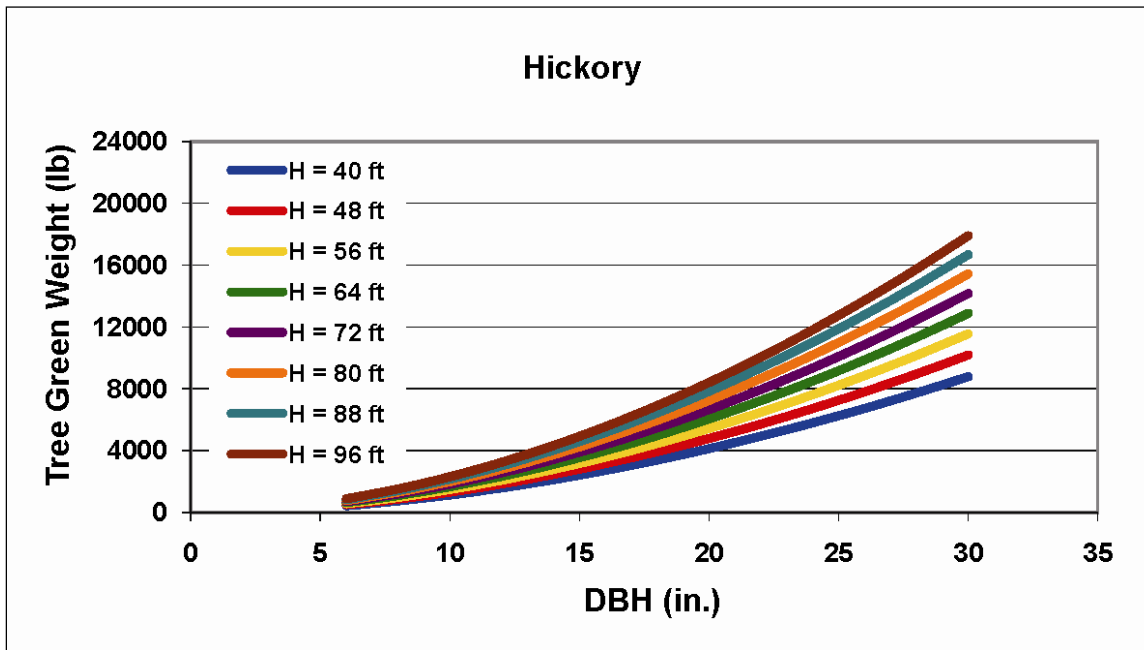


Figure 172. Relationship between weight and DBH for different heights of hickory tree.

Another equation used for tree weight estimation was developed by Jenkins et al. (2004). Based on 180 publications concerning regressions on tree weight, Jenkins et al. developed a relationship between total aboveground biomass for all hardwoods and softwoods as a function of DBH. The biomass equation is expressed using the metric system as:

$$bm = \text{Exp} (\beta_0 + \beta_1 \ln \text{DBH}) \quad (14)$$

where:

$bm$  = total aboveground biomass (kg)  
DBH = diameter at breast height (cm).

The parameters  $\beta_0$  and  $\beta_1$  are regression constants, which vary for different species. For example, the value of  $\beta_0$  is -2.2094 and  $\beta_1$  is 2.3867 for cottonwood (Jenkins et al. 2004). Jenkins found that the coefficient of determination ( $R^2$ ) of 0.953 shows an excellent correlation between the two parameters.

## Wind load

Wind blowing the tree crown creates pressure on the upper part of the tree and this in turn causes a moment loading to the bottom of the tree. The Beaufort scale suggests that wind load is substantial when the wind is stronger than Scale 6. A wind at Beaufort Scale value of 7 causes the entire tree to be in motion, and this scale value may be translated as a wind velocity of 32 to 38 mph. Uphill winds acting on well rooted trees will cause a downhill moment, which adds to the driving force in slope stability calculations. On the other hand, downhill winds acting on shallow rooted trees will add downhill shear forces that destabilize the slope. In general, drag forces caused by trees are influenced by wind velocity, tree height, crown size, and the slope angle.

Hsi and Nath (1970) conducted wind tunnel experiments on a model forest for estimating wind pressure caused by wind parallel to the ground surface. They found that the wind pressure ( $p$ ) measured in pounds per square foot ( $\text{lb}/\text{ft}^2$ ) is expressed as:

$$p = 0.5 * \rho_a V^2 C_D \quad (15)$$

where:

- $\rho_a$  = air density, in slug/ft<sup>3</sup> (0.0024 flug/ft<sup>3</sup> at 12 °C and 1013 mb pressure)  
 $V$  = wind velocity, ft/sec  
 $C_D$  = dimensionless drag coefficient.

Brown and Sheu (1975) formulated equations to estimate shear force and overturning moment caused by wind pressure. For a tree on a slope inclined at angle  $\beta$  with respect to the ground with wind blowing parallel to the slope, the wind pressure normal to the tree is:

$$p_s = p \cos^2 \beta \quad (16)$$

Drag force (D) can be calculated by multiplying  $p_s$  by the area of the tree crown. Coder (2007) tabulated wind pressure of different wind velocities using Equation 14 by assuming the value of drag coefficient equals to one. Depending on the shape of the tree crown, the wind load is applied at the center of the tree crown. For conic shape of the crown, the drag force may be assumed to be located at approximately 1/3 of the tree height.

## Procedure

The procedure used in this study is shown in Figure 173. Although there are techniques and methods available to study root systems, and slope stability other than the ones used here, the procedure described in this section is repeatable in different geographical regions. In addition, the results of the ERDC slope stability analyses were verified when compared to previous research.

Figure 174 gives an example of a conceptual model for slope stability analyses to display where the steps within the procedure apply to a study of woody vegetation on a levee. The input parameters, levee profile (includes specific aspects of the levee, such as the SBC slurry wall and ground surface), phreatic surface, wind load, root ball, tree weight, and root reinforcement are described in the following paragraphs.

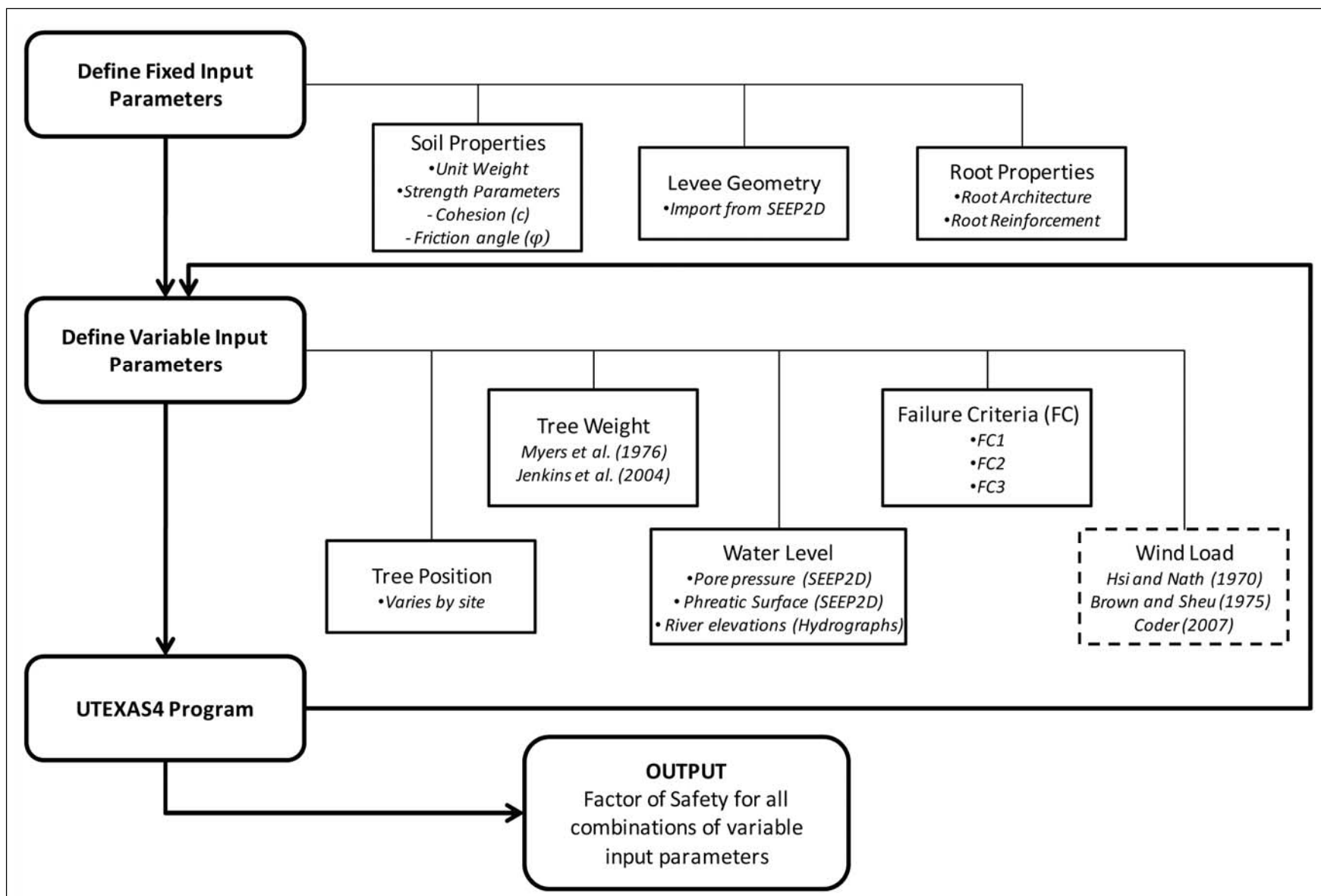


Figure 173. Procedure used by ERDC for the slope stability analysis.

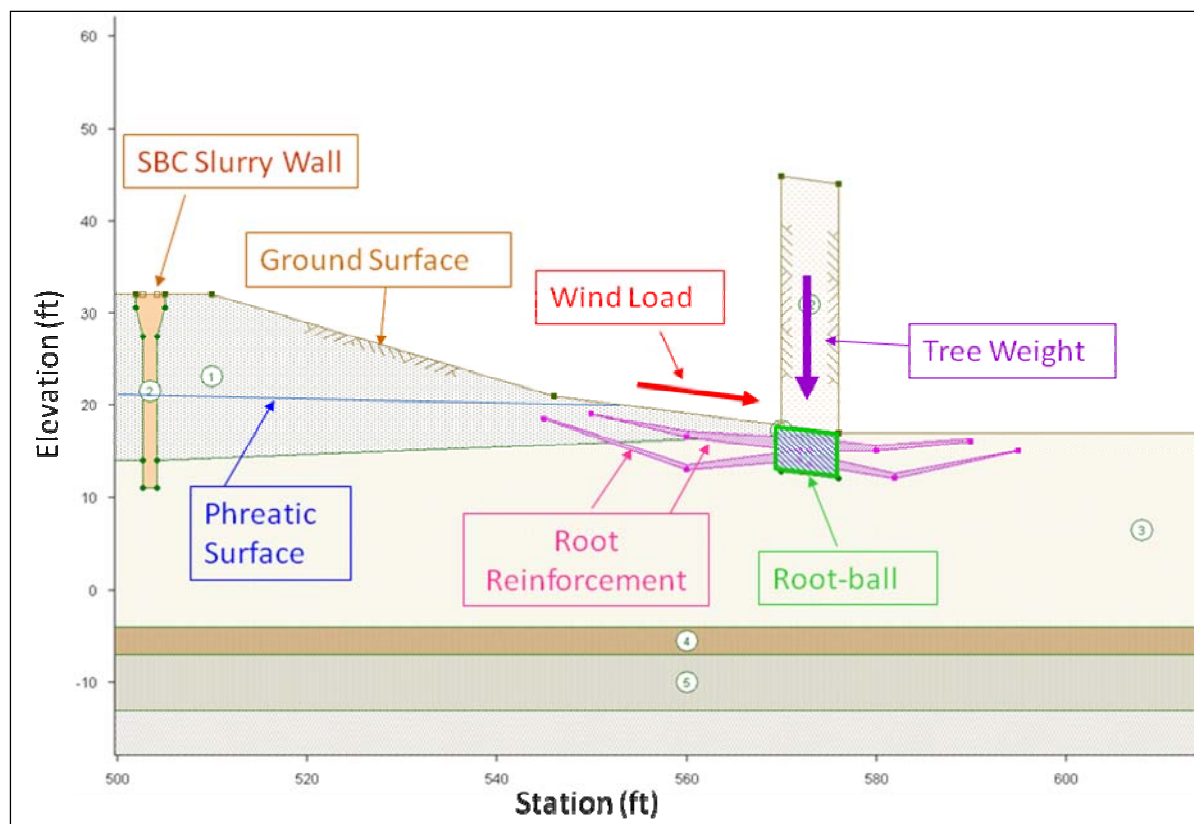


Figure 174. Conceptual diagram of tree and levee interaction in slope stability analysis.

Before we discuss the specifics of the slope stability model, an overview of the model selected for these analyses is needed. The 2-D slope stability analyses for the ERDC study were performed using UTEXAS4, a program based on conventional limit equilibrium methods (Wright 1999). This method examines the equilibrium of a soil mass, which is inclined to slide down the slope because of its self-weight and external loading. The calculations consider all forces, moments, and stresses that trigger the instability, as well as those resisting the movement. Limit equilibrium methods assume the shear strengths of materials along the shear plane, and are regulated by a linear or non-linear relationship between shear strength and normal stress. In general, the 2-D slope stability analysis assumes a plain strain condition. The output of UTEXAS4 is a factor of safety defined by the following equation:

$$FS = \frac{\text{Available Shear Resistance}}{\text{Equilibrium Shear Stress}} \quad (17)$$

When the factor of safety is greater than 1.0, the slope is considered stable, and when the factor of safety is less than 1.0, it is considered unstable.

The most familiar procedure of the limit equilibrium analysis is the slice method, in which the soil mass is divided into many vertical slices for calculations. Based on various assumptions, several different methods of creating the slices have been developed. In this study, the Spencer Method was selected as the limit equilibrium method for the slope stability analyses. This method takes into account both force and moment equilibrium, assumes all inter-slice forces are parallel, and shows consistency in the results. The Spencer Method is recommended by USACE (2003).

The following sections include details from the procedure and the conceptual model for each study location:

1. Soil properties and levee geometry. As described in Volume II of this report series, the soil properties and levee geometry were obtained from existing geotechnical reports and imported from SEEP2D for each of the sites analyzed in the slope stability models.
2. Root properties (root architecture and root reinforcement). For the root architecture, the root ball area is estimated by geophysical tests conducted for this study, and described in Volume II. Two reinforcing roots represent the boundary (upper and lower) of the root architecture.

The root reinforcement consists of two aspects: the root ball, and the area outside the root ball. At the root ball, the additional shear strength is calculated using Equations 9 and 10. The value of  $t_R$  is the pullout strength obtained from field test data for this study, and described in greater detail in Volume II. In the case of the Pocket Levee in Sacramento, CA, the value of RAR is estimated to be 0.5% as reported by Gray et al. (1991). If the RAR is not available, then the RAR data gathered by Norris and Greenwood (2006) can be used. At the area outside the root ball, the reinforcement is applied through the group of individual, long roots. The estimated strength of the root is calculated from pullout test data. For these analyses, root length is based on the following observational data:

1. Tree position. Because the influence of a tree on different positions along a levee is unknown, several different locations for a tree were used in the analyses.

2. Water level (river elevation, pore pressure, and phreatic surface). Hydrographs are used to identify the peak elevation. Several river elevations are used in developing the model to identify the influence of fluctuating water levels on the stability calculations. The phreatic surface, and pore pressures of  $\beta = 100$  from a root system are calculated and imported from SEEP2D. A thorough discussion of the seepage models is included previously in this volume.
3. Failure criteria. In most slope stability analyses, finding the absolute minimum factor of safety is a goal. This is easily accomplished in UTEXAS4 through the use of the built-in automated search routine, in which a floating search grid is used to search all possible circle locations. However, in sites with cohesionless soils, this feature is of little use because the failure circle with the lowest factor of safety is always a shallow, local failure circle near the surface. To gain an understanding of how the tree position affected overall levee stability, three failure criteria were defined by limiting the software's search routine to failure circles passing through three points (Figure 175). These limitations are designated as failure criteria because they determine which factor of safety value is identified as being closest to failure. While this procedure may not find the absolute minimum factor of safety for a given slope, it will serve as definitive criteria for quantifying the effects of trees on levees.
4. Wind load. The wind load is calculated using the equation proposed by Hsi and Nath (1970) with correction by Brown and Sheu (1975), or a table proposed by Coder (2007). The table proposed by Coder (2007) was used for the analysis because the published values are considered to be conservative.
5. Tree weight. The tree weight is calculated using equations developed by Myers et al. (1976), or Jenkins et al. (2004).

## **Study locations for analyses**

Slope stability analyses were conducted for Sacramento, CA; Burlington, WA; and Albuquerque, NM, and are described in this order in the following sections. Because of time constraints, the Portland, OR, site was not used in the slope stability analysis.

### **Sacramento, CA**

The levee profile (including levee geometry and material properties) used for the Pocket Levee analysis is shown in Figure 176. The approximate dimensions of the levee are 15 ft in height, 32-ft crest elevation, and 22-ft

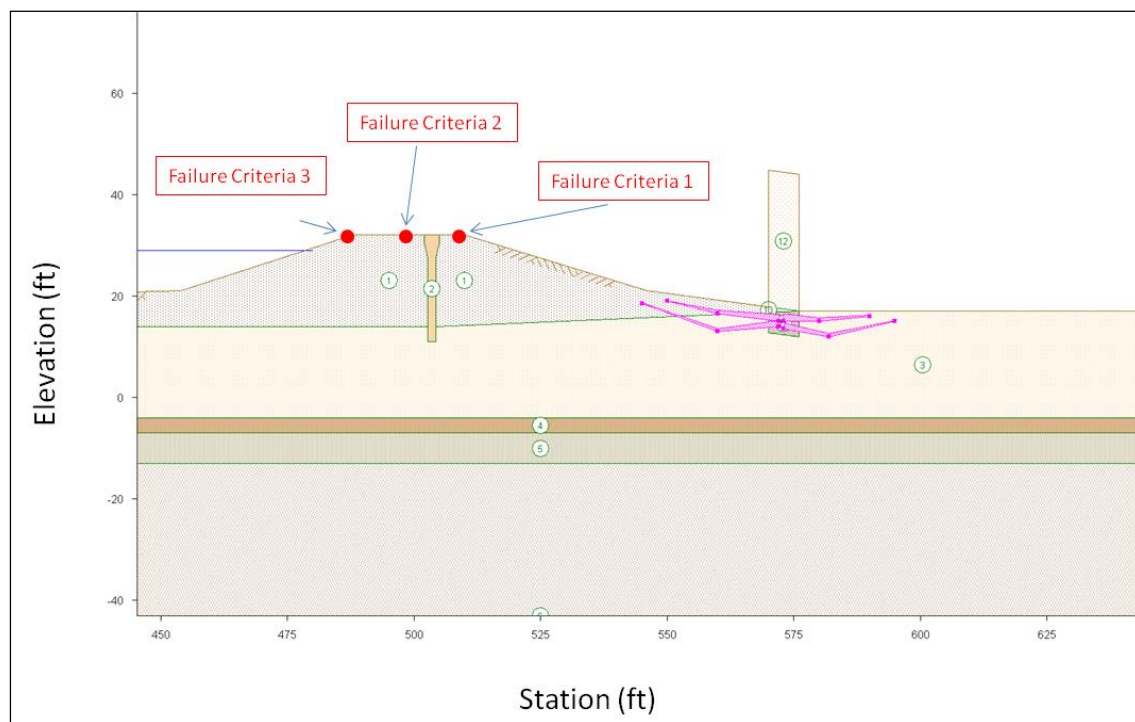


Figure 175. Three failure criteria used for calculating the factor of safety on the landside at the Pocket Levee, Sacramento, CA.

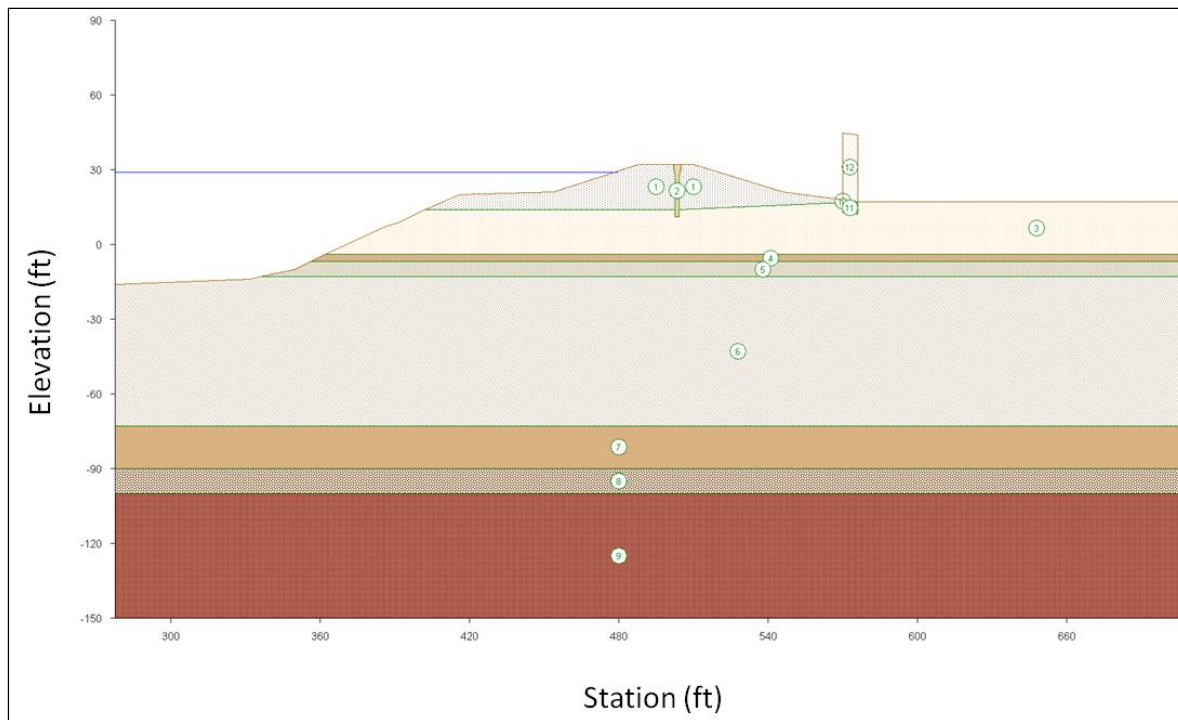


Figure 176. Typical levee profile of the Pocket Levee area, Sacramento, CA.

crest width. The landside slope is 18 deg, and the riverside slope is 18 deg with an approximate 38-ft-wide berm. Recent geotechnical investigations show that the main levee material is sandy with a density of 110 lb/ft<sup>3</sup> (URS 2010a). The friction angle is 34 deg, and the levee material is assumed to not have cohesion. To reduce seepage during flood events, a SBC slurry wall was constructed at the center off the levee. The SBC slurry wall is approximately 18 in. thick, and 21 ft deep. Recent tests show the wall has a density of 120 lb/ft<sup>3</sup>, and a cohesion of 500 lb/ft<sup>2</sup> (Harder et al. 2010). The material properties of the foundation are shown in Table 78. The numbers in Figure 177 correspond to material properties on Table 78. The geology and material properties are detailed in Volume II.

**Table 78. Foundation material properties of the Pocket Levee, Sacramento, CA.**

Material	Material	Unit Weight (lb/ft <sup>3</sup> )	Cohesion (lb/ft <sup>2</sup> )	Friction Angle (deg)
1	Levee Sand	110	0	34
2	SBC slurry wall	120	500	0
3	Clay and Silty Clay	100	0	29
4	Clay Mixed with Sand	120	0	29
5	Clay and Silty Clay	100	0	29
6	Silty Sand	115	0	35
7	Silty Gravel	135	0	35
8	Silt	120	0	29
9	Poorly Graded Sand with Silt	130	0	40
10	Levee Sand with Root	120	50	34
11	Clay and Silty Clay with Root	120	100	29

The most common tree in the Pocket Levee area is the valley oak (Gray et al. 1991). As discussed in Volume II, geophysical tests suggest that the size of the root ball of this tree has approximate dimensions of 6 ft (length) × 6 ft (width) × 5 ft (depth). In the 2-D analysis, tree weights and wind loads are divided by six based on the 6-ft width because only a 1-ft-wide slice is considered. Gray et al. (1991) stated that the RAR of the area surrounding the root ball is approximately 0.2. Because pullout tests were not conducted at the Pocket Levee owing to time constraints, the results from pullout tests and tree parameters on a cottonwood tree in Portland, OR, (Figure 178) were used for the Pocket Levee analysis. Based on pullout tests conducted for this study, it was found that cottonwoods exhibit a higher root strength than other species studied. However, similarities among tree species cannot be categorized; therefore, the species is insignificant in this analysis. The tree is 81 ft high, and the DBH is 42 in. The tree weight is calculated from the equation by Jenkins et al. (2004)

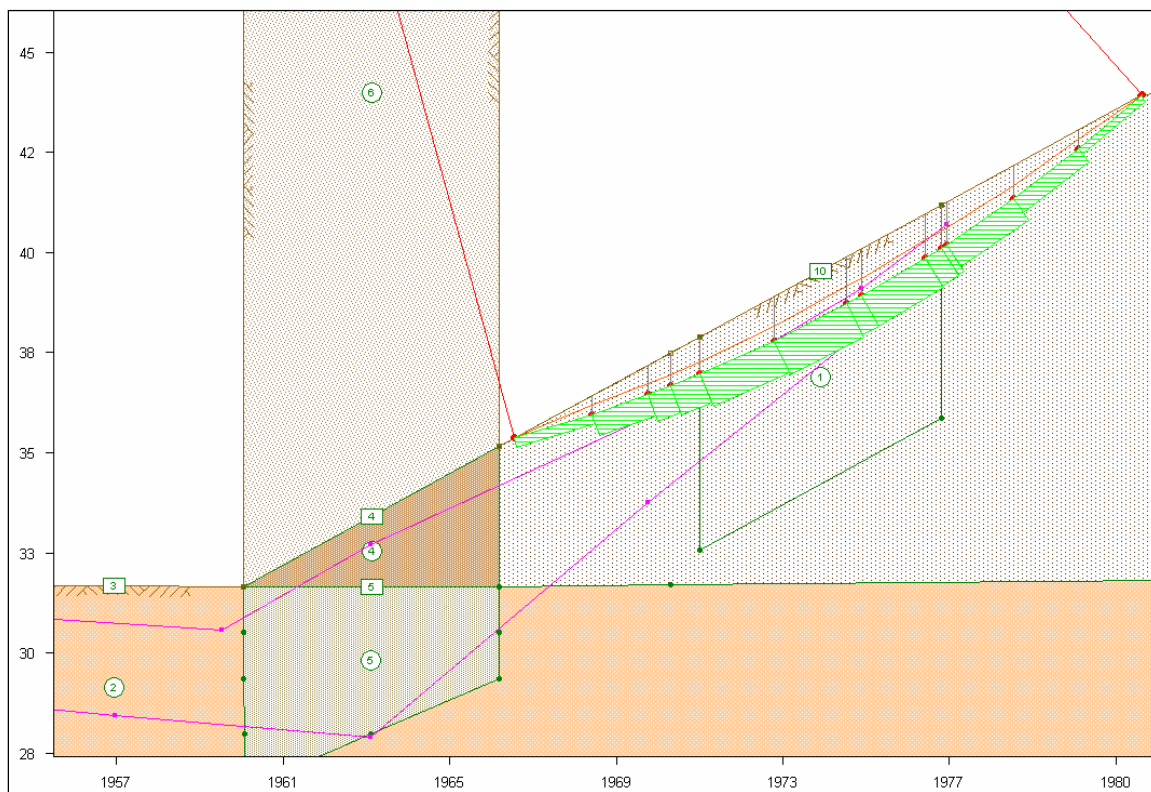


**Figure 177. Tree 2 Failure Criterion 1.**

discussed earlier in this section. For the cottonwood, the tree weight is calculated to be 17,000 lb.

#### *Sensitivity analysis*

Because of the unknown effects of the tree at different positions on the levee, as well as a fluctuating water level, a sensitivity analysis was needed. The parameters used in the sensitivity analyses are described in this section.

In this study, water elevations of 23, 26, and 29 ft are used, and three different locations of trees are considered: toe, midslope, and top of the levee on each side (riverside and landside) (Figure 179).

The following calculation was performed without considering the effect of wind loads on trees to isolate the influence of tree weight and root reinforcement on slope stability. The sensitivity of the effects of wind loads is discussed later in this section.

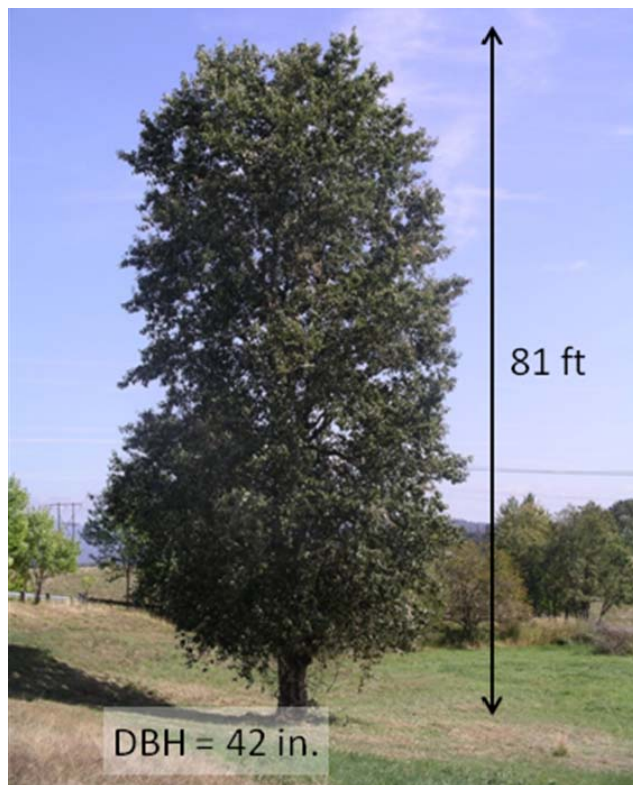


Figure 178. The cottonwood tree in Portland, OR, used in the slope stability analyses for the Pocket Levee, Sacramento, CA.

The first failure criterion limits the critical circle to pass through the downstream edge of the levee crest, and is similar to the analysis performed by Gray et al. (1991) on a sandy levee in Sacramento, CA. The second and third failure criteria have deeper critical circles, passing through the center and the upstream edge of the levee crest, respectively (Figure 176).

Sensitivity analyses were conducted without a tree for each failure criterion at three different river elevations. Because these analyses do not include a tree, the factor of safety calculated for these situations serves as a baseline for comparing the factor of safety calculations to those analyses with a tree.

#### *Landside analysis*

A sensitivity analysis was first conducted without a tree with a flood elevation of 29 ft using the second failure criterion. The factor of safety for this case is equal to 1.60 (Figure 180). The plus sign in the center of the contour lines represents the factor of safety noted on the figure. The contour lines correspond to the factor of safety at a particular point. In the second case, the second failure criterion was again used, but in this analysis, a tree

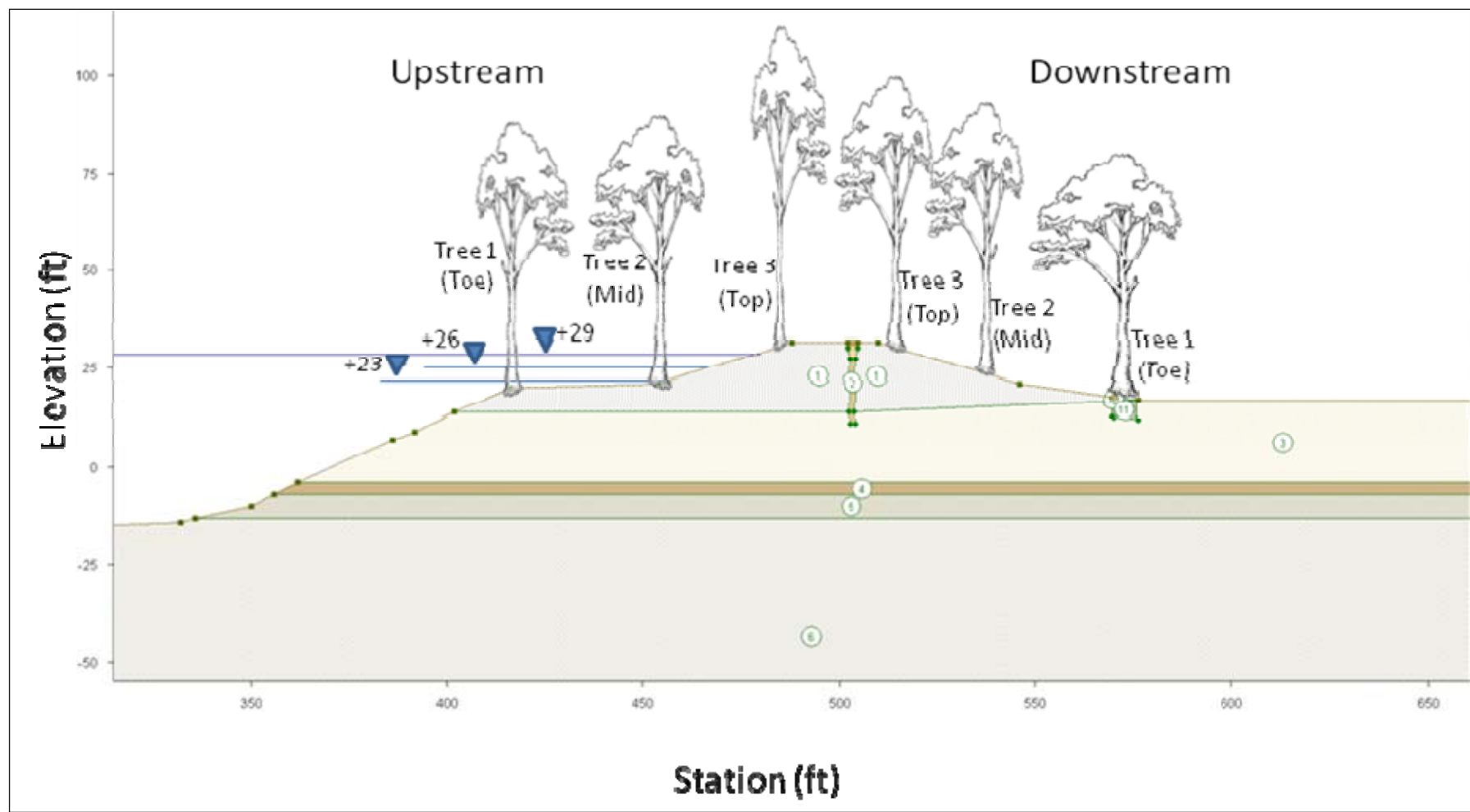


Figure 179. Tree positions and water levels used in the sensitivity analysis for the slope stability analyses, Pocket Levee, Sacramento, CA.

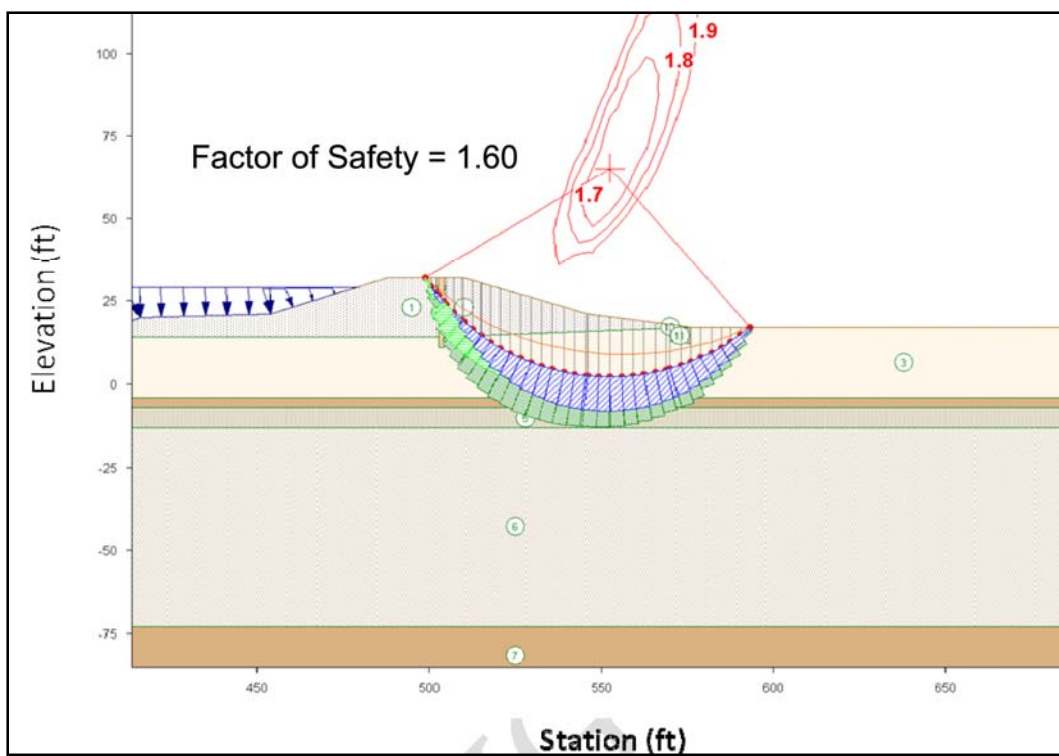
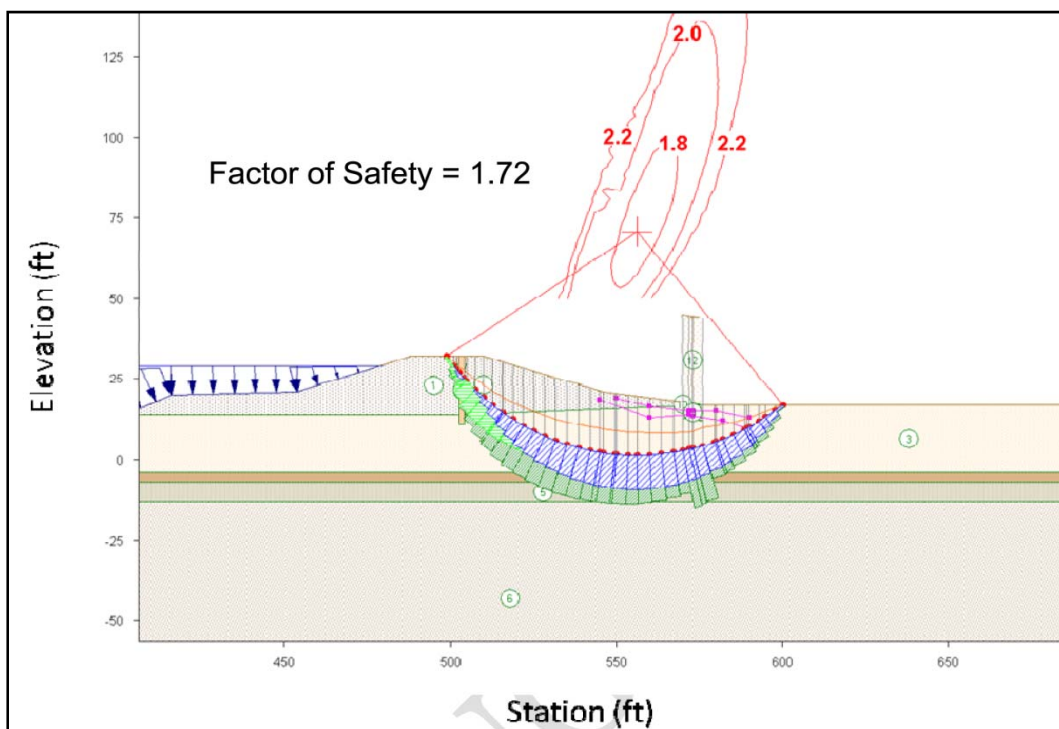


Figure 180. Landside slope stability analysis with no tree, assuming Failure Criterion 2, El. 29 ft, Pocket Levee, Sacramento, CA. This analysis serves as a baseline comparison for failure criterion to different positions of a single tree.

was positioned at the downstream toe. The factor of safety for this case is 1.72, which is approximately a 7.5% increase from the original analysis of a levee without a tree (Figure 181). The presence of a tree at the toe gives an additional counterweight against the sliding forces. This result is consistent with the previous finding by Coppins and Richards (1990), and Norris and Greenwood (2006).

Figures 182 and 183 show the slope stability analysis of the same levee conditions and tree locations, using Failure Criteria 1 and 3, respectively. The parameters used in the sensitivity analysis and the factor of safety results for all failure criteria with and without trees are shown in Table 79.

Data for each case are plotted using the ratio of flood height ( $w$ ) to levee height ( $h$ ) versus factor of safety (Figures 184 through 186). The general trend shows the decrease of the factor of safety as flood elevation increases. As the flood elevation increases, pore pressures increase and shear strength decreases. If only Failure Criterion 1 occurs, a single tree at the downstream toe increases the factor of safety by 6%; a single tree at the



**Figure 181.** Landslide slope stability analysis with a single tree at the toe of the levee, assuming Failure Criteria 2, Pocket Levee, Sacramento, CA.

middle of the downstream slope decreases the factor of safety by 4%; and a single tree at the top of the downstream slope decreases the factor of safety by 2%. These results are consistent with the findings of Gray et al. (1991).

Based on the limited cases of slope stability assessments using limit equilibrium analysis, calculations show that a tree at the toe increases the factor of safety by 6% on average. On the other hand, trees at the mid-section and the top of the levee decrease the factor of safety by 3%. However, these numbers are generated by the program and do not necessarily reflect the actual factor of safety of the levee. Norris and Greenwood (2006) also concluded that a single tree at the top of the slope decreases the factor of safety. A tree at the downstream toe produces an additional counterweight to support the levee slope against sliding, and, at the same time, tree roots reinforce the soil around the trees intersecting the failure circle. Trees at the top of the slope give an additional weight to the slope to produce sliding, and small portions of the tree root may intersect the failure circle. Trees at the middle of the levee slope give an additional weight that cause sliding, and the roots may not intersect the failure circle at any point. Of the three locations, woody vegetation located midslope

presents the most impact to levee integrity. Wind was applied in all directions but it became

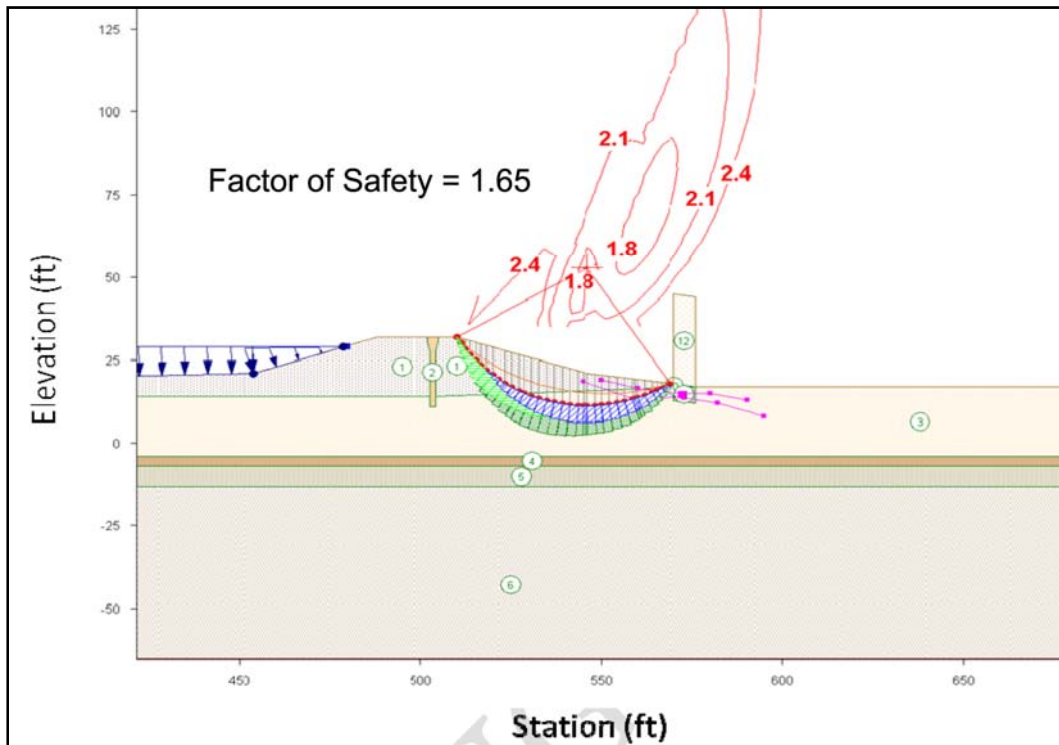


Figure 182. The factor of safety with a single tree at the toe of the levee, Failure Criterion 1, Pocket Levee, Sacramento, CA.

apparent after many model runs that UTEXAS4 could not model a moment. Therefore, the impact of the wind was assumed on the root ball. Wind direction used in this research presented the worst case for a 2-D limit equilibrium model even though it might not be the worst case for a stress-strain analysis.

#### Riverside analysis

The procedure used in the riverside slope stability analysis is the same as for the landside slope stability analysis. The failure criteria begin at the same origin as in the landside analysis only these move toward the riverside. The first failure criteria limits the critical circle to passing through the upstream edge of the levee crest. The second and the third failure criteria let the critical circle pass through the center and the downstream edge of the levee crest, respectively.

With the use of Failure Criterion 2 and a flood elevation of 29 ft, the factor of safety is 2.21 (Figure 187). As described in the landside analysis, this calculation serves as the baseline value of factor of safety for Failure Criterion 2 because of the lack of trees.

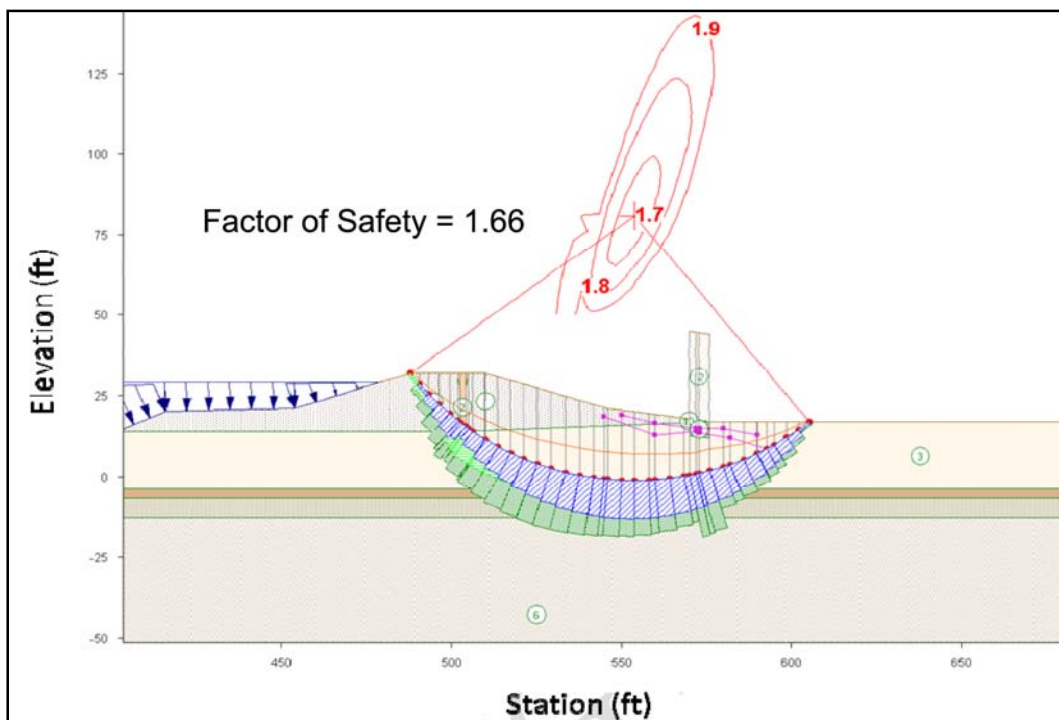


Figure 183. The factor of safety with a single tree at the toe of the levee, Failure Criteria 3, El. 29 ft, Pocket Levee, Sacramento, CA.

Table 79. Factor of Safety for the Pocket Levee (landside) with no tree, three different tree locations, and three different flood water levels.

Failure Criteria	Water Level	Factor of Safety			
		No Tree	Tree at toe	Tree at midslope	Tree at top slope
1	23	1.87	2.00	1.81	1.86
	26	1.70	1.77	1.62	1.66
	29	1.54	1.65	1.47	1.51
2	23	1.92	2.08	1.87	1.86
	26	1.76	1.89	1.71	1.66
	29	1.60	1.72	1.56	1.52
3	23	1.98	2.09	1.94	1.92
	26	1.79	1.88	1.75	1.71
	29	1.56	1.66	1.55	1.51

In the first case considered in the analysis, a single tree is located at the downstream toe assuming Failure Criterion 2. The factor of safety is 2.30, which is a 4.1% increase from the original analysis of a levee without trees (Figure 188). The presence of a tree at the toe gives an additional counter-weight against the sliding forces.

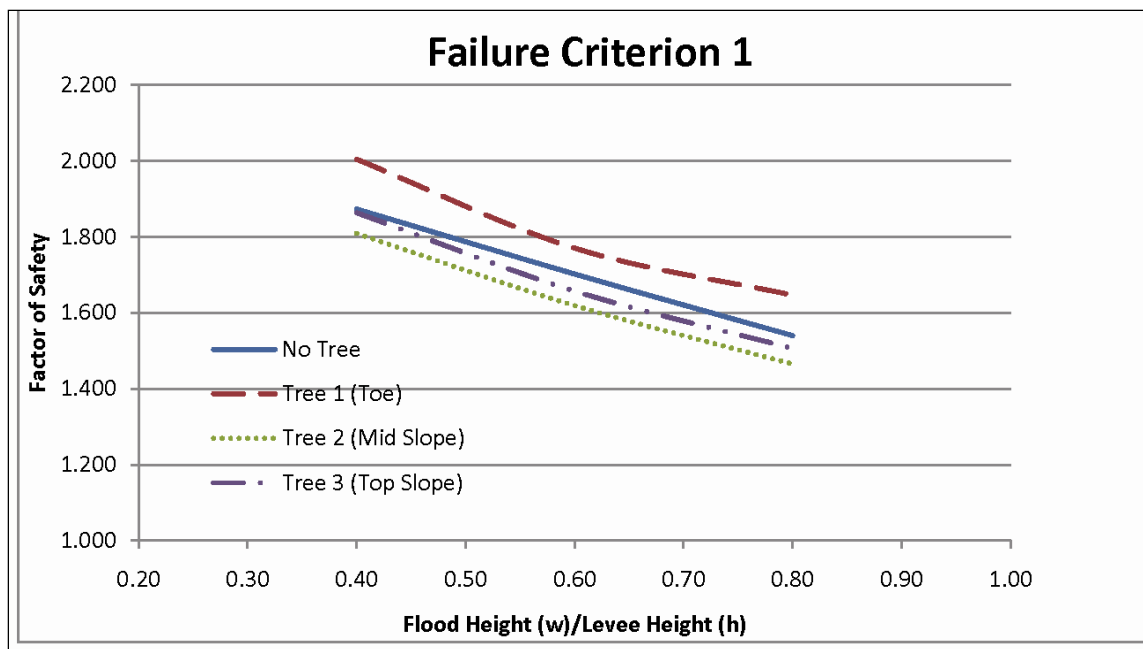


Figure 184. Sensitivity analysis of the factor of safety for Failure Criterion 1 on the landside of the levee with no tree, and three different locations of a single tree. Three different flood elevations are used in the analysis for the Pocket Levee, Sacramento, CA.

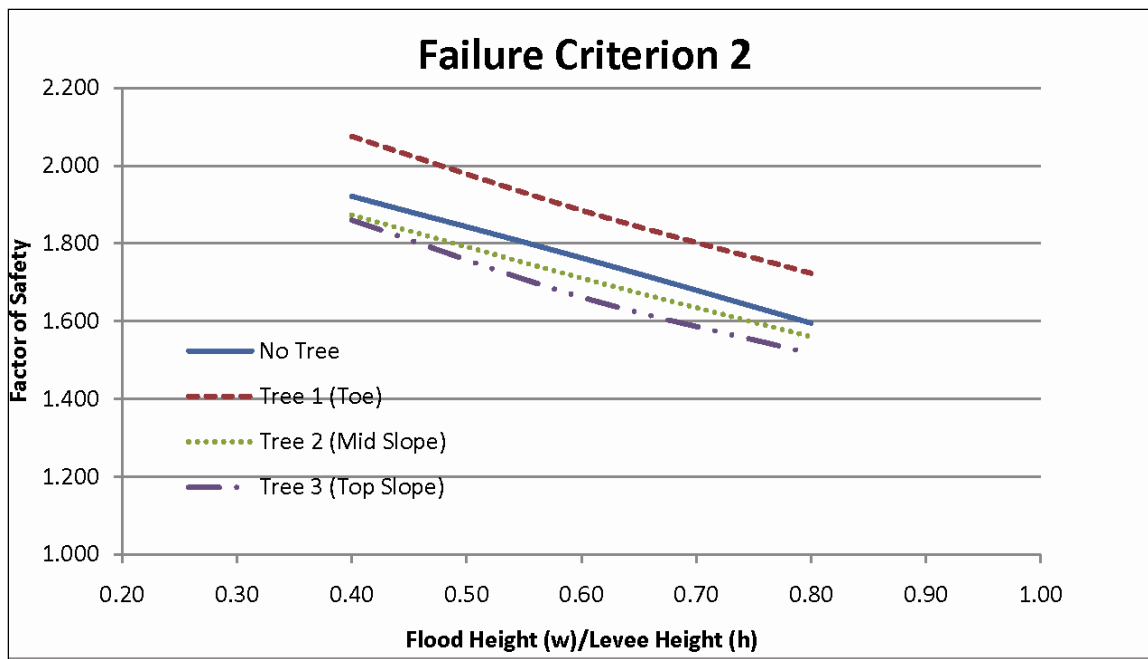


Figure 185. Sensitivity analysis of the factor of safety for Failure Criterion 2 on the landside of the levee with no tree, and three different locations of a single tree. Three different flood elevations are used in the analysis for the Pocket Levee, Sacramento, CA.

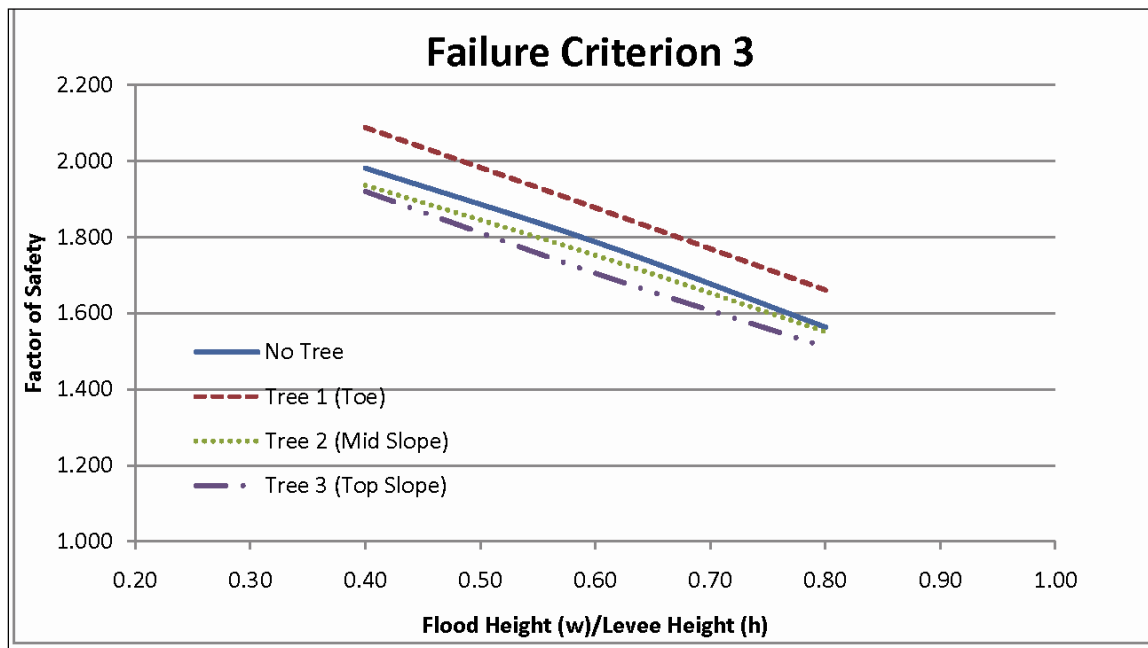


Figure 186. Sensitivity analysis of the factor of safety for Failure Criterion 3 on the landside of the levee with no tree, and three different locations of a single tree. Three different flood elevations are used in the analysis for the Pocket Levee, Sacramento, CA.

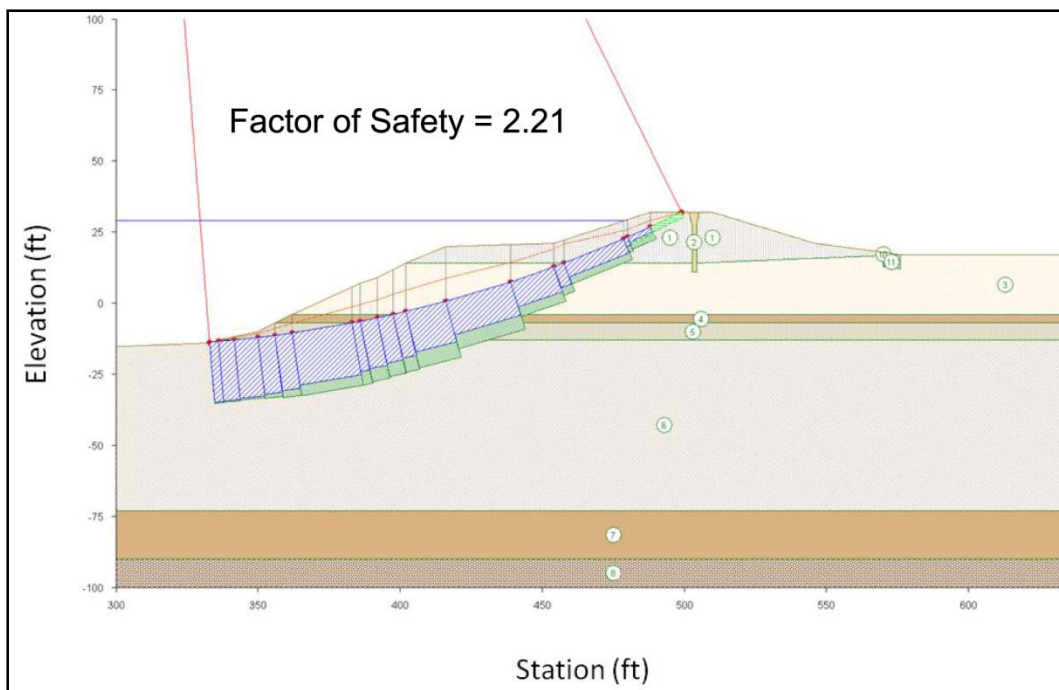


Figure 187. Riverside slope stability analysis with no tree, assuming Failure Criterion 2, Pocket Levee, Sacramento, CA. This analysis serves as a baseline comparison for additional analyses using different locations of a single tree.

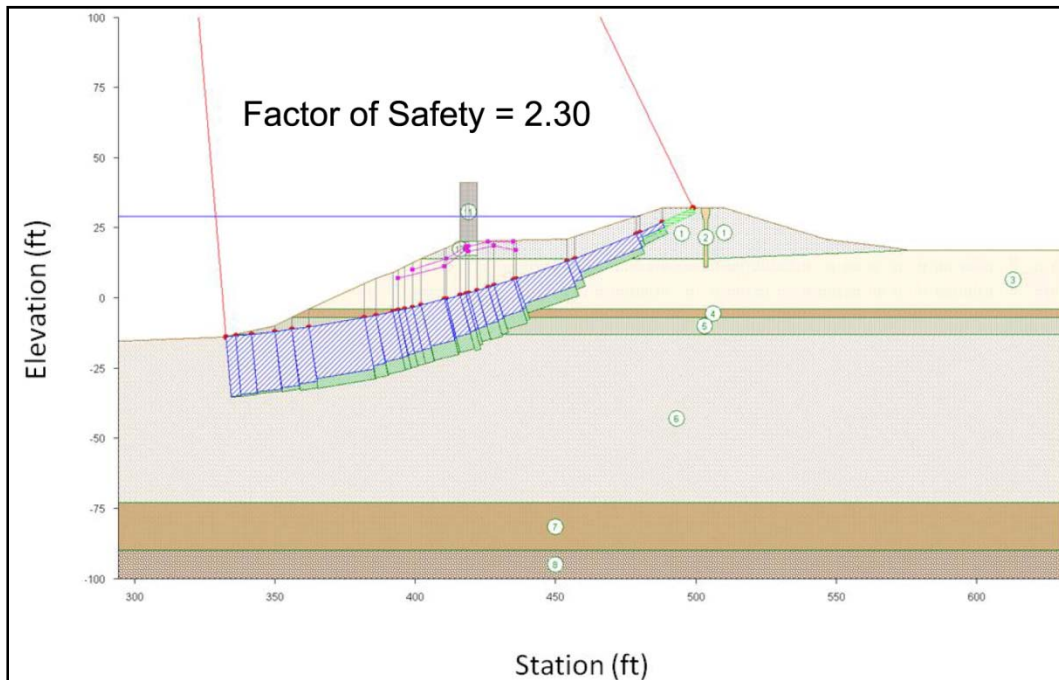


Figure 188. Riverside slope stability analysis with a single tree at the toe of the levee, assuming Failure Criterion 2, Pocket Levee, Sacramento, CA.

The factor of safety is slightly higher compared to the levee condition without a tree when the slope stability analyses for Failure Criterion 1 and

Failure Criterion 3 are computed (Figures 189 and 190). The results of the sensitivity analysis for the factor of safety with different tree locations and flood elevations for each failure criterion are depicted in Figures 191, 192, and 193. The curves correlate the ratio of flood height ( $w$ ) to levee height ( $h$ ) versus factor of safety. A general trend shows an increase in the factor of safety as flood elevation increases. As the flood elevation increases above the existing ground level, the effective stress in the soil remains constant. This indicates that the available shear resistance in the soil is not changing. However, the surface loads are increasing because of increased water depths, resulting in higher hydrostatic pressures. Because the hydrostatic pressures are acting against the sliding motion of a failure mass on the upstream slope, the factor of safety increases with increasing water level. Considering only Failure Criterion 1, a single tree at the upstream toe increases the factor of safety by 5%, a single tree at the middle of the upstream slope increases the factor of safety by 1%, and a single tree at the top of the upstream slope increases the factor of safety by 8%. Table 8o shows the factor of safety calculated in the slope stability analysis for different flood elevations, and tree positions.

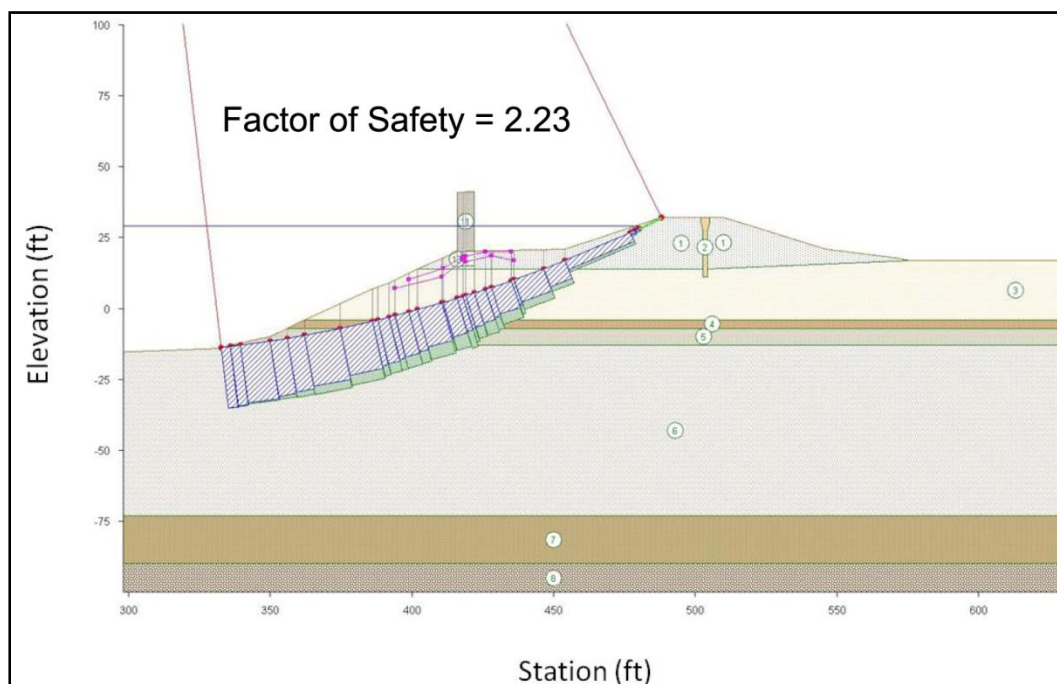


Figure 189. Riverside slope stability analysis with a single tree at the toe of the levee, assuming Failure Criterion 1, Pocket Levee, Sacramento, CA.

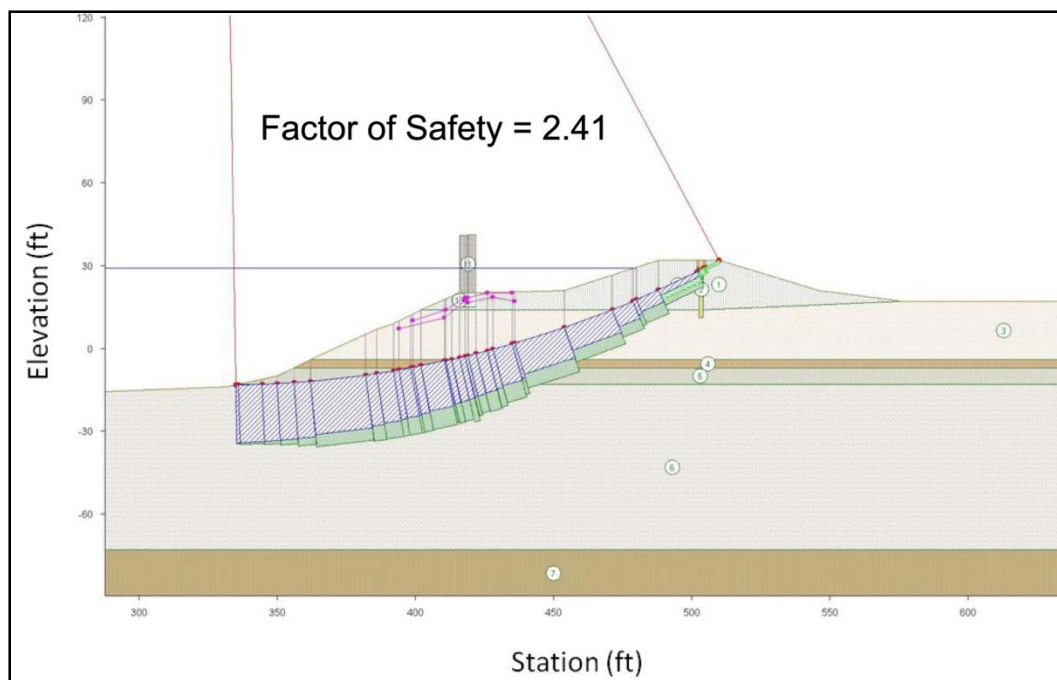


Figure 190. Riverside slope stability analysis with a single tree at the toe of the levee, assuming Failure Criterion 3, Pocket Levee, Sacramento, CA.

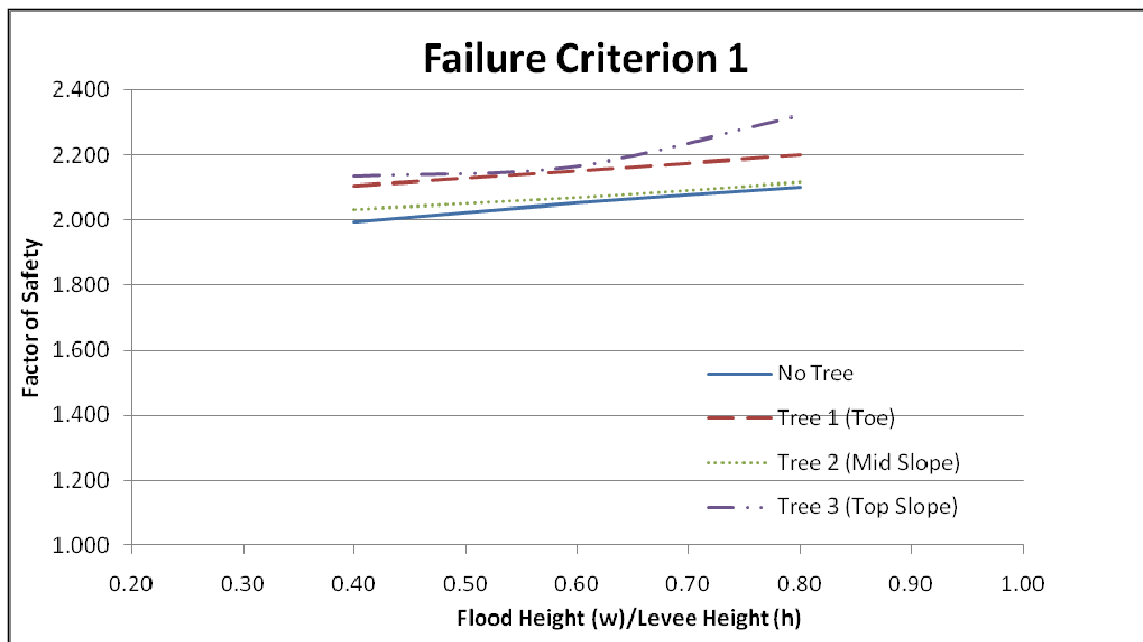


Figure 191. Sensitivity analysis of the factor of safety for Failure Criterion 1 on the riverside of the levee with no tree, and three different locations of a single tree. Three different flood elevations are used in the analysis for the Pocket Levee, Sacramento, CA.

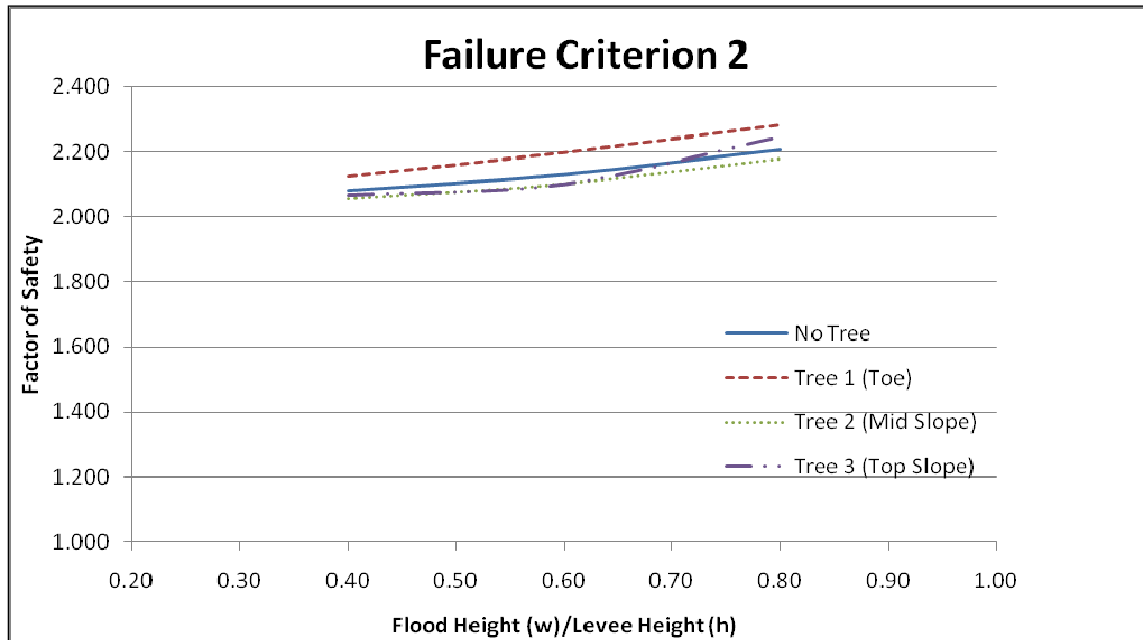


Figure 192. Sensitivity analysis of the factor of safety for Failure Criterion 3 on the riverside of the levee with no tree, and three different locations of a single tree. Three different flood elevations are used in the analysis for the Pocket Levee, Sacramento, CA.



Figure 193. Sensitivity analysis of the factor of safety for Failure Criterion 3 on the riverside of the levee with no tree, and three different locations of a single tree. Three different flood elevations are used in the analysis for the Pocket Levee, Sacramento, CA.

Table 80. Factor of Safety for the Pocket Levee (riverside) with no tree, three different tree locations, and three different flood water levels.

Failure Criteria	Water Level	Factor of Safety			
		No Tree	Tree at toe	Tree at midslope	Tree at top slope
1	23	2.00	2.11	2.04	2.13
	26	2.05	2.15	2.07	2.17
	29	2.10	2.23	2.12	2.32
2	23	2.08	2.12	2.05	2.07
	26	2.13	2.20	2.10	2.10
	29	2.21	2.30	2.18	2.25
3	23	2.15	2.21	2.15	2.14
	26	2.24	2.30	2.22	2.21
	29	2.34	2.41	2.32	2.36

#### Sensitivity analysis of wind load

The wind load was calculated using an equation proposed by Hsi and Nath (1970) with computed values tabulated by Coder (2007). The maximum and average wind speed are from statistical data collected by the National Oceanic and Atmospheric Administration (USDC 2010).

Wind speed for Sacramento, CA, is shown in Figure 194. Two data were observed, i.e., monthly maximum wind speed and average monthly wind speed. For the cottonwood tree shown in Figure 178, the area of crown is 2625 ft<sup>2</sup>. Because the calculations for wind load use 1-ft-wide slice of the slope, the crown is divided by six. Coppins and Richards (1990) and Greenwood et al. (2004) suggested applying the wind load as a line force at the base of the tree.

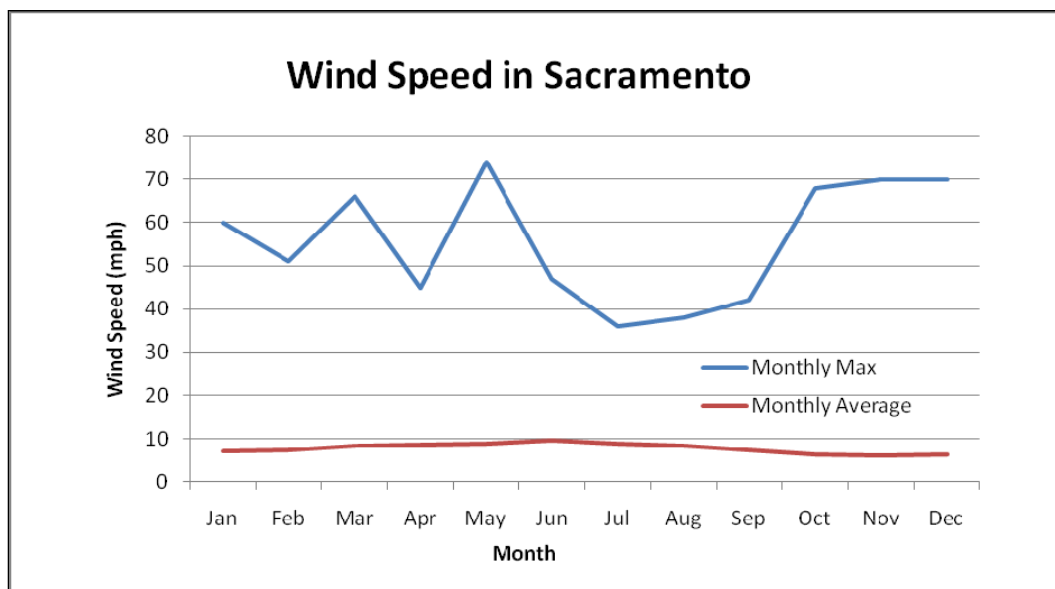


Figure 194. Monthly maximum and average wind speed in Sacramento, CA.

Using this suggestion, ERDC performed a sensitivity analysis on the effects of wind loads on levee stability. The analyses were done on the landside stability, assuming Failure Criterion 2 occurs with a flood elevation of 29 ft. Figure 195 and Table 81 show the results of the sensitivity analysis. The factor of safety, shown in Table 86, is calculated using data gathered on a specific cottonwood tree. For trees of other dimensions (i.e., tree height), the calculated factor of safety might be different. As the wind speed exceeds 40 mph, the factor of safety decreases, especially for a tree at the top of the levee. By review of these data, it appears that if the wind is very strong, the slope may fail due to lower factors of safety. However, there is no case history to support this failure mechanism and further investigation is needed.

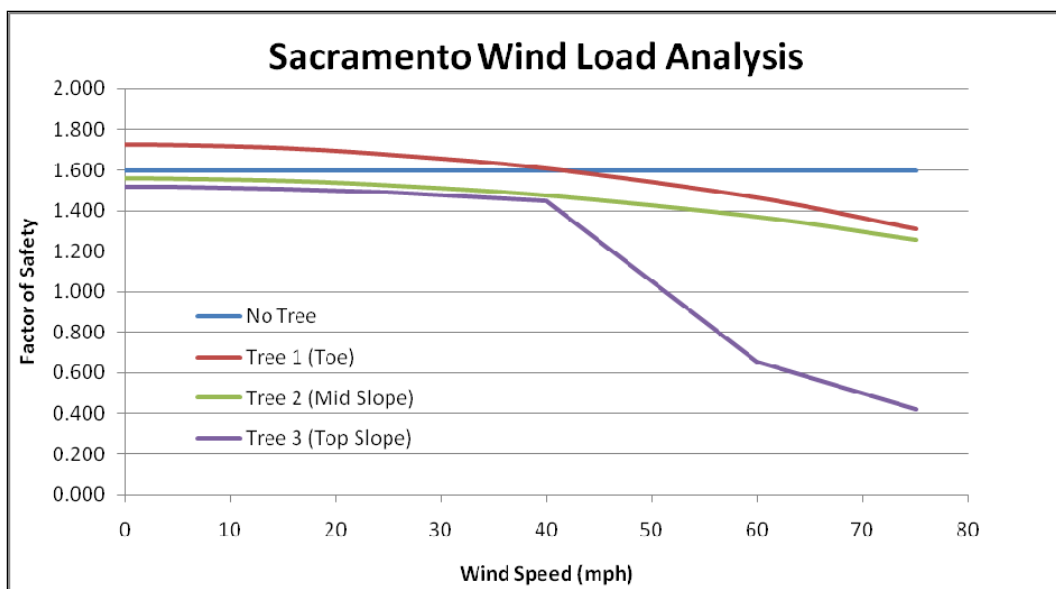


Figure 195. Sensitivity analysis of factor of safety of landside levee attributable to varying wind speed using no tree, and a single tree at three different locations on the levee. The analysis also uses three different flood elevations, and Failure Criterion 2.

Table 81. Factor of Safety for the Pocket Levee, Sacramento, CA, (landside) with three different tree locations, and flood water elevation at 29 ft with varying wind speeds. The crown area of the cottonwood is 2625 ft<sup>2</sup>.

Failure Criteria	Water Level	Wind Speed (mph)	Wind Pressure (lb/ft <sup>2</sup> )	Wind Load (lb)	Factor of Safety			
					No Tree	Tree at Toe	Tree at MidsSlope	Tree at Top Slope
2	29	0	0	0	1.60	1.72	1.56	1.52
		5	0.1	44	1.60	1.72	1.56	1.52
		15	0.6	263	1.60	1.71	1.55	1.51
		25	1.7	744	1.60	1.67	1.53	1.49
		40	4.2	1838	1.60	1.61	1.48	1.45
		60	9.5	4156	1.60	1.46	1.37	0.66
		75	15	6563	1.60	1.31	1.26	0.42

### Burlington, WA

Figure 196 shows a typical cross section of the Burlington, WA, levee section analyzed in this study. The levee is approximately 13 ft high with a crest elevation of 32 ft. The crest width is 20 ft, with an upstream slope of approximately 1.8H (horizontal):1V (vertical) and a downstream slope of approximately 2.3H:1V. A recent geotechnical investigation (Golder Associates 2009) shows that the levee is composed entirely of silty sand overlying a foundation composed of similar materials. Material properties

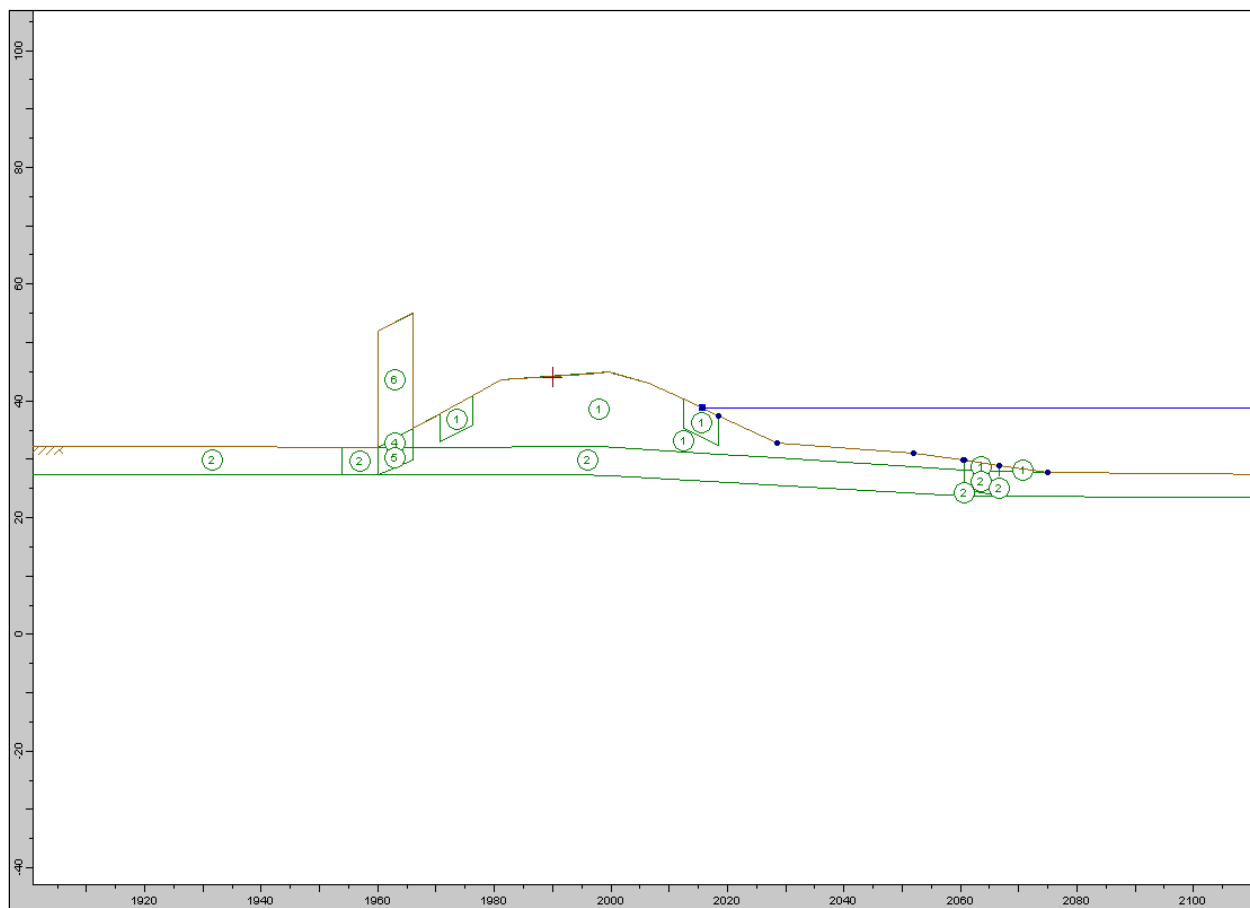


Figure 196. Typical section of the levee in Burlington, WA.

for the profile are summarized in Table 82. Each number shown on Figure 196 corresponds to the material numbers assigned in Table 82.

A slope stability analysis was conducted for the Burlington Levee to determine the sensitivity of the levee stability to tree position and flood level. Five tree positions used in the seepage analysis were also analyzed at three flood levels: 32.7, 38.7, and 45 ft. Tree positions and water levels are shown in Figure 197.

Table 82. Burlington Levee material properties.

Material Number	Material	Unit Weight (lb/ft <sup>3</sup> )	Cohesion (lb/ft <sup>3</sup> )	Friction Angle (deg)
1	Silty Sand	125	0	32
2	Silt	120	0	30
3	Poorly-graded sand	125	0	32
4	Silty Sand with roots	125	200	32
5	Silt with roots (root ball)	120	200	30
6	Tree	--	--	--

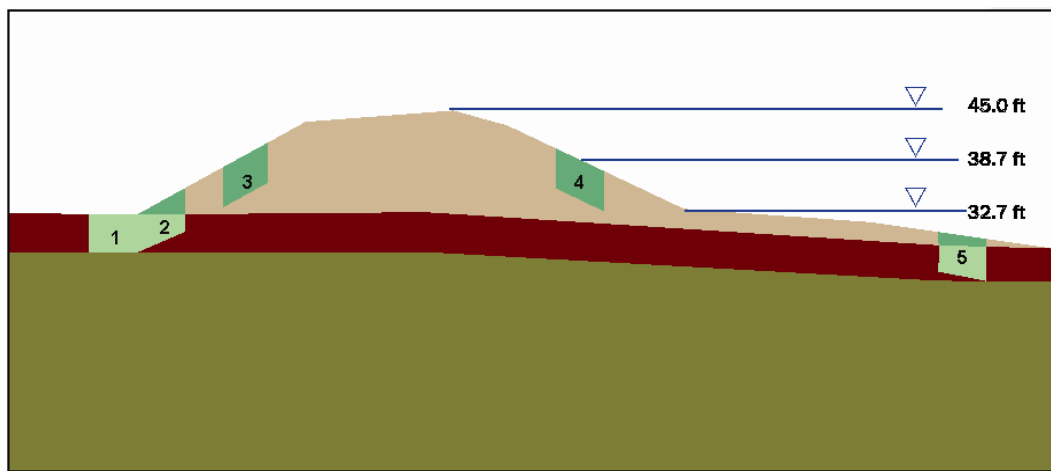


Figure 197. Tree position and water elevation scenarios.

The tree used for the Burlington Levee analysis is an 85-ft-tall Western cedar (Figure 198). This tree was chosen because of its close proximity to the downstream levee toe. The tree weight was estimated to be 20,000 lb using the tree regressions by Jenkins et al. (2004) previously discussed. The regression used for cedar used 196 data points, resulting in a  $R^2$  of 0.981.

The tree roots were estimated to extend 15 ft horizontally in both directions and to no more than a depth of 5 ft. These data were based on the combination of geophysical site investigations done in Burlington and a physical tree root characterization study performed on a tree of similar size. The tree roots were represented in the slope stability analysis by soil reinforcement with strength values characteristic of tree roots, as determined by root pullout tests. The tree weight was represented by a column of material of equivalent weight. Figure 199 shows the tree as modeled in UTEXAS4.

The three points used to define the failure criteria for the downstream slope analysis are shown in Figure 200, and the resulting failure circles

obtained are shown in

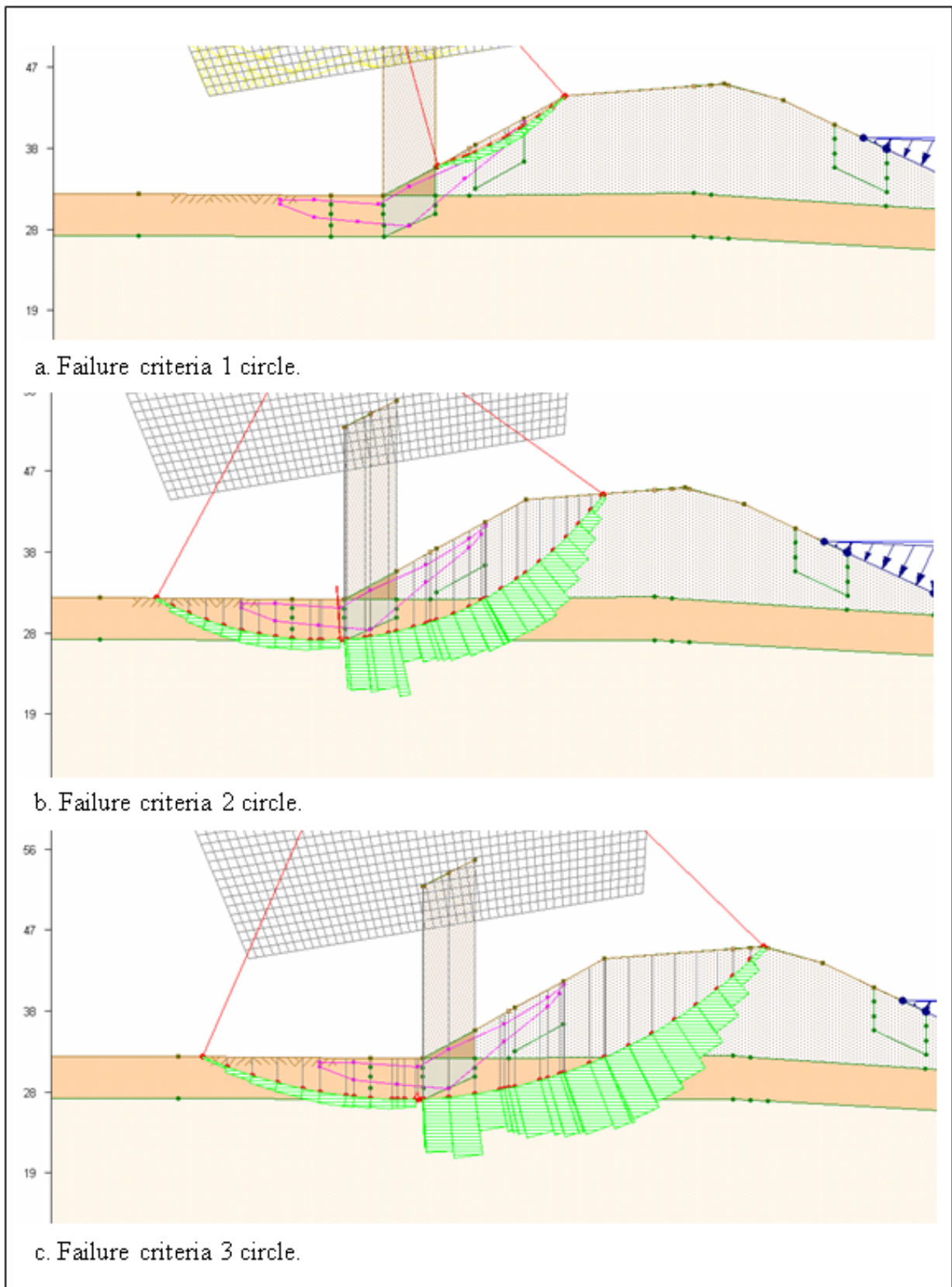


Figure 201. Note that for Failure Criteria 2 and 3, the roots were not effective reinforcement because they exist inside the failure circle.

The variation in factor of safety for each tree position is plotted for varying flood levels for Failure Criteria 1, 2, and 3 in Figures 202, 203, and 204, respectively.

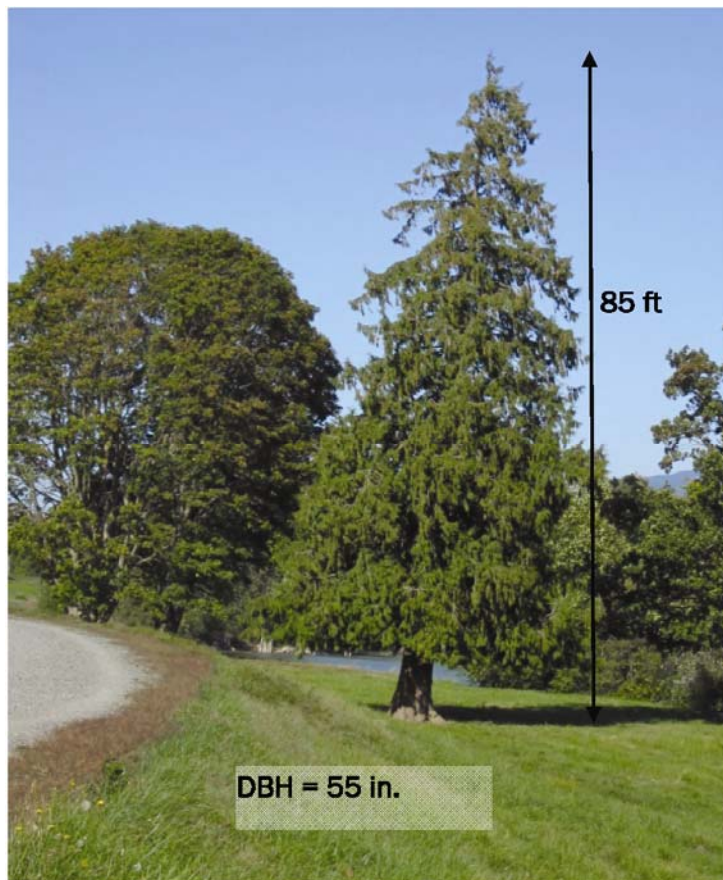


Figure 198. The Western cedar used in the Burlington Levee analysis.

Tables 83 and 84 are a summary of the factor of safety calculated for the different tree positions on the landside and riverside with varying water levels.

Failure Criterion 1 resulted in the largest variations of the factor of safety, up to 75%. A closer view of the failure circle for tree position 2 with the water level at 38.7 ft is shown in Figure 205. It shows that the failure circle is shallow and small, resulting in small stresses along the failure surface. Because the circle is small, minute variations in internal forces and stresses will result in large factor of safety variations.

The pore pressures in the region of the failure circle increase because the tree root ball blocks groundwater flow in the 2-D model. This concept is illustrated in Figure 206. As the pore pressures rise, the effective stress drops, and in turn, decreases the soil strength. This is one possible explanation for the large factor of safety variation seen with Failure Criterion 1.

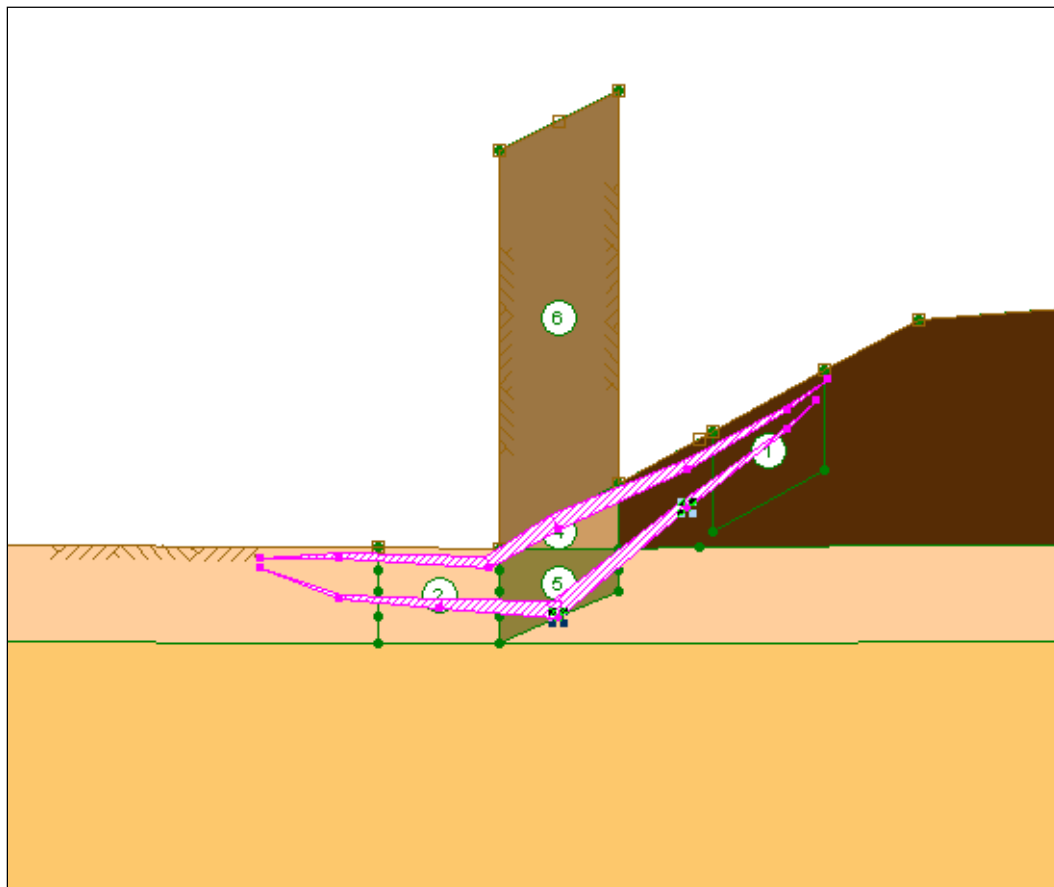


Figure 199. Tree representation in UTEXAS4, Burlington, WA.

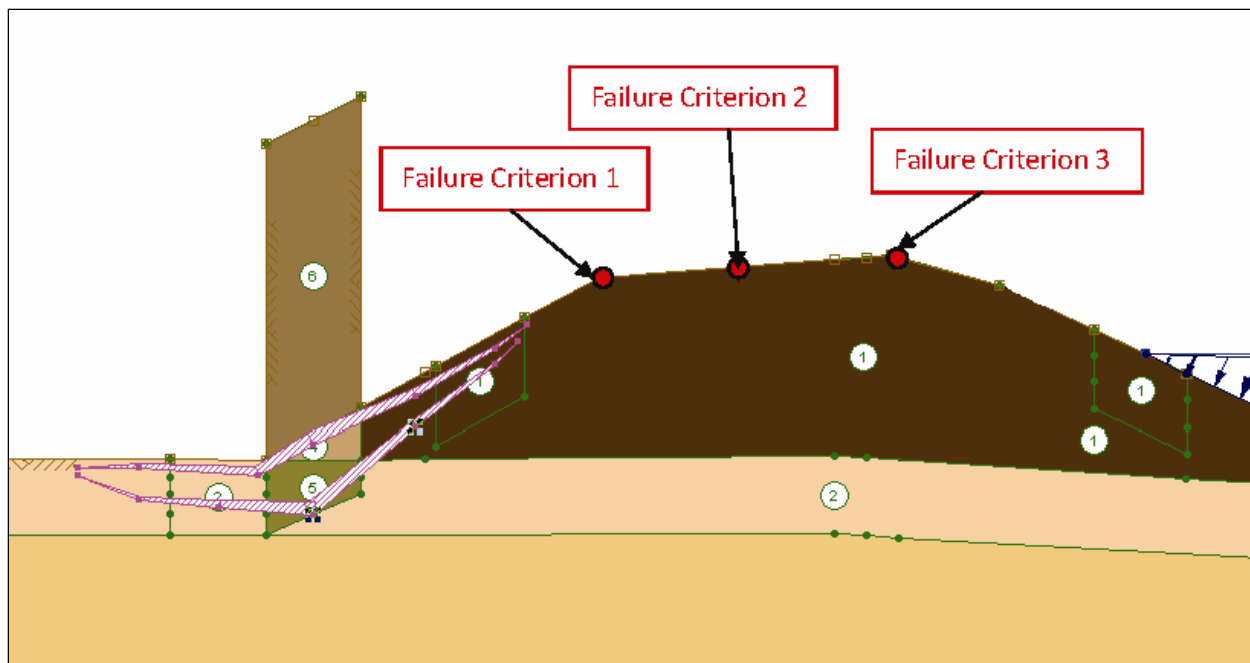


Figure 200. The locations of the failure criteria used in the slope stability analysis for Burlington, WA.

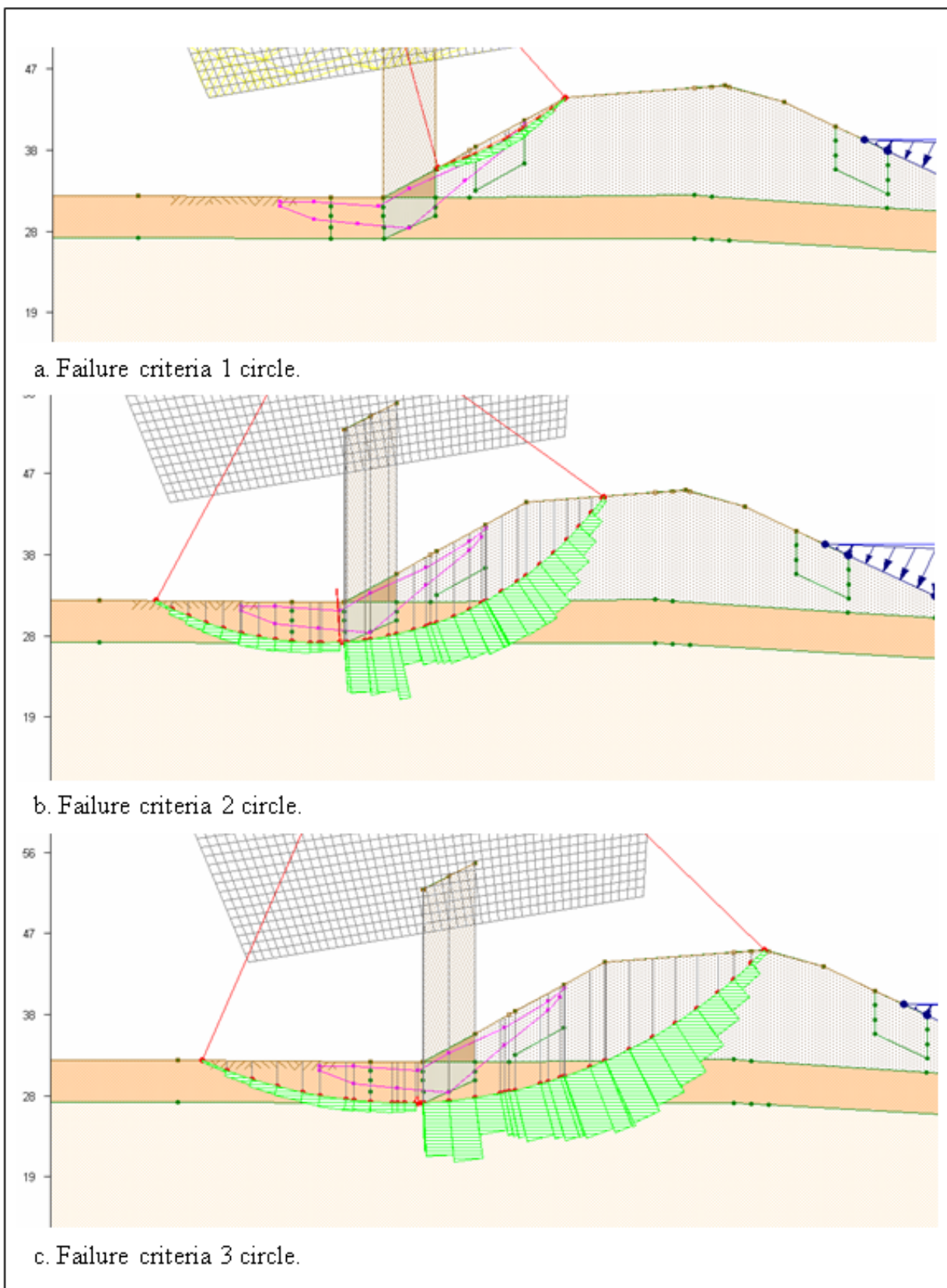


Figure 201. Typical failure circles used in the slope stability analyses for the Burlington Levee.

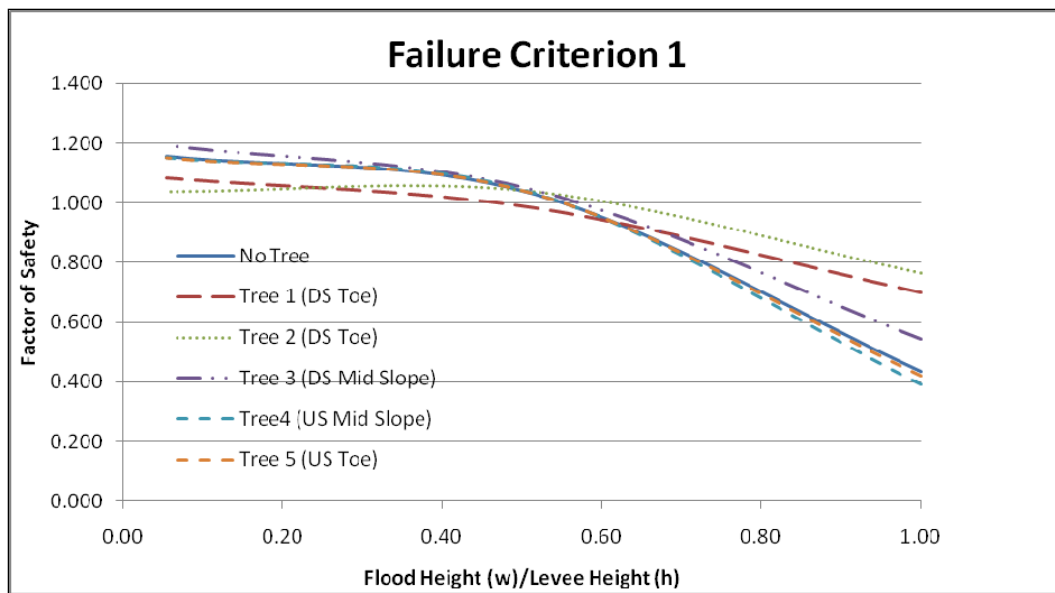


Figure 202. Sensitivity analysis of the factor of safety for Failure Criterion 1 with no tree, and five different locations of a single tree.



Figure 203. Sensitivity analysis of the factor of safety for Failure Criterion 2 with no tree, and five different locations of a single tree.

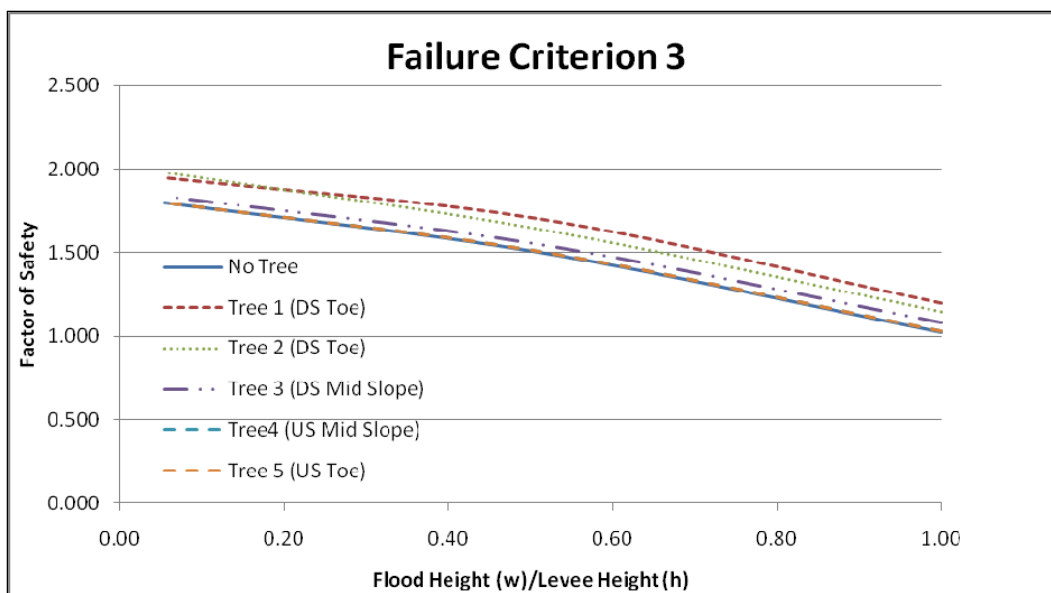


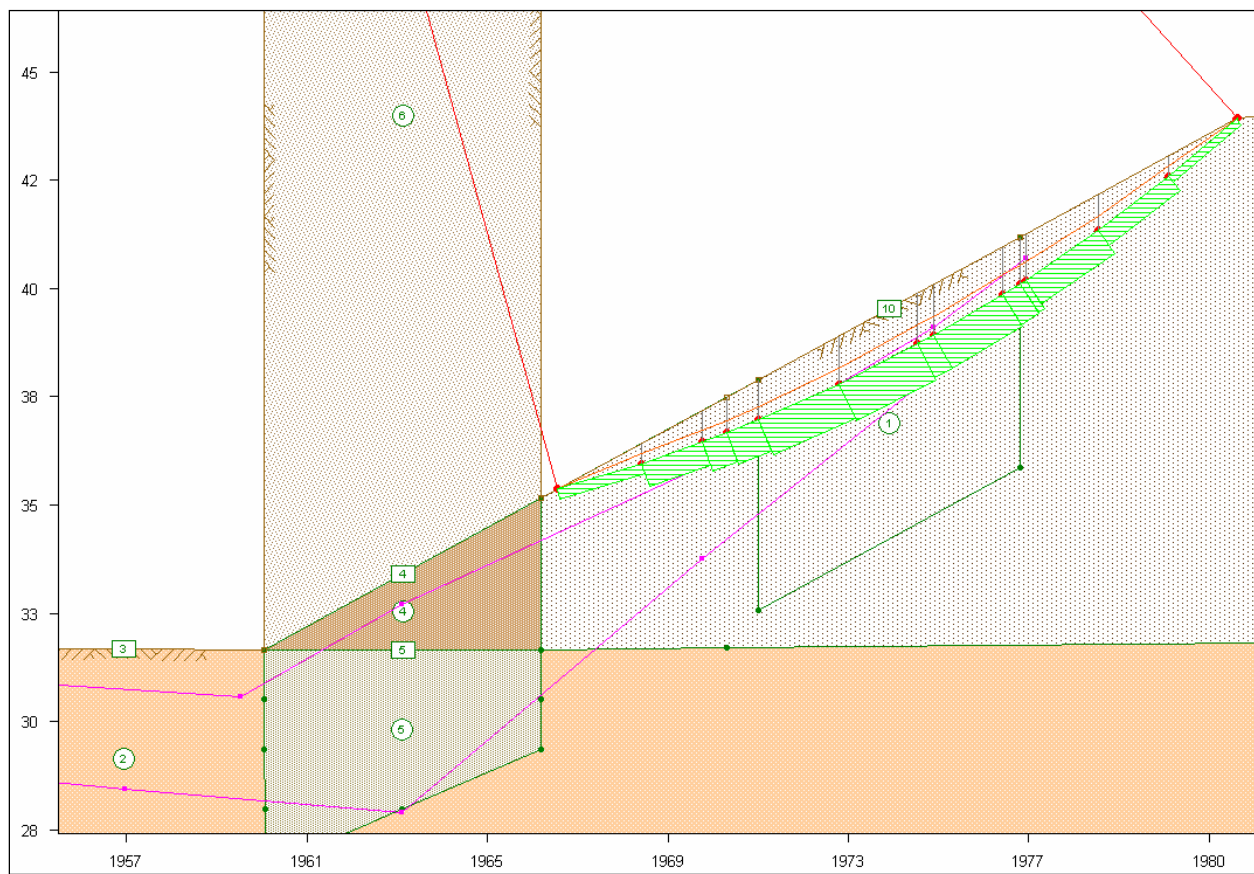
Figure 204. Sensitivity analysis of the factor of safety for Failure Criterion 3 with no tree, and five different locations of a single tree.

Table 83. Factor of Safety for the Burlington, WA, Levee (landside) with no tree, five different tree locations, and three different flood water levels.

Failure Criteria	Water Level	Factor of Safety					
		No Tree	Tree 1	Tree 2	Tree 3	Tree 4	Tree 5
1	32.7	1.16	1.09	1.04	1.19	1.15	1.15
	38.7	1.03	0.99	1.04	1.04	1.03	1.03
	45.0	0.44	0.70	0.76	0.54	0.39	0.42
2	32.7	1.51	1.46	1.57	1.53	1.51	1.52
	38.7	1.24	1.37	1.41	1.27	1.25	1.25
	45.0	0.80	1.02	0.91	0.83	0.79	0.79
3	32.7	1.80	1.95	1.98	1.84	1.80	1.80
	38.7	1.50	1.70	1.64	1.55	1.50	1.50
	45.0	1.02	1.20	1.15	1.08	1.03	1.03

Table 84. Factor of Safety for Burlington, WA, Levee (riverside) with five different tree locations and three different flood water levels.

Failure Criteria	Water Level	Factor of Safety					
		No Tree	Tree 1	Tree 2	Tree 3	Tree 4	Tree 5
2	32.7	1.88	1.88	1.88	1.88	1.92	1.88
	38.7	2.14	2.13	2.13	2.15	2.26	2.14
	45.0	3.21	3.18	3.19	3.25	3.34	3.21



**Figure 205. Tree 2 Failure Criterion 1.**

However, the 3-D seepage analysis shows that the variation in pore pressure is minimal. This observation suggests that the 2-D seepage analysis introduces error into the 2-D slope stability results. Another potential explanation for the large variation in factor of safety is that the root reinforcement causes the failure circle to change positions. The failure circles with no tree were generally very small, while the failure circles with trees were larger.

Failure Criteria 2 and 3 show minimal variation in the factor of safety as the tree position changes, as can be seen in Figures 203 and 204. However, wind loading was not taken into consideration in the values shown, so that the influence of tree weight and root reinforcement could be isolated from the effects of external loading. A wind analysis was done using accepted wind pressure values (Coder 2007), and a graphically measured tree frontal area. A crown area of  $1828 \text{ ft}^2$  is used for the cedar tree shown in Figure 198. Given the tree dimensions of 6 ft (length)  $\times$  6 ft (width)  $\times$  5 ft (depth), the wind force is calculated by dividing the crown area by six because the calculations are based on a 1-ft-wide slope. The

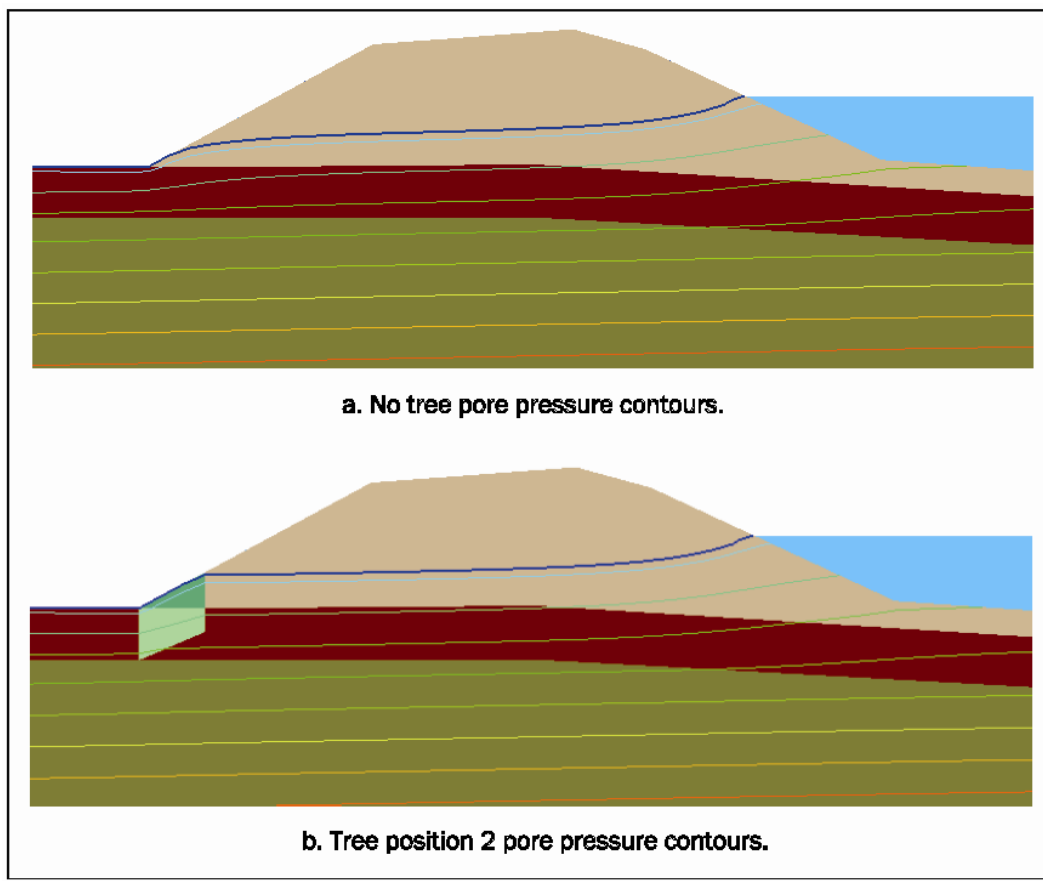


Figure 206. The variation in pore pressures between no tree, and a tree near the levee toe.

results obtained are shown in Table 85. Wind speeds beyond those shown were not analyzed because of the limitations of limit equilibrium methods. Using forces larger than those in Table 85 resulted in nonmeaningful results. The results show that wind does have the potential to lower the factor of safety regarding slope stability (Figure 207).

In general, trees in the locations studied for this analysis increase slope stability during high flow events, provided wind loading is not a factor. Wind loading on trees will decrease slope stability, but the extent of the wind effects is not currently known.

Trees located on the downstream slope appear to decrease stability with respect to localized surface failures because of changes in seepage conditions during low flood events, but increase surface stability during high flood events. Surface stability refers to shallow, local failure defined by Failure Criterion 1. This failure criterion may not be as reliable of an assessment as the other failure criteria because of the shallow depth of the failure.

**Table 85.** Wind load results for downstream tree positions.  
The crown area of the cedar tree is 1828 ft<sup>2</sup>.

Wind Speed (mph)	Pressure (lb/ft <sup>2</sup> )	Horz. Force (lb)	Force per Foot (lb/ft)	Factor of Safety			
				No Tree	Tree 1	Tree 2	Tree 3
0	0	0	0	1.24	1.39	1.41	1.27
5	0.1	182.8	30	1.24	1.39	1.41	1.26
15	0.6	1096.8	183	1.24	1.39	1.39	1.25
25	1.7	3107.6	518	1.24	1.39	1.34	1.22
40	4.2	7677.6	1280	1.24	1.37	1.25	1.15
60	9.5	17366	2894	1.24	1.18	1.09	0.98

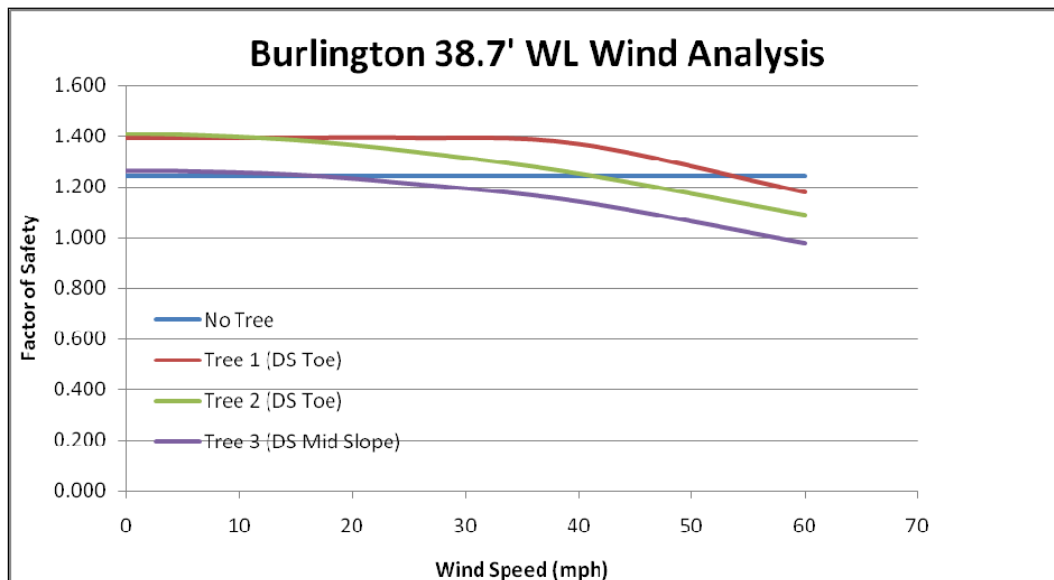


Figure 207. Wind loading effects on the factor of safety.

### Albuquerque, NM

A typical cross section of the Albuquerque Levee section being analyzed in this study is shown in Figure 208. The levee is approximately 6 ft high with a crest elevation of 4,995 ft. The crest is 10 ft wide with an upstream slope of 3H:1V and a downstream slope of 3.7H:1V. Soil properties are summarized in Table 86 and have been obtained from a geotechnical investigation conducted nearby. The material numbers in Figure 208 correspond to material numbers in Table 86. A limitation to evaluating this site is that the levee used in the analysis is very short with a flat landside slope. The effect of clogging the drain only results in a slight decrease in the factor of safety. Other levee systems where toe drains are critical to the stability of a levee should be evaluated.

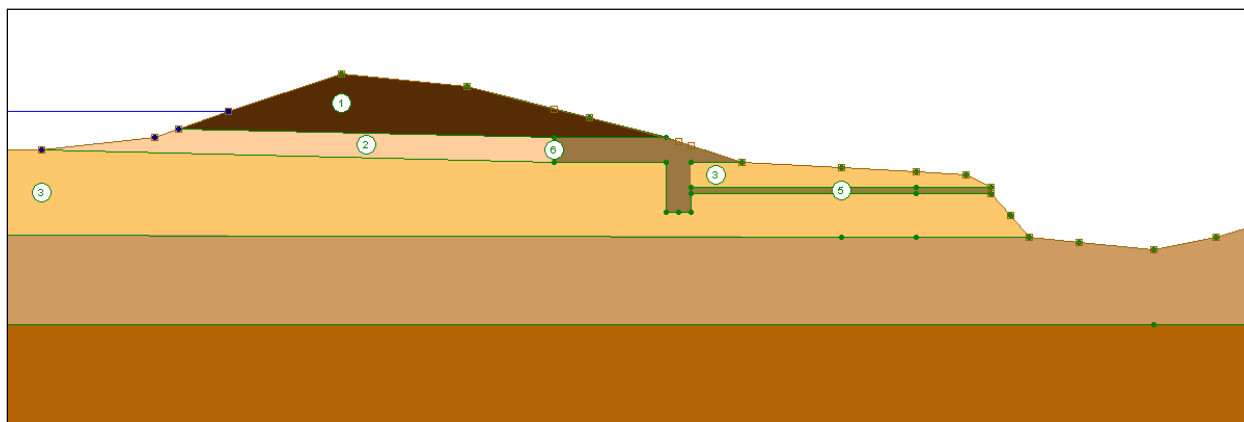


Figure 208. A typical section for a levee in Albuquerque, NM.

Table 86. Soil properties for the levee section in Figure 208, Albuquerque, NM.

Material Number	Soil Classification (USCS)	Unit Weight (lb/ft <sup>3</sup> )	Cohesion (lb/ft <sup>3</sup> )	Friction Angle (deg)
1	Levee Sand (SP)	130	0	31
2	Levee Silty Sand (SM)	119	0	31
3	Blanket Sandy Silt (ML)	102	400	9.9
4	Aquifer Silty Sand (SP)	130	0	38
5	Pipe Drain	NA	NA	NA
6	Toe Drain Gravel (GM)	125	0	34
7	Aquifer Sand (SP)	130	0	38

The soil characteristics and geometry at Albuquerque were similar to those of Burlington. Because of this, the slope stability response to tree position was expected to be similar. The toe drain presents a unique factor, however, that had not previously been analyzed. The purpose of the toe drain is to dissipate pore pressures within the slope and increase global stability. The possibility exists that roots from woody vegetation could reduce the effectiveness of the drain and lower slope stability. Therefore, a single scenario was analyzed for Albuquerque in which a tree was assumed to be located directly on the toe drain, as shown in Figure 209.

For this analysis, no root ball soil properties were assumed, as the change in drainage was achieved by varying the permeability of the entire toe drain. Tree properties of a cottonwood were used in the analysis. The tree is estimated to weigh 17,000 lb using the tree biomass regressions by Jenkins et al. (2004) previously discussed. The roots were modeled as extending 15 ft radially and 5 ft deep on the basis of physical root characterization data collected from a similarly sized tree in Vicksburg, MS.

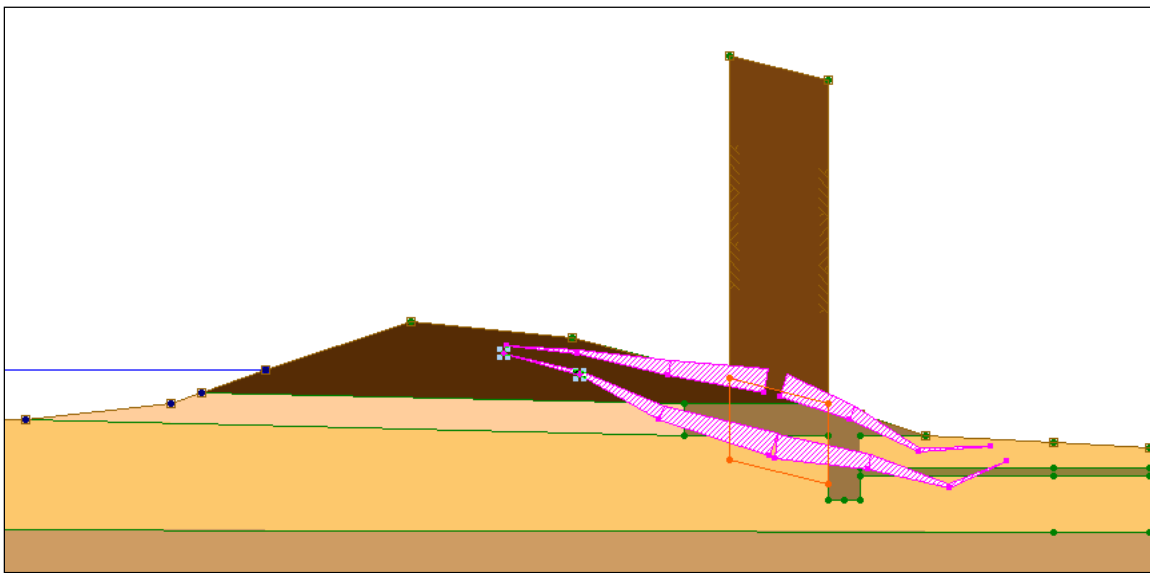


Figure 209. The tree position at the toe drain used in the slope stability analysis for Albuquerque, NM.

As discussed in the seepage model section of this volume, the toe drain had a significant effect on seepage conditions, but it did not appear to affect the slope stability based on the analysis for this study. The soil profile included a cohesive layer, which forced deep failure circles, so it was unnecessary to define various failure criteria for Albuquerque. The results of the slope stability analysis are shown in Figure 210.

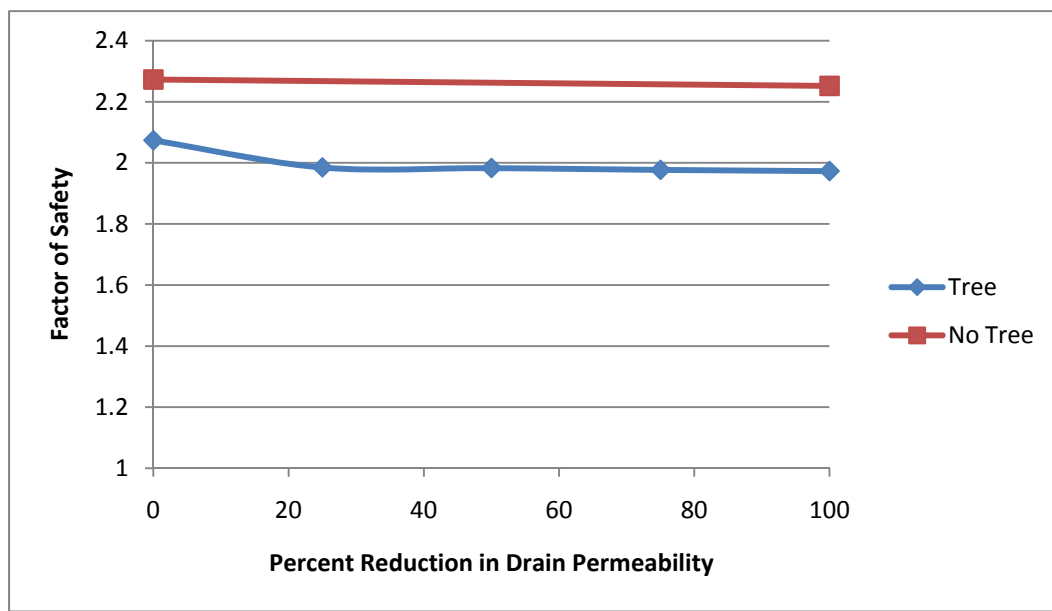


Figure 210. The results of the slope stability analysis for Albuquerque, NM.

Varying the toe drain had little to no effect on the factor of safety values. This is likely ascribable to the failure circles being relatively deep. With deep failure circles, the changes in the phreatic surface have a proportionally smaller effect on the soil stresses because of the larger stresses along the failure circle. A typical failure circle is shown in Figure 211.

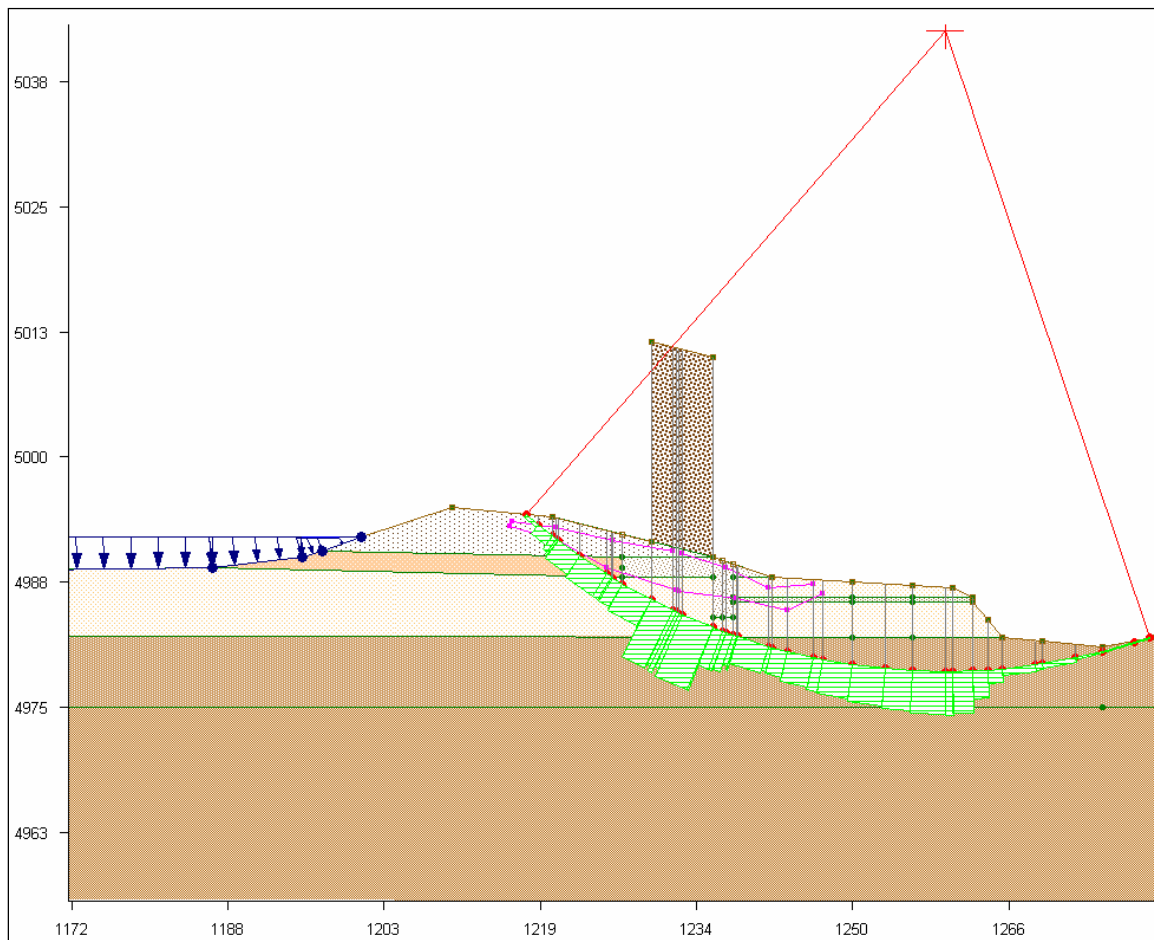


Figure 211. Typical failure circle for the Albuquerque Levee.

The tree position itself had the largest effect on the factor of safety. As shown in Figure 210, locating the tree at the downstream, midslope position resulted in an average reduction in the factor of safety of 12%, regardless of drainage conditions. Trees in general will lower the factor of safety at Albuquerque if located on the slope.

## Vicksburg, MS

### *Introduction*

Two sites at a local sand and gravel pit in Warren County, Mississippi, (Figures 212 to 216) were evaluated for targeted studies of trees for mapping individual roots and the rootball. Studies were performed on an oak tree and involved terrestrial LiDAR, ground-penetrating radar (GPR), and resistivity surveys beneath the tree. Studies conducted at the pine tree were limited to GPR surveys. Both of the tree sites were later excavated by using an air compressor and air lance to expose the root system to map the



Figure 212. Location of the Vicksburg study site. The study site is in a gravel pit south of Vicksburg in hills bordering the Mississippi River Alluvial Valley. These hills are composed of Tertiary Age sediments veneered by windblown silt (loess) derived from exposed fine-grained Mississippi River sediments from melting Pleistocene Age glaciers in the northern latitudes.

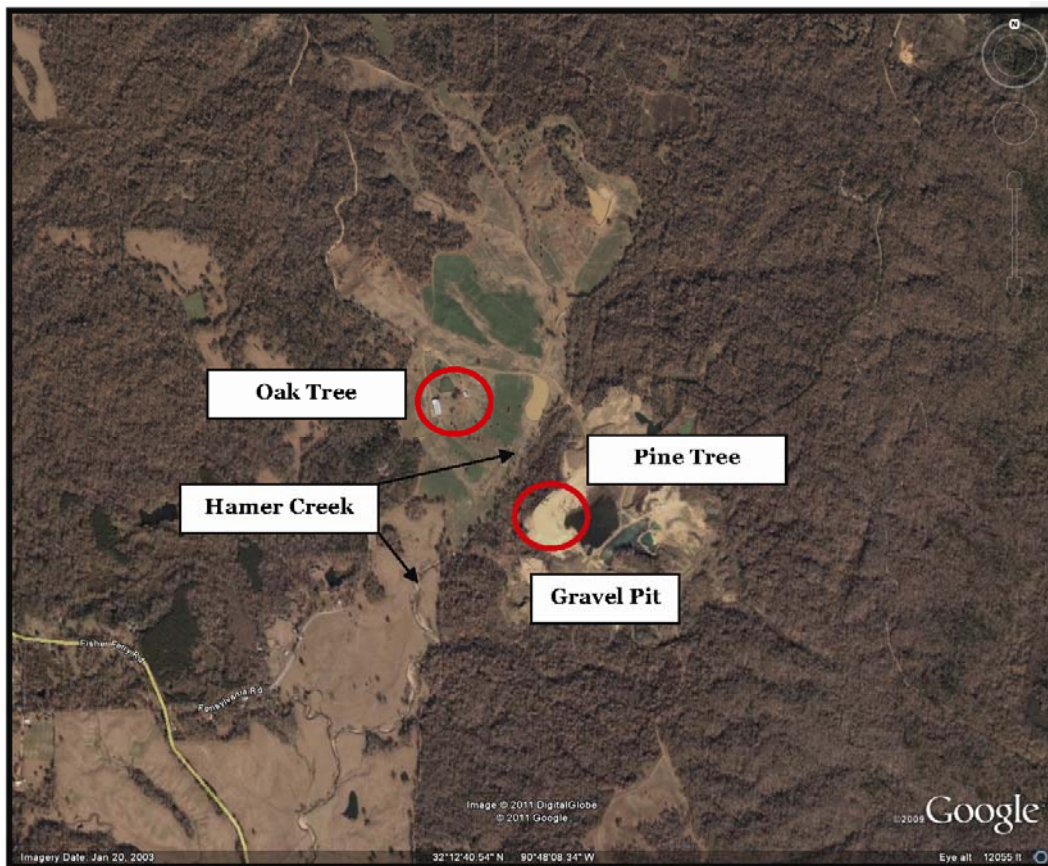


Figure 213. Aerial view of the Vicksburg Site where an oak tree and pine tree were studied. The pine tree lies within an active sand and gravel operation. Geophysical surveys were performed at both sites. LiDAR surveys were performed only at the Oak site. Excavation of roots was performed at both tree sites. Hamer Creek is the local drainage and is a tributary to the Big Black River, which in turn drains into the Mississippi River.

roots and to verify the results of the geophysical methods for noninvasive mapping.

The purpose for conducting the LiDAR survey at the oak site was to obtain a detailed morphometric map of the tree and its root system and obtain physical properties of the roots for modeling purposes. Terrestrial LiDAR surveys were performed to obtain a detailed map of the tree canopy and its rootball after being excavated with the air lance. LiDAR data were incorporated into the geotechnical modeling by providing physical dimensions and characteristics of the tree, the roots, and the rootball extent. GPR and resistivity surveys were used prior to any excavation to determine the worth of these techniques for mapping individual roots and their extent as



Figure 214. Closeup view of the oak tree where LiDAR and geophysical surveys were conducted.



Figure 215. Top photo is view of pine tree at the Warren County gravel pit used to test ground-penetrating radar for mapping roots. Bottom photo shows the underlying sand and gravel foundation being mined for aggregate. The tree being studied is the farthest tree in the right side of photograph.

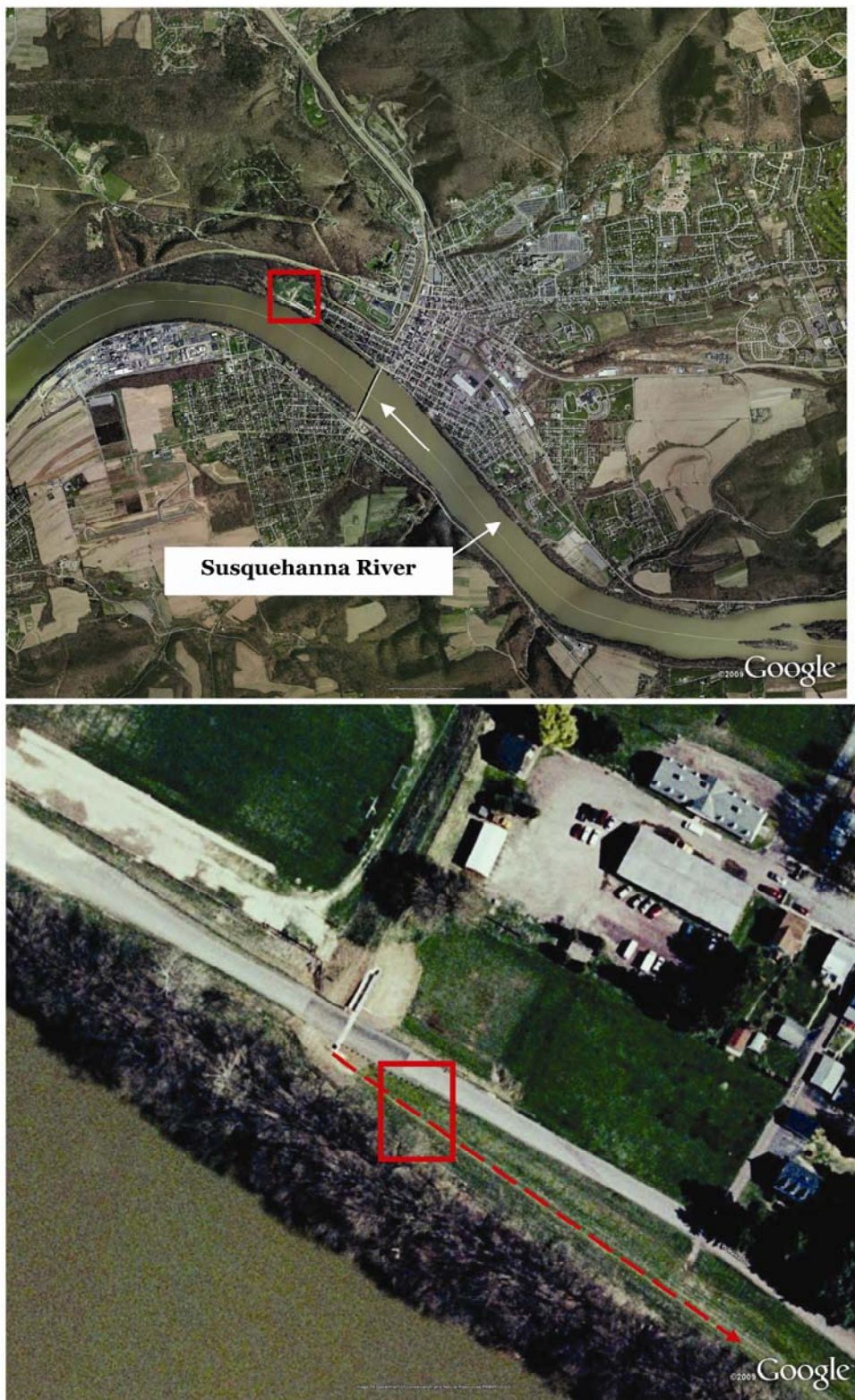


Figure 216. Study area along the Susquehanna River at Danville, Pennsylvania. Closeup view in bottom of photo shows the levee centerline and the site studied at Station 122 + 90. Note the trees growing at the edge of the vegetation-free zone (VFZ).

part of the evaluation of noninvasive techniques for subsurface mapping of woody vegetation. Geophysical surveys were performed adjacent to and around the root zone, before the excavation of the root mass was initiated.

#### *Geologic setting*

The Vicksburg, MS, area is nationally noted for its thick occurrence of loess (wind blown silt) soils, and is the type locality for one of several different loess sheets in the Mississippi River Alluvial Valley (Clark et al. 1989; Krinitzsky and Turnbull 1967; Kolb and Durham 1967; Saucier 1994). Loess deposits are present along the bluffs bordering the Mississippi River's alluvial valley. These deposits occur as a thick accumulation of wind blown dust, composed primarily of silt-sized, quartz particles. The origin for the loess is from fine-grained outwash plain deposits derived from melting continental glaciers during the Pleistocene Age. The Mississippi River at Vicksburg was a conduit for massive quantities of glacial sediment transported by the Mississippi and Ohio rivers during the Pleistocene. Prevailing winds blowing across the alluvial valley entrained silt-sized particles from the exposed outwash plain deposits, and transported these sediments onto the high bluffs bordering the present day Mississippi River's alluvial valley. Loess deposits are present along both sides of the bluffs flanking the Mississippi River in the central U.S. Extensive loess deposits are present in Arkansas, Illinois, Louisiana, Mississippi, Missouri, and Tennessee (Krinitzsky and Turnbull 1967; Saucier 1994) and decrease in thickness with increasing distance from the Mississippi River's floodplain.

In the Vicksburg area, loess deposits can attain a thickness of nearly 100 ft adjacent to the river, as evidenced by road cut exposures and numerous soil borings that have been drilled through the loess (Krintszky and Turnbull 1967; Kolb and Durham 1967; Mellen, McCutcheon, and Livingston 1941). The thicker accumulations of loess sediments in the Vicksburg area correspond to multiple periods of deposition, associated with different glacial melting and waning episodes in the Pleistocene. In the Vicksburg area, at least three different loess sheets are present.

The age of the loess sheets in Vicksburg was tentatively characterized by Krinitzsky and Turnbull (1967) as ranging from the Early Holocene (8,000 years BP) to Late Pleistocene (125,000 years BP).

The Vicksburg site likely contains the youngest of the loess sheets present in the Vicksburg area. The oak tree in Figures 213 and 214 corresponds to a site situated in loess soils, which were subsequently modified by Holocene pedogenic (i.e., weathering and soil formation) processes, and historic (man-made) processes. The Warren County soil survey bulletin (USDA 1964) indicates the tree site as being composed of Memphis-Natchez soils on 12 to 17% slopes. The tree site is located on a gentle southeast facing slope overlooking Hamer Creek (Figure 213), which is a tributary to the Big Black and Mississippi rivers. ML and silt loam (CL-ML) are present beneath the oak tree. The total thickness reported for the C-horizon (unmodified parent horizon in soil taxonomy) for Memphis and Natchez soils is estimated to be 10 to 20 ft deep (USDA 1964).

The foundation geology at the pine tree is entirely different compared to the oak tree location. Obvious differences between the two sites are the different tree species, and also that the pine tree is on highly disturbed ground compared to the oak tree location. The ground is actually a large man-made gravelly sand (SW) hill, which was stockpiled many years earlier for the aggregate (Figure 215). The stockpile was derived from a 10- to 40-ft-thick layer of naturally occurring coarse sands and gravels, which lie unconformably beneath the loess deposits.

The sand and gravel pit in relationship to Hamer Creek's floodplain (Figure 213) occurs as a pronounced topographic high, and is representative of many similar quarrying operations throughout the central Mississippi region and the Southeast Gulf Coastal Plain. These pits typically occupy topographically higher elevations than the surrounding terrain. They are an erosional vestige or remnant of a much larger and geographically widespread alluvial fan complex, formed by ancestral rivers draining the Appalachian Mountains during the Pliocene and Early Pleistocene (5 to 1.5 million years BP) across much of the southeastern U.S. coastal plain (Ispahordig and Lamb 1971). Local drainage, established after deposition of this coarse-grained fan complex in the early to middle Pleistocene, has eroded this extensive fan in response to tectonic uplift and eustatic sea level fluctuations. The end result is the presence of these isolated knolls occupying topographic high areas throughout the central Mississippi and the Vicksburg area. This sand and gravel unit is relatively continuous, extending from Texas to Florida and across southern Louisiana, Mississippi, and Alabama, and is mapped as the Citronelle Formation in Louisiana and Mississippi (Moore 1976; Ispahordig and Lamb 1971).

*Laboratory soils data and hydraulic conductivity*

Soil samples were collected beneath the canopy of the two trees to characterize soil texture and their grain size distribution. These samples classify as clayey ML beneath the oak tree, and gravelly sand (SW) beneath the pine tree. The gravel in the sand was previously washed and concentrated to primarily a pea gravel size with approximately 10 to 15% volume.

*Groundwater conditions*

The Vicksburg site is much different in comparison to any of the previous sites examined as no levees exit at this location, and the site is well removed from the active floodplain. The purpose for studying the Vicksburg site was to perform LiDAR and geophysical experiments locally, in order to develop and improve field data collection methods. Groundwater was observed in the gravel pit as occupying lower elevations than either the oak or pine locations.

**Danville, PA***Introduction*

Danville, PA, is located in Montour County on the Susquehanna River (Figure 216). This location was included in the levee sites studied by ERDC because of its eastern U.S. setting, the existence of a comprehensive engineering assessment of the levee system for the Federal Emergency Management Agency (FEMA) certification process (Schnabel 2010), and the willingness of the levee owner to support the ERDCs research effort. The engineering analysis by Schnabel (2010) included a study on the impacts of silver maples to the reliability of the flood protection system.

The Danville levee system is owned, operated, and maintained by the local Borough. The levee system is approximately 5 miles in length and borders the Susquehanna River. The system provides flood protection from the Susquehanna River and its tributaries flowing within the Borough limits. The flood protection system was originally built in the mid-1950s, and has been subsequently upgraded in response to large magnitude flood events over the past 50 years (Schnabel 2010). The levee system involves earthen levees, flood walls, and interior drainage control structures, which pass drainage behind the levee to the Susquehanna River during low water.

The typical levee prism contains a 12-ft-wide crown with side slopes of 1 vertical and between 2.0 to 2.5 horizontal (Figure 217). The Borough removed all woody vegetation from the levee toe in 2009 to meet the standards for the USACE vegetation-free zone (VFZ) along the levee right-of-way. Most of the woody vegetation deficiencies at Danville involved the presence of mature silver maples within the flood side 15-ft-wide VFZ corridor (Figure 217).

ERDC activities at Danville involved a reconnaissance survey of the levee system and limited study of a site where preexisting engineering data were available. Time permitting, the Danville location was considered to be a worthy candidate for a more focused study by the ERDC modeling team. ERDC performed additional data collection at Station 122+90, which was a study profile in the engineering assessment by Schnabel (2010). ERDC personnel obtained hydraulic conductivity, Troxler density, and Troxler soil moisture measurements.

#### *Geologic setting*

Danville is located in a narrow alluvial valley cut into sedimentary rocks of Silurian (443 to 416 million yr BP) and Devonian (416 to 359 million years BP) by the Susquehanna River during geologic time (Berg et al. 1984; Berg and Dodge 1981; Hoskins 1976a, 1976b; Schnabel 2010). The borough is located in the region of Pennsylvania that was covered by Pleistocene continental glaciers as evidence by the presence of glacial tills in Montour County (Sevon and Braun 2007; USDA 1985). Additionally, this region was further modified by the discharge of glacial melt waters into the Susquehanna River system during the Pleistocene. Boring data drilled for the geotechnical evaluation of the Danville levee system by Schnabel (2010) indicates that the alluvial deposits are generally less than 20 to 30 ft thick. The undisturbed alluvium in descending order consists of a thin top blanket of silt and clay, a pervious substratum of coarse-grained sand and gravel, a lower coarse gravel unit containing disintegrated bedrock, and rock (Schnabel 2010).

A representative boring from Station 122 + 90 at the levee center line is presented in Figure 218 (Schnabel 2010). This boring is representative of similar conditions for the levee and its foundation for the Danville flood protection system. The levee at this location is approximately 15 ft above the levee toe. The levee embankment is composed of fill material, consisting of sandy clay and silty to clayey sand. The levee foundation is



Figure 217. View of Danville levee looking southwest at Station 122 + 90. Silver maple stumps along edge of the vegetation free zone were removed in 2009.

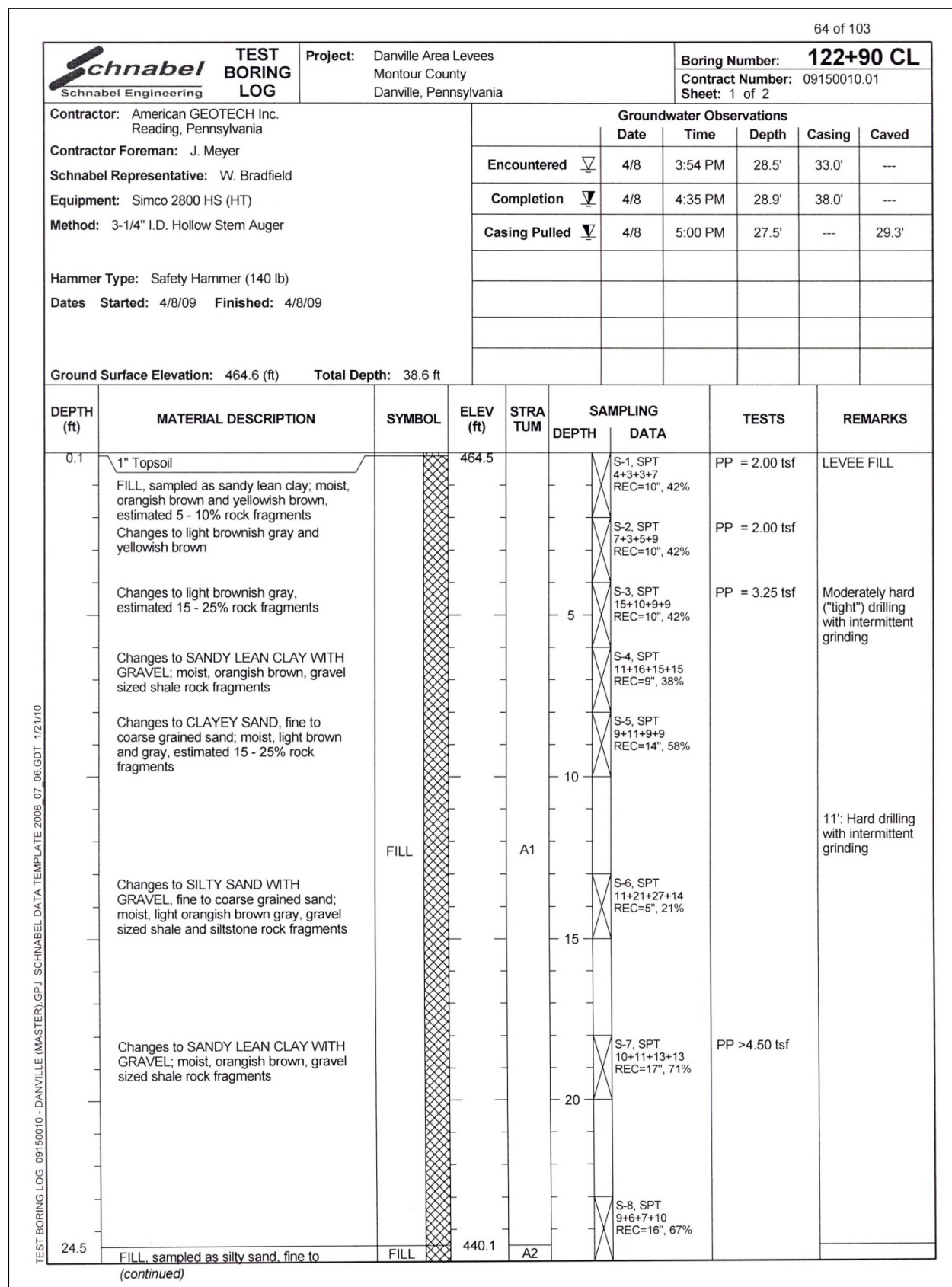


Figure 218a. Center line boring from Station 122 + 90, continued (Schnabel 2010).

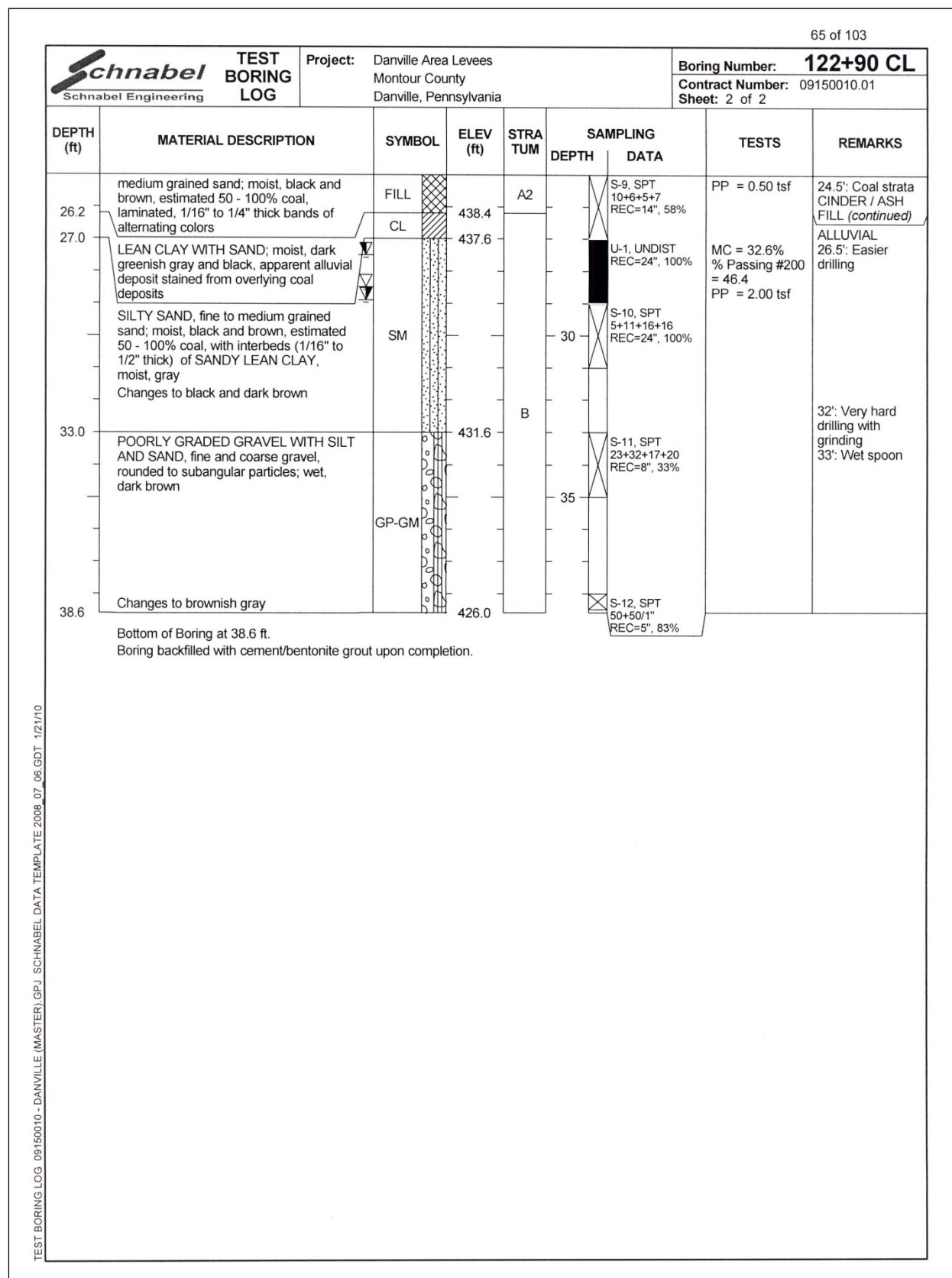


Figure 218b. Concluded.

**Table 87. Stratum designation for the SEEPW analysis of the Danville Levee system (Schnabel 2010). See Figure 218 for stratum designation of this boring.**

<b>Soil Description</b>	<b>Classification <sup>(1)</sup></b>	<b>Density <sup>(2)</sup></b>	<b>Designation on Plates</b>
FILL: Levee Fill (A1)	Fine	Loose/Soft	A1-F-L
	Fine	Dense/Firm	A1-F-D
	Coarse	Loose	A1-C-L
	Coarse	Dense	A1-C-D
FILL: Cinder/Ash Fill (A2)	Coarse	Loose	A2-C-L
	Coarse	Dense	A2-C-D
FILL: Soil Fill (A3)	Fine	Loose/Soft	A3-F-L
	Fine	Dense/Firm	A3-F-D
	Coarse	Loose	A3-C-L
	Coarse	Dense	A3-C-D
ALLUVIAL: Fine-Grained (B1) <sup>(3)</sup>	Low plasticity	Loose/Soft	B1-L-L
	Low plasticity	Dense/Firm	B1-L-D
ALLUVIAL: Coarse-Grained (B2)	SP (poorly-graded sand)	Loose	B2-SP-L
	SP (poorly-graded sand)	Dense	B2-SP-D
	SM (silty sand)	Loose	B2-SM-L
	SM (silty sand)	Dense	B2-SM-D
ALLUVIAL: Coarse-Grained (B3)	GP (poorly-graded gravel)	Loose	B3-GP-L
	GP (poorly-graded gravel)	Dense	B3-GP-D
	GM (silty gravel)	Loose	B3-GM-L
	GM (silty gravel)	Dense	B3-GM-D
DISINTEGRATED ROCK (C)	Disintegrated Rock		C
ROCK (Rx)	Rock		D

- (1) Fine – classifies as fine-grained based on gradation (greater than 50% passing the No. 200 sieve).  
Coarse – classifies as coarse-grained based on gradation (less than 50% passing the No. 200 sieve).
- (2) Indicates the basic consistency/density of a soil based on unit weight/shear strength. Note fine-grained soils are not typically classified as “loose” or “dense,” but this nomenclature was used for simplicity.
- (3) Fine-grained alluvial were originally subdivided into low and high plasticity soils, but based on interpretation of the data, the high plasticity designation was not necessary.

composed of fill, which becomes coarser grained with depth and includes coal, cinders, slag, and ash. The presence of these materials in the levee and foundation fill is a legacy of Danville's history as an important iron manufacturing center during the 1800s to support the development of railroads in the U.S (Schnabel 2010). The fill transitions to natural alluvial sediments at 26-ft depth in the centerline boring in Figure 218 and terminates in the coarse gravels above the bedrock contact.

#### *Danville Borough levee assessment and results*

The Borough of Danville contracted an engineering assessment of their levee system to AMEC and Schnabel Engineering to comply with the FEMA levee certification process (Scott Raschke<sup>1</sup>, 2011; Schnabel 2010). The engineering assessment by Schnabel Engineering included drilling of additional geotechnical borings in the levee right-of-way (centerline, flood side toe, and river side toe), digging of test pits in the levee section, and elevation surveys of representative sections. Furthermore, test pits were dug adjacent to mature silver maple trees to map the root extent and determine the impact to the levee prism. A steady state seepage analyses using SEEP/W was performed on representative profile sections to assess underseepage impacts because of pervious geologic conditions, pervious levee soils, and possible impacts related to woody vegetation growing within the VFZ. Stratigraphic models of the levee and foundation were developed for the SEEP/W analysis using the boring data, as shown in Table 87, and the stratum designation identified on the boring log in Figure 218. ERDC obtained additional field measurements at Station 122 + 90, which was one of the levee sections evaluated by Schnabel (2010).

Included in the Schnabel (2010) seepage study was a sensitivity analysis to better understand the impacts to levee reliability from the root zone of silver maple trees growing into the VFZ and the levee prism. One of the purposes for the sensitivity analysis was to determine the practical root excavation depth needed for the mitigation of woody vegetation and roots growing into the levee slope and the VFZ from encroaching flood side tree growth.

Tree data were obtained from excavation of test pits adjacent to mature silver maples to provide information for the sensitivity modeling and

---

<sup>1</sup> Personal communication. 2011. Scott Rachke, Schnabel Engineering, Danville, PA.

analysis. Test pit excavation was performed with the collaboration of an arborist. The sensitivity analyses used a 1-, 2-, and 3-ft root plate or zone along the flood side to assess the exit gradient and the factor of safety at each representative site evaluated by increasing the permeability of the root zone or plate, in comparison to the underlying embankment levee soils. One of the seepage analysis conducted for the ERDC study used the same approach.

Test pit studies indicated the majority of mature silver maple roots were shallow in nature, being less than 18 in. deep. The maximum root size was limited to about 6 in. in diameter adjacent to the tree, and diminished significantly in size within three stump diameters (Schnabel 2010).

Furthermore, it was found that silver maple roots, where present, did not penetrate deep into the main body of the levee prism, but rather were confined to only the upper 18 in. Tree mitigation within the VFZ at the levee toe was restricted to cutting the tree and leaving the stump in place (Figure 217), because the seepage analysis indicates only a 5% difference in the factor of safety between areas where trees were present and those without.

#### *Laboratory soils data and hydraulic conductivity*

Laboratory soil testing was conducted as part of the Danville levee assessment by Schanabel (2010) to assign engineering properties to the various stratigraphic layers (Table 87) in their SEEPW cross sections. Test data from selected samples were included on the boring logs (Figure 218), and included standard engineering related tests for moisture content, grain size distribution, Atterberg limits, dry unit weight, bulk density, hydraulic conductivity, direct shear, and triaxial shear. Additionally, ERDC supplemented these data with in situ Troxler density, soil moisture, and falling head permeameter tests at levee Station 122 + 90.

#### *Groundwater conditions*

As the levee system is located adjacent to the river, groundwater levels are governed by stage of the Susquehanna River. The pervious nature of the alluvial soils in the levee foundation allow for rapid changes in groundwater elevation as the stage of the river rises or falls. Groundwater was encountered at the base of the fill sequence in the centerline boring in Figure 218.

## Boca Raton, FL

### *Introduction*

The last site studied is located in southern Palm Beach County, near Boca Raton, FL (Figure 219). The site contains a back levee, which protects against storm surge from rising water levels in the Arthur R. Marshall Loxahatchee National Wildlife Refuge. This site contains fig trees that were outside of the VFZ (Figure 220), but were representative of vegetation from this region. A view of the levee system is shown in Figure 221a. These levees have a crown width of 10 to 12 ft and are about 10 ft in height, with side slopes of 1V:3H.

The levees are owned by the South Florida Water Management District (SFMD), which was originally created in 1949 as the Central and Southern Florida Flood Control District. The District became the SFWMD in 1972 to provide flood protection and irrigation to farmers and overseas Everglade restoration projects. This District has over 1,700 employees and 2000 miles of canals, levees, pumps, and other types of water related infrastructure.

### *Geologic setting*

A unique feature of this site, compared to other sites studied, was the presence of shallow limestone bedrock, typically less than 4 ft deep beneath the ground surface. The bedrock for this area is mapped as the Miami Limestone, which is described as white to light gray in color, fossiliferous, contains variable percentage of sand, and often grades into calcareous sand (Scott 1993; Scott et al. 2001). Bedrock was frequently encountered at shallow depths in the auger holes for permeameter testing.

Soils overlying the bedrock are marsh deposits, fine-grained sand, and shell used for fill. The soils series in the area studied are classified as being either Dania or Lauderhill (USDA 1978). These soils correspond to organic marsh deposits overlying bedrock. This area has been extensively disturbed during historic time by construction of the nearby canal, roads, and the flood protection levees.

### *Laboratory soils data and hydraulic conductivity*

No geotechnical data were obtained for this site from the SFWMD to characterize the engineering properties of the levee fill and the shallow



Figure 219. Study site at Boca Raton, FL, where a fig tree was evaluated.



Figure 220. View of fig trees studied at the Boca Raton, FL. Top photo is view looking south on the east side of the canal. This tree was tested for soil hydraulic conductivity using a permeameter. Bottom photo is view looking north and shows another fig tree adjacent to the wildlife refuge. Levee is to the right of photo. Both trees were measured with the Troxler for soil moisture and density.



Figure 221. View looking south of the levee system adjacent to the Arthur R. Marshall Loxahatchee National Wildlife Refuge. Top photo shows the canal on the protected side and marsh on the flood side. Pervious nature of the levee soils are reflected by seepage at the levee toe on the landside. Water level in the marsh was about 1 to 2 ft higher than the protected side.

foundation. Levee soils were observed to be fairly pervious, containing silty sands and fine-grained sands with shell fragments. The levees were likely built from material dredged from near the toe of the levee.

*Groundwater conditions*

The water table is at ground surface to less than 3 ft below the ground surface near the canal. As shown in Figure 221b, through seepage is ponding at the surface because of the differential head between the flood and protected sides of the levee.

## 4 3-D Numerical Modeling

Though not fully understood, the effect of a root system on subsurface material properties related to hydrodynamics and structural mechanics is often limited in extent and is both anisotropic and heterogeneous in nature (Schwarz et al. 2010). For example, roots may penetrate only the first few feet of soil, and the density of roots in soil may decrease sharply at some lateral distance from the base of a tree (Schwarz et al. 2010). Seepage and stability analysis for engineered levees is typically carried out on vertical cross sections (Griffiths and Lane 1999), which is equivalent to an assumption of an infinitely long levee in the upstream direction with uniform properties and boundary conditions in the direction normal to the vertical cross section.

In the ERDC research, two approaches for 3-D modeling are used to represent root systems. The first is a direct extension of the 2-D hydraulic conductivity (rectangular block) approach, discussed previously in this volume, to 3-D, while the second employs a higher fidelity approximation to a root geometry reconstructed from LiDAR scans taken at the ERDC test site in Vicksburg, MS. The resulting levee conceptual models are essentially extruded cross sections with trees positioned every 20 or 30 ft, depending on the assumed root zone geometry. Because highly local modifications to subsurface hydrodynamic and/or soil mechanical properties can generate genuinely 3-D phenomena, full 3-D finite element models were used for seepage and slope stability, and included woody vegetation effects. Kees et al. (2008) describe the 3-D seepage model in more detail. The elasto-plastic soil mechanics is a new in-house implementation of the approach described in Griffiths and Lane (1999) extended to continuous tetrahedral finite element methods, and the common Backward Euler integration method for plasticity constitutive equations, described by Belytschko et al. (2000). The 3-D finite element analysis uses a standard elastic-plastic constitutive law for soils based on the Mohr-Coulomb failure criteria. Griffiths and Lane (1999) describe this method for slope stability analysis. The algorithm used in the ERDC study to integrate the constitutive law is from Belytschko et al. (2000), which is also the standard for elastic-plastic materials including soils, as well as a much wider class of solids encountered in structural engineering.

The seepage model is based on Richards' equation with the Mualem-van Genuchten constitutive relations, while the soil mechanics is based on small deformation plasticity using the Mohr-Coulomb yield surface and the Drucker-Prager plastic potential. While these models are widely used and described in much more detail in the references previously, some of the limitations of these models are listed to make it clear what phenomena can and cannot be modeled. The assumptions for seepage and stability include the following:

- Seepage is modeled as if the geometry of the pore space is fixed (i.e., not deforming or eroding in time).
- Seepage is modeled as pure water, ignoring the effects of air-water or sediment-water mixing and evaporation/erosion/deposition.
- Inertial effects in the seepage are neglected.
- The pore fluids affect the soil mechanics only through the steady-state pore pressures applied in water-saturated pores, thereby neglecting surface tension effects on the soil and the effect of deformation on the pore pressure.
- Soil deformation is small, and no changes in density or material properties occur due to flow.
- On-set of plastic strain is governed by the Mohr-Coulomb failure surface, and no hardening or softening occurs.
- The parameters for the constitutive relations in these theoretical models are not known for mixed root-soil systems at the centimeter scale or smaller.

Due to these limitations, 3-D modeling is used in the form of parameter sensitivity studies primarily to assess the 2-D results and to gain some insight into the important processes governing levee performance. Use of 3-D modeling in a more predictive mode will require more integrated advances in constitutive theory, parameter identification, and computational methods guided by extensive lab and field work at a range of space and time scales.

## **Model input**

Because the objective in considering 3-D models is to assess the validity of the 2-D seepage model and stability model, straightforward extensions of the 2-D Pocket Levee models developed for seepage and stability analyses were used in the 3-D analyses. The Pocket Levee is used as an example of the 3-D model analysis. Specifically, the 2-D geometry and seepage

parameters were read directly from the SEEP2-D input files with the values and distributions discussed earlier in this volume. The geometry of the slice was extruded along the levee to consider either a 10- or 30-ft section of the levee, depending on the root-zone representation. In both cases, symmetry boundary conditions were used to model a periodic vegetation distribution along the levee.

The block root-zone consists of a 6-ft-wide vegetated region with a 14-ft-wide separation zone (Figure 222). The 14-ft separation zone was chosen because it was wide enough that seepage in the unmodified soil zone was comparable to the 2-D unmodified profile, indicating that the separation was wide enough that the majority of the tree's effect was isolated to a local zone. Actually trying to model a case of an isolated tree would require specifying head values that are either correct, which is unknown, or far enough away that their effect is essentially negligible, which for this equation is of such great of a distance that far away, it could require as much in the  $y$ -direction as is currently used in the  $x$ -direction. The separation zone is the unmodified soil between the trees in the  $y$ -direction, which is 14 ft in reality, or 7 ft in the computational domain. The levee profile is periodic in the  $y$ -direction in that conceptually it goes from  $y = -\infty$  to  $y = +\infty$  with a repeating pattern. These zones replace what would have been a uniform woody vegetation zone in the 2-D models. The 2-D solution structure is recovered by setting the properties in the woody vegetation zone and separation zone to the same value. The mesh for the computation is highlighted in Figure 223.

One half-period cell is composed of a wood vegetation zone and separation zone. The computational meshes were adaptively refined, unstructured tetrahedral mesh generated using the TetGen mesh generator (Si 2006). The mesh representation of the 3-D levee profile results in a set of solids (regions). These solids are recognized by the mesh generator to adapt the mesh to the solution variation, which is high in the neighborhood of a predictable set of regions: the SBC slurry wall, the sand core, and the woody vegetation zone and surrounding soil. Using this technique, the resulting mesh is a solution-adapted mesh that adds refinement in regions where greater accuracy is needed, rather than just a fixed mesh controlled only by the boundaries and geometry of the soil strata. For the final large-scale seepage results discussed subsequently, the mesh consisted of slightly more than 3 million tetrahedra. Due to the need for additional resolution for the stability analysis, a smaller subdomain (identified by the red block

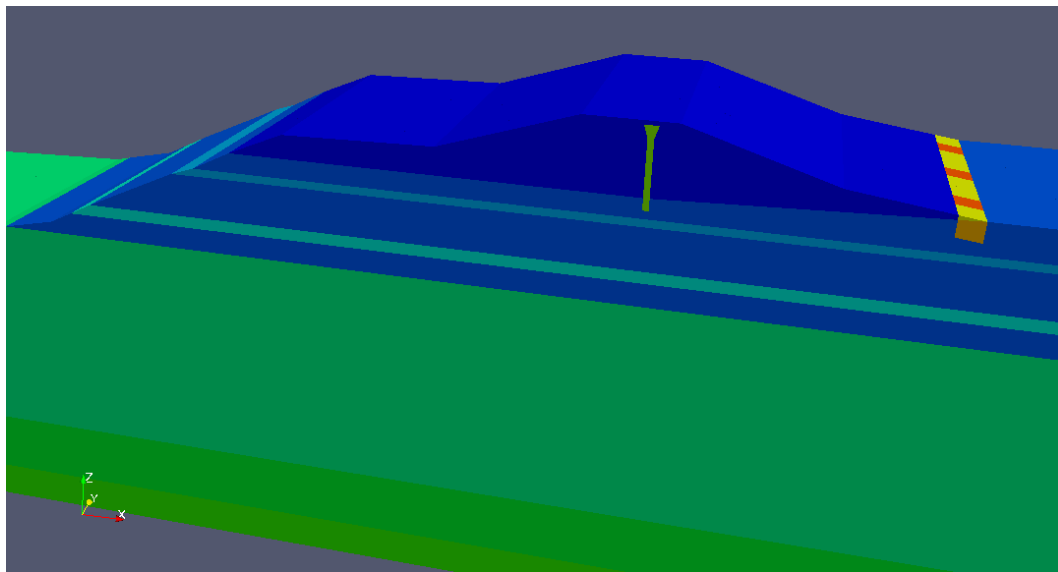


Figure 222. Periodic domain and material layout for 3-D modeling with the woody vegetation zone (red) and separation zone (yellow), Pocket Levee, Sacramento, CA.

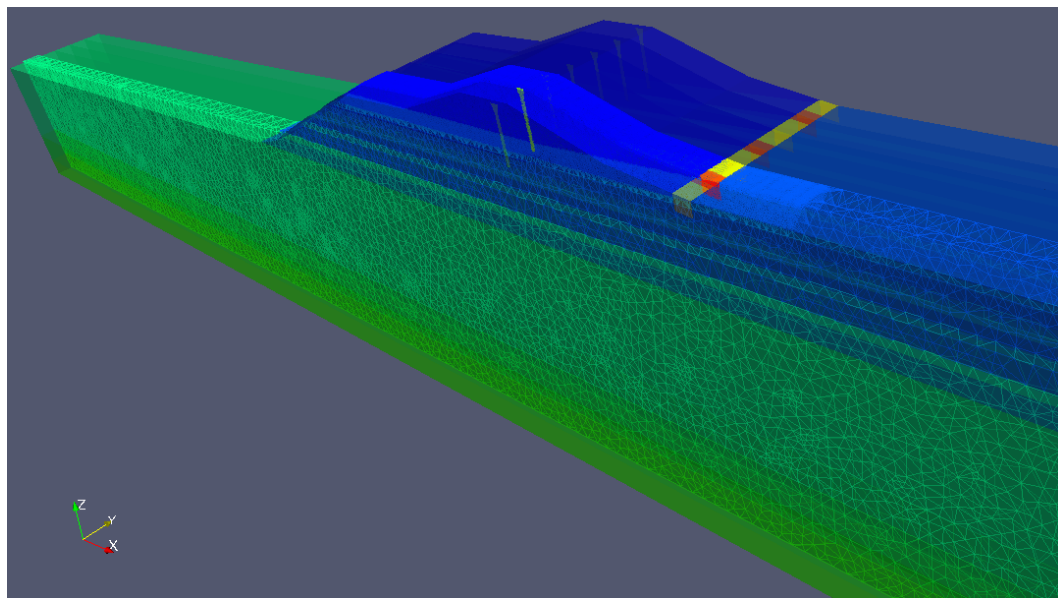


Figure 223. Mesh for the 10-ft half-period cell used as the computational domain, Pocket Levee, Sacramento, CA.

in Figure 224) was constructed from the full levee. The cutout domain was needed to obtain higher resolution in the region where slope failures are likely to occur. Seepage boundary conditions on the cutout domain corresponded to those computed using the full domain. It was verified in doing this that the pore pressures computed in the smaller cutout domain were accurate. Figure 224 shows the cutout domain with respect to the full domain. The mesh for the cutout domain consisted of slightly more than 5 million tetrahedra.

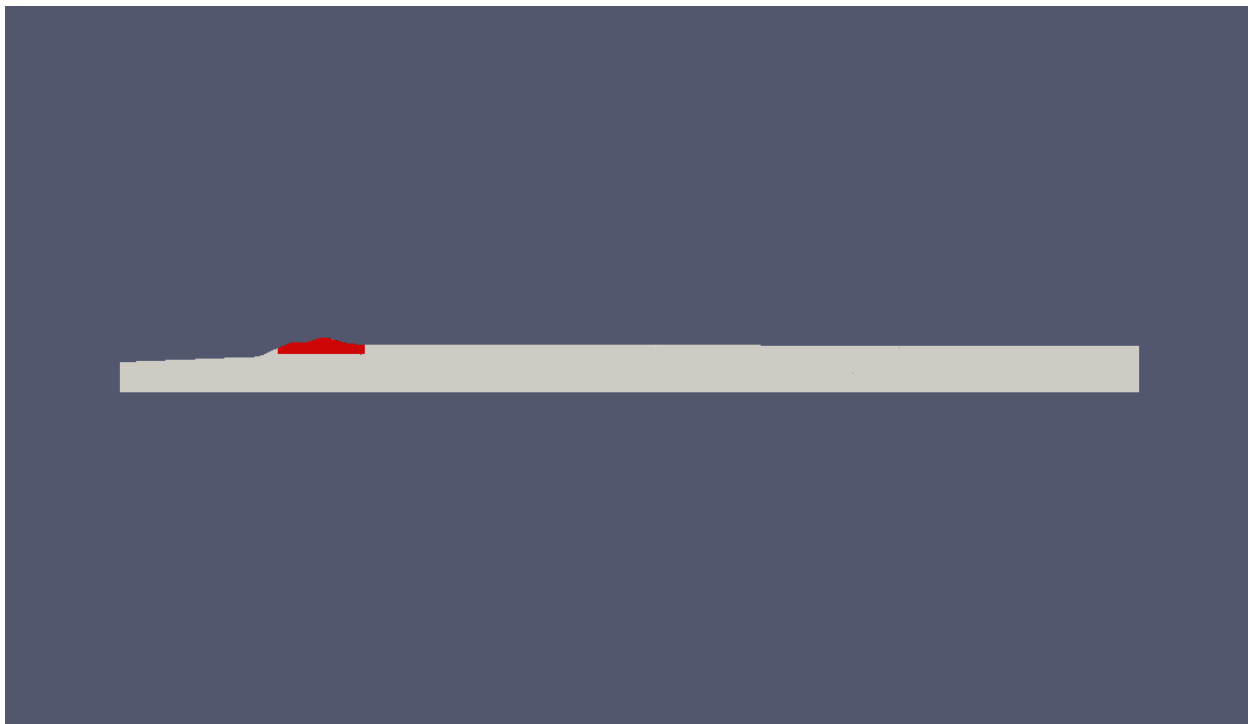


Figure 224. Levee domain (grey) and cutout domain (red).

Material properties and units for seepage modeling were similar to the 2-D seepage analysis except, for the modifications to the 3-D woody vegetation zone discussed previously. Unit weight, cohesion, and friction angle were taken from the 2-D slope stability model generated for this research and discussed earlier in this volume.

In addition to 3-D extrusions of the 2-D numerical models, the use of fully 3-D representations of root geometry was considered. Using the current tetrahedral mesh generation, the root geometry must be approximated as a set of closed (watertight) piecewise linear complexes. A piecewise linear complex is basically a solid that is described by a set of polyhedra. A LiDAR scan of a root system at the ERDC test site in Vicksburg, MS, was used in the 3-D analysis. LiDAR scanning is a technology that provides both points and (outward) normal vectors for the surfaces in the boundaries of the scan; thus, it is capable of providing a precise, but incomplete description of the root geometry. Forming a complete and explicit description of solid geometry based on point cloud information is known as a surface reconstruction problem. Solution algorithms for surface reconstruction problems have been studied intensely for several decades due in part to the increased availability of LiDAR scans, though the application to root geometry extraction has received relatively little

attention. An open source implementation of the Poisson reconstruction technique (Kazhdan et al. 2006) was selected because it is appropriate for noisy data and returns a watertight triangulated surface that is appropriate for the existing mesh generation capabilities.

Figure 225 shows the surface reconstructed from the ERDC LiDAR scan. The reconstruction appears to resolve much of the root structure accurately, but contains over 20 million points, which is currently beyond the 3-D modeling capability in the sense that it represents only a small block of the full levee domain.



Figure 225. Poisson surface reconstruction of ERDC LiDAR scan, Vicksburg, MS.

To obtain a more tractable representation, a two-step approach was taken. First, a high-quality surface triangulation was generated to capture roots with a diameter greater than 3 cm (Ballard 2011). While much sparser than the Poisson reconstruction in Figure 225, the triangulated surface in Figure 226 still contains more than 450,000 triangles and 160,000 points. Embedding the geometry in Figure 226 with sub-inch resolution into a computational mesh for a domain like the Pocket Levee, which is on the scale of hundreds and thousands of feet, is nontrivial.

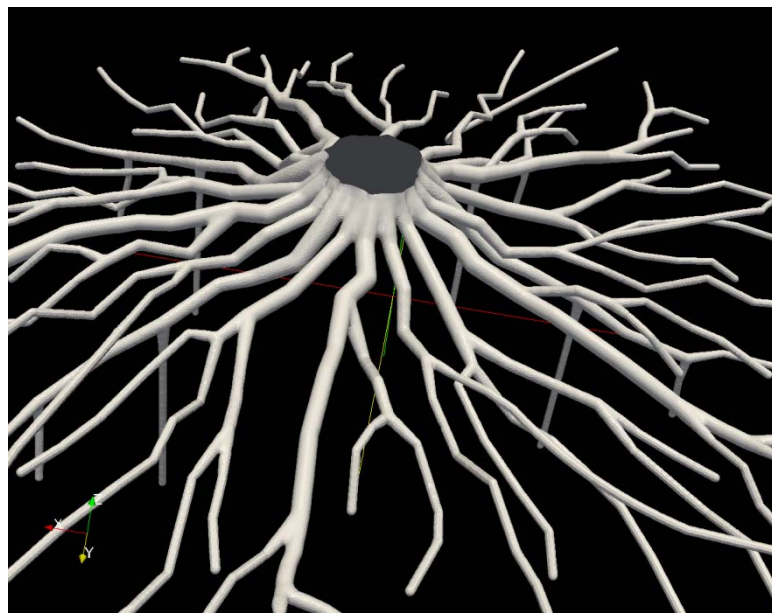


Figure 226. Reconstructed surface mesh for root system from the ERDC LiDAR scan, Vicksburg, MS.

Root system geometry was further approximated by using a “classification” approach to obtain a representation more suitable for 3-D analysis of the full levee domain. Specifically, the soil region impacted by the root system was identified using a local neighborhood search radius,  $\delta$ . Any tetrahedral element in the computational mesh with a barycenter (centroid) lying within a sphere of radius  $\delta$  from the triangulated root surface was then considered part of the root zone. Figure 227 illustrates the subsurface root zone for an intermediate level (Level 2) of refinement and a neighborhood radius of 0.3 ft. In this case, the soil-root zone contained 84,113 elements and 24,904 nodes, and the full computational mesh consisted of approximately 1.9 million elements and 300,000 nodes.

The corresponding region with  $\delta = 0.1$  ft, and an additional level (Level 3) of mesh refinement is shown in Figure 228. At this level of resolution, the soil-root zone contained 167,237 elements and 53,699 nodes, while the full computational mesh contained more than 15 million elements and 2.6 million nodes. Figure 229 illustrates the final root system embedded at the toe of the Pocket Levee in Sacramento, California.

### Conceptual models for seepage and slope stability

The seepage model used the same model formulation and material parameters as the 2-D analysis, except that it was extended to 3-D on tetrahedral meshes, as described in Kees et al. (2008).



Figure 227. Soil-root zone for intermediate (Level 2) computational mesh.

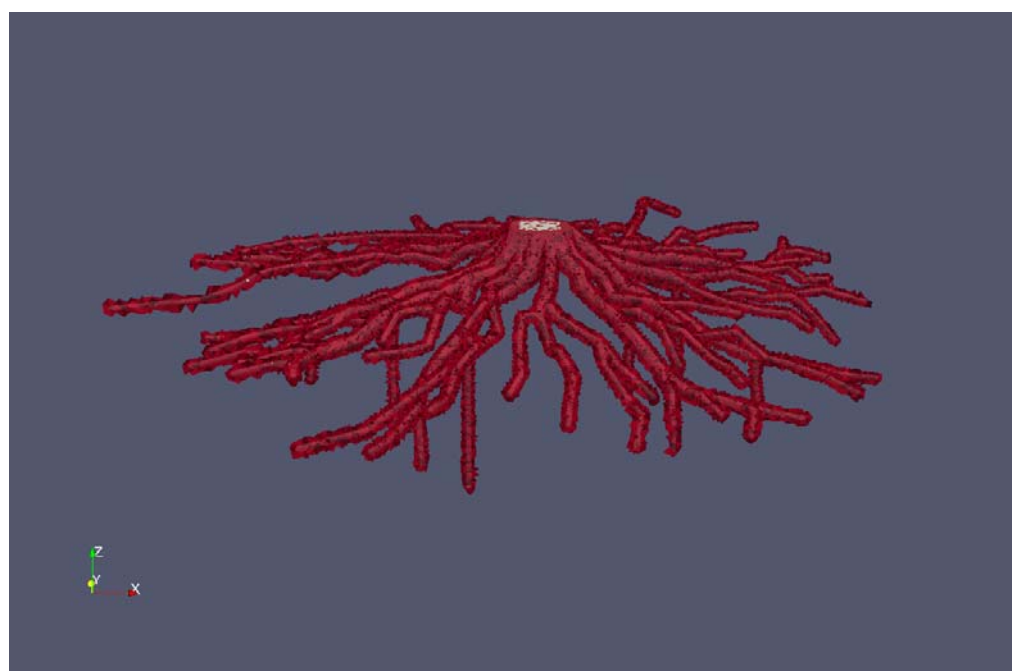


Figure 228. Soil-root zone for highest resolution  
(Level 3) computational mesh.

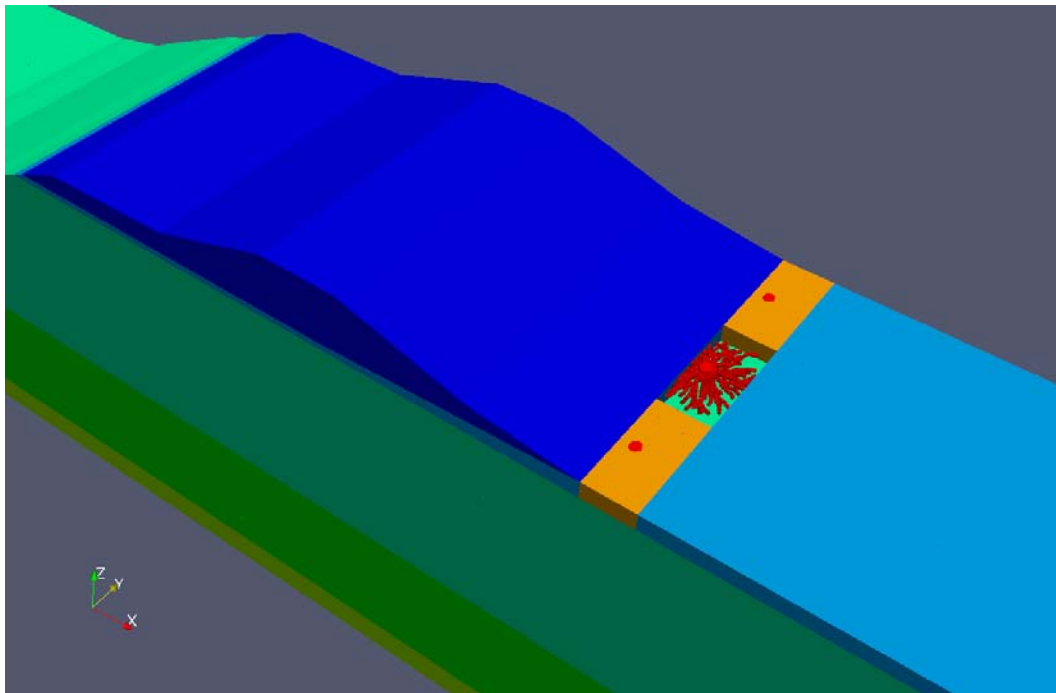


Figure 229. Periodic domain and material layout for 3-D root geometry (red) embedded in the 5 ft clay blanket (light blue) at the toe of the Pocket Levee, Sacramento, CA.

Only steady-state simulations were considered. Nodal quadrature was used for integration of the volume integrals in the weak formulation, and 5th order Gauss-Legendre quadrature, a numerical integration method, was used for the surface integrals. New boundaries parallel to the  $xz$  plane were specified as no flow to reflect the symmetry of the 3-D domain.

The slope stability was modeled with a 3-D continuum soil mechanics approach following Griffiths and Lane (1999). The Mohr-Coulomb constitutive relation was used for the elasto-plastic yield surface, and the Drucker-Prager relation was used for the plastic flow rule. Material properties were taken from the 2-D slope stability analysis, except that a minimum cohesion of 100 lb/ft<sup>2</sup> was enforced to eliminate shallow surface failures, and the silty-sand forming the base of the cutout domain was given a cohesion of 200 lb/ft<sup>2</sup>. Nodal quadrature and linear tetrahedral elements were used in the finite element method.

## Sensitivity analysis

The magnitude of the 3-D effects was first analyzed on the phreatic surface distribution, pore pressure gradients, and flow paths generated from the 2-D seepage models for the ERDC research. A representative case from the

2-D analysis of the Pocket Levee with a steady flood stage of 29 ft and the woody vegetation zone on the toe of the levee was selected. Seven cases were run varying the hydraulic conductivity with  $\beta = 0.001, 0.01, 0.1, 1, 10, 100$ , and  $1000$  in the vegetation zone, as well as seven 2-D cases, where the same value of  $\beta$  was used in both the woody vegetation and separation zones. In the following analysis, red is the 2-D reference case, and blue is the 3-D case.

First, seepage velocities in a horizontal plane in the extreme cases of  $\beta = 0.001$  are considered. The plane is located near the vertical midpoint of the woody vegetation zone. Figure 230 shows that, as expected, local 3-D effects emerge near the woody vegetation zone with flow bypassing the low hydraulic conductivity woody vegetation zone. Likewise, total head contours, shown in Figure 231, demonstrated significant 3-D effects on the flow field in the vicinity of the woody vegetation zone. The total head contours near the 3-D woody vegetation zone are deformed in a manner consistent with variation of hydraulic conductivity in the  $x$ - $y$  plane. The deformation in total head contours results in flow lines, which deflect both vertically and horizontally away from the woody vegetation zone when  $\beta = 1000$ . The flow lines move vertically and horizontally into the woody vegetation zone.

Despite the significant local effects on the flow field, the relatively small extent of the woody vegetation region in both 2-D and 3-D cases, particularly the shallow depth relative to any deeper confining layers, results in very little change to the global flow field, location of the seepage face, or pore pressure gradients, as seen in Figure 232.

Finally, when considering the symmetry plane at  $y = 0$ , the results in the 2-D and 3-D calculations are quite similar along the plane of symmetry, as shown in Figure 233.

In the other extreme case  $\beta = 1000.0$ , changes of the flow paths due to the 3-D effects are expected. Figure 234 shows the head gradients in a horizontal slice through the root zone. Total head gradients show some bypassing of the lower hydraulic conductivity zone, which in this case is the separation zone.

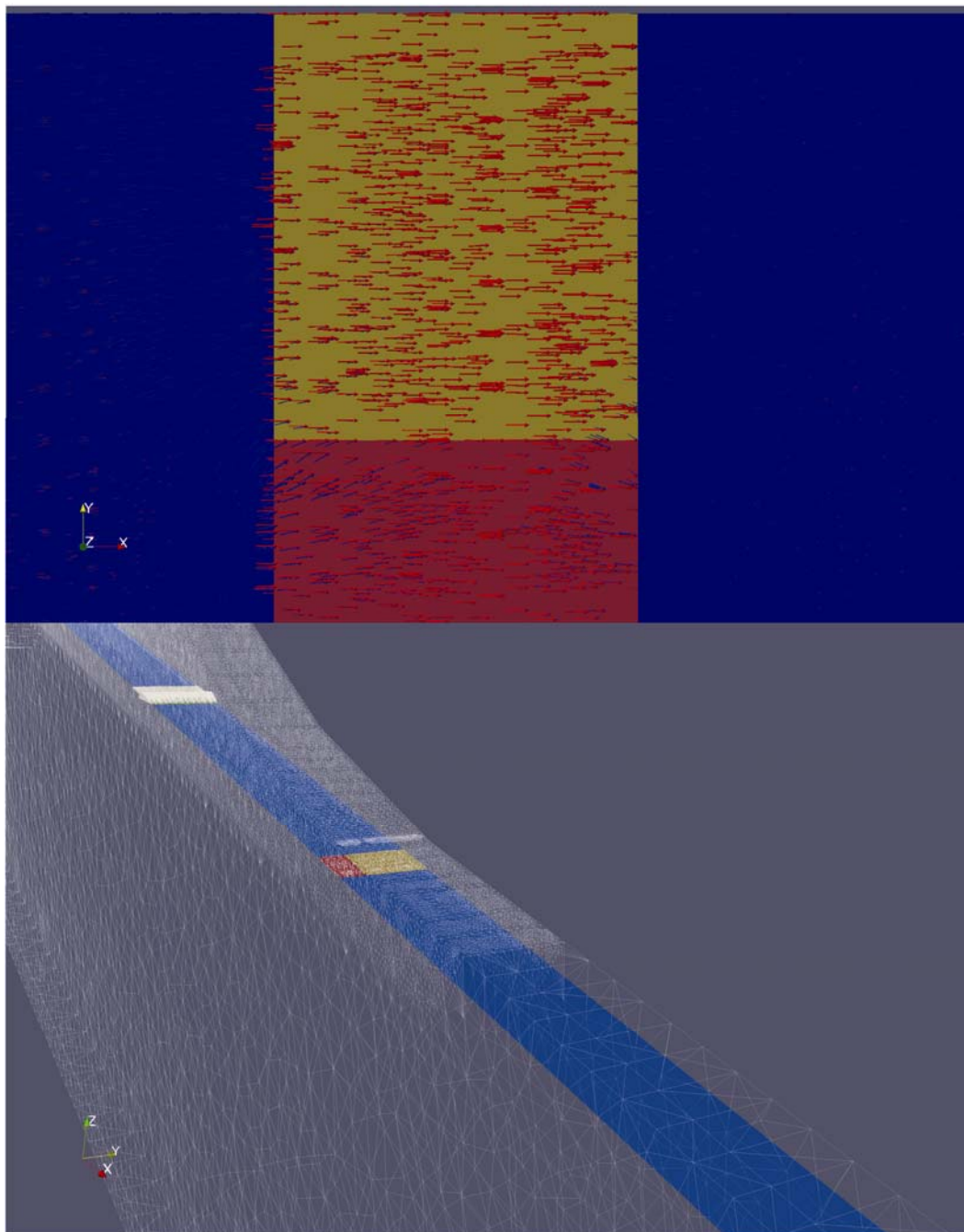


Figure 230. (Top) total head gradients for 2-D (red) and 3-D (blue) cases,  $\beta = 0.001$ , (Bottom) location of slice in the 3-D domain, Pocket Levee, Sacramento, CA.

Figure 235 shows a comparison between the 2-D (red) and 3-D (blue) total head contours in the vicinity of the woody vegetation zone. A small perturbation due to the effect of the 3-D woody vegetation zone is apparent, which decays rapidly away from the zone. The large-scale hydrodynamics of the 2-D and 3-D cases are essentially identical, as shown in Figure 236,

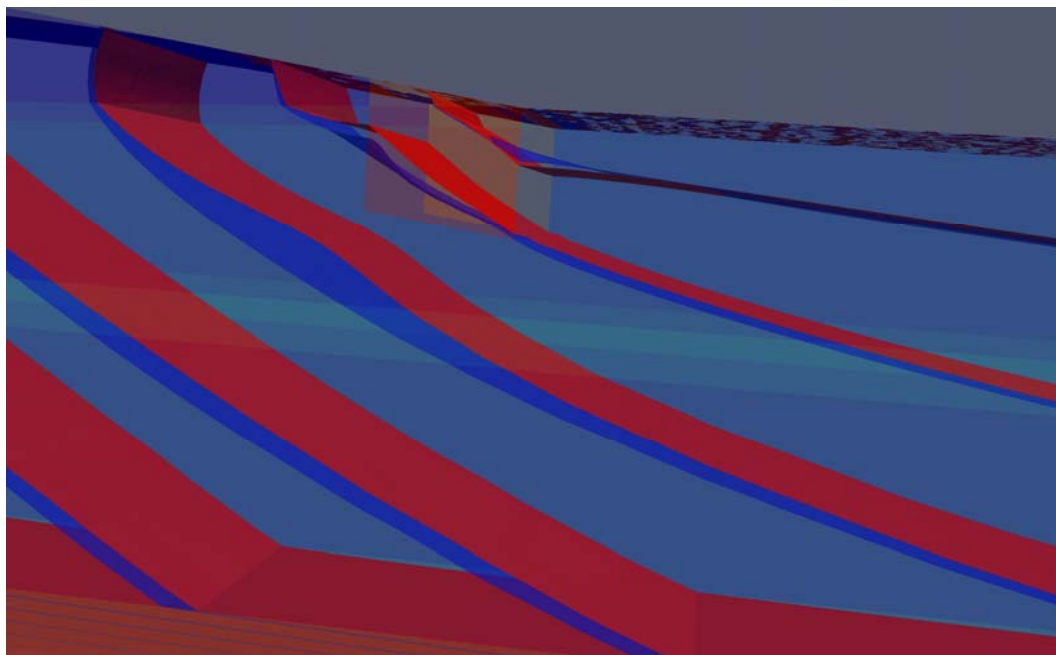


Figure 231. Total head contours of 2-D (red) and 3-D (blue) cases,  
 $\beta = 0.001$ , Pocket Levee, Sacramento, CA.

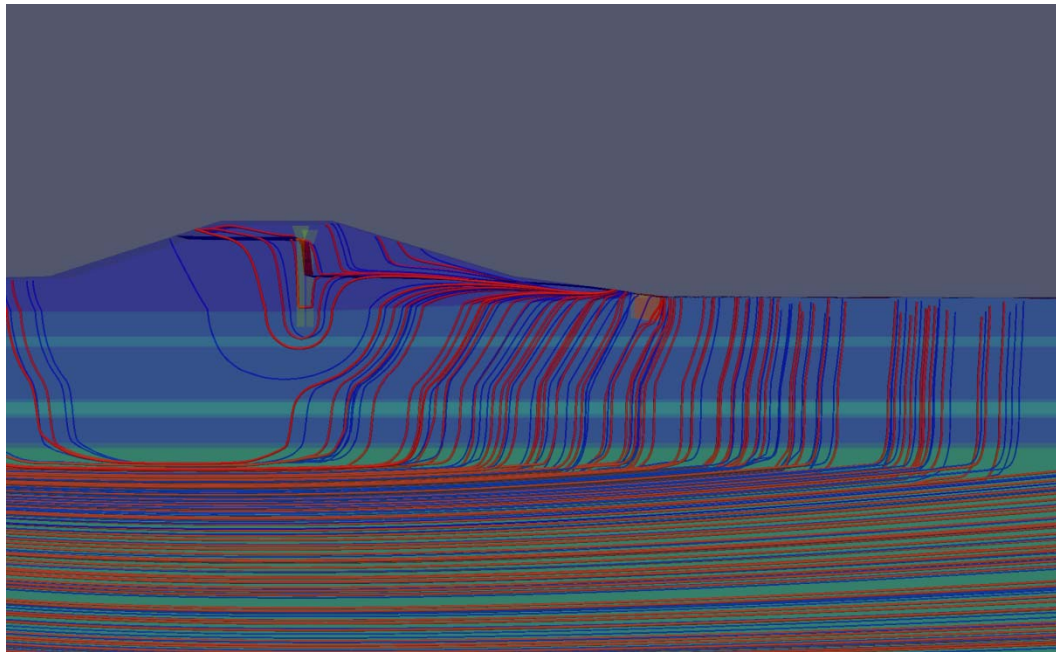


Figure 232. Phreatic surface and flow lines for 2-D (red) and 3-D  
(blue) cases,  $\beta = 0.001$ , Pocket Levee, Sacramento, CA.

where the 2-D and 3-D head contours and streamlines are superimposed. Figure 237 shows the total head gradients in a vertical plane through the woody vegetation zone for the 2-D and 3-D cases, which demonstrates again that the 2-D simulation closely approximates the 3-D data along that

plane. Figure 238 shows the superimposed total head contours for the less extreme case of  $\beta = 0.1$ . The “spottiness” of the surface is due to the fact that the 3-D rendering cannot cleanly differentiate between the 3-D contours (blue) and 2-D contours (red).

As an additional computational experiment, the same hydraulic conductivity sensitivity study was run using the first levee profile in Burlington, WA. Figures 239 through 244 contain visualizations of the cases  $\beta = 0.01$ , and  $\beta = 100.0$ . We see some local 3-D effects, but the deviations from the 2-D case do not appear to be significant.

### Complex root zone geometry

To address the impact of a more realistic root system geometry, a subset of the previous sensitivity analysis using the approximate soil-root zones, shown in Figures 227 and 228, is repeated. For simplicity, only the Pocket Levee domain with a 5-ft clay blanket and no slurry wall is considered, which represents a limiting case. Figure 245 shows the root system location at the levee toe and the intersection of the sinker roots with the bottom of the clay blanket (see Figure 229 for the full levee domain).

As in the previous analysis, saturated hydraulic conductivity for the soil-root region is scaled across several orders of magnitude, and a steady-state seepage analysis assuming a flood stage of 29 ft is performed. Figures 246 through 248 illustrate the impact of different setting scaling factors, ( $\beta = 1$ ,  $0.01$ , and  $100$ ) on subsurface flow and pressure distributions in the levee for the highest resolution computational mesh (Level 3). Each plot contains a contour for the phreatic surface, as well as 1-ft total head contours between the flood stage (left), a boundary condition of 29 ft, and a right boundary value of 12 ft specified at  $x = 2500$  ft. In addition, select flow lines passing through planes at  $x = 400$  ft and  $x = 530$  ft are included. Flow lines are colored by the pressure head gradient, which is shown in the color bar of each figure. Figures 249 through 251 provide a closer view at the level toe.

As with the 2-D and 3-D seepage results for the block root zone geometries, changing  $\beta$  over several orders of magnitude had only a minor impact on the bulk flow. For example, the flow line exit points are shifted slightly in the negative  $x$  direction for  $\beta > 1$  and in the positive  $x$  direction for  $\beta < 1$ . A similar effect can be seen in the total head contours as well.

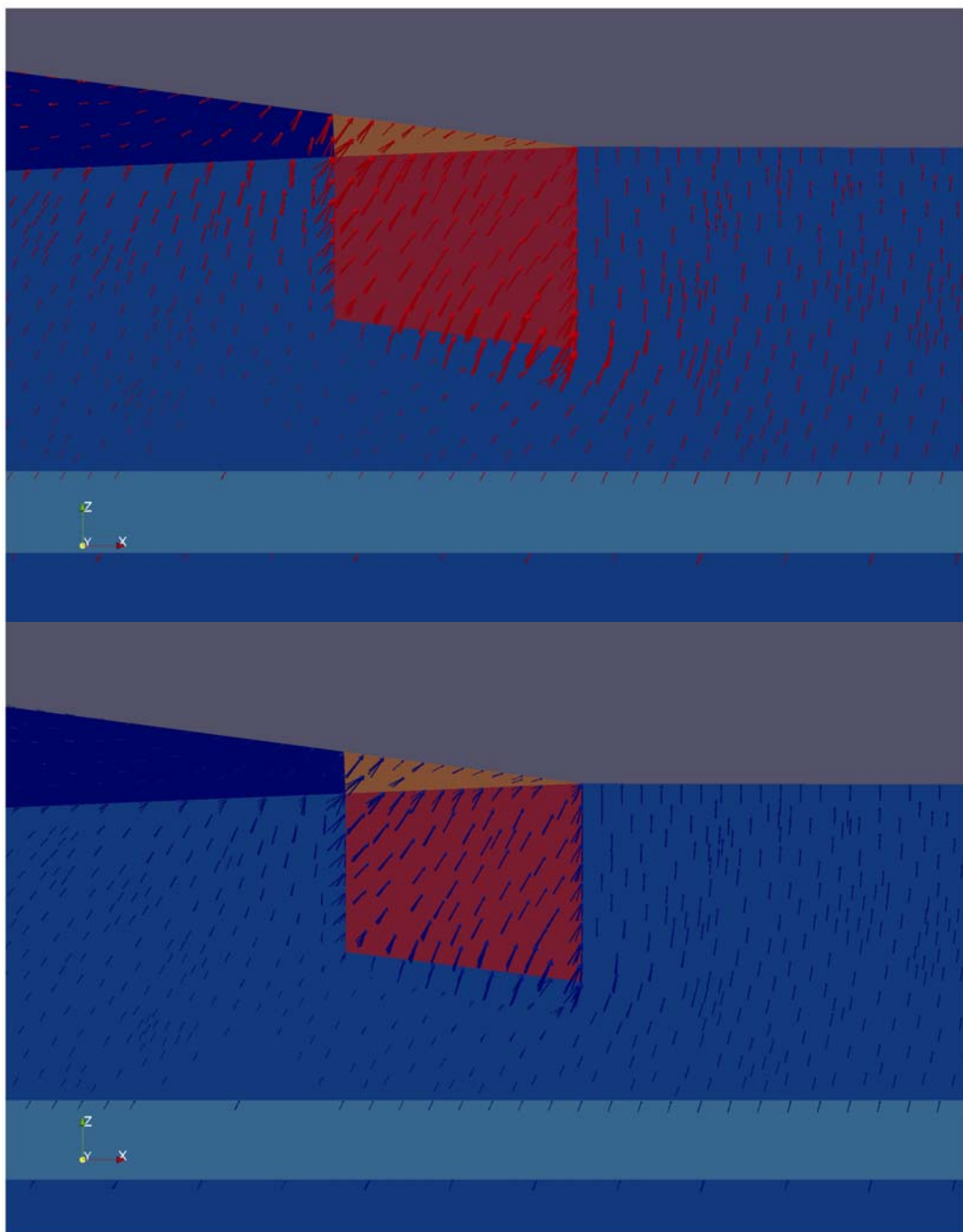


Figure 233. Total head gradients in 2-D (red, top) and 3-D (blue, bottom) cases along the plane  $y = 0$ ,  $\beta = 0.001$ , Pocket Levee, Sacramento, CA.

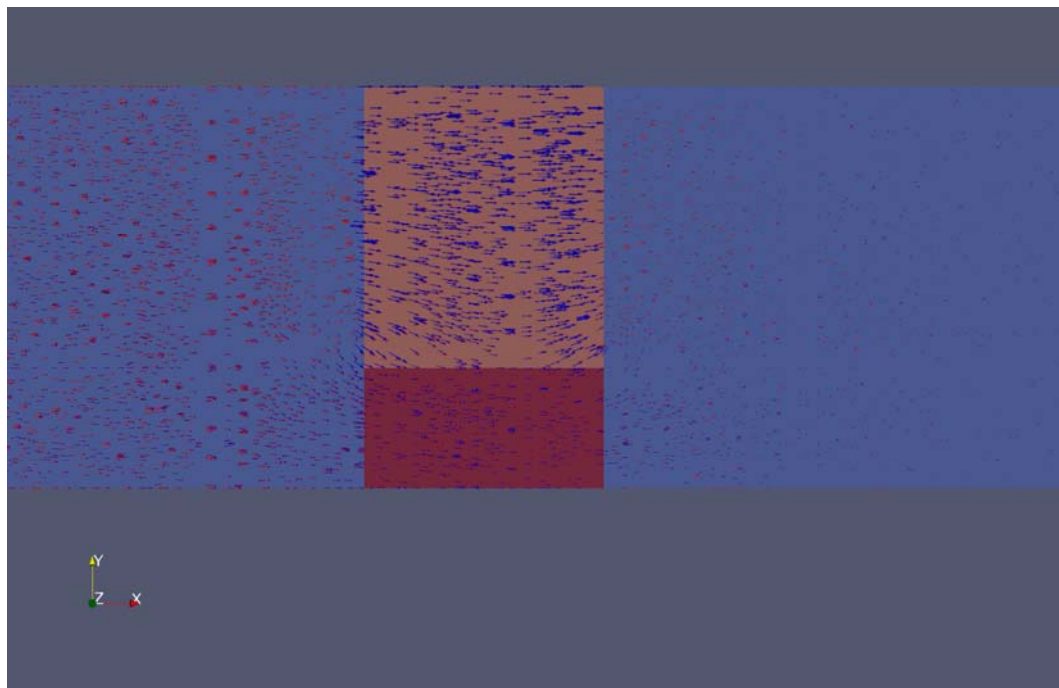


Figure 234. Total head gradients for 2-D (red) and 3-D (blue) cases,  
 $\beta = 1000.0$ , Pocket Levee, Sacramento, CA.

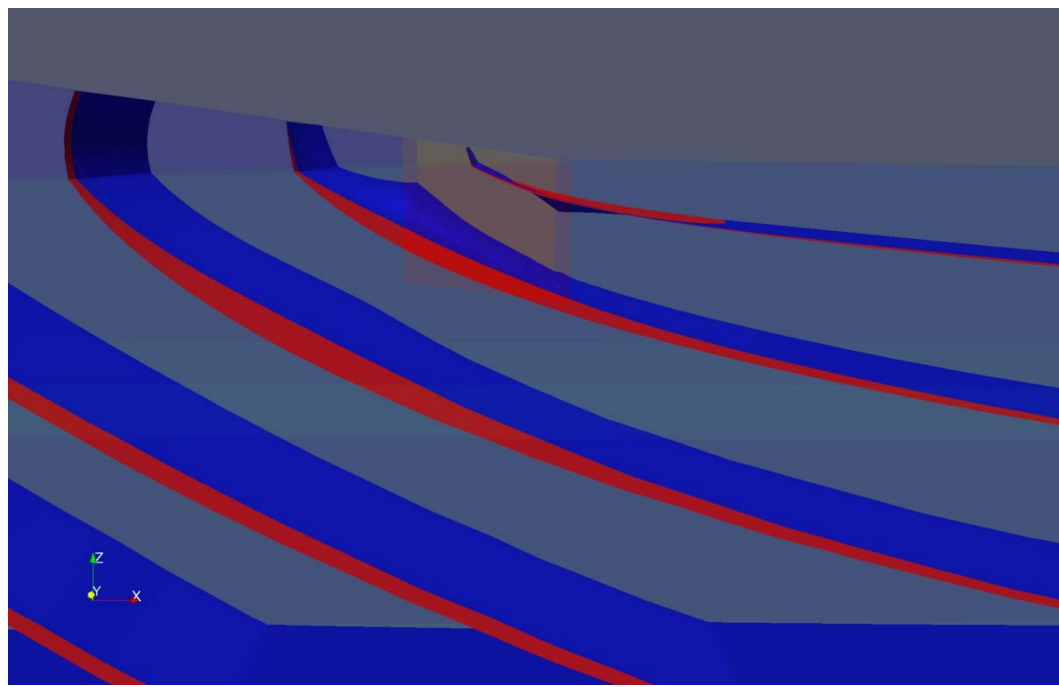


Figure 235. Total head contours of 2-D (red) and 3-D (blue) cases,  
 $\beta = 1000.0$ , Pocket Levee, Sacramento, CA.

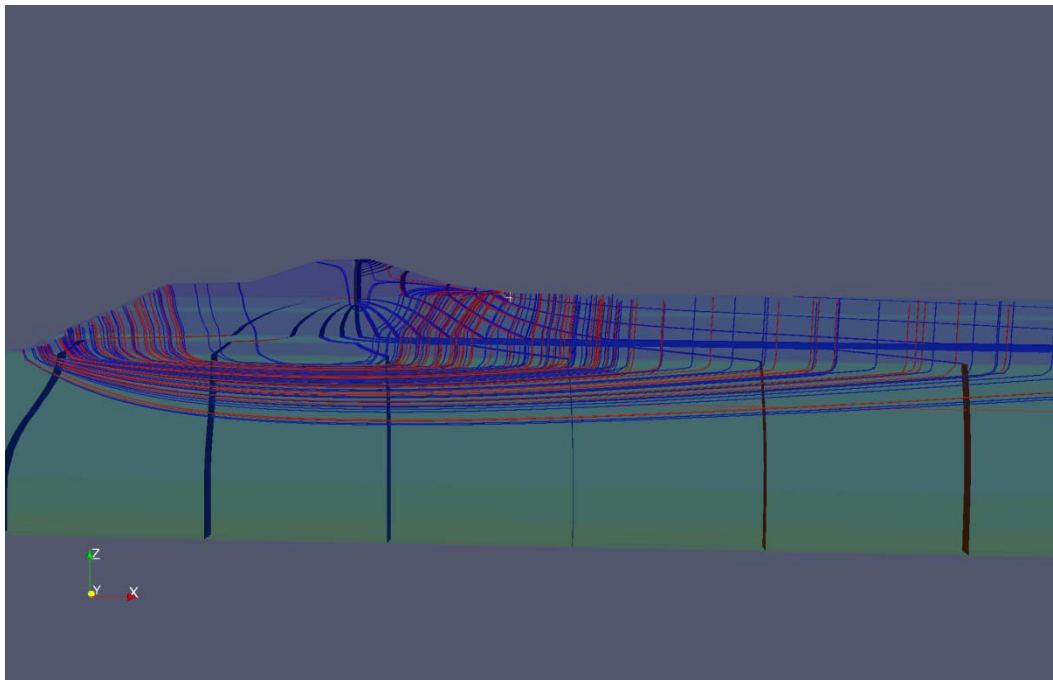


Figure 236. Phreatic surface and flow lines for 2-D (red) and 3-D (blue) cases,  $\beta = 1000.0$ , Pocket Levee, Sacramento, CA.

Although varying the hydraulic conductivity scaling had a relatively minor impact on the global (levee) scale subsurface flow and head distribution,  $\beta$  did affect the local behavior around the root zone. The impact of  $\beta$  on pressure head gradients in the root-zone can be seen more clearly in Figure 252, where the pressure head gradient is projected onto the root surface for the Level 2 mesh. In the unmodified case ( $\beta = 1$ ), gradients increase through the clay layer as one would expect. Gradient distribution for the vertical sinker roots, which puncture the clay blanket, remains similar for  $\beta = 100$ , but the overall gradient across the areal extent of the root system decreases. The reverse is seen for  $\beta < 1$ , where there is a marked increase in pressure gradients across the root system. Results are shown only for the intermediate level of refinement because pressure distributions and gradients were very similar for the finest level of refinement.

Figure 253 illustrates the groundwater velocity distribution near the root zone for the unmodified case ( $\beta = 1$ ). Although decreasing  $\beta$  increased pressure and exit gradients across the root zone significantly, it had little effect on subsurface velocities (see Figure 254, which compares velocity fields for  $\beta = 1$  and  $\beta = 0.01$ ). On the other hand, when  $\beta = 100$ , the soil-root zone served as a high conductivity pathway through the clay blanket,

and local focusing of velocities is seen around the roots and much greater velocity magnitudes in Figure 255.

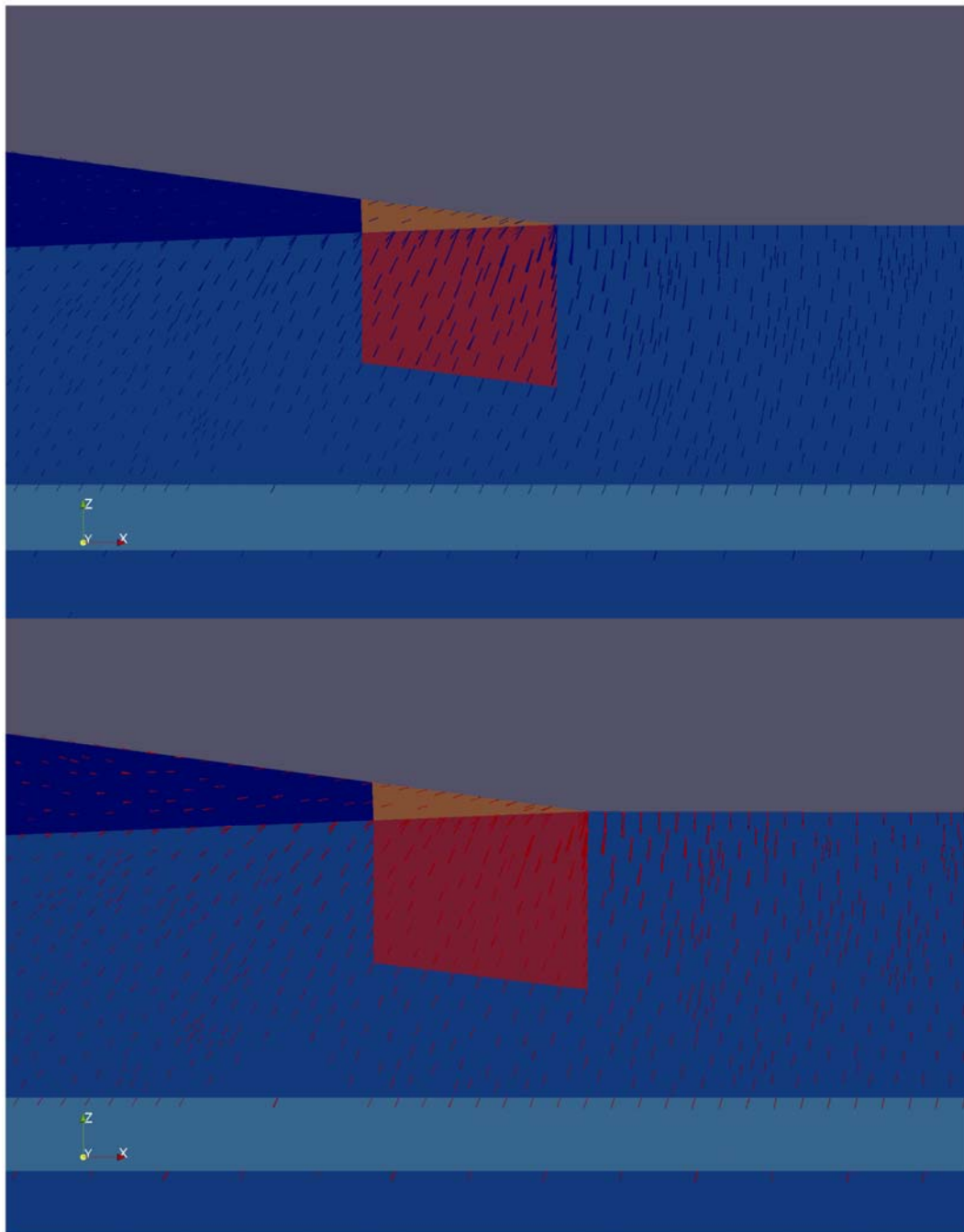


Figure 237. Total head gradients for 2-D (red, top) and 3-D (blue, bottom) cases along the plane  $y = 0$ ,  $\beta = 1000.0$ , Pocket Levee, Sacramento, CA.

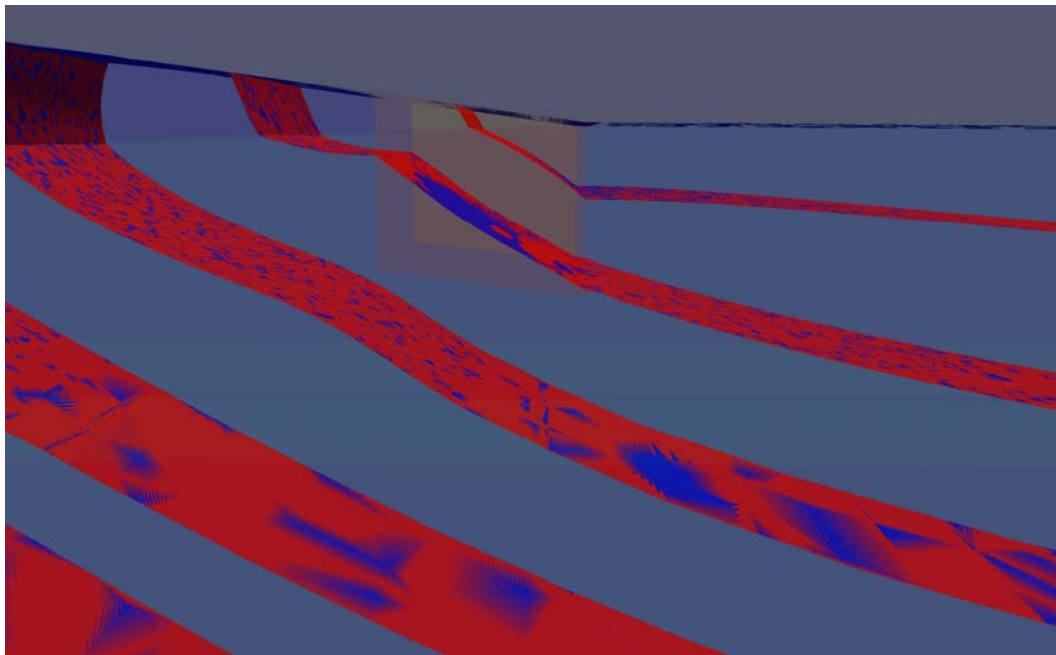


Figure 238. Total head contours of 2-D (red) and 3-D (blue) cases,  
 $\beta = 0.1$ , Pocket Levee, Sacramento, CA.

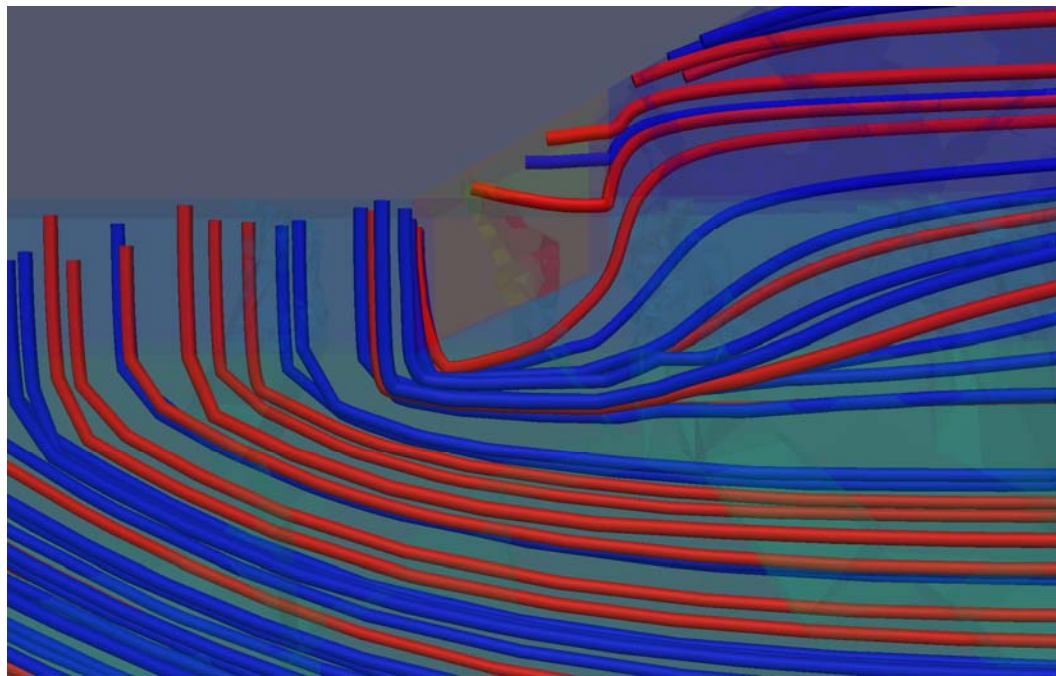


Figure 239. Flow lines for 2-D (red) and 3-D (blue) test cases near the  
woody vegetation zone,  $\beta = 0.01$ , Levee Profile 1, Burlington, WA.

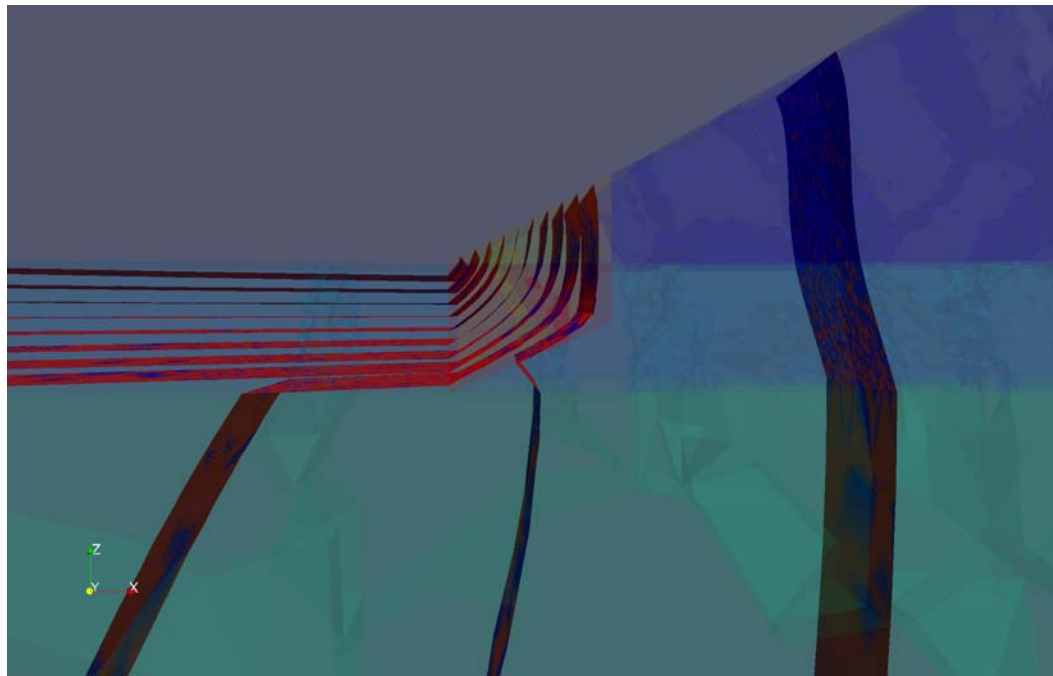


Figure 240. Total head contours near the woody vegetation zone,  
 $\beta = 0.01$ , Levee Profile 1, Burlington, WA.

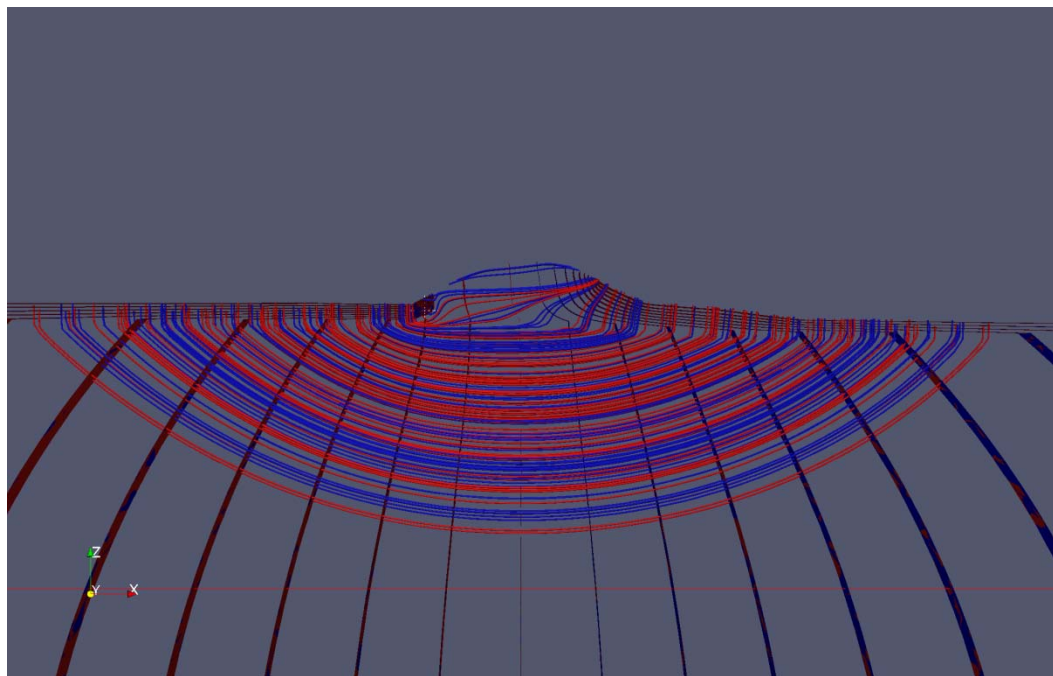


Figure 241. Total head contours and flow lines for 2-D (red) and 3-D (blue)  
test cases,  $\beta = 10.0$ , Levee Profile 1, Burlington, WA.

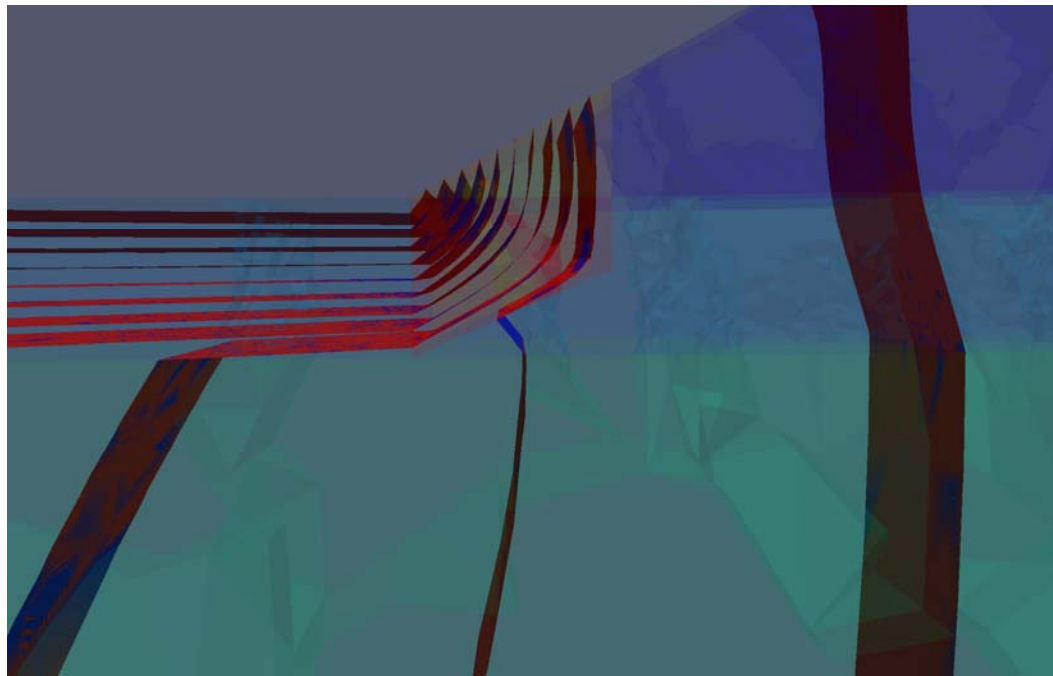


Figure 242. Total head contours for 2-D (red) and 3-D (blue) cases near the woody vegetation zone,  $\beta = 10.0$ , Levee Profile 1, Burlington, WA.

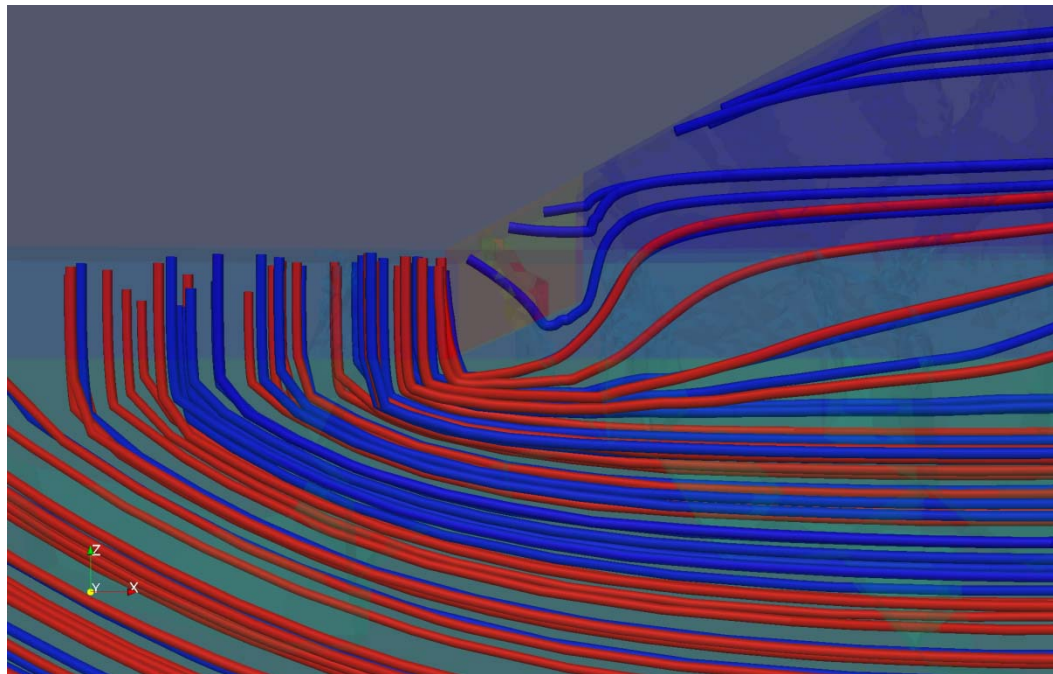


Figure 243. Flow lines for 2-D (red) and 3-D (blue) cases near the woody vegetation zone,  $\beta = 10.0$ , Levee Profile 1, Burlington, WA.

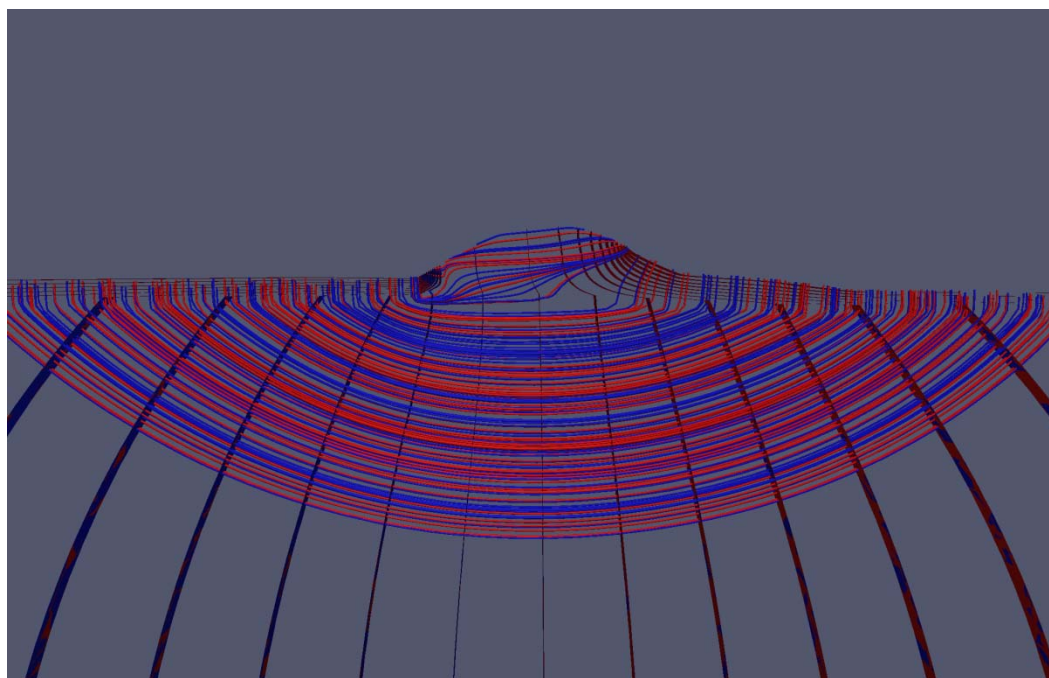


Figure 244. Phreatic surface and flow lines for 2-D (red) and 3-D (blue) cases,  $\beta = 0.01$ , Levee Profile 1, Burlington, WA.

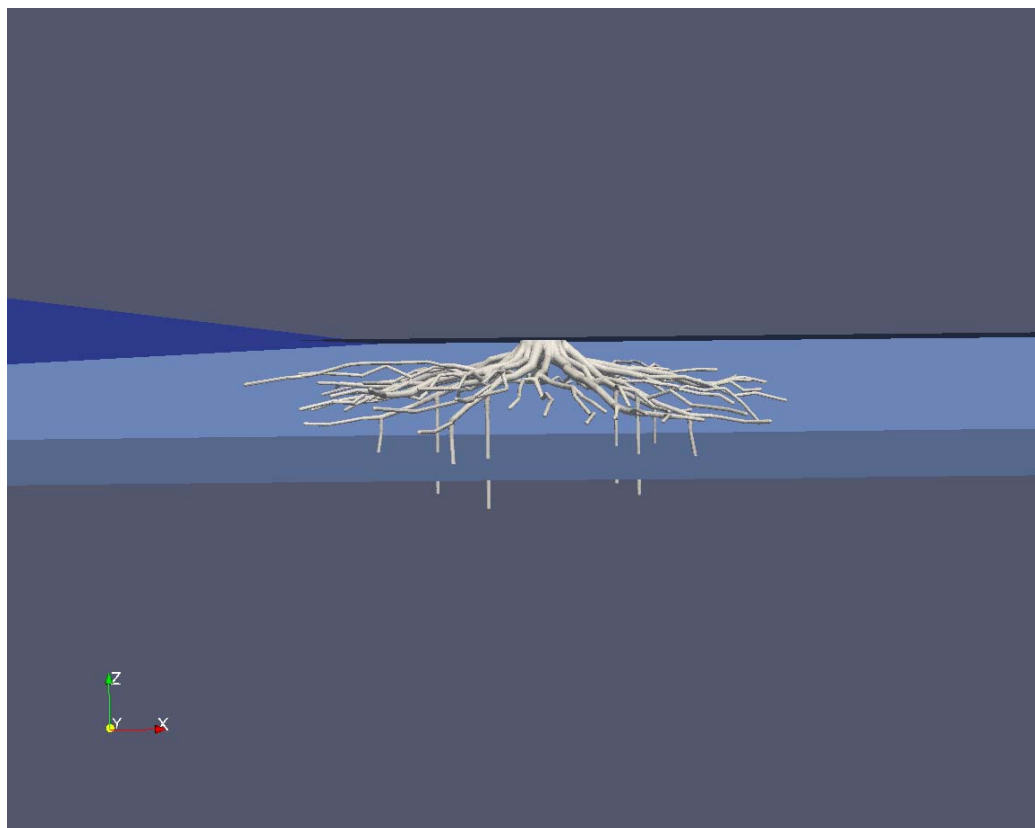


Figure 245. Intersection of the root system at the levee toe with the clay blanket, Pocket Levee, Sacramento, CA.

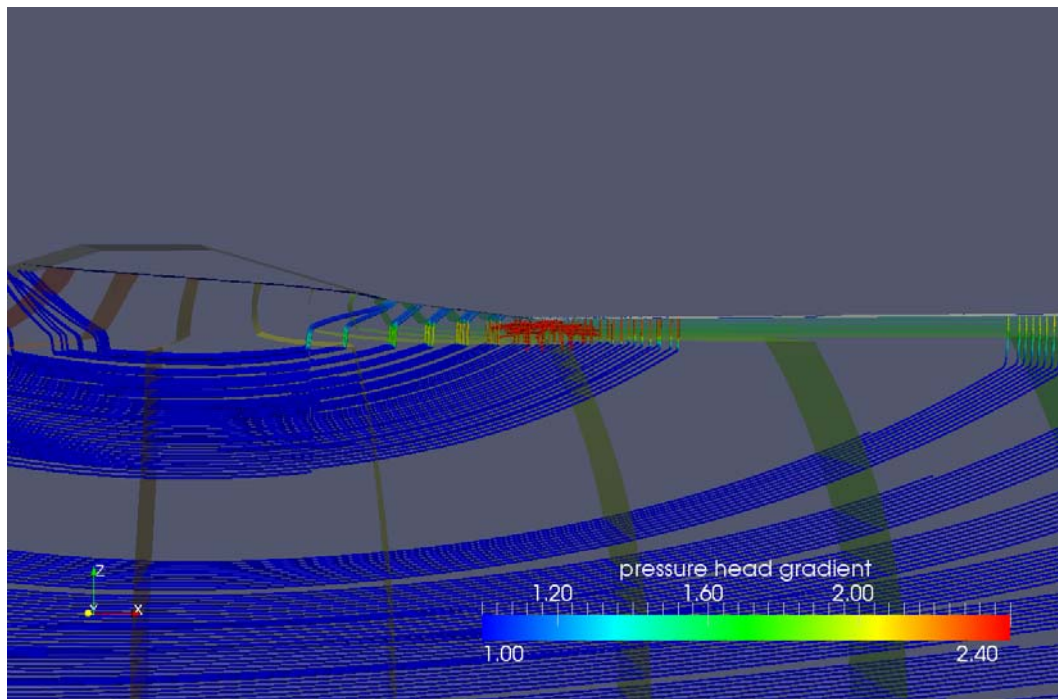


Figure 246. Phreatic surface with total head contours and flow lines colored by pressure head gradient,  $\beta = 1$ , Pocket Levee, Sacramento, CA.

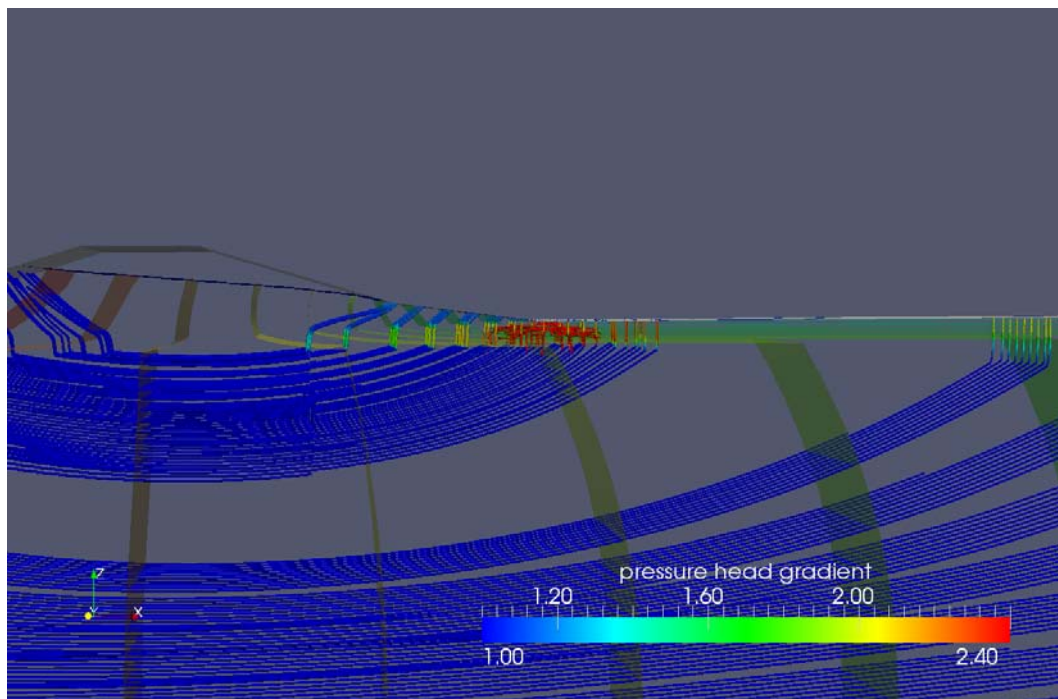


Figure 247. Phreatic surface with total head contours and flow lines colored by pressure head gradient,  $\beta = 100$ , Pocket Levee, Sacramento, CA.

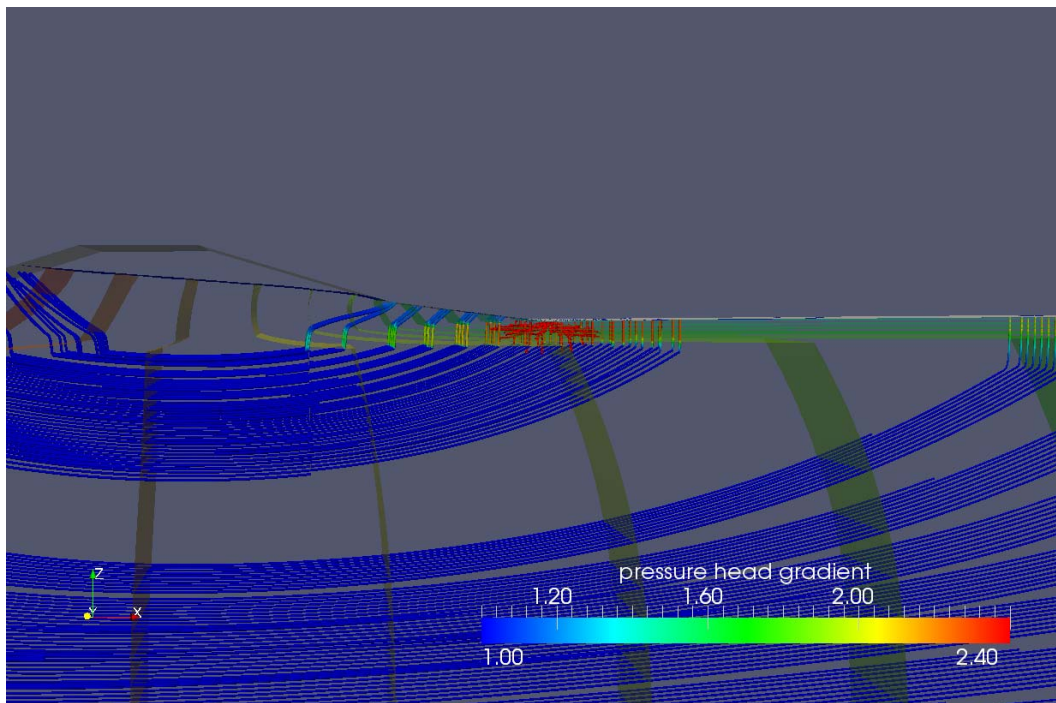


Figure 248. Phreatic surface with total head contours and flow lines colored by pressure head gradient,  $\beta = 0.01$ , Pocket Levee, Sacramento, CA.

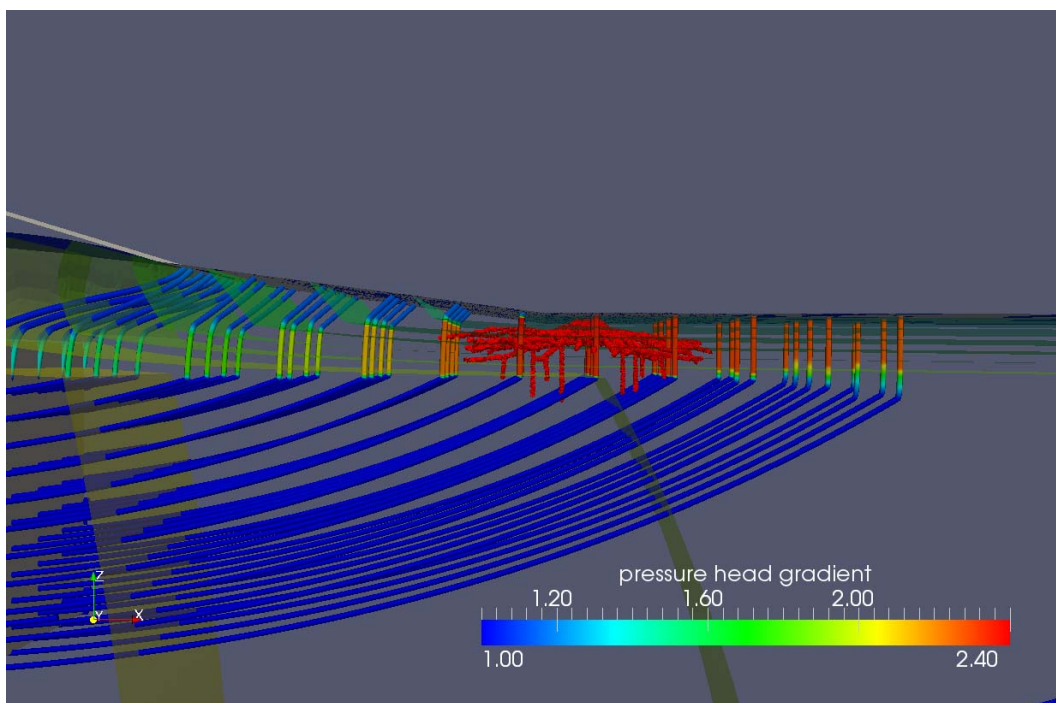


Figure 249. Close-up of soil-root region,  $\beta = 1$  (unmodified case),  
Pocket Levee, Sacramento, CA.

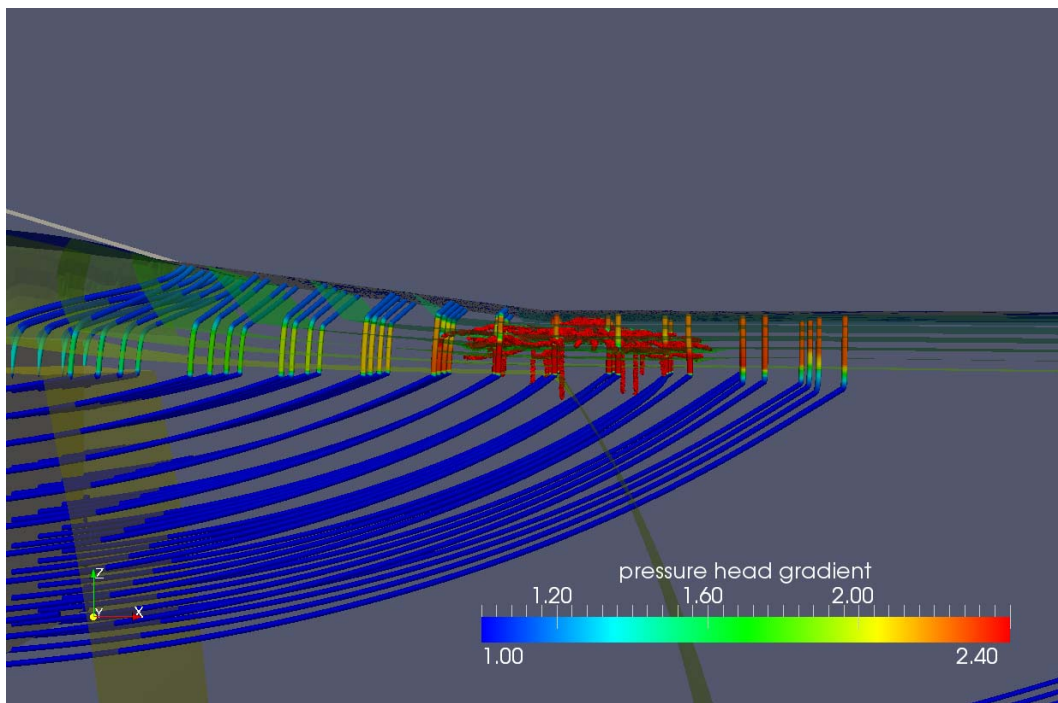


Figure 250. Close-up of soil-root zone,  $\beta = 100$ ,  
Pocket Levee, Sacramento, CA.

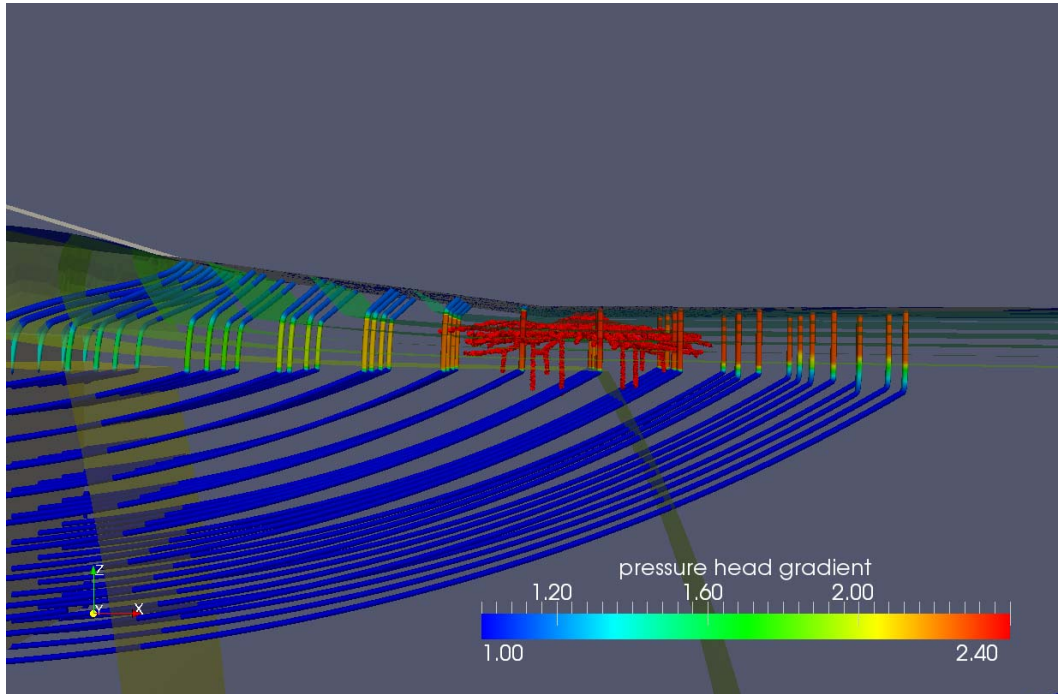


Figure 251. Close-up of soil-root zone,  $\beta = 0.01$ ,  
Pocket Levee, Sacramento, CA.

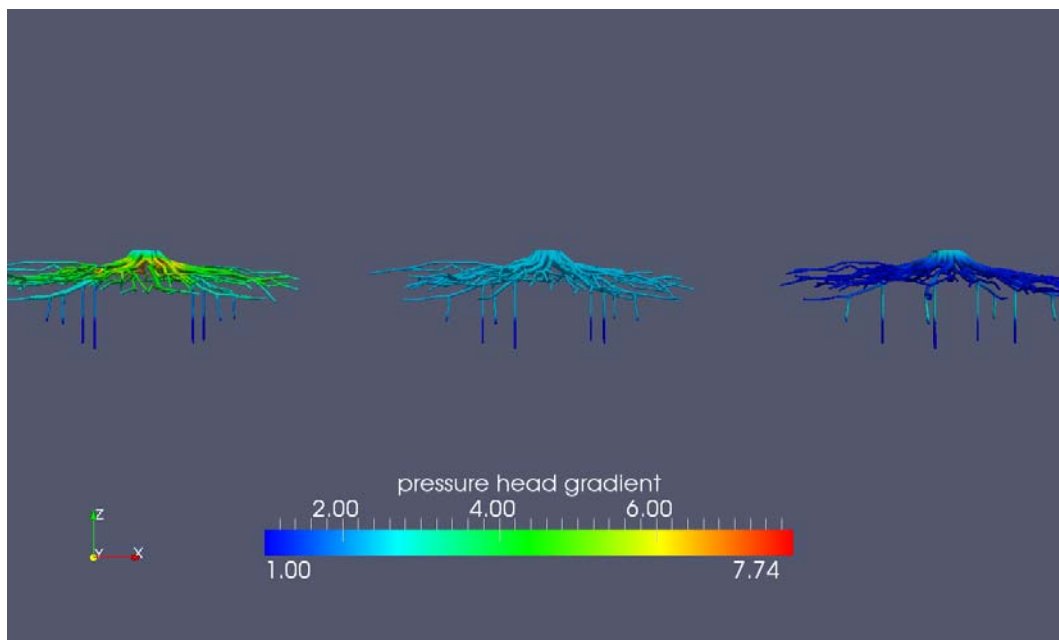


Figure 252. Root geometry with projected pressure head gradient,  
 $\beta = 0.01, 1$ , and  $100$ , Level 2, Pocket Levee, Sacramento CA.

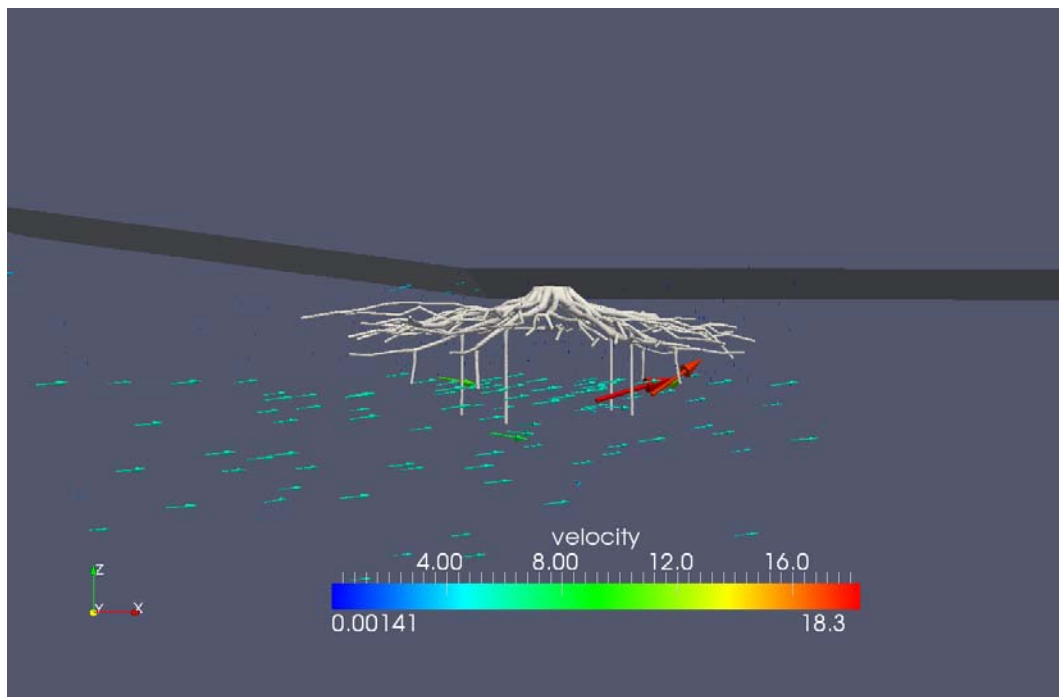


Figure 253. Groundwater velocity field in (ft/day) around root zone,  $\beta = 1$   
(unmodified case), Pocket Levee, Sacramento, CA.

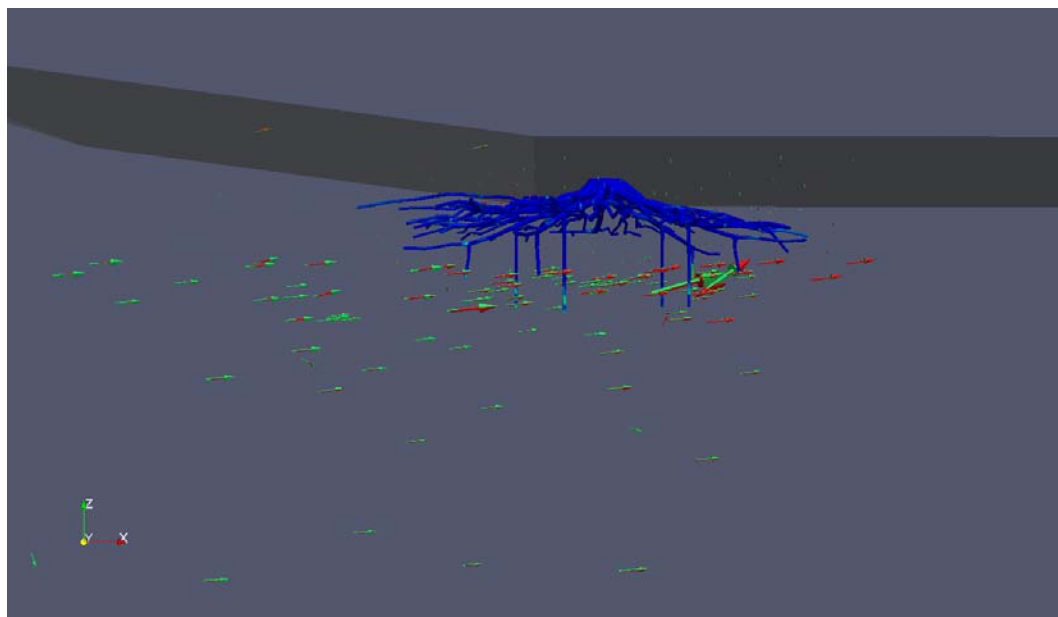


Figure 254. Comparison of groundwater velocity field around soil-root zone for unmodified case (red) and  $\beta = 0.01$  (green), Pocket Levee, Sacramento, CA.

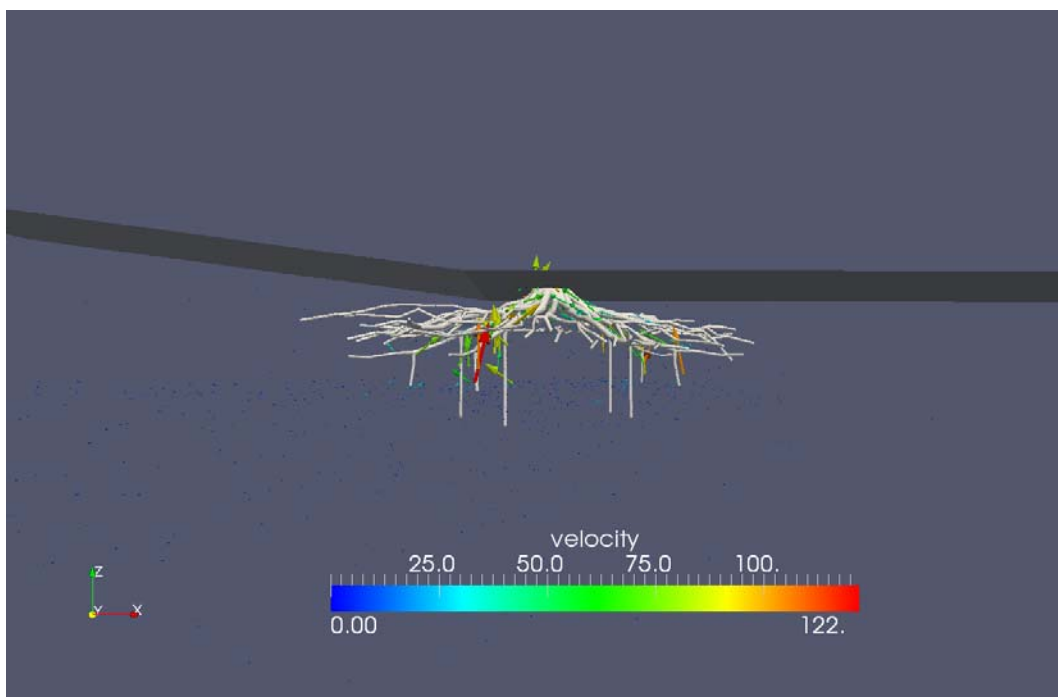


Figure 255. Groundwater velocity field in (ft/day) around root zone for  $\beta = 100$ , Pocket Levee, Sacramento, CA.

For further comparison to the 2-D work, we also provide the following table of values near the toe of the levee in Figures 256 through 258.

	$\beta_r = 1$	$\beta_r = 0.01$	$\beta_r = 100$
Level 0	$\bar{\nabla}h/\nabla h_{max}$		
$\bar{\nabla}h/\nabla h_{max}$	1.40/1.54	1.27/1.55	1.52/3.29
Level 1	$\bar{\nabla}h/\nabla h_{max}$		
$\bar{\nabla}h/\nabla h_{max}$	1.35/1.55	1.15/1.56	1.38/3.23
Level 2	$\bar{\nabla}h/\nabla h_{max}$		
$\bar{\nabla}h/\nabla h_{max}$	1.35/1.60	1.31/1.59	1.25/2.52

Figure 256. Average and maximum total head gradients at levee toe excluding vegetated region.

	$\beta_r = 1$	$\beta_r = 0.01$	$\beta_r = 100$
Level 0	$\bar{\nabla}h/\nabla h_{max}$		
$\bar{\nabla}h/\nabla h_{max}$	1.40/1.54	1.28/2.54	1.51/3.28
Level 1	$\bar{\nabla}h/\nabla h_{max}$		
$\bar{\nabla}h/\nabla h_{max}$	1.35/1.55	1.16/3.27	1.37/3.19
Level 2	$\bar{\nabla}h/\nabla h_{max}$		
$\bar{\nabla}h/\nabla h_{max}$	1.35/1.60	1.30/1.59	1.25/2.30

Figure 257. Average and maximum total head gradients at levee toe.

	$\beta_r = 1$	$\beta_r = 0.01$	$\beta_r = 100$
Level 0	$\bar{\psi}$ [psf]		
$\bar{\psi}$ [psf]	740.	741.	719.
Level 1	$\bar{\psi}$ [psf]		
$\bar{\psi}$ [psf]	724.	726.	707.
Level 2	$\bar{\psi}$ [psf]		
$\bar{\psi}$ [psf]	726.	725.	718.

Figure 258. Average pressure at base of clay blanket beneath root zone.

### Cutout domain seepage and stability

In the finite element-based slope stability analysis following Griffiths and Lane (1999), the shear strength properties at every quadrature point are modified by a Strength Reduction Factor (SRF) using the relations

$$C'f = c' / FOS \quad (17)$$

$$\varphi'f = \arctan\left(\frac{\tan\varphi'}{FOS}\right) \quad (18)$$

where  $c$  is the cohesion and  $\varphi$  is the friction angle of the material, and the quantities with the asterisks are used in the model. The SRF was incrementally increased until failure occurs. In Griffiths and Lane (1999), failure is identified with a sudden increase in the displacements that prevents convergence of the quasi-equilibrium step of the nonlinear material code. Thus, the maximum SRF is essentially defined as the point at which the nonlinear iteration fails, but this result can be cross-checked with a plot of the maximum displacement versus SRF and the solution to demonstrate that the slope is clearly approaching failure before the step is taken that causes nonlinear iteration failure. The factor of safety is then identified with the maximum SRF. Thus, each factor of safety computation is composed of a sequence of soil mechanics simulations. Because both the 2-D analysis and the 3-D seepage analysis identified the levee toe as a region of likely instability and of high pore pressure gradients, the root system is again placed near the levee toe (Figure 259), and the hydraulic conductivity is scaled by  $\beta = 0.0001$  to approximate nearly impermeable roots.

As Figure 260 shows, the overall seepage characteristics for this configuration are similar to the results above. Looking more closely at the root zone in Figure 261, it shows significant local distortion in the total head contours due to the effect of the low permeability in the root zone. The effect on the flow can be seen more clearly in Figures 262 and 263, where flow lines are clearly curving around the roots and pressure head gradients are significantly elevated.

To study the effect of tree roots on the stability of the slope, the friction angle is set to zero, and the cohesion and Young's modulus is modified by factors of  $\Gamma = 1, 10, 100$ , and  $1000$ . The initial configuration, where the root system has the same cohesion and Young's modulus ( $\Gamma = 1$ ), is given in Figure 264. Because the root system has the same strength as the surrounding , the three-dimensional failure mode is due to the higher clay

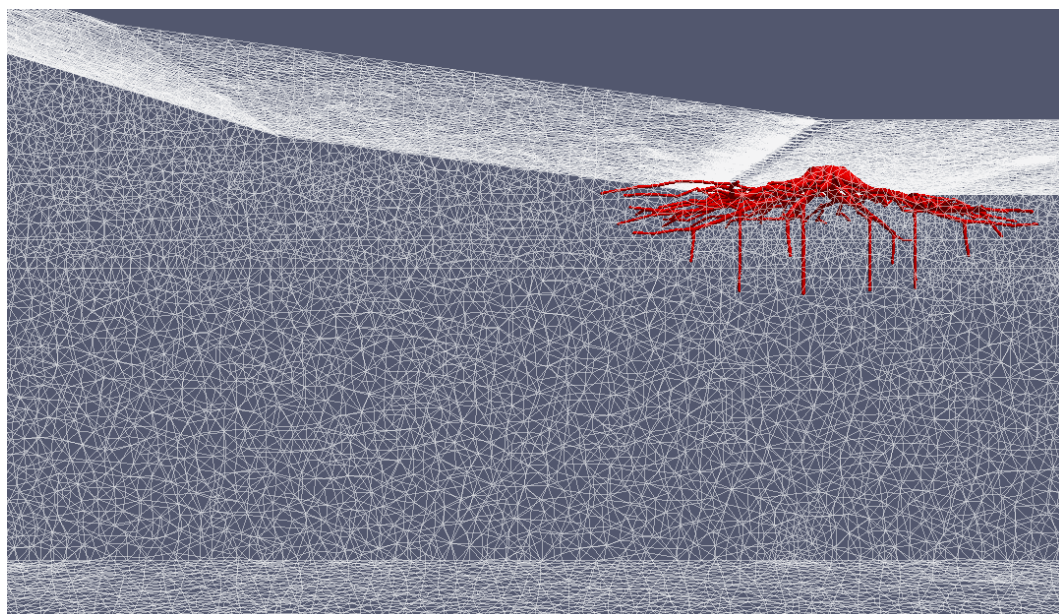


Figure 259. Root system location at levee toe.

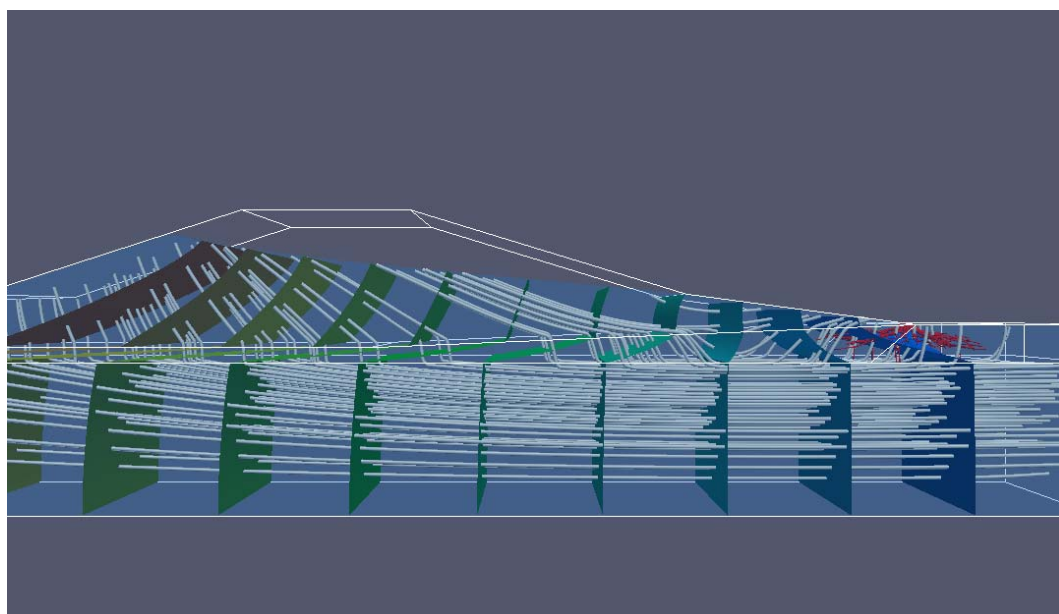


Figure 260. Cutout domain contours (1-ft intervals) and flow lines.

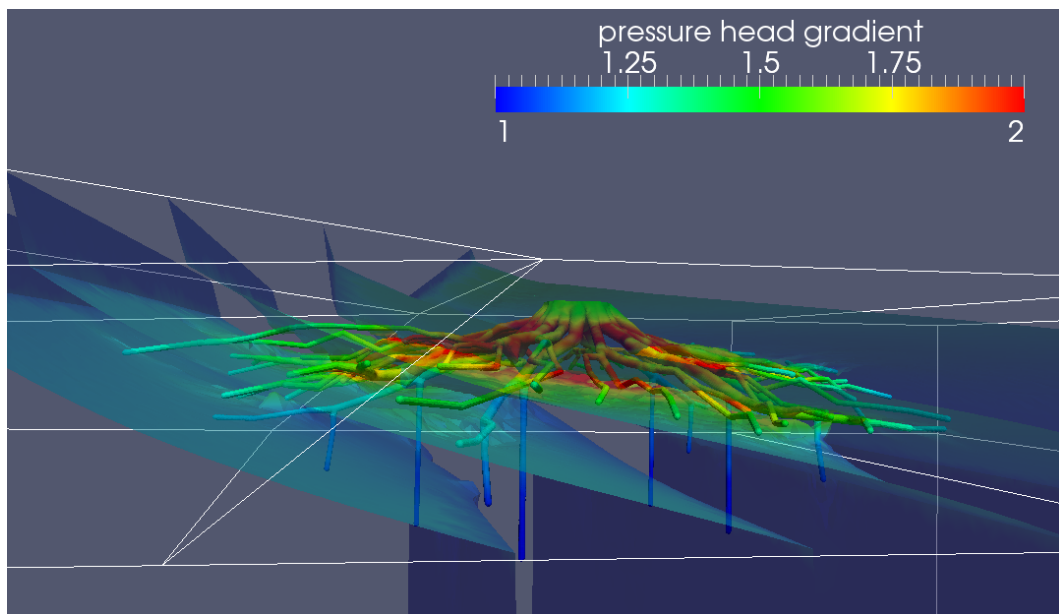


Figure 261. Total head contours and pressure head gradients in root zone.

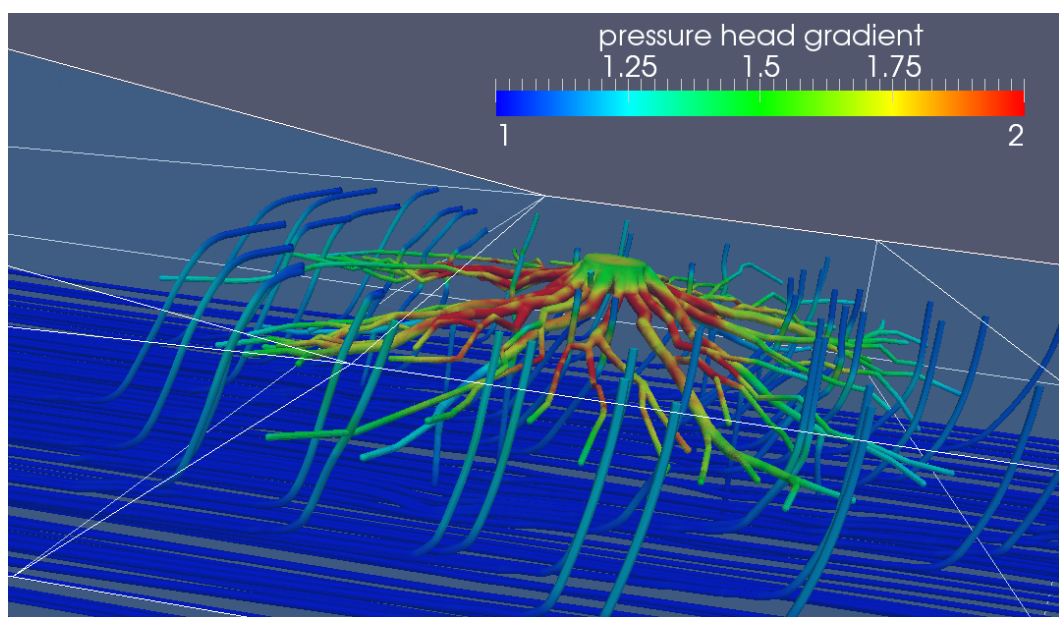


Figure 262. Root zone flow lines and pressure head gradients.

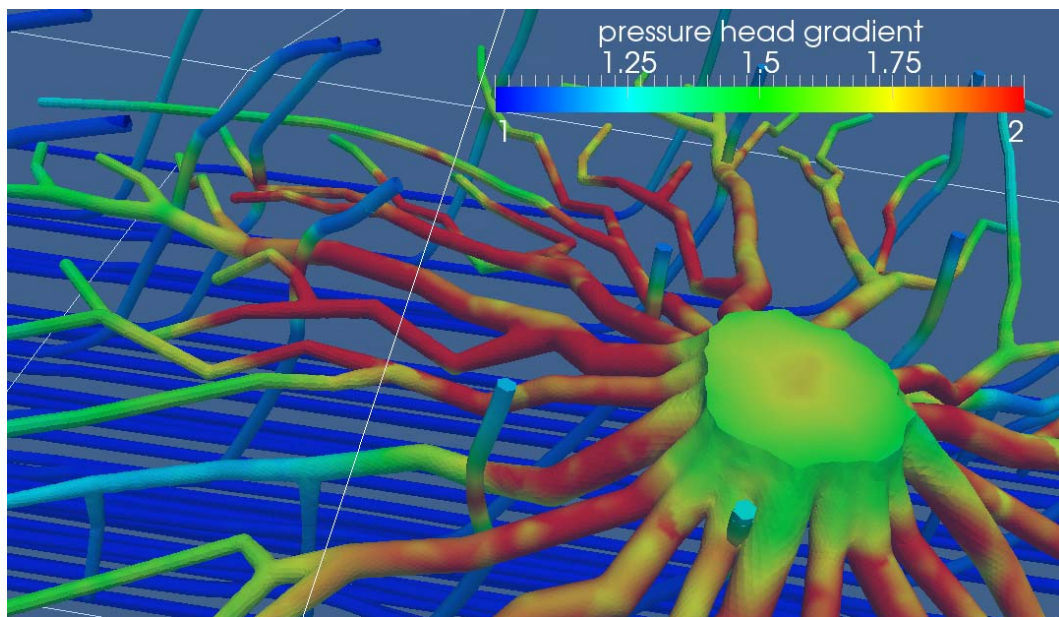


Figure 263. Close-up of root zone flow lines and pressure head gradients with large three-dimensional effects on the flow lines.

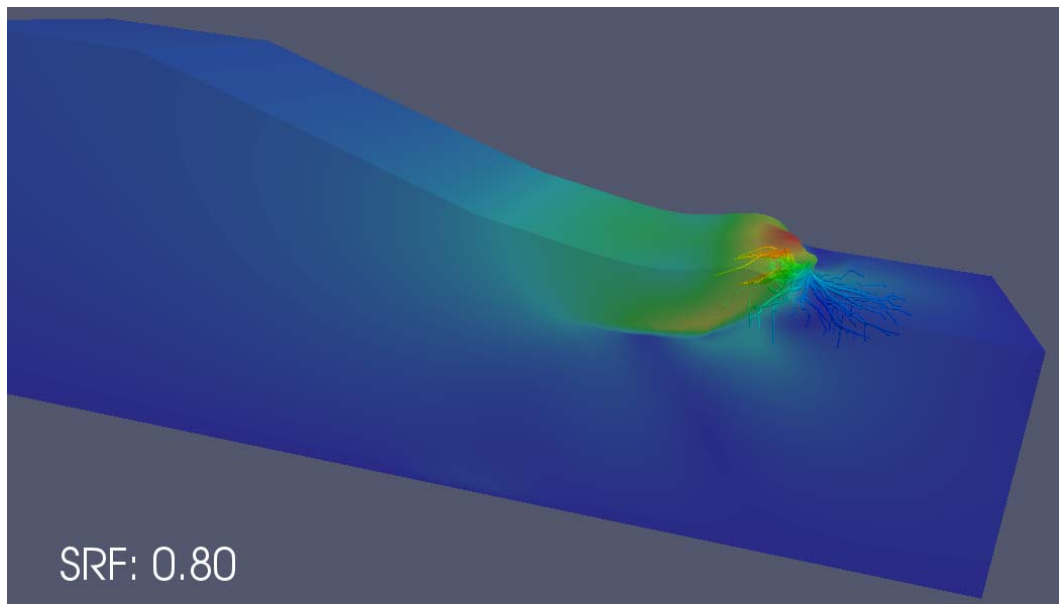


Figure 264. Scaled deformation at failure (SRF=factor of safety=0.80) for the case  $\Gamma = 1$ .

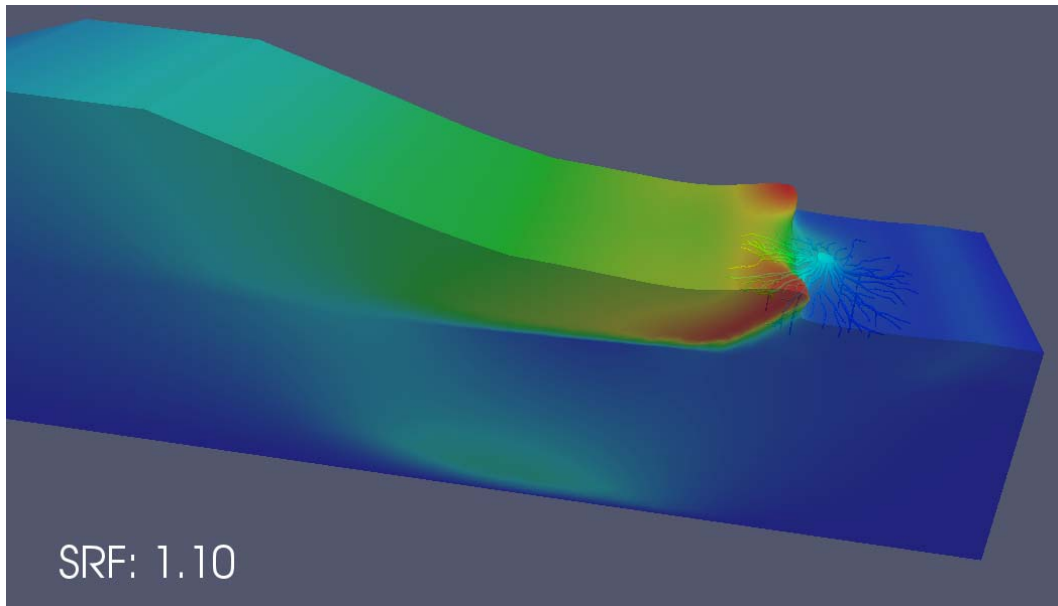


Figure 265. Scaled displacements at failure (SRF = factor of safety = 1.10) for  $\Gamma = 1000$ .

pore pressure gradients in the neighborhood of the roots. For reference, the “base” case is also simulated (Figure 266) where the root system parameters were set equal to the surrounding clay both seepage and stability ( $\beta = \Gamma = 1$ ), which yielded a factor of safety of 0.9, indicating that the increased pressure gradients due to the lower permeability representation of the roots could have some effect on factor of safety by lowering it.

For the remaining cases where the root system is strengthened by factors of  $\Gamma = 10, 100$ , and  $1000$ , the factor of safety increased to 1.1. Figure 265 shows the failure surface clearly forming in the separation zone and soil containing few roots. Table 88 provides a summary of the sensitivity study of root system strength.

## Discussion

The three-dimensional analysis clearly shows the potential for local modifications to the seepage and soil mechanics. Without more detailed characterization of the actual material properties (hydraulic and structural) of the root-soil system, it is difficult to make precise conclusions. If the root-soil system has significantly enhanced strength, then the sensitivity study indicates that the factor of safety would be increased, as fits with common intuition. On the other hand, if the root-soil system has significantly reduced permeability without significantly enhanced strength, then the factor of safety could actually be reduced due to the higher pressure

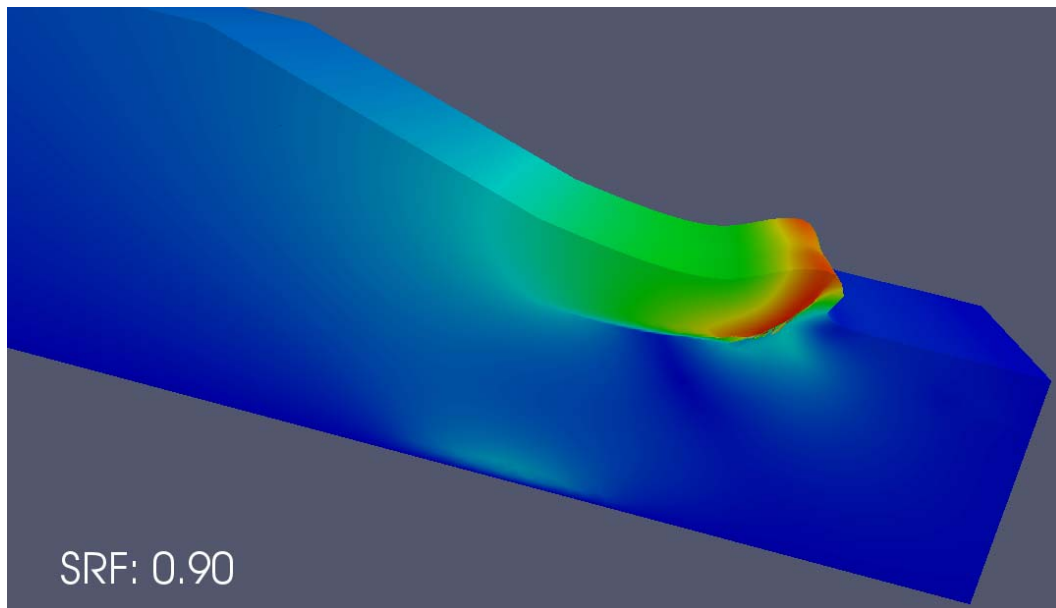


Figure 266. Scaled displacements at failure (SRF = factor of safety = 0.90) for  $\Gamma = 1$  and  $\beta = 1$ .

Table 88. Stability sensitivity study to root system strength.

Unmodified root system	$\beta = \Gamma = 1$	FS=0.9
Low permeability root system and unmodified strength	$\beta = 0.001 \quad \Gamma = 1$	FS=0.8
Low permeability and strengthened root system	$\beta = 0.001 \quad \Gamma = 10$	FS=1.1
Low permeability and strengthened root system	$\beta = 0.001 \quad \Gamma = 100$	FS=1.1
Low permeability and strengthened root system	$\beta = 0.001 \quad \Gamma = 1000$	FS=1.1

FS = factor of safety.

gradients. Modeling cannot be used to its fullest potential because of the need for more precise material characterization through both measurements and constitutive theory for root-soil systems.

From the three-dimensional analysis, the following observations were made:

- Root system effects on the hydrodynamics are local (confined to the root system). Large-scale seepage characteristics like the location of seepage face are not affected, which validates the use of 2-D seepage models for determining seepage behavior at the large (levee) scale.

- Large local increases in pore pressure gradients may occur if the root system is assumed to cause large decreases in hydraulic conductivity near the surface.
- Large local increases in seepage velocity may occur if the root system is assumed to cause large increases in hydraulic conductivity.
- A small increase in the factor of safety against slope instability is seen for a root system located at the toe if the affect of the roots can be represented as significantly strengthened soil.

### **Limitations**

- A process model is needed to properly assess internal erosion to link the affect of higher seepage velocities. With such a model, no link can be drawn between high internal seepage velocities and a factor of safety.
- The study is a parametric analysis using hypothetical material properties and not actual properties; therefore, fine scale material properties are needed for more detailed seepage or stability analyses.
- Potential fine scale mechanisms not addressed in this research might lead to slope instability.

### **Conclusions**

- Models developed in this research provides advances in detailed seepage and stability analyses, specifically when introducing a root system into a soil profile.

### **Future research**

- Methods to develop detailed properties for soil-root systems
- Integrated field and model characterization efforts to fully exploit the capabilities of the models
- Process models (constitutive relations) to capture internal erosion and other hydraulic and mechanical coupling.

## References

- Angers, D. A., and J. Caron. 1998. Plant-induced changes in soil structure: Processes and feedbacks. *Biogeochemistry* 42:55-72.
- Baker, D. L. 2003. Sensing breaches in earthen dams. *IEEE Instrumentation and Measurement Magazine* 6(2):13-18.
- Baker, K. J., P. G. Bonnier, T. Damsma, B. Safari, G. Soltys, and D. D. Haag. 2006. PLAXIS: *PlaxFlow- Version 1.4.*, ed. R.B.J. Brinkgreve, R. Al-Khoury, and J. M. van Esch. DELFT, The Netherlands.
- Ballard, Jerrell R., Jr. (2011). A Three-Dimensional Heat and Mass Transport Model for a Tree Within A Forest. (Doctoral dissertation) Mississippi State University, Mississippi State, MS.
- Belytschko, T., W. K. Liu, and B. Moran. 2000. *Nonlinear finite elements for continua and structures*. John Wiley and Sons.
- Berg, T. M., and C. M. Dodge. 1981. Atlas of preliminary geologic quadrangle maps of Pennsylvania. Commonwealth of Pennsylvania. Harrisburg, PA: Bureau of Topographic and Geologic Survey.
- Berg, T. M., W. D. Sevon, and R. Abel. 1984. Rock types of Pennsylvania. Map 63, 1:500,000 scale map. Commonwealth of Pennsylvania. Harrisburg, PA: Bureau of Topographic and Geologic Survey.
- Beven K., and P. Germann. 1982. *Macropores and water flow in soil*. *Water Resources Research* 18:1311-1325.
- Bowles, J. E. 1995. *Foundation analysis and design*. McGraw-Hill Higher Education.
- Brown, C. B., and M. S. Sheu. 1975. Effects of deforestation on slopes. ASCE, *Journal of Geotechnical Engineering Division* 101:147-165.
- Clark, P. U., A. R. Nelson, W. D. McCoy, B. B. Miller, and D. K. Barnes. 1989. Quaternary aminostratigraphy of Mississippi Valley loess. *Geological Society of America Bulletin* 101:918-926.
- Coder, Dr. Kim D. 2007. Storm wind loads on trees. *Outreach Publication SFNR07-3*. University of Georgia.
- Coppins, N. J., and L. G. Richards. 1990. *Use of vegetation in civil engineering*, Butterworths, London.

- Crow, T. R., and G. G. Erdmann. 1983. Weight and volume equations and tables for red maple in the Lake States. Research Paper NC-242, U.S. Department of Agriculture, Forest Service, North Central Forest Experiment Station, St. Paul, MN.
- Daniels, H. E. 1945. The statistical theory of the strength of bundles of threads. *Proceedings of the Royal Society of London* 183(995):405-435.
- Fisk, Harold N. 1947. Fine-grained alluvial deposits and effects on Mississippi River activity. Volumes I and II. Vicksburg MS: Waterways Experiment Station.
- Golder Associates Inc. 2009. Final Report: Geotechnical Investigation and Levee Analysis. City of Burlington and Dike District 12 Levee Certification Project. Burlington, WA. Prepared for: Pacific International Engineering. Edmonds, WA.
- Gray, D. H., and A. T. Leiser. 1982. *Biotechnical slope protection and erosion control*. New York: Van Nostrand Reinhold Company.
- Gray, D. H., and W. F. Megahan. 1981. Forest vegetation removal and slope stability in the Idaho Batholith. U.S. Department of Agriculture, Forest Service, Intermountain Forest and Range Experiment Station. Research Paper INT-271. Ogden, UT.
- Gray, D. H., and H. Ohashi. 1983. Mechanics of Fiber Reinforcement in Sand. *Journal of Geotechnical Engineering* 109(3):335-353.
- Gray, D. H., A. MacDonald, T. Thomann, I. Blatz, and F. D. Shields, Jr. 1991. *The effects of vegetation on the structural integrity of sandy levees*. Technical Report No. REMR-EI-5. Vicksburg, MS: U.S. Army Engineer Waterways Experiment Station.
- Greenwood, J. R., J. E. Norris, and J. Wint. 2004. Assessing the contribution of vegetation to slope stability. *Proceedings of the Institution of Civil Engineers, Geotechnical Engineering* 157, October 2004 Issue GE4, 199-207.
- Griffiths, D. V., and P. A. Lane. 1999. Slope stability analysis by finite elements. *Géotechnique* 49(3):387-403.
- Guardo, M., and K. P. Rohrer. 2000. Calibration of a steady-state seepage model from transient recovery of field data. *Journal of the American Water Resources Association* 36(1):87-94.
- Gurwin, J., and M. Lubczynski. 2005. Modeling of complex multi-aquifer systems for groundwater resources evaluation - Świdnica study case (Poland). 4(4):1431-2174.
- Harder, Jr., L. F., R. Kroll, V. Claaseen, P. E. F. Buck, and A. M. Berry. 2010. *Investigation of tree root penetration into a levee soil-cement-bentonite slurry cutoff wall*. Seattle, Washington: Association of State Dam Safety Officials. 19-23.

- Hoskins, D. M. 1976a. Danville geologic quadrangle. Map 160, 1:24,000 scale map. Atlas of Preliminary Geologic Quadrangle Maps of Pennsylvania. Harrisburg, PA: Pennsylvania Geological Survey.
- Hoskins, D. M. 1976b. Riverside geologic quadrangle. Map 483, 1:24,000 scale map. Atlas of Preliminary Geologic Quadrangle Maps of Pennsylvania. Harrisburg, PA: Pennsylvania Geological Survey.
- Hsi, G., and J. H. Nath. 1970. Wind drag within a simulated forest. *Journal of Applied Meteorology* 9:592-602.
- Isphording, W. C., and G. M. Lamb. 1971. Age and origin of the Citronelle Formation in Alabama. *Geological Society of America Bulletin* 82:775-780.
- Jenkins, J. J., D. C. Chojnacky, L. S. Heath, and R. A. Birdsey. 2004. *Comprehensive database of diameter-based biomass regressions for North American tree species*. USDA General Technical Report NE-319. Burlington, VT.
- Johnson, M. S., and J. Lehmann. 2006. Double-funneling of trees: Stemflow and root-induced preferential flow. *Ecoscience* 13(3):324-333.
- Jones, N. L. 1999. *SEEP2D Primer*. Groundwater Modeling System, Environmental Modeling Research Laboratory. Provo, UT: Brigham Young University.
- Kaestner A., M. Schneebeeli, and F. Graf. 2006. Visualizing three-dimensional root networks using computed tomography. *Geoderma* 136:459-469.
- Kazhdan, M. M., M. Bolitho, and H. Hoppe. 2006. Poisson surface reconstruction. *Eurographics Symposium on Geometry Processing*.
- Kees, C., M. Farthing, and C. Dawson. 2008. Locally conservative, stabilized finite element methods for variably saturated flow. *Computer Methods in Applied Mechanics and Engineering* 197:4610-4625.
- Kolb, C. R., and C. O. Durham. 1967. Field trip guidebook, Lower Mississippi Alluvial Valley and Terraces. *Geological Society of America 1967 Annual Meeting*. New Orleans, Louisiana.
- Kolb, Charles R. 1975. Geologic control of sand boils along Mississippi River levees. Miscellaneous Paper S-75-22. Vicksburg MS: U.S. Army Engineer Waterways Experiment Station.
- Krinitzsky, E. L., and W. J. Turnbull. 1967. *Loess deposits of Mississippi*. Special Paper 94. New York: Geological Society of America.
- Mellen, F. F., T. E. McCutcheon, and M. R. Livingston. 1941. Warren County mineral resources. Bulletin 43. University, MS: Mississippi State Geological Survey.

- Moore, W. H. 1976. Geologic map of Mississippi. University, MS: Mississippi Mineral Resources Institute.
- Mualem, Y. 1976. A new model predicting the hydraulic conductivity of unsaturated porous media. *Water Resources Research* 12:513–522.
- Myers, C., D. Polak, and L. Stortz. 1976. Full tree weight equations and tables for selected central hardwoods. In *Proceedings of the Central Hardwood Forest Conference, 17-19 October 1976, Carbondale, IL*, ed. J. S. Fralish, G. T. Weaver, and R. C. Schlessinger, 401-407. Carbondale, IL.
- Noguchi, S., N. Abdul Rahim, K. Baharuddin, T. Sammori, M. Tani, and K. Morisada. 1997. Soil physical properties and preferential flow pathways in tropical rain forest, Bukit Tarek, Peninsular Malaysia. *Journal of Forestry Research* 2:115-120.
- Norris, J., and J. R. Greenwood. 2006. Assessing the role of vegetation on soil in urban area. IAEG 2006 Paper number 744. The Geological Society of London.
- Pollen, N., and A. Simon. 2005. Estimating the mechanical effects of riparian vegetation on stream bank stability using fiber bundle model. *Water Resources Research* 41.
- Saucier, R. T. 1994. *Geomorphology and quaternary geologic history of the Lower Mississippi Valley*. Volumes I and II. Vicksburg, MS: Mississippi River Commission.
- Schaefer, J. A., T. M. O'Leary, N. D. Vroman, R. Fell, M. Foster, J. Cyganiewicz, G. Sills, and R. Davidson. 2010. *Internal erosion toolbox: A method for estimating probabilities of failure of embankment dams due to internal erosion*. Best Practices Guidance Document. Final draft. Vicksburg, MS: U.S. Army Corps of Engineers.
- Schmertmann, J. H. 2000. The non-filter factor of safety against piping through sands. ASCE Geotechnical Special Publication No. 111, Judgement and Innovation. Edited by F. Silva and E. Kavazanjian, ASCE, Reston.
- Schnabel Engineering. 2010. Phase 2 - Geotechnical data collection and evaluation/assessment Danville Area Flood Protection System (FPS) Borough of Danville, Montour County Pennsylvania. Project 09150010.A2. West Chester, PA: Schnable Engineering.
- Schwarz, M., P. Lehmann, and D. Or. 2010. Quantifying lateral root reinforcement in steep slopes - from a bundle of roots to tree stands. *Earth Surface Processes and Landforms* 35:354–367.
- Scott, T. M. 1993. Geologic map of Palm Beach County. Florida Geological Survey, Open File Map Series No. 65. Tallahassee, FL: Department of Natural Resources.

- Scott, T. M., K. M. Campbell, F. R. Rupert, J. D. Arthur, R. C. Green, G. H. Means, T. M. Missimer, J. M. Lloyd, J. W. Yon, and J. G. Duncan. 2001. Geologic map of the State of Florida. 1:1,000,000 scale, Map Series 145. Tallahassee, FL: Department of Natural Resources.
- Sevon, W. D., and D. D. Braun. 2000. Glacial deposits of Pennsylvania. Map 59, Commonwealth of Pennsylvania, Department of Conservation and Natural Resources, Bureau of Topographic and Geologic Survey, Harrisburg, PA. [www.dcnr.state.pa.us/topogeo/index.aspx](http://www.dcnr.state.pa.us/topogeo/index.aspx) (accessed 8 June 2011).
- Si, H. 2006. TetGen: A quality tetrahedral mesh generator and three-dimensional Delaunay triangulator. *Mohrenstr.* 39:10117. Berlin, Germany: Weierstrass Institute for Applied Analysis and Stochastics.
- Toto, E., L. Zouhri, and A. Jgounni. 2009. Direct and inverse modelling of the groundwater flow in porous media. *Hydrological Sciences Journal* 54(2):327-337.
- Tracy, F. T. 1983. *User's guide for a plane and axisymmetric finite element program for steady-state seepage problems*. Instruction Report No. IR K-83-4. Vicksburg, MS: U.S. Army Engineer Waterways Experiment Station.
- Tracy, F. T. 2006. Clean two- and three-dimensional analytical solutions of Richards equation for testing numerical solvers. *Water Resources Research* 42:W08503.
- U.S. Army Corps of Engineers (USACE). 2003. *Slope stability*. Engineer Manual EM 1110-2-1902. Washington, DC.
- U.S. Army Corps of Engineers (USACE). 2005a. *Geotechnical evaluation of safety, Sacramento Rivers east bank levees from approximately RM 53.7 to RM 45.3, Pocket Area to New North Beach Levee*. Draft, American River Watershed Project (Common Features) California. Sacramento, CA: U.S. Army Corps of Engineers, Soil Design Section, Sacramento District.
- U.S. Army Corps of Engineers (USACE). 2009. *Guidelines for landscape planting and vegetation management levees, floodwalls, embankment dams, and appurtenant structures*. Engineering Technical Letter (ETL) 1110-2-571, 10 April, Washington, DC.
- U.S. Army Corps of Engineers (USACE). 2011. RiverGages.com. Water levels of rivers and lakes. <http://www2.mvr.usace.army.mil/WaterControl/new/layout.cfm>. (Accessed 26 April 2011).
- U.S. Department of Commerce (USDC). 2010. National Environmental Satellite, Data, and Information Service (NESDIS): National Climatic Data Center. <http://www.ncdc.noaa.gov/oa/ncdc.html>. (Accessed 19 August 2010).
- U.S. Department of Agriculture (USDA). 1964. Soil survey of Warren County, Mississippi. Washington, DC: U.S. Department of Agriculture.

U.S. Department of Agriculture (USDA). 1978. Soil survey of Palm Beach County area, Florida. Washington, DC: U.S. Department of Agriculture.

U.S. Department of Agriculture (USDA). 1985. Soil survey of Montour County, Pennsylvania. Washington, DC: U.S. Department of Agriculture.

URS. 2010a. *Phase 1 geotechnical evaluation report (P1GER), Sacramento River study area*. Urban Levee Geotechnical Evaluations Program Contract 4600007418, Prepared for Department of Water Resources, Division of Flood Management, URS, Gateway Oaks Drive, Sacramento, CA, 369.

van Genuchten, M. Th. 1980. A closed-form equation for predicting the hydraulic conductivity of unsaturated soils. *Soil Science Society of America Journal* 44:892–898.

Waldron, L. J. 1977. The shear resistance of root-permeated homogeneous and stratified soil. *Soil Science Society American Journal* 41:843–849.

Western Regional Climate Center (WRCC). Prevailing Wind Direction.  
<http://www.wrcc.dri.edu/htmlfiles/westwinddir.html>. (Accessed 19 August 2010).

Wright, S. G. 1999. UTEXAS4, a computer program for slope stability calculations. Tutorial prepared for Department of the Army, U.S. Army Corps of Engineers Washington, DC. Shinoak Software, Austin Texas.

Wu, T. H. 1976. Investigation of landslides on Prince of Wales Island, Alaska, Geotechnical Engineering Report No. 5, Dept. of Civil Engineering, Ohio State University, Columbus, Ohio, 94.

Wu, T. H., W. P. McKinnel III, and D. N. Swanston. 1979. Strength of tree root and landslides on Prince of Wales Island, Alaska. *Canadian Geotechnical Journal* 16:19–33.

Yang, F. R., C. H. Lee, W. J. Kung, and H. F. Yeh. 2009. The impact of tunneling construction on the hydrogeological environment of Tseng-Wen Reservoir Transbasin Diversion Project in Taiwan. *Engineering Geology* 103(1-2):39–58.

Zee, C. H., and R. Zee. 2006. Earthquake hydrodynamic pressure on dams. *Journal of Hydraulic Engineering* 132(11):1128–1133.

## Appendix A: Glossary<sup>1</sup>

### A

#### **Alluvial Deposit**

Clay, silt, sand, gravel, or other sediment deposited by the action of running or receding water.

#### **Alluvium**

A general term for all detrital deposits resulting directly or indirectly from the sediment transported by (modern) streams; thus, including the sediments laid down in river beds, floodplains, lakes, fans, and estuaries.

### B

#### **Bank**

The rising ground bordering a lake, river, or sea; or of a river or channel, for which it is designated as right or left as the observer is facing downstream.

#### **Baseline**

The primary reference line defining a construction coordinate system.

#### **Bathymetry**

The measurement of water depths in oceans, seas, and lakes; also information derived from such measurements.

#### **Bed**

The bottom of a watercourse, or any body of water.

#### **Bedrock**

The solid rock that underlies gravel, soil, and other superficial material. Bedrock may be exposed at the surface (an outcrop), or it may be buried under a few centimeters to thousands of meters of unconsolidated material.

#### **Bench Mark**

A permanently fixed point of known elevation. A primary bench mark is one close to a tide station to which the tide staff and tidal datum originally are referenced.

#### **Berm**

On a structure: a nearly horizontal area, often built to support or key-in an armor layer.

**Boil**

An upward flow of water in a sandy formation due to an unbalanced hydrostatic pressure resulting from a rise in a nearby stream, or from removing the overburden in making excavations.

**Boring**

A hole advanced into the ground by means of a drilling rig.

**Breaching**

(1) Formation of a channel through a barrier spit or island by storm waves, tidal action, or river flow. Usually occurs after a greater than normal flow, such as during a hurricane. (2) Failure of a dike, levee, or dam allowing flooding.

**Bulk density**

Bulk density is the mass of material per unit volume.

**C****Channel**

A natural or artificial waterway of perceptible extent, which either periodically or continuously contains moving water, or which forms a connecting link between two bodies of water.

**Clay**

A fine grained, plastic, sediment with a typical grain size less than 0.004 mm. Possesses electromagnetic properties, which bind the grains together to give a bulk strength or cohesion.

**Cohesive Sediment**

Sediment containing significant proportion of clays, the electromagnetic properties of which cause the sediment to bind together.

**D****Datum**

A horizontal or vertical reference system for making survey measurements and computations. The vertical datum used in the United States is the National Geodetic Vertical Datum of 1929 (NGVD 29), formerly referred to as the Sea Level Datum of 1929. This datum has been upgraded to the North American Vertical Datum of 1988 (NAVD 88).

**Degradation**

The geologic process by means of which various parts of the surface of the earth are worn away and their general level lowered, by the action of wind and water.

**Dike**

In most areas of the United States, a structure (earth, rock, or timber) built part way across a river for the purpose of maintaining a navigation channel. In other areas, the term is used synonymously with levee. Generally constructed of earth, stone, timber, concrete, or similar material.

**Discharge**

The discharge, usually abbreviated as "Q", is the volume of a fluid or solid passing a cross section of a stream per unit time.

**E****Embankment**

Fill material, usually earth or rock, placed with sloping sides and with a length greater than its height. Usually an embankment is wider than a dike.

**Eolian (also Aeolian)**

Pertaining to the wind, especially used with deposits such as loess and dune sand, and sedimentary structures like wind formed ripple marks.

**Erosion**

The wearing away of land by the action of natural forces. On a beach, the carrying away of beach material by wave action, tidal currents, littoral currents, or by deflation.

**F****Flood**

Abnormally high water flows or water level that overtops the natural or artificial confining boundaries of a waterway. A general and temporary condition of partial or complete inundation of normally dry land areas from the overflow of river and/or tidal waters and/or the unusual accumulations of waters from any sources.

**Flood Plain**

A flat tract of land bordering a river consisting of alluvium deposited by the river when the river overflows its banks.

**Flood Stage**

The water surface elevation of a river, stream, or body of water, above which flooding and damages normally begin to occur, normally measured with respect to a specific reference gage. Flood stage is normally the level at which a river overflows its banks. Flood stage for any particular geographic area is unique to that geographic area.

**Fluvial**

Of or pertaining to rivers; produced by the action of a river or stream (e.g., fluvial sediment).

**G****Geographical Information System (GIS)**

Database of information, which is geographically referenced, usually with an associated visualization system.

**Geotechnical Investigations**

Subsurface investigation of soils, rock, and other strata for the purposes of engineering design.

**Global Positioning System (GPS)**

A navigational and positioning system developed by the U.S. Department of Defense, by which the location of a position on or above the Earth can be determined by a special receiver at that point interpreting signals received simultaneously from several of a constellation of special satellites.

**Gradient**

A measure of slope (soil- or water-surface) in meters of rise or fall per meter of horizontal distance.

**Gravel**

Unconsolidated natural accumulation of rounded rock fragments coarser than sand but finer than pebbles (2 to 4 mm diameter).

**Ground-penetrating radar (GPR)**

The use of high frequencies of electromagnetic waves, which are propagated in a straight line into the ground to depths, which vary from a few feet to tens of feet, depending on the electrical conductivity of the terrain. The use of GPR is similar to the seismic reflection technique because both methods record the time required for a wave to travel to an interface between two formations and then reflect to the surface.

**Groundwater**

The water contained in interconnected pores located below the water table.

**H****Head, Total Hydraulic**

The sum of the elevation head, the pressure head, and the velocity head at a given point in an aquifer.

**Headwaters**

A continuous graph showing the properties of stream flow with respect to time.

**Hydrograph**

A continuous graph showing the properties of stream flow with respect to time.

**Hydraulic Conductivity**

The rate at which water of a specified density and kinematic viscosity can move through a permeable medium.

**Hydraulic Gradient**

The change in total head with a change in distance in a given direction, which yields a maximum rate of decrease in head.

**I****Infiltration**

Water entering the groundwater system throughout the land surface.

**J K****L****Levee**

An embankment raised along a river to protect adjoining lands from inundation.

**Light Detection And Ranging (LIDAR)**

Laser range and distance measurements of the earth from an aircraft; can be used to generate a dense grid of elevation points for various mapping products to include DEM, and DTM data sets.

**Load**

The quantity of sediment transported by a current. It includes the suspended load of small particles and the bed load of large particles that move along the bottom.

**M****Mean Sea Level (MSL)**

A tidal datum that is the mean of hourly water elevations observed over a specific 19-year metonic cycle (the National Tidal Datum Epoch). The abbreviation amsl refers to annual mean sea level.

**Mud**

A fluid-to-plastic mixture of finely divided particles of solid material and water.

**N****Natural Levee**

A natural embankment that parallels the course of a river. A natural levee is built up over time by sediment deposition associated with seasonal flooding.

**O****Overtopping**

Passing of water over the top of a structure as a result of wave runup or surge action.

**P****Permeability**

The property of bulk material (sand, crushed rock, and soft rock in situ), which permit movement of water through its pores.

**Piezometer**

A nonpumping well, generally of small diameter, that is used to measure the elevation of the water table or potentiometric surface. A piezometer generally has a short well screen through which water can enter.

**Piping**

Erosion of closed flow channels (tunnels) by the passage of water through soil; flow underneath structures, carrying away particles, may endanger the stability of the structure.

**Pore Pressure**

The interstitial pressure of water within a mass of soil or rock.

**Porosity**

Percentage of the total volume of a soil sample not occupied by solid particles but by air and water, =  $Vv/VT \times 100$ .

**Q R****S****Sand**

Sediment particles, often largely composed of quartz, with a diameter of between 0.062 mm and 2 mm, generally classified as fine, medium, coarse or very coarse. Beach sand may sometimes be composed of organic sediments such as calcareous reef debris or shell fragments.

**Saturation**

(1) Soil Saturation. A condition in soil in which all spaces between the soil particles are filled with water. Such conditions normally occur after prolonged periods of rainfall and/or snowmelt. (2) Levee saturation. Soil saturation that has occurred in an earthen levee because of floodwaters remaining above flood stage for extremely long periods of time. This condition can lead to catastrophic failure of the levee.

**Sediment**

(1) Loose, fragments of rocks, minerals, or organic material, which are transported from their source for varying distances and deposited by air, wind, ice, and water. Other sediments are precipitated from the overlying water, or form chemically, in place. Sediment includes all the unconsolidated materials on the sea floor. (2) The fine grained material deposited by water or wind.

**Seepage**

The movement of water through small cracks, pores, interstices, out of a body of surface or subsurface water. The loss of water by infiltration from a canal, reservoir, or other body of water, or from a field. It is generally expressed as flow volume per unit of time.

**Seepage Velocity**

Also known as pore water velocity. The rate of movement of fluid particles through porous media along a line from one point to another.

**Silt**

Sediment particles with a grain size between 0.004 mm and 0.062 mm, i.e., coarser than clay particles but finer than sand.

**Soil**

A layer of weathered, unconsolidated material on top of bed rock; in geologic usage, usually defined as containing organic matter and being capable of supporting plant growth.

**Stage**

The elevation of a river or confined water area, usually referred to a low water datum plane.

**T****Thalweg**

The line following the lowest part of a valley, whether under water or not. Usually the line following the deepest part, or middle, of the bed or channel of a river.

**U****Unconsolidated**

In referring to sediment grains, loose, separate, or unattached to one another.

**Universal Transverse Mercator (UTM) Coordinate System**

A worldwide metric military coordinate system rarely used for civil works applications.

**Unsaturated Zone**

Also known as the zone of aeration and the vadose zone. The zone between the land surface and the water table. It includes the root zone, intermediate zone, and capillary fringe. The pore spaces contain water at less than atmospheric pressure, as well as air and other gases. Saturated bodies, such as perched groundwater, may exist in the unsaturated zone.

**V****W****Water Level**

Elevation of still water level relative to some datum.

**Water Table**

The surface in an unconfined aquifer or confining bed at which the pore water pressure is atmospheric. It can be measured by installing shallow wells extending just into the zone of saturation and then measuring the water level in those wells.

**X Y Z**

<sup>1</sup>The definitions in this glossary are from the following references:

U.S. Army Corps of Engineers. 1987. *Reservoir Water Quality Analyses*. Engineer Manual (EM) 1110-2-1201. Washington, DC.

U.S. Army Corps of Engineers. 1993. *River Hydraulics*. Engineer Manual (EM) 1110-2-1416. Washington, DC.

U.S. Army Corps of Engineers. 1995. *Geophysical Exploration for Engineering and Environmental Investigations*. Engineer Manual (EM) 1110-1-1802. Washington, DC.

U.S. Army Corps of Engineers. 1999. *Groundwater Hydrology*. Engineer Manual (EM) 1110-2-1421. Washington, DC.

U.S. Army Corps of Engineers. 2001. *Emergency Employment of Army and Other Resources Civil Emergency Management Program*. Engineer Regulations (ER)500-1-1. Washington, DC.

U.S. Army Corps of Engineers. 2002. *Hydrographic Surveying*. Engineer Manual (EM) 1110-2-1003. Washington, DC.

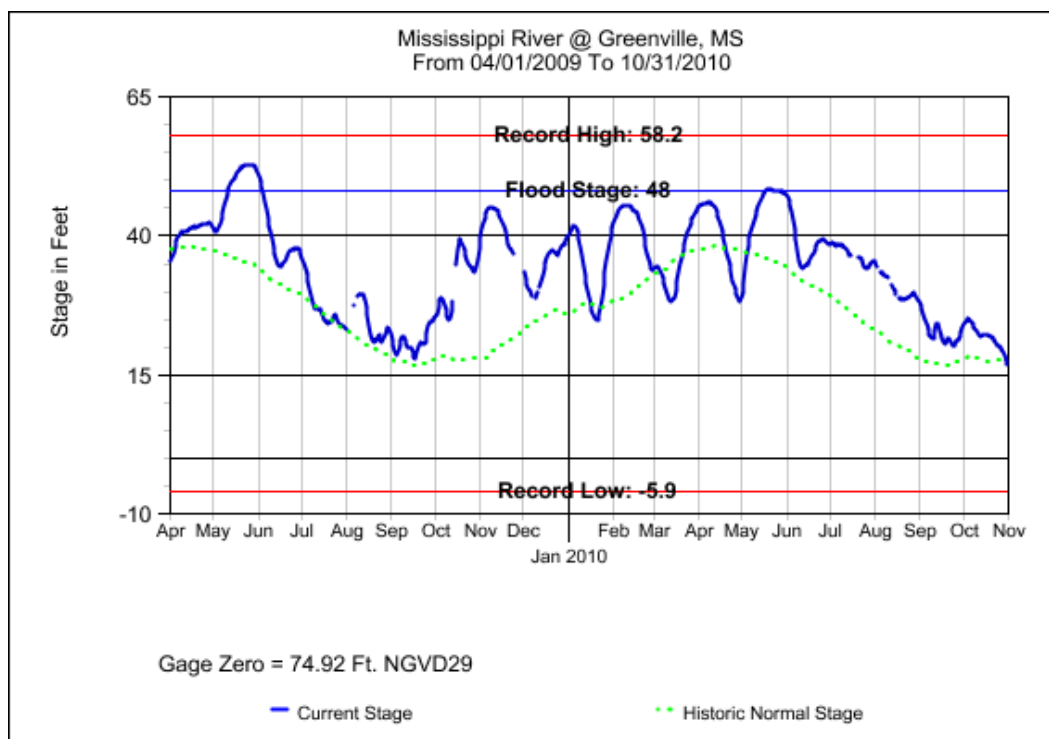
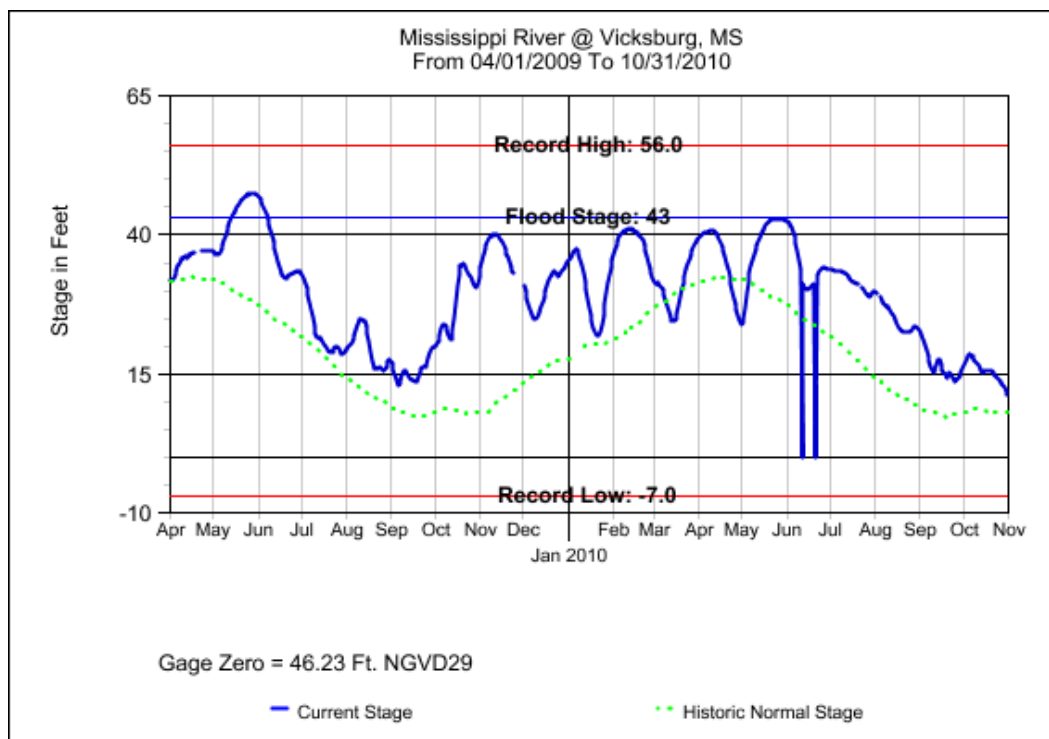
U.S. Army Corps of Engineers. 2002. *Photogrammetric Mapping*. Engineer Manual (EM) 1110-1-1000. Washington, DC.

U.S. Army Corps of Engineers. 2003. *Coastal Engineering Manual - Appendix A - Glossary of Coastal Terminology*. Engineer Manual (EM) 1110-2-1100. Washington, DC.

U.S. Army Corps of Engineers. 2007. *Engineering and Design: Control and Topographic Surveying*. Engineer Manual (EM) 1110-1-1005. Washington, DC.

U.S. Army Corps of Engineers. 2011. *NAVSTAR Global Positioning System Surveying*. Engineer Manual (EM) 1110-1-1003. Washington, DC.

## **Appendix B: Mississippi River Stage Data**



Mississippi River @ Greenville, MS					Gage Zero - 74.92 Ft. NGVD29					
Flood Stage - 48.0 Ft.					Record High Stage - 58.2 Ft. (05/12/1973)					
River Mile - 531.3										
Location of Gage - Located near the Greenville bridge which crosses at mile 531.3										
2009 Stage (Ft)	Day	APR	MAY	JUN	JLY	AUG	SEP	OCT	NOV	DEC
1	35.59	41.24	50.83	35.84	M	21.17	25.48	39.73	33.44	
2	36.08	40.83	49.89	35.06	M	20.3	25.87	41.32	32.1	
3	36.94	40.83	48.89	34.22	M	19.39	27.08	42.39	31.16	
4	38.02	41.34	47.68	33.15	M	18.54	28.44	43.08	30.51	
5	39.16	42.2	46.23	31.72	M	19.37	28.89	44.05	30.08	
6	39.98	43.26	44.64	30.56	27.5	20.28	28.55	44.81	29.33	
7	40.31	44.22	43.23	29.17	M	21.13	27.44	45.12	29.07	
8	40.56	45.37	41.98	27.96	29.33	21.97	26.72	45.15	M	
9	40.83	46.38	40.66	27.04	29.57	21.74	25.62	45.14	29	
10	40.86	47.47	39.35	26.83	M	21.4	24.83	45.2	29.86	
11	40.8	48.37	37.98	26.83	29.45	20.49	25.21	44.92	M	
12	40.85	49.15	36.72	26.99	29.5	19.79	26.44	44.68	31.01	
13	41.14	49.79	35.69	26.72	28.46	19.75	28.2	44.34	31.73	
14	41.19	50.26	34.8	26.48	27.29	19.85	M	43.79	32.75	
15	41.36	50.52	34.35	25.72	25.72	19.3	34.98	43.2	34.15	
16	41.55	50.91	34.36	24.9	23.89	18.34	37.59	42.56	35.09	
17	41.67	51.33	34.68	24.56	22.08	18.07	39.02	41.79	36.19	
18	41.59	51.76	35.04	24.61	21.21	19.32	39.35	40.81	36.71	
19	41.56	52.09	35.6	24.29	21.08	20.32	38.92	M	37.21	
20	41.73	52.45	36.24	24.54	20.96	20.77	38.21	38.63	37.66	
21	41.93	52.57	36.67	24.5	21.09	21.07	37.47	37.67	37.57	
22	42.09	52.77	37.03	25.1	21.94	20.52	36.54	37.44	37.31	
23	42.2	52.83	37.34	25.68	22.08	20.6	35.49	37.51	36.96	
24	42.16	52.83	37.47	25.88	21.38	20.94	34.76	36.7	36.47	
25	42.15	52.9	37.62	25.05	20.95	22.43	34.49	M	36.91	
26	42.27	52.9	37.77	24.13	21.45	23.96	34.2	M	37.58	
27	42.43	52.85	37.83	23.79	22.11	24.52	33.81	M	38.13	
28	42.38	52.8	37.88	23.8	23.26	24.68	33.58	M	38.53	
29	42.02	52.55	37.49	23.79	23.61	24.84	34.41	M	38.58	
30	41.63	52.11	36.7	23.45	23.12	25.06	35.89	M	39.03	
31		51.59		23.28	22.55		37.75		39.81	
MIN	35.59	40.83	34.35	23.28	20.95	18.07	24.83	36.7	29	
MAX	42.43	52.9	50.83	35.84	29.57	25.06	39.35	45.2	39.81	
MEAN	40.77	48.98	39.42	26.96	24.15	21	32.17	42.18	34.62	

Mississippi River @ Greenville, MS							Gage Zero - 74.92 Ft. NGVD29			
Flood Stage - 48.0 Ft.							Record High Stage - 58.2 Ft. (05/12/1973)			
River Mile - 531.3										
Location Located near the Greenville bridge which crosses at mile 531.3										
2010 Stage (Ft)										
Day	JAN	FEB	MAR	APR	MAY	JUN	JLY	AUG	SEP	OCT
1	40.31	42.62	34.14	45.3	29.83	46.97	38.65	35.1	27.52	24.07
2	40.91	43.28	34.52	45.51	31.66	46.42	38.7	34.65	26.89	24.6
3	41.46	43.81	34.67	45.72	34.6	45.59	38.59	M	25.95	24.95
4	41.75	44.29	34.4	45.72	36.76	44.38	38.38	33.61	24.97	25.08
5	41.79	44.83	33.86	45.75	38.2	42.81	38.32	33.46	24.3	24.94
6	41.44	45.18	33.28	45.84	39.7	41.26	38.5	33.21	23.15	24.69
7	40.7	45.32	32.4	46.04	40.87	39.45	38.39	32.92	22.13	24.21
8	39.48	45.56	31.48	46.05	41.89	37.61	38.41	32.96	21.76	23.71
9	38.15	45.61	30.64	45.87	42.94	35.63	38.22	32.56	21.54	23.36
10	36.53	45.62	29.61	45.7	43.72	34.67	38.05	32.38	21.69	22.94
11	34.6	45.62	28.4	45.53	44.55	34.34	37.82	M	23.01	22.4
12	32.82	45.33	28.15	45.09	45.47	34.24	37.52	31.2	24.39	21.97
13	31.46	45	28.37	44.33	46.04	34.53	36.83	30.57	24.39	21.88
14	30.2	44.66	28.61	43.51	46.76	34.74	36.34	30.13	22.77	22.18
15	28.71	44.51	29.03	42.88	47.29	34.76	36.45	29.6	21.81	22.17
16	27.6	44.31	30.09	41.8	47.75	35.29	M	M	21.58	22.21
17	26.49	44.2	31.7	40.91	48.18	35.94	M	29.01	21.04	22.24
18	25.81	43.64	33.53	39.71	48.5	36.36	M	28.71	20.53	22.2
19	25.18	42.86	35.18	38.43	48.61	36.82	M	28.47	21.15	22.06
20	24.76	42.08	36.29	36.86	48.59	37.52	36.3	28.58	21.7	21.86
21	24.9	41	37.46	35.69	48.33	38.19	36.09	28.56	21.65	21.48
22	25.86	39.57	38.62	34.71	48.24	38.81	35.7	28.81	20.81	21.17
23	27.31	38.21	39.68	33.72	48.18	39.21	35.4	28.81	20.38	20.8
24	28.94	36.87	40.67	31.93	47.99	39.3	34.47	28.73	20.09	20.38
25	31.19	35.75	41.43	31.31	48.18	39.39	34.27	29.15	20.72	20.22
26	33.52	34.82	42.28	30.68	48.02	39.36	34.16	29.59	21.13	19.92
27	35.66	34.09	43.04	29.57	47.98	39.06	34.39	29.99	21.4	19.54
28	37.27	33.83	43.6	28.88	47.85	38.93	34.82	29.42	21.83	19.14
29	38.68		44.01	28.33	47.98	38.57	35.24	29.14	22.6	18.64
30	40.16		44.59	28.95	47.77	38.57	35.55	28.66	23.52	17.55
31	41.42		44.91		47.4		35.46	28.07		17.07
MIN	24.76	33.83	28.15	28.33	29.83	34.24	34.16	28.07	20.09	17.07
MAX	41.79	45.62	44.91	46.05	48.61	46.97	38.7	35.1	27.52	25.08

Mississippi River @ Vicksburg, MS					Gage Zero - 46.23 Ft. NGVD29				
Flood Stage - 43.0 Ft.					Record High Stage - 56.0 Ft. (05/04/1927)				
River Mile - 435.7									
Location of Gage -					1.6 miles downstream of the mouth of the Yazoo diversion canal. Vicksburg Quadrangle.				
2009 Stage (ft)									
Day	APR	MAY	JUN	JLY	AUG	SEP	OCT	NOV	DEC
1	31.73	36.81	46.78	32.77	19.44	16.81	20	34.05	30.73
2	31.93	36.49	46.35	32.08	20.01	15.72	20.42	35.34	29.87
3	32.33	36.34	45.74	31.36	20.34	14.83	20.88	36.65	28.5
4	32.79	36.48	45.16	30.42	20.6	13.84	21.79	37.58	27.48
5	33.54	36.84	44.53	29.3	21.12	13.04	23.35	38.25	26.71
6	34.39	37.49	43.66	27.91	21.91	13.41	23.89	38.89	25.85
7	34.9	38.3	42.75	26.71	22.86	14.04	24.04	39.39	25.53
8	35.51	39.04	41.86	25.13	23.75	14.92	23.47	39.68	24.99
9	35.79	39.93	40.92	23.61	24.44	15.66	22.81	39.96	24.98
10	35.85	40.72	39.86	22.4	24.74	15.73	21.99	40.1	25.16
11	36.02	41.56	38.74	21.72	24.73	15.41	21.25	40.19	25.72
12	35.9	42.42	37.64	21.59	24.65	14.78	21.26	40.08	26.23
13	36.19	43.04	36.47	21.45	24.52	14.18	22.78	39.79	27.15
14	36.43	43.64	35.34	21.3	23.62	14.05	25.04	39.69	27.75
15	36.49	44.17	34.23	20.96	22.39	14.08	28.01	39.26	28.87
16	36.74	44.6	33.29	20.34	20.86	13.96	30.89	38.67	29.82
17	36.79	45.17	32.74	19.78	19.02	13.45	32.97	38.13	30.74
18	M	45.54	32.42	19.3	17.37	13.57	34.35	37.57	31.79
19	M	46	32.16	19.1	16.34	14.5	34.65	36.63	32.39
20	M	46.22	32.25	18.85	15.82	15.35	34.93	36.1	32.87
21	M	46.54	32.42	18.78	15.82	15.9	34.63	35.06	33.21
22	37.03	46.85	32.7	19.04	15.78	16.13	34.12	34.23	33.43
23	37.09	47.11	32.88	19.66	16.32	16.12	33.61	33.68	33.27
24	37.17	47.28	33.2	19.99	16.38	16.26	32.95	33.33	32.82
25	37.13	47.44	33.23	20.07	15.92	16.72	32.36	M	32.67
26	37.19	47.4	33.35	19.43	15.55	17.77	31.83	M	33.01
27	37.2	47.51	33.47	18.87	15.83	19	31.46	M	33.48
28	37.26	47.56	33.58	18.56	16.36	19.5	31.02	M	33.91
29	37.25	47.47	33.62	18.64	17.24	19.88	30.68	M	34.24
30	37.09	47.39	33.33	19.02	17.5	19.83	31.06	M	34.66
31		47.1		19.25	17.38		32.48		35.21
MIN	31.73	36.34	32.16	18.56	15.55	13.04	20	33.33	24.98
MAX	37.26	47.56	46.78	32.77	24.74	19.88	34.93	40.19	35.21
MEAN	35.68	43.24	37.16	22.5	19.63	15.61	27.9	37.6	30.1

Mississippi River @ Vicksburg, MS						Gage Zero - 46.23 Ft. NGVD29						
Flood Stage - 43.0 Ft.						Record High Stage - 56.0 Ft. (05/04/1927)						
River Mile - 435.7												
Location of Gage -						1.6 miles downstream of the mouth of the Yazoo diversion canal. Vicksburg Quadrangle.						
2010 Stage (ft)												
Day	JAN	FEB	MAR	APR	MAY	JUN	JLY	AUG	SEP	OCT		
1	35.43	36.66	31.6	39.59	24.23	42.45	33.72	29.9	22.39	16.62		
2	36	37.65	31.11	39.95	24.89	42.23	33.69	29.69	21.84	17.29		
3	36.4	38.32	31.39	40.31	26.96	41.88	33.67	M	21.09	17.81		
4	36.9	38.92	31.24	40.47	29.63	41.38	33.63	28.93	20.16	18.27		
5	37.22	39.73	30.97	40.5	31.55	40.65	33.41	28.3	19.21	18.52		
6	37.34	40.14	30.62	40.59	33.02	39.74	33.37	27.99	18.25	18.35		
7	37.11	40.37	30.05	40.57	34.4	38.62	33.42	27.54	17.22	18.13		
8	36.55	40.61	29.11	40.81	35.49	37.12	33.46	27.36	16.23	17.68		
9	35.63	40.8	28.12	40.79	36.48	35.61	33.44	27.07	15.72	17.23		
10	34.57	40.94	27.15	40.86	37.44	33.86	33.29	26.85	15.37	16.81		
11	33.18	41.06	26.13	40.74	38.2	0	33.09	26.51	15.48	16.45		
12	31.6	41	25.24	40.57	38.94	31.24	32.8	26.02	16.53	15.94		
13	30.04	41.01	24.62	40.28	39.65	30.51	32.52	25.59	17.66	15.56		
14	28.45	40.82	24.56	39.82	40.34	30.32	32.06	24.95	17.56	15.39		
15	26.99	40.69	24.64	39.24	40.76	30.24	31.77	24.47	16.65	15.51		
16	25.58	40.57	24.91	38.65	41.31	30.28	31.55	23.88	15.76	15.56		
17	24.5	40.48	25.78	37.97	41.76	30.43	31.49	23.32	15.29	15.66		
18	23.36	40.31	27.27	37.16	42.09	30.86	31.4	22.97	14.77	15.46		
19	22.72	39.98	28.88	36.21	42.39	31.23	31.18	22.78	14.37	15.53		
20	21.81	39.5	30.38	35	42.64	0	31.15	22.41	14.72	15.45		
21	21.8	39.07	31.24	33.78	42.7	0	M	22.41	15.12	15.27		
22	21.86	38.23	32.53	32.42	42.67	32.82	M	22.48	14.92	14.86		
23	22.56	37.21	33.8	31.15	42.77	33.38	30.52	22.61	14.43	14.63		
24	23.9	36.17	34.71	29.74	42.75	33.82	30.13	22.61	13.97	14.21		
25	25.48	35.01	35.67	28.55	42.76	34.02	29.51	22.72	13.75	13.85		
26	27.44	33.98	36.54	27.67	42.72	34.22	29.09	22.94	14.06	13.56		
27	29.41	33.19	37.18	26.69	42.76	34.17	28.92	23.4	14.35	13.36		
28	31.49	32.11	37.74	25.66	42.74	33.94	29.09	23.7	14.68	12.99		
29	32.93		38.48	24.55	42.74	33.83	29.25	23.61	15.19	12.67		
30	34.21		38.84	23.88	42.67	33.76	29.74	23.33	15.9	12.02		
31	35.53		39.29		42.59		29.91	22.91		11.13		
MIN	21.8	32.11	24.56	23.88	24.23	0	28.92	22.41	13.75	11.13		
MAX	37.34	41.06	39.29	40.86	42.77	42.45	33.72	29.9	22.39	18.52		
MEAN	30.26	38.73	30.96	35.81	38.45	31.42	31.73	24.98	16.42	15.54		

## **Appendix C: Review of VPlants Model**

---

Biedenharn Group

---

**Vegetation Root Architecture  
Analysis for River Bank Stability  
Applications**

VPlants Evaluation

---

August 2009

---

**FINAL REPORT**

---

Department of Geography  
University of Portsmouth  
Buckingham Building  
Lion Terrace  
Portsmouth  
PO1 3HE  
UK  
t: +44 (0)23 9284 2482  
f: +44 (0)23 9284 2512  
e: philip.soar@port.ac.uk

Biedenharn Group Llc  
3303 Woodlands Pl  
Vicksburg  
Mississippi 39180-5759  
USA

Biedenharn Group  
Vegetation Root Architecture Analysis for River Bank Stability Applications  
Final Report



## REVISION HISTORY

Revision Ref./ Date Issued	Amendments	Issued to
Draft Report (v1) January 2009		Dr David Biedenharn 1 electronic copy (pdf)
Final Report August 2009		Dr David Biedenharn 1 electronic copy (pdf)

## CONTRACT

This report describes work commissioned by the Biedenharn Group Llc under University of Portsmouth project number 14696, of 10<sup>th</sup> November 2008.

Prepared by: ..... *Philip Soar*

Philip Soar, BSc PhD CEnv CSci MCIWEM  
*Senior Lecturer in Physical Geography*

Date: August 2009

## DISCLAIMER

This document has been prepared solely as a research report for the internal use of the contractor, the Biedenharn Group and the US Government. The University of Portsmouth accepts no responsibility or liability for any use that is made of this document other than by the Client for the purposes for which it was originally commissioned and prepared.

## CONTENTS

	Page
<b>REVISION HISTORY</b>	<b>i</b>
<b>CONTRACT</b>	<b>i</b>
<b>CONTENTS</b>	<b>ii</b>
<b>LIST OF FIGURES</b>	<b>iv</b>
<b>LIST OF TABLES</b>	<b>iv</b>
<b>CONVERSION OF SI TO US CUSTOMARY UNITS</b>	<b>iv</b>
<b>ACKNOWLEDGEMENTS</b>	<b>v</b>
<b>1 INTRODUCTION.....</b>	<b>1</b>
1.1 Background.....	1
1.2 Research Objectives.....	3
<b>2 DEVELOPMENT OF PLANT ARCHITECTURE MODELING.....</b>	<b>5</b>
2.1 Plant Architecture Defined .....	5
2.2 History .....	5
2.3 OpenAlea .....	6
2.3.1 The Platform .....	7
2.3.2 Licensing.....	8
2.3.3 Software Components.....	8
<b>3 VISUALEA AND VPLANTS OPERATION .....</b>	<b>9</b>
3.1 Installation .....	9
3.2 Guidance and Support.....	10
3.3 Graphical User Interface (GUI) .....	10
3.3.1 Nomenclature.....	10
3.3.2 Using the Graphical Components .....	12
3.3.3 Using the Python Shell .....	14
<b>4 APPLICATION OF VPLANTS FOR ROOT ARCHITECTURE ANALYSIS.....</b>	<b>15</b>
4.1 Data Input .....	15
4.1.1 Multiscale Tree Graphs.....	15
4.1.2 Data Capture Methods for Root Architecture.....	17
4.2 VPlants Primitives .....	19
4.3 Visualization of PlantFrames.....	21
4.4 Root Architecture Analysis.....	22
4.5 VPlants Functionality for River Bank Stability Models .....	25
4.6 Data Output and Post-Processing.....	27

Biedenharn Group  
Vegetation Root Architecture Analysis for River Bank Stability Applications  
Final Report



<b>5</b>	<b>CONCLUSIONS – VPLANTS ‘SWOT’ ANALYSIS.....</b>	<b>29</b>
5.1	Strengths .....	29
5.2	Weaknesses .....	29
5.3	Opportunities .....	30
5.4	Threats .....	30
<b>6</b>	<b>REFERENCES.....</b>	<b>31</b>

**APPENDICES:**

**APPENDIX A: - EXAMPLE MTG FILE**

**APPENDIX B: - PYTHON MODULE FOR ROOT ARCHITECTURE ANALYSIS**

**APPENDIX C: - VISUAL BASIC CODE FOR DISCRETIZING AN MTG**

## LIST OF FIGURES

Figure 3-1 The VisuAlea Graphical User Interface.....	11
Figure 3-2 Example of dataflow created within a workspace: Volume of a cone frustum .....	13
Figure 4-1 The VPlants Process (Godin et al., 1999a) .....	15
Figure 4-2 Example MTG structure for a root system (from Danjon and Reubens, 2008).....	17
Figure 4-3 Preparing <i>Pinus Pinaster</i> root system for 3D digitizing (photograph: Frédéric Danjon).....	18
Figure 4-4 Example dataflow for importing and plotting a root system MTG.....	21
Figure 4-5 Example 3D representation of <i>Pinus pinaster</i> root system (data from Frédéric Danjon).....	22
Figure 4-6 Vertical distributions of a number of root parameters where roots intersect planes parallel to the slope at 0.1 m intervals (example from Danjon et al., 2008) .....	25
Figure 4-7 Multiple 2D distribution of root area ratio in four planes parallel to the slope at 0.3 m intervals (from Danjon et al., 2008) .....	26

## LIST OF TABLES

Table 3-1 Default packages available in OpenAlea .....	12
Table 4-1 Standard Python functions for extracting individual root segment characteristics .....	24

## CONVERSION OF SI TO US CUSTOMARY UNITS

The following units are used in this report and may be converted as indicated:

Length	1 m = 3.281 ft
	1 cm = 0.394 inches = 0.03281 ft
Area	1 m <sup>2</sup> = 10.764 ft <sup>2</sup>
	1 cm <sup>2</sup> = 0.155 inches <sup>2</sup> = 0.00108 ft <sup>2</sup>
Volume	1 m <sup>3</sup> = 35.315 ft <sup>3</sup>
	1 cm <sup>3</sup> = 0.06102 inches <sup>3</sup> = 0.000035 ft <sup>3</sup>

Biedenharn Group  
Vegetation Root Architecture Analysis for River Bank Stability Applications  
Final Report



## ACKNOWLEDGMENTS

---

This evaluation has been greatly assisted through discussions with M Christophe Pradal from UMR-DAP (l'Unité Mixte de Recherche - Développement et Amélioration des Plantes - Joint Research Unit for Plant Development and Genetic Improvement), Montpellier, France, and Dr Frédéric Danjon from the Site de Recherche Forêt-Bois (Forest Wood Research Site) in Pierroton, near Bordeaux.

## 1 INTRODUCTION

### 1.1 Background

The following background statement is provided by Dr Maureen Corcoran of the US Army Corps of Engineers (USACE), Engineer Research and Development Center (ERDC), Vicksburg, Mississippi:

In February 2007, the US Army Corps of Engineers (USACE) released a list of 122 levee segments in the United States identified as a safety risk because of poor maintenance. Two of the contributors to the safety risk were woody vegetation and vegetation overgrowth. In some areas, trees were allowed to grow closer than the 15 ft required in USACE guidance. After the inspection, levee districts were instructed to remove trees on and close to the levee or risk de-certification by the Federal Emergency Management Agency. As trees provide habitat, are aesthetically pleasing and would incur significant costs for removal, many state and local governments are reluctant to remove any trees. They argue that there is no documentation that trees have ever contributed to a levee failure.

At the request of the USACE Headquarters (HQ), in July 2007, the US Army Engineer Research and Development Center (ERDC), Vicksburg, Mississippi, conducted an extensive literature review focusing on the effects of woody vegetation on levees. The findings of the review found that no documented evidence exists to prove trees negatively influence levee integrity. However, research is very limited that addresses specifically the roles of woody vegetation on levee systems. The literature review was then extended to include subjects pertaining to root systems, slope stability, hydraulic processes, and wind force that would prove helpful in future.

Based on the results of the literature review, the USACE HQ recognized that without further research, the question of the effects of woody vegetation on levees would remain unanswered. In April 2008, USACE HQ requested that ERDC begin research on this issue. In response, ERDC formed a team of scientists and engineers with geotechnical, environmental, geological, and geophysical expertise. As California has the most levee segments with heavy tree growth, the Sacramento Flood Control Agency (SAFCA) proposed a similar investigation into levee vegetation. The SAFCA proposal is unfunded at this time, but ERDC has coordinated efforts with SAFCA and is making every effort to include the views and input of scientists and engineers involved in developing the SAFCA proposal. In addition to SAFCA, ERDC is coordinating with the USACE districts of New Orleans, Seattle, Albuquerque, and Portland to select field sites and to include local expertise in vegetation in the research methodology.

In 1991, ERDC published a comprehensive technical report entitled: 'The Effects of Vegetation on the Structural Integrity of Sandy Levees' (Gray et al., 1991), under the Repair, Evaluation, Maintenance, and Rehabilitation (REMR) Research Program, to specifically address scientific and engineering aspects of vegetation on levees. This research concluded that woody vegetation did not appear to adversely affect the structural integrity of a levee. Despite this finding, however, scientists and engineers involved in the research recognized that this study was not inclusive of all potential conditions, but rather provided a foundation for future research. Unfortunately, almost 20 years later, research into the effects of vegetation on levees has not even slightly advanced. In fact, since the REMR report, there has not been any research on levee vegetation at a similar level of detail.

In response to this need for further research on the effects of vegetation on levees, the USACE has formed an interdisciplinary team of scientists and engineers to support a detailed study of the interaction of vegetation and levees. The scope of work discussed herein represents a sub-component of the larger USACE study.

The influence of vegetation in ‘improving’ the stability of soil on slopes is widely documented in the engineering, geomorphological and botanical literature, in particular the impact of root tensile strength (however, it is not an objective of this research to revisit this literature).

In summary, vegetation can protect embankments from slope failure and fluvial erosion through above and below ground mechanisms, for example:

#### *Surface protection*

- Shielding the soil surface from overtopping flow
- Intercepting and alleviating the effect of direct precipitation on the levee surface
- Reducing the velocity of overbank flow
- Reducing the effect of trampling and wind-related erosion
- Maintaining moisture levels in the soil to reduce the formation of fissures

#### *Sub-surface protection*

- Soil ‘fixing’ and reinforcing action of the root network, mainly through strong tensile forces. The presence of roots provides additional shear strength to the soil column, or ‘apparent cohesion’.

However, it is also common for published reports and research papers to acknowledge that, in some circumstances, the presence of vegetation can have a deleterious impact on the structural integrity of levees. For example, the recently co-published report by the Department for Environment, Food and Rural Affairs (Defra) in the UK and the Environment Agency in England and Wales, entitled: ‘Management of Flood Embankments: A Guide to Good Practice’ (Morris et al., 2007) presents the potentially damaging effects of vegetation as follows:

- Poorly controlled maintenance activities can result in bank steepening through excessive removal of soil when removing vegetation leading to a progressive reduction in the factor of safety.
- The strengthening influence of plant and tree roots in the near surface soil zone can theoretically push failure surfaces deeper into the levee structure.
- Trees and bushes, in particular, can lead to destruction of the embankment body through root growth and may provide a focal point for local scour during extreme flood conditions.
- Root systems can provide a preferential route for seepage flow or failure paths through a levee.
- Dying roots, particularly of trees, can leave behind pore spaces, increasing the risk of seepage flow and associated erosion at the bank face.
- Root systems can have non-uniform distributions, leading to differences in the erosion resistance of soil.
- Large trees can transmit the dynamic effects of heavy wind onto structures, leading to movement or failures.

One of the Defra/EA conclusions is that specific research and better guidance is required to establish how vegetation type affects the performance of levees, including the influence on stability.

There is also a growing body of research and literature that focuses more specifically on the modeling of plant ‘root architecture’ and, recently, on the interaction of physical plant root ‘geometrical’ and ‘topological’ characteristics on slope stability. While this is only an emerging field of science, notable advances have been made by Danjon (eg. Reubens et al., 2007; Danjon and Reubens, 2008; Danjon et al., 2008), in particular, which are discussed within this report.

The main focus of this research effort is to evaluate the VPlants software, which is recognized as a principle tool for analyzing plant architecture including root systems, and to comment on its potential use for deriving input data to slope stability models and to aid further research into the influence vegetation roots on levee stability. The software was identified through the literature review undertaken by ERDC, where it was anticipated to have considerable utility value in the assessment of bank stability for levees with woody vegetation.

VPlants comprises a set of modules to analyze, model and visualize plant architecture at different spatial scales (tissue, organ, axis and plant). The software has been developed by the Virtual Plants project team, which is an INRIA imitative, joint with CIRAD and INRA. It is located at UMR-DAP, within CIRAD, Montpellier, France. The long-term focus of the project is to study plant development and its control by genetic processes.

INRIA (Institut National Recherche en Informatique et en Automatique) is the French National Institute for Research in Computer Science and Control. CIRAD (Centre de coopération Internationale en Recherche Agronomique pour le Développement) is the French Agricultural Research Centre for International Development. INRA (l’Institut National de la Recherche Agronomique) is the French National Institute for Agricultural Research. UMR-DAP (l’Unité Mixte de Recherche - Développement et Amélioration des Plantes) is the Joint Research Unit for Plant Development and Genetic Improvement (<http://umr-dap.cirad.fr>) , which is based at the CIRAD office in Montpellier, France (CIRAD TA A 96/03, Avenue. Agropolis, 34398 Montpellier Cedex 5, France).

The VPlants software was previously (in a less advanced version) a stand-alone package called AMAPmod but, since 2003, is now is a component of OpenAlea, which is an open source software platform and research project primarily aimed at the plant research community and with a particular focus on Plant Architecture Modeling. OpenAlea includes a range of modules to represent, analyze, and model the functioning and growth of plant architecture. The evolution of the software has progressed through collaborative investigations to develop libraries, coded in the Python programming language, and tools for addressing the needs of current and future work in Plant Architecture modeling.

## **1.2 Research Objectives**

The aim of this research project is to evaluate the ability of the VPlants software (which includes the previously separate AMAPmod model) with respect to its ability to represent and display the biological architecture of plant root systems and analyze vegetation parameters that influence slope and riverbank stability.

Specific objectives of the evaluation are to:

- review existing literature that specifically includes the use of AMAPmod and/or VPlants in investigations of plant root architecture.
- obtain the VPlants software and undertake a general familiarization of its interface, components and methods. (This has been supported by visits in December 2008 to UMR-DAP to discuss the software with Christophe Pradal, one of the main developers, and to the Site de Recherche

Biedenharn Group  
Vegetation Root Architecture Analysis for River Bank Stability Applications  
Final Report



Forêt-Bois of INRA in Pierrotin, near Bordeaux, to discuss applications of the software with Dr Frédéric Danjon, one of the main scientists researching 3D architecture of coarse root systems)

- assess the functionality of the software in terms of input data and pre-processing requirements, representation and display of plant root architecture, analyzing methods, (with particular emphasis on use in slope stability applications), 'operability' (user-friendliness), output data and limitations and constraints in using VPlants as a practical tool for application.

As the USACE has already undertaken a comprehensive literature review, it is not the purpose of this study to re-examine the literature related to the interaction of vegetation on slope stability, nor to evaluate existing slope stability models. In addition, it is not the aim of this research to provide a user guide or technical reference for VPlants (although, it is understood from the VPlants development team that a VPlants user manual will be developed and made available during 2009).

## 2 DEVELOPMENT OF PLANT ARCHITECTURE MODELING

### 2.1 Plant Architecture Defined

'Plant architecture is the three dimensional (3D) structure of an individual plant, including both the topological arrangement of components and their coarse geometric characteristics' (Reubens et al., 2007). For plant roots, it is the complete set of variables that characterize the 3D structure of a root system. Root 'topology' is concerned with the branching pattern and physical connections between root components and root 'geometry' defines the shape, size, orientation and location of root entities. Root branches can be defined as axes, each of which is linked at branch junctions and each includes a series of segments with interior links. The branching system is the basic object of the topology and the root segment is the fundamental unit of the geometry

### 2.2 History

The Functional-Structural Plant Modeling (FSPM) community aims to improve the understand of the biological processes involved in plant development and how plants function and is increasingly turning to mathematical models and computational models from various scientific disciplines to enable this objective to be met. Through this paradigm, the obvious need to develop routine and practical methods for describing and characterizing plant architecture and describing biological phenomena with respect to topological location became of paramount importance.

Emerging in the 1970s, plant architecture modeling is still a science in its infancy. Its application has since spread into a number of disciplines (Godin et al., 1997; Godin et al., 1999a) including computer simulation, botany, agronomy, forestry and plant-environment interaction modeling. Progression has been made through advances in organizing plant component information into structured formats according to topology. This was achieved through the AMAPmod system, enabling plants to be represented in a single model with different scales of description (eg. nodes, annual shoots, axes, etc).

AMAPmod was developed by C. Godin, Y. Guédon in the late 1990s at UMR-AMAP (l'Unité Mixte de Recherche - botAnique et bioinforMatique de l'Architecture des Plantes, which is the Joint Research Unit for Botany and Computational Plant Architecture), the former name of UMR-DAP. Its main functionality enables users to adopt a consist methodology to measure plant geometry and topology, to create plant databases in a formalized, structured format and to analyze and visualize information extracted from the data. Information from detailed field observations is initially represented in a delimited file using a dedicated encoding language. The AMAPmod system then reads this dataset and decodes the descriptions of plant geometry and topology before building a representation of the entire plant architecture. Once represented in AMAPmod, the user has a flexible range of tools to analyze, deconstruct, visualize and better understand the plant architecture in three dimensions.

The software focuses on plant architecture rather than simulating plant growth and has a dedicated programming language, AML (AMAP Modeling Language), so that, by writing AML script, users can have a high degree of interaction with their data. AMAPmod was pioneered for the Linux operating system, although an in-house Windows version was also developed. Using AMAPmod involves executing lines of AML code within a shell interface (with no graphical user interface) and requires specialist programming knowledge, which arguably limits its use within the FSPM community and beyond. In the AML shell, each line of code is executed in turn; the system evaluates the commands and returns a message displaying the output object. All operations are expressed as calls to 'functions' and AML includes a wide range of built-in functions (termed primitives). These functions can be split into

three groups: i) a kernel of standard functions for arithmetic calculations, reading and writing data, storing data, displaying graphs, etc.; ii) functions for exploring the plant architecture database, comparing the attributes of branching systems at different scales and extracting geometric and topological information for user-specified criteria, and; iii) a dedicated suite of general and advanced statistical tools to facilitate research on structures and regularities in plant architecture. The strength of AMAPmod is that the user can develop new functions based on the in-house primitives that can be reused for a number of applications (eg. the user can define a function to calculate the volume of a cone frustum, simulating the geometry of a plant root segment, which can then be queried by another function to calculate the entire volume of the root system or just the combined volume of roots for a specified branching order). For complex model applications, a series of sophisticated functions need to be developed and tested, which can potentially be a lengthy process.

The development, functionality and application of AMAPmod are described in Godin et al., 1997a; Godin and Caraglio, 1998; Godin et al., 1999a, b, and other publications). Applications in the field of agronomy are numerous and are not reviewed here. Godin et al. (1999a) notes that the focus in AMAPmod, and the purpose of most of the built-in statistical tools, is on data analysis tools for samples of sequences. In particular, the system is suited to investigate advanced research on the succession of architectural attributes along branching systems, for example exploring the distribution of leaves along tree branches using (hidden) semi-Markov chains, segmentation analysis, autocorrelation functions and smoothing functions. AMAPmod was not designed specifically for the purpose of analyzing tree root systems as the focus was directed at characteristics of architecture above the ground. However, the utility value of the AMAPmod for the study of root systems has been recognized since 1999 (Danjon et al., 1999a, b).

Although the various sources of literature over the past 10 years or so provide a general overview of the AMAPmod system, the principle source of ‘guidance’ for the actual use of the software is available for version 1.8 as an online manual (<http://amap.cirad.fr/amapmod/refermanual18/partHome.html>) and as a hard copy by request from UMR-DAP (Godin and Guédon, 2001). These references provide an overview of the system, and descriptions of input data formatting but the main feature is a list of all AML functions with brief descriptions of their operation and convention. However, the documents do not provide step-by-step guidance for new users and are really a source of reference for scientists already familiar with the basics of the software and the coding language of AML (for example gained from training courses or self-taught). This is a particular limitation of AMAPmod.

In 2003, the development of AMAPmod was then abandoned and is no longer available today. It has now been upgraded, reengineered and repackaged as the VPlants (Virtual Plants) module of the OpenAlea software platform, described below, and forms the focus for this evaluation. However, as OpenAlea is still relatively new, it is inevitable that the transition to VPlants from AMAPmod is a gradual process, particularly with the need to convert existing AML code to Python script in order to be processed within OpenAlea.

It is important to note at this point that OpenAlea is not the only software package of interest to the FSPM community. Other available software (not reviewed here) include: ‘L-Studio’ (Prusinkiewicz and Lindenmayer, 1990; Mech and Prusinkiewicz, 1996); VLab (Federl and Prusinkiewicz, 1999) and GrolMP (Kniemeyer et al., 2006), however they are more related to plant growth and development simulation rather than architectural analysis (Pradal, 2008).

## **2.3 OpenAlea**

ALEA refers to ‘Atelier Logiciel en Ecophysiologie et en Architecture 3D des plantes’, or the ‘Workshop for software in ecophysiology and in 3D architecture of plants’ and the software is primarily under development at the UMR-DAP research centre at CIRAD, Montpellier.

### 2.3.1 The Platform

The ALEA project seeks to provide biologists with a ‘homogeneous’ and accessible software platform, integrating a range of ‘tools’ for investigating plant architecture in a modeling framework. The software itself, OpenAlea, is not a model but rather a ‘framework, within which biologists can ask ‘questions’ about the architectural properties and characteristics of plants and gain an improved understand of these attributes through visualization. The way in which OpenAlea, and any of its components, are approached by a user really depends on the type of questions being asked. A simple analogy can be made with Microsoft Excel as it is not a model, per se, but rather a platform from which users can construct their specific queries by linking the various tools available to create a flow of data that generates a solution (a ‘dataflow’).

The OpenAlea platform is designed to foster scientific collaboration within the FSPM community through:

- free access to the software, tools, models and source code, encouraging model reusability and a continuous program of development
- support through training, e-learning, online documentation and an online forum accessible at <http://openalea.gforge.inria.fr>
- a common high-level language interface to all tools and models
- a user-friendly graphic user interface (GUI) called VisuAlea, for operating the various modules (by bringing together plant architecture analysis and visual programming).
- a set of general-purpose tools (eg. 3D plant representation, data structure) that can be reused by different modelers.
- availability on both Linux and Windows operating systems.

OpenAlea provides the computational environment to build models within a visual programming interface dedicated to plant modeling. At its simplest, OpenAlea is a collection of components with clearly defined input and output interfaces that can be designed into a ‘dataflow’ through their interconnection. These data structures (called composite nodes) can then be reused for other datasets and applications, modified by other modelers and inserted into more complex models comprising many composite nodes. Through this ethos of portability, reusability and interoperability of computational methods, scientists from different disciplines can progress research using a common modeling platform and the functionality of OpenAlea can be continually extended. OpenAlea is described in various sources of literature but a general overview is provided by Pradal et al., 2008.

The OpenAlea system is based on the Python script language (<http://www.python.org>), a common programming language in many scientific areas. It is a high-level, object-orientated script language that is ‘interpreted’, rather than ‘compiled’, providing a more open approach for model development between research teams. The performance of OpenAlea components themselves can be improved by including ‘extension modules (Python ‘wrappers’) that are written in other programming languages (eg. Fortran, C++) to optimize speed. Essentially, Python is the language that ‘glues’ the components together in a model. Unfortunately, the disadvantage of using a script language is that errors in the code syntax only become known at run-time and are not detected during compilation. This means that for complicated models, relying on hundreds of lines of Python script, it can be very time consuming for generating individual Python functions and modules (Python files containing a number of functions and script) from scratch. However, once the modules have been developed, they can be reused, modified and extended for other applications so the investment in time at the start is considered worthwhile. In summary, the use of Python is considered to represent a balance between interactivity, efficiency, stability, expressive power and legibility both for expert programmers and beginners (Pradal et al., 2008).

### 2.3.2 Licensing

One of the aims of the OpenAlea project is to share knowledge, experiences, methodologies and, importantly, development between various teams. Therefore, the source code of OpenAlea is offered under a free license and is available to run on both Windows and Linux platforms. In addition, all packages distributed in OpenAlea must have a free/Open Source license. To support this, OpenAlea is released under CECILL-C and CECILL-v2 licenses which define the principles of use and dissemination of free software in conformance with French law, granting the recipients of the computer program the following rights:

- the right to run the program, for any desired purpose
- the right to study how the program works, and modify it.
- the right to redistribute copies
- the right to improve the program, and release the improvements to the public.

These details are further elaborated on the OpenAlea licensing website and the development team at CIRAD, Montpellier can advise on the type of license needed for developers of new components. ([http://openalea.gforge.inria.fr/dokuwiki/doku.php?id=documentation:guidelines:license\\_guidelines](http://openalea.gforge.inria.fr/dokuwiki/doku.php?id=documentation:guidelines:license_guidelines)). For users that will not be distributing new programs under the OpenAlea framework but just operating the software for research purposes need not seek further information on licensing requirements, however the OpenAlea program should be mentioned in all research publications.

### 2.3.3 Software Components

OpenAlea includes the following modules:

#### *Plant Architecture Analysis (VPlants)*

Multiscale plant architecture datasets are developed from raw field measurements of plant measurements (usually made in the field). The geometry and topology of plants can then be visualized in 3D and explored at different scales through a suite of tools and functions. Collectively, these tools are available in the VPlants (Virtual Plants) module of OpenAlea.

#### *Plant Geometry Modeling*

A range of tools are available dedicated to investigating the geometry of plant assemblages (known as 'scene graphs) constructed from geometric objects. An entire forest can be created from a library of geometric objects (primitives), visualized in 3D and analyzed interactively. Scenes can then be used to investigate ecophysiological processes, particularly related to tree canopies (see below). These tools are available in a dedicated graphic library called PlantGL (Pradal et al., 2007) and are fully compatible with the VPlants module. In particular, the PlantGL Viewer is a powerful visualization tool that provides users with functionality to display and interactively explore in 3D 'PlantFrames' created from queries on plant architecture data.

#### *Ecophysiological Process Modeling*

Highly specialized models have been developed for the simulation of rainfall interception on multiple plants, assessing the biological implications of different light conditions within and below 3D canopies and for calculating radiation interception. As the OpenAlea community develops it is envisaged that these specialize components will become more numerous.

#### *Meristem Modeling*

A dedicated toolkit is available to botanists for investigating meristem properties, phyllotaxis (leaf development and arrangement) and the growth of plant tissue at the cellular level.

### 3 VISUALEA AND VPLANTS OPERATION

#### 3.1 Installation

A graphical tool has been developed to enable installation/removal of OpenAlea modules. The available packages are downloaded from the repository server at:

- <http://openalea.gforge.inria.fr>

and instructions for installation of OpenAlea are provided at:

- <http://openalea.gforge.inria.fr/dokuwiki/doku.php?id=download>

Before installing OpenAlea and its modules, a user must first install Python. Currently, OpenAlea is based on Python version 2.5. This is achieved via a link to the Python download page and for Windows using x86 processors, the current release is python-2.5.2.msi and is an automatic installation (other releases are available for different platforms and processors):

- <http://www.python.org/download/releases/2.5.2/>

OpenAlea includes its own installer package, with functionality to install and remove separate packages, for example VPlants. To begin, the user must download and run a Python script: 'ez\_alea\_setup.py', which then downloads the relevant files and enables the Installer to be opened from the Windows Start Menu under the OpenAlea group. Failure to download and run the installer (due to network problems or security issues), the individual packages of OpenAlea can be installed manually, although this is a rather cumbersome and time-consuming process.

Using the Installer software, the 'base' packages of OpenAlea that are the core of the software platform can be installed. VPlants itself contains all the packages developed and distributed by the Virtual Plants teams at UMR-DAP, Montpellier, France. In particular, it contains the functionalities of the redundant software AMAPmod as well as new components. The principal packages that should be installed comprise the following Python files:

- vplants.aml - the AML language and Python wrappers. The AML language has been developed by the VPlants team to use the primitives (functions) of the AMAPmod software. In Vplants, though, the AML coding convention has been replaced by the general purpose language, Python. However, all the functionalities of AMAPmod remain available in Python through the vplants.aml package.
- vplants.plantgl - the open-source toolkit for the creation and 3D visualization of virtual plants. This package offers extended functionality to vplants.aml, in particular for visualizing PlantFrame objects of queried plant architecture datasets.
- vplants.mtg - the MTG (Multi-scale Tree Graph) data structure. This package contains components to enable the input of structured plant datasets into VPlants and their manipulation.
- vplants.stat-tool - components for general statistical analysis

In addition, VPlants include packages for undertaking advanced statistical functions (particularly sequence analysis) and fractal analysis.

For ease of installation, it is recommended that all OpenAlea and VPlants packages be installed. Upon successful installation, an OpenAlea program folder is created under the Windows Start Menu containing the following: OpenAlea Installer (installation/removal of individual packages); a Python Shell (coding dialog box for interacting with the primitives of VPlants without using the graphical user interface and suitable for developing advanced functions); VisuAlea (the graphical user interface of OpenAlea, see below), and the PlantGL Viewer (for displaying 3D representations of plant architecture). The version of OpenAlea and VPlants used in this evaluation was 0.6.

### **3.2 Guidance and Support**

The OpenAlea website is a collaborative forum where content is provided by users and developers, enabling the sharing of tools, documentation and news. The site also provides user tutorials and some general guidelines for using OpenAlea, together with short presentations of the various components (within an elearning environment):

- <http://openalea.gforge.inria.fr>

In addition, the VPlants team maintains an additional website including supporting information on the software, publications, contacts and useful links:

- <http://www-sop.inria.fr/virtualplants>

Unfortunately, a user manual or reference manual for VPlants is not available. The OpenAlea website includes guidance on installation and 'getting started', however for new users there are no step-by-step instructions for navigating and operating the various functionalities of the OpenAlea platform or VPlants packages. This is a major limitation of the software. In addition, there is no guidance for script writing in Python and interacting with the VPlants functions using the Python shell facility. Although, improved guidance documents are planned for the future, currently the best support remains the AMAPmod reference manual (Godin and Guédon, 2001), for very brief descriptions on all the functions available in AMAPmod and now reengineered in VPlants, and discussing the software, examples and experiences with the developer and end-user communities.

### **3.3 Graphical User Interface (GUI)**

The OpenAlea GUI, VisuAlea comprises three areas (Figure 3-1): i) a central 'design' area containing workspaces, where each workspace can include a graphical description of the model or models being built (by linking 'component nodes' into 'dataflows'; ii) a package manager pane located on the left of the interface where a user can browse and select component nodes from available libraries installed on the user's computer and insert them into a model in an open workspace; iii) a Python interpreter (a dialog box or 'shell' below the design area where Python code can be entered and executed), which provides both a companion and sometimes alternative approach for designing models. The shell can also be used for outputting the results when running an individual model component or the entire dataflow to generate final scenarios.

#### **3.3.1 Nomenclature**

When working with objects within a workspace, the following nomenclature is important:

##### *Node*

This is an individual software unit or component, which performs a specific operation or process on data passed to it from its input ports, before outputting results through its output ports. The nodes can be edited simply by clicking on them, enabling a model to be explored interactively and different model scenarios to be run quickly. When a node is 'opened', a small dialog box is generated (termed a widget), where data can be edited.

#### *Dataflow*

This is a graph (similar to a flow chart) composed of nodes connected at their top and bottom edges by lines which transport data around the graph. Nodes can be connected if their data types are compatible. The idea of the dataflow graph is that users can generate models without needing to know advanced Python and can better understand the structure of models.

#### *Composite Node*

Often called a macro node, this node represents a single dataflow (comprising a range of nodes) and can be saved for later reuse or assigned its own input and output ports so that they can be inserted into other dataflows, enabling a nested hierarchy of components and a flexible means of reusing complex functions for different modeling purposes. Dataflows containing nodes and composite nodes can be saved as a standalone application or written to a python script file.

#### *Package*

This is a deployment unit containing a set of nodes, data, associated files and, if needed, meta information such as authors, license, version, etc.

#### *Package Manager*

This is a tree-like browsing facility, enabling users to browse or search for specific components within the library saved on a computer.

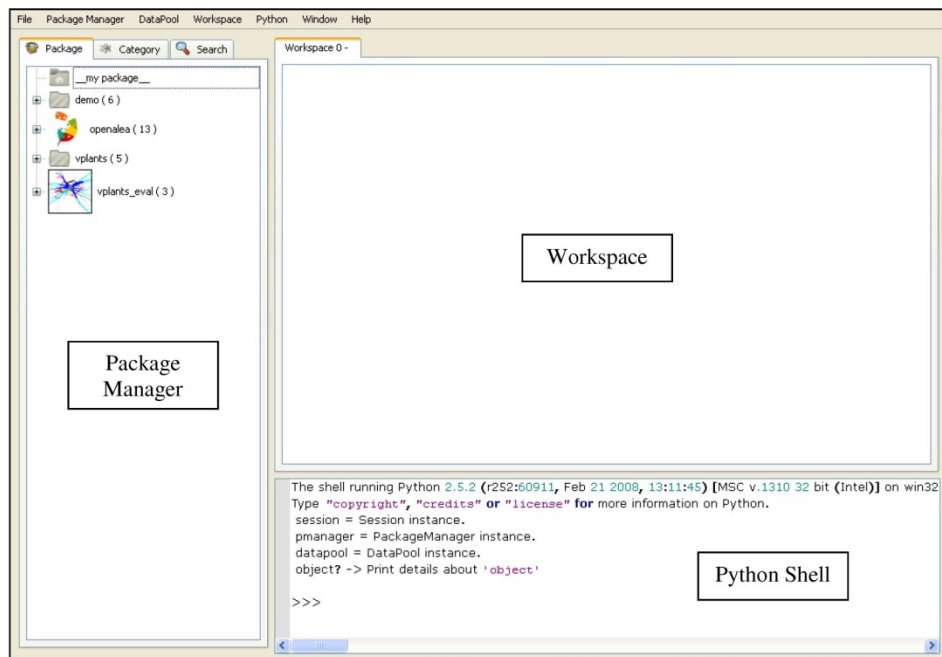


**Figure 3-1 The VisuAlea Graphical User Interface**

### 3.3.2 Using the Graphical Components

Although there is no ‘standard’ modeling process, after opening VisuAlea a user might start by creating a new package where all the components, dataflows and associated files for a modeling application can be grouped together. Creating a new package also creates a new folder in Windows Explorer where the python package files and any user files are stored. At any time during the model compilation, a dataflow in an open workspace can be saved as a composite node to the package. Composite nodes can then be opened in a workspace (by dragging into the workspace or clicking from the package manager). In this way, several versions of the same dataflow with different parameters can be quickly investigated.

Within the package manager, OpenAlea contains the default packages (or node libraries) listed in Table 3-1:

OpenAlea Package	Description
Color	Color map and color type objects
Data structure	Data type nodes (integer, float, string, etc.) and nodes for simple operations on raw data (eg. joining strings, operations for dealing with sets)
File	Input-output operations on files
Flow control	Operations related to the flow of data between nodes (eg. writing annotations next to nodes in a dataflow, writing data to a ‘pool’, which is a type of clipboard, for later retrieval)
Function Operator	Operations on functions (in particular the ‘function’ node enables users to define their own data operations for input to another node, providing data types are compatible).
Image	Image querying and physical manipulation
Math	A wealth of basic mathematical operators
Plottools	Creation of sequences, histograms
Python Method	A very useful package containing familiar Python data operations, querying and looping
Spatial	Creation of simple distributions (eg. dataset of 2D random data for creating a stand of trees)
Stat	A very useful package containing a wide-range of basic statistical functions, analysis of different types of statistical distributions, plotting histograms and functions, regression analyses and test statistics (eg. student t test).
System	Functions in this package are uncertain

Note: The components in each of the above packages do not have any documentation associated with them, therefore only the operation of nodes with intuitive titles can be discerned. In evaluating the software the functionality of a number of nodes was unclear.

**Table 3-1 Default packages available in OpenAlea**

When nodes are inserted into a workspace, they are shown as blue rectangles. They can be added, moved, copied, pasted or deleted and connected together by dragging the mouse cursor between output and input ports, assuming data are compatible between components (inputs are yellow dots on the top of the components and outputs are yellow dots on the bottom). By hovering the mouse cursor over a component, a tooltip shows the name of the node, input and output values, the operation described in Python convention and the name of the package that the node is catalogued under. When building a

dataflow, it is useful to add annotations to the workspace to describe the various data and functions. For complex models, ‘function’ nodes can be added to the graphical dataflow, where users can enter lines of dedicated Python script that comprise the function.

To illustrate the creation of a dataflow, Figure 3-2 shows the calculation of the volume of a cone frustum (dimensions in centimeters), which can simulate the shape of a plant root segment (a cone with the tip removed to derive a volume with two parallel circular edges of different diameters separated by a height at right angles to the circles). The equation for the volume,  $V_s$ , of the frustum is given in Equation 3-1:

$$V_s = \frac{\pi h}{12} (d_1^2 + d_1 d_2 + d_2^2) \quad (3-1)$$

where  $d_1$  and  $d_2$  are the top and bottom diameters and  $h$  is the perpendicular length.

The entire dataflow can be run from the Workspace menu and the ‘Print’ function outputs the result to the Python shell (alternatively, if the output was a graphical object the results can be ‘sent’ to the PlantGL Viewer (eg. a 3D scene of a forest).

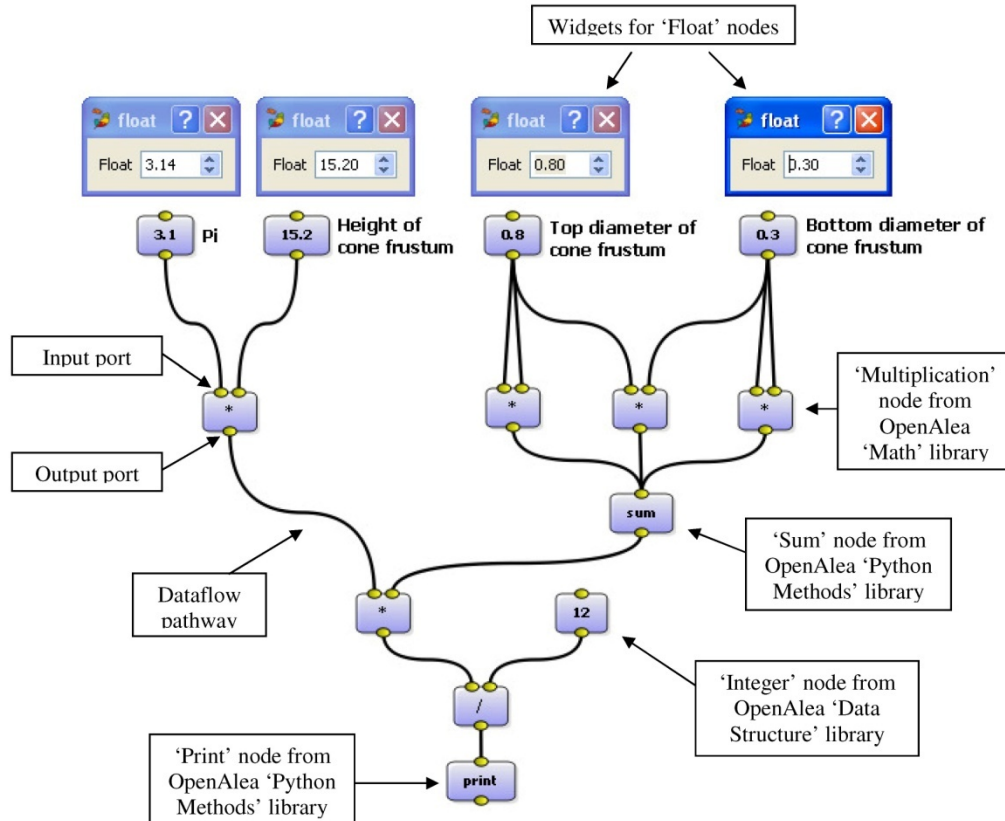


Figure 3-2 Example of dataflow created within a workspace: Volume of a cone frustum

By completing these types of functions in ‘graphical’ format, it quickly becomes clear that the process can be very time consuming and other methods (spreadsheets or dedicated macros) would be more suited. However, the advantage of developing functions within OpenAlea is that once the work has been undertaken in constructing the dataflows (and composite nodes), they can be reused quickly, inserted into other dataflows and shared between the user community. The VPlants components are discussed in Section 4.

An alternative to generating dataflows within workspaces is to write and execute the Python code directly within a Python shell. A shell facility has been added to OpenAlea and provides the user with functionality for performing complex data operations and advanced querying of the primitives in the vplants.aml package (in a very similar fashion to the previous AMAPmod software).

### 3.3.3 Using the Python Shell

The Python shell (see Figure 3-1) is suited to users with previous programming experience as script is written in Python as a series of operations and functions on a line by line basis. Although the downside is that a working knowledge of Python is required (which can be a major investment in time), once familiar with the Python syntax and AML primitives, direct coding in this way provides considerable flexibility and range of data queries that can be performed. The user has access to all the primitives in OpenAlea and VPlants as well as the built-in functionality of Python for data manipulation and input-output operations. For example, the Python function for calculating the volume of a root segment, described as a cone frustum, could be written as (compare with Figure 3-2):

```
# Volume of a segment is a cone frustum
#-----
def volume_conefrustum(h,d1,d2):
    return Pi*h*(d1**2+d1*d2+d2**2)/12
```

The built-in shell is limited to single line execution, which severely limits its use in running tens or hundreds of lines of script (which is quite normal in AMAPmod). However, there is no real reason why users must use the built-in shell as more flexible alternatives are available. For example, the standard Python interpreter (downloaded when installing Python itself), called IDLE, can run an entire module (text file usually with extension .py) of Python script (containing a large number of functions) in a fraction of a second. Alternatively, a user can select one of a number of other available interpreters (eg. iPython). All that is required is that the user references the VPlants primitives at the start of the python file. The actual programming itself can be undertaken either within a Python editor or in any text editor (eg. Textpad). Once a series of dedicated script has been written, it can be reused for any number of datasets. Programming in Python for root architecture analysis is discussed in Section 4.

## 4 APPLICATION OF VPLANTS FOR ROOT ARCHITECTURE ANALYSIS

### 4.1 Data Input

The operational process of using VPlants is schematized in Figure 4-1, below, and involves five stages: i) initially the subject plant or tree is observed and raw data collected on the geometry and topology; ii) this input dataset is reworked into the standard format of a Multiscale Tree Graph (see Section 4.1.1), essentially a text file with a strict coding convention; iii) the MTG is read by VPlants and deconstructed into a model comprising ‘vertices’ (physical plant components) and ‘edges’ (links between vertices) at various scales; iv) using the range of Python, OpenAlea and VPlants primitives (functions), the MTG can then be queried using Python script (either coded directly or through the GUI) to answer user-defined questions on the plant architecture; v) a range of basic and sophisticated models and statistical tools can then be applied for further analysis (either within VPlants itself or, by writing the processed data to a file, using a different software package or coding language).

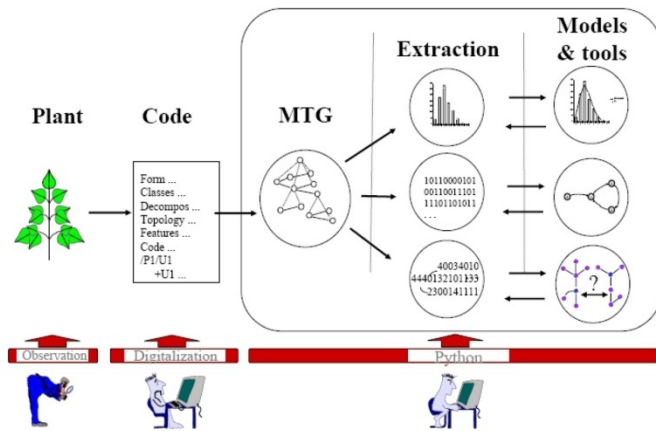


**Figure 4-1 The VPlants Process (Godin et al., 1999a)**

#### 4.1.1 Multiscale Tree Graphs

The plant representation format used in VPlants is the Multiscale Tree Graph (or MTG), which is able to integrate different scales of description within a single data structure. The MTG system was forwarded by Godin and Caraglio (1998) as a means of inputting a consistent data structure into AMAPmod and to enable a formalization suited to decoding and interrogation by the AMAPmod system. The coding language of MTG files also enables field observations of plant architecture (eg. through digitization) to be preprocessed in a standard and repeatable format, familiar to the FSPM community. VPlants uses the same MTG convention and once loaded into the software, an MTG database can be analyzed through the VPlants primitives (see Section 4.2).

An MTG includes data not only the geometry and location of plant attributes but also the topological relationships between these attributes. To construct an MTG, a plant is first ‘deconstructed’ into

physical components at different scales. For the portion of a plant above the surface, there are potentially a wide range of scales that can be included in the MTG (for example, internodes, growth units, flowering sites, branches, etc). In addition, the MTG captures the ‘order’ of the different components (for example the trunk is order 0, the first branches off the trunk might be order 1, etc). Notably, growth units might extend across more than one order (for example, the growth of a new branch might occur during the same growing period as the continued extension of the parent branch). In the MTG file, each attribute is conventionally referred to as a ‘vertex’ and the physical connection between adjacent vertices is termed an ‘edge’. The relationship between plant components can be of two types: i) a ‘precedes’ relation, denoted by a ‘<’ sign represents the ‘apical’ growth (ie. the extension of branches) and joins two components of the same type (eg physical indicators on branches or distinct changes in geometry); ii) a ‘bears’ relation, denoted by a ‘+’ sign, refers to the creation of a new axis with its own apical growth. In addition, a ‘/’ symbol means the vertex is nested within a vertex at a larger scale (eg. the first vertex along a branch will have this symbol)

The MTG system is described in numerous papers by Godin (eg. Godin et al., 1999a, for an apple tree orchard), however a detailed description and coding convention of the MTG file is provided in the AMAPmod reference manual (Godin and Guédon, 2001). Each MTG is different and is related to the convention used to define the scales of plant architecture. The majority of MTGs described in the literature refer to plant systems above the ground and often include data for more than one tree. In particular cases, with several scales of analysis, the MTG code file can be very complex. In contrast, the typical convention for coding MTG files for plant ‘root’ systems is more straightforward as there are generally only three scales of analysis: i) the plant or tree itself at Scale 0; ii) a root branch (or axis) at Scale 1, and; iii) individual branch segments that are defined in the field either by changes in physical characteristic (eg. diameter or direction) or, for relatively uniform branches, at user defined intervals. Growth units are not normally recorded as they are not clearly defined.

Each vertex in a root MTG has an alphabetical Label, and an Index. The label refers to the Scale (eg. ‘P’ is often used for Plant, ‘A’ for Axis and ‘S’ for root Segment). The convention of using the symbols ‘+’, ‘<’ and ‘/’ for root architecture are illustrated in Figure 4-2. Indices do not have to be unique but should increase incrementally for vertices with the same ‘complex’ (the vertex at the next higher scale; for example, all root segments along a particular axis). It is conventional to code an MTG file so that vertices for a particular branching order lie in the same data column, such that the number of columns listing the vertices corresponds to the number of branching orders. Any vertex which is prefixed by the ‘^’ symbol is connected to the next vertex up in the same column.

To illustrate the above coding convention, a partial MTG text file for a root system is provided in Appendix A). The example dataset has been provided by Dr Frédéric Danjon, from the Site de Recherche Forêt-Bois of INRA in Pierrotton, near Bordeaux, with permission to be used as a demonstration file for this project. The data include plant architecture for two *Pinus pinaster* trees. At the start of the file, there are several headers (the most important describe the symbols used for each scale and how vertices in each scale can be connected). The full structure of the header rows are described at the end of the AMAPmod reference manual (Godin and Guédon, 2001) and are not described further here. The first few columns of the MTG describe the topology of the root architecture and the remaining columns describe the coordinates (measured to the centre of the object) and top diameter of each vertex. This dataset comprises the minimum required for reconstructing the plant in 3D. Coordinates refer to the end of segments and the start of root branches for axes. Additional ‘features’ can be added to the MTG file, if needed and all ‘feature’ data can be read by the VPlants ‘Feature’ function.

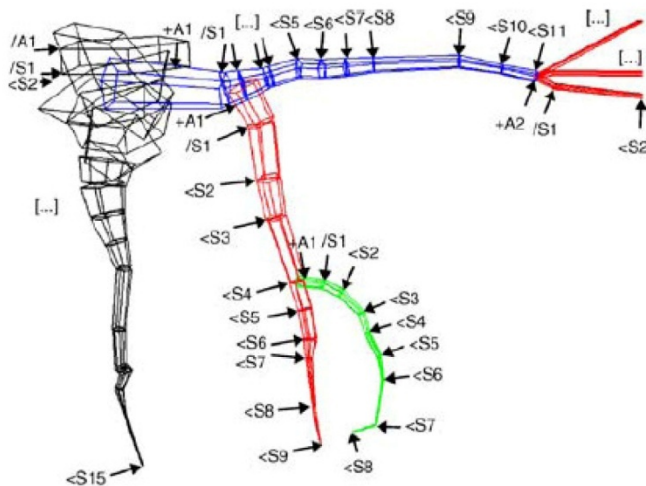


Figure 4-2 Example MTG structure for a root system (from Danjon and Reubens, 2008)

In summary, the coding convention of the MTG file is not immediately straightforward but for root systems the code files usually only contain three scales (plant, axis and segment), which is comparatively easier to understand by non-botanists (and new users to VPlants) than for files that represent tree canopies. Once the MTG is defined, input, analysis and output of data (assuming familiarity with Python and AML) can be performed very quickly and in a routine fashion. However, potentially the most intensive and challenging stage in the entire process is the measurement and collation of raw data, which is discussed in Section 4.1.2, below).

#### 4.1.2 Data Capture Methods for Root Architecture

Measuring and collecting root architecture data is a skilled and often lengthy process, normally performed by experienced botanists or tree scientists. There is no question that this stage in the VPlants process presents the most constraints for root architecture analysis. As part of this evaluation, data collection methods were discussed with Dr Frédéric Danjon and a brief overview of root measurement and detection methods is provided here. Importantly, the measurement process must preserve the information related to plant 3D structures, including both the type of entities and their topological relationships, as these data are required to build the MTG.

##### 3D Digitizing

The conventional method for measuring roots is invasive and involves manual excavation using spades and hand tools to delicately separate the roots from the soil matrix. A detailed description is provided by Danjon and Reubens (2008), who note that full excavation of a root system in 5 m<sup>3</sup> of soil volume and recuperation all coarse roots can take up to 8 man-days. In sandy soils, the process can be aided by wetting, however in most soils dry excavation is preferred aided by a high pressure air lance. In many cases, a substantial volume of horizontal roots are broken. Once the root system is exposed it can either be measured in situ or taken out of the soil and measured in a laboratory or under a makeshift shelter, holding the roots within a makeshift frame (Figure 4-3). It is important that roots are measured quickly

to prevent sagging of horizontal and oblique roots due to gravity and warping due to drying (thus changing the architecture). Unfortunately, some degree of error must be accepted in the measurement process as it is impossible to maintain the ‘exact’ position of all root segments as they were in the soil.



**Figure 4-3 Preparing *Pinus Pinaster* root system for 3D digitizing (photograph: Frédéric Danjon)**

Once removed from the soil, measurement is conventionally performed by 3D digitizing, which can be achieved using a number of methods. In many cases, roots of plants and small trees can be measured manually using a frame consisting of moveable rulers in the X and Y planes and a plumb bob to ascertain the 3D coordinates. Alternatively, the length, vertical angle and azimuth (using a clinometer) of each root segment can be measured, together with recording the topology, root axis base and segment end diameter (using a caliper). A system is now available (see Dupuy et al., 2007), called ArchiRoot, to program these measurements and automatically construct the MTG file (<http://www.archiroot.org.uk>).

Ideally, a semi-automatic digitizing device should be used, which was adapted to root systems by Danjon et al. (1999a). Although expensive to purchase, requiring specialist technical skills to operate and requiring a lengthy period to complete the measurements, this method is highly accurate. In addition, dedicated software can be used, such as ‘3A’ (Adam et al., 1999), to automatically capture the digitized data in MTG coding format. A caliper is used to measure axis base (proximal end) and segment end diameter (often two diameters are recorded), which is manually entered into the MTG feature columns (the topology also has to be set manually). A comprehensive review of using contact 3D digitizers for root measurement is given by Danjon and Reubens (2008) and example of an application is given by Danjon et al. (1999a).

In all cases of digitizing and to facilitate MTG coding, root measurement should start from the collar and work progressively downwards and outwards, undertaking measurements for each root branch to its tip and then returning to the main root (its parent) and continuing the processes (pruning each measured root along the way). The coordinates are actually measured on the external surface of the bark and then an adjustment is made to calculate the coordinates in the centre of the cross section. Further advice on root system excavation and digitizing can be acquired from Dr Frédéric Danjon at fred@pierrotin.inra.fr).

### Ground Penetrating Radar (GPR)

In contrast to manual excavation, Ground Penetrating Radar (GPR) offers a non-destructive geophysical technique for detecting changes in sub-surface materials and potentially a tool for mapping root architecture for the research community. The objective is to estimate the depth, position and size of roots from the character of reflected waveform.

Discussions on the use of GPR to detect plant roots are provided in several research papers (eg. Danjon and Ruebens, 2008; Dannoura et al., 2008; Hirano et al., 2009). The research indicates that GPR has mostly been applied for measurement of coarse root 'biomass' rather than geometry and topology. Attempts at measuring the size of individual roots has had only limited success, recognizing the inherent problem of radar methods with changes in soil moisture and other environmental factors. The limiting factors are outlined by Hirano et al. (2009) who conclude that where there are small intervals between neighboring roots (less than 20cm) and the volumetric water content of roots is less than 20% in sandy soil, GPR failed to detect the presence of *Cryptomeria japonica* roots. Roots were only visible to GPR with a cross section diameter greater than 19 mm at soils depths less than 80 cm. Danjon (2008, pers. comm.) and Danjon and Reubens (2008) elaborated on these finds with the following points:

- When there is little difference between the water content in the soil and that of a root, GPR has difficulty in detecting even the presence of the root (particularly the case in clayey soils)
- The central part of the root system produces confusing GPR profiles due to the density of roots
- Where roots overlap or are located in close proximity to each other, GPR results can be misleading and underestimate the biomass. Dense systems of fine roots are particularly problematic. This is also the case for 3D laser scanning techniques, which appear to be useful only to measure very simplistic root systems.
- Where roots are orientated vertically (for example, tap roots and sinkers), the GPR signal cannot identify objects running parallel to the scan properly.
- Research undertaken so far on using GPR to detect roots appears to have been undertaken in very controlled conditions and, in addition, has focused on the 'detection' of roots rather than the measurement of root characteristics.
- To measure root diameter from a GPR signal, the results are only as good as the correlation between waveform and diameter and in most cases there is a high degree of uncertainty.
- The main weakness of GPR is that it cannot measure architecture. Even if the geometry can be measured accurately, the topology cannot be ascertained.

In summary, it appears that GPR offers an 'opportunity for further research' rather than a reliable technique to capture the dynamics of 3D root architecture for use in VPlants at the precision required. With advances in resolution, GPR might, for example, be applicable to sandy levees (such as those in Sacramento, CA) but for soils with high clay content (for example, the Mississippi River levees) GPR is not applicable.

## 4.2 VPlants Primitives

VPlants includes a wide range of primitives (mirroring the functionality of AMAPmod) for querying root architecture. The only guidance available to users is the AMAPmod reference manual (Godin and Guédon, 2001), which includes a catalogue of the functions, albeit with very brief descriptions.

All operations on the primitives are expressed as function calls from Python script. The primitives are classified under the following modules:

- Kernel: these are general functions for undertaking mathematical operations, reading/writing data, storing variables, etc. The kernel functions are also available as graphical nodes under the OpenAlea package in VisuAlea.
- MTG: At the heart of VPlants, these dedicated functions enable users to access and query the plant root database. Primitives are available for MTG construction, retrieving information on MTG features (topology, geometry and location), navigating through an MTG and interpretation of vertex geometry (namely axis or segment for roots). For example, users can perform operations to move along axes, read successive segment data and classify segments according to branching order or location within the soil column. For exploring and classifying root segments according to geometry, topology and location, the MTG primitives are the most useful for root architecture analysis involving parameterization for slope stability studies.
- Stat: Dedicated statistical tools (mainly suitable for sequence analysis)

The full list of primitives is not repeated here and reference should be made to the AMAPmod reference manual.

Interestingly, not all of the primitives appear to be available as graphical ‘nodes’ in the OpenAlea and VPlants package libraries in VisuAlea. For example, the MTG package includes only 16 of the 55 primitives listed in the AMAPmod reference manual. The graphical nodes do, however, permit users to create dataflows for reading and plotting MTG data. An example of how a dataflow can be constructed to enable a user to visualize a plant root system in 3D is illustrated in Figure 4-4. In this example, annotations are used to provide short descriptions of the data operations. The main components of the data flow are:

- MTG: Interpretation by VPlants of the MTG coding file (entered in the top most ‘filename’ node)
- PlantFrame: The geometric representation of an MTG in 3D, according to user criteria (namely the list of vertices to show and ‘Scale’ for filtering the dataset). A number of additional input ports can be added, but typically users might require specifying: the distance between trunks (if the MTG contains more than one plant); the top and bottom diameters of each vertex to enable the volume of root material to be plotted rather than a skeleton (these data are extracted from the MTG ‘feature’ columns but require Python functions to be written); dressing data (see below)
- DressingData: This is a text file that enables users to control the geometric representation of MTG vertices (the actual plant root entities). Only limited guidance on the content and format of a dressing file is provided in the AMAPmod Reference Manual, however the file includes any changes the user would like to make to the default values used by VPlants to actually construct the geometry. For example, the default method for drawing the top and bottom of each entity’s volume is a hexagon, which can be changed to a circle to permit a more realistic visual representation, as adopted here.
- PlotPlantFrame: This function sends the constructed PlantFrame to the PlantGL 3D viewer (see Section 4.3). Additional data screening and option setting can be performed at this stage. For example, Figure 4-4 shows a function for filtering out vertices in the PlantFrame according to branching order (here, all axes are shown as the maximum order in the dataset is 3) and a particularly useful function for coloring axes according to their order). It is important to note here that these additional ‘functions’ are not available as drag-and-drop components but have to be manually typed or pasted into the widget dialog boxes.

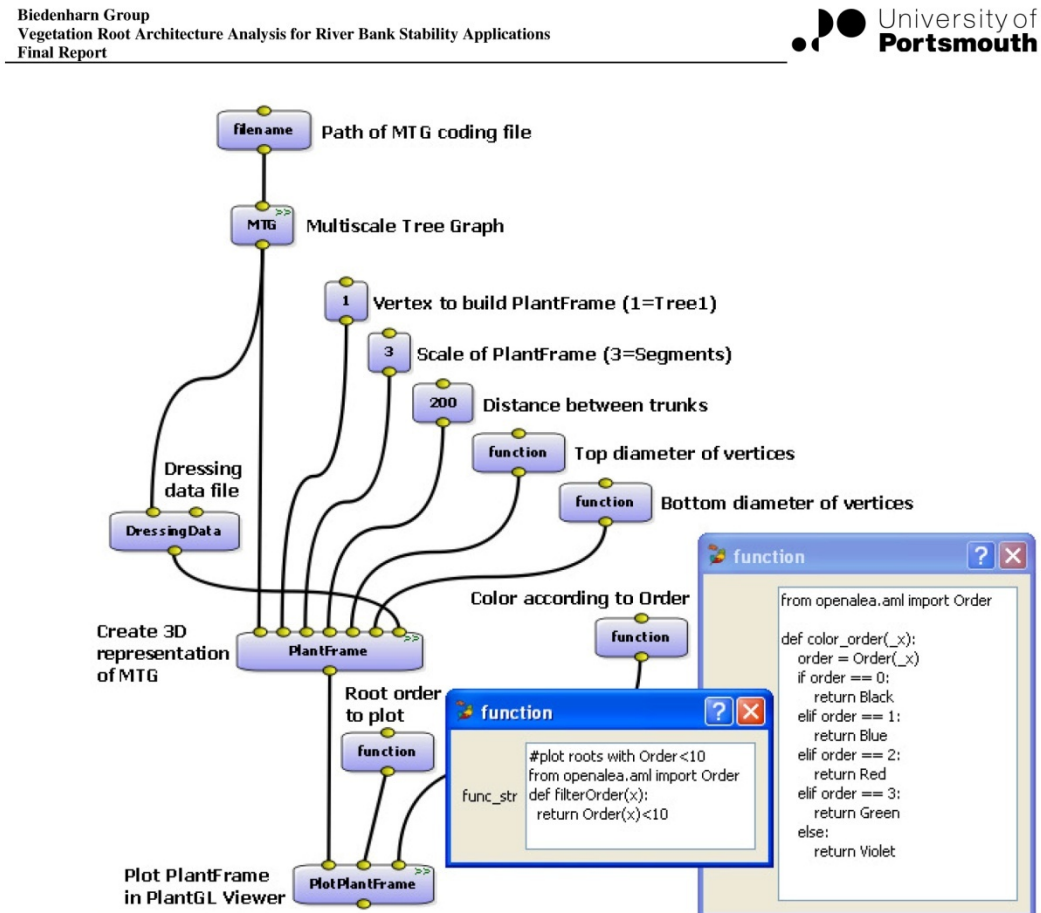


Figure 4-4 Example dataflow for importing and plotting a root system MTG

#### 4.3 Visualization of PlantFrames

Executing the PlantFrame primitive in VPlants, according to user defined criteria (MTG, Scale, etc), automatically opens the PlantGL viewer and displays the PlantFrame object in 3D. The PlantGL viewer interface is illustrated in Figure 4-5 for a *Pinus pinaster* root system. The functionality of the viewer centers on visualization and operation is straightforward. The PlantFrame can be displayed as a solid object, wireframe or skeleton and can be rotated in 3D and moved within the display area (either using the mouse or entering ‘camera’ parameters). A useful feature for assessing spatial scale is to display a grid on the x-y plane and/or the x-z plane (according to user-defined cell size). Secondary features include the ability to alter light conditions, select individual or groups of components (eg. root segments) and either remove the selection or replace it with a different representation (eg. solid volume to wireframe), display the PlantFrame in ‘perspective’ view and save the scene as a bitmap file. Finally, the viewer enables users to save the image in ‘POV-Ray’ format, which is a useful feature for producing lifelike 3D graphics that are suitable for publications and presentations (although not evaluated here). POV-Ray stands for Persistence of Vision Raytracer and is a freeware program for ‘ray-tracing’, which

is a rendering technique that calculates an image of a scene by producing realistic simulations of light on objects (pixel-by-pixel) according to the user-defined position of the camera. In this way, POV-ray can produce realistic reflections, shading, perspective and other effects. Danjon has used POV-ray for photo-realistic imagery in publications (eg. Danjon and Reubens, 2008).

In summary, the visualization functionality of VPlants and the flexibility of the PlantFrame primitive to deconstruct an MTG, according to user defined topological criteria, are extremely powerful features of VPlants for studying plant root architecture.

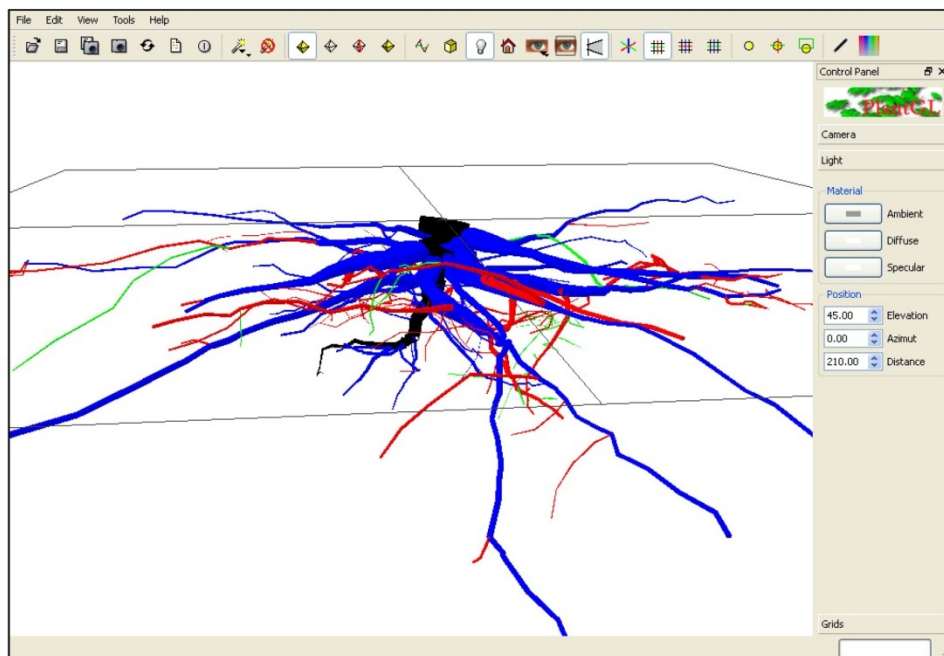


**Figure 4-5 Example 3D representation of *Pinus pinaster* root system (data from Frédéric Danjon)**

#### 4.4 Root Architecture Analysis

Although to visualize plant roots using the 3D PlantGL viewer requires little code-writing (only to manipulate the function nodes in a dataflow, as in Figure 4-4), to yield quantitative outputs from VPlants (eg. lengths, volumes, branching angles, etc) requires a degree of programming and familiarity with many of the AML and Python primitives. While the graphical user interface of VisuAlea and the composite node facility are very useful for simplistic operations and querying, to really interrogate an MTG (eg. to compare root architecture within different spatial domains around the tree, to meet radial distance, azimuth, depth and other criteria), the appropriate method is to write dedicated code in Python using the built-in Python shell feature or external Python interpreter. Based on this evaluation, it would just not be sensible or practical to use the composite, graphical node structure for complex queries.

There are potentially a large number of outputs that can be generated from an MTG in VPlants but they can broadly be classified into three groups depending on the scale of analysis:

- Summary characteristics of the entire root system (eg. total root volume, biomass, length, number of roots, maximum rooting depth, radial extension)
- Characteristics of individual root entities or those for a particular root axis or order of root axis (a user-defined 'scale' domain)
- Bulk characteristics of roots that fall within a zone of soil relative to the plant collar (a user-defined 'spatial' domain)

An initial evaluation might involve calculating a 'standard' range of root characteristics for every single root segment. This dataset can then be used to determine summary characteristics for the entire root system (for example, summing each root segment volume to calculate the entire volume of the root system), or used to perform further analysis specific to the type of application, which could be achieved either within VPlants using advanced Python script or in a different coding or software package (eg. spreadsheets, Visual Basic or the 'R Project' software for statistical computing, as used by Danjon for post processing).

Appendix B is a Python module developed for this project that can be used to output an extensive suite of root characteristics for individual root segments and axes. A substantial portion of the code has been converted and modified from AMAPmod functions written in AML, made available by Dr Frédéric Danjon for this project and used in his research. However, much of the script is entirely new, particularly for the analysis of root properties crossing a potential failure plane and for writing results to text files. The objective of this Python module is to provide a routine mechanism of outputting results in a standardized format. Of course, further functions and operations can be added to this module for specific applications. The module uses script that interacts with the VPlants primitives and includes operations for loading and displaying a PlantFrame object (to mirror the dataflow in Figure 4-4) and the 'standard' functions listed in Table 4-1.

Secondary functions are used to calculate the length, volume, position, orientation and branching angle for all axes. In this way, the characteristics of axes alone can be investigated, for example a user might want to calculate the total volume (hence biomass, if root material density is known) or maximum radial distance of all axes of a particular branch order.

Building on these datasets, it is possible to subdivide the soil column around a tree collar into distinct volumes (defined according to ranges of azimuth, perpendicular distance to surface and radial distance from the centre of the collar) and derive bulk root characteristics for these areas or for planes within the soil column. Using AMAPmod, this type of spatial analysis can be adopted to assess the impact on root asymmetry in response to wind and slope direction (eg. Danjon, 2005). In addition, Reubens et al. (2007) and Danjon et al. (2008) used a spatial analysis approach to explore the use of plant root architecture for inputs to models of shallow slope stability (see Section 4.5, below).

Python Function	Description
coord_seg_bot	Relative coordinates of bottom (start) of segment (relative to plant origin)
coord_seg_mid	Relative coordinates of the middle of a segment
coord_seg_top	Relative coordinates of top of segment
diam_seg_bot	Bottom diameter of segment
diam_seg_mean	Mean diameter of segment
diam_seg_top	Top diameter of segment
length_seg	Length of segment (unlike the standard 'Length' function in VPlants, this new function calculates the length of the first segment in an axis from the point where the new axis starts on the outside of the bearing axis and not from the centre of the bearing axis. This prevents double counting when calculating the segment volumes)
length_to_bottom_axis	Length between end (top) of segment and proximal end (start) of axis
length_to_top_axis	Length between end (top) of segment and distal end (tip) of axis
length_to_branch	Length of axis from segment to previous ramification on same axis
length_hor_seg	Horizontal length of a segment (projection on to x-y plane)
length_vert_seg	Vertical length of segment
dist_radial_seg_bot	Radial distance from the center of the collar to the bottom of a segment
dist_radial_seg_mid	Radial distance from the center of the collar to the middle of a segment
dist_radial_seg_top	Radial distance from the center of the collar to the top of a segment
volume_seg	Volume of segment (based on a cone-frustum)
azimuth	Azimuth of segment direction from 0 to 360 degrees (north is +x direction)
vert_angle	Vertical angle of segment between 0 and 90 with horizontal (horizontal=0)
vert_angle_class	Classification of vertical angle of segment (user defined to enable deviding roots into classes of inclination, eg. vertical, oblique and horizontal)
branching_angle_seg	Branching angle of the axis containing the segment

Note: 'bottom' refers to the proximal end (nearest the base of an axis) and 'top' refers to the distal end (nearest the tip of an axis)

**Table 4-1 Standard Python functions for extracting individual root segment characteristics**

By adopting a spatial analysis approach, it is possible to examine how root properties vary with depth (perpendicular distance to surface if on a slope) or across planes parallel to the x-z axis. For example, Danjon (1999a) plotted the 2D spatial distribution of root volume as a continuous function of depth and radial distance. This was achieved by extracting discrete data for a series of planes at increments of depth and interpolating the results. Notably, while the data extraction was undertaken in AMAPmod, post-processing and graphing was performed in the R Project software package. In a similar approach, Danjon et al. (2008) explored the relationships of several bulk root properties with depth (Figure 4-6). These types of analyses can be performed through application of the Python script in Appendix B.

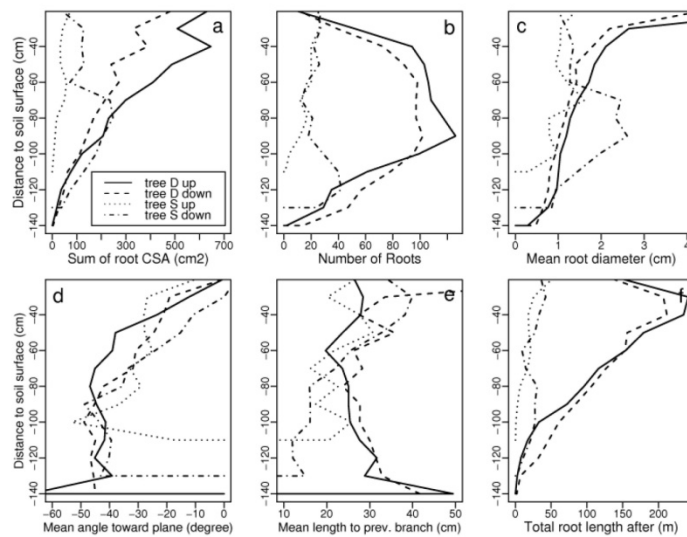


**Figure 4-6** Vertical distributions of a number of root parameters where roots intersect planes parallel to the slope at 0.1 m intervals (example from Danjon et al., 2008)

#### 4.5 VPlants Functionality for River Bank Stability Models

There is very limited research on using plant architecture analysis methods for aiding slope stability assessment and control and there is a complete absence of literature bringing together root architecture analysis using dedicated software and river bank stability models. Notable published research includes Reubens et al. (2007) and Danjon et al. (2008). The functions in Table 4-1 provide an insight into root parameters but they are not all directly linked to slope stability processes. While it would be useful if VPlants could calculate at the press of a button all parameters that are thought to have an influence on soil mass movement, unfortunately the user must develop further dedicated python scripts.

Reubens et al. (2007) provide a table of influencing root parameters, which includes:

- root density (RD): dry mass of living roots in a unit volume of soil
- root length density (RLD): length of root present in a unit volume of soil
- root area ratio (RAR): root cross sectional area per unit soil surface
- inclination: angle of root crossing a potential failure plane
- maximum root depth
- mean length to previous branch
- total length after intersection point: length of root after the potential failure plane
- branching pattern: undefined
- angle between laterals: possibly defined as the branching angle

The Python module in Appendix B includes a ‘horizontal plane analysis’, which involves the calculation of root characteristics for those segments crossing a user-defined horizontal plane. For vegetation on slopes, the coordinate system should first be rotated so that the x-y plane is parallel to the ground surface. This can be done, for example, by loading the MTG file into a spreadsheet and changing the coordinates using a simple trigonometric equation for rotating coordinate systems about the origin. The user can then enter (by changing default values within the Python module) the depth (perpendicular length from soil surface to the potential failure plane) and constraints of radial distance, inclination, azimuth, minimum length of branch above the plane and minimum length of branch below the plane. For every segment crossing the plane that meets these criteria, the same suite of parameters in Table 4-1 are generated. In particular, this analysis outputs the inclination of roots crossing a potential failure plane and the axis length either side of the potential failure plane.

One of the most important parameters in consideration of the impact of plant roots on slope stability is the ‘root area ratio’. Danjon et al. (2008) demonstrates how root architecture can be used to compute accurately the factor of safety of a forested slope, primarily by calculating root area ratio and root inclination at potential failure planes (as an improvement on less rigorous methods or the use of default values). The root area ratio is an important ‘physical’ vegetation parameter in influencing slope stability because it measures the proportion of a failure plane that is occupied by roots and can be easily converted into a measure of root force per square meter by multiplying by the mean tensile strength of roots, if known). This ‘additional’ force is used in models such as SLIP4EX (Greenwood, 2006) that attempt to account for vegetation in slope stability analysis. However, it is important to realize that root area ratio is not constant across a plane but varies significantly with distance from the soil surface and collar. Recognizing this, Danjon et al. (2008) used AMAPmod to perform a spatial analysis and output root area ratio for different radial slices within a potential failure plane (Figure 4-7).

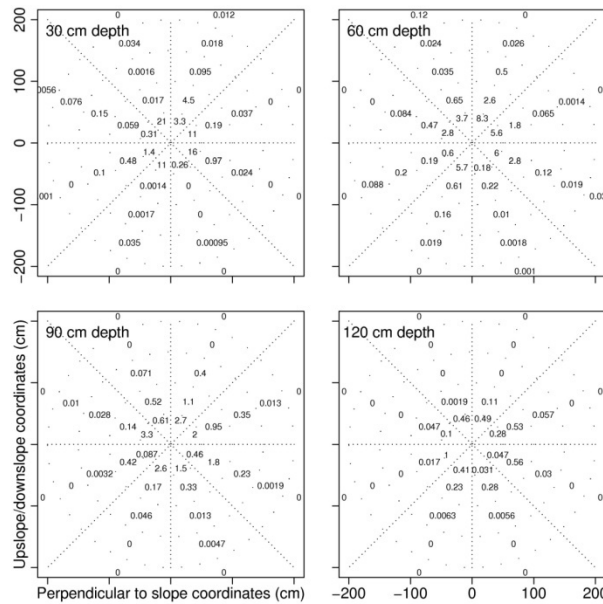


**Figure 4-7 Multiple 2D distribution of root area ratio in four planes parallel to the slope at 0.3 m intervals (from Danjon et al., 2008)**

Using a dedicated Python function ('root\_area\_ratio\_hor\_plane') in Appendix B, this type of approach can be performed routinely on an MTG in VPlants.

A similar approach could be adopted in VPlants for vertical planes (or perpendicular to the ground surface, if on a slope) at increasing distances from the core, or an oblique plane could be defined to simulate a levee face in order to examine root architecture near levee sides and the potential risk, albeit qualitatively, of piping and subsequent erosion

In undertaking any type of spatial analysis on root architecture, results can potentially be misleading if root segments are particularly long as they can cross the user-defined spatial boundaries by significant lengths. This has been recognized by Danjon et al. (2008), who developed a method for discretizing root segments into 10mm sub-segments, thus overcoming this problem when assessing spatial distributions. It is understood that this process was performed in AMAPmod. As an alternative, it is possible to rework an existing MTG coding file to perform this segment division. Visual Basic code in Appendix C has been written specifically to meet this objective, outputting a much longer MTG file for a user-defined maximum segment length. The new PlantFrame in VPlants is visually identical to the original and the same set of functions in Appendix A can be applied to the new MTG.

#### 4.6 Data Output and Post-Processing

VPlants provides very little functionality for outputting data to file. In particular, there is no quick method for creating an ASCII text file of large datasets for segment characteristics, which would be very useful for post-processing within other software packages. To overcome this weakness, the Python module in Appendix B includes a series of statements for creating four text files, as follows:

1. A file called 'Segments\_all.txt' includes an extensive table of all root architecture properties in Table 4-1 for the entire set of segments (based on either the original or discretized MTG).
2. A file called 'Axes\_all.txt' includes all root architecture properties for the entire set of axes, written for each branching order to enable bulk characteristics to be calculated.
3. A file called 'Segments\_hor\_plane.txt' includes all root architecture properties in Table 4-1 for the entire set of segments crossing a horizontal plane (assuming coordinates in an MTG file have first been rotated, if the vegetation is sited on a slope). This dataset is extremely useful for plotting root cross sections within different planes or for informing slope stability studies (eg mean angle of vertical inclination). This file can be rewritten for different sets of spatial constraints (enabling plots such as Figure 4-7 to be produced).
4. By repeating the analysis used in (3), a file called root-area-ratios.txt includes a list of root area ratios for user-defined increments of depth up to a set depth limit. This file can then be loaded into any plotting software to generate a graph similar to Figure 4-6. Clearly, this script can be extended to write depth profiles for any parameter.

The Python script for generating these files has been developed purely with a view to undertaking a comprehensive review of the VPlants software. The Python module can be developed further to provide additional functionality and output other types of data depending on the type(s) of application (for example, to add a function to estimate root density could be achieved relatively easily).

---

**Biedenharn Group**  
Vegetation Root Architecture Analysis for River Bank Stability Applications  
Final Report



This page is intentionally left blank.

## 5 CONCLUSIONS – VPLANTS ‘SWOT’ ANALYSIS

SWOT Analysis is a strategic method used to evaluate the Strengths, Weaknesses, Opportunities, and Threats involved in a project, venture or approach. For the evaluation of the VPlants: ‘Strengths’ are attributes of the software that are helpful in achieving the objective of using vegetation root architecture for deriving outputs that can be used in river bank and levee stability applications; ‘Weaknesses’ are attributes that present limitations and difficulties in achieving this objective; ‘Opportunities’ are external conditions that might be helpful to achieving the objective, and; ‘Threats’ are external conditions that might inhibit the use of VPlants for these types of applications.

### 5.1 Strengths

- VPlants is a flexible software package, enabling users to construct graphical dataflows and/or modules of Python script in order to answer specific questions on root architecture for different scales of analysis. For example, through a series of dedicated functions, it is possible to calculate root inclination, root area ratio and other parameters for all roots crossing a potential failure plane. Through a comprehensive suite of built in functions, users can explore root architecture and output a potentially wide range of parameters.
- Data input to VPlants is via a Multiscale Tree Graph (MTG) coding file, which is a recognized formulation within the end user community, enabling geometry and topology at multiple scales to be structured in a standard configuration. Reading an MTG file is extremely fast.
- The graphical user interface, VisuAlea, provides users with a graphically-structured approach for generating root architecture parameters for simplistic applications, without the need for more than a basic knowledge of Python programming.
- The PlantGL 3D viewer is a powerful feature of VPlants for visualizing and exploring root architecture. ‘PlantFrame’ objects can be developed by querying input datasets and then plotted in the viewer using a simple dataflow in VisuAlea.
- Once a dataflow or Python module has been developed, processing tasks in VPlants and outputting results can be undertaken in seconds and routinely for numerous MTGs.

### 5.2 Weaknesses

- A major weakness of VPlants is that, for complex querying, the graphical user interface is considered cumbersome and impractical and a substantial investment in learning the Python programming language is needed (particularly for users with little or no previous programming experience).
- The general front end of VPlants is not particularly user-friendly as it is very different from conventional software with Windows interfaces and operation is not straightforward. There are no Windows toolbars for completing tasks and users must ‘design’ their own functions and operations which can be very time consuming.
- VPlants has no ‘built-in’ functionality for outputting data for use in slope stability or river bank stability models. Users have to develop their own functions.

### 5.3 Opportunities

- VPlants exists within an open source software platform. It is free to use and develop and is constantly being improved. There are very supportive developer and end-user communities.
- The operational flexibility of VPlants means that packages, Python script and outputs could potentially be interfaced with other software packages or models, including those for assessing stability on slopes with vegetation.
- The Python coding language has a strong following within the scientific community, which will facilitate future improvements within VPlants.

### 5.4 Threats

- The collection of raw data to develop an MTG file is considered to be the main constraint to the routine and practical use of VPlants. Data collection is resource intensive and requires specialist knowledge of tree root systems to record the topology and specialist skills to excavate and measure the roots for developing the MTG file. There are numerous sources of difficulty, error and uncertainty in the data collection phase. Ground Penetrating Radar cannot be used to generate a dataset that can be read by VPlants due to errors in root detection, limitations in different environmental conditions, inability to reproduce topological relationships and uncertainty in correlating waveform with root diameter.
- Existing input datasets are limited. Ideally, a database of MTGs is needed for a range of species (and vegetation of different ages) to enable VPlants to have wide-ranging utility value. Relying on an MTG for a single root system presents uncertainty as outputs are just a snap-shot of the total population of root systems for the target vegetation species.
- A major limitation of VPlants is the absence of a user-guide. Although the existing reference manual for AMAPmod is useful for understanding the functionality of VPlants, for new users the software can appear quite alien and a step-by-step guidance document for different examples and applications would be very useful.
- Existing users of AMAPmod have invested significant time and resources in developing coding modules written in the dedicated programming language AML and moving to VPlants requires converting these code files to Python. This factor could affect the general uptake of VPlants.
- The application of root architecture analysis to slope stability and river bank stability modeling is not widely-reported in the literature.
- Post-processing and some functions of VPlants can quite easily be undertaken using a different software package or just a spreadsheet and attempting to keep all activity within the OpenAlea framework is potentially very challenging. Exporting data from VPlants for further analysis is not embracing the objective of OpenAlea for a collaborative expansion of reusable functionality.

## 6 REFERENCES

- Adam B, Sinoquet H, Godin C, Dones N. 1999. 3A - A software for the acquisition of plant architecture. Version 2.0. Clermont-Ferrand: UMR PIAF INRA-UBP.
- Danjon, F, Reubens, B. 2008. Assessing and analyzing 3D architecture of woody root systems, a review of methods and applications in tree and soil stability, resource acquisition and allocation. *Plant Soil* **303**: 1-34.
- Danjon F, Fourcaud T, Bert D. 2005. Root architecture and wind-firmness of mature *Pinus pinaster*. *New Phytologist* **168**: 387-400.
- Danjon F, Barker D, Drexhage M, Stokes A. 2008. Using 3D root architecture in models of shallow slope stability. *Annals of Botany* **101**: 1281-1293.
- Danjon F, Bert D, Godin C, Trichet P. 1999a. Structural root architecture of 5-year-old *Pinus pinaster* measured by 3D digitising and analysed with AMAPmod. *Plant Soil* **217**: 49-63
- Danjon F, Sinoquet H, Godin C, Colin F, Drexhage M. 1999b. Characterisation of structural tree root architecture using 3D digitising and AMAPmod software. *Plant Soil* **211**: 241-258
- Dannoura M, Hirano Y, Igarashi T, Ishii M, Aono K, Yamase K, Kanazawa Y. 2008. Detection of *Cryptomeria japonica* roots with ground penetrating radar. *Plant Biosystems* **142**(2): 1-16.
- Dupuy L, Fourcaud F, Lac P, Stokes A. 2007. A generic 3D finite element model of tree anchorage integrating soil mechanics and real root system architecture. *American Journal of Botany* **94**:1506-1514.
- Federl P, Prusinkiewicz P. 1999. Virtual laboratory: an interactive software environment for computer graphics. In *Proceedings of Computer Graphics International*. IEEE Computer Society: Washington, DC; 93-100.
- Godin C, Caraglio Y. 1999. A multiscale model for plant topological structures. *Journal of Theoretical Biology* **191**: 1-46.
- Godin C, Costes E, Caraglio Y. 1997. Exploring plant topological structure with the AMAPmod software: an outline. *Silva Fennica* **31**: 355-366.
- Godin C, Guédon Y, Costes E. 1999a. Exploration of a plant architecture database with the AMAPmod software illustrated on an apple tree hybrid family. *Agronomie* **19**: 163-184.
- Godin C, Costes E, Sinoquet H. 1999b. A method for describing plant architecture which integrates topology and geometry. *Annals of Botany* **84**: 343-357.
- Godin C, Guédon Y. 2001. *AMAPmod - Installation and Reference Manual*. Version 1.8. CIRAD/INRA - UMR Modelisation des Plantes, Montpellier, France
- Godin C, Sinoquet H. 2005. Functional-structural plant modelling. *New Phytologist* **166**: 705-708.
- Gray DH, MacDonald A, Thomann T, Blatz I, Shields FD Jr. 1991. Repair, Evaluation, Maintenance, and Rehabilitation Research Program: The Effects of Vegetation on the Structural Integrity of Sandy Levees. Army Engineer Waterways Experiment Station, Vicksburg, Mississippi, Environmental Lab. Final Report. August, 1991.
- Greenwood JR. 2006. SLIP4EX - A program for routine slope stability analysis to include the effects of vegetation, reinforcement and hydrological changes. *Geotechnical and Geological Engineering* **34**: 449-465.

- Hirano Y, Dannoura M, Aono K, Igarashi T, Ishii M, Yamase K, Makita N, Kanazawa Y. (2009, in press). Limiting factors in the detection of tree roots using ground-penetrating radar. *Plant and Soil*.
- Kniemeyer O, Buck-Sorlin G, Kurth W. 2006. GroIMP as a platform for functional-structural modelling of plants. In Functional-Structural Plant Modelling in Crop Production. Springer-Verlag: Dordrecht, The Netherlands; 43–52.
- Mech R, Prusinkiewicz P. 1996. Visual models of plants interacting with their environments. In *SIGGRAPH '96*, Rushmeier H (ed). Addison-Wesley: New York; 397–410.
- Morris M, Dyer M, Smith P. 2007. Management of flood embankments: A good practice review. R&D Technical Report FD2411/TR1, Joint Department for Environment, Food and Rural Affairs (Defra), Environment Agency (EA) Flood and Coastal Erosion Risk Management R&D Programme. November, 2007.
- Pradal C, Boudon F, Nouguier C, Chopard J, Godin C. 2007. PlantGL: a Python-based geometric library for 3D plant modeling at different scales. Research Report 6367. Centre de recherché, INRIA, Sophia Antipolis Cedex, France.
- Pradal C, Dufour-Kowalski S, Boudon F, Fournier C, Godin C. 2008. OpenAlea: a visual programming and component-based software platform for plant modeling. *Functional Plant Biology* **35**: 751–760.
- Prusinkiewicz P, Lindenmayer A. 1990. *The Algorithmic Beauty of Plants*. Springer-Verlag: New York.
- Reubens B, Poesen J, Danjon F, Geudens G, Muys B. 2007. The role of fine and coarse roots in shallow slope stability and soil erosion control with a focus on root system architecture: a review. *Trees* **21**: 385–402.

---

**Biedenharn Group**  
Vegetation Root Architecture Analysis for River Bank Stability Applications  
Final Report

---



---

**APPENDICES**

---

---

**Biedenharn Group**  
Vegetation Root Architecture Analysis for River Bank Stability Applications  
Final Report

---



This page is intentionally left blank.

**Biedenharn Group**  
**Vegetation Root Architecture Analysis for River Bank Stability Applications**  
**Final Report**



## **Appendix A: - Example MTG File**

Extract from MTG coding file for root system of *Pinus pinaster* (dataset courtesy of Frederic Danjon, measurements in cm; full file comprises two trees and 10728 lines):

CODE				
CLASSES:				
SYMBOL	SCALE	DECOMPOSITION	INDEXATION	DEFINITION
\$	0	FREE	FREE	IMPLICIT
P	1	CONNECTED	FREE	EXPLICIT
A	2	LINEAR	FREE	EXPLICIT
S	3	FREE	FREE	EXPLICIT
DESCRIPTION:				
LEFT	RIGHT	RELTYPE	MAX	
A	A	+	?	
S	S	+	?	
S	S	<	1	
FEATURES:				
NAME	TYPE			
XX	REAL			
YY	REAL			
ZZ	REAL			
TopDia	REAL			
MTG:				
ENTITY-CODE	XX	YY	ZZ	TopDia
/P28	0	0	0	9.93
/A1	0	0	0	9.93
^/S1	0.440345	0.20326	-2.65884	9.93
+A1	-3.43982	4.01468	-4.79205	4.5
^/S1	-3.33728	6.39602	9.22514	4.5
+A1	-4.88007	8.08308	9.46345	2.12
^/S1	-6.23842	15.4519	-8.77316	1.8
^/S2	-10.3791	22.8726	9.45847	1.2
+A1	-11.8292	22.9782	9.36703	1.2
^/S1	-14.6768	23.0855	-11.5733	0.2
^/S2	-16.5385	21.8188	-13.8863	0.18
^/S3	-17.4745	18.3855	-16.7719	0.15
^/S3	-12.8905	27.7095	9.80002	1.2
^/S4	-12.6599	28.2702	9.55196	0.8
^/S5	-10.5943	30.1042	-7.6011	0.7
^/S6	-4.53266	34.0461	-3.58035	0.7
^/S7	-0.665474	35.1898	-2.33567	0.7
^/S8	3.7749	38.0844	-0.567882	0.55
+A1	5.09431	38.4719	-0.212859	0.28
^/S1	6.34993	36.9666	-0.35734	0.25
^/S2	8.0968	35.5688	-0.659749	0.25
^/S3	10.2653	33.2743	-1.85473	0.23
^/S4	10.8883	31.3326	-1.77017	0.23
^/S5	11.5745	28.9154	-2.59256	0.25
^/S9	5.43477	38.9821	-0.0260875	0.46
^/S10	10.1235	41.5962	-0.096798	0.46
+A1	10.6639	41.6541	-0.0594279	0.23
^/S1	12.453	37.8551	-2.14903	0.2
^/S2	13.9522	34.468	-5.95149	0.28
^/S3	16.8322	32.2798	-9.12324	0.1
^/S11	10.7845	41.8738	-0.088829	0.4
^/S12	14.6203	43.4	-0.0111011	0.4
^/S13	15.6075	44.3225	-0.708802	0.4
+A1	16.1313	44.5074	-1.27701	0.24
^/S1	16.7407	44.5757	-2.94411	0.22
^/S2	17.3776	43.8332	-6.48647	0.2
^/S3	16.8395	43.4313	-8.89719	0.2
^/S4	17.3912	41.9022	-10.1554	0.2
^/S14	16.2779	44.8416	-0.458097	0.3
^/S15	22.0107	49.957	-0.46401	0.25
^/S16	26.0012	53.5043	-2.83457	0.25
^/S17	30.5475	56.2021	-0.455048	0.25

---

**Biedenharn Group**  
Vegetation Root Architecture Analysis for River Bank Stability Applications  
Final Report

---



This page is intentionally left blank.

## Appendix B: - Python Module for Root Architecture Analysis

The following Python module contains a suite of functions and commands that interact with the functions of VPlants to generate root architecture parameters for user-defined root segments, axes or entire root systems for different criteria. A portion of this Python script has been converted and modified (with permission) from AML script used previously by Frédéric Danjon in AMAPmod. The script relating to the calculation of root characteristics along a potential failure plane parallel to the soil surface, calculations for root area ratio and all code for outputting results to text files is completely new.

```
#-----
# Enable VPlants aml functions
#-----
from openalea.aml import *

#-----
# Enable standard math functions in Python (eg degrees)
#-----
from math import *

#NB function names are case sensitive
#s refers to vertex number of a segment (scale 2)
#a refers to vertex number of an axis (scale 1)

import os
prev_dir=os.getcwd()

#-----
# Set default directory for file input-output
#-----
dir='C:\\\\Vplants\\\\' #change directory accordingly
os.chdir(dir)

# General functions for vector calculations
#-----
# i) Addition of two vectors, v1 and v2
#-----
def vplus(v1,v2):
    if len(v1) == len(v2):
        return [v1[i] + v2[i] for i in range(len(v1))]
    else:
        return Undef

#-----
# ii) Subtraction of vector v2 from vector v1
#-----
def vminus(v1,v2):
    if len(v1) == len(v2):
        return [v1[i] - v2[i] for i in range(len(v1))]
    else:
        return Undef

#-----
# iii) Division of vector v1 by a scalar value k
#-----
def vdiv(x,v1):
    return [v/x for v in v1]

#-----
# iv) Multiplication of vector v1 by a scalar value k
#-----
def vmul(x,v1):
    return [v*x for v in v1]
```

**Biedenharn Group**  
**Vegetation Root Architecture Analysis for River Bank Stability Applications**  
**Final Report**



```

#-----
# Distance between two points (two sets of coordinates)
# NB v1,v2 here are vectors
#-----
def dist(v1,v2):
    x1,y1,z1=v1
    x2,y2,z2=v2
    return ((x2-x1)**2 +(y2-y1)**2 +(z2-z1)**2 )**0.5

#-----
# Volume of a segment is a cone frustum
#-----
def volume_conefrustum(h,diam1,diam2):
    return Pi*h*(diam1**2+diam1*diam2+diam2**2)/12

#-----
# Load MTG file
#-----
g=MTG(dir+'MTGdemol.txt')

#-----
# Set Dressing file (to override defaults for PlantFrame)
#-----
dressing=DressingData(dir+'dressingdemol.txt')

#-----
# For plotting : each segment are coloured as a function of his order
#-----
def color_order(s):
    order = Order(s)
    if order == 0:
        return Black
    elif order == 1:
        return Blue
    elif order == 2:
        return Red
    elif order == 3:
        return Green
    else:
        return Violet

#-----
# 1) Bottom diameter of segment
#-----
def diam_seg_bot(s):
    if Rank(s) == 0: return Feature(Complex(s), "TopDia")
    else: return Feature(Father(s), "TopDia")

#-----
# Compute the PlantFrame for plant stemming from Vertex 1
# (NB First argument: 0=all data, 1=Plant1, x=Plant2 where x is vertex number of Plant2)
#-----
f0 = PlantFrame(1, Scale=3,BottomDiameter=diam_seg_bot,DressingData=dressing, TrunkDist=200)

#-----
# Plot the PlantFrame
#-----
Plot(f0,Color = color_order) # to plot in colors according to the ramification order

#-----
# 2) Diameter of top of segment
#-----
def diam_seg_top(s):
    return TopDiameter(f0,s)

#-----
# 3) Mean diameter of segment
#-----
def diam_seg_mean(s):
    diam_mean=(diam_seg_top(s)+diam_seg_bot(s))/2
    return diam_mean

```

```

-----#
# 4-6) Coordinates in MTG
#-----
def xx(v):
    return Feature(v, "XX")

def yy(v):
    return Feature(v, "YY")

def zz(v):
    return Feature(v, "ZZ")

#-----
# 7) Coordinates of proximal bottom (start) of an axis (relative to plant origin)
#-----
def coord_axis_bot(a):
    return [xx(a),yy(a),zz(a)]

#-----
# 8) Coordinates of distal end of an axis (relative to plant origin)
#-----
def coord_axis_top(a):
    return coord_seg_top(Components(a)[-1])

#-----
# 9) Relative coordinates of proximal bottom (start) of segment (relative to plant origin)
#-----
def coord_seg_bot(s):
    if Rank(s) > 0:
        return RelBottomCoord(f0,s)
    else:
        return coord_axis_bot(Complex(s))

#-----
# 10) Relative coordinates of top of segment (relative to plant origin)
#-----
def coord_seg_top(s):
    return RelTopCoord(f0,s)

#-----
# 11) Length of a segment
#-----
def length_seg(s):
    # if not first segment of axis
    if Rank(s) > 0:
        return Length(f0,s)
    else:
        return dist(coord_seg_bot(s),coord_seg_top(s))
    #NB this equation is the same as Length(f0,s) if Rank>0

#-----
# 12) Length of an axis
#-----
def length_axis(a):
    return sum(length_seg(s) for s in Components(a))

#-----
# 14) Length between end (top) of segment and proximal end (start) of axis
#-----
def length_to_bottom_axis(s):
    if Index(s)==1:
        return length_seg(s)
    else:
        return sum(length_seg(s) for s in Path(Components(Complex(s))[0],s))

#-----
# 15) Length between end (top) of segment and distal end (tip) of axis
#-----
def length_to_top_axis(s):
    return length_axis(Complex(s))-length_to_bottom_axis(s)

```

```

#-----
# 16) Length of axis from segment to previous ramification on same axis
#-----
def length_to_branch(s):
    if len(Sons(Complex(s)))>0:
        if s>Sons(Complex(s))[0]:
            #define vertex of next branch on current axis closest to axis base
            branch=max([branch for branch in Sons(Complex(s)) if branch<s])
            return sum(length_seg(s) for s in Path(branch-1,s))
        else:
            #segment is below the first branch off axis
            return length_to_bottom_axis(s)
    else:
        #there are no ramifications off axis
        return length_to_bottom_axis(s)

#-----
# 17) Diameter of proximal (start) end of axis, at the branch
#-----
def diam_axis_bot(a):
    return diam_seg_bot(Components(a)[0])

#-----
# 18) Diameter of distal end (top) of axis
#-----
def diam_axis_top(a):
    return diam_seg_top(Components(a)[-1])

#-----
# 19) Mean diameter of axis
#-----
def diam_axis_mean(a):
    diam_mean=sum(diam_seg_mean(s)*length_seg(s) for s in Components(a))/length_axis(a)
    return diam_mean

#-----
# 20) Volume of segment
#-----
def volume_seg(s):
    vol=volume_coneFrustum(length_seg(s),diam_seg_top(s),diam_seg_bot(s))
    return vol

#-----
# 21) Volume of axis, where a is Index of an axis
#-----
def volume_axis(a):
    vol=sum(volume_seg(s) for s in Components(a))
    return vol

#-----
# 22) Horizontal length of a segment (projection on to x-y plane)
#-----
def length_hor_seg(s):
    # [0] is x value, [1] is y value and z coordinate is fixed at 0
    # so distance calculated for x-y plane only
    return dist([coord_seg_bot(s)[0],coord_seg_bot(s)[1],0.0],
               [coord_seg_top(s)[0],coord_seg_top(s)[1],0.0])

#-----
# 23) Vertical length of a segment
#-----
def length_vert_seg(s):
    return fabs(coord_seg_top(s)[2]-coord_seg_bot(s)[2])

#-----
# 24) Vertical length of an axis
#-----
def length_vert_axis(a):
    return sum(length_vert_seg(s) for s in Components(a))

```

**Biedenharn Group**  
**Vegetation Root Architecture Analysis for River Bank Stability Applications**  
**Final Report**



```

#-----
# 25) Horizontal length of an axis
#-----
def length_hor_axis(a):
    return sum(length_hor_seg(s) for s in Components(a))

#-----
# 26) Coordinates of the middle of a segment - returns list [x,y,z]
#-----
def coord_seg_mid(s):
    return vplus(coord_seg_bot(s),vdiv(2,vminus(coord_seg_top(s),coord_seg_bot(s)))) 

#-----
# 27) Radial distance from the center of the collar to the middle of a segment
#-----
def dist_radial_seg_mid(s):
    return (coord_seg_mld(s)[0]**2+coord_seg_mid(s)[1]**2)**0.5

#-----
# 28) Radial distance from the center of the collar to the bottom of a segment
#-----
def dist_radial_seg_bot(s):
    return (coord_seg_bot(s)[0]**2+coord_seg_bot(s)[1]**2)**0.5

#-----
# 29) Radial distance from the center of the collar to the top of a segment
#-----
def dist_radial_seg_top(s):
    return (coord_seg_top(s)[0]**2+coord_seg_top(s)[1]**2)**0.5

#-----
# 30) Radial distance from the center of the collar to the bottom of an axis (proximal end)
#-----
def dist_radial_axis_bot(a):
    return (coord_axis_bot(a)[0]**2+coord_axis_bot(a)[1]**2)**0.5

#-----
# 31) Radial distance from the center of the collar to the top of an axis (distal end)
#-----
def dist_radial_axis_top(a):
    return (coord_axis_top(a)[0]**2+coord_axis_top(a)[1]**2)**0.5

#-----
# 32) Horizontal angle of segment on x-y plane between 0 and pi rads
# Values in Angle function have to be floats, hence decimal points included
# Angle function is angle subtended by the two lists of 'directions' and the origin
# The second set of directions is for the segment examined
# 'Direction' refers to the difference in coordinates (x,y,z) between the top and bottom of a segment
#-----
def hor_angle(s):
    direction_seg=[float(coord_seg_top(s)[0]-coord_seg_bot(s)[0]),
                  float(coord_seg_top(s)[1]-coord_seg_bot(s)[1]),0.]
    if direction_seg==[0.,0.,0.]:
        ang=Angle([1.,0.,0.],[float(coord_seg_top(s)[0]-coord_seg_bot(s)[0]),
                           float(coord_seg_top(s)[1]-coord_seg_bot(s)[1]),0.])
        return ang
    else:
        return -999

#-----
# 33) Azimuth of segment direction from 0 to 360 degrees (north is +x direction)
#-----
def azimuth(s):
    ang=hor_angle(s)
    if hor_angle(s)==-999:
        return "none"
    else:
        #if change in y coordinates is positive
        if float(coord_seg_top(s)[1]-coord_seg_bot(s)[1])>0.0:
            return degrees(hor_angle(s))
        else:
            return 360-degrees(hor_angle(s))

```

**Biedenharn Group**  
**Vegetation Root Architecture Analysis for River Bank Stability Applications**  
**Final Report**



```

#-----
# 34) Vertical angle of segment between 0 and 90 with horizontal (horizontal=0)
#-----
def vert_angle(s):
    #if change in coordinates is positive
    direction_seg=[float(coord_seg_top(s)[0]-coord_seg_bot(s)[0]),
                  float(coord_seg_top(s)[1]-coord_seg_bot(s)[1]),
                  float(coord_seg_top(s)[2]-coord_seg_bot(s)[2])]
    if direction_seg!= [0.,0.,0.]: # the segment has zero length so does not have an angle
        return 90.0-degrees(Angle([0.,0.,1.],[float(coord_seg_top(s)[0]-coord_seg_bot(s)[0]),
                                    float(coord_seg_top(s)[1]-coord_seg_bot(s)[1]),
                                    float(coord_seg_top(s)[2]-coord_seg_bot(s)[2]))))
    else:
        return "none"

#-----
# 35) Classification of vertical angle of segment (user defined)
# User can change these criteria
#-----
def vert_angle_class(s):
    # NB fabs is absolute value of float
    ang=vert_angle(s)
    if ang=="none":
        return "none"
    else:
        if fabs(ang)>=60:
            return "vertical"
        elif fabs(ang)>30 and fabs(ang)<60:
            return "oblique"
        else:
            return "horizontal"

#-----
# 35) This function is used to calculate the branching angle
# If the topological father segment has a length of zero,
# it is because there is more than one branch from the same point in the MTG
# If this is the case then the direction of the predecessor segment is used
#-----
def father_haslength(s):
    if length_seg(Father(s))< 0.0001: # ie length is zero
        return father_haslength(Father(s))
    # continuos recall of function until length of predecessor segment is greater than zero
    else:
        return Father(s)

#-----
# 36) Branching angle for an axis vertex
# This is the angle subtended between the direction of the first segment of an axis
# and that of its topological father
# The topological father of a segment is another segment,
# so it is the joining segment on the lower order branch
#-----
def branching_angle(a):
    if Order(a)> 0: # Tap root obviously doesn't have a branching angle
        seg1=Components(a)[0]
        seg2=father_haslength(seg1)
        direction_seg1=[float(coord_seg_top(seg1)[0]-coord_seg_bot(seg1)[0]),
                      float(coord_seg_top(seg1)[1]-coord_seg_bot(seg1)[1]),
                      float(coord_seg_top(seg1)[2]-coord_seg_bot(seg1)[2])]
        direction_seg2=[float(coord_seg_top(seg2)[0]-coord_seg_bot(seg2)[0]),
                      float(coord_seg_top(seg2)[1]-coord_seg_bot(seg2)[1]),
                      float(coord_seg_top(seg2)[2]-coord_seg_bot(seg2)[2])]
        if direction_seg1== [0.,0.,0.]: # the first segment has zero length so does not have an angle
            return "none"
        else:
            return degrees(Angle(direction_seg1,direction_seg2))
    else:
        return "none"

```

**Biedenharn Group**  
**Vegetation Root Architecture Analysis for River Bank Stability Applications**  
**Final Report**



```

#-----
# 37) Branching angle of axis containing the segment (the Complex is the vertex at Scale=1, ie parent)
#-----
def branching_angle_seg(s):
    return branching_angle(Complex(s))

#-----
# List of all vertices in MTG
#-----
vlist=VtxList()

#-----
# Lists of vertices according to criteria
#-----
plants=VtxList(Scale=1)
axes=VtxList(Scale=2)
segments=VtxList(Scale=3)

#-----
# 38) Extract segments crossing a horizontal (potential failure) plane according to criteria
#-----
def segments_hor_plane(depth,rad_min,rad_max,incline,az_min,az_max,len1,len2):
    # If vertex number is less than the second plant (data for first plant only)
    # This can be amended according to requirements, or criterion removed is only one plant
    segments_plane=[s for s in segments if s<plants[1] and
                    max(coord_seg_top(s)[2],coord_seg_bot(s)[2])>-depth and
                    min(coord_seg_top(s)[2],coord_seg_bot(s)[2])<-depth and
                    dist_radial_seg_mid(s)>rad_min and dist_radial_seg_mid(s)<rad_max and
                    vert_angle(s)<incline and az_min<=azimuth(s)<az_max and
                    (length_to_bottom_axis(s)-length_seg(s)/2)>=len1 and
                    length_to_top_axis(s)+length_seg(s)/2>=len2]
    return segments_plane

#-----
# 39) Root area ratio for root segments crossing horizontal plane
#-----
def root_area_ratio_hor_plane(segs,rad_min,rad_max,az_min,az_max):
    if len(segs)>0:
        area_annulus_sector=pi*(rad_max**2-rad_min**2)*(az_max-az_min)/360
        area_roots=sum((pi*(diam_seg_mean(s)/2)**2) for s in segs)
        return area_roots/area_annulus_sector
    else:
        return 0

#-----
# Define lists of axes according to order
# Axes_p1 are axes for the first plant
# ie. all axes with a vertex number less than the vertex number of the second plant
# This can be amended to extract data for any plant (but plant would need to be included in PlantFrame)
# or criterion removed if only one plant in TG
#-----
axes_p1=[axis for axis in axes if axis<plants[1]]
axes_order0=[axis for axis in axes_p1 if Order(axis)==0] # tap root
axes_order1=[axis for axis in axes_p1 if Order(axis)==1]
axes_order2=[axis for axis in axes_p1 if Order(axis)==2]
axes_order3=[axis for axis in axes_p1 if Order(axis)==3]
axes_order4=[axis for axis in axes_p1 if Order(axis)==4]

length_axes_order0=sum(length_axis(a) for a in axes_order0)
length_axes_order1=sum(length_axis(a) for a in axes_order1)
length_axes_order2=sum(length_axis(a) for a in axes_order2)
length_axes_order3=sum(length_axis(a) for a in axes_order3)
length_axes_order4=sum(length_axis(a) for a in axes_order4)

volume_axes_order0=sum(volume_axis(a) for a in axes_order0)
volume_axes_order1=sum(volume_axis(a) for a in axes_order1)
volume_axes_order2=sum(volume_axis(a) for a in axes_order2)
volume_axes_order3=sum(volume_axis(a) for a in axes_order3)
volume_axes_order4=sum(volume_axis(a) for a in axes_order4)

```

**Biedenharn Group**  
**Vegetation Root Architecture Analysis for River Bank Stability Applications**  
**Final Report**



```

#-----
# Write data for ALL segments in first plant
#-----
f1=open("Segments_all.txt","w")
# Write descriptions
f1.write("coord_seg_bot is relative coordinates of bottom (start) of segment (relative to plant origin)+"\n")
f1.write("coord_seg_mid is relative coordinates of the middle of a segment)+"\n")
f1.write("coord_seg_top is relative coordinates of top of segment)+"\n")
f1.write("diam_seg_bot is bottom diameter of segment)+"\n")
f1.write("diam_seg_mean is mean diameter of segment)+"\n")
f1.write("diam_seg_top is top diameter of segment)+"\n")
f1.write("length_seg is length of segment)+"\n")
f1.write("length_to_bottom_axis is length between end (top) of segment and proximal end (start) of axis)+"\n")
f1.write("length_to_top_axis is length between end (top) of segment and distal end (tip) of axis)+"\n")
f1.write("length_to_branch is length of axis from segment to previous ramification on same axis)+"\n")
f1.write("length_hor_seg is horizontal length of a segment (projection on to x-y plane)+"\n")
f1.write("length_vert_seg is vertical length of segment)+"\n")
f1.write("dist_radial_seg_bot is radial distance from the center of the collar to the bottom of a segment)+"\n")
f1.write("dist_radial_seg_mid is radial distance from the center of the collar to the middle of a segment)+"\n")
f1.write("dist_radial_seg_top is radial distance from the center of the collar to the top of a segment)+"\n")
f1.write("volume_seg is volume of segment)+"\n")
f1.write("azimuth is azimuth of segment direction from 0 to 360 degrees (north is +x direction)+"\n")
f1.write("vert_angle is vertical angle of segment between 0 and 90 with horizontal (horizontal=0)+"\n")
f1.write("vert_angle_class is classification of vertical angle of segment (user defined)+"\n")
f1.write("branching_angle_seg is branching angle of the axis containing the segment)+"\n"+'\n')

# Write column titles
f1.write("coord_seg_bot(x)+"'\t'+"coord_seg_bot(y)+"'\t'+"coord_seg_bot(z)+"'\t'+
"coord_seg_mid(x)+"'\t'+"coord_seg_mid(y)+"'\t'+"coord_seg_mid(z)+"'\t'+
"coord_seg_top(x)+"'\t'+"coord_seg_top(y)+"'\t'+"coord_seg_top(z)+"'\t'+
"diam_seg_bot)+"'\t'+"diam_seg_mean)+"'\t'+"diam_seg_top)+"'\t'+"length_seg)+"'\t'+
"length_to_bottom_axis)+"'\t'+"length_to_top_axis)+"'\t'+"length_to_branch)+"'\t'+
"length_hor_seg)+"'\t'+"length_vert_seg)+"'\t'+"dist_radial_seg_bot)+"'\t'+
"dist_radial_seg_mid)+"'\t'+"dist_radial_seg_top)+"'\t'+"volume_seg)+"'\t'+
"azimuth)+"'\t'+"vert_angle)+"'\t'+"vert_angle_class)+"'\t'+
"branching_angle_seg)+"'\n')

for s in segments:
    # If vertex number is less than the second plant
    # This can be amended to extract data from a specific plant in MTG,
    # or criterion removed if only one plant in MTG
    if s<plants[1]:
        f1.write(str(coord_seg_bot(s)[0])+'\'t'+str(coord_seg_bot(s)[1])+'\'t'+
            str(coord_seg_bot(s)[2])+'\'t'+str(coord_seg_mid(s)[0])+'\'t'+
            str(coord_seg_mid(s)[1])+'\'t'+str(coord_seg_mid(s)[2])+'\'t'+
            str(coord_seg_top(s)[0])+'\'t'+str(coord_seg_top(s)[1])+'\'t'+
            str(coord_seg_top(s)[2])+'\'t'+str(diam_seg_bot(s))+'\'t'+
            str(diam_seg_mean(s))+'\'t'+str(diam_seg_top(s))+'\'t'+str(length_seg(s))+'\'t'+
            str(length_to_bottom_axis(s))+'\'t'+str(length_to_top_axis(s))+'\'t'+
            str(length_to_branch(s))+'\'t'+str(length_hor_seg(s))+'\'t'+
            str(length_vert_seg(s))+'\'t'+str(dist_radial_seg_bot(s))+'\'t'+
            str(dist_radial_seg_mid(s))+'\'t'+str(dist_radial_seg_top(s))+'\'t'+
            str(volume_seg(s))+'\'t'+str(azimuth(s))+'\'t'+str(vert_angle(s))+'\'t'+
            str(vert_angle_class(s))+'\'t'+str(branching_angle_seg(s))+'\'n')
    f1.close()

#-----
# Write data for ALL axes (ORDER 0 TO 4) in first plant, according to branch order
#-----
f2=open("Axes_all.txt","w")
# Write descriptions
f2.write("coord_axis_bot is relative coordinates of proximal bottom (start) of axis (relative to plant origin)+"\n")
f2.write("coord_axis_top is relative coordinates of distal end of an axis)+"\n")
f2.write("diam_axis_bot is bottom diameter of axis)+"\n")
f2.write("diam_axis_mean is mean diameter of axis)+"\n")
f2.write("diam_axis_top is diameter of distal end (top) of axis)+"\n")
f2.write("length_axis is length of axis)+"\n")

```

```

f2.write("length_hor_axis is horizontal length of an axis (projection on to x-y plane)+"'\n')
f2.write("length_vert_axis is vertical length of axis)+"'\n')
f2.write("dist_radial_axis_bot is radial distance from the center of the collar to the bottom of an
axis (proximal end)+"'\n')
f2.write("dist_radial_axis_top is radial distance from the center of the collar to the top of an axis
(distal end)+"'\n')
f2.write("volume_axis is volume of axis)+"'\n')
f2.write("branch_angle is branching angle for an axis)+"'\n'+"'\n')

# Write column titles
f2.write("coord_axis_bot(x)+"'\t'+str(coord_axis_bot(y)+"'\t'+str(coord_axis_bot(z)+"'\t'+
"coord_axis_top(x)+"'\t'+str(coord_axis_top(y)+"'\t'+str(coord_axis_top(z)+"'\t'+
"diam_axis_bot)+"'\t'+str(diam_axis_mean)+"'\t'+str(diam_axis_top)+"'\t'+str(length_axis)+"'\t'+
"length_hor_axis)+"'\t'+str(length_vert_axis)+"'\t'+str(dist_radial_axis_bot)+"'\t'+
"dist_radial_axis_top)+"'\t'+str(volume_axis)+"'\t'+str(branching_angle)+"'\n'+"'\n')

# If vertex number is less than the second plant
# This can be amended to extract data from a specific plant in MTG,
# or criterion removed if only one plant in MTG

f2.write("AXES: ORDER 0 (TAP ROOT)+"'\n')
for a in axes_order0:
    f2.write(str(coord_axis_bot(a)[0])+'\t'+str(coord_axis_bot(a)[1])+'\t'+
    str(coord_axis_bot(a)[2])+'\t'+str(coord_axis_top(a)[0])+'\t'+
    str(coord_axis_top(a)[1])+'\t'+str(coord_axis_top(a)[2])+'\t'+
    str(diam_axis_bot(a))+'\t'+str(diam_axis_top(a))+'\t'+str(length_axis(a))+'\t'+
    str(length_hor_axis(a))+'\t'+str(length_vert_axis(a))+'\t'+
    str(dist_radial_axis_bot(a))+'\t'+str(dist_radial_axis_top(a))+'\t'+
    str(volume_axis(a))+'\t'+str(branching_angle(a))+'\n')

f2.write('\'\n')
f2.write("AXES: ORDER 1)+"'\n')
for a in axes_order1:
    f2.write(str(coord_axis_bot(a)[0])+'\t'+str(coord_axis_bot(a)[1])+'\t'+
    str(coord_axis_bot(a)[2])+'\t'+str(coord_axis_top(a)[0])+'\t'+
    str(coord_axis_top(a)[1])+'\t'+str(coord_axis_top(a)[2])+'\t'+
    str(diam_axis_bot(a))+'\t'+str(diam_axis_top(a))+'\t'+str(length_axis(a))+'\t'+
    str(length_hor_axis(a))+'\t'+str(length_vert_axis(a))+'\t'+
    str(dist_radial_axis_bot(a))+'\t'+str(dist_radial_axis_top(a))+'\t'+
    str(volume_axis(a))+'\t'+str(branching_angle(a))+'\n')

f2.write('\'\n')
f2.write("AXES: ORDER 2)+"'\n')
for a in axes_order2:
    f2.write(str(coord_axis_bot(a)[0])+'\t'+str(coord_axis_bot(a)[1])+'\t'+
    str(coord_axis_bot(a)[2])+'\t'+str(coord_axis_top(a)[0])+'\t'+
    str(coord_axis_top(a)[1])+'\t'+str(coord_axis_top(a)[2])+'\t'+
    str(diam_axis_bot(a))+'\t'+str(diam_axis_top(a))+'\t'+str(length_axis(a))+'\t'+
    str(length_hor_axis(a))+'\t'+str(length_vert_axis(a))+'\t'+
    str(dist_radial_axis_bot(a))+'\t'+str(dist_radial_axis_top(a))+'\t'+
    str(volume_axis(a))+'\t'+str(branching_angle(a))+'\n')

f2.write('\'\n')
f2.write("AXES: ORDER 3)+"'\n')
for a in axes_order3:
    f2.write(str(coord_axis_bot(a)[0])+'\t'+str(coord_axis_bot(a)[1])+'\t'+
    str(coord_axis_bot(a)[2])+'\t'+str(coord_axis_top(a)[0])+'\t'+
    str(coord_axis_top(a)[1])+'\t'+str(coord_axis_top(a)[2])+'\t'+
    str(diam_axis_bot(a))+'\t'+str(diam_axis_top(a))+'\t'+str(length_axis(a))+'\t'+
    str(length_hor_axis(a))+'\t'+str(length_vert_axis(a))+'\t'+
    str(dist_radial_axis_bot(a))+'\t'+str(dist_radial_axis_top(a))+'\t'+
    str(volume_axis(a))+'\t'+str(branching_angle(a))+'\n')

f2.write('\'\n')
f2.write("AXES: ORDER 4)+"'\n')
for a in axes_order4:
    f2.write(str(coord_axis_bot(a)[0])+'\t'+str(coord_axis_bot(a)[1])+'\t'+
    str(coord_axis_bot(a)[2])+'\t'+str(coord_axis_top(a)[0])+'\t'+
    str(coord_axis_top(a)[1])+'\t'+str(coord_axis_top(a)[2])+'\t'+
    str(diam_axis_bot(a))+'\t'+str(diam_axis_top(a))+'\t'+str(length_axis(a))+'\t'+
    str(length_hor_axis(a))+'\t'+str(length_vert_axis(a))+'\t'+
    str(dist_radial_axis_bot(a))+'\t'+str(dist_radial_axis_top(a))+'\t'+
    str(volume_axis(a))+'\t'+str(branching_angle(a))+'\n')

f2.write('\'\n')
f2.close()

```

```

-----  

# Horizontal plane analysis (roots crossing plane)  

#-----  

# NB For plants on slopes, must first rotate x,z coordinates,  

# so that x is positive up-slope and z is perpendicular to slope plane  

# Set criteria:  

# depth is vertical distance (positive) from ground level  

# rad_min is radial distance from origin (centre of collar) (user enters min value)  

# rad_max is radial distance from origin (centre of collar) (user enters max value)  

# incline is vertical angle (degrees) with horizontal plane:  

# ie. positive is up and negative is down (user enters max value: neg for roots)  

# az_min is the azimuth on horizontal x-y plane (user enter min value)  

# az_max is the azimuth on horizontal x-y plane (user enter max value)  

# NB rad and az allows creation of an annular sector (annulus cut by circular sector),  

# for analysis of specific areas around root zone  

# len1 is length of axis from middle of segment to bottom (distal end) of exis (user enters min value)  

# len2 is length of axis from middle of segment to top (proximal end) of axis (user enters min value)  

# NB depth, radius, len1 and len2 must be in same units as PlantFrame (eg cm)

-----  

# SET CRITERIA HERE FOR HORIZONTAL PLANE ANALYSIS
-----  

depth=10
rad_min=0
rad_max=30
incline=-30
az_min=0
az_max=360
len1=1
len2=1

-----  

# Write data for subset of segments crossing horizontal (potential failure) plane
-----  

f3=open("Segments_hor_plane.txt","w")
# Write descriptions
f3.write("coord_seg_bot is relative coordinates of bottom (start) of segment (relative to plant
origin)+"'\n')
f3.write("coord_seg_mid is relative coordinates of the middle of a segment "+"'\n')
f3.write("coord_seg_top is relative coordinates of top of segment "+"'\n')
f3.write("diam_seg_bot is bottom diameter of segment "+"'\n')
f3.write("diam_seg_mean is mean diameter of segment "+"'\n')
f3.write("diam_seg_top is top diameter of segment "+"'\n')
f3.write("length_seg is length of segment "+"'\n')
f3.write("length_to_bottom_axis is length between end (top) of segment and proximal end (start) of
axis)+"'\n')
f3.write("length_to_top_axis is length between end (top) of segment and distal end (tip) of axis "+"'\n')
f3.write("length_to_branch is length of axis from segment to previous ramification on same axis "+"'\n')
f3.write("length_hor_seg is horizontal length of a segment (projection on to x-y plane)+"'\n')
f3.write("length_vert_seg is vertical length of segment "+"'\n')
f3.write("dist_radial_seg_bot is radial distance from the center of the collar to the bottom of a
segment)+"'\n')
f3.write("dist_radial_seg_mid is radial distance from the center of the collar to the middle of a
segment)+"'\n')
f3.write("dist_radial_seg_top is radial distance from the center of the collar to the top of a
segment)+"'\n')
f3.write("volume_seg is volume of segment "+"'\n')
f3.write("azimuth is azimuth of segment direction from 0 to 360 degrees (north is +x direction)+"'\n')
f3.write("vert_angle is vertical angle of segment between 0 and 90 with horizontal
(horizontal=0)+"'\n')
f3.write("vert_angle_class is classification of vertical angle of segment (user defined)+"'\n')
f3.write("branching_angle_seg is branching angle of the axis containing the segment)+"'\n'+")'\n')

# Write criteria
f3.write("CRITERIA FOR PLANE ANALYSIS:"+'\n')
f3.write("depth is vertical distance (positive) from ground level)+"'\n')
f3.write("rad_min is minimum radial distance from origin (centre of collar)+"'\n')
f3.write("rad_max is maximum radial distance from origin (centre of collar)+"'\n')
f3.write("incline is maximum vertical angle (degrees) with horizontal plane: positive is up and
negative is down)+"'\n')
f3.write("az_min is the minimum azimuth on horizontal x-y plane)+"'\n')
f3.write("az_max is the azimuth on horizontal x-y plane)+"'\n')
f3.write("len1 is min length of axis from middle of segment to bottom (distal end) of exis)+"'\n')

```

```

f3.write("len2 is length of axis from middle of segment to top (proximal end) of axis)+"\n")
f3.write("NB depth, radius, len1 and len2 must be in same units as PlantFrame (eg cm)+"\n"+'\n')
f3.write("depth"+'\t'+str(depth)+"\n")
f3.write("rad_min"+'\t'+str(rad_min)+"\n")
f3.write("rad_max"+'\t'+str(rad_max)+"\n")
f3.write("incline"+'\t'+str(incline)+"\n")
f3.write("az_min"+'\t'+str(az_min)+"\n")
f3.write("az_max"+'\t'+str(az_max)+"\n")
f3.write("len1"+'\t'+str(len1)+"\n")
f3.write("len2"+'\t'+str(len2)+"\n"+'\n')

# Write column titles
f3.write("coord_seg_bot(x)+"'\t'+"coord_seg_bot(y)+"'\t'+"coord_seg_bot(z)+"'\t'+
"coord_seg_mid(x)+"'\t'+"coord_seg_mid(y)+"'\t'+"coord_seg_mid(z)+"'\t'+
"coord_seg_top(x)+"'\t'+"coord_eg_top(y)+"'\t'+"coord_seg_top(z)+"'\t'+
"diam_seg_bot)+"'\t'+"diam_seg_mean)+"'\t'+"diam_seg_top)+"'\t'+"length_seg)+"'\t'+
"length_to_bottom_axis)+"'\t'+"length_to_top_axis)+"'\t'+"length_to_branch)+"'\t'+
"length_hor_seg)+"'\t'+"length_vert_seg)+"'\t'+"dist_radial_seg_bot)+"'\t'+
"dist_radial_seg_mid)+"'\t'+"dist_radial_seg_top)+"'\t'+"volume_seg)+"'\t'+
"azimuth)+"'\t'+"vert_angle)+"'\t'+"vert_angle_class)+"'\t'+
"branching_angle_seg)+"'\n')

for s in segments_hor_plane(depth,rad_min,rad_max,incline,az_min,az_max,len1,len2):
    f3.write(str(coord_seg_bot(s)[0])+'\t'+str(coord_seg_bot(s)[1])+'\t'+
    str(coord_seg_bot(s)[2])+'\t'+str(coord_seg_mid(s)[0])+'\t'+
    str(coord_seg_mid(s)[1])+'\t'+str(coord_seg_mid(s)[2])+'\t'+
    str(coord_seg_top(s)[0])+'\t'+str(coord_seg_top(s)[1])+'\t'+
    str(coord_seg_top(s)[2])+'\t'+str(diam_seg_bot(s))+'\t'+
    str(diam_seg_mean(s))+'\t'+str(diam_seg_top(s))+'\t'+str(length_seg)+"\t"+
    str(length_to_bottom_axis)+"\t"+str(length_to_top_axis)+"\t"+
    str(length_to_branch(s))+'\t'+str(length_hor_seg(s))+'\t'+
    str(length_vert_seg(s))+'\t'+str(dist_radial_seg_bot(s))+'\t'+
    str(dist_radial_seg_mid(s))+'\t'+str(dist_radial_seg_top(s))+'\t'+
    str(volume_seg(s))+'\t'+str(azimuth(s))+'\t'+str(vert_angle(s))+'\t'+
    str(vert_angle_class(s))+'\t'+str(branching_angle_seg(s))+'\n')

f3.close()

#-----
# Write root area ratios on horizontal plane for increments of depth
#-----
f4=open("Root_area_ratios.txt","w")
# Write criteria
f4.write("CRITERIA FOR PLANE ANALYSIS:"+'\n')
f4.write("depth is vertical distance (positive) from ground level)+"'\n')
f4.write("rad_min is minimum radial distance from origin (centre of collar)+"'\n')
f4.write("rad_max is maximum radial distance from origin (centre of collar)+"'\n')
f4.write("incline is maximum vertical angle (degrees) with horizontal plane: positive is up and negative is down)+"'\n')
f4.write("az_min is the minimum azimuth on horizontal x-y plane)+"'\n')
f4.write("az_max is the azimuth on horizontal x-y plane)+"'\n')
f4.write("len1 is min length of axis from middle of segment to bottom (distal end) of axis)+"'\n')
f4.write("len2 is length of axis from middle of segment to top (proximal end) of axis)+"'\n')
f4.write("NB depth, radius, len1 and len2 must be in same units as PlantFrame (eg cm)+"'\n"+'\n')
f4.write("rad_min"+'\t'+str(rad_min)+"\n")
f4.write("rad_max"+'\t'+str(rad_max)+"\n")
f4.write("incline"+'\t'+str(incline)+"\n")
f4.write("az_min"+'\t'+str(az_min)+"\n")
f4.write("az_max"+'\t'+str(az_max)+"\n")
f4.write("len1"+'\t'+str(len1)+"\n")
f4.write("len2"+'\t'+str(len2)+"\n"+'\n')
f4.write("Depth"'\t'+"RAR)+"\n")

#-----
# SET MAXIMUM DEPTH AND DEPTH INCREMENT HERE
#-----
d_max=200 # cm
d_interval=2 # cm. NB. other criteria set above

for d in range(0,int(d_max),int(d_interval)):
    segs=segments_hor_plane(d,rad_min,rad_max,incline,az_min,az_max,len1,len2)
    root_area=root_area_ratio_hor_plane(segs,rad_min,rad_max,az_min,az_max)
    f4.write(str(d)+"\t"+str(root_area)+"\n")
f4.close()
os.chdir(prev_dir)

```

---

**Biedenharn Group**  
Vegetation Root Architecture Analysis for River Bank Stability Applications  
Final Report

---



This page is intentionally left blank.

### Appendix C: - Visual Basic Code for Discretizing an MTG

```

Option Explicit
'set reference to Microsoft Scripting Runtime

Private Sub Main()
'mtg file (dimensions in cm)
Dim i As Long
Dim y As String
Dim openfilename As Integer
Dim savefilename As Integer
Dim openfilename_original As String
Dim openfilename As String
Dim savefilename As String
Dim mtg
Dim label As String
Dim xx As String
Dim yy As String
Dim zz As String
Dim TopDia As String 'top diameter
Dim xx_father As String
Dim yy_father As String
Dim zz_father As String
Dim Topdia_father As String
Dim dist_segment As Single
Dim xx_new As String
Dim yy_new As String
Dim zz_new As String
Dim Topdia_new As String
Dim label_no As Integer
Dim fs As New FileSystemObject
Close
openfilename = FreeFile()
openfilename_original = OpenSave(0)
Open openfilename_original For Input As openfilename
savefilename = FreeFile()
savefilename = "C:\temp1.txt"
Open savefilename For Output As savefilename
DoEvents
Do Until EOF(openfilename)
  Line Input #openfilename, y
  If Left(Trim(y), 11) = "ENTITY-CODE" Then
    Print #savefilename, y
    Line Input #openfilename, y 'P/
    Print #savefilename, y
    Exit Do
  Else
    Print #savefilename, y
  End If
Loop
'1. Discretise segments on axis of Order 0 (column 2)
label_no = 1
Do Until EOF(openfilename)
  Line Input #openfilename, y
  mtg = Split(y, vbTab)
  'set x in mtg(x) according to axis order (column)
  label = mtg(1) 'Top root is second column
  If label <> "" Then
    xx = mtg(5)
    yy = mtg(6)
    zz = mtg(7)
    TopDia = mtg(8)
    If InStr(1, label, "S") Then 'segment
      dist_segment = ((xx - xx_father) ^ 2 + (yy - yy_father) ^ 2 + _
                     (zz - zz_father) ^ 2) ^ 0.5
      If dist_segment > 1 Then '1 cm
        For i = 0 To Fix(dist_segment / 1) - 1
          Line Input #openfilename, y
          If Left(Trim(y), 11) = "ENTITY-CODE" Then
            Print #savefilename, y
            Line Input #openfilename, y 'P/
            Print #savefilename, y
            Exit Do
          Else
            Print #savefilename, y
          End If
        Next i
      End If
    End If
  End If
  'Print #savefilename, y
  'Line Input #openfilename, y
  'Print #savefilename, y
  'Exit Do
End If
Loop

```

```

xx_new = Round(xx_father + (i + 1) * 
    (xx - xx_father) / (dist_segment / 1), 5)
yy_new = Round(yy_father + (i + 1) * 
    (yy - yy_father) / (dist_segment / 1), 5)
zz_new = Round(zz_father + (i + 1) * 
    (zz - zz_father) / (dist_segment / 1), 5)
TopDia_new = Round(TopDia_father + (i + 1) * (TopDia - TopDia_father) / _ 
    (dist_segment / 1), 5)
If i = 0 And InStr(1, label, "/") > 0 Then
    label = "^/S" & label_no
Else
    label = "^<S" & label_no
End If
'set tabbed data in Print statement according to axis order (column)
Print #savefilenumber, vbTab & label & vbTab & vbTab & vbTab & _ 
    xx_new & vbTab & yy_new & vbTab & zz_new & vbTab & TopDia_new
label_no = label_no + 1
Next i
label = "^<S" & label_no
Print #savefilenumber, vbTab & label & vbTab & vbTab & vbTab & vbTab & xx & _ 
    vbTab & yy & vbTab & zz & vbTab & TopDia
Else
    'short segment so no discretisation but just update label_no if needed
    label = Left(label, 3) & label_no
    'set tabbed data in Print statement according to axis order (column)
    Print #savefilenumber, vbTab & label & vbTab & vbTab & vbTab & xx & _ 
        vbTab & yy & vbTab & zz & vbTab & TopDia
    label_no = label_no + 1
End If
Else 'it is an Apex label
    Print #savefilenumber, y
    label_no = 1
End If
xx_father = xx
yy_father = yy
zz_father = zz
TopDia_father = TopDia
Else
    Print #savefilenumber, y
End If
Loop
Close
openfilenumber = FreeFile()
openfilename = savefilename
Open openfilename For Input As openfilenumber
savefilenumber = FreeFile()
savefilename = "c:\temp2.txt"
Open savefilename For Output As savefilenumber
DoEvents
Do Until EOF(openfilenumber)
    Line Input #openfilenumber, y
    If Left(Trim(y), 11) = "ENTITY-CODE" Then
        Print #savefilenumber, y
        Line Input #openfilenumber, y 'P/
        Print #savefilenumber, y
        Exit Do
    Else
        Print #savefilenumber, y
    End If
End If
Loop
'2. Discretise segments on axis of Order 1 (column 3)
label_no = 1
Do Until EOF(openfilenumber)
    Line Input #openfilenumber, y
    mtg = Split(y, vbTab)
    'set x in mtg(x) according to axis order (column)
    label = mtg(2)
    If label <> "" Then
        xx = mtg(5)
        yy = mtg(6)
        zz = mtg(7)
        TopDia = mtg(8)
        If InStr(1, label, "S") Then 'segment

```

```

dist_segment = ((xx - xx_father) ^ 2 + (yy - yy_father) ^ 2 + _
               (zz - zz_father) ^ 2) ^ 0.5
If dist_segment > 1 Then '1 cm
    For i = 0 To Fix(dist_segment / 1) - 1
        xx_new = Round(xx_father + (i + 1) * (xx - xx_father) / (dist_segment / 1), 5)
        yy_new = Round(yy_father + (i + 1) * (yy - yy_father) / (dist_segment / 1), 5)
        zz_new = Round(zz_father + (i + 1) * (zz - zz_father) / (dist_segment / 1), 5)
        TopDia_new = Round(TopDia_father + (i + 1) * _
                           (TopDia - TopDia_father) / (dist_segment / 1), 5)
        If i = 0 And InStr(1, label, "/") > 0 Then
            label = "^/S" & label_no
        Else
            label = "^<S" & label_no
        End If
        'set tabbed data in Print statement according to axis order (column)
        Print #savefilenumber, vbTab & vbTab & label & vbTab & vbTab & vbTab & _
               xx_new & vbTab & yy_new & vbTab & zz_new & vbTab & TopDia_new
        label_no = label_no + 1
    Next i
    label = "^<S" & label_no
    Print #savefilenumber, vbTab & vbTab & label & vbTab & vbTab & vbTab & xx & _
           vbTab & yy & vbTab & zz & vbTab & TopDia
Else
    'short segment so no discretisation but just update label_no if needed
    label = Left(label, 3) & label_no
    'set tabbed data in Print statement according to axis order (column)
    Print #savefilenumber, vbTab & vbTab & label & vbTab & vbTab & vbTab & xx & _
           vbTab & yy & vbTab & zz & vbTab & TopDia
    label_no = label_no + 1
End If
Else 'it is an Apex label
    Print #savefilenumber, y
    label_no = 1
End If
xx_father = xx
yy_father = yy
zz_father = zz
TopDia_father = TopDia
Else
    Print #savefilenumber, y
End If
End If
Loop
Close
openfilenumber = FreeFile()
openfilename = savefilename
Open openfilename For Input As openfilenumber
savefilenumber = FreeFile()
savefilename = "c:\temp3.txt"
Open savefilename For Output As savefilenumber
DoEvents
Do Until EOF(openfilenumber)
    Line Input #openfilenumber, y
    If Left(Trim(y), 11) = "ENTITY-CODE" Then
        Print #savefilenumber, y
        Line Input #openfilenumber, y 'P/
        Print #savefilenumber, y
        Exit Do
    Else
        Print #savefilenumber, y
    End If
Loop
'3. Discretise segments on axis of Order 2 (column 4)
label_no = 1
Do Until EOF(openfilenumber)
    Line Input #openfilenumber, y
    mtg = Split(y, vbTab)
    'set x in mtg(x) according to axis order (column)
    label = mtg(3)
    If label <> "" Then
        xx = mtg(5)
        yy = mtg(6)
        zz = mtg(7)
        TopDia = mtg(8)
    End If
Loop

```

**Biedenharn Group**  
**Vegetation Root Architecture Analysis for River Bank Stability Applications**  
**Final Report**

---



```
'Display the Open dialog box
.Action = 1 'Show open dialog box
End Select
OpenSave = .FileName
Unload frmCommonBack
End With
Exit Function
ErrorHandler1:
    MsgBox Err.Number
End
End Function
```

